CRANFIELD INSTITUTE OF TECHNOLOGY

COLLEGE OF AERONAUTICS

Ph.D THESIS

Academic Year 1988-9

R. SLADE

Composite Faced Sandwich Construction for Primary Spacecraft Structures.

Supervisor : Prof. D. HOWE

September 1989

SUMMARY

This study investigated the application of fibre reinforced composite materials to spacecraft sandwich structures. In particular, aspects of the manufacture, analysis and design optimisation of components fabricated using the co-cure process were studied. The manufacturing process was developed to ultimately enable a full size thrust tube structure to be built using a single step cure, the design of which was verified by a modal survey test. Techniques for the analysis of stiffness, strength, vibration frequencies and local instability were established and found to correlate well with tests on co-cured sandwich specimens. The current wrinkling theory for composite faced sandwich was extended to the more general case to allow facesheet constitutive matrix coupling and multiaxial loding to be accomodated. The analytical methods were incorporated within simple optimisation schemes, amenable to employment at the preliminary design stage, to allow alternative feasible designs for panel and thrust tube structures to be generated. These illustrated the benefits of the use of composite materials and the co-cure manufacturing technique for spacecraft sandwich components.

CONTENTS

FIGURES

Chapter 9

Appendix A

NOTATION

A_{ij}	Elements of Membrane Constitutive Matrix
A_s	Effective Shear Area
a	Panel Length
B_{ij}	Elements of Coupling Constitutive Matrix
BI	Buckling Interaction Index
b	Panel Width
b_{ij}	Elements of Layer Reduced Stiffness Matrix
C_{ij}	Elements of Wrinkling Equation Stiffness Matrix
C_f	Spacecraft Lateral Frequency Coefficient
D_{ij}	Elements of Flexural Constitutive Matrix
d_c	Honeycomb Cell Size
E_1	Longitudinal (Fibre Direction) Young's Modulus
E_2	Transverse Young's Modulus
E_c	Core Through-Thickness Modulus
E_f	Effective Facesheet Modulus
F_i	First Order Strength Tensors
F_{ij}	Second Order Strength Tensors
F_{ijk}	Third Order Strength Tensors
f	Natural Frequency (Hz)
f_D	Design Frequency (Hz)
G_{12}	Shear Modulus
G_{xz}	Core Longitudinal Shear Modulus
G_{yz}	Core Transverse Shear Modulus
g_j	Constraint Functions
h	Core Depth
h_k	Position of k^{th} Layer relative to mid-plane

h_1	Position of Upper Facesheet relative to sandwich mid-plane
h_2	Position of Lower Facesheet relative to sandwich mid-plane
I	Second Moment of Area
I_i	Moment of Inertia at i^{th} node
K_{ij}	Elements of Vibration Stiffness Matrix
K_A	Tolerance Limit Factor for 'A' Design Allowables
K_{x1}, K_{x2}	Longitudinal Facesheet Stress Resultant Ratios
K_{xy1}, K_{xy2}	Shear Facesheet Stress Resultant Ratios
k_i	Knockdown Factors for Panel Optimisation
k_T	Constant in equation (8.20)
k_x	Longitudinal Curvature
k_y	Transverse Curvature
k_{xy}	Twisting Curvature
L	Thrust Tube Element Length
L	Cylinder Length
L_e	Effective cylinder length of cone
l*	Critical Wrinkling Half-Wavelength
M_i	Lumped Mass at i^{th} node
M_{ij}	Elements of Vibration Mass Matrix
M_x	Longitudinal Bending Moment Resultant
M_y	Transverse Bending Moment Resultant
M_{xy}	Twisting Moment Resultant
m	Number of Half-Wavelengths in x-direction
m*	Critical Number of Half-Wavelengths in x-direction
N_x	Longitudinal Stress Resultant
Nx_d	Critical Dimpling Compression Stress Resultant (single f/s)
Nx_{wr}	Critical Wrinkling Compression Stress Resultant
N_y	Transverse Stress Resultant
N_{xy}	Shear Stress Resultant
N_I	Principal Stress Resultant

n	Number of Half-Wavelengths in y-direction
n	Sample Size
P_{ij}	Elements of Wrinkling Equation Load Matrix
Q_{ij}	Elements of Layer Stress-Strain Relation Matrix
Q_x	Core Shear Stress Resultant on xz-plane
Q_y	Core Shear Stress Resultant on yz-plane
Q_1	G_{xz}/E_c
Q_2	G_{yz}/E_c
R	Radius of Curvature
R_1	Small radius of truncated cone
R_2	Large radius of truncated cone
R_e	Effective cylinder radius for cone
S	Shear Strength
S	Population Standard Deviation
S_{xz}	Core Longitudinal Shear Rigidity
S_{yz}	Core Transverse Shear Rigidity
s	Sample Standard Deviation
TW	Tsai-Wu Index
t	Facesheet Thickness
t_{ply}	Single Ply Thickness
T_{ij}	Elements of Layer Angle Transformation Matrix
u	Displacement in x-direction
u_f	Facesheet x-direction displacement
v	Displacement in y-direction
v_f	Facesheet y-direction displacement

w	Displacement in z-direction
w_f	Facesheet z-direction displacement
X	Population Mean
XA	'A' Design Allowable
X_T	Longitudinal Tension Strength
X_C	Longitudinal Compression Strength
x	Longitudinal Coordinate
x	General Design Variable
Y_T	Transverse Tension Strength
Y_C	Transverse Compression Strength
y	Transverse coordinate
z	Out-of-Plane coordinate

$\alpha_{\frac{1}{2}}$	Cone Semi-Angle
α	$m\pi/a$
β_x	Slope of Normal to Mid-Plane in x-direction
β_y	Slope of Normal to Mid-Plane in y-direction
β_θ	Slope of Normal to Mid-Plane in θ-direction
β	$n\pi/b$
γ_{xy}	In-plane Shear Strain
γ_{xz}	Core Shear Strain on xz-plane
γ_{yz}	Core Shear Strain on yz-plane

ϵ_x	Longitudinal Strain
ϵ_y	Transverse Strain
ϵ_z	Core Through-Thickness Direct Strain
ζ	Bending/Shear stiffness ratio (see eq.(8.1))

θ	Layer Angle relative to x-direction
θ	Circumferential coordinate
λ , γ	Eigenvalue
μ	$m\pi R/L$
ρ	Radius of Gyration
ρ	Uniform Mass per Unit Area
ρ_A	Adhesive Mass per Unit Area
ρ_c	Core density
σ_1	Longitudinal (Fibre Direction) Layer Stress
σ_2	Transverse Layer Stress
σ_d	Critical Facesheet Dimpling Stress
σ_{z0}	Core Through-Thickness Direct Stress at mid-plane
τ_{12}	Layer Shear Stress
τ_{xz}	Core Shear Stress on xz-plane
τ_{yz}	Core Shear Stress on yz-plane
ν_{12}	Major Poissons Ratio
ν_{21}	Minor Poissons Ratio
ϕ	Skew Angle of Wrinkle Nodal Lines
χ	Defined in equation (B.9), Appendix B

CHAPTER 1 INTRODUCTION

In the past ten years, continuous fibre reinforced composite materials have emerged as contenders to replace traditionally used aluminium, titanium, magnesium and beryllium alloys in spacecraft primary structures. Although initially limited to secondary structure in which low thermal expansion, R/F transparency and thermal isolating properties were exploited, the improvements in modern composite prepreg systems, their properties and manufacturing techniques has seen their potential high stiffness and strength to weight ratios realised in practical primary structures. The driving force behind this movement towards composites is the overriding requirement to produce lighter structures and so enhance spacecraft payload and/or lifetime. The importance attached to the weight of spacecraft and launcher structures is more so than any other vehicle. This can be appreciated by the following sums of money put on a 1 kg weight saving in flight vehicle structures, from reference [1] :

Light Aircraft	£30 / kg
Transport Aircraft	£100 / kg
Fighter Aircraft	£250 / kg
Spacecraft	£10 000 / kg

Larger sums than this are reputed to be acceptable to certain spacecraft prime contractors in an effort to save structure mass. Aerospatiale for example, are prepared to spend in the region of $32K to save a kilogramme in the structure of a geostationary spacecraft[2], and Hughes are prepared to spend $10K - $40K per pound of weight saved ($22K - $88K per kg) depending on the location in the spacecraft and its mission[3]. The greatest premium is on interplanetary missions where some programmmes are reputed to be prepared to spend $50K per pound ($110K per kg) of structure weight saved[4].

A large proportion of most spacecraft structures is composed of honeycomb sandwich constuction as panels and shell components. These are characterised by very thin core-stabilised facesheets and are consequently amenable for the application of thin composite prepregs. The research

presented here concentrated on the investigation of the efficient application of composites to this type of construction. The basic aims of the research were as follows :

(1) To develop co-curing manufacturing techniques for typical spacecraft sandwich structure components.

The term 'co-cure' refers to a method in which the composite facesheets of a sandwich component are simultaneously cured and bonded to the honeycomb core. The conventional method is to pre-cure the facesheets and then bond these to the core in a secondary operation. The co-cure method has advantages in terms of reduced cost, and possible weight savings because the facesheet lay-up is no longer constrained to be 'balanced' about its own mid-plane to prevent curing distortion. The aim was to develop the practicalities of the method sufficiently to produce representative complex spacecraft structure components.

(2) To evaluate the structural performance of co-cured sandwich by testing.

Co-cured sandwich must be cured at a lower pressure than pre-cured facesheets and this leads to an increased void content and reduced performance. By testing co-cured sandwich samples, the aim was to assess the degradation of strength and stiffness and compare with predictions using laminate stiffness and failure theories.

(3) To extend current analytical techniques for the prediction of composite faced sandwich performance to include facesheet coupling effects.

Currently used methods for the prediction of sandwich panel local instability behaviour (wrinkling and dimpling) assume special orthotropy for the facesheets. The aim was to extend these to more general lay-ups which exhibit coupling (such as co-cured facesheets), evaluate the effect on the critical instability loads and validate the predictions by testing.

(4) To incorporate analytical techniques for the prediction of strength, stiffness, general and local instability of sandwich components into schemes for preliminary design optimisation.

Because of the additional variables open to the designer of composite structures, namely fibre/matrix system, fibre angles and stacking sequence, there is a need to quickly assess all the alternatives and produce optimum 'tailored' designs. The aim was to develop methods for the initial design optimisation of sandwich panel and thrust tube components. The emphasis was on optimisation from the preliminary stages of design, to enable material trade-offs to be performed for example, and to increase its cost effectiveness. The intention was also to use the optimisation techniques to compare the relative merits of co-cured and pre-cured composite faced sandwich in different components.

As a background to this research, work carried out on the design study of a Molniya orbit mobile communications satellite, T-Sat[5], provided a useful focus for the design optimisation of realistic spacecraft structure sandwich components. This study was sponsored by the Science and Engineering Research Council. The spacecraft and its structure are described in Appendix A .

CHAPTER 2 SPACECRAFT STRUCTURES

2.1 STRUCTURE CONFIGURATIONS

The structural configurations of spacecraft are determined largely by the requirements of the missison and by constraints imposed by the launcher(s). The mission type (communications, earth observation or interplanetary) and the method of spacecraft stabilisation (3-axis or spin-stabilised) primarily determines the overall shape of the spacecraft and positions of payload, service systems and sensors. The launch vehicle will imposes constraints on the spacecraft mass and volume.

Several structural configuration solutions may be possible within the outline of the general spacecraft configuration. The basic function of the structure is to provide a stiff mounting platform for the payload and systems, and to provide a path for the inertia and vibration loads down to the launcher interface. This interface is usually a circular separation frame and has a large impact on the structure configuration since all loads must pass through it. The three most commonly adopted spacecraft structure types are :

1. Thrust Tube & Platforms
2. Frame Assembly
3. Panel Assembly

2.1.1 Thrust Tube & Platform Structures

This category of structure is the most common. Numerous examples include all INTELSAT series satellites, ECS, Olympus and Giotto. Sometimes known as a 'cakestand' arrangement, the primary structural member is a central thrust tube, which interfaces at its lower edge to the launcher, and supports several platforms up its length. Fig. 2.1a illustrates the concept in the MARECS maritime communications satellite. The platforms are either rectangular or circular depending on whether the spacecraft is 3-axis or spin-stabilised. Equipment loads are transferred from the sidewalls, for 3-

axis stabilised spacecraft, to the central thrust tube via the platforms and shear webs and/or struts. Equipment in spin-stabilised spacecraft is generally concentrated on the platforms.

The advantage of this type of structural configuration is that the launch loads are efficiently diffused through the thrust tube down to the circular launcher interface. The thrust tube also acts as the primary stiffening element for the structure and provides a convenient mounting location for a solid boost motor or liquid propellant tanks. Disadvantages are that the central tube is a large, complex component to manufacture, and that it disturbs the internal volume of the satellite and the layout of harnesses and pipes.

2.1.2 Frame Assembly Structures

In this type of structure, the primary support is a framework or space-frame to which secondary structure or modular equipment boxes are fixed. This category covers a range of concepts from those which adopt a space-frame as an alternative to a shell type thrust tube, such as Viking shown in fig. 2.1b, to full trellis structures such as used for EURECA. The latter is driven by its unusual launcher interface across the shuttle payload bay. In some cases, the Galileo spacecraft for example, a hybrid type of structural configuration is employed in which the lower part of the primary structure is a space frame of struts and the upper part is built round a closed thrust tube.

This type of structure will in general be more inefficient than a shell central structure because of the number of joints and the introduction of load at a few points. The main advantage of this arrangement is that it is highly suited to a modular design. This makes it particularly amenable to adaptable spacecraft bus concepts since it can be rapidly reconfigured simply by interchanging module boxes on the frame.

2.1.3 Panel Assenbly Structures

Panel assembly structures employ an internal arrangement of web and keel flat panels to transfer the primary loads from the equipment sidewalls to the launcher. Examples of this 'egg-crate' structure concept are to be found in the TDF1/TV-SAT Franco-German broadcasting satellite shown in fig. 2.1c, and the DSCS III U.S. military communications satellite series. This type of structure has been proposed for the future 2000 kg class Japanese communications spacecraft.

A panel assembly structure can be advantageous if the spacecraft incorporates a liquid propellant motor, because large tanks can be incorporated in the available volume between internal webs. These can also be arranged to form stiff compartments to which modular sidewall equipment can be attached. The structure is highly redundant with multiple load paths, but interface with the launcher or transfer stage will be at only a few hard points.

2.2 COMPOSITE APPLICATIONS TO SPACECRAFT STRUCTURES

Composite materials (mainly carbon fibre epoxies) have been proposed and adopted for use in primary spacecraft and launcher structures in recent years. In launchers, applications have been mainly in the upper stages where the greatest returns in increased payload capability are to be made. Notable examples are the 2nd/3rd interstage on the Ariane launcher (Fokker) and SPELDA payload support structure (B.Ae). Carbon composites are also proposed for the Ariane V vehicle.

Probably the first spacecraft to employ composites in the primary structure was the UK X3 chassis (1971). This was composed of an assembly of flat carbon-epoxy faced sandwich panels. However, limitations on available thicknesses of prepreg at the time prevented the structure making any mass savings over an equivalent aluminium alloy one.

In the following sections composite applications in a number of spacecraft structure projects and design studies are reviewed. These include work carried out in Europe, the U.S & Japan, and cover all structural configuration types. In most instances the greatest benefits from the use of composites in terms of mass savings are to be found in thrust tube and strut components, since these can best exploit the unidirectional properties. The application of composites to flat sandwich panels such as platforms, sidewalls and webs has been less widespread as a result of minimum material thicknesses and poor conductivity. The application of composites in frames, brackets and connection elements has also been fairly restricted even though these can make up over a quarter of a typical spacecraft structure mass. This is as a result of poor interlaminar strength and manufacturing difficulties with thick section components.

2.2.1 ACESM (Rockwell International)

Rockwell International[6] performed a development study in 1983 for the U.S.A.F Flight Dynamics Lab. to investigate the feasibilty of carbon-epoxy application to satellite primary structure. The Advanced Composites Equipment Support Module (ACESM) provided the focus for the study, which was based on the NAVSTAR spacecraft for the 18 satellite Global Postioning System.

Work performed included material testing of T-300, PAN 50 & P75S fibres combined with Fiberite 934 epoxy, detail component testing and fabrication of a full scale structure. Over 80% of the original aluminium structure was redesigned in composites, making a weight saving of 19%.

The thrust cone and cylinder were of monocoque construction incorporating 0.127 mm thick P75S/934 prepreg. All attachment rings were machined aluminium alloy which were bonded on. Bulkheads, equipment platforms, shear and access panels were of composite faced aluminium honeycomb. The honeycomb density being predominantly 2.3lb/cuft, increasing to 6.1lb/cuft in load concentration areas, and having thicknesses between 6mm and 25mm. Lay-ups for the facesheets were of the pseudo-isotropic type [0/+60/-60] or

[0/+45/-45/90], and of either PAN50/934 or P75S/934 prepregs of 0.064mm ply thickness. A number of solid laminated components were also incorporated into the design as replacements for alumimium longerons. These were of hybrid T-300/934 UD tape and woven fabric.

A modal survey test carried out on the complete structure showed natural frequencies 30-50% higher than the aluminium baseline. Damping was found to be about the same since the main mechanism for loss was through joints. The acoustic response was also found to be comparable with the aluminium structure.

2.2.2 DSCS III (General Electric)

The DSCS III (Defense Satellite Communication System), shown in fig. 2.2, is a geostationary 3-axis stabilised military communications satellite. The structure is a six bay 'egg-crate' arrangement made up of honeycomb sandwich panels and bulkheads. In its original form, these were of 0.15 mm 7075 aluminium alloy on a 2.0lb/cuft core. The north and south equipment (radiator) panels were of integrally machined magnesium alloy. Only struts, of which there were a total of 70 in the structure including 8 for the spacecraft adaptor truss, used composite materials. HM-S fibres in a CE339 120°C curing epoxy were used after a trade off evaluation with T-300 high strength and GY-70 ultra high modulus fibres.

In 1978 General Electric conducted a study programme for the USAF Flight Dynamics Lab. to assess the feasability of composites application to this structure[7]. Carbon-epoxy was adopted as a replacement for the facesheets of the honeycomb panels, and in built-up laminated form for a number of longerons and the south equipment panels. The magnesium north equipment panel was retained because of higher heat dissipation requirements. The composite structure showed a 19% (30kg) saving over the metallic baseline.

To assess manufacturing techniques representative sandwich shear panels were fabricated. These consisted of a single ply of woven GY-70/CE339 (0.127 mm) at 45° bonded with FM73 film adhesive to an aluminium honeycomb

core. A 2.0lb/cuft core was used in the centre of the panel and 4.0lb/cuft around the edge. The panels were manufactured using a one step operation in which doublers (T-300 fabric), facesheets, film adhesive and core were co-cured at 120°C.

The overall conclusions from this study were that composite spacecraft structures were a practical proposition, saving 15-20% in structure mass for acceptable cost. The low conductivity of carbon-epoxies was considered only to limit their usage in high heat dissipation surfaces. Electrical requirements were satisfied with metallization only necessary in some local areas.

2.2.3 INTELSAT V A (Ford, Aerospatiale)

The third block of INTELSAT V communications spacecraft, designated V-A, incorporated an enhanced payload which was in some part due to a saving of 9 kg made by replacing the aluminium corrugated thrust tube with one of carbon-epoxy faced honeycomb construction[8]. This thrust tube was developed by Aerospatiale. The basic structure is shown in fig. 2.3.

Monocoque, integrally stiffened and honeycomb shell design concepts were all evaluated. The solution adopted was a honeycomb shell construction with unsymmetric facesheets. The external facesheets were of hybrid unidirectional high modulus and T-300 prepreg (a total thickness of 0.6 mm in the cylindrical section and 0.7 mm in the conical section). The internal facesheets were 0.3 mm thick which stabilised the 2.0lb/cuft aluminium honeycomb core which was 5 mm thick in the cylindrical and 7 mm in the conical section. The shells were " panned" at ring interfaces to ensure load transfer to both the facesheets. The lower Marman clamp ring and the apogee motor ring were retained as aluminium alloy because of the complexity of manufacturing in composites. The antenna deck ring and internal fuel tank however, were made of high modulus carbon-epoxy.

The conical and cylindrical sections were fabricated separately and subsequently bonded together with the apogee motor ring. The manufacturing

sequence involved curing the external skin in one piece and the outer skin in four segments, and then bonding the honeycomb in a further cure cycle. The inner skin segments were spliced together with composite overlaps. Composite and metallic fittings were cold bonded to the completed tube.

Static testing of the composite thrust tube showed it to be laterally stiffer than its aluminium counterpart. Modal survey testing, however, showed only a slight shift in the spacecraft first lateral frequency. This was intentional since part of the design concept was to enable full interchangeability with the original tube to have minimum impact on the spacecraft behaviour.

2.2.4 Shuttle Pallet Satellite (MBB)

The Shuttle Pallet Satellite (SPAS) is a modular truss type structure composed of carbon fibre reinforced tubular struts[9]. This type of structure formed the primary support structure for the European Bridge Assembly on the Spacelab mission D1, and provides the backbone for EURECA (European Retrievable Carrier).

Composite materials provided an ideal design solution because of the unidirectional nature of the strut loading and low thermal expansion requirements. High modulus Toray 40 fibres in an Araldite 209/HT 972 epoxy resin were selected as the composite material. The strut nodes were cold bonded titanium, preferred over aluminium because of its lower thermal expansion.

2.2.5 DFS Kopernikus (MBB/Erno)

In 1978 MBB/Erno completed the development of an alternative composite corrugated thrust cone based on the European Orbital Test Satellite (OTS) to demonstrate its superiority over the metallic design. Subsequently the German communications satellite DFS Kopernikus[10] was designed from the outset with a composite central thrust structure.

A preparatory development programme defined a corrugated construction with external frame belts utilising high modulus carbon fibres in an epoxy matrix. Although a honeycomb construction was recognised as having comparable structural efficiency, the corrugated construction was considered to be better from the point of view of inspection and the provision of hard points for connections via rivets. The thrust tube was built up from three segments which had a lay-up of the form: $[+32.5/0_i/-32.5]$ where i = 0, 1 and 3 at different sections along the length. The prepreg thickness was 0.10 mm. Two platform rings of triangular section and a top U-section ring for the antenna platform were also made of carbon-epoxy. Only the launch vehicle attachment ring was aluminium alloy to meet separation system requirements. The rings were cold bonded and rivetted to the cylinder.

The assembled cylinder weighed 15 kg, of which 4.3 kg was attributable to the LVA ring. This cylinder was statically tested and a number of premature failures were detected in the region of shear loaded rivets. These were subsequently strengthened with co-cured doublers in later cylinders. the material was also switched from high modulus to high strength fibres because of susceptibility to handling damage. The later cylinders successfully passed static, dynamic and acoustic qualification tests.

2.2.6 SKYNET IV (B Ae)

The Skynet IV U.K. military communications satellite, shown in fig. 2.4, incorporated a carbon composite thrust cone[11]. This was of sandwich construction utilising unidirectional HM/Code 87 prepreg in the facesheets with a lay-up of [+10/-10/+50/-50/-10/+10]. The inner and outer facesheets were cured separately in three 120° segments each, and then bonded to an aluminium honeycomb core. The three sandwich shell segments were finally bonded together with longitudinal butt straps. The almost balanced lay-up of the facesheets enabled them to be cured separately without excessive distortion. Circumferential reinforcing plies in the region of attachment rings were incorporated by co-curing them to the inner facesheet, and bonding in a secondary operation to the outer facesheet (to avoid machining

a taper in the tooling). The attachment rings for the payload module, solid boost motor, service module and mating with the launcher were all aluminium alloy. These were bonded, or bonded and bolted through inserts to the cone.

2.2.7 ARABSAT (Aerospatiale)

The contract for the production of three ARABSAT communications satellites for the League of Arab States was awarded to Aerospatiale in 1981. The spacecraft were 3-axis stabilised with a launch weight of about 1200 kg.

The spaceraft structure incorporated a carbon-epoxy sandwich thrust tube[12] and a number of other composite panels in the service and payload modules. The thrust tube was based on the experience gained from the Intelsat V central tube. The facesheets, this time identical, were a hybrid mixture of woven high modulus G837 at 45° and unidirectional HM/V108 epoxy at 0°. The number of 0° UD plies was increased from one to three down the length of the cylinder to match the increased loading. The facesheets themselves were balanced and so fabricated separately, the inner on a male mould and the outer on a female mould. The honeycomb was bonded to the outer facesheet, and the inner facesheet previously cut into two segments, was added with two splices.

In 1986 Aerospatiale performed their own study to investigate a co-curing fabrication technique for sandwich thrust tubes. The ARABSAT central tube was used as the reference for this study. In this scheme, both facesheets and the facesheet to core adhesive bonds were cured simultaneously in a single operation. Use of a co-cure technique enabled the facesheet lay-up to be changed to one incorporating only UD high modulus prepreg. This was unbalanced about its midplane since it was only necessary to achieve a balanced sandwich. The resin was also switched to the lower flow 914 epoxy system. Curing was carried out on a female mould. The main drive behind the investigation of this method was to reduce manufacturing cost. This goal was achieved because of a reduction in the number of tools and processing operations.

2.2.8 Olympus (Fokker)

A recent design study was carried out by Fokker under an ESA contract to investigate a composite replacement for the propulsion module part of the Olympus satellite (L-Sat) central cylinder[13]. This is currently a ring and corrugation aluminium alloy design.

Initially a trade off was carried out to select the best method of construction. Externally blade stiffened, corrugated and sandwich constructions were all evaluated. Of these, the corrugated option resulted in the lowest bare mass for the cylinder, but once reinforcements at the load introduction rings were taken into consideration, the sandwich gave the lowest overall mass. The selected design had a facesheet lay-up of [+25/-25/0/-25/+25] built up from 0.05mm T-300/Code 92 prepreg on an 8mm 2.0-3/16"-0.0007" core. The aluminium end frames were bonded on because bolted connections were found to incur a 2 kg penalty. The facesheets were reinforced by 0° and +45/-45 plies to a thickness of 0.40mm in the vicinity of the end frames.

A cylinder was manufactured in a two step process. Firstly two inner and two outer facesheets were cured on a half cylinder male mould. The faces were then bonded to the core on the same mould to form two half shells which were subsequently bonded together with splices. The full cylinder was statically tested and failed at 1.85 times ultimate load level. Failure was at the tension side of the cylinder at the end ring bonded joint. The study concluded that a mass saving of 41% could be achieved for only a modest cost increase of 6% (based on a run of 10 spacecraft).

2.2.9 CS-3 (Mitsubishi)

The Japanese CS-3 spin-stablised communications satellite made widespread use of carbon-epoxy composites[14]. The structure, shown in fig. 2.6, had a weight of only 53 kg (out of a total launch weight of 1988 kg).

The basic configuration consisted of upper and lower circular equipment panels supported by a central thrust tube and a number of struts. The thrust tube attachment rings, brackets, struts and thruster support panels incorporate composites. Only the equipment panels and launcher interface ring were of aluminium alloy because of heat conduction requirements. The thrust tube was a monocoque utilising a lay-up incorporating +20°/-20° and +70°/-70° orientated plies, these directions being selected to optimise the buckling strength. The number of plies was reduced above the apogee boost motor. The boost motor support ring was of triangular section and used a polyimide rather then epoxy matrix because of the motor soak back temperatures. The weight of the thrust tube was 17.5 kg - an estimated 30% saving over an aluminium one. Composite brackets were also estimated to save 30% over alloy counterparts.

This structure successfully passed static and vibration tests to ultimate level.

2.2.10 Future Japanese GEO Satellite (Toshiba, Kawasaki)

A future 3-axis, 580 kg (on-orbit) Japanese communications satellite was studied as an application for composite materials[15]. The structural configuration, shown in fig. 2.7, consisted of a centre-body, equipment panels and fuel tank support structure. The centre-body was a permanently bonded assembly made up of a central thrust tube, three deck panels and shear webs. All of this assembly was constructed of carbon-epoxy faced sandwich ranging in thickness from 5mm for the upper central tube to 15mm for the upper deck panel. The fuel tank support structure also utilised carbon-epoxy face sandwich components and struts. The removable equipment panels were aluminium faced sandwich because of thermal and electrical conductivity requirements.

High modulus (Toray M40) unidirectional prepreg was used for most of the composite components along with some high strength (Toray T-300) unidirectional and woven prepreg. A full scale structure was built and

successfully proof tested. A modal survey test demonstrated the structure met stiffness requirements. The total weight of the structure was 54 kg.

2.2.11 T-SAT Study

This spacecraft formed the focus of a design study into a mobile communications and technology demonstrator platform for a Molniya type orbit[5] (see Appendix A). As part of this study, a trade off comparison between aluminium alloy and high modulus carbon-epoxy for the primary structure was performed. This was a two-part thrust tube and platfrom structure with stiffening struts. The lower, conical part of the thrust tube formed an Orbit Transfer Module (O.T.M) housing a solid boost motor which was separated once on-orbit, and the upper part was cylindrical. A co-cured composite sandwich construction was specified for both parts of the thrust tube, saving an estimated total of 10.1 kg, or 22%, over an aluminium alloy faced sandwich design. The cylinder had $[0_2/\pm45]$ HM-S/CYCOM 985 facesheets and the OTM $[0_4/\pm20_2]$ HM-S/CYCOM 985 facesheets, both on predominantly 10 mm thick 2.0lb/cu.ft honeycomb cores. The facesheets were reinforced and a denser honeycomb was employed at attachment frame positions.

Savings of 31 % were also identified for the strut components, although in terms of actual weight these were less spectacular because of their small proportion of the total. Modest savings were apparent in some of the other sandwich components. In some instances these could have been more significant with other carbon fibre prepregs. Only a single material system: HM-S/CYCOM 985 was considered in order to minimise the development testing effort, and this material was the optimum solution for the thrust tube where the weight savings were greatest. Composites were precluded from the major equipment mounting and radiator panels because of poor thermal conductivity. Overall, composites were employed in 36 % of the structure, saving an estimated 17 kg.

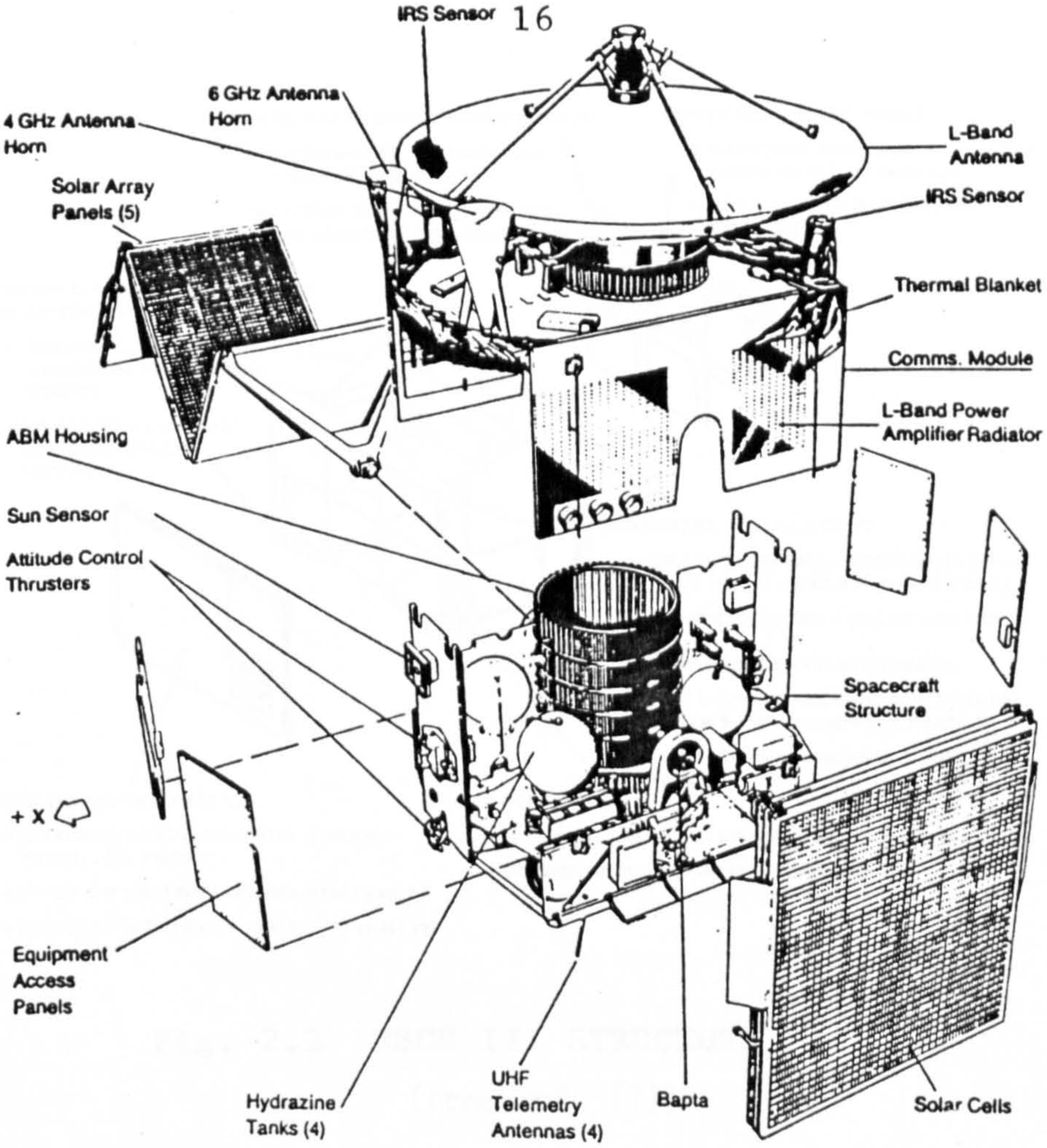

(a) Thrust tube and platforms (MARECS)

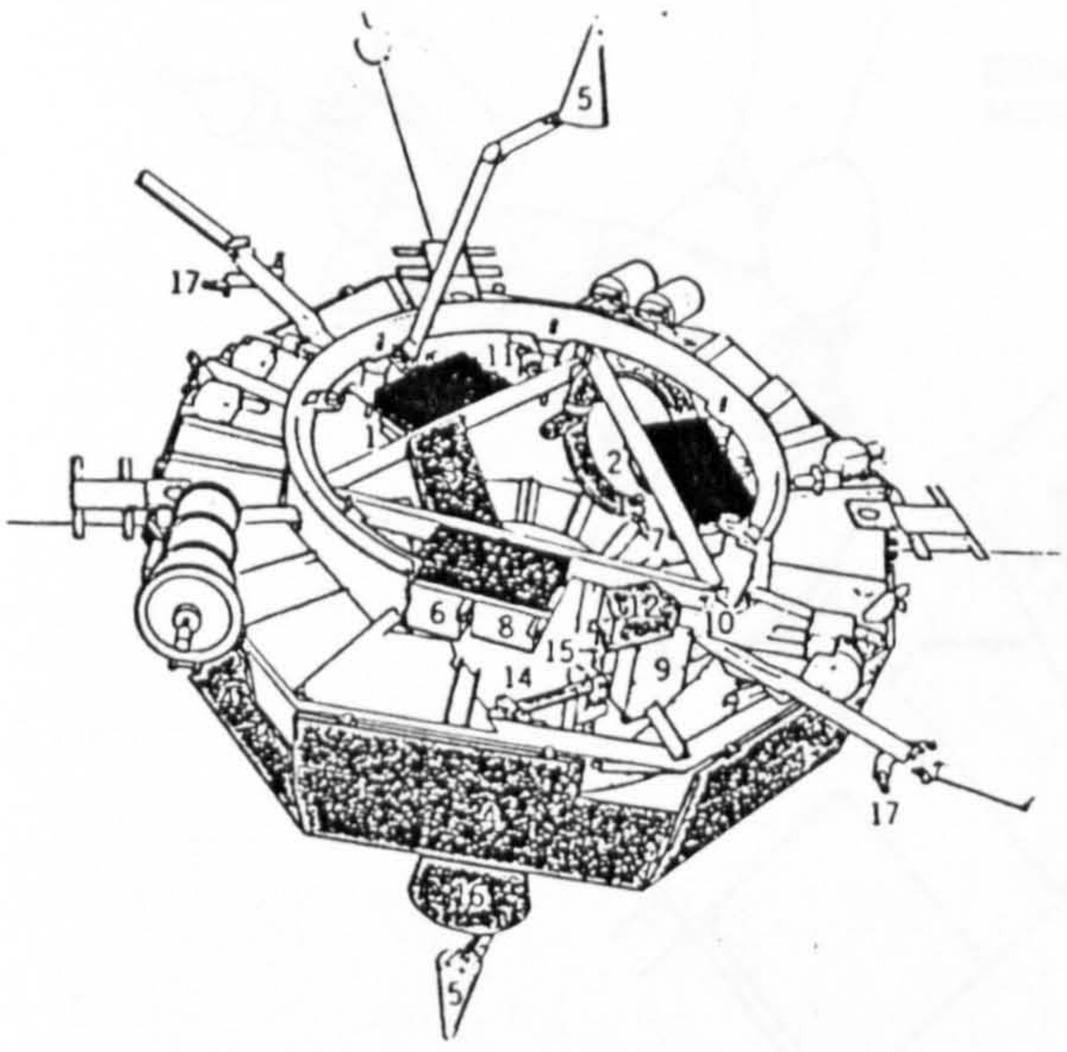

(b) Frame assembly (VIKING)

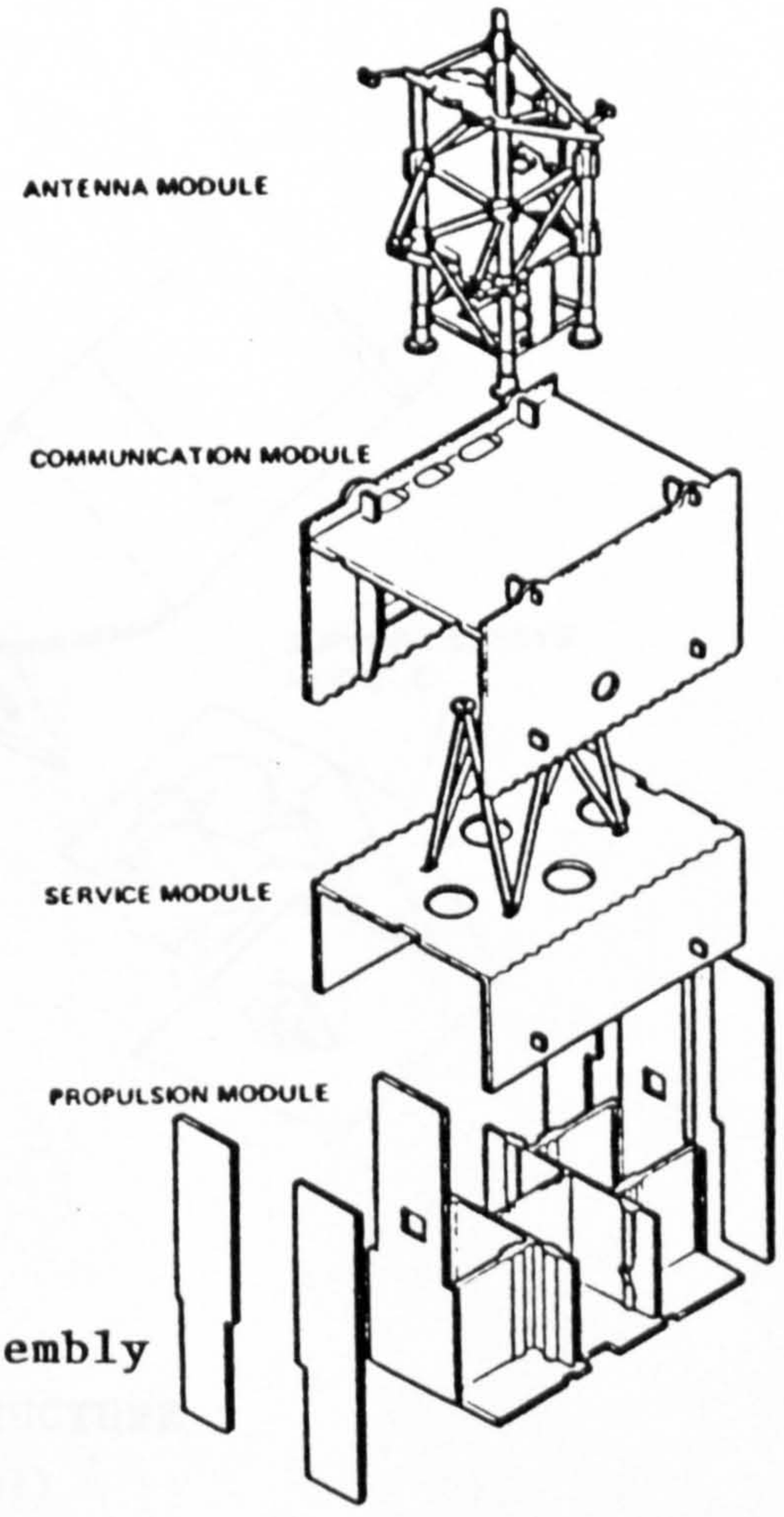

(c) Panel assembly (TDF1/TV SAT)

Fig. 2.1 EXAMPLES OF STRUCTURE CONFIGURATION TYPES

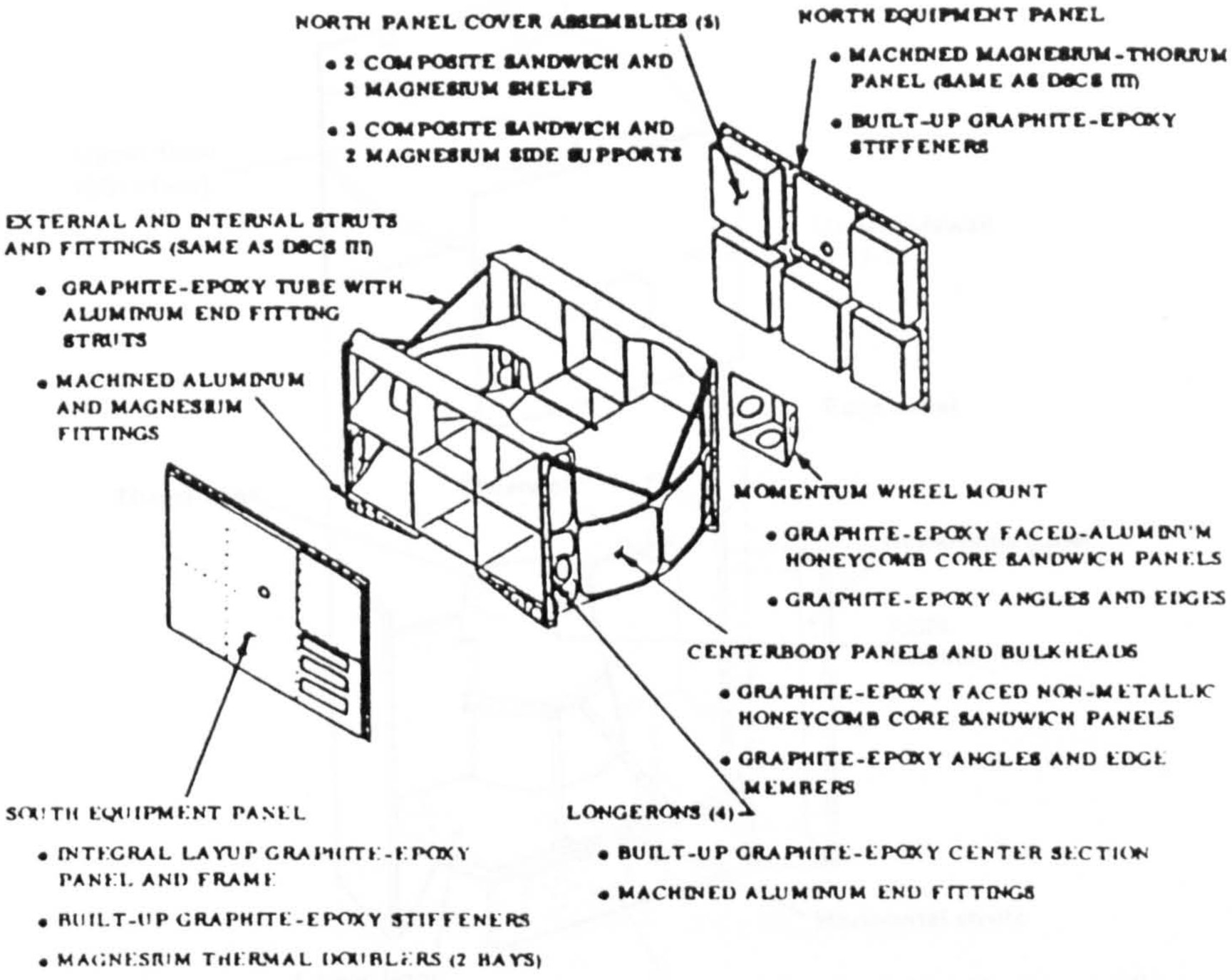

Fig. 2.2 DSCS III STRUCTURE

(from ref. [7])

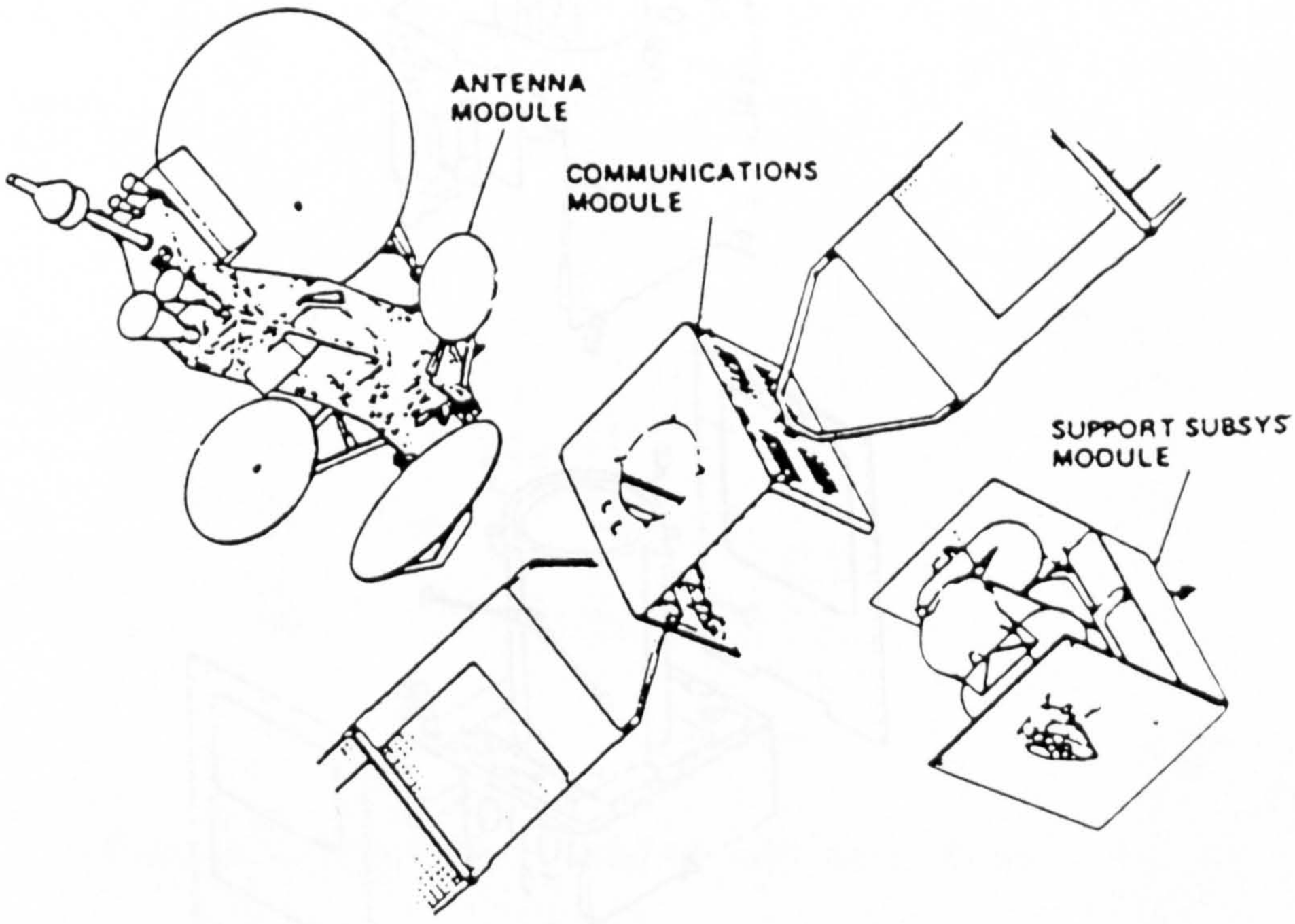

Fig. 2.3 INTELSAT V STRUCTURE

(from ref. [8])

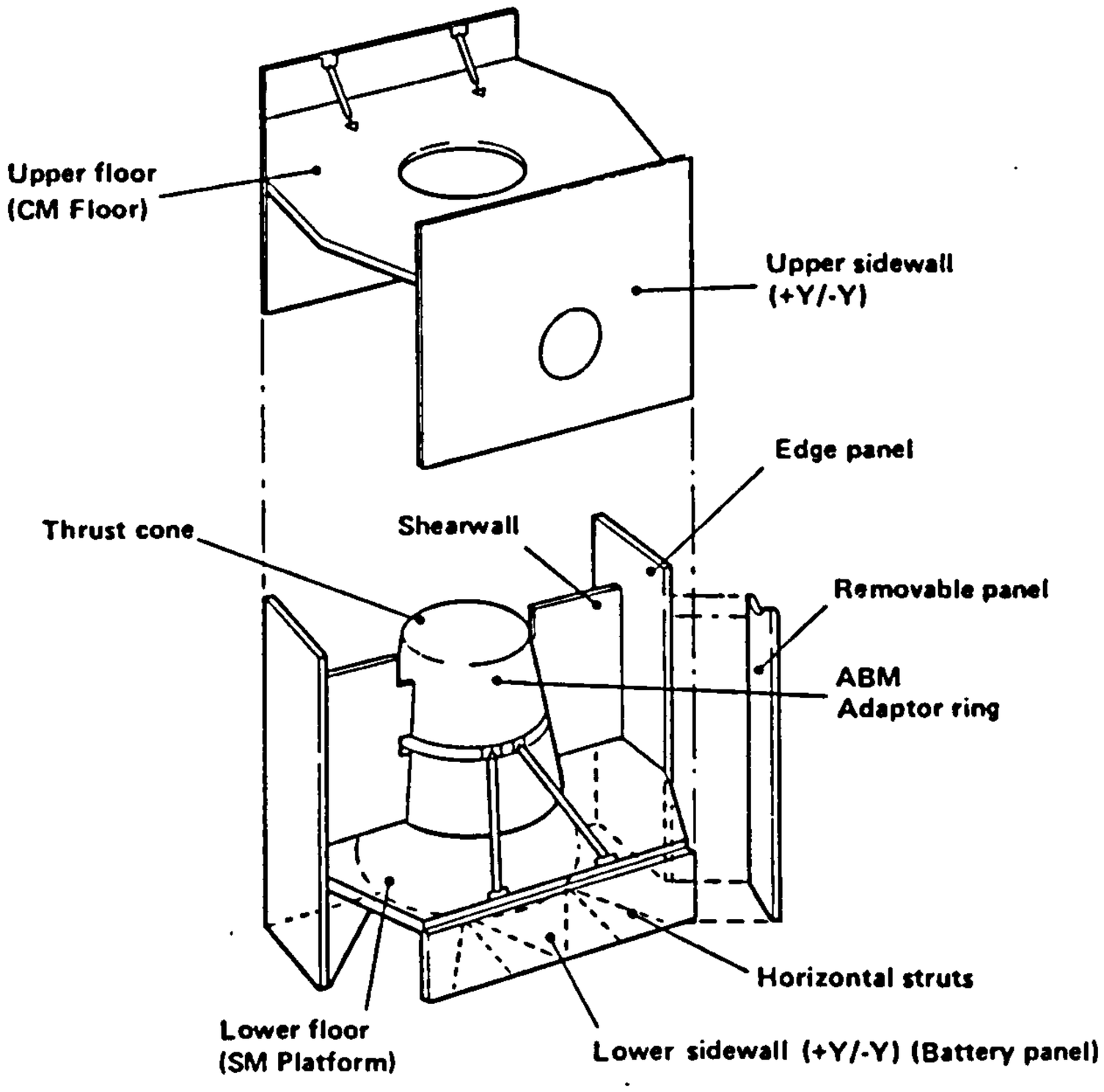

Fig. 2.4 SKYNET IV STRUCTURE

(from ref. [11])

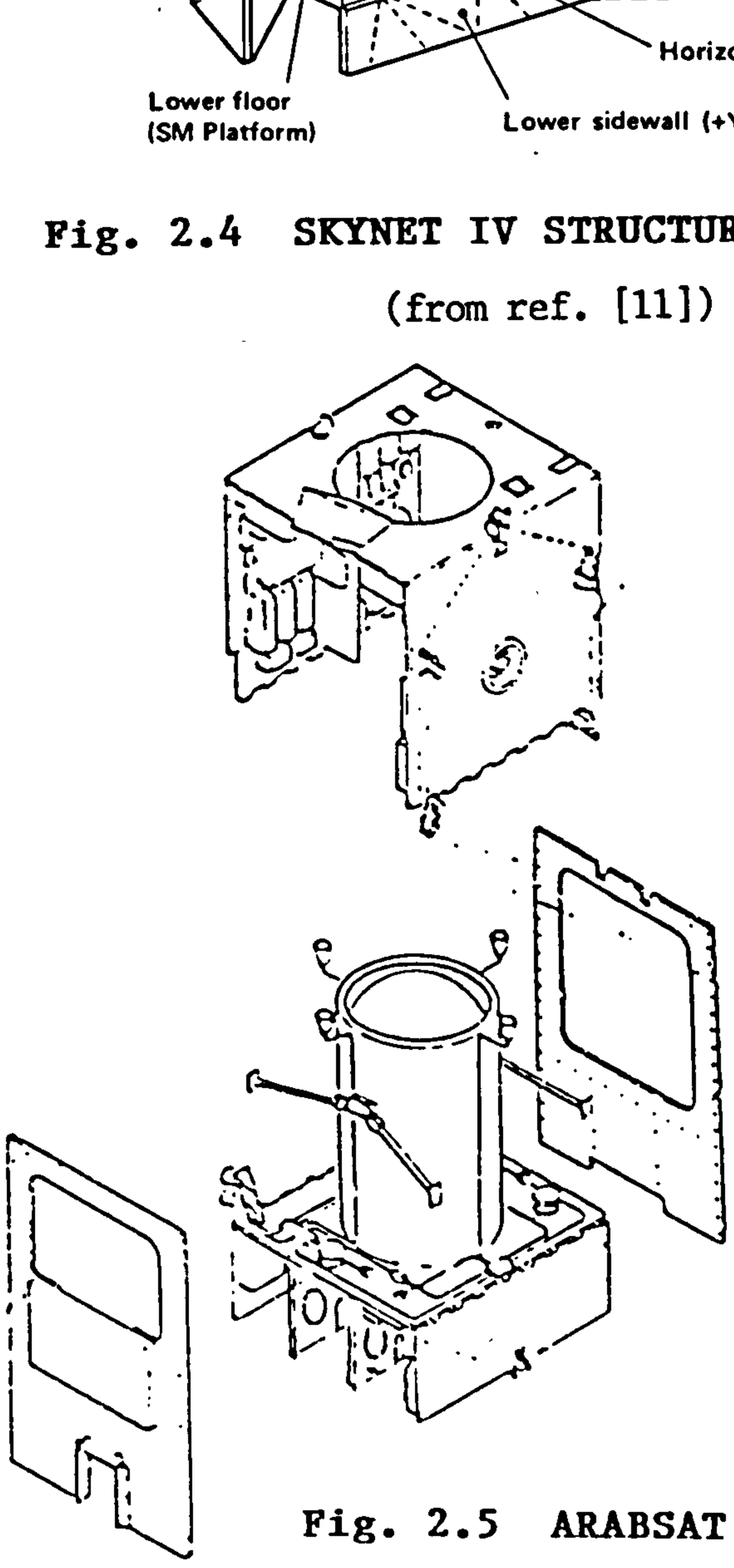

Fig. 2.5 ARABSAT STRUCTURE

(from ref. [12])

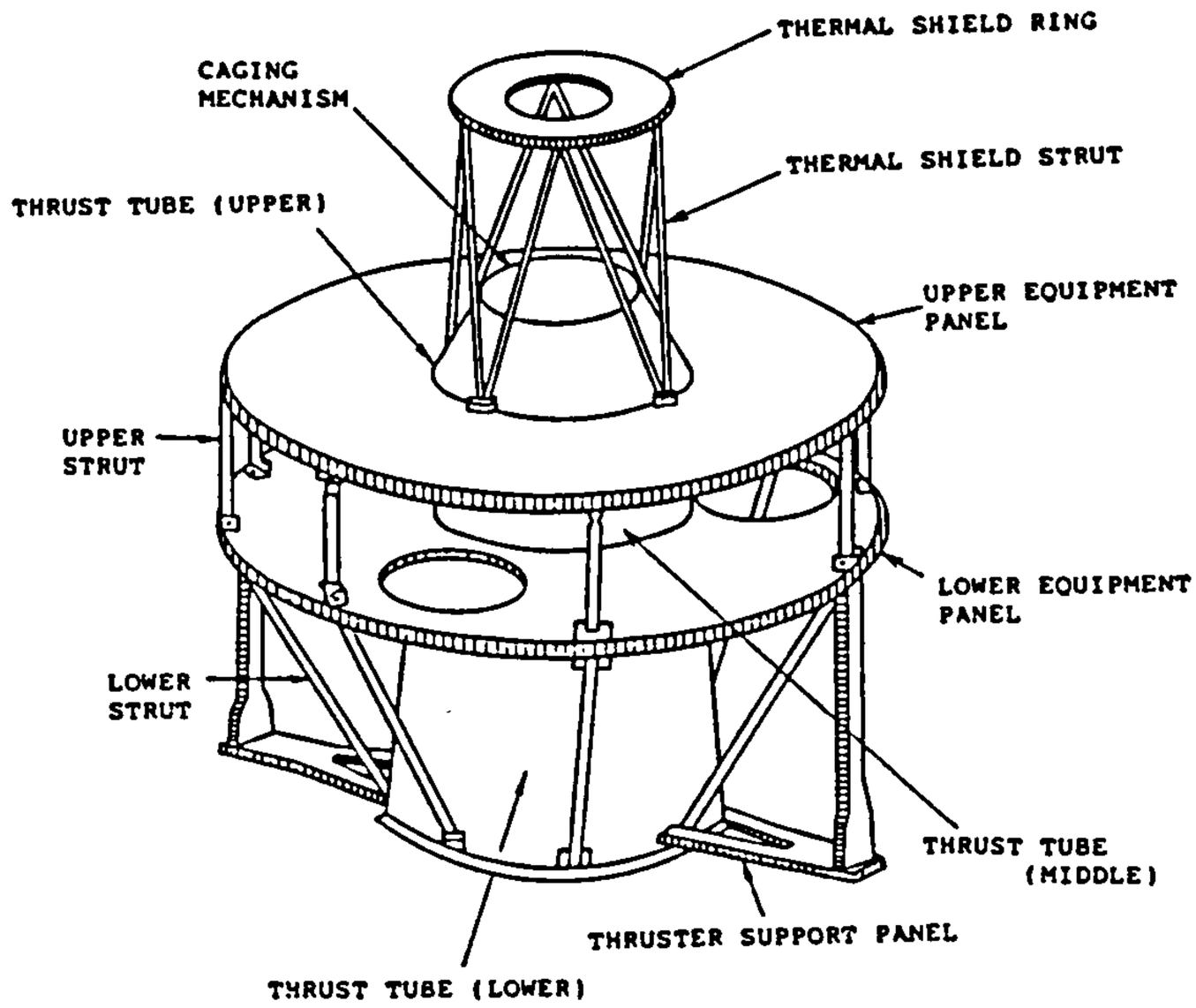

Fig. 2.6 CS-3 STRUCTURE

(from ref. [14])

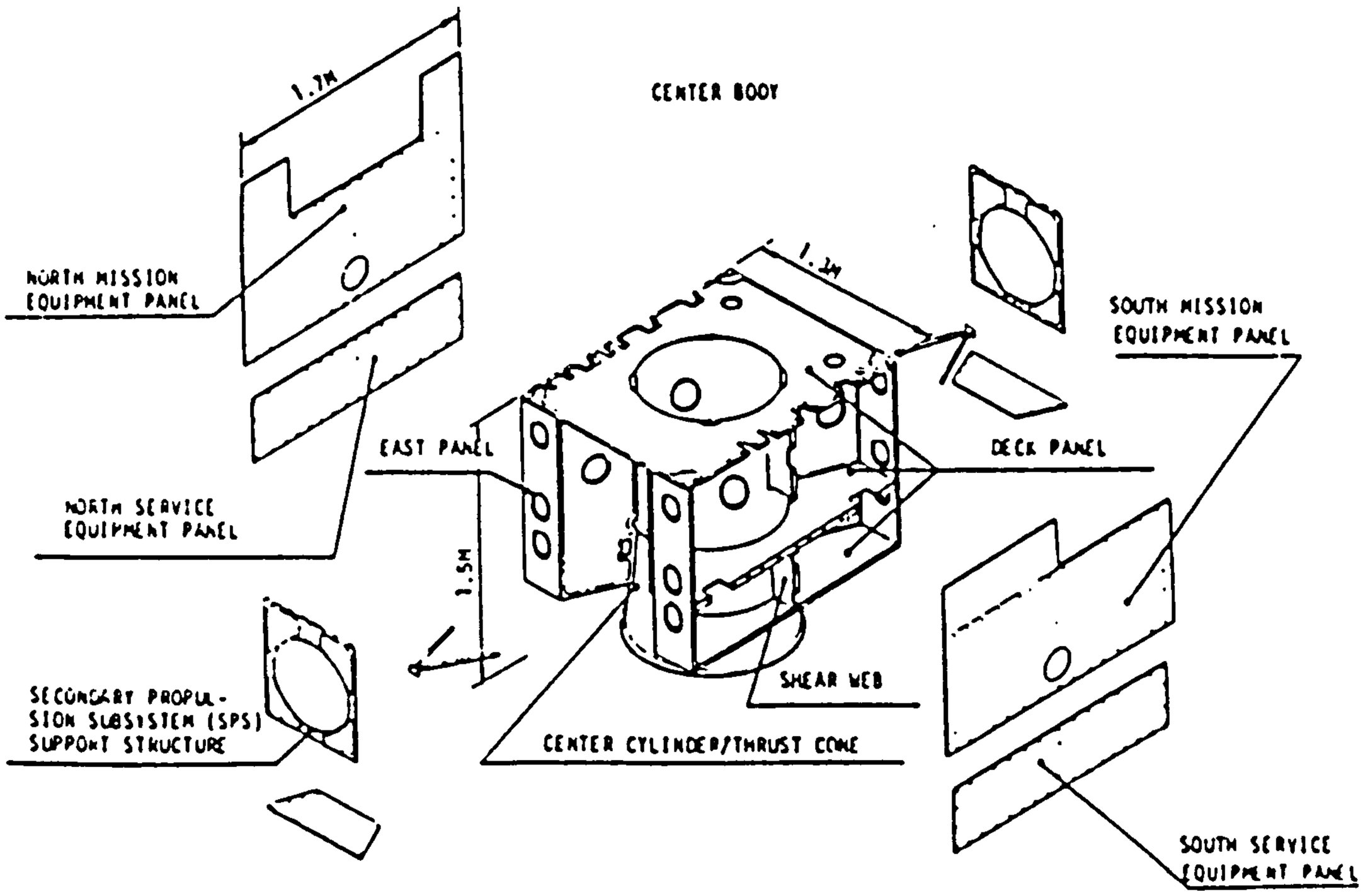

Fig. 2.7 FUTURE JAPANESE GEO STRUCTURE

(from ref. [15])

CHAPTER 3 COMPOSITE MATERIALS

3.1 ADVANTAGES & DISADVANTAGES OF COMPOSITES APPLIED TO SPACECRAFT STRUCTURES

This section discusses the basic advantages and disadvantages of fibre-reinforced composite materials compared to metal alloys for primary spacecraft structures. These are discussed with respect to mechanical properties (strength and stiffness), fabrication methods, thermal & electrical conductivity, effect of the space environment and cost.

3.1.1. Strength and Stiffness

The high specific strengths and stiffnesses of modern fibre reinforced-polymer composites are well known, making them attractive for application in primary flight structures where such properties are highly desirable. The term 'composite' here refers to continuous unidirectional or woven reinforcing fibres embedded in a polymer matrix. The structural properties are determined largely by the reinforcing fibres and the polymer matrix holds the fibres together, transfers load between them and performs a stabilising role under compression. Consequently, the properties are highly orthotropic, with those in the fibre (or longitudinal) direction vastly superior to those perpendicular to the fibres (in the transverse direction). Shear properties, which rely on the polymer matrix, are also inferior to isotropic metallic materials. It is therefore not correct to make direct comparisons between isotropic metals and orthotropic composites based only on directional strength and stiffness properties.

The highly orthotropic nature of composites has its advantages and disadvantages. On the positive side it enables the designer to tailor the reinforcing fibre orientations to meet requirements more effectively. This can result in more efficient structures because there is less 'wasted' material adding weight without performing a useful function. Fibres need only be incorporated in the directions of applied loads or in directions where stiffening is necessary. A particular example is the central thrust

tube found in most spacecraft structures. Composite ply angles can be suitably arranged to meet the launcher-imposed lateral frequency requirements and the applied axial, shear and bending loads with the minimum of material. Struts are other components which benefit from composite orthotropic properties. The fibres can be arranged in the axial or near axial direction to resist the predominant loading in this direction.

For many sandwich stabilised panels in spacecraft structures however, composite material orthotropy can be less advantageous. These components are often multi-axially loaded and rely on the sandwich core for their bending strength and stiffness properties. Efficient constructions utilise thin facesheets on a low density core. Because of limitations on the minimum available prepreg thickness (0.05-0.10 mm), it can be difficult to incorporate all the necessary fibre directions and still yield a lower weight design than a metallic faced alternative.

The non-isotropic properties of composites complicates the analysis of stiffness, strength and stability. Although several analytical techniques are now widely accepted (laminate failure theory for example) these are considerably more complex than the equivalent analysis for isotropic structures and require computer programs to perform the calculations. Other aspects of analysis are less well developed due to the difficulty in handling coupling effects inherent in many laminated constructions. Incorporation of these effects in a form amenable to preliminary design is a particular problem which can be a hinderence to efficient usage because the uncertainties introduce conservatism. Generally the composite analyst is faced with a larger number of variables than are necessary to analyse a metal structure so the analysis effort is consequently more complicated and costly.

Orthotropy also adds to the material development costs. Composites are generally characterised by 4 stiffness properties and 5 strength properties as a minimum for plane stress analysis. Derivation of these properties requires tension, compression and shear testing of longitudinally and transversely orientated samples. In addition interlaminar shear strength is

often used as a material characteristic. This increases the development effort over conventional metallic structures, particularly if a number of composite fibre-resin systems are to be evaluated. Greater material variability and sensitivity to enviromental factors also increases inspection and testing effort at all stages in the structure development.

3.1.2 Method of Fabrication

The matrix material of a composite system governs the method of manufacture. The majority of composites presently used in aerospace applications involve thermoplastic or thermosetting resins, with thermosetting epoxies dominating for low temperature applications. The most widely adopted manufacturing methods are autoclave curing of prepreg lay-ups and filament winding. The use of preimpregnated unidirectional tapes or woven fabrics has superceded wet lay-up techniques because of improved consistency and control over quality, and a reduction in production time. Machine filament winding also improves consistency because of less dependence on operator skill than hand lay-up techniques. This method is restricted mainly to shell type structures however.

The key difference between the manufacture of composite and metal structural components is that with composites, in addition to the shape and form of the component, the material itself is manufactured. Although this has the advantages of tailoribility previously noted, it does put the responsibility of material consistency on the component manufacturer. In spite of modern manufacturing techniques, the variables of processing lead to a much greater scatter in material properties compared with metals. This variability puts a greater emphasis on manufacturing development and quality control. Accounting for the variability of properties reduces the potential benefits over metal alternatives.

Since composite manufacturing methods are basically those of plastic moulding by the application of heat and pressure, these can allow a reduction in the number of parts in an assembly, which translates as a mass and cost saving. This advantage can be exploited in integrally bonded

stiffeners and sandwich panel facesheet doublers, reducing the number of components and secondary bonding operations. The co-cure method of sandwich panel manufacture, in which composite facesheets are simultaneously cured and bonded to the core, also exploits this advantage and offers a reduction in the number of processing operations over metal faced sandwich fabrication. Extending the concept of single piece mouldings further, to reduce the number of components in an assembly, is however restricted in most spacecraft structures because of the requirement for disassembly for access during the Integration and Test phase.

3.1.3 Conductivity

Potential major drawbacks for the application of plastic based composites to many parts of spacecraft primary structures are poor thermal and electrical conductivites. Although advantageous for certain secondary components (R/F transparent and thermally insulating structures, for example), much of the primary structure requires good conductivity properties. Good electrical conductivity is fundamental for a spacecraft that uses the structure as the electrical ground plane. It also provides a degree of interference shielding and a conducting path around the exterior of the spacecraft to prevent charge build-up. Good thermal conductivity is a requirement for equipment mounting panels to dissipate waste heat over a large area and improve radiative heat exchange. These are the north and south panels for 3-axis stabilised geostationary satellites and the deck panels for spin stabilised satellites.

The inferior electrical conductivity of composites over metals is not an overriding disadvantage because most modern spacecraft utilise a harness-provided electrical ground, and conductivity requirements for shielding and external charge dissipation are not great. Carbon-epoxy composites have been shown to have the necessary conductivity to meet these requirements[16], with additional conductive layers only necessary in locallised areas (eg. at joints).

Poor thermal conductivity, on the other hand, can prevent composite application in equipment mounting and radiator panels. A greater thickness of material is needed in the facesheets of these panels to provide the necessary medium for heat transfer than is required for structural efficiency. The provision of metallic doublers to boost performance will often negate any mass savings over an all-metallic faced panel and thermal cycling at the interface can be problematical because of the differential thermal expansion. This is a particular drawback for equipment panels on most geostationary communications satellite applications with high power electrical components and passive thermal control systems.

3.1.4 Space Environment

Composite materials are more sensitive to the space envoronment than their metallic counterparts although composite material behaviour in space is not considered to preclude their use in the majority of possible applications. The observed effects relate mainly to the plastic matrix.

The most commonly used thermosetting resins, such as epoxies, tend to absorb moisture. This can cause expansion and stressing of the composite, but more significantly for space use, can outgas once in vacuum, although oven drying and a controlled environment are sufficient to reduce this. Thermosets themselves also tend to outgas volatiles, but most epoxies (used widespreadly for potting and bonding in spacecraft for many years) meet standard outgassing test requirements. Thermoplastics are much better in this respect and can offer advantages for use in sensitive instrumentation, for example.

Plastic composites retain their structural properties only up to relatively modest temperatures compared to metals. The properties most affected are those in which the resin performance is important. For example, the longitudinal compression strength of a typical high strength carbon-epoxy is reduced by about 25% at 100°C. At temperatures above the glass transition temperature (120-200°C for most epoxies) the material stability is lost. Fortunately thermal protection, provided for the benefit of the

payload, results in a reasonably benign thermal environment for the spacecraft structure during launch and on-orbit, which is within the capabilities of even the lowest temperature composite systems. For the T-Sat spacecraft the structure operating temperature limits were -41°C to +65°C for the worst cases, with normal cycling between lower maximum and minimum temperatures. Temperatures during the launch phase, when the structure is being most severely tested, are usually controlled to be below 50°C. The most temperature sensitive properties are strengths rather than stiffnesses, and these are no longer important once on-orbit.

The longer term effects of the space environment have not shown any major deterioration in composite material systems to date. Microcracking of some epoxy matrix materials has been shown to occur as a result of thermal cycling over extreme temperature ranges, although the temperature limits of a thermally protected spacecraft structure are generally less than the exposed temperatures used in tests, and modern toughened epoxies have reduced this[17]. Microcracking has not been shown to significantly effect properties in any case[18]. Test programmes carried out to investigate the effects of radiation and ultraviolet exposure have not highlighted any problems. In some instances, improvements in properties have even been observed[19].

Atomic oxygen erosion has recently been a cause for some alarm for the integrity of spacecraft structures in low earth orbits. Polymer matrices are particularly susceptible to this type of damage. However, for internal structure or surfaces with thermal protection this is not a serious problem.

3.1.5 Cost

The low volume of production of prepreg materials results in a much higher raw material cost than most metals. An approximate cost guide for carbon-epoxy prepregs is given in Table 3.1. The major cost penalty associated with composite materials for a typical spacecraft project however, is associated with the additional analysis and development test effort,

resulting from non-isotropic properties and material variability as noted previously. Table 3.2 (taken from reference [20]) indicates the relatively high cost of these activities for typical, primarily metal, spacecraft structure projects. These would be increased with a composite structure, but manufacturing cost, which can account for up to 45% of a metal structure can be reduced. This is primarily through a reduction in the number of parts in an assembly and the number of manufacturing operations. For example, an aluminium faced sandwich structure would require the facesheets etched to the required thickness, prepared for bonding, bonded to the honeycomb, and attachments, doublers and reinforcements fastened or bonded in position. By contrast, a composite sandwich can be layed up and co-cured with integral doublers and reinforcements in a single operation. The relative costs of the overall project would therefore tend to shift more towards analysis and development (which would reduce with increased experience) away from the manufacture.

Detailed trade-off studies between carbon-epoxy composites and aluminium alloy for spacecraft structure components, have shown only modest cost increases for small production runs[13,16]. These were easily justified by the large savings in structure weight.

3.2 FIBRE AND MATRIX MATERIALS

3.2.1 Fibres

Four types of fibre are commonly used in aerospace composites :

1. Glass
2. Boron
3. Kevlar (or aramid)
4. Carbon (or graphite) .

Glass fibres are the cheapest form of reinforcement and those most often used in general purpose composites. S-glass, with substantially higher strength than the commercial grade E-glass, is used in aerospace

applications. It has good insulating properties and reasonable specific strength which has seen application in R/F trasnsparent and thermally isolating spacecraft components. However, it has a relatively low modulus of elasticity making it uncompetitive for many stiffness critical structures.

Boron fibres have very high modulus and yield composites of high compressive strength making them attractive for use in compression loaded stability-critical and stiffness-critical spacecraft structures. However their use has not been widespread because of the emergence of very high modulus carbon fibres at lower cost and without many of the inherent disadvantages. These are attributable to boron fibres being denser, thicker, more brittle and harder than carbon. This results in thick plies, results in poor drapability, prevents them being woven and makes machining difficult.

Kevlar is the most often used organic man-made fibre in composites. These have the lowest density of the four fibres listed, have good specific tensile strength, high failure strains, excellent dielectric properties and are easily formed and machined. The biggest shortcomings of these fibres are a low specific modulus and poor compressive strength. Application of Kevlar composites on spacecraft has therefore been limited mainly to pressure vessels and antennas.

Carbon fibres are the most widely used reinforcement in aerospace composite structures. This is attributable to the wide range of fibre types available with good combinations of specific strengths and stiffnesses. There are four basic fibre type classifications :

1. High Strength
2. Intermediate Modulus
3. High Modulus
4. Ultra High Modulus

There is an increase in fibre modulus going down the list, but for a sacrifice in strength and an increase in cost.

In addition to good structural properties, carbon fibres have a small negative coefficient of expansion. When combined with a plastic matrix and suitable fibre orientation, near-zero thermal expansion can be achieved in a given direction. This has been exploited in a number of thermally stable platforms, antennas and optical benches on spacecraft. As confidence in composite materials has grown, carbon fibres have also become the most popular form of reinforcement for both strength and stiffness critical spacecraft primary structure. All of the examples described in Chapter 2 employed carbon fibre composites.

3.2.2 Matrix Materials

Matrix materials for fibre-reinforced composites fall into three categories :

1. Thermosets
2. Thermoplastics
3. Metals

The thermosetting class of plastics are those most often used at present. These are characterised by an irreversible polymer cross-linking reaction during the cure process - usually through the application of heat. Phenolics, polymides and epoxies are the three most commonly used types. Choice of a particular thermosetting resin type is mainly dependent on the in-service temperature. Phenolics were used in many early composite applications but problems resulting from the large release of volatiles during processing has seen them largely replaced by other resins. For high service temperatures of up to 350°C, polyimides are often used, but consequently require a high cure temperature (approx. 300°C) and poor resin flow requires high pressures of 200 p.s.i and above.

Where these additional manufacturing complications are not warranted because of fairly low service temperatures, epoxies are the most commonly adopted design solution. For most satellite structure applications, the service temperatures are well within the capabilities of epoxy resins. The

popularity of epoxies has seen a vast range of these resins become commercially available with fibre reinforcement in composite prepreg form. These fall basically into two groups :120°C curing epoxies (eg. Cyanamid Code 92) and 180°C curing epoxies (eg. Cyanamid Code 69, Ciba-Geigy Fibredux 914) which offer slightly better property retention at elevated temperatures.

Thermoplastics differ from the thermosets in that they are characterised by a reversible reaction with the application of heat. Thermoplastics which have been incorporated in fibre reinforced composites include polyether-etherketone (PEEK), polyetherimide (PEI), polysulphone (PS) and polyethersulphone (PES). Fabrication techniques include multi-stage processing in which layers of reinforced plastic film can be built up by temperature and pressure and subsequently re-formed to the final shape of the component by further application of heat and pressure. This offers advantages over thermosets in terms of the speed of production, particularly for complex shapes, but requires higher temperatures and pressures. PEEK for example is formed at 400°C. Commercially available PEEK with intermediate modulus carbon fibre reinforcement (known as APC 2), has been shown to exhibit other advantages over carbon-thermoset composites such as reduced outgassing and moisture absorption, better atomic oxygen and radiation resistance, improved impact tolerance and superior hot/wet performance[21]. At present, thermosets dominate in spacecraft composite applications, but thermoplastics are likely to see increasing use in the near future. Brackets and attachments are particular components which could exploit the multi-stage processing capability of thermoplastics. Such small and complex shapes are expensive to produce by hand lay-up in thermosetting composites.

Metal matrix composites are still at the development stage. The use of a metal matrix, usually aluminium, magnesium, titanium or nickel, can overcome many of the disadvantages inherent in plastics such as poor electrical and thermal conductivity and restricted high temperature performance. Manufacture involves the bonding of layers of fibre reinforced metal tape through brazing, diffusion or eutectic bonding by the application of very high temperatures and pressure. Such fabrication

techniques and high raw material cost currently restrict metal matrix composites to only specialised applications.

3.3 CARBON-EPOXY COMPOSITES

Carbon fibre reinforced epoxies are currently the most widely used composites in spacecraft and launcher structures. Control of the in-service behaviour of the material is determined largely by the particular carbon fibre type, whereas the particular epoxy is essentially selected with regard to the method of fabrication. For space use, the epoxy should also have low outgassing characteristics and microcracking resistance.

3.3.1 Mechanical Properties

Tables 3.3 and 3.4 list average strength and stiffness properties of commonly used unidirectional and woven carbon-epoxies (plus carbon-PEEK and a couple of carbon-polyimides for comparison).

Prepreg properties are essentailly governed by the fibre modulus. This is illustrated by fig. 3.1 which shows specific unidirectional tension and compression strengths plotted against specific unidirectional tension modulus. The trend is a reduction in strength for increasing modulus, with compression strengths significantly lower than tension strengths for most material systems. Selection of a particular carbon fibre type will depend on the particular application - whether stiffness or strength critical. For the majority of spacecraft components, which are loaded in direct compression or bending, it is the specific compression strength which is the relevant figure of merit as regards strength. At one end of the range are the high strength fibres, typified by Toray T-300 which are widely available in a number of alternative resin systems at fairly low cost. Improved stiffness can be gained for a small increase in cost by utilising high modulus fibres such as Grafil HM-S, again these are readily available. Where stiffness is the overriding concern, ultra high modulus fibres such as Celion GY-70 may be used, but at a significant cost penalty and with a

large reduction in strength compared to lower modulus fibres. At the top end of the ultra-high modulus pitch based fibre range are Thornel P-100, P-120 and P-140. These are very stiff but have low compression strength, are very expensive and are susceptible to handling damage. Newer high strain carbon fibres such as Hercules AS6 and IM6 and Toray T-50 offer a better compromise between strength and stiffness.

3.3.2 Design Allowables

For design purposes "allowable" material properties are used to take into account scatter, particularly in the strength properties. Tables 3.5 and 3.6 give design allowables for a number of carbon-epoxy systems used on several space structure projects. A comparison with Tables 3.3 and 3.4 shows the large reductions in the design allowables over the average properties necessary to account for the statistical variability.

TABLE 3.1 TYPICAL PREPREG COSTS (from numerous sources)

FIBRE TYPE	FORM	PLY THICKNESS (mm)	APPROX. COST (£ per kg)
High Strength	U.D	0.10	100
High Strength	Woven	0.20	100
High Modulus	U.D	0.10	130
Ultra-High Modulus	U.D	0.06	2000
2024 ALUMINIUM ALLOY		0.60	30

TABLE 3.2 TYPICAL STRUCTURE COST BREAKDOWN (from ref. [20])

ACTIVITY		PERCENTAGE OF TOTAL COST
MANAGEMENT		8-20
ENGINEERING	ANALYSIS	15-30
	DRAWINGS	10-20
MANUFACTURING		20-45
TESTING		15-30

TABLE 3.3 **AVERAGE U.D. MATERIAL PROPERTY DATA**

COMPOSITE MATERIAL SYSTEM				STIFFNESS (GPa)						STRENGTH (MPa)					SOURCE
FIBRE	MATRIX	DENSITY	V_f	E_{1T}	E_{1C}	E_{2T}	E_{2C}	ν_{12}	G_{12}	X_T	X_C	Y_T	Y_C	S	
CELION 32msi	CYCOM 985	—	60%	128	124	8.3	-	—	-	1724	1241	40	-	-	[22]
AS	4397[a]	—	63%	126	129	9.6	-	—	-	1401	1420	37	-	-	[23]
T-300	CYCOM 985	1560	60%	133	114	8.2	-	0.34	4.8	1642	977	52	-	33	[5]
AS-6	F'DUX 6376	—	60%	136	-	9.5	-	—	-	2690	1572	83	-	-	[24]
T-300	F'DUX 914	1580	62%	138	121	8.9	10.3	0.37	5.0	1573	—	37	-	87	[25]
AS-4 "APC 2"	PEEK[b]	1600	-	139	102	10.4	5.7	0.33	4.5	2131	1116	64	253	175	[26]
T-300	F-178[a]	—	65%	140	125	10.3	-	—	-	1080	1240	20	-	-	[23]
IM-6	F'DUX 6376	—	60%	172	148	9.4	-	—	-	2696	1614	73	-	-	[24]
HM-S	CYCOM 985[c]	1600	60%	192	157	6.8	-	0.30	3.8	1202	882	38	139	47	Chapt.4
PAN-50	F'RITE 934	—	-	214	197	12.4	7.7	0.36	-	916	895	19	110	78	[6]
HM-S	F'DUX 914	1640	-	222	-	7.3	-	—	-	1121	898	46	-	-	[25]
T-50	ERL 1962	1600	60%	241	-	-	-	—	-	1413	965	-	-	-	[27]
P-55	ERL 1962	1710	60%	241	-	-	-	—	-	931	510	-	-	-	[27]
P-75S	ERL 1962	—	65%	289	-	20.0	-	—	-	972	441	25	-	-	[6]
GY-70	CODE 87	—	60%	290	-	-	-	—	-	600	520	-	-	-	[22]
GY-70	CODE 92	1600	60%	300	276	5.2	-	0.39	3.5	712	510	9	-	-	[25]
P-100	ERL 1962	1830	60%	421	310	-	-	0.30	4.8	1034	255	-	-	-	[27]
P-120S	ERL 1962	—	50%	525	-	5.7	-	—	5.5	1441	-	23	-	-	[27]

NOTES:-

(a) Polyimide resin
(b) Thermoplastic resin
(c) Data for 30 psi cured laminate

TABLE 3.4 **AVERAGE WOVEN MATERIAL PROPERTY DATA**

COMPOSITE MATERIAL SYSTEM				STIFFNESS (GPa)						STRENGTH (MPa)					SOURCE
FIBRE	MATRIX	DENSITY	V_f	E_{1T}	E_{1C}	E_{2T}	E_{2C}	ν_{12}	G_{12}	X_T	X_C	Y_T	Y_C	S	
T-300	F593 EPOXY	1450	44%	52	45	51	46	0.06	3.5	554	574	553	625	-	[25]
T-300	CYCOM 985	1600	60%	58	54	58	-	0.12	2.3	504	513	484	-	100	[5]
M-40B	F'DUX 914	1560	50%	95	-	88	-	—	-	341	312	352	298	-	[25]
UHM	ERL 1962	1800	-	152	152	-	-	0.09	4.8	345	152	-	-	-	[27]

TABLE 3.5 **UD MATERIAL DESIGN ALLOWABLES**

COMPOSITE MATERIAL SYSTEM				STIFFNESS (GPa)						STRENGTH (MPa)					SOURCE
FIBRE	MATRIX	DENSITY	V_f	E_{1T}	E_{1C}	E_{2T}	E_{2C}	ν_{12}	G_{12}	X_T	X_C	Y_T	Y_C	S	
T-300	CODE 69	—	60%	115	115	7.1	7.1	0.30	4.0	1050	660	48	220	60	[13]
T-300	F'RITE 934	1600	63%	118	118	8.4	8.4	—	5.9	1120	1000	80	71	68	[25]
HM-S	CYCOM 985[a]	1600	60%	175	175	6.8	6.8	0.30	3.8	574	344	23	70	15	Chapt.4
HM-S	EPOXY	—	-	185	185	7.6	7.6	—	5.1	736	756	27	150	50	[10]
HM-S	CODE 69	—	-	191	167	6.1	6.4	0.37	2.9	432	546	15	61	45	[28]
GY-70	CODE 69	—	-	252	263	4.7	7.4	—	4.2	400	441	16	108	41	[25]
GY-70	CODE 95	—	60%	264	245	-	-	0.30	3.5	405	470	-	-	117	[25]
GY-70	CODE 92	1600	-	275	251	4.6	-	0.35	2.7	612	391	15	-	-	[25]
P-75S	F'RITE 934[b]	—	-	336	255	6.0	6.8	0.37	4.9	848	294	10	90	21	[6]

NOTES :-

(a) Data for 30 psi cured laminate
(b) "B" Allowables

TABLE 3.6 **WOVEN MATERIAL DESIGN ALLOWABLES**

COMPOSITE MATERIAL SYSTEM				STIFFNESS (GPa)						STRENGTH (MPa)					SOURCE
FIBRE	MATRIX	DENSITY	V_f	E_{1T}	E_{1C}	E_{2T}	E_{2C}	ν_{12}	G_{12}	X_T	X_C	Y_T	Y_C	S	
KEVLAR	F-161 (SATIN)	1400	48%	29	27	27	27	0.05	2.0	285	113	270	113	30	[25]
T-300	F-263 (PLAIN)	1500	60%	57	57	57	57	0.06	4.8	280	280	284	284	36	[25]
T-300	F-263 (SATIN)	1500	63%	60	60	60	60	0.06	5.8	296	284	296	284	44	[25]

Fig. 3.1 SPECIFIC UNIDIRECTIONAL TENSION & COMPRESSION STRENGTH VS. SPECIFIC MODULUS OF CARBON COMPOSITES.

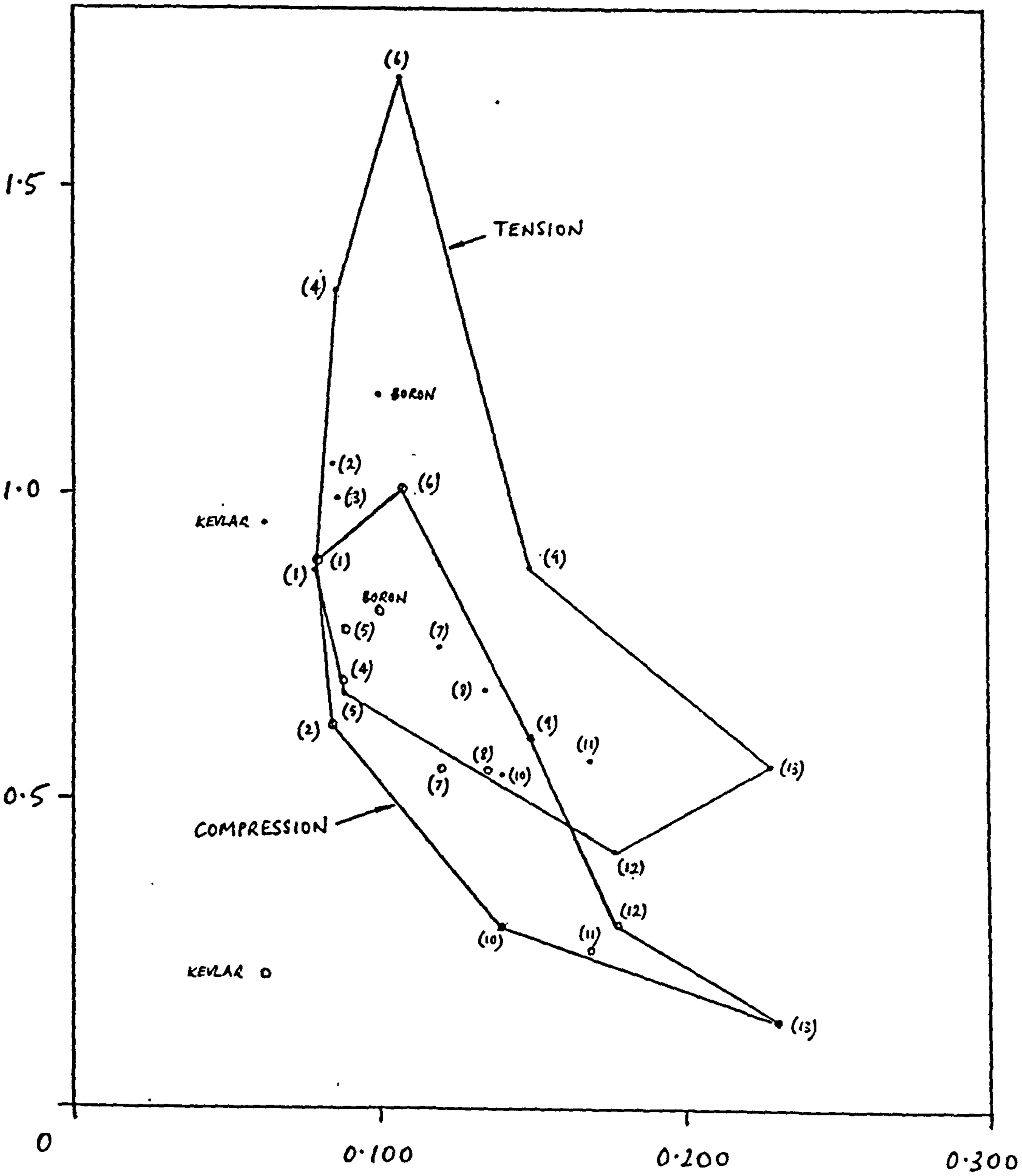

CHAPTER 4 COMPOSITE SANDWICH PANEL MANUFACTURE

4.1 SANDWICH CONSTRUCTION

Sandwich construction is the most commonly adopted design solution for the flat platform, sidewall and shear web components of spacecraft structures. It is also the most popular form of construction for composite thrust tube shells. The advantages of sandwich construction are its high structural efficiency in terms of strength, stiffness and buckling stability plus the provision of a smooth mounting surface for equipment attachment. Composite materials can be readily incorporated into the facesheets or skins of sandwich components because these are generally only very thin, perhaps only several plies thick. The sandwich core is usually aluminium or NOMEX honeycomb bonded to the facesheets by a film adhesive. Such cores are lightweight, have good shear strength and stiffness properties and are available in a range of densities.

Sandwich panels can be locally reinforced by thicker facesheets (or doublers) and by the use of higher density honeycomb in particular regions. Attachment of equipment or other structure components is usually with inserts which are adhesively potted into the panel.

4.2 CO-CURE MANUFACTURING TECHNIQUE

This chapter describes the development of a 'co-cure' manufacturing technique for the production of composite faced sandwich components. Co-curing refers to a method in which thermosetting composite facesheets are simultaneously cured and bonded to the core in a single operation. This contrasts with the more commonly adopted technique, which will be referred to as a 'pre-cure' method, in which the facesheets are cured separately and subsequently bonded to the core.

4.2.1 Advantages & Disadvantages over Conventional Methods

The co-cure method can offer two major advantages over the pre-cure method. These are :-

1. The facesheets of a co-cured sandwich need not be "balanced", ie. have a symmetric lay-up about the facesheet mid-plane. Only the complete sandwich needs to be balanced to prevent distortion of the component on cool down from the cure temperature. In certain cases this can imply lighter designs because the plies can be more efficiently tailored to the structural requirements, without the constraint of having to achieve symmetry in facesheet lay-up. Pre-cured facesheet lay-ups often have to include unecessary plies simply to fulfill this manufacturing requirement. To remain competitive with alloy faced designs it may be necessary to resort to very thin and more costly prepreg for pre-cured facesheets, whereas co-cured facesheets can incorporate standard thickness prepregs.

2. Co-cured sandwich components can be manufactured at significantly lower cost. This is mainly as a direct result of the reduction in the number of processing steps. A saving in recurrent costs is achieved simply because there is only a single cure cycle. A sandwich component with pre-cured facesheets requires a cure cycle for the two facesheets, followed by an additional cycle to bond the honeycomb core. Non-recurrent costs are saved by a reduction in the tooling requirements. Pre-cured facesheets require tooling for the facesheet lay-ups and a jig for positioning and bonding the honeycomb, whereas a single tool is the only requirement for a co-cured sandwich. Certain pre-cured components can save on tooling expense by utilising the same tool for both facesheets, although this then requires a separate cure cycle for each.

The additional design freedom offered by the co-cure method to the facesheet lay-ups can reduce the number of plies and this can also translate into cost savings. Pre-cured facesheets may require 6 x 0.05 mm plies for example, to achieve lay-up symmetry, whereas a co-cured facesheet may be able to adopt a 3 x 0.10 mm unbalanced lay-up. The

cutting and lay-up time is reduced and the thicker 0.10 mm prepreg is more cost-effective. The fewer number of plies will also reduce the liklihood of interlaminar defects being introduced.

The major disadvantage of the method is that a low pressure must be used in the cure cycle to prevent collapse of the honeycomb core. This results in a higher void content and a consequent degradation in structural performance compared to pre-cured laminated facesheets. The co-cure technique has therefore been mainly limited to secondary stiffness-critical sandwich components in various applications, using an oven cure and a pressure of only 1 atmosphere applied by a vacuum bag.

The use of higher autoclave pressures to reduce the degradation effect in the co-cure method was therefore investigated and developed for application to typical spacecraft sandwich components.

4.2.2 Co-cure Manufacture Development

The co-cure technique was developed by investigating in turn the effects of various parameters on manufactured composite sandwich. The effects of cure pressure, curved geometry, honeycomb venting, honeycomb splices, facesheet thickness changes and requirements for the lay-up stack were all investigated in a series of manufacturing trials.

4.2.2.1 Selection of Cure Pressure

In the first set of manufacturing trials the aim was to establish a maximum cure pressure, in order to produce low void content facesheets, without crushing the honeycomb. To establish a common cure pressure suitable for a wide range of spacecraft sandwich component constructions, a 'worst case' construction with a low crush strength was used. This consisted of single ply woven T-300/CYCOM 985 facesheets, FM300M film adhesive and a 1¼" deep low density 2.0-3/16"-0.0007" perforated 5056 aluminium honeycomb core. A film adhesive and low flow resin were used to ensure good facesheet-

honeycomb bond integrity, whilst controlling resin content. This was considered preferable to a higher flow resin and no film adhesive, which although lighter would not guarantee a good facesheet-honeycomb bond.

In the first trial, these layers were built up on a flat tool plate with an aluminium caul plate placed on top. The lay-up was sealed in a vacuum bag and autoclave cured according to the standard CYCOM 985 cure schedule, but with the maximum autoclave pressure limited to 50 psi (about half the pressure used for solid laminates). The resulting panel was extensively collapsed as a consequence of pressure on the exposed edges of the honeycomb which pushed it inwards towards the centre of the panel before the prepreg had cured.

The tooling was modified to include an angle section dam around the periphery to protect the edges. A second panel was cured on the modified tooling at the same pressure of 50 psi. This too was badly collapsed although not to the same extent as the first. Collapse was initiated by crushing of the honeycomb adjacent to one edge which spread across half the panel area. The edge is weakest because the honeycomb cell walls here are unsupported by surrounding cells so consequently have a lower buckling strength. The honeycomb cells which were uncrushed had small wavelength buckles down the foils.

In a third trial, the panel was cured at a pressure of 35 psi. This was successful, with no core crushing evident. Some cell wall buckles were apparent around the panel periphery, but this effect was confined to outside the 15 mm trim line. A maximum cure pressure of 30 psi, to give a margin of safety, was therefore specified for all subsequent co-cure manufacturing.

4.2.2.2 Effect of Curved Geometry

The additional complexities of curved geometry on the co-cure method were investigated by fabricating a cylindrical sandwich component. This had a diameter of 1000 mm, length of 300 mm and core thickness of 10 mm. These

dimensions were chosen to be representative of a thrust tube section. The sandwich construction consisted of 2-ply UD T-300/CYCOM 985 prepreg facesheets, FM300M film adhesive and a 5.7-3/16"-0.0020" unperforated 5056 aluminium core. A facesheet lay-up of [0/90] was arbitarily selected and the choice of an unvented core was forced by material availability.

The prepreg and film adhesive were layed up flat and a pre-consolidation de-bulking cycle was used to compact the layers prior to positioning on the cylindrical tooling. This consisted of 1 hour at 80 psi in the autoclave at room temperature. The cylindrical tooling was fabricated from rolled sheet steel and incorporated two end rings as edge protection dams. The tool was orientated with its axis vertical for lay-up on its exterior surface and rotated horizontal for curing in the autoclave. The inner facesheet was positioned on the tool surface first in one third segments by taping around the top and bottom edges. Honeycomb segments rolled to the correct curvature were placed on this layer with foaming adhesive strips between to splice them together. The lay-up was completed by the outer facesheet plies and film adhesive which had also been pre-consolidated in one third segments. Two thin aluminium caul plate halves were positioned on the top porous release cloth layer and the stack was completed with a glass cloth breather and vacuum bag. The lay-up stack is shown in fig. 4.1.

Under vacuum the thin caul plate formed buckles rather than following the curved profile of the lay-up. To overcome this it was replaced by thicker 28 swg sheet that was rolled to the correct curvature. Small gaps were left at the joins between the caul plate halves to allow these to close up freely when pressure was applied. At one gap a free floating overlap plate was positioned over the join and the other was left open.

The cylinder was cured according to the standard CYCOM 985 schedule but with autoclave pressure limited to 30 psi. Several defects were observed in the cured cylinder which is shown still in position on the tooling in fig. 4.2. Dimpling of the facesheets was apparent over most of the component surface, both on the inside and the outside. This was believed to be a result of using an unperforated honeycomb because the effect was not observed on the earlier manufactured flat panels with perforated cores.

Ridges in the outer facesheet were apparent at both of the caul plate joins where the outer facesheet plies had ridden up at the gaps. Some creasing was also evident at the positions of honeycomb section splices, this was thought to be due to poor application of the foaming adhesive. Other, smaller longitudinal pits and resin rich areas at the cylinder ends were attributed to the non-porous release cloth. This had not been put on sufficiently tightly to prevent creases forming. By being non-porous it had acted as a barrier to outwards resin flow, causing resin to flow under the surface and out to the cylinder ends where it formed resin-rich pools.

4.2.2.3 Effects of Caul Plate & Honeycomb Venting and Changes in Facesheet Thickness

Following on from the co-cured cylinder trial, a further flat panel was manufactured with the following aims :

1. To investigate whether a caul plate was really necessary, since this caused problems on the cylinder component.

2. To confirm that the dimpling effect observed on the cylinder was caused by the use of an unvented core.

3. To demonstrate the possibility of incorporating changes in facesheet thickness (such as local doublers or reinforcement on an actual panel).

The panel construction illustrated in fig. 4.3 was used to investigate these effects. This was divided into three equal regions. In each region the facesheets consisted of 4-ply [0/90/0/90] HM-S/CYCOM 985 in one half stepping down to 2-ply [0/90] in the other half. The change in thickness was stepped over a 5 mm width where the facesheets consisted of 3 plies. In region (1) a perforated honeycomb was employed as the core and no caul plate was use. The perforated honeycomb extended into region (2) but in this region a 28 swg aluminium caul plate was used. In region (3) the core was unperforated and a caul plate was used. A porous release cloth was

adopted on both sides of the lay-up over the full area. The cure cycle was identical to the cylinder, with autoclave pressure limited to 30 psi.

The upper side of the cured panel in region (1) had a fairly uniform dimpled appearance, whereas the lower (tool side) facesheet had a good flat finish. This was attributable to the omission of the caul plate in this region. Pressure applied during the early stages of the cure had caused the still flexible prepreg to be pushed into the cell cavities. Dimpling was also apparent in region (3) which incorporated unperforated honeycomb. This occured on both the upper and lower facesheets - reproducing the effect found on the cylinder. The dimpling was more pronounced in the thinner 2-ply half of the region. The central region : region (2), gave a very satisfactory finish. The porous relaease cloth gave a uniform matt appearance with no resin-rich areas. The caul plate followed the change in panel thickness without any bridging effects or prepreg ridges forming at the step.

Based on these trials, the following recommendations were drawn up for the co-curing technique :-

1. Cure pressure to be limited to 30 psi. This limit is sufficient to prevent collapse in 2.0lb./cu.ft. aluminium cores up to 1¼" in thickness.

2. A perforated honeycomb is essential for an undimpled finish. Such a core would be specified in any case for space hardware to enable air pressure to escape during launch.

3. A caul plate is necessary to prevent dimpling of the upper facesheet. The caul plate should be sufficiently thick to spread the pressure evenly yet deform to follow the component. Buckling can occur on a curved component if the caul plate is too thin, 28 swg aluminium was found to be satisfactory.

4. Pre-consolidation of the facesheet plies may be beneficial. This enables a greater compaction of the plies than can be achieved during the low pressure cure. A pre-consolidation at 80 psi and room temperature was used.

5. Changes in facesheet thickness can be accomadated. Ply increments of 0.10 mm were satisfactorily incorporated over 5 mm wide steps.

6. A porous release cloth gives a more uniform finish, prevents the formation of resin-rich areas and gives a better surface for any subsequent bonding. A low flow resin system such as CYCOM 985 used here is essential for resin control during the co-cure process.

4.3 EFFECT OF THE CO-CURE TECHNIQUE ON SANDWICH MECHANICAL PROPERTIES

Because of the low pressure employed during the co-cure process (30 psi as opposed to 80-100 psi used for solid laminates), a degradation in mechanical properties is expected. This is a consequence of increased void content with decreasing cure pressure. The properties most affected are longitudinal compression and inter-laminar shear strength. This is illustrated for solid laminates in fig. 4.4 (reproduced from reference [29]) which plots longitudinal compression strength against void content for two high strength carbon-epoxy systems. The corresponding cure pressures for the observed void contents are given along the top of the graphs. These show that the application of quite modest pressures results in significant improvements in performance over vacuum only cured laminates. The graph indicates that longitudinal compression strength is reduced by a factor of about 0.85 at a cure pressure of 30 psi, whereas the reduction factor falls to about 0.50 for zero autoclave pressure. Table 4.1 (from reference [30]) lists knock-down factors for vacuum-only cured AS-1/3501-5A carbon-epoxy laminates compared to their autoclave cured counterparts. These were derived by comparing average properties of test coupons manufactured by the two different processes. Most properties show relatively small degradations but the longitudinal compression strength

(F_c in this table) is halved. This is reasonably consistent with the findings of refernce [29].

An estimation of the reduction in compression strength of the facesheets of co-cured sandwich panels, or any other properties, based on the observed reductions for solid laminates is not strictly valid. This is because the relationship between void content, and hence strength, and the applied cure pressure is much more complex.

The primary function of the applied pressure during any composite cure process is to compact the plies and assist resin flow, and in so doing reduce voids and improve the quality of the laminate. For a solid laminate stack the effect of the applied pressure and the resulting distribution of pressure and resin flow in the layers is well understood. Several thermophysical models exist (eg. reference [29]) to explain this behaviour during the cure. The applied pressure results in a cascading compaction of the plies and a flow of resin both between the plies and along the interfaces between them. In the co-cure process however, the uniform pressure distribution over the surface of the plies is altered by the presence of the honeycomb, since only the cell walls provide a stiff path to react the applied pressure. As highlighted by the manufacturing trials, the caul plate plays an important role in spreading the pressure to the cell walls by bridging the prepreg and preventing its collapse into the cell cavities. Consequently the applied pressure distribution will be concentrated in an hexagonal pattern at the facesheet-cell wall interfaces. One might therefore not expect much compaction of the plies in the central regions of the honeycomb cells other than that obtained during pre-consolidation of the facesheets. Nevertheless, because the effect of the pressure is to induce resin flow both parallel and perpendicular to the plies, it is likely to be squeezed out from the cell wall interface regions into the low pressure areas in the centre of the cells, as illustrated in fig. 4.5.

The resulting facesheet-honeycomb interface is shown in the photograph of fig. 4.6 for a 4-ply faced panel (magnified 5 times). The upper dark layer is the prepreg plies (the irregular surface is a consequece of the cut but

unpolished edge), the lower lighter layer is the film adhesive and the bright vertical band is a honeycomb cell foil. Good filleting of the adhesive at the cell wall evident in this picture resulted in a very strong facesheet-core bond in all manufactured panels. Although subsequent testing in some cases resulted in facesheet delamination the facesheet bond always remained intact. The picture also shows local distortion of plies at the cell wall junction which is consistent with the assumption of locallised high pressure and radial resin flow. Measurements from this picture show that the facesheet is compacted locally to a thickness of 0.34 mm - about 20% less than in other regions, at this position. The local compaction and distortion of the fibres at the cell wall interfaces may result in a decrease in dimpling strength, although the caul plate and tool surface ensure that the facesheet surfaces are flat.

The dimpling effect which was observed on both facesheets of co-cured sandwich with unperforated cores, even with a caul plate, can probably be attributed to a pressure differential set up across the facesheet during the cure. At some point hot air is trapped in the honeycomb cells as the prepreg and adhesive seal the facesheet-honeycomb interface. On cooling this air contracts and the pressure difference across the facesheets causes them to buckle inwards forming dimples.

4.4 CONCLUSION

Manufacturing trials carried out using the co-cure process indicated that the method is feasible for most envisaged spacecraft composite faced sandwich components. The method was developed sufficiently to enable cylindrical components and flat panels with integral core and facesheet reinforcements to be successfully produced. These techniques were later extended to fabricate a single piece central thrust tube structure, which is described later in detail in Chapter 9.

The adoption of a high pressure compaction cycle of the facesheets prior to lay-up and a cure pressure of 30 psi was expected to improve the structural integrity over vacuum-only co-cure methods. It was not possible to predict

the performance of co-cured sandwich manufactured in this way by direct comparison with data for low pressure cured laminates, because of the more complex pressure distribution and resin flow. In the following chapter the compression strength of a typical co-cured sandwich construction is determined by test and the results compared with predictions made based on data for low pressure cured laminates.

TABLE 4.1 RATIO OF VACUUM CURED TO AUTOCLAVE CURED PROPERTIES FOR AS-1/3501 CARBON-EPOXY LAMINATES

(from ref. [30])

Property	Ratio of VPC to Autoclave-Cured Dry Laminate at RT
F_t^d/F_t	0.88
F_c^d/F_c	0.50
F_s^d/F_s	0.90
E_t^d/E_t	1.00
E_c^d/E_c	0.87
G^d/G	0.91

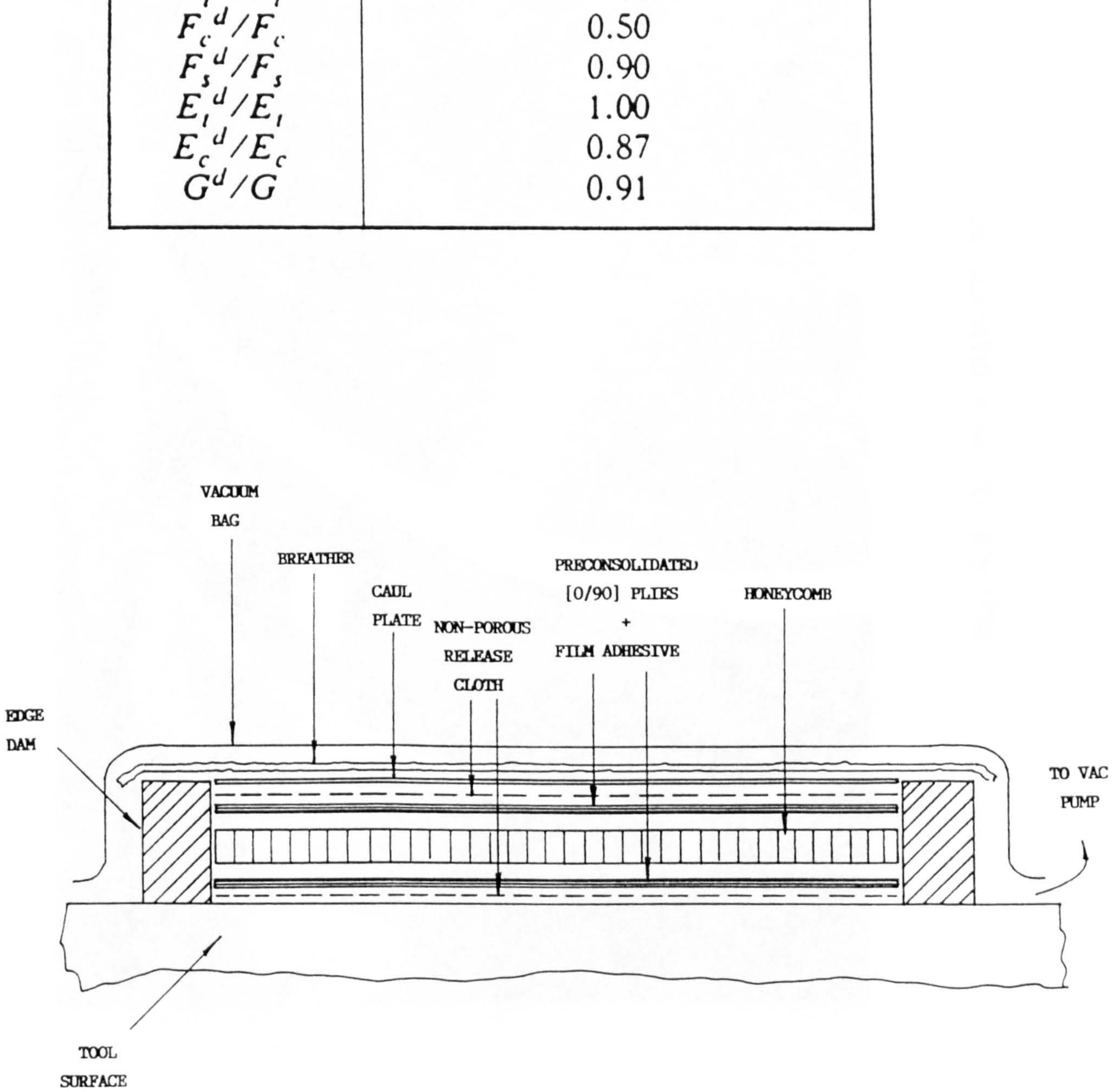

Fig. 4.1 LAY-UP STACK FOR CYLINDER CO-CURING TRIAL

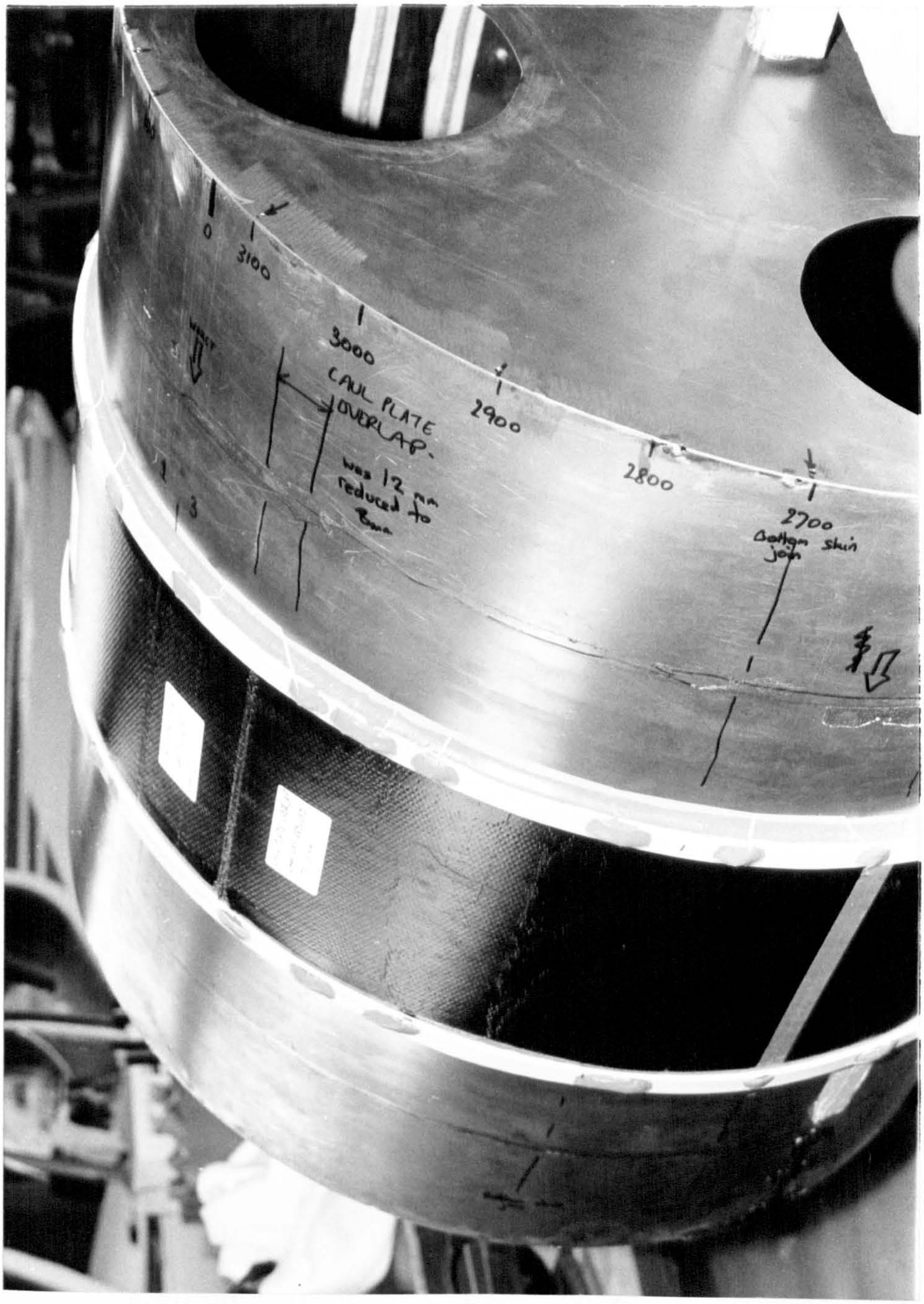

Fig. 4.2 CO-CURED TRIAL CYLINDER

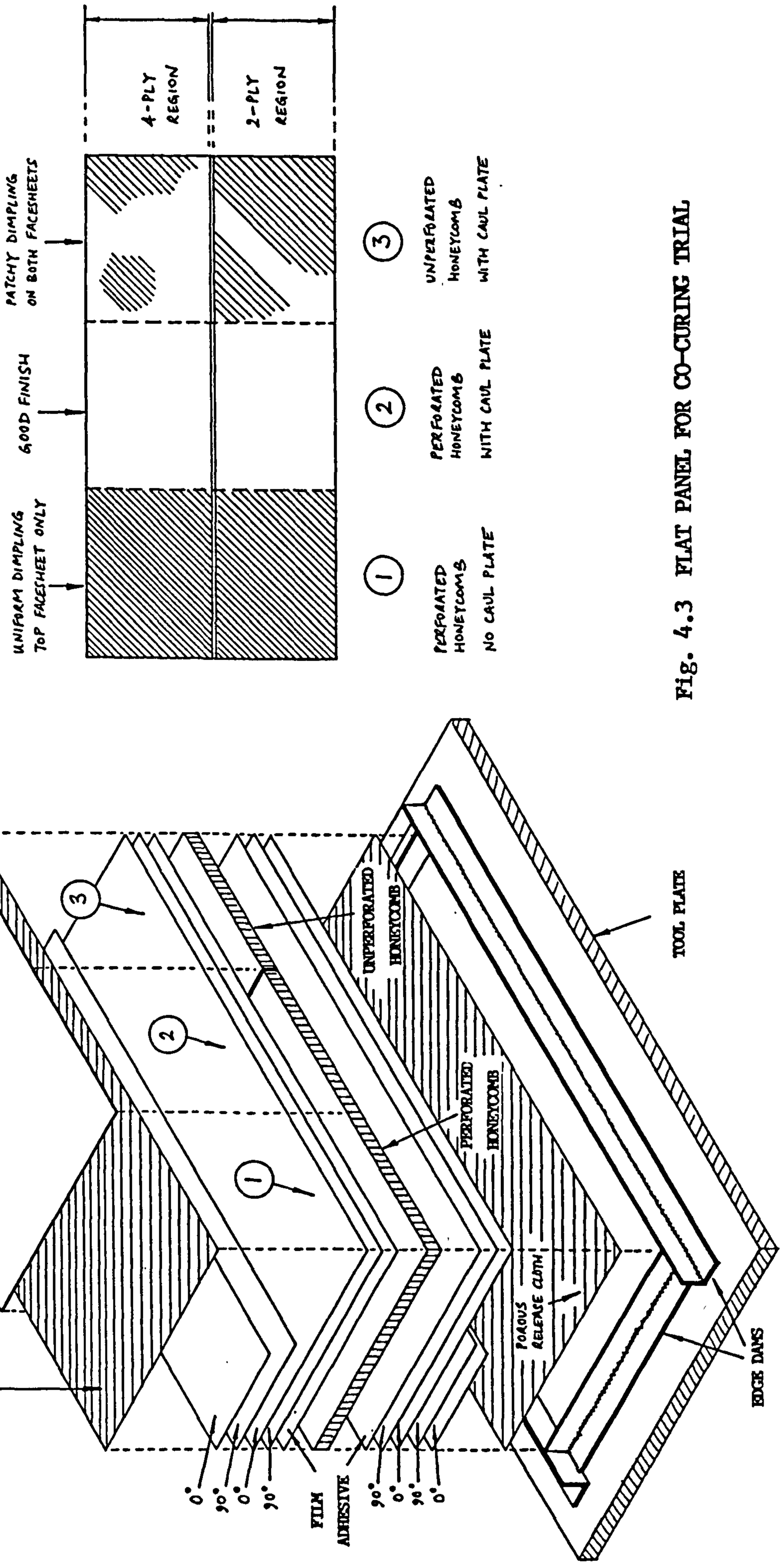

Fig. 4.3 FLAT PANEL FOR CO-CURING TRIAL

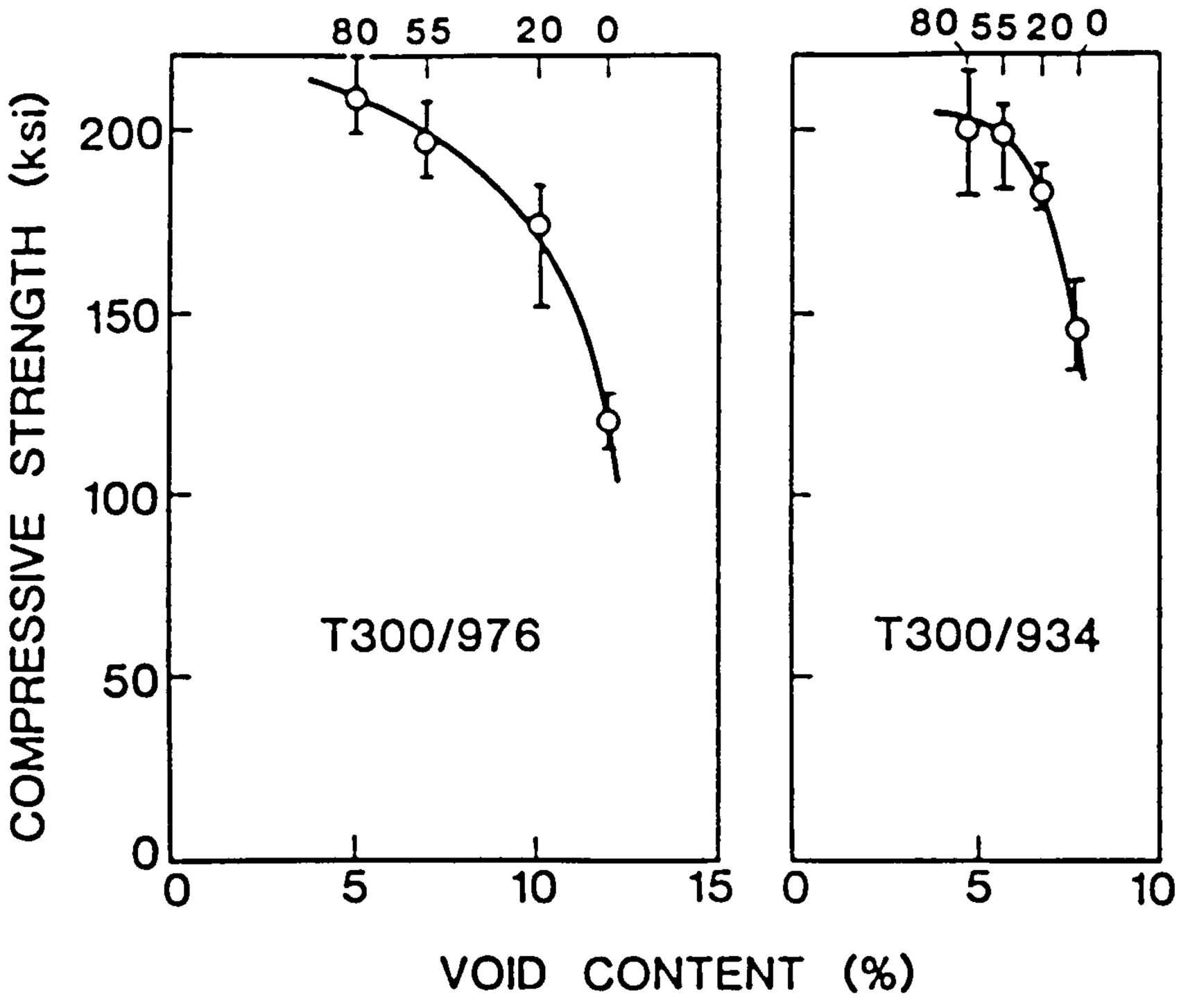

Fig. 4.4 EFFECT OF CURE PRESSURE & VOID CONTENT ON THE LONGITUDINAL COMPRESSIVE STRENGTH OF CARBON-EPOXY LAMINATES (from ref. [29])

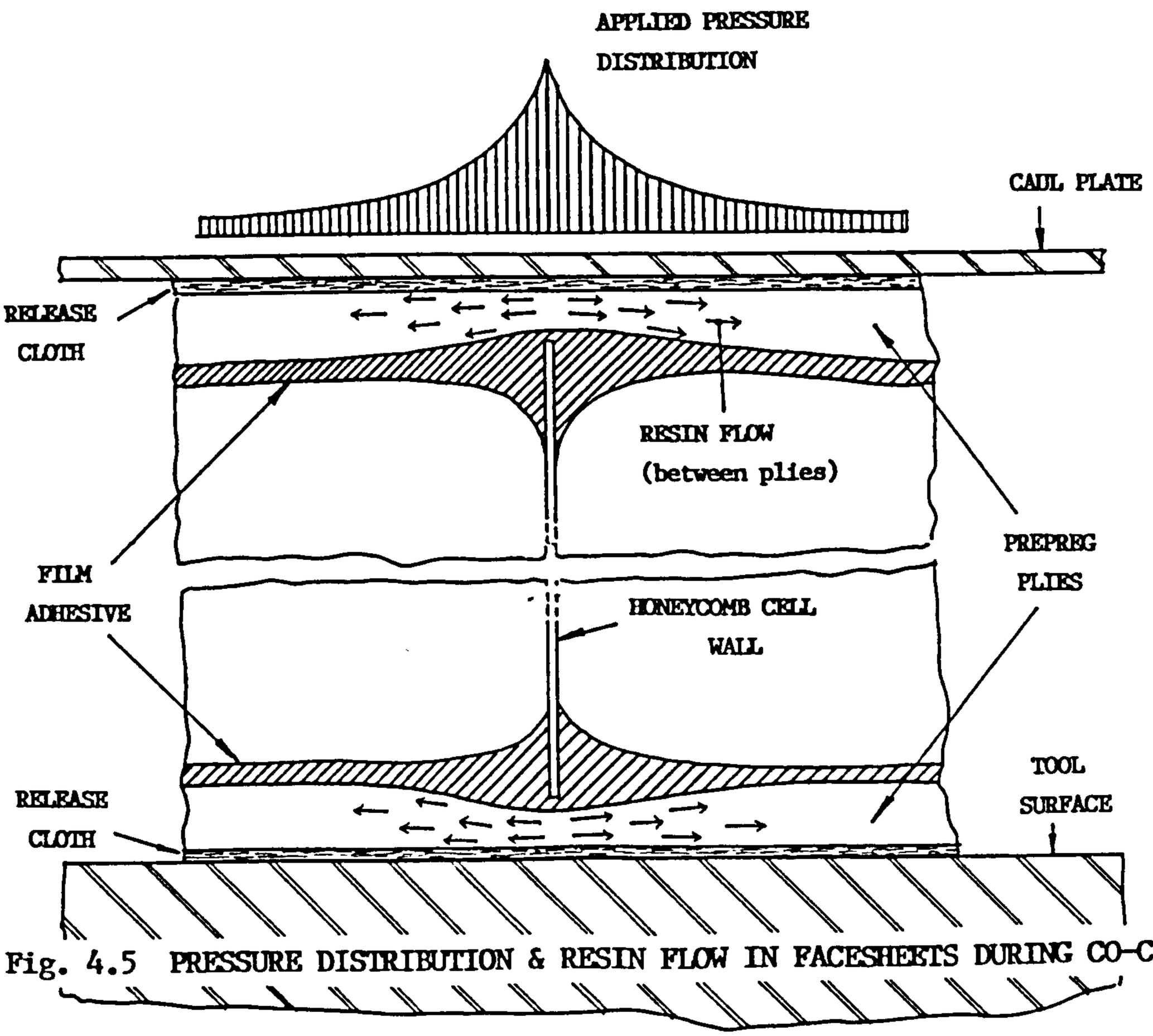

Fig. 4.5 PRESSURE DISTRIBUTION & RESIN FLOW IN FACESHEETS DURING CO-CURE

Fig. 4.6 FACESHEET-ADHESIVE-HONEYCOMB INTERFACE OF CO-CURED PANEL
(Magnification x 5)

CHAPTER 5 COMPOSITE SANDWICH STIFFNESS & STRENGTH

5.1 PHILOSOPHY FOR MECHANICAL PROPERTY PREDICTION

The prediction of the mechanical properties of composite laminates built up from a number of differently orientated plies is normally carried out by the use of a laminated plate analysis technique. This uses unidirectional material properties found from coupon tests to predict the strength and stiffness of more complex lay-ups. The advantage of this approach is a drastic reduction in the test effort since, theoretically at least, an infinite number of lay-ups and loading conditions can be investigated based on a relatively small series of unidirectional tests.

In this chapter the derivation of the constitutive matrix which characterises a composite laminate is outlined using laminated plate theory. The constitutive matrices for both the individual facesheets and the complete sandwich of a composite faced sandwich panel are essential for the prediction of overall panel behaviour, such as resonant frequencies and general buckling, and local behaviour, such as wrinkling and dimpling instability. Inversion of the constitutive matrix and the application of a laminate failure theory enables panel material strength to be predicted. Several of the more generally adopted laminate strength theories and the necessary manipulation to generate sandwich failure envelopes are described.

Underpinning laminated plate analysis, and hence the prediction of stiffness, vibration behaviour, material strength, and general & local buckling strengths, are the longitudinal and transverse material properties. These are normally derived by a series of tests on standard tension, compression and shear coupons. Ideally the manufacture of these coupons should reflect the manufacture of more complex constructions, the behaviour of which they are used to predict. For sandwich panels in which the facesheets are pre-cured prior to bonding, this is a straightforward matter of curing the coupons at the same pressure as the facesheets. However, an accurate reproduction of the pressure distribution and resin

flow in the facesheets of co-cured sandwich panels is not possible. It is necessary to either perform material testing on co-cured panels with unidirectional facesheets or rely on standard test coupons which are cured only under approximately the same conditions. The problem with the former approach is developing satisfactory test specimens and methods which overcome load introduction effects, achieve pure uniform loading conditions and avoid local instability failure modes. The latter approach enables data to be obtained using simple standard test methods but does not accurately reproduce the true facesheet co-cure conditions. An attempt was made to predict co-cured sandwich performance using this latter approach with laminate coupons cured at 30 psi.

5.2 STIFFNESS PREDICTION

5.2.1 Constitutive Matrix

The constitutive equation relates the strains and curvatures of a sandwich panel or individual facesheet to the applied stress and bending moment resultants. In matrix form, the equation is :

$$\begin{Bmatrix} N_X \\ N_Y \\ N_{XY} \\ M_X \\ M_Y \\ M_{XY} \end{Bmatrix} = \left[\begin{array}{ccc:ccc} A_{11} & A_{12} & A_{13} & B_{11} & B_{12} & B_{13} \\ & A_{22} & A_{23} & & B_{22} & B_{23} \\ \text{SYM} & & A_{33} & \text{SYM} & & B_{33} \\ \hdashline B_{11} & B_{12} & B_{13} & D_{11} & D_{12} & D_{13} \\ & B_{22} & B_{23} & & D_{22} & D_{23} \\ \text{SYM} & & B_{33} & \text{SYM} & & D_{33} \end{array}\right] \begin{Bmatrix} \epsilon_X \\ \epsilon_Y \\ \gamma_{XY} \\ k_X \\ k_Y \\ k_{XY} \end{Bmatrix} \qquad \text{(eq. 5.1)}$$

For a curved panel, the membrane strains and curvatures are given by :

$$\epsilon_x = \frac{\partial u}{\partial x} \quad \epsilon_y = \frac{\partial v}{\partial y} - \frac{w}{R} \quad \gamma_{xy} = \frac{\partial u}{\partial y} + \frac{\partial v}{\partial x}$$

$$k_x = \frac{-\partial^2 w}{\partial x^2} \quad k_y = \frac{-\partial^2 w}{\partial y^2} - \frac{1}{R}\frac{\partial v}{\partial y} \quad k_{xy} = \frac{-2\partial^2 w}{\partial x \partial y} - \frac{1}{R}\frac{\partial v}{\partial x}$$

where R refers to the radius of curvature in the Y-direction. For flat plates R approaches infinity. The sign of the curvatures is negative as a consequence of the sign convention adopted, which is shown in fig. 5.1. Bending moments are positive if they cause tension in the uppermost surface (or inside surface if cylindrical). This convention is retained throughout this report. Also, the twisting curvature, k_{xy}, includes the factor of 2. In some of the literature the factor of two is not included in k_{xy}, so that the A_{i3}, B_{i3} and D_{i3} elements of the constitutive matrix are factored by 2 instead.

The [A] extensional stiffness, [B] coupling stiffness, and [D] flexural stiffness matrix elements are calculated from :

$$A_{ij} = \sum_{k=1}^{n} (Q_{ij})_k \, (h_{k+1} - h_k)$$

$$B_{ij} = \frac{1}{2}\sum_{k=1}^{n} (Q_{ij})_k \, (h_{k+1}^2 - h_k^2) \qquad \text{(eqs. 5.2)}$$

$$D_{ij} = \frac{1}{3}\sum_{k=1}^{n} (Q_{ij})_k \, (h_{k+1}^3 - h_k^3)$$

by summing over all n layers of the laminate. The h_k are the relative positions of the k^{th} layer from the mid-plane of the stack as shown in fig. 5.2. The Q_{ij} represent the terms of the stress-strain relation matrix for each individual layer in the laminated plate axes. These depend on the

stiffness properties and orientation of the layer. The Q matrix is defined by the relationship:

$$[Q] = [T]^{-1}\,[b]\,[T]^{-T} \qquad \text{(eq. 5.3)}$$

where [b] is the layer reduced stiffness matrix given by :

$$[b] = \begin{bmatrix} \dfrac{E_1}{(1-\nu_{12}\nu_{21})} & \dfrac{\nu_{12}\,E_2}{(1-\nu_{12}\nu_{21})} & 0 \\ & \dfrac{E_2}{(1-\nu_{12}\nu_{21})} & 0 \\ \text{SYM} & & G_{12} \end{bmatrix} \qquad \text{(eq. 5.4)}$$

and [T] is the transformation matrix

$$[T] = \begin{bmatrix} \cos^2\theta & \sin^2\theta & 2\sin\theta\cos\theta \\ \sin^2\theta & \cos^2\theta & -2\sin\theta\cos\theta \\ -\sin\theta\cos\theta & \sin\theta\cos\theta & (\cos^2\theta-\sin^2\theta) \end{bmatrix} \qquad \text{(eq. 5.5)}$$

The expanded values of [Q] are :

$$Q_{11} = b_{11}\cos^4\theta + 2(b_{12} + 2b_{33})\sin^2\theta\cos^2\theta + b_{22}\sin^4\theta$$

$$Q_{12} = (b_{11} + b_{22} - 4b_{33})\sin^2\theta\cos^2\theta + b_{12}(\sin^4\theta + \cos^4\theta)$$

$$Q_{13} = (b_{11} - b_{12} - 2b_{33})\sin\theta\cos^3\theta + (b_{12} - b_{22} + 2b_{33})\sin^3\theta\cos\theta$$

$$Q_{22} = b_{11}\sin^4\theta + 2(b_{12} + 2b_{33})\sin^2\theta\cos^2\theta + b_{22}\cos^4\theta$$

$$Q_{23} = (b_{11} - b_{12} - 2b_{33})\sin^3\theta\cos + (b_{12} - b_{22} + 2b_{33})\sin\theta\cos^3\theta$$

$$Q_{33} = (b_{11} + b_{22} - 2b_{12} - 2b_{33})\sin^2\theta\cos^2\theta + b_{33}(\sin^4\theta + \cos^4\theta)$$

The [A], [B] and [D] matrices for a sandwich construction can be evaluated in the same way as a solid laminate by assuming the honeycomb to be a layer with near zero stiffness in the plane of the panel. For the honeycomb used in spacecraft sandwich construction, such an assumption is reasonable. Alternatively, the constitutive matrix for the sandwich can be derived from the constitutive matrices for the individual facesheets. This approach is useful when the constitutive matrices for both the separate facesheets and complete sandwich are required. The relationships are :

$$A_{ij}^{S/W} = A_{ij}^{F/S1} + A_{ij}^{F/S2}$$

$$B_{ij}^{S/W} = B_{ij}^{F/S1} + B_{ij}^{F/S2} + \bar{h}_1 A_{ij}^{F/S1} + \bar{h}_2 A_{ij}^{F/S2}$$

$$D_{ij}^{S/W} = D_{ij}^{F/S1} + D_{ij}^{F/S2} + 2\bar{h}_1 B_{ij}^{F/S1} + 2\bar{h}_2 B_{ij}^{F/S2} + \bar{h}_1^2 A_{ij}^{F/S1} + \bar{h}_2^2 A_{ij}^{F/S2}$$

(eqs. 5.6)

where the superscripts F/S1 and F/S2 refer to the upper and lower facesheets respectively and S/W to the complete sandwich. The relative positions of the facesheets are shown in fig. 5.3.

For a symmetric sandwich ie. one facesheet lay-up the mirror image of the other (as required for an undistorted co-cured panel) :

$$A_{ij}^{FS/1} = A_{ij}^{F/S2}$$

$$B_{ij}^{FS/1} = - B_{ij}^{F/S2}$$

$$D_{ij}^{F/S1} = D_{ij}^{F/S2}$$

and,

$$\bar{h}_1 = -\bar{h}_2$$

so the sandwich - facesheet constitutive relationship simplifies to :

$$A_{ij}^{S/W} = 2A_{ij}^{F/S1}$$

$$B_{ij}^{S/W} = 0 \qquad \text{(eqs. 5.7)}$$

$$D_{ij}^{S/W} = 2D_{ij}^{F/S1} + 2hB_{ij}^{F/S1} + \frac{1}{2}h^2A_{ij}^{F/S1}$$

where h is the separation distance of the facesheets. For typical spacecraft thin faced sandwich construction, the facesheet separation can be equated to the core thickness with little loss in accuracy.

5.2.2 Facesheet and Sandwich Coupling Effects

Coupling in the individual facesheet lay-ups or complete sandwich is governed by the terms of the corresponding constitutive matrices. The possible modes of coupling for non-zero constitutive terms are :

A_{13}, A_{23} = 0 : In-Plane Extension-Shear Coupling
B_{ij} = 0 : Extension-Flexural Coupling
D_{13}, D_{23} = 0 ; Bending-Twisting Coupling

For a co-cured sandwich construction, a balanced sandwich (facesheets symmetric) is a prerequisite to ensure $[B]_{S/W} = 0$ and no warpage occurs during the cure. However, no such requirement exists for the facesheets themselves, and because panel weight is optimised with a minimum of plies, these will in general have B_{ij} coupling present. In-plane coupling between extension and shear, A_{13} and A_{23} terms, can be avoided by ensuring that there is a ply orientated at $+\theta$ for every one at $-\theta$. Such an arrangement of facesheet plies is adopted in nearly all cases because it prevents shear strength being dependent on the shear direction. Consequently, extension-shear coupling is avoided in the complete sandwich also. Bending-twisting Coupling, D_{13} and D_{23} terms, can only be prevented by the use of special stacking sequences which cannot be efficiently utilised for thin sandwich

facesheets. Hence D_{13} and D_{23} terms will be present in general facesheet lay-ups. This coupling will also be present in the complete sandwich matrix, but these terms are small compared to the other D_{ij} terms. This is because, for large h and thin facesheets, the following approximation is valid :

$$D_{ij}{}^{S/W} \simeq \frac{1}{2} h^2 A_{ij}{}^{F/S}$$

Since A_{13} and A_{23} for the facesheets are generally zero, then D_{13} and D_{23} for the sandwich will be approximately zero.

This assumption is important, because the sandwich constitutive matrix then becomes effectively uncoupled since $A_{13} = A_{23} = D_{13} = D_{23} = 0$ and $B_{ij} = 0$. Consequently the analysis of spacecraft sandwich panels for material strength, vibration and compressive buckling is greatly simplified. However, coupling in the form of non-zero B_{ij} and D_{13} and D_{23} terms will in general be present for the individual facesheets. These complicate the analysis of the local instability phenomena of wrinkling and dimpling.

5.3 FACESHEET STRENGTH PREDICTION

5.3.1 Ply Stresses

Individual ply stresses under a given set of applied stress and moment resultants can be determined by inversion of the sandwich constitutive matrix and transformation of the resulting plate strains to ply stresses. This procedure can be greatly simplified for the case of an uncoupled symmetric sandwich by considering equivalent membrane stress resultants only, with little loss in accuracy. For a thick core and thin facesheets, the applied bending and twisting moments can be replaced by an equivalent membrane stress resultant couple with opposite signs in the two facesheets by applying simple bending theory. Adding the membrane loads applied to the complete sandwich, which are shared equally between the symmetric facesheets, the equivalent facesheet membrane loads become :

$$\begin{Bmatrix} N_X \\ N_Y \\ N_{XY} \end{Bmatrix}_{F/S} = \frac{1}{2} \begin{Bmatrix} N_X \\ N_Y \\ N_{XY} \end{Bmatrix}_{S/W} \pm \frac{1}{h} \begin{Bmatrix} M_X \\ M_Y \\ M_{XY} \end{Bmatrix} \qquad \text{(eq. 5.8)}$$

The ply stresses can then be obtained by pre-multiplying the equivalent membrane loads by the inverted facesheet [A] matrix, and transformation of the facesheet strains to individual ply stresses in the local material axes. The matrix transformation is :

$$\begin{Bmatrix} \sigma_1 \\ \sigma_2 \\ \tau_{12} \end{Bmatrix}_K = [b]_K \, [T]_K \, [A]^{-1}_{F/S} \begin{Bmatrix} N_X \\ N_Y \\ N_{XY} \end{Bmatrix}_{F/S} \qquad \text{(eq. 5.9)}$$

By considering the two facesheets as a balanced pair, loaded only by membrane stress resultants, it is only necessary to invert the facesheet [A] matix, rather than the full sandwich constitutive matrix. The [B] and [D] matrices are neglected because these govern only the small stress resultant gradient through the facesheet thickness under bending. The use of equivalent membrane loads assumes a uniform stress through the thickness so that this gradient becomes zero. For all practical purposes therefore, the stresses in the facesheet plies, and hence the panel strength, are essentially independent of the facesheet ply stacking sequence, since this only affects the [B] and [D] facesheet constitutive matrices. The above can be shown to be a valid approximation for core to facesheet thickness ratios of 20 or more, which covers the majority of spacecraft sandwich constructions.

5.3.2 Laminate Failure Theories

The sandwich facesheet strength margin under load can be predicted by applying one of numerous laminate failure theories to the computed ply stresses given by equation (5.4). An excellent review of the various theories is given in reference [31]. No one theory has emerged as superior to any of the others. The Maximum Stress and Minimum Strain theories, and a

number of stress interaction theories including those of Hoffmann, Tsai-Wu and Tsai-Hill are commonly used. All of these theories compare the direct stresses (or strains) parallel and perpendicular to the fibre direction and the shear stress in each layer with a particular failure criteria. Failure is normally considered to occur once the stresses in one ply are such that the criteria is exceeded. A more rigorous application of the theories considers a redistribution of load in the laminate after first ply failure, and failure of the laminate is then deemed to occur when all the plies have failed. For most practical purposes, first ply failure is a sufficiently accurate criterion for failure.

The Maximum Stress and Maximum Strain Theories are perhaps the simplest of those commonly used. No account is taken of any interaction between the stresses in each ply, but nevertheless they do indicate the possible mode of failure which is a limitation of the interaction theories. Failure is deemed to occur when the longitudinal, transverse or shear stresses (or strains for the Maximum Strain Theory) in a ply exceed the corresponding unidirectional laminate strengths. Correlation between experimental and theoretical strengths using the Maximum Stress or Strain Theories is not good for combined loading actions.

Stress interaction failure theories for composites are based on extensions of Von Mises failure criteria for isotropic materials. Most of these theories have failure criteria of the following form :

$$F_i \sigma_i + (F_{ij} \sigma_i \sigma_j)^{\alpha} = 1 \qquad \text{(eq. 5.10)}$$

where the σ_i are ply stresses (i = 1 longitudinal, i = 2 transverse, i = 3 shear) and F_i are strength tensors found from the unidirectional laminate strengths, α = 1 or 1/2. Interaction theories of this form are summarised in Table 5.1, which is reproduced from reference [31]. In this table, X and Y are the longitudinal and transverse tension strengths, and X' and Y' are the corresponding compression strengths. These are given as X_T, Y_T, X_C and Y_C throughout the rest of this work. S is the unidirectional laminate shear strength.

The theory of Tsai and Hill can be expressed by the following criterion equation :

$$\left(\frac{\sigma_1}{X}\right)^2 + \left(\frac{\sigma_2}{Y}\right)^2 + \left(\frac{\tau_{12}}{S}\right)^2 - \left(\frac{\sigma_1 \sigma_2}{X}\right)^2 = 1 \qquad \text{(eq. 5.11)}$$

Usually this criteria is employed with $X = X_T$ or X_C and $Y = Y_T$ or Y_C depending on the sign of the stresses σ_1 and σ_2. The shortcoming of this theory is that the interaction effect is fixed between the stress components.

The Tsai-Wu theory was developed to more adequately predict experimental results. This criteria is expressed by :

$$F_{11}\sigma_1^2 + F_{22}\sigma_2^2 + F_{33}\tau_{12}^2 + F_1\sigma_1 + F_2\sigma_2 + F_3\tau_{12} + 2F_{12}\sigma_1\sigma_2 = 1 \quad \text{(eq. 5.12)}$$

where the strength tensors are :

$$F_{11} = 1/X_T X_C \qquad F_1 = 1/X_T - 1/X_C$$
$$F_{22} = 1/Y_T Y_C \qquad F_2 = 1/Y_T - 1/Y_C$$
$$F_{33} = 1/S_T S_C \qquad F_3 = 1/S_T - 1/S_C$$

S_T and S_C are the tension and compression shear strengths which are equal if testing is carried out in the principal directions, then the F_3 term vanishes. The F_{12} off-diagonal tensor term accounts for independent interaction between the stress components and must be determined by biaxial tests. Performing reliable biaxial testing is difficult and is a drawback of this theory. In some cases for carbon-epoxy the F_{12} term, which is difficult to derive from test, is neglected. Reference [32] suggests using :

$$F_{12} = -\frac{1}{2}\sqrt{F_{11}\ F_{22}}$$

when bi-axial test data is not available.

The theories of Ashkenazi and Malmeister are similar to that of Tsai-Wu except for differences in the determination of the F_{12} interaction term. Theories suggested by Cowin and by Hoffman are also similar but have fixed interaction coefficients which can be derived from uniaxial test data. In the Cowin theory, the interaction term is given by :

$$F_{12} = \sqrt{F_{11}\ F_{22}} - \frac{1}{2S^2}$$

and in the Hoffmann theory the interaction term is :

$$F_{12} = -\frac{1}{F_{11}}$$

The theory of Tsai-Wu was extended by Tennyson to include cubic terms. The failure criterion is given by :

$$F_{11}\sigma_1^2 + F_{22}\sigma_2^2 + F_{33}\tau_{12}^2 + F_1\sigma_1 + F_2\sigma_2 + 2F_{12}\sigma_1\sigma_2 + 3F_{112}\sigma_1^2\sigma_2 + 3F_{221}\sigma_2^2\sigma_1 + 3F_{133}\sigma_1\tau_{12}^2 + 3F_{233}\sigma_2\tau_{12}^2 = 1 \qquad \text{(eq. 5.13)}$$

where the linear and quadratic terms are those of the Tsai-Wu theory and the cubic terms F_{112}, F_{221}, F_{133} and F_{233} are evaluated from biaxial test data and constraint equations. The further reliance on biaxial test data has meant that this theory has not been readily adopted.

The quadratic interaction theories give quite good correlation with observed strengths under combined loads. Of these, the Tsai-Wu type have enjoyed the most popularity but usually with the F_{12} term assumed zero or based on uniaxial test data. In the current work, the Tsai-Wu theory has generally been adopted, although because no biaxial testing was performed F_{12} was taken to be :

$$F_{12} = -\frac{1}{2}\sqrt{F_{11}\ F_{22}}$$

5.3.3 Failure Envelopes

It is possible to substitute the equation for ply stresses, equation (5.9) into one of the quadratic interactive failure criteria, such as the Tsai-Wu criteria of equation (5.12), to yield an ellipsoidal failure surface for each ply in stress-resultant space. The intersection of the individual ply ellipsoid surfaces defines the failure surface for the laminate. For a component with only two of the three membrane stress resultants : N_X, N_Y and N_{XY} applied, the failure surface is 2-dimensional and can be readily plotted to give a meaningful failure envelope. This is a useful visual aid for the comparison of several possible facesheet lay-ups under several design load cases, which can be more effective than numerous failure index computations.

For sandwich constructions loaded predominantly by axial and shear stress resultants, such as thrust tube shells for example, the ply failure envelopes can be determined by substituting equation (5.9) with $N_Y = 0$ into equation (5.12). This results in a quadratic of the following form for each ply :

$$a\,N_{XY}^2 + b\,N_{XY} + c = 0 \qquad \text{(eq. 5.14)}$$

where,

$$a = F_{11}X_{13}^2 + F_{22}X_{23}^2 + F_{33}X_{33}^2 + F_{12}X_{13}X_{23}$$

$$b = N_X(2F_{11}X_{11}X_{13} + 2F_{22}X_{21}X_{23} + 2F_{33}X_{31}X_{33} + F_{12}(X_{13}X_{21} + X_{23}X_{11})) + (F_1X_{13} + F_2X_{23})$$

$$c = N_X^2(F_{11}X_{11}^2 + F_{22}X_{21}^2 + F_{33}X_{31}^2 + F_{12}X_{11}X_{21}) + N_X(F_1X_{11} + F_2X_{21}) - 1$$

and X_{ij} refer to elements of matrix [X], for each ply, given by :

$$[X] = [b]_K\,[T]_K\,[A]_{F/S}^{-1}$$

F_i, F_{ii}, F_{ij} are strength tensors for the Tsai-Wu failure criterion given in equation (5.12).

Similar quadratics can be derived for intersections of the ply failure surfaces on other stress resultant planes. For a panel loaded predominantly by bending moments it is possible to derive the quadratic in terms of N_X and N_Y to represent the equivalent facesheet membrane stress resultants for example.

A computer program was written to generate the elliptical ply failure curves on the $N_Y = 0$ plane. An example of the resulting failure envelope for a $[0_2/\pm45]$ HM-S/CYCOM 985 faced sandwich construction is given in fig. 5.4. This is discussed later in this chapter.

Particular points on the ply failure ellipse can be determined by substitution into equation (5.14). For example, the axial tension and compression strengths of a given construction can be found by setting $N_{XY} = 0$. The lowest positive solution for N_X, for each of the constituent ply orientations, is the tension strength, and the lowest negative solution is the compression strength. The solution is :

$$N_X = \frac{-d \pm \sqrt{d^2 - 4c}}{2c} \qquad \text{(eq. 5.15)}$$

where,

$$c = F_{11}X_{11}^2 + F_{22}X_{21}^2 + F_{33}X_{31}^2 + F_{12}X_{11}X_{21}$$
$$d = F_1X_{11} + F_2X_{21}$$

and [X], F_{ij} are defined previously.

5.4 GENERATION OF 30 PSI CURED MATERIAL PROPERTY DATA FOR HM-S/CYCOM 985 CARBON-EPOXY

Longitudinal, transverse and shear data for undirectional HM-S/CYCOM 985 laminates cured at 30 psi were derived from a series of tests. The following stiffness and strength properties are required in order to formulate the constitutive matrices and predict laminate strength:

STIFFNESS:	E_1	Longitudinal Young's Modulus
	E_2	Transverse Young's Modulus
	v_{12}	Major Poissons Ratio
	G_{12}	In-Plane Shear Modulus
STRENGTH:	X_T	Longitudinal Tension Strength
	X_C	Longitudinal Compression Strength
	Y_T	Transverse Tension Srength
	Y_C	Transverse Compression Strength
	S	In-Plane Shear Strength

These were derived from tension, compression and shear tests on coupon specimens with fibres orientated in the longitudinal and transverse directions.

5.4.1 Laminate Panel Manufacture

Two unidirectional laminated panels were manufactured using the same cure cycle used to manufacture the co-cured sandwich panels. This consisted of a room temperature pre-consolidation cycle at 80 psi prior to cure at 180°C and 30 psi. One panel was built up of 10 plies (nominal thickness 1 mm) for the tension and shear coupons, the other of 20 plies (nominal thickness 2 mm) for the compression coupons. Fibre volume fraction was quoted as 60.1% by the manufacturer's outgoing inspection. All tests were carried out at room temperature and nominal moisture contents.

5.4.2 Tension Tests

Tension tests were carried out on longitudinal and transversely orientated unwaisted coupons of nominal dimensions : 250 mm L x 20 mm W x 1 mm T. Aluminium end tags were bonded to each end with REDUX 403 two-part epoxy to facilitate gripping in the test machine. The test machine was an Instron 1195 run at a cross head speed of 0.5 mm/min.

A total of 13 longitudinal coupons were cut from the panel and tested, of which 3 were strain gauged with cruciform gauges to enable Modulus and

Poissons Ratio data to be derived. In all cases failure was near the centre of the coupon. The results are summarised in Table 5.2. The mean ultimate longitudinal tension stress (X_T) was 1202 MPa, but the data showed quite large scatter with a Coefficient of Variation of 13.7%. The stress-strain curves for the strain gauged coupons given in fig. 5.5 exhibit high linearity. The mean longitudinal tension modulus (E_{1T}) found from these curves was 192.4 GPa with only a small variation.

Of the 13 transverse coupons, 4 failed prematurely whilst setting up in the machine because of the low strength in this direction. Results for the other coupons are summarised in Table 5.3. The mean transverse tension strength (Y_T) was 37.7 MPa with a Coefficient of Variation of 9.3%. None of the coupons were strain gauged, but a surface mounted extensometer was used to enable stress-strain curves (fig. 5.6) and a transverse tension modulus (E_{2T}) to be derived. The mean modulus found was 6.8 GPa.

5.4.3 Compression Tests

The derivation of reliable compression strength data is difficult because of the problem of specimen buckling. A number of methods have been proposed for composite material compression testing. The method adopted in this work was the ASTM method D3410-75, sometimes known as the Celanese Method. This relies on a very short unsupported gauge length to prevent buckling. The test fixture is shown in fig. 5.7. Conical shaped grips centered by tapered collets are designed to transfer a uniform non-eccentric compression load into the specimens, which measure 140 mm L x 6.35 mm W x 2.0 mm T, via bonded aluminium end tags. The tags are bonded over almost the entire length of the coupons other than a 12.7 mm unsupported gauge length.

A total of 20 coupons were cut from the thicker panel with fibres orientated longitudinally. All but 2 were successfully set up and tested. The test machine was an Instron 1195, the cross head speed was 0.5 mm/min. The ultimate longitudinal compressive strengths (X_T) are summarised in Table 5.4. The mean strength was 882 MPa, somewhat lower than the tension strength as expected, and the scatter in the data was also larger having a Coefficient of Variation of 17.6%. Four of the coupons were strain gauged

with back-to-back cruciform gauges. Output from these gauges and a dial gauge indicated no evidence of buckling prior to failure. The average of the gauges was used to generate the compression stress-strain curves shown in fig. 5.8. A slight non-linearity is evident. Modulus values were calculated at the 0.2% strain level. The mean longitudinal compression modulus (E_{1C}) found was 157.4 GPa, significantly lower than the tension modulus. The Poissons Ratio found from the transverse strain data had a mean value of 0.305 which was comparable to the value calculated from the tension tests.

5.4.4 Shear Tests

In-plane shear testing was carried out using the ASTM D4255-83 method, sometimes known as the 2-rail shear method. In this method specimens are loaded in shear by opposed tension loads in two steel loading rails. The rails are clamped to the specimen edges by bolts which pass through over-size holes drilled through the specimen, fig. 5.9. The specimens measure 152 mm L x 63.5 mm W x 1.0 mm T and have six holes of 12.7 mm diameter. Testing was carried out on a Dartec hydraulic machine.

A total of 8 coupons were cut and drilled but the brittle nature of the material meant 4 of these failed during mounting in the test rig. Another failed at a very low load and this was thought to be a result of damage during setting up. The ultimate shear stresses (S) are summarised in Table 5.5. The mean value, excluding the damaged coupon (no. 3), was 46.8 MPa and the data from the 3 successful tests was very consistent. All the coupons were instrumented with cruciform strain gauges at 45° to enable shear stiffness data to be derived. The averages of the two gauges were used to produce the shear stress-strain curves shown in fig. 5.10. These exhibit the high strain and non-linear behaviour of the resin dominated shear properties. Tangent shear moduli (G_{12}) were calculated at the 0.2% strain level and are given in Table 5.5 also. The mean value found from 4 tests was 3.75 GPa.

5.4.5 Average Properties and Design Allowables

The average material properties found from the above tests were subsequently used with laminate theory to generate constitutive matrices for sandwich constructions. These enabled strength, stiffness and stability predictions to be compared with test results on co-cured sandwich incorporating this facesheet material. For design purposes however, the average property values are statistically reduced to 'allowable' values to account for material variability. This variability can be quite large for composite materials, strength properties in particular, as shown by the data scatter in the tests described above.

Reducing the test data to formulate design allowables is achieved by fitting a statistical model to the data. For composite material properties either Normal, Log-Normal, 2-Parameter Weibull or 3-Parameter Weibull distribution models are usually assumed. All of these distributions have been shown to be reasonable descriptions based on 'goodness of fit' tests[33]. Design allowables calculated using different distribution models show only small variations (less than 1% in reference [33] for a sample of 25 composite longitudinal tension strength data). The Normal distribution was therefore adopted in the current work because of its simplicity. The mean properties are reduced to 'A' design allowables by the following formula :

$$X_A = \overline{X} - K_A S \qquad \text{(eq. 5.16)}$$

where,

X_A = 'A' Design Allowable - exceeded by 99% of the population with 95% confidence.

$\overline{X}$ = Population Mean (= Sample Mean)

K_A = 'A' Tolerance Limit Factor. Found from tables for a given sample size, eg. reference [34].

S = Population Standard Deviation

$$S^2 = \frac{n}{(n-1)} s^2$$

s = Sample Standard Deviation

n = Sample Size

'A' allowables were only calculated for the strength properties since the strain gauged sample sizes were too small to produce statistically meaningful modulus properties. Mean modulus values were used for design because the data showed small scatter and for the overall stiffness of a large component local changes in modulus will be averaged out. For the analysis of sandwich panel bending, vibration and buckling instability (where the assumed modes are dominated by flexure) an average of the longitudinal tension and compression moduli was taken.

Because no compression tests were carried out on transversely orientated coupons, an estimate of the average transverse compression strength (Y_C) was assumed based on similar material systems. This value was simply halved to give a design allowable.

The average and allowable material properties for the 30 psi cured HM-S CYCOM 985 UD material are given in Table 5.6. The large reductions in the average strengths to produce the design allowables is evident from this table. The longitudinal tension and compression strengths are reduced by factors of 0.48 and 0.39 respectively to account for the high material property variability.

5.4.6 Effect of Low Pressure Cure on Material Properties

A test program was not carried out on laminated coupons cured at higher pressures so a direct comparison with properties derived from the low pressure cured HM-S/CYCOM 985 system was not possible. Nonetheless it was possible to gauge the effect of low cure pressure on properties by comparison with existing test data for similar material systems cured under standard conditions.

Table 5.7 compares average properties of the 30 psi cured HM-S/CYCOM 985 system with HM-S/Fibredux 914 cured under standard pressure (from reference

[25]). Both systems contain identical carbon fibres at 60% volume fractions in similar 180°C curing epoxies. A direct comparison between fibre dominated longitudinal properties is therefore reasonable. The longitudinal modulus (E_1), and longitudinal strengths (X_T and X_C) are similar in both cases. The similarity between the compression strengths is perhaps a little surprising given the sensitvity of this property to cure pressure, but the big difference in this respect seems to be in the data scatter, with the low pressure cured material exhibiting a much larger Coefficient of Variation. If the 'A' allowable strengths are calculated from these data, one finds that the low cure pressure material compression strength allowable is only 46% that of the standard cure pressure material, and the ratio for tension strength is 79%. However, the Coefficient of Variation for the longitudinal compression strength of the standard pressure cured HM-S/Fiberite 914 is unusually low, indicating a particularly high quality laminate and this results in a high design allowable value. A more typical Coefficient of Variation is 10%.

Table 5.8 compares the design allowable properties for low pressure cured HM-S/CYCOM 985 material with allowables generated for the similar HM-S/Code 69 system used for design of the Ariane 4 SPELDA structure[28]. This data refered to material cured at standard pressure. Comparing the two sets of data shows the allowable stiffness properties are similar. The allowable longitudinal tension stress of the low pressure cured material is actually higher, and the longitudinal compression stress is 63% of the corresponding allowable for the standard cure pressure material. This ratio of compression stress allowables for 30 psi and 100 psi cured material is more representative of the expected property reduction, being slightly higher than the ratio of 50% for vacuum cured to autoclave cured material given in Table 4.1. The allowable transverse strength properties are higher for the low pressure cured material, but this is likely to be a consequence of the different resins. The allowable shear stress is considerably smaller for the low pressure cured material. This can be mainly attributed to the small number of data points used to generate the allowable value and reflects statistical uncertainty rather than a reduction in performance.

In order to reduce design allowable data for a material system cured at standard autoclave pressure to that cured at low pressure (30 psi), such as the facesheets of a co-cured sandwich, the reduction factors given in Table 5.9 are suggested, based on Table 5.8 and the above discussion. These were used in later numerical examples to estimate co-cured material properties where low cure pressure data was unavailable.

5.5 EXPERIMENTAL STIFFNESS & STRENGTH OF [0/±45/0] HM-S/CYCOM 985 FACED SANDWICH CONSTRUCTION

A test program was undertaken to obtain compressive strength and stiffness data for a co-cured sandwich construction to check the validity of strength and stiffness predictions using 30 psi cured coupon data and Laminate Theory. The sandwich lay-up used for these tests was that of the T-Sat thrust cylinder shell construction which enabled the compression strength to be compared with the design compression loading, since the actual cylinder was not statically tested to destruction.

5.5.1 Panel Construction

A flat sandwich panel was manufactured using the co-cure cycle described in the previous chapter, and identical to the cycle used to manufacture the full thrust cylinder. This cycle included a cold pre-consolidation of the facesheet plies at 80 psi and cure of the sandwich at 30 psi and 180°C. The panel construction was :

Facesheets : [0/±45/0] HM-S/CYCOM 985 UD
V_f = 60%, t_{ply} = 0.10 mm
Adhesive : FM300M
Core : 5056 5.7-3/16"-0.0020" Aluminium honeycomb
h = 10 mm

5.5.2 Compression Specimens

Specimens were all cut from the one panel with nominal dimensions of 50 mm length x 70 mm width with the honeycomb ribbon aligned with the specimen length. Twenty millimetre 18 SWG aluminium tags were bonded with room temperature REDUX 403 adhesive at each end with an overlap of 10 mm. The cavity formed by the end tags was filled with epoxy and subsequently machined flat. The dimensions of the specimens are shown in fig. 5.11. The purpose of the filled ends was to facilitate compression load introduction to the facesheets and stabilise the loaded edges of the sandwich against local buckling. The original design for the specimens did not incorporate aluminium tags, and instead required honeycomb to be cut out at the ends and the cavity so formed filled with epoxy. However, because the co-cured facesheets themselves were unbalanced, it was found that removal of the honeycomb caused the facesheets to warp inwards. The tagged system was therefore adopted to avoid this effect.

The relatively small specimen length - 30 mm between the end tags, was selected to give a high overall buckling resistance. Similarly a 5.7 lb/cu ft core was used to improve overall buckling and local wrinkling instability strength. This core had the same cell size as the 2.0 lb/cu ft core used in the T-Sat thrust cylinder wall construction, so manufacturing aspects governed by the core were the same.

5.5.3 Predicted Specimen Stiffness & Strength

The specimen stiffness and critical loads for different modes of failure were predicted based on the unidirectional properties found from the 30 psi cured coupons summarised in Table 5.6. The membrane stiffness of the sandwich was calculated using laminated plate theory outlined in section 5.2.1. The [A] matrix for the complete sandwich was :

$$[A] = \begin{bmatrix} 94020 & 18690 & 0 \\ & 23800 & 0 \\ \text{SYM} & & 20100 \end{bmatrix} \text{ N/mm}$$

A strength envelope under combined axial and shear loading (the dominant loads on the thrust cylinder) was calculated using the method described in section 5.3.3. This is plotted in fig. 5.4. The resulting envelopes for average strength properties and design allowables from laminated coupon test data are both shown. These are defined by the intersection of the failure ellipses for the 0° plies, the +45° ply and the -45° ply. The large reduction in the design allowable envelope is evident. The principal design load vectors, (N_x = -96 N/mm, Nxy = 14 N/mm) and (Nx = -32 N/mm, N_{xy} = 20 N/mm) for the thrust cylinder are safely encompassed by this lay-up with the critical case being high axial compression. The average compression strength predicted for the sandwich is given by the intersection of the average strength failure envelope with the negative N_x axis. This was calculated to be 290 N/mm using equation (5.15). The corresponding 'A' allowable was found to be 124 N/mm.

Other stability failure modes : overall (Euler) buckling, wrinkling and facesheet dimpling were calculated from the predicted constitutive matrix using theory described later in Chapter 6. Overall instability assumed a free length of 50 mm and simply supported loaded ends. The predicted failure loads are summarised in Table 5.10.

TABLE 5.10 PREDICTED FAILURE MODES

FAILURE MODE	COMPRESSION LOAD N_X (N/mm)
Facesheet Compression	290 (av.) 124 ("A")
Overall Buckling	3798
Wrinkling	2372
Dimpling	728

The likely mode of failure was therefore facesheet compression.

5.5.4 Compression Tests

The sandwich specimens were positioned between the loading platens of an Instron 1195 machine, with a self-aligning lower table to ensure an even load introduction, see fig. 5.12. Sixteen specimens were tested. 3 of which were strain gauged with 0°/90° cruciform gauges. Load and strain data for the strain gauged specimens was recorded on a data logger, and load only data was recorded by a chart recorder for the others. Load data was converted to an N_x stress resultant by dividing by the specimen width.

The specimens were found to exhibit linear behaviour up to failure which occured as fracture of the facesheets. Generally, failure of both facesheets was virtually instantaneous, and along a line perpendicular to the load direction in the centre of the specimen. In some cases the line of failure was saw-toothed as it followed the +45° and -45° plies. The observed mode of failure was in agreement with the facesheet compression failure predicted. The position of the failure surface away from the end tags and on both facesheets, indicated that a reasonably uniform load introduction to the specimens had been achieved. In one case, specimen No. 3, failure occured in one facesheet only. This specimen failed at a particularly low load and suggested an uneven load distribution between the two facesheets, possibly because of non-flat ends. This data point was cast out when calculating the mean failure strength.

5.5.5 Comparison of Test Results and Predictions

The ultimate loads for the 16 specimens are given in Table 5.11. The mean failure load, based on 15 data points, was 321 N/mm, 11% greater than the predicted failure load of 290 N/mm. The coefficient of variation on the data was 10.9% which was significantly better than the variation found for the unidirectional coupon compression data. The "A" value calculated from these sandwich test data of 194 N/mm, is consequently over 50% higher than the "A" allowable of 124 N/mm based on coupon test results. This would tend to suggest that the co-cured facesheet quality is better than solid laminates cured at the same low pressure. This may be as a result of

improved resin flow arising from high local pressure on co-cured facesheets at the honeycomb cell wall interfaces.

Fig. 5.13 shows plots of the compressive load-strain curves for the three strain gauged specimens. Also plotted on the same figure is the predicted longitudinal stiffness. The slope of this line is found by inverting the sandwich [A] matrix. The longitudinal load-strain relationship is then given by :

$$N_x = \frac{A_{11}A_{22} - A_{12}^2}{A_{22}} \epsilon_x \qquad \text{(eq. 5.16)}$$

The slope can be regarded as an equivalent Young's modulus multiplied by the combined facesheet thicknesses, assuming the stiffness contribution of the core and film adhesive is negligible. The equivalent facesheet Young's modulus, E_x, was predicted to be 95.4 GPa. The values found from the strain gauged specimens at the 0.2% strain strain level are given in Table 5.9. These assume a cured ply thickness of 0.104 mm (measured from cured laminates). The average equivalent modulus was 93.6 GPa which is in good agreement with the prediction, although with greater variability over the 3 specimens than for the unidirectional coupon modulus.

In fig. 5.14 the compressive load is plotted against the transverse strain across the specimen width. The transverse strain results from the Poisson's effect. The relationship can be predicted by :

$$N_x = - \frac{(A_{11}A_{22} - A_{12}^2)}{A_{12}} \epsilon_y \qquad \text{(eq. 5.17)}$$

and an equivalent major Poisson's ratio from :

$$\nu_{xy} = \frac{A_{12}}{A_{22}} \qquad \text{(eq. 5.18)}$$

The transverse strains found from the tests were somewhat smaller than predicted, indicating a lower Poisson's ratio. The equivalent Poisson's

ratios found are given in Table 5.9. The mean value was 0.559 compared with the predicted value of 0.785. There was a large variablity between specimens and also at different strains resulting from the non-linearity of the curves in fig. 5.14. The discrepency was attributed to the linear assumptions of laminate theory which do not match the non-linear resin-dominated transverse behaviour observed for this lay-up.

5.6 CONCLUSIONS

Mechanical property data derived from a test program conducted on low pressure cured laminates were used in conjunction with laminated plate theory and the Tsai-Wu failure theory to predict co-cured sandwich panel performance.

The low pressure cured laminate property data showed only small differences with average laminate properties for a similar carbon-epoxy system cured at standard autoclave pressure. The average longitudinal compression strength, X_C, was anticipated to be significantly degraded as a result of the low cure pressure (due to increased void content), but this was not observed. However, there was a large scatter in the test data. The calculated 'A' design allowable longitudinal compression strength was consequently significantly lower than the corresponding value for a similar material system cured at standard pressure. The ratio for the 30 psi to 100 psi cured laminates was 0.63. The other principal structural properties were comparable with the standard cure pressure material, and no differences could be attributed to the reduced cure pressure. The longitudinal Young's Modulus, E_1, which governs the important stiffness behaviour of spacecraft sandwich components and instability failure modes, was degraded only by 2%.

The predicted sandwich compression strength based on the low pressure cured laminate data was in reasonable agreement with tests on sandwich samples representative of a spacecraft thrust tube construction. The average compression strength from the tests was 11% higher than predicted. The Tsai-Wu theory was hence found to be reasonably consistent for this particular case. More significantly from the point of view of establishing

the quality of co-cured sandwich facesheets, the large scatter found in the laminate compression tests was not reflected by the sandwich compression specimens. This suggested either a greater sensitivity in the Celanese coupon compression test method for the laminates, or an improvement in co-cured facesheet quality over laminates cured at the same pressure. The latter could be explained by better resin flow, and hence a reduction in void content, arising from the uneven pressure distribution on the co-cured sandwich facesheets, as described in section 4.3. Consequently, the 'A' allowable compression strength found from the sandwich test data was 50% higher than the value predicted from laminate coupons. The method of 'allowable' strength prediction of co-cured sandwich, based on laminate coupons cured at the same autoclave pressure, was hence considered to be conservative.

The prediction of co-cured sandwich stiffness was found to be in good agreement with test results. The prediction of Poissons ratio was less successful. This was attributed to resin dominated non-linear behaviour across the specimens which was not included in the linear laminate theory prediction.

Theory	Criterion equation	F_1	F_2	F_{11}	F_{12}	F_{22}	F_{66}
Ashkenazi	$F_i\sigma_i\sigma_j = 1$	-	-	$\frac{1}{X^2}$	$\frac{1}{2}\left[\frac{4}{U^2} - \frac{1}{X^2} - \frac{1}{Y^2} - \frac{1}{S^2}\right]$	$\frac{1}{Y^2}$	$\frac{1}{S^2}$
Chamis	$F_i\sigma_i\sigma_j = 1$	-	-	$\frac{1}{X^2}$	$-\frac{K_i'K_j}{2XY}$	$\frac{1}{Y^2}$	$\frac{1}{S^2}$
Cowin	$F_i\sigma_i + F_{ij}\sigma_i\sigma_j = 1$	$\frac{1}{X} - \frac{1}{X'}$	$\frac{1}{Y} - \frac{1}{Y'}$	$\frac{1}{XX'}$	$\sqrt{F_{11}F_{22}} - \frac{1}{2S^2}$	$\frac{1}{YY'}$	$\frac{1}{S^2}$
Fischer	$F_{ij}\sigma_i\sigma_j = 1$	-	-	$\frac{1}{X^2}$	$-\frac{K}{2XY}$	$\frac{1}{Y^2}$	$\frac{1}{S^2}$
Gol'denblat-Kopnov	$F_i\sigma_i + \sqrt{F_{ij}\sigma_i\sigma_j} = 1$	$\frac{1}{2}\left(\frac{1}{X} - \frac{1}{X'}\right)$	$\frac{1}{2}\left(\frac{1}{Y} - \frac{1}{Y'}\right)$	$\frac{1}{4}\left(\frac{1}{X} + \frac{1}{X'}\right)^2$	$\frac{1}{8}\left[\left(\frac{1}{X} + \frac{1}{X'}\right)^2 + \left(\frac{1}{Y} + \frac{1}{Y'}\right)^2 - \left(\frac{1}{S_{45}} + \frac{1}{S_{45}'}\right)^2\right]$	$\frac{1}{4}\left(\frac{1}{Y} + \frac{1}{Y'}\right)^2$	$\frac{1}{S^2}$
Hoffman	$F_i\sigma_i + F_{ij}\sigma_i\sigma_j = 1$	$\frac{1}{X} - \frac{1}{X'}$	$\frac{1}{Y} - \frac{1}{Y'}$	$\frac{1}{XX'}$	$-\frac{1}{2XX'}$	$\frac{1}{YY'}$	$\frac{1}{S^2}$
Malmeister	$F_i\sigma_i + F_{ij}\sigma_i\sigma_j = 1$	$\frac{1}{X} - \frac{1}{X'}$	$\frac{1}{Y} - \frac{1}{Y'}$	$\frac{1}{XX'}$	$\frac{1}{2}\left[\frac{1}{S_{45}'}(F_1 - F_2) + F_{11} + F_{22} - \left(\frac{1}{S_{45}'}\right)^2\right]$	$\frac{1}{YY'}$	$\frac{1}{S^2}$
Marin	$F_i\sigma_i + F_{ij}\sigma_i\sigma_j = 1$	$\frac{1}{X} - \frac{1}{X'}$	$\frac{XX' - YY}{XX'Y}$	$\frac{1}{XX'}$	$\frac{1}{XX'} - \frac{XX' - S[X' - X - X'(X/Y) + Y]}{2S^2XX'}$	$\frac{1}{XX'}$	-
Norris	$F_{ij}\sigma_i\sigma_j = 1;\ \sigma_1^2 = X^2\ \&\ \sigma_2^2 = Y^2$	-	-	$\frac{1}{X^2}$	$-\frac{1}{2XY}$	$\frac{1}{Y^2}$	$\frac{1}{S^2}$
Tsai-Hill	$F_{ij}\sigma_i\sigma_j = 1$	-	-	$\frac{1}{X^2}$	$-\frac{1}{2X^2}$	$\frac{1}{Y^2}$	$\frac{1}{S^2}$
Tsai-Wu	$F_i\sigma_i + F_{ij}\sigma_i\sigma_j = 1$	$\frac{1}{X} - \frac{1}{X'}$	$\frac{1}{Y} - \frac{1}{Y'}$	$\frac{1}{XX'}$	$\leqslant \pm\sqrt{F_{11}F_{22}}$ and determined under biaxial stress	$\frac{1}{YY'}$	$\frac{1}{S^2}$

$K_i = \dfrac{(1 + 4\nu_{12} - \nu_{13})E_{22} + (1 - \nu_{23})E_{11}}{[E_{11}E_{22}(2 + \nu_{12} + \nu_{13})(2 + \nu_{21} + \nu_{23})]^{1/2}}$ K_i' experimentally determined correlation coefficient $K = \dfrac{E_{11}(1 + \nu_{21}) + E_{22}(1 + \nu_{12})}{2\sqrt{E_{11}E_{22}(1 + \nu_{12})(1 + \nu_{21})}}$

Table 5.1 LAMINA STRENGTH THEORIES HAVING STRESS INTERACTION (from ref. [31])

TABLE 5.2 LONGITUDINAL TENSION TESTS ON 30 psi CURED UD HM-S/CYCOM 985

COUPON NO.	ULTIMATE STRESS X_T (MPa)	ULTIMATE STRAIN e_{1T} (%)	YOUNGS MODULUS E_{1T} (GPa)	POISSONS RATIO v_{12}
1	1346	0.67	194.4	0.350
2	1434			
3	1287			
4	1421	0.71	193.2	0.275
5	1175			
6	1110			
7	1190			
8	865			
9	1296			
10	1039	0.545	189.7	0.275
11	987			
12	1298			
13	1182			
mean	1202	0.642	192.4	0.300
S.D.	165	0.067	4.1	0.035
C.o.V	13.7%	10.5%	2.1%	11.8%

TABLE 5.3 TRANSVERSE TENSION TESTS ON 30 psi CURED UD HM-S/CYCOM 985

COUPON NO.	ULTIMATE STRESS Y_T (MPa)	YOUNGS MODULUS E_{2T} (GPa)
1	42.5	6.6
2	37.7	-
3	38.6	6.8
4	u/s	-
5	38.0	6.9
6	34.5	6.8
7	38.5	7.1
8	u/s	-
9	39.7	6.7
10	37.6	6.8
11	u/s	-
12	29.0	6.9
13	40.9	6.2
mean	37.7	6.8
S.D.	3.5	0.24
C.o.V	9.3%	3.5%

TABLE 5.4 LONGITUDINAL COMPRESSION TESTS ON 30 psi CURED UD HM-S/CYCOM 985

COUPON NO.	ULTIMATE STRESS X_C (MPa)	ULTIMATE STRAIN e_{1C} (%)	YOUNGS MODULUS E_{1C} (GPa)	POISSONS RATIO v_{12}
1	958			
2	750	0.480	152	0.275
3	813			
4	876	0.620	154	0.300
5	867			
6	u/s			
7	927	0.595	163	0.325
8	966			
9	948			
10	1049			
11	700	0.450	159	0.325
12	660			
13	895			
14	1149			
15	715	0.455	159	0.300
16	1165			
17	1057			
18	u/s			
19	749			
20	930			
mean	882	0.520	157.4	0.305
S.D.	155	0.073	3.9	0.019
C.o.V	17.6%	14.0%	2.5%	6.1%

TABLE 5.5 2-RAIL SHEAR TESTS ON 30 psi CURED UD HM-S/CYCOM 985

COUPON NO.	ULTIMATE SHEAR STRESS S (MPa)	ULTIMATE SHEAR STRAIN γ_{12} (%)	SHEAR MODULUS G_{12} (GPa)
1	u/s	-	-
2	46.9	1.53	3.97
3*	(19.7)	(0.50)	3.95
4	u/s	-	-
5	u/s	-	-
6	43.9	1.57	3.73
7	u/s	-	-
8	49.7	2.15	3.34
mean	46.8	1.75	3.75
S.D.	2.4	0.28	0.21
C.o.V	5.2%	16.0%	5.6%

* Defective coupon, premature failure.

TABLE 5.6 AVERAGE & ALLOWABLE PROPERTY DATA FOR 30 psi CURED UD HM-S/CYCOM 985

PROPERTY	UNITS	AVERAGE	DESIGN ALLOWABLE
E_{1T}	GPa	192	175
E_{1C}	GPa	157	
E_{2T}	GPa	6.8	6.8
v_{12}	-	0.30	0.30
G_{12}	GPa	3.75	3.75
X_T	MPa	1202	574
X_C	MPa	882	344
Y_T	MPa	37.7	23
Y_T	MPa	140*	70*
S	MPa	46.8	15

* Estimated

TABLE 5.7 PROPERTIES OF HM-S/CYCOM 985 CURED AT 30 psi AND HM-S/FIBREDUX 914 CURED AT STANDARD PRESSURE

PROPERTY		HM-S/ (1) CYCOM 985 30 PSI	HM-S/ (2) FIBREDUX 914 (STANDARD CURE)
E_1 (TENSION)	AV.	192.4 GPa	221.7 GPa
	CoV	2.1%	1.5%
	n	3	6
E_2 (TENSION)	AV.	6.8 GPa	7.31 GPa
	CoV	0.24	1.8%
	n	9	6
X_T	AV.	1202 MPa	1121 MPa
	CoV	13.7%	10.9%
	n	13	25
X_C	AV.	882 MPa	898 MPa
	CoV	17.6%	5.0%
	n	18	25
Y_T	AV.	37.7 MPa	46 MPa
	CoV	9.3%	13.0%
	n	10	25

(1) Test data from this study

(2) ESA Composites Handbook (source: DFVLR)

TABLE 5.8 ALLOWABLE PROPERTIES OF HM-S/CYCOM 985 CURED AT 30 psi AND HM-S/CODE 69 CURED AT STANDARD PRESSURE

PROPERTY	HM-S/ CYCOM 985 30 PSI (1)	HM-S/ CODE 69 STANDARD CURE (2)
E_1	175 GPa	179 GPa
E_2	6.8 GPa	6.3 GPa
ν_{12}	0.30	0.37
G_{12}	3.8 GPa	2.9 GPa
X_T	574 MPa	432 MPa
X_C	344 MPa	546 MPa
Y_T	23 MPa	15 MPa
Y_C	70 MPa	61 MPa
S	15 MPa	45 MPa

(1) Test data from this study

(2) Allowables for Ariane SPELDA

TABLE 5.9 ASSUMED REDUCTION FACTORS FOR CO-CURED FACESHEET MATERIAL PROPERTIES

PROPERTY	REDUCTION FACTOR
E_1	0.98
E_2	1.00
12	1.00
G_{12}	1.00
X_T	1.00
X_C	0.63
Y_T	1.00
Y_C	1.00
S	1.00

TABLE 5.11 COMPRESSION TEST RESULTS ON [0/±45/0] HM-S/CYCOM 985 FACED SANDWICH SPECIMENS

COUPON NO.	ULTIMATE LOAD N_x (N/mm)	EFFECTIVE YOUNGS MODULUS E_x (GPa)	EFFECTIVE POISSONS RATIO ν_{xy}
1	295		
2	279		
3	(219)*		
4	372		
5	344	82.7	0.461
6	319		
7	327		
8	308		
9	372		
10	261		
11	342	109.8	0.614
12	318		
13	336	88.2	0.603
14	288		
15	377		
16	283		
mean	321	93.6	0.559
S.D.	35	11.4	0.072
C.o.V	10.9%	12.2%	12.9%
A allowable	194		

* discarded data pt. due to failure of one facesheet only

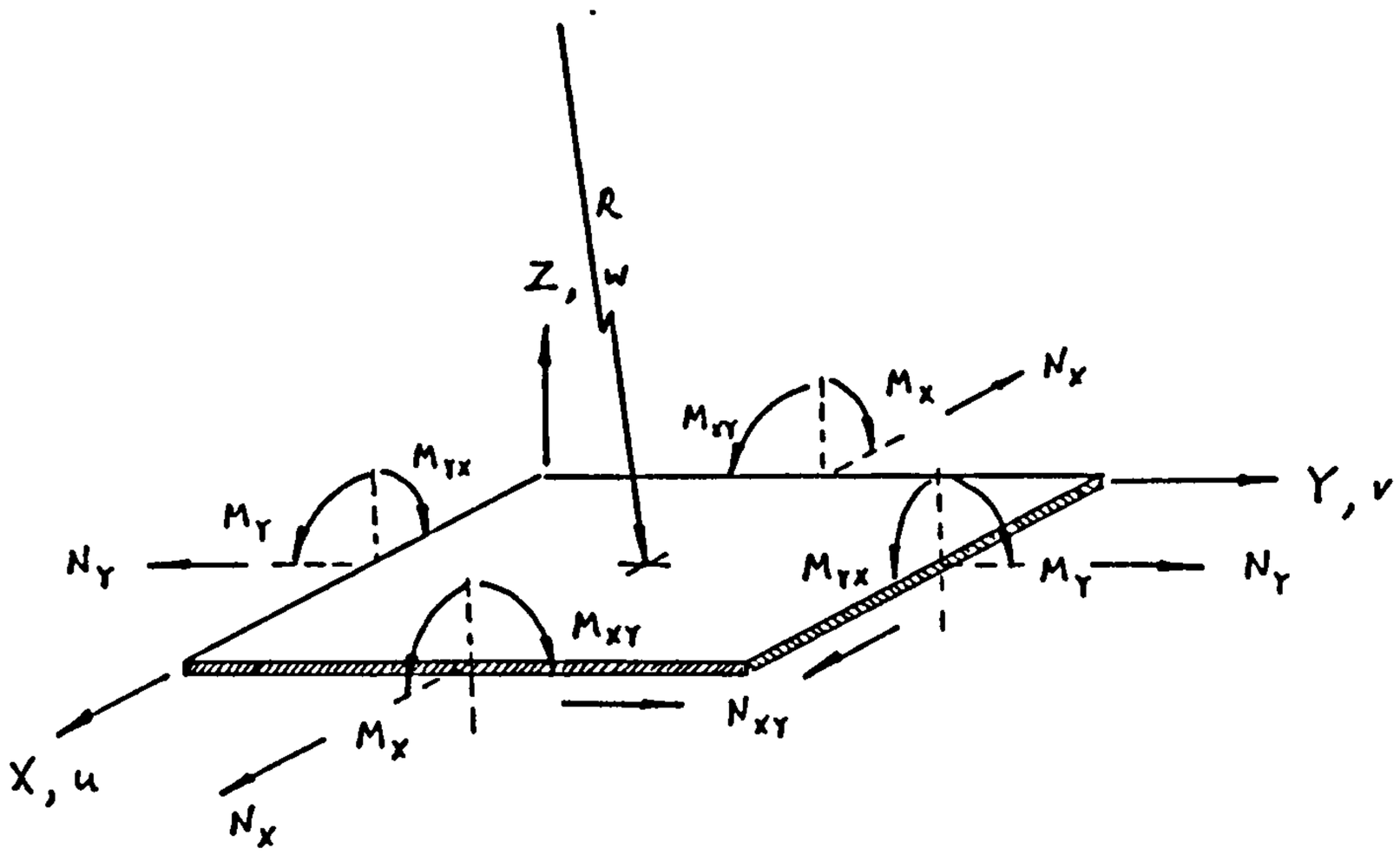

Fig. 5.1 SIGN CONVENTION FOR STRESS AND MOMENT RESULTANTS

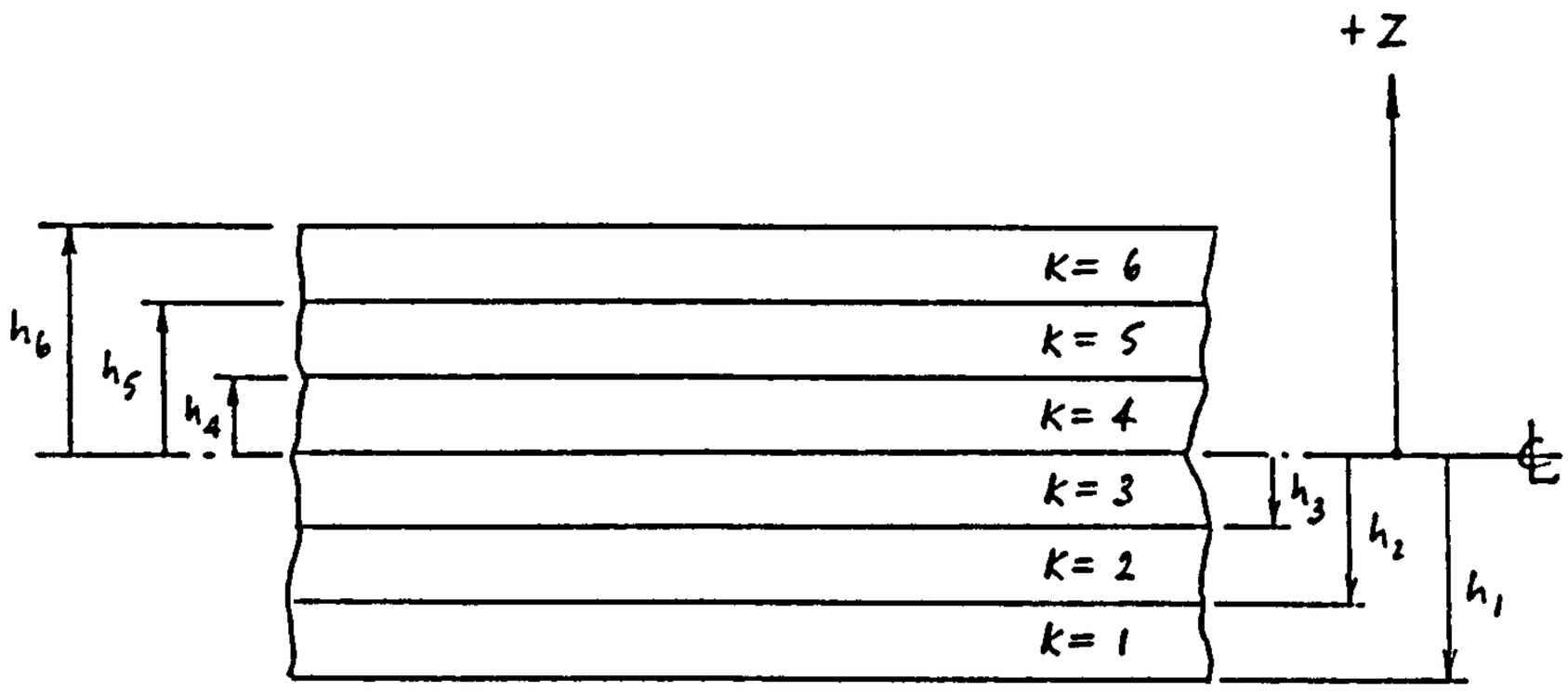

Fig. 5.2 LAMINATE STACKING SEQUENCE

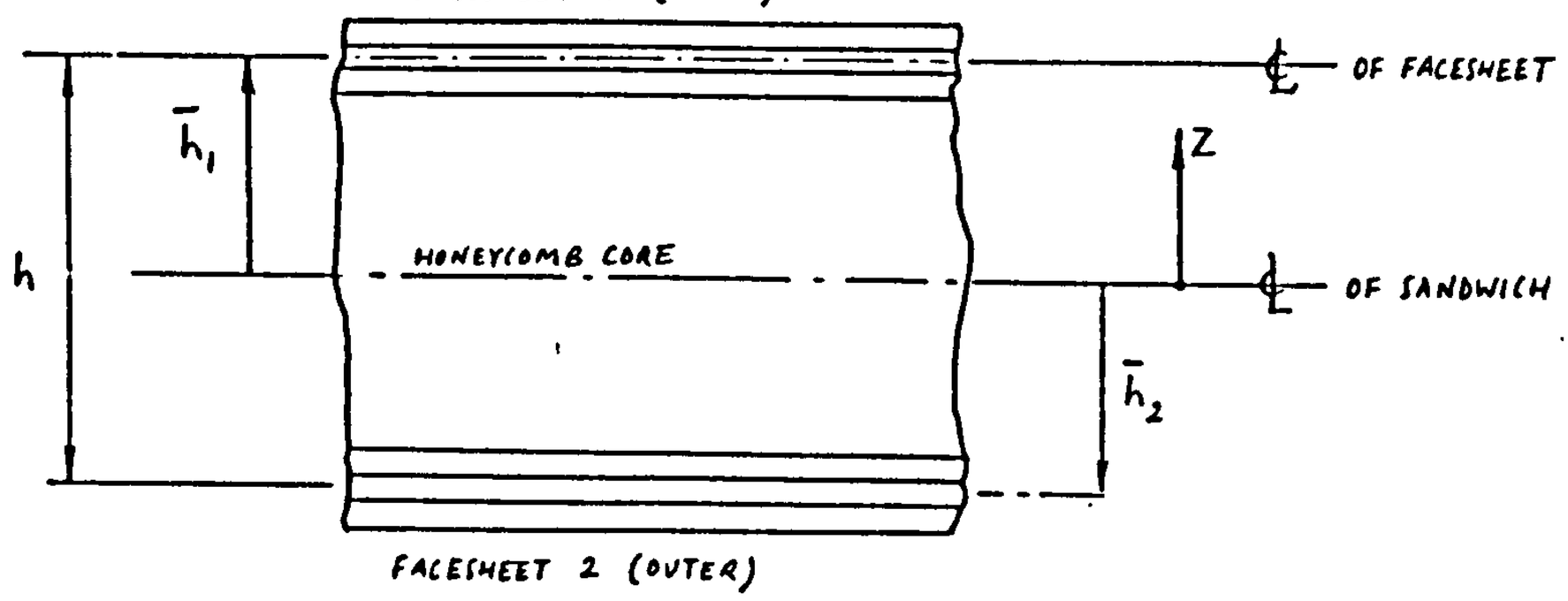

Fig. 5.3 SANDWICH PANEL STACK

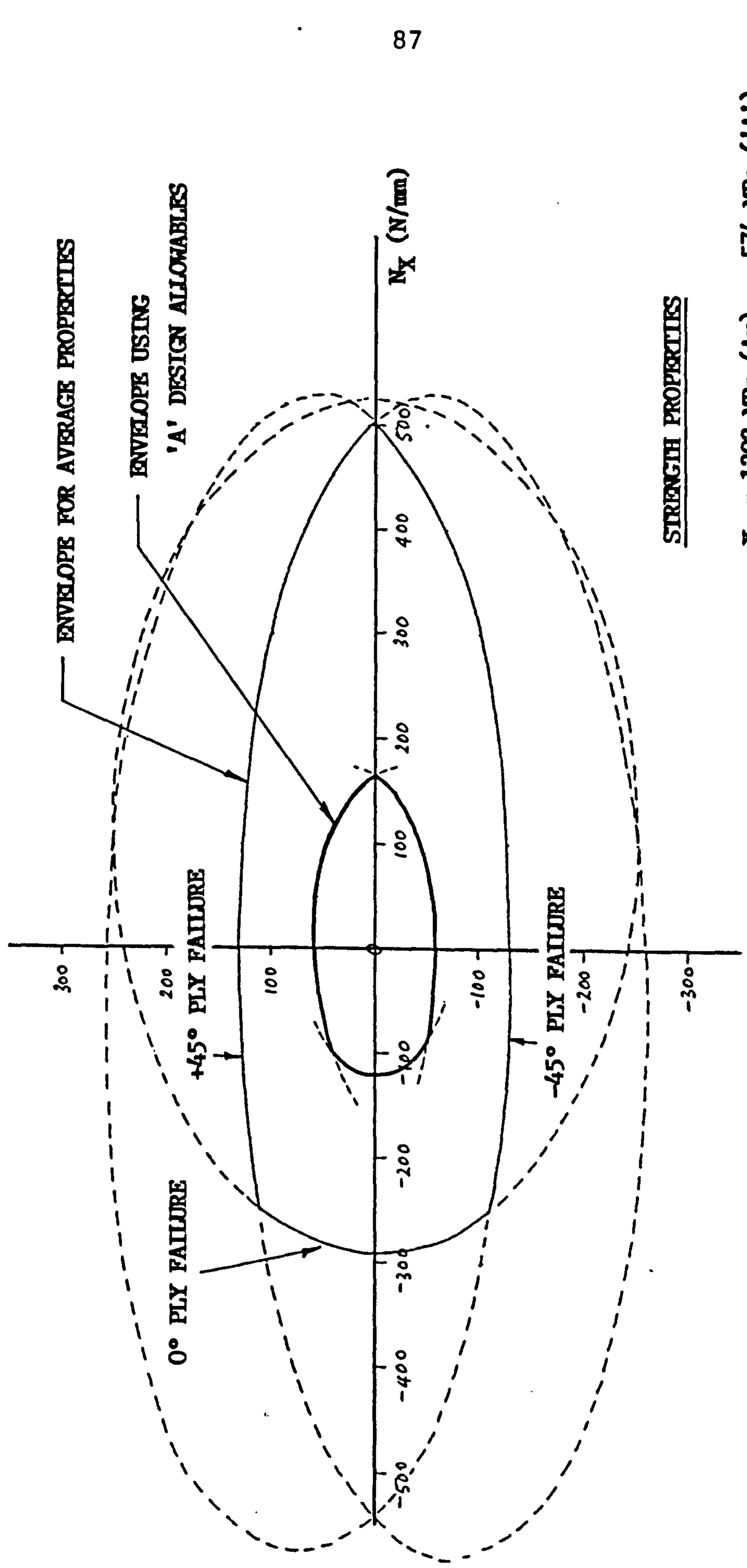

STRENGTH PROPERTIES

X_T = 1202 MPa	(Av)	574 MPa ('A')
X_C = 882 MPa	(Av)	344 MPa ('A')
Y_T = 38 MPa	(Av)	23 MPa ('A')
Y_C = 139 MPa	(Av)	70 MPa ('A')
S = 47 MPa	(Av)	15 MPa ('A')

Fig 5.4 STRENGTH ENVELOPE FOR [0/0/±45] FACED HMS/CYCOM 985 SANDWICH

Fig. 5.5

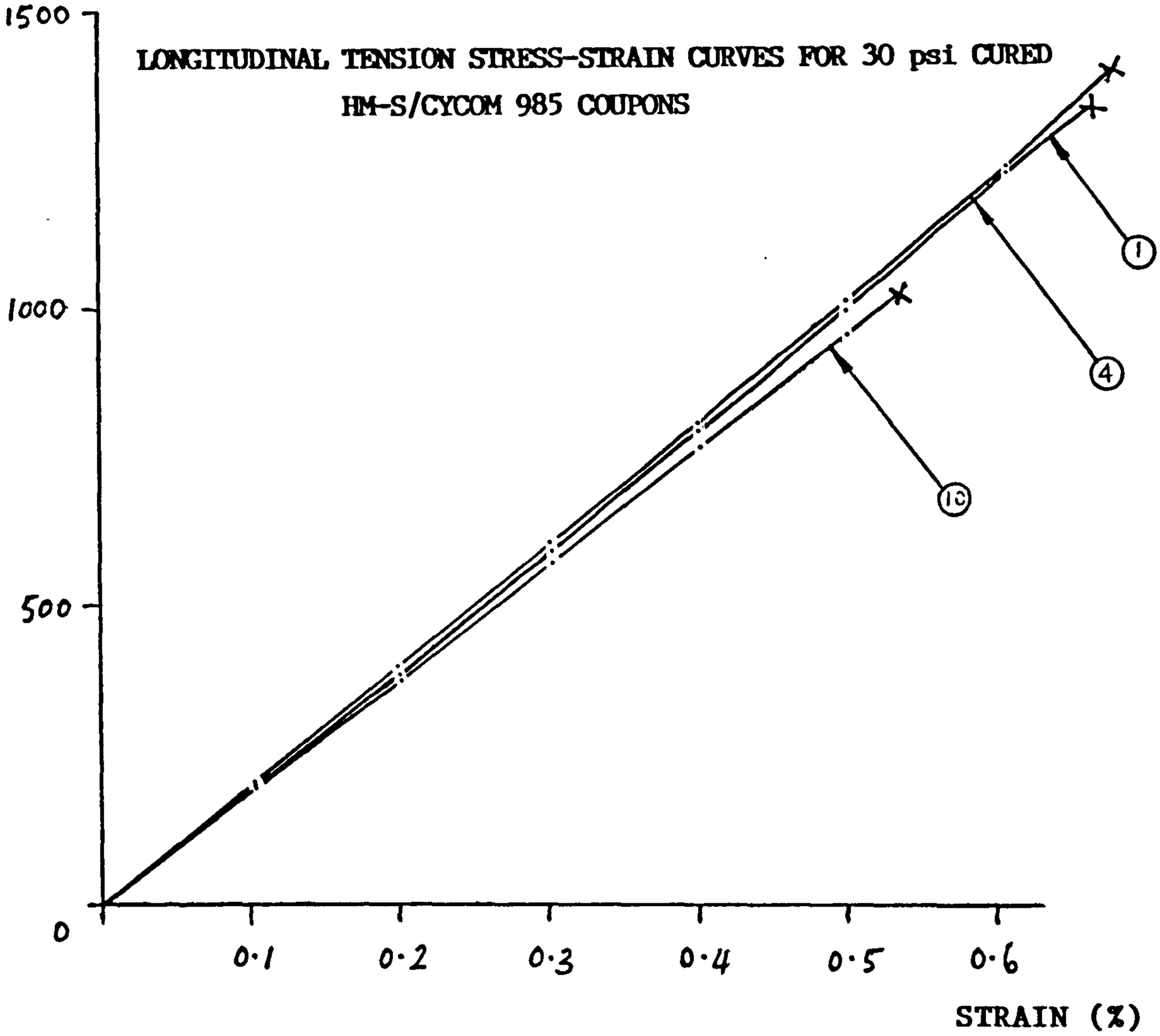
LONGITUDINAL TENSION STRESS-STRAIN CURVES FOR 30 psi CURED
HM-S/CYCOM 985 COUPONS
1500
1000
500
0
0·1
0·2
0·3
0·4
0·5
0·6
TENSION STRESS (MPa)
STRAIN (%)
1
4
12

Fig. 5.6

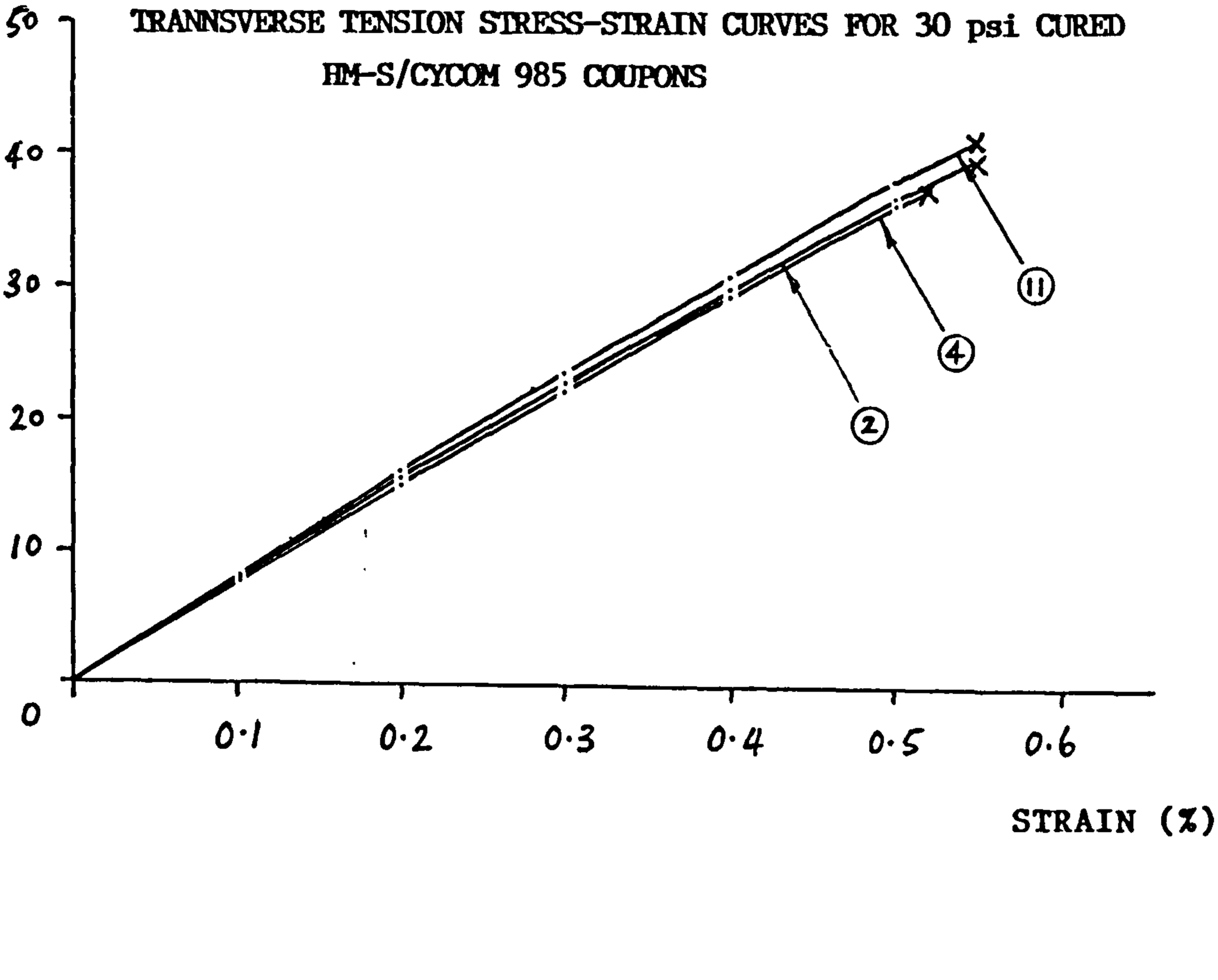
TRANNSVERSE TENSION STRESS-STRAIN CURVES FOR 30 psi CURED
HM-S/CYCOM 985 COUPONS
50
40
30
20
10
0
0·1
0·2
0·3
0·4
0·5
0·6
STRAIN (%)
2
4
11

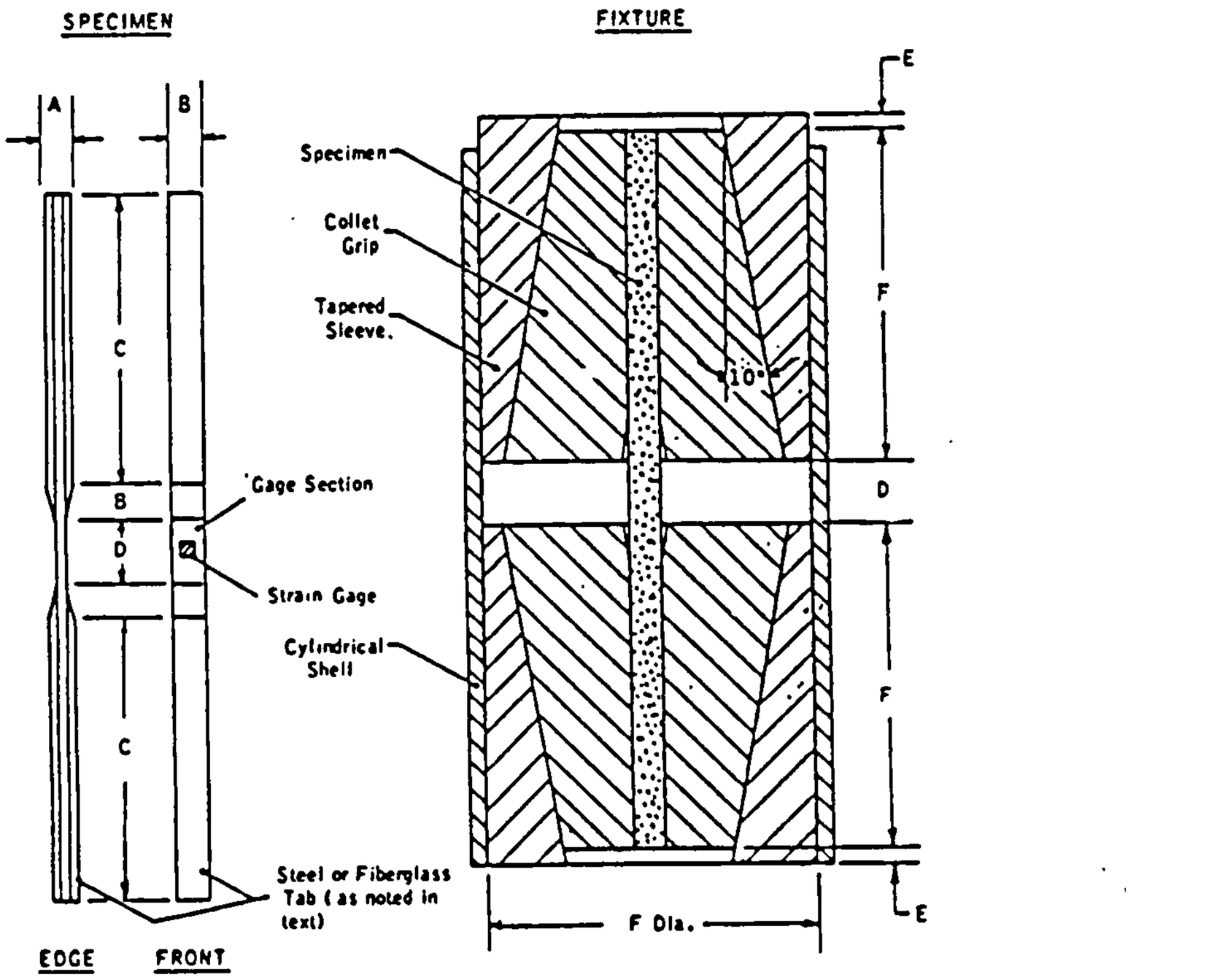

Dimensions	m	in.	Dimensions	m	in.
A	0.00399	0.157	D	0.01270	0.500
B	0.00635	0.250	E	0.00318	0.125
C	0.05715	2.250	F	0.06350	2.500

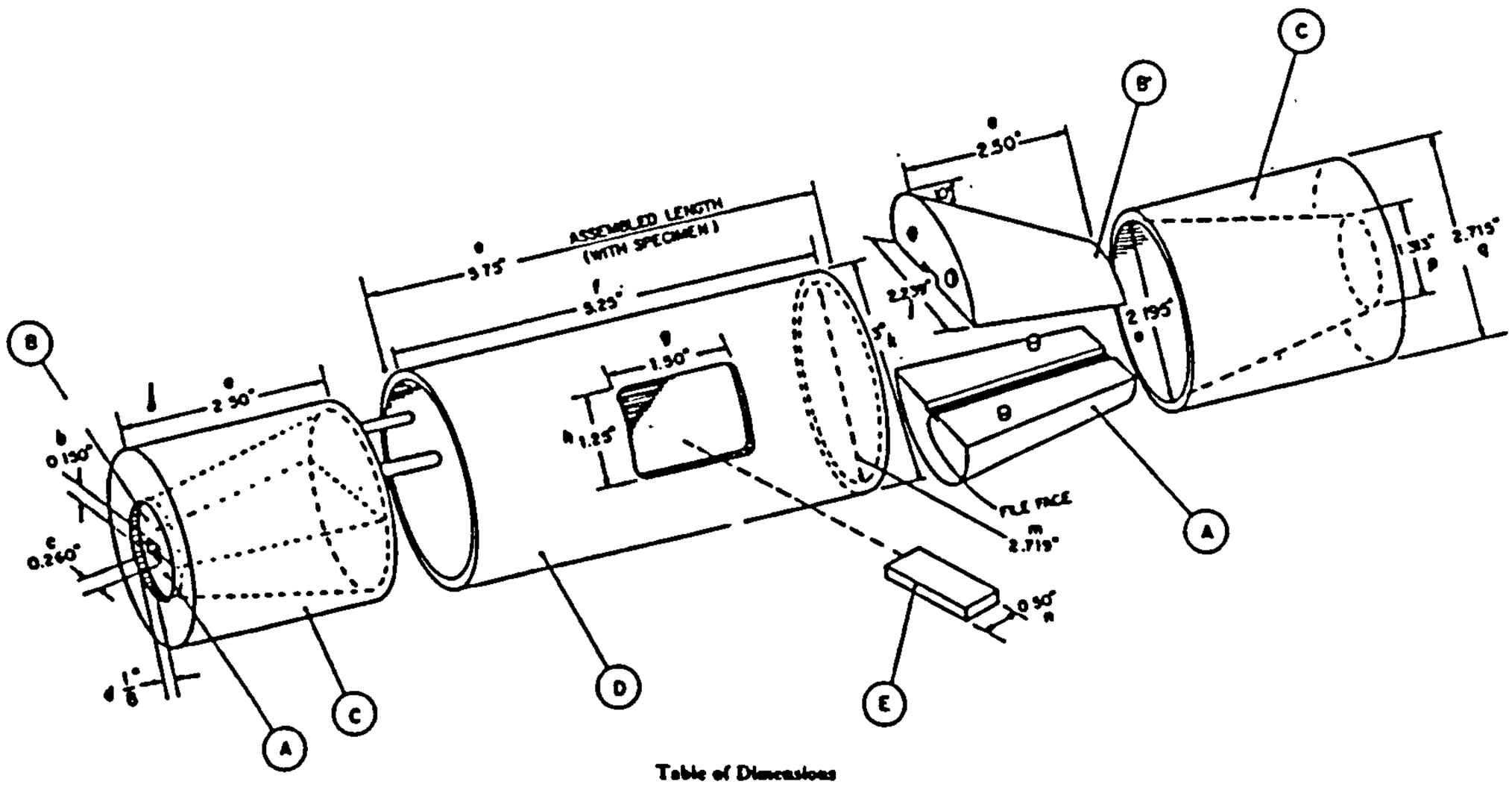

Table of Dimensions

	mm		in.			mm		in.	
	Dimension	Tolerance	Dimension	Tolerance		Dimension	Tolerance	Dimension	Tolerance
a	63.5	±0.10	2.500	±0.005	j	56.87	±0.03	2.239	±0.000
b	3.81	±0.05	0.150	±0.002	k	76.20	±0.30	3.000	±0.010
c	6.60	±0.025	0.260	±0.001			−0.00		−0.00
					m	69.06	+0.08	2.719	+0.003
d	3.18	±0.075	0.125	±0.003	n	12.70	±0.03	0.500	±0.002
e	146.0	±0.50	5.75	±0.010	o	55.75	±0.03	2.195	±0.001
f	133.0	±0.50	5.25	±0.01	p	33.35	±0.03	1.313	±0.001
g	38.1	±0.30	1.50	±0.01	q	68.96	+0.00	2.715	+0.000
							−0.05		−0.002
h	31.8	+0.30	1.25	±0.01					

Fig. 5.7 CELANESE COMPRESSION TEST FIXTURE

(from ASTM D3410-75)

Fig. 5.8

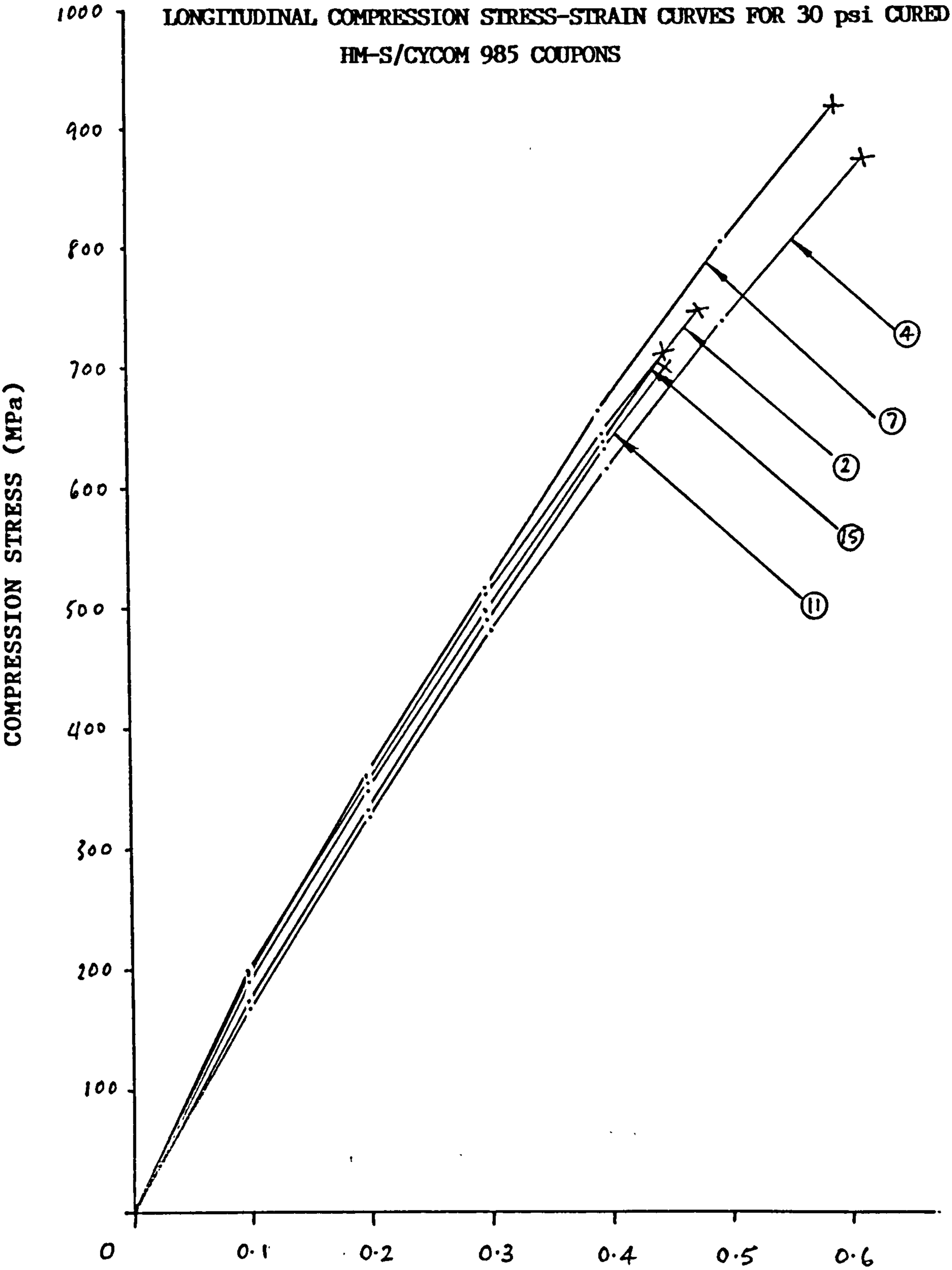
LONGITUDINAL COMPRESSION STRESS-STRAIN CURVES FOR 30 psi CURED
HM-S/CYCOM 985 COUPONS
COMPRESSION STRESS (MPa)
1000
900
800
700
600
500
400
300
200
100
0
0·1
0·2
0·3
0·4
0·5
0·6
STRAIN (%)
4
7
2
15
11

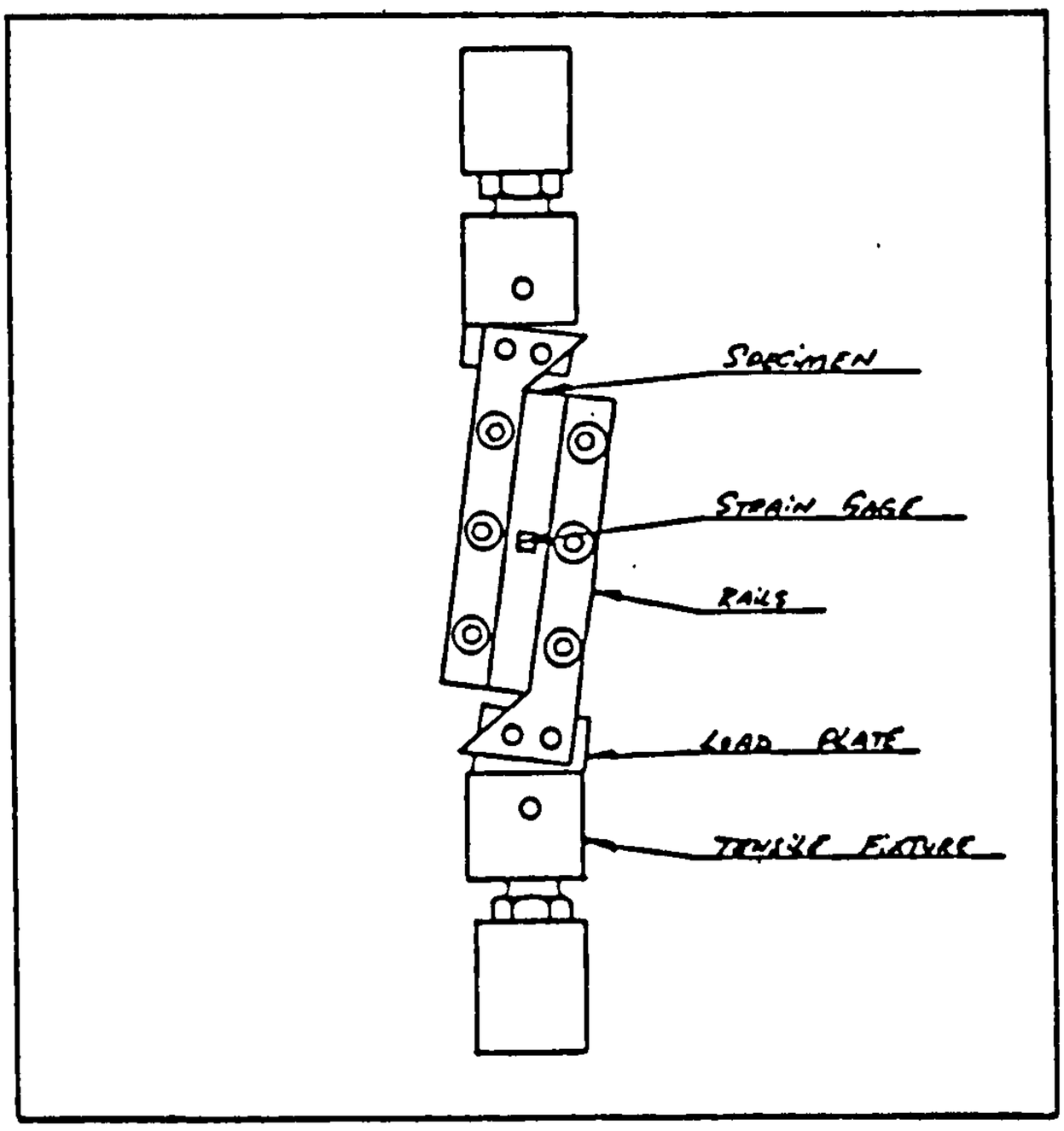

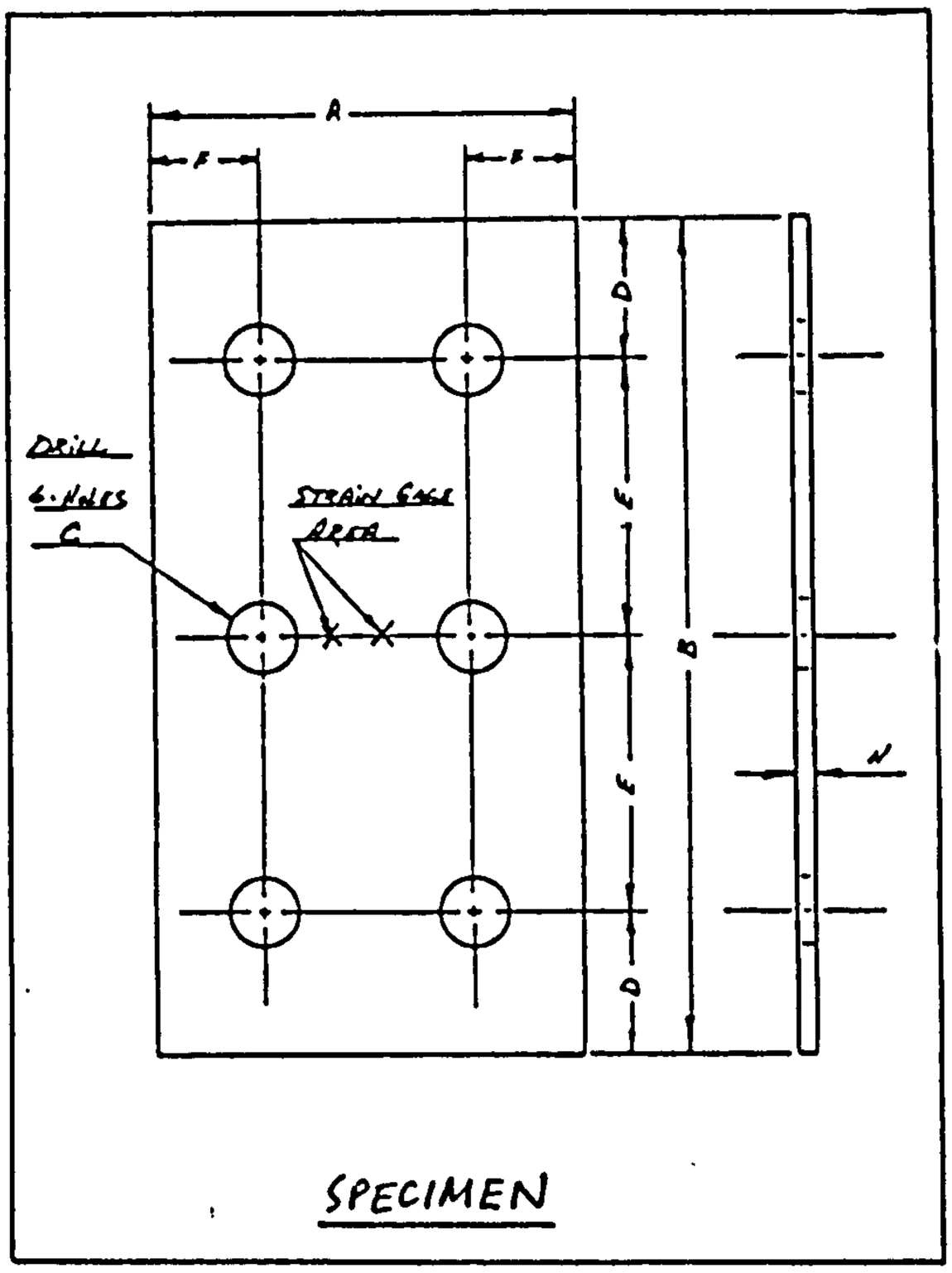

Dimension	mm	in.
A	76.0	3.0
F	15.9	0.625
C	12.7	0.50
D	25.0	1.0
E	51.0	2.0
B	152.0	6.0
N	To be measured	

Fig. 5.9 TWO-RAIL SHEAR TEST FIXTURE

Fig. 5.10 IN-PLANE SHEAR STRESS-STRAIN CURVES FOR 30 psi CURED HM-S/CYCOM 985 COUPONS

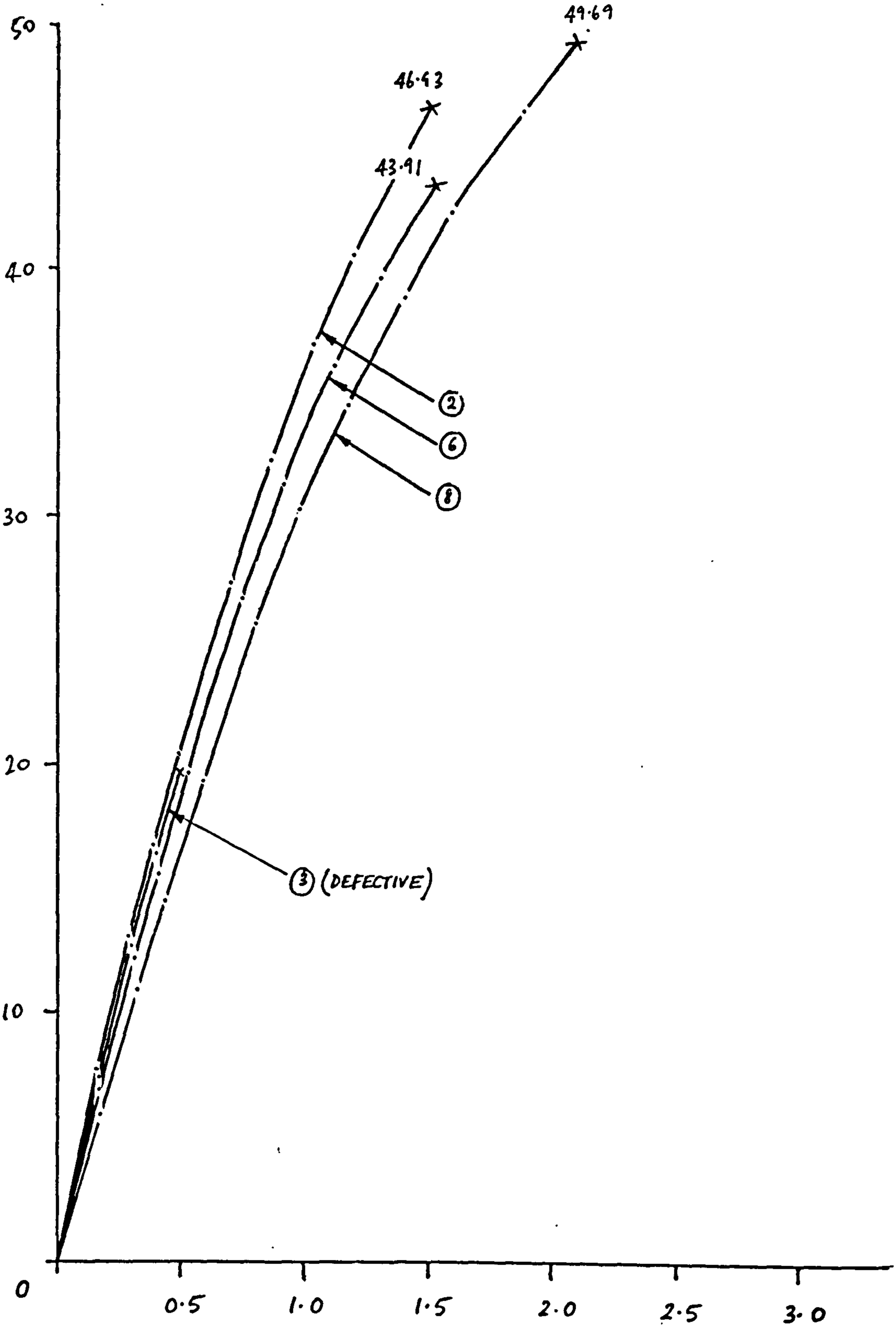

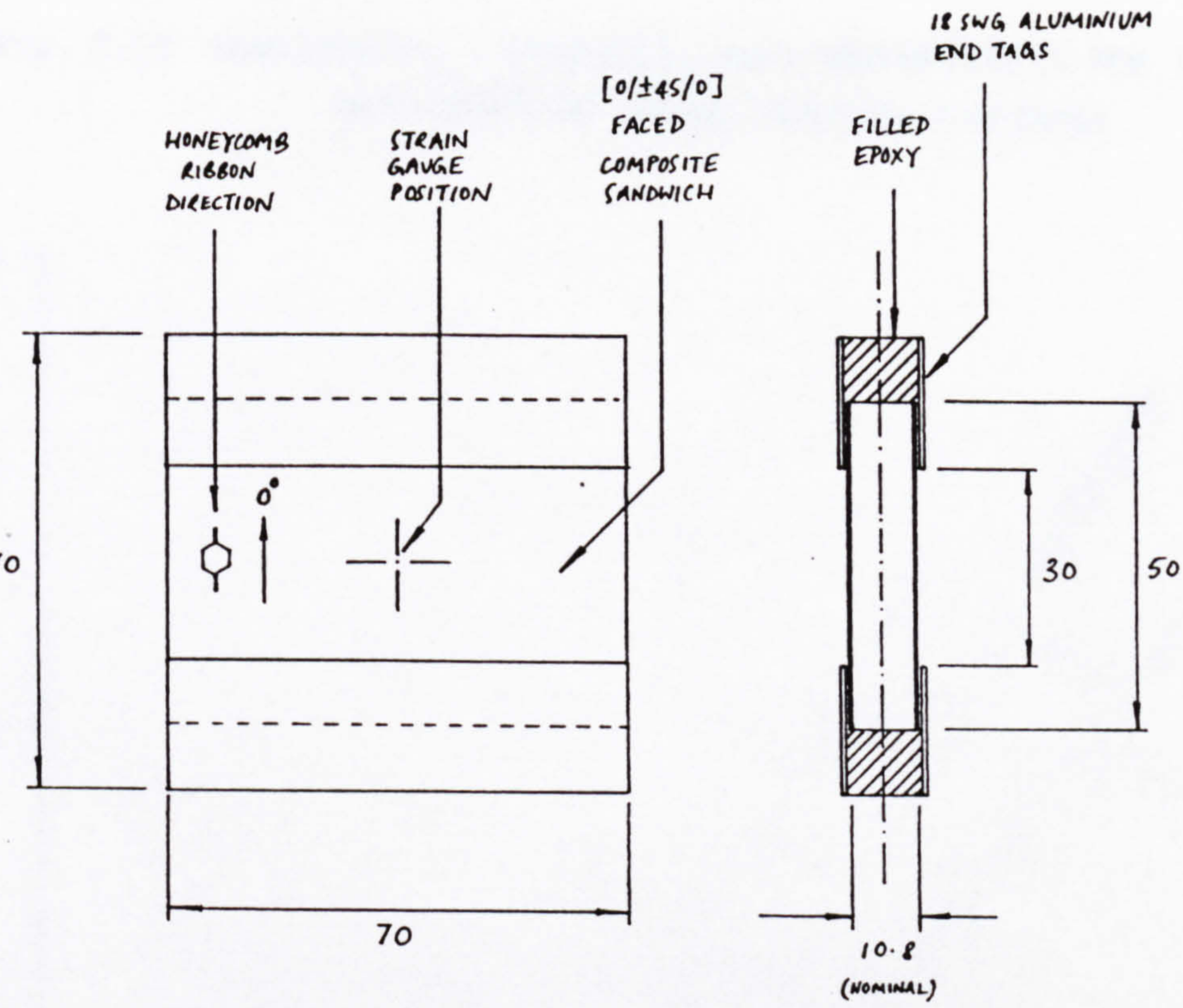

Fig. 5.11 SANDWICH COMPRESSION SPECIMEN

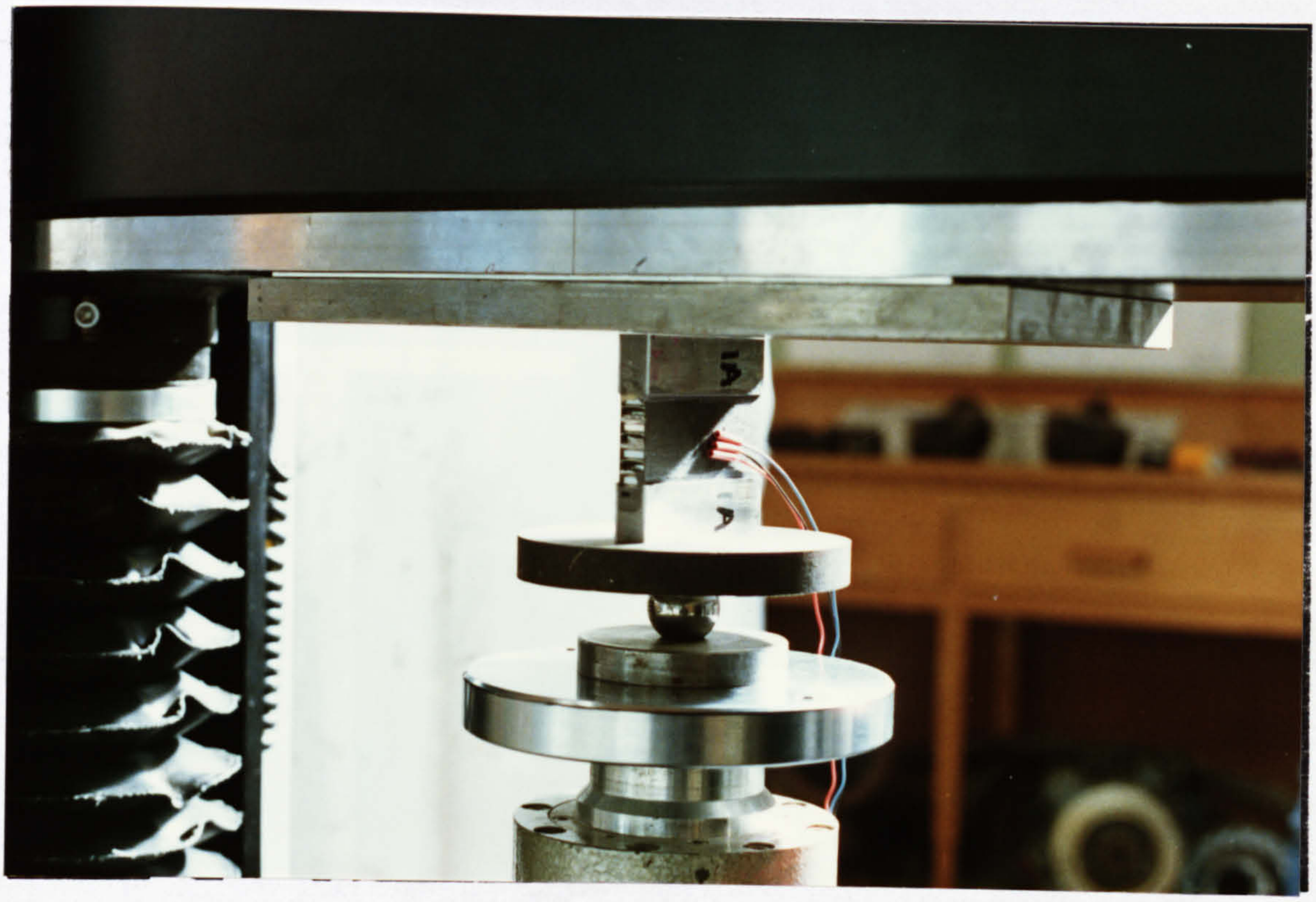

Fig. 5.12 SANDWICH COMPRESSION SPECIMEN IN TEST MACHINE

Fig. 5.13 LONGITUDINAL COMPRESSION LOAD-STRAIN CURVES FOR [0/±45/0] UD HM-S/CYCOM 985 FACED SANDWICH SPECIMENS

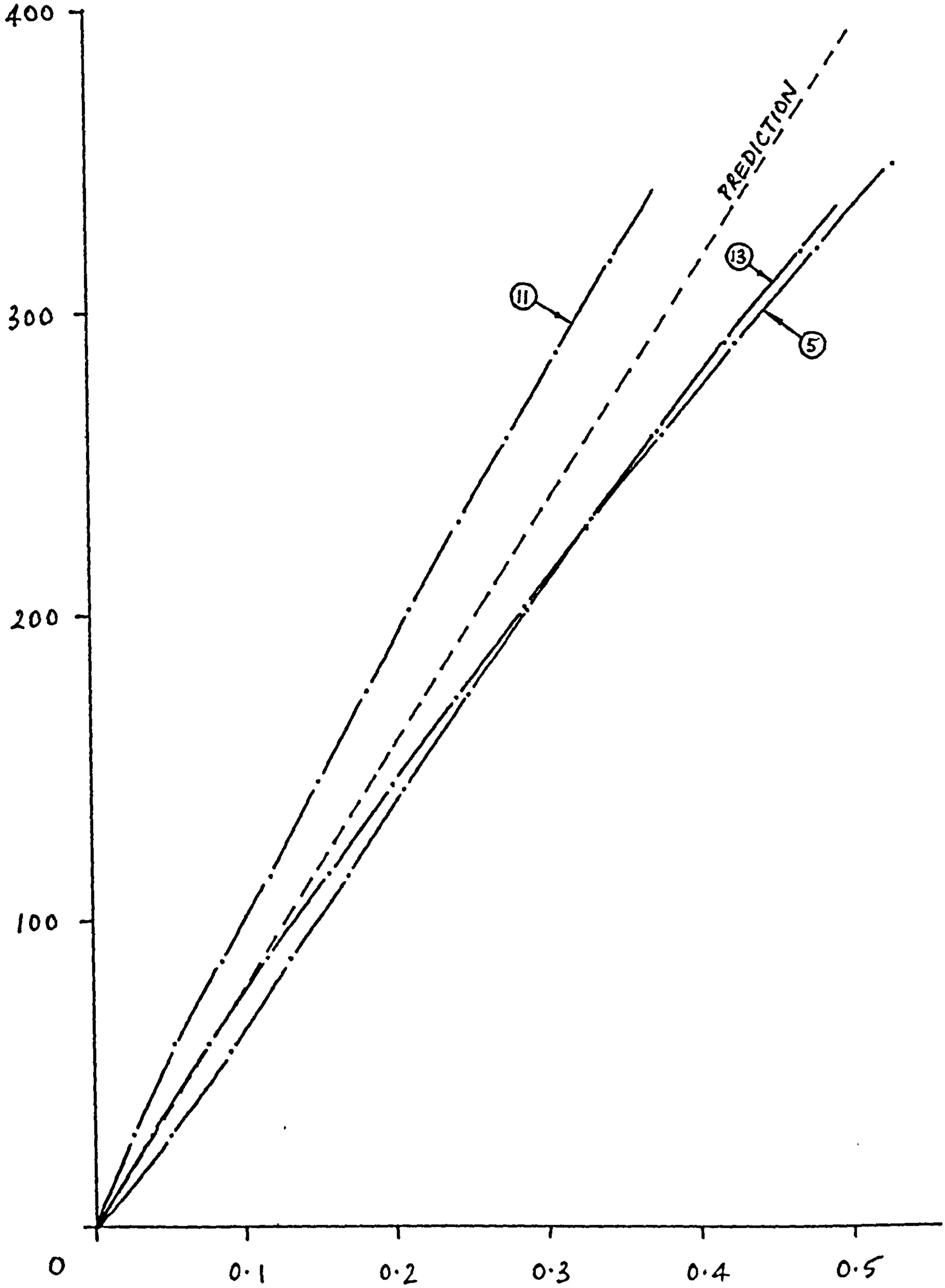

Fig. 5.14 LONGITUDINAL COMPRESSION LOAD Vs TRANSVERSE STRAIN FOR [0/±45/0] UD HM-S/CYCOM 985 FACED SANDWICH SPECIMENS

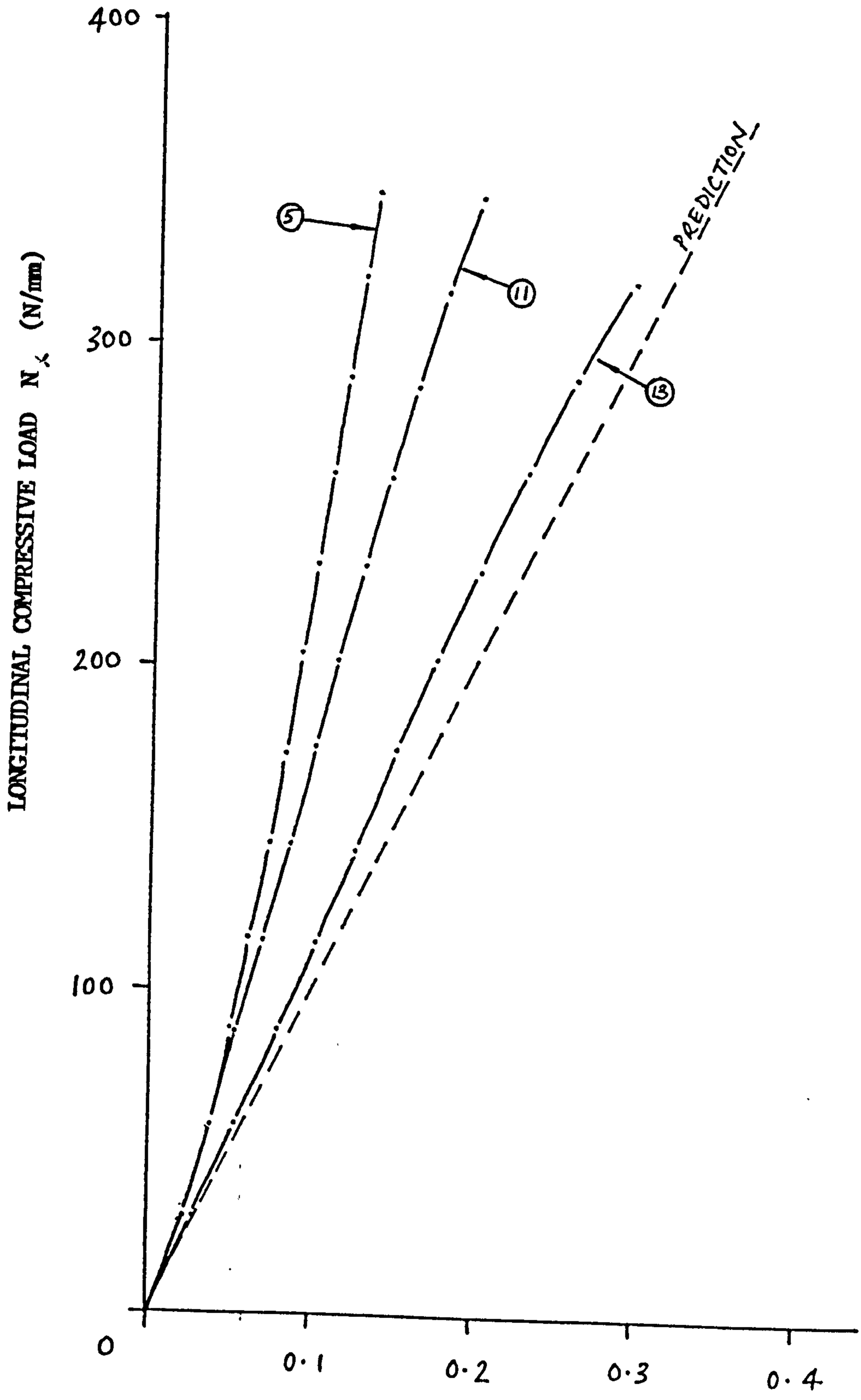

CHAPTER 6 COMPOSITE SANDWICH LOCAL INSTABILITY

Two forms of local instability are encountered in honeycomb sandwich construction: wrinkling and dimpling. Both forms of instability can occur under pure compression, bending (one facesheet in compression), shear or combinations of these loading actions. Methods of predicting the critical instability loads is therefore essential for the analysis and design optimisation of spacecraft composite faced sandwich components.

The major focus of this chapter is wrinkling instability since this mode in particular constitutes a failure mechanism and can often be a critical design constraint. Current techniques for analysing this mode are extended to include co-cured constructions with unsymmetric facesheet lay-ups under various load combinations. These were incorporated in a computer program which was used to investigate several numerical examples. The method was used to predict wrinkling instability for a number of co-cured sandwich constructions with typical spacecraft panel facesheet lay-ups which were tested in compression.

6.1 CURRENT METHODS OF WRINKLING ANALYSIS

Wrinkling is a short wavelength local buckling phenomenon which can occur in sandwich panels. Two different buckling modes are theoretically possible under compression loading. These are a symmetric and an anti-symmetric mode as shown in fig. 6.1. Generally, the symmetric mode, in which the core has a sinusoidally varying through-thickness tension-compression strain, occurs at a lower load than the anti-symmetric mode. The panel loses its load carrying capability once wrinkling occurs and hence it can be considered as a failure mode. Actual failure often manifests itself as a tension rupture of the core to facesheet bond, interlaminar separation or core compression. Panels most susceptible to wrinkling failure are those with thin facesheets and thick cores.

6.1.1 Simple Design Formulae

The design formulae currently in widespread use[25,28,35,36] are simply extensions of isotropic metal faced sandwich wrinkling analysis with some allowance made for material in-plane orthotropy. This is based on linear small deflection theory with an assumed sinusoidal symmetric buckled waveform. The critical compressive wrinkling load is often given in the following form :

$$Nx_{wr} = 1.633\left(\frac{E_f t^3 E_c}{h}\right)^{\frac{1}{2}} \qquad \text{(eq. 6.1)}$$

where, Nx_{wr} = Critical compression stress resultant
(total on both facesheets)
E_f = Effective Youngs Modulus in the load direction
t = Facesheet thickness
E_c = Core compression modulus
h = Core thickness

Material orthotropy is incorporated by the use of an effective (flexural) facesheet modulus in the load direction. This approach is therefore only valid if the facesheets are specially orthotropic (ie. no coupling) and is hence somewhat limited.

The notable features of equation (6.1) are that the wrinkling load is independent of the core shear modulus - a consequence of the symmetric instability mode, and inversely proportional to the square root of the core depth. Observed wrinkling instability on metal faced sandwich panels is usually found to occur at a lower load than predicted by this formula. This is believed to be as a result of initial waviness in the facesheets not incorporated in the linear small deflection model. To account for any initial waviness, the formula is sometimes used in the modified form[35] :

$$Nx_{wr} = 1.633\left(\frac{E_f t^3 E_c}{h}\right)^{\frac{1}{2}} \Big/ \left(1 + 0.64K_\delta\right) \qquad \text{(eq. 6.2)}$$

where $K_\delta = \dfrac{E_c}{hF_c}$

F_c = flatwise sandwich strength

For initial design purposes, where the waviness is unknown, reference [35] recommends a lower bound prediction for compressively loaded isotropic faced sandwich given by :

$$Nx_{wr} = 0.66\left(\frac{E_f t^3 E_c}{h}\right)^{\frac{1}{2}} \qquad \text{(eq. 6.3)}$$

This is an empirical relationship based on tests, and it can be seen to reduce the theoretical prediction by a factor of 0.40. In reference [36] experimental wrinkling loads for composite faced sandwich under compression loading, 4-point bending and shear led to the following factors replacing the 0.66 factor in equation (6.3):

CFRP & AFRP facesheets, compression	0.80
CFRP & AFRP facesheets, bending	0.84
CFRP & AFRP facesheets, shear	0.84
Filament wound CFRP faces, compression	0.66

For shear, the facesheet modulus (E_f) was taken in the 45° direction. A correlation of test results with the simple isotropic based design formula is not strictly valid because the test specimens (for Exosat & Intelsat development) consisted of [0/90], [±45] and 'quasi-isotropic' facesheet lay-ups which are not specially orthotropic. Similarly reference [25] recommends a factor of 0.66 to be applied in equation (6.3) for the design of composite faced sandwich panels. These again are based on tests on panels without specially orthotropic facesheets.

6.1.2 Compressive Wrinkling of Specially Orthotropic Faced Panels

Pearce & Webber[37] developed a more rigourous analytical technique to study the problem of wrinkling of simply supported rectangular panels with fibre reinforced facesheet materials. They extended the analysis of reference [38] for isotropic faced panels to the more general case of orthotropic faces. In this method, equilibrium relations for the upper and lower facesheets are related to the core mid-plane displacements, u_0, v_0, w_0 and stresses, σ_{z0}, τ_{xz}, τ_{yz}. The problem becomes one of six simultaneous partial differential equations in these six unknowns.

A solution was obtained for the case of symmetric buckling by assuming w_0, $\tau_{xz}, \tau_{yz} = 0$, that the facesheets were specially orthotropic ie. A_{13}, $A_{23} = 0$, D_{13}, $D_{23} = 0$ and $B_{ij} = 0$, and assuming a variation for σ_{z0} of :

$$\sigma_{z0} = k \sin \frac{m\pi x}{a} \sin \frac{\pi y}{b} \qquad \text{(eq. 6.4)}$$

This reduced the problem to a single equation with the solution :

$$N_x = \frac{2\pi^2}{a^2}\left\{ D_{11}m^2 + 2\,(D_{12} + 2D_{66})\,(a/b)^2 + \frac{D_{22}}{m^2}(a/b)^4 \right\} + \frac{E_c a^2}{m^2\pi^2 h}$$

(eq. 6.5)

The critical value of N_x for symmetric buckling can simply be found by minimising with respect to m, the buckle half wavelength. The value of m to make N_x a minimum is :

$$m^* = a\left\{ \frac{1}{D_{11}}\left(\frac{D_{22}}{b^4} + \frac{2E_c}{\pi^4 h} \right) \right\}^{1/4} \qquad \text{(eq. 6.6)}$$

and the critical symmetric wrinkling load is then :

$$Nx_{wr} = 2\left\{\pi^2 D_{11}k + \frac{2E_c}{\pi^2 hk} + \frac{2\pi^2}{b^2}(D_{12} + 2D_{33}) + \pi^2 \frac{D_{22}}{k}\frac{1}{b^4}\right\} \quad \text{(eq. 6.7)}$$

where $k = \frac{1}{D_{11}}\left(\frac{D_{22}}{b^4} + \frac{2E_c}{4h}\right)$

Noticable from this equation is that the panel length, a, does not affect the critical load. Only the panel width, b, appears in the equation. However, for practical constructions, the terms containing b^2 and b^4 can be shown to be insignificant when compared to the other terms for values of b of the order of the core depth. The wrinkling load is therefore effectively independent of the panel dimensions. Ignoring these terms, the critical buckle wavelengths and critical load become :

$$m^* = \frac{a}{\pi}\left(\frac{2E_c}{D_{11}h}\right)^{\frac{1}{4}} \quad \text{(eq. 6.8)}$$

$$Nx_{wr} = 5.657\left(\frac{D_{11}E_c}{h}\right)^{\frac{1}{2}} \quad \text{(eq. 6.9)}$$

This equation for the wrinkling load is then equivalent to (eq. 6.1) provided flexural Poissons effects are ignored.

For the case of anti-symmetric buckling a solution was obtained by assuming $\sigma_{z0} = 0$, special orthotropy and a variation for w_0 of :

$$w_0 = W \sin\frac{m\pi x}{a} \sin\frac{\pi y}{b} \quad \text{(eq. 6.10)}$$

This reduced the problem to a single equation with two minima. One had a wavelength of the order of the panel length, and the other a wavelength of the order of the symmetric solution. The former was the overall panel buckling solution. Pearce & Webber found for all cases they obtained numerical results, that the short wavelength antisymmetric solution was always greater than the symmetric solution.

6.1.3 Compressive Wrinkling of Cross-Ply Faced Columns

Subsequent experimental work carried out by Pearce & Webber[39] indicated a large discrepancy between test failure loads and theoretical predictions using the specially orthortropic formula (equation (6.9)) particularly for [0/90] faced panels which have large B_{11}, B_{22} coupling terms. These terms were not included in the analysis. In a later paper by Webber, Kyriakides & Lee[40] an attempt was made to account for the B_{11} and B_{22} terms, both to enable [0/90] facesheet lay-ups to be analysed and also to include the effect of the core-facesheet adhesive which can be incorporated by considering the adhesive as an additional laminate. The adhesive layer increases the flexural stiffness and B_{ij} coupling of the facesheets and was thought to be the major discrepency between predictions and test results.

Inclusion of B_{11}, B_{12} and B_{22} was accomplished by reducing the 3 dimensional elasticity equations for core and facesheets to 2 dimensions by taking average quantities with respect to y (the column width). The stress resultants N_y and M_y were assumed zero for a narrow strut, since both quantities must be zero at the free edges. The symmetric wrinkling solution obtained can be expressed in the following form :

$$Nx_{wr} = 5.657 \left\{ \left(D_e - \frac{B_e^2}{A_e} \right) \frac{E_c}{h} \right\}^{\frac{1}{2}} \qquad \text{(eq. 6.11)}$$

where :

$$A_e = A_{11} + \frac{A_{12}B_{12}B_{22} - A_{12}^2D_{22} - B_{12}^2A_{22} + B_{12}A_{12}B_{22}}{(A_{22}D_{22} - B_{22}^2)}$$

$$B_e = B_{11} + \frac{A_{12}D_{12}B_{22} - A_{12}B_{12}D_{22} - B_{12}D_{12}A_{22} + B_{12}^2B_{22}}{(A_{22}D_{22} - B_{22}^2)}$$

$$D_e = D_{11} + \frac{B_{12}D_{12}B_{22} - B_{12}^2D_{22} - D_{12}^2A_{22} + D_{12}B_{12}B_{22}}{(A_{22}D_{22} - B_{22}^2)}$$

For [B] = 0 the solution reduces to the specially orthotropic equation. Further tests carried out gave closer agreement to the above theoretical prediction if the adhesive layer was included. It was therefore concluded that the major source of discrepancy in the specially orthotropic prediction (eq. 6.9) was due to neglect of the adhesive layer and coupling in the facesheet-adhesive lay-up.

The column formula (equation (6.11)) is not applicable to panels in general because of the assumption of zero N_y and M_y over the whole width. For low Poissons ratio lay-ups, such as [0/90] the column formula will give a reasonable approximation to the wrinkling load for panels of greater width, but for facesheet lay-ups which have a high effective Poissons ratio, such as [+45/-45], the formula is restricted to narrow columns only.

6.1.4 Flexural Wrinkling of Cross Ply Beams

In reference [41] Gutierrez & Webber extended the orthotropic theory further to investigate the wrinkling problem for cross ply faced sandwich beams in bending. Under this loading action, local wrinkling instability can occur in the compression face. Bending was incorporated into the equilibrium equations by considering the facesheets to be acted upon by an equivalent tension and compression stress resultant couple. It was assumed that the initial facesheet out-of-plane displacements were zero. Although this is clearly not the case for a beam under bending, such an assumption is still reasonable for wrinkling analysis. This is because the overall bending displacement distribution has a large wavelength compared to the wrinkling wavelength, and so can be considered as the zero displacement reference plane. Solutions obtained for [0/90] faced panels showed that the facesheet wrinkling stress resultant was slightly higher than that calculated for a column under pure compression.

6.2 GENERALISED WRINKLING THEORY

In this current work, linear small displacement wrinkling theory was extended to comprehensively take into account all facesheet coupling effects. Both membrane-flexural coupling and bending-twisting coupling of the facesheet lay-up were accomodated. This allows facesheets with fully populated [B] and [D] matrices to be analysed. Membrane coupling effects (A_{13}, A_{23} terms) were not included since these terms are zero for all practical lay-ups ($+\theta$ and $-\theta$ plies always occur in pairs to prevent warping during manufacture and to give equal shear strength in positive and negative senses).

The theory was also extended to allow critical wrinkling loads to be calculated for combinations of axial compression, in-plane shear and bending loading actions. As such, the theory enables effective wrinkling analysis to be performed for all practical composite faced honeycomb panels and load combinations that are likely to be encountered in spacecraft structures.

The development of the theory is described fully in Appendix B. It follows the methods of Hemp[38] and Pearce & Webber[37] by setting up six facesheet-core interface equilibrium equations in terms of mid-plane displacements and through-thicknesses strains for the panel in its buckled condition (three for each facesheet). The stresses acting on an element of the panel and the assumed sign convention are given in fig. 6.2. The method departs from that for specially orthotropic facesheet lay-ups by allowing for shear and differential axial loading of the facesheets in the equilibrium equations, and by introducing extra terms associated with coupling. Because this results in mixed derivatives in the equilibrium equations it was necessary to resort to a skew-sinusoidal function to describe the assumed buckled waveform. Functions of the following form were assumed :

$$w_0 = W \sin\left(\frac{m\pi x}{a} - \frac{n\pi y}{b}\right) \qquad \text{(eq. 6.12a)}$$

which alternatively can be re-expressed as

$$w_0 = W \sin \frac{m\pi}{a}(x - \phi y) \qquad \text{(eq. 6.12b)}$$

This function has a sinusoidal variation across the plate (y direction) of n half waves in addition to m half waves along the length. Alternatively, the shape function can be considered as sinusoidal waves skewed at an angle with half wavelength $(a/m).\cos\phi$, see fig. 6.3.

Although this form of shape function satisfied the equilibrium equations, in general simply supported or fixed boundary conditions will not be satisfied. This means that other than for the special case of axially loaded, specially orthotropic faced panels, calculated values of the overall (single half wave) panel buckling mode using these assumed shape functions will be invalid. The skew shape function can however be used to predict symmetrical and anti-symmetrical wrinkling modes. This is because the wrinkling mode wavelengths are very much smaller than the panel dimensions in all practical cases. Consequently violated edge conditions have little influence over the behaviour of the majority of the panel area.

For the general case, the use of skew-sinusoidal shape functions to represent mid-plane strains and displacements prevents any simplifications to the six equilibrium equations. It is not possible to reduce the problem to a closed form solution and all six equations must be retained. After lengthy substitutions it is possible to condense them into a 6 degree of freedom eigen-problem which can be expressed in more convenient matrix form as :

$$([C] - \lambda[P])\{U\} = 0 \qquad \text{(eq. 6.13)}$$

where, [C] is a 6 x 6 matrix of stiffness coefficients

[P] is a 6 x 6 matrix of load coefficients

$\{U\}$ is the 6 degree of freedom vector of mid-plane displacement and strain amplitudes

λ is the buckling eigenvalue

The stiffness and load matrix coefficients are listed in Appendix B. Appendix C describes a FORTRAN program which was written to generate the matrices and solve the eigenvalue problem. There are six eigenvalue solutions, of which only some are finite. These correspond to different buckling modes (eg. symmetric and anti-symmetric). The critical eigenvalue for a particular mode was found by varying the buckled waveform parameters m & n until a minimum was found. The program described in Appendix C included a facility for performing this minimisation automatically.

6.3 COMPRESSION WRINKLING

To test the program and make comparisons with existing solutions, the case of a cross-ply laminated sandwich panel under axial loading was investigated. The example is the same as that given in reference [40], other than an infinite width panel rather than a narrow column is considered. The facesheets are two ply [0/90] CFRP on a 25 mm deep low density NOMEX core. The panel length is 400 mm. Full details of the panel construction are shown on fig. 6.4.

Because the loading is longitudinal compression only and B_{13}, B_{23}, D_{13} & D_{23} are all zero for this facesheet lay-up, the buckled waveform has nodal lines of zero slope, so m is the only minimisation parameter. Eigenvalue buckling loads were calculated using the program for different half-wave numbers, m. Six eigenvalues were extracted, corresponding to the number of equations. Of these, only two had finite values. These were the symmetric (ϵ_{z0} dominated) and anti-symmetric (W_0 and γ_{xz} dominated) modes. The variations of the eigenvalues for these modes with assumed half-wavelength are shown in fig. 6.4.

The overall buckling load for the panel (simply supported loaded edges, free unloaded edges) is the eigenvalue for the antisymmetric mode with m=1.

The calculated value was 268 N/mm which is in agreement with the value calculated in reference [40]. Minima for the symmetric and anti-symmetric modes occur for values of m of approximately 75 and 90 respectively, with eigenvalues of 103 N/mm and 166 N/mm. These are also in agreement with the symmetric and anti-symmetric wrinkling loads calculated in reference [40]. Good agreement between infinite-width panel and column buckling loads is to be expected for this example because of the low effective Poisson's ratio of the facesheets.

The influence of the B_{11} and B_{22} facesheet coupling terms which are present for [0/90] lay-ups can be determined by performing the calculations with all B_{ij} set to zero. These show that there is no significant effect on overall Euler buckling loads because this mode is dominated by the panel's overall flexural stiffness, so coupling effects of the facesheets themselves will be negligible. The symmetrical wrinkling load, on the other hand, is increased to 155 N/mm by neglecting facesheet coupling. Hence, neglecting coupling by assuming special orthotropy leads to unconservative results of 50% in this case.

6.4 SHEAR WRINKLING

Calculation of shear wrinkling loads requires a skewed buckling waveform to be assumed, so the minimum load has to be located with respect to both m and n. The example considered is a 300mm square sandwich panel with [0/90] 2-ply HM-S/CYCOM 985 carbon-epoxy facesheets on a 10mm deep 2.0 lb/cu-ft aluminium honeycomb core. Facesheet properties were calculated based on the material testing performed in this study. Full details of the panel are given in fig. 6.5.

Symmetric and anti-symmetric modes were obtained for different values of m and n. The minimum wrinkling load was found to occur for the symmetric mode. The variation of the symmetric mode eigenvalue with m and n is shown in fig. 6.5 for the cases in which B_{11}, B_{12} coupling was included and for the case when they were neglected. The minima are seen to occur when m and n are equal, implying a nodal slope of the buckled waveform of 45°; ie.

perpendicular to the principal compression direction. The critical shear load was computed as 118 N/mm if B_{11} and B_{22} were included, and as 186 N/mm if they were excluded. This latter value agreed with that found using the specially orthotropic formula with E_f calculated for the facesheets in the 45° direction i.e. for [0/90] rotated to [±45]. As with the compression loaded example, it can be seen that the use of the specially orthotropic formula leads to an unconservative result of over 50%.

The calculated wrinkling wavelength was shorter (larger m & n) when the coupling terms were included. This feature was also found for compression wrinkling. In both examples, the wrinkling wavelength was slightly less than the honeycomb 3/16" cell size. The theoretical derivation assumed a continuous orthotropic core medium so the validity of this assumption is debatable for such small critical wavelengths. Nevertheless it can be argued that the facesheets are supported by the core at smaller intervals than a single cell diameter, both as a consequence of the staggered arrangement of the cells and the slope of the nodal lines, see fig. 6.6.

Where the calculated wrinkling wavelength is of the order of the cell size, the possibility of coupling between inter-cell dimpling and wrinkling instability will exist, and this could have the effect of reducing the calculated critical loads. Unfortunately, for many typical spacecraft carbon-epoxy faced aluminium honeycomb panel constructions critical wrinkling wavelengths are of the order of the honeycomb cell size. Tests reported later in this Chapter however, found no evidence of reduced critical wrinkling loads due to wrinkling-dimpling coupling.

6.5 FLEXURAL WRINKLING

For flexural wrinkling, the example given in reference [41] was run using the program to enable a direct comparison to be made. The panel construction is exactly the same as the compressive wrinkling example of section 6.3.

Flexural wrinkling was accomodated in the analysis in the same way as reference [41] by considering equal but opposite tension and compression N_x stress resultants in the facesheet equilibrium equations. This stress resultant couple is equivalent to an applied bending moment provided that the assumption of thin facesheets and thick core is valid. For input to the program (Appendix C) this meant setting the facesheet direct stress resultant factors K_{x1} = +1 and K_{x2} = -1 or vice versa. (See Appendix B for the definition of these terms.)

As with compression wrinkling, flexural wrinkling of [0/90] faced panels will have waveforms with no nodal line slope, ie. m is the only necessary minimisation parameter. Fig. 6.7 shows the variation in the wrinkling load with m for the panel, for the cases of pure compression and pure bending. For pure compression the load axis refers to the single facesheet compressive load, and for bending it refers to the equivalent tension and compression facesheet couple. This figure shows that the critical flexural wrinkling load is higher than that for the panel loaded by an equivalent compression load in both facesheets. The computed critical loads were in agreement with those found in reference [41]. The higher critical load for flexure was also in agreement with test results of reference [36] which found in general higher wrinkling loads for 4-point bending specimens over those loaded in pure compression.

Two finite eigenvalues of equal magnitude but opposite sign were found for the case of flexural loading. The corresponding eigenvectors consisted of W_0, γ_{xz} and ϵ_{z0} deflections and strains, which differed only in sign between the eigenvalue pair. The W_0 deflection component diminished in comparison to the γ_{xz} and ϵ_{z0} strains as m increased. The two eigenvalues referred to positive and negative applied bending moments. The difference between the buckled mode shapes for bending to those for compression was that the symmetric and anti-symmetric modes were combined rather than distinct.

The assumption made in reference [41] for flexural wrinkling analysis was that the tension facesheet remains undistorted by buckling in the compression face. This assumption is bourne out by the results found from

the generalised wrinkling analysis here. The facesheet lateral deflection w_f is given by equation (B.10) of Appendix B. For the assumed shape functions and zero nodal line slope, the facesheet deflection amplitudes become

$$w_f = \frac{h^2}{8E_c} G_{xz} \gamma_{xz} \left(\frac{m\pi}{a}\right) \pm \frac{h}{2} \bar{\epsilon}_{z0} \qquad \text{(eq. 6.14)}$$

where + & - signs in the second term refer to upper and lower facesheets. The program results showed that at the critical wavelength (a/m^*) the shear and direct core strains were such that the two terms in the above equation were equal in magnitude and cancelled in the tension facesheet. Hence there is no lateral deflection in the tension facesheet at wrinkling. The increase in the critical wrinkling load over the pure compression case can therefore be explained by the constraining influence of the tension facesheet, which results in a mode shape which is a combination of the classical compression symmetric and anti-symmetric modes.

The wrinkling analysis approach often used for panels under bending loads is that of an equivalent compression in both facesheets. For this example, such an approach yields an underestimate of 23%. The equivalent compression approach is often used in combination with a specially orthotropic wrinkling formula which neglects [B] matrix coupling. Neglecting B_{11} and B_{22} in the current example, as shown previously for compression wrinkling, results in a serious overestimate. The net effect is a reduced overestimate of 17%.

6.6 EFFECT OF SANDWICH PANEL DESIGN PARAMETERS ON CALCULATED WRINKLING LOADS

The wrinkling program was used to investigate the effect of sandwich panel design parameters, namely core depth and facesheet lay-up, on the calculated wrinkling loads.

6.6.1 Facesheet Lay-up

The effect of the facesheet lay-up on the calculated wrinkling loads under compression, shear and bending was investigated for typical spacecraft composite sandwich panels. To enable direct comparisons to be made, a 20mm deep 2.0-3/16"-0.0007" 5056 aluminium honeycomb was adopted for all of the differently faced constructions. Two facesheet materials were considered : unidirectional T-300/CYCOM 985 and plain woven T-300/CYCOM 985, to allow a comparison between the prepreg types to be made. Mechanical property data for these materials was obtained from tests performed in reference [5], and these are summarised here in Table 6.1 .

Three commonly used lay-up types were investigated : bi-directional, 3-fibre direction quasi-isotropic and 4-fibre direction quasi-isotropic. The facesheet lay-ups and their calculated constitutive matrices are listed in Tables 6.2 to 6.4. The [0/90] facesheet lay-ups are typical of rectangular exterior spacecraft panels, the [±45] are typical of shear panels and the quasi-isotropic lay-ups typify multiaxially loaded panels such as platforms. The 3-fibre direction quasi-isotropic facesheet lay-ups offer the possibility of reduced mass design solutions over those incorporating 4 fibre directions.

With 3 or more plies, an additional design freedom is the ply stacking sequence. This freedom is reflected in the lay-ups investigated. Altering the stacking sequence does not affect the overall stiffness properties of the panel, since these are determined primarily by the facesheet [A] matrix, which is stacking sequence independent. However the stacking sequence does alter the [B] and [D] matrices and hence the panel's wrinkling behaviour.

Calculated wrinkling loads for pure compression, pure shear and pure bending for the differently faced panels are given in Tables 6.5 to 6.7 along with the half-wavelengths and nodal line slopes of the wrinkling modes. The critical wrinkling loads are given for a single facesheet (the critical compression and shear loads on the complete panel are simply twice the single facesheet figure, for flexure the figure refers to the critical

tension/compression equivalent membrane load). Figures in brackets refer to calculations using the specially orthotropic wrinkling formula which ignore coupling effects, given for comparison. For shear, these are calculated by using D_{11} for the facesheets when rotated to the 45° principal compression directions. For bending, the equivalent compression of both facesheets is used. The notation and sign convention for shear direction, fibre angles, θ nodal line slope, ϕ, and half-wavelength, l^*, are those of fig. 6.3.

6.6.1.1 Bi-directional Lay-ups

Table 6.5 shows that for the single woven ply faced panels there is complete agreement between the compression and shear wrinkling loads calculated using the program and the specially orthotropic design formula. This is to be expected, for compression at least, since there are no coupling effects for these facesheets: [B] = 0 and $D_{13} = D_{23} = 0$. For the case of flexural wrinkling, the simple approach neglects the alleviating effect of the tension facesheet and underestimates the critical load by about 25% for both [0°] and [45°] orientated woven faces. Results for shear of the [0°] woven and compression of the [45°] woven orientated faces are interchangeable because the buckle nodal line slope is in both cases perpendicular to the principal compression direction. This is also true for the [0/90] and [+45/-45] UD faced panels. This may seem intuitive, and is the recommended assumption of reference [35] when applying the simple design formula to panels under combined shear and compression loads. However as will be shown for other lay-ups, this is not always the case.

Coupling terms are present in the 2-ply unidirectional facesheets because there is no symmetry about the facesheet mid-plane. For [0/90] lay-ups there is membrane-bending coupling (B_{11} and B_{22}) and for [+45/-45] lay-ups there is membrane-twisting/shear-bending coupling (B_{13} and B_{23}), see Table 6.2. This coupling results in wrinkling loads lower than those calculated using the specially orthotropic formula which neglects B_{ij} terms. The reduction effect of B_{11}, B_{22} coupling in the [0/90] lay-up is 35%, slightly larger than the reduction effect of B_{13}, B_{23} coupling in the [±45] lay-up

which is 30%. As well as reducing wrinkling loads, the coupling terms have the effect of reducing the wrinkling wavelengths.

Where wrinkling is the critical design case, these results suggest that woven facesheets provide a better solution. The slightly lower stiffness of a single woven ply compared to two unidirectional cross plies is more than offset by the increase in wrinkling strength as a result of no facesheet coupling.

6.6.1.2 3-Fibre Direction Quasi-Isotropic Lay-Ups

Three ply quasi-isotropic facesheet lay-ups are built up from 0°, +60° and -60° plies, or +90°, +30° and -30° if referenced to the perpendicular direction. Quasi-isotropy refers only to the membrane stiffness or [A] matrix which is invariant with direction. The other constitutive matrices, [B] and [D] do differ both with direction and the ply stacking sequence. These differences are shown for the 3-ply quasi-isotropic lay-ups given in Table 6.3.

The specially orthotropic wrinkling formula shows that the important facesheet stiffness term is D_{11} - the flexural rigidity in the load direction. This is reflected in the ranking of the compression wrinkling loads for the four lay-ups given in Table 6.6. The [+30/90/-30] and [0/+60/-60] lay-ups have the highest critical loads because the 0° or near load direction 30° fibres are furthest from the mid-plane and so yield larger D_{11} terms. Coupling in all the lay-ups reduces the compression wrinkling loads compared to the calculated values when these effects are neglected. The reduction effect varies between 26% and 37%. No obvious correlation between the reduction effect and the relative magnitudes of the B_{ij} and D_{13}, D_{23} coupling terms is apparent.

A feature of the lay-ups in which the 0° or 90° ply is displaced from the centre of the stack, is that the resulting wrinkling mode shape has sloping nodal lines. The nodal line slope is the same for both compression and flexural wrinkling. These lay-ups have fully populated [B] and [D]

matrices, but no conclusions can be drawn as to which terms have the greatest contributory effect.

As a result of D_{13} coupling, the critical shear wrinkling loads of the [0/+60/-60] and [90/+30/-30] faced panels depends on the direction of the applied shear. There is no such dependence for lay-ups with no D_{13} coupling, a situation analogous to the dependence of material strength on shear direction. This effect is accounted for in the simple formula by the difference in the effective D_{11} terms for the facesheet in the +45° and -45° directions. Neglecting the coupling however, overestimates the shear wrinkling loads by 23% to 37%. For all of the lay-ups considered, the critical slopes of the wrinkles under shear are not perpendicular to the principal compression direction (ie. not at +45° or -45° to the x-direction). This is a consequence of facesheet coupling and further invalidates the use of the specially orthotropic formula with an equivalent modulus (E_f) in the principal compression direction.

Based on these results, some recommendations can be made on the best 3-ply quasi-isotropic lay-up to adopt for a wrinkling critical panel. The fundamental point is that wrinkling strength depends on the load direction. If a [+60/0/-60] lay-up is adopted, with the 0° ply central, it should be aligned perpendicular to the highest compressive load or moment. This means the lay-up is effectively [+30/90/-30] in the highest load direction, which yields a significantly higher wrinkling strength. Material strength is also higher in this orientation and shear wrinkling strength is not direction dependent.

If instead, the 0° ply is positioned away from the centre of the lay-up i.e. [0/+60/-60], the wrinkling strength becomes highest in the longitudinal (0°) direction and lowest in the transverse (90°) direction. By aligning the 0° ply parallel to the highest loading there are small increases in wrinkling strengths over the [+30/90/-30] lay-up in both directions. However, the material strength for a sandwich panel with thin facesheets in bending or under compression, is not dependent on the stacking sequence. Strength is still therefore highest in the 90° direction. Hence, for this lay-up sequence, the direction of highest

wrinkling strength (0°) is perpendicular to the direction of highest material compression strength (90°). Such a situation is not desirable from the point of view of optimising the design. In addition, such a lay-up results in a panel shear wrinkling strength which is directionally dependent. No significant gains in wrinkling strength are made by positioning the 0° ply away from the lay-up mid-plane and with the other attendant disadvantages, positioning it in the centre of the stack is recommended.

6.6.1.3 4-Fibre Direction Quasi-Isotropic Lay-Ups

Four fibre direction quasi-isotropic lay-ups have layers orientated at 0°, ±45° and 90°. The wrinkling behaviour of three lay-ups of this type were compared using the program. Two have 4 unidirectional layers, one with the ±45° layers on the outside and one with them in the centre, and the third has 2 woven layers. As with the 3-fibre direction quasi-isotropic lay-ups these all have similar [A] matrices but greatly different [B] and [D] matrices, see Table 6.4.

The results for these panels are given in Table 6.7. Under pure compression, the program predicts wrinkling loads 28-32% lower than those predicted by the specially orthotropic formula for the UD lay-ups due to [B] coupling. The [0/+45/-45/90] facesheet lay-up gives the higher load of the two because the 0° ply is further from the mid-plane, and hence has a higher D_{11}. For both lay-ups the wrinkling mode shape has a slight skew. Rather surprisingly, the coupling present in the [0/45] woven lay-up has only a small effect on the compression and shear wrinkling loads. The reduction is only 2%, so that predicted wrinkling performance of the lay-up is superior to both the UD lay-ups.

Shear wrinkling loads of all three facesheet lay-ups are the same for both shear directions because D_{13}, D_{23} terms are not present. Improved shear wrinkling strength is gained by placing the ±45° plies furthest from the mid-plane as would be expected. Note that the shear wrinkling strength of [0/+45/-45/90] roughly equals the compression wrinkling strength of

[+45/0/90/-45] and vice-versa since one lay-up is the other rotated through 45°. The agreement is not exact because the nodal line slope is rotated slightly away from the principal compression perpendicular direction. Choice between one lay-up sequence or the other would depend on whether the panel loading was dominated by direct or shear stresses. If wrinkling is critical, a 2-ply woven lay-up may offer the best solution because of higher wrinkling strengths at the cost of only a small facesheet stiffness reduction. Additionally, a woven lay-up can offer some advantages for manufacturing.

6.6.2 Core Thickness

The specially orthotropic formula which neglects coupling, predicts that compression wrinkling strength is inversely proportional to the square root of the core depth. This is shown graphically for a [0/90] HM-S CYCOM 985 faced panel with 2.0 lb/cu ft core in fig 6.8. Also shown on the same graph is the theoretical wrinkling strength predicted using the program which includes [B] coupling. Other than the downwards displacement, due to the coupling effect, the curve is of the same form - also inversely approximately proportional to the square root of core depth.

In fig. 6.9 the compression wrinkling strength of [0/+45/-45/90] faced panels is plotted against core depth. The buckled waveform for this construction is skewed at -21°, and this angle is found to be constant for all core depths. Hence the nodal line skew effect under pure compression is a result of facesheet coupling only. The compression wrinkling strength also varies inversely with the square root of h for this lay-up.

For flexural wrinkling, the bending moment to cause wrinkling is the important measure of strength. For facesheets which are thin compared to the core depth, the approximate relationship between the equivalent facesheet membrane loading and applied moment is :

$$N_x = \pm \frac{M_x}{h}$$

Hence, using the specially orthotropic formula and the assumption that both facesheets are loaded by the equivalent membrane compression, the critical bending moment becomes :

$$M_x = 5.657 \, (D_{11} \, E_c \, h)^{\frac{1}{2}} \qquad \text{(eq. 6.15)}$$

This relationship assumes flexural wrinkling bending moment capacity is directly proportional to the square root of the core depth. Fig. 6.10 plots the computed wrinkling bending moment against core depth for [0/90] faced panel construction. The variation of moment :

$$M_x \propto h^r$$

is found to have an exponent r slightly greater than ½ when the tension facesheet alleviation effect is taken into account.

6.6.3 Summary

Based on the results of the numerical calculations performed for commonly used panel constructions described above, it is possible to make a number of general observations regarding wrinkling behaviour under separately applied compression, shear and flexural loading actions.

(1) Facesheet coupling reduces the predicted wrinkling loads. Compression and shear wrinkling loads are reduced typically by about 30% for the 2,3 and 4 ply lay-ups considered, and can be up to 50%.

(2) It is not readily apparent which coupling terms dominate the reduction effect. There is a complex inter-relationship between the B_{ij} and D_{13}, D_{23} terms which causes the reduction. Therefore it is not possible to estimate a reduction factor from the facesheet constitutive matrix to apply to the specially orthotropic prediction formula.

(3) The wrinkled mode shapes have buckles which are not necessarily perpendicular to the principal compression direction. Coupling terms can result in buckles which are skewed through small angles away from the principal compression perpendicular directions.

(4) Certain facesheet lay-ups have shear wrinkling strengths which are dependent on the direction of the applied shear. This is a result of D_{13}, D_{23} coupling.

(5) Flexural wrinkling strengths are higher than the equivalent wrinkling strengths of both facesheets in compression. This is because the tension facesheet remains unbuckled and so disturbs the stress/strain distribution in the core from the classic symmetric wrinkling mode.

(6) For compression and shear, the symmetric wrinkling mode is always lower than the anti-symmetric mode.

(7) The critical half-wavelengths are smaller when facesheet coupling is taken into account. Critical half-wavelengths increase with facesheet stiffness and core depth. For the constructions considered, critical half-wavelengths are in the range 3-6 mm. This wavelength is of the order of commonly used honeycomb cell sizes which contravenes the assumption of a continuous core and could lead to possible wrinkling-dimpling interaction.

(8) Compression wrinkling strength is decreased with increasing core depth but flexural wrinkling bending moment capability is increased.

(9) Ply stacking sequences must be carefully considered when designing wrinkling critical panels. The fibres furthest from the facesheet mid-plane should ideally be orientated near to the principal compression direction and coupling minimised.

(10) Woven materials can offer improved wrinkling strengths over equivalent uni-directional lay-ups because the coupling reduction effects are less severe.

6.7 WRINKLING UNDER COMBINED LOADS

6.7.1 Compression and Shear

To investigate wrinkling behaviour under combined compression and shear, calculations were performed using the program for a [0/90] HM-S/CYCOM 985 faced panel with 10mm deep 2.0lb/cu ft aluminium honeycomb core. This is the same example described in section 6.4 for pure shear loading. Under combined loading, the critical compression and shear stress resultants are found for a prescribed compression/shear ratio from the symmetric mode eigenvalue, minimised with respect to the mode shape parameters m & n. In the program this is carried out by specifying shear and compression factors K_x and K_{xy} for each facesheet in the proportion of the applied load. The critical compression and shear resultants are then found by multiplying the minimum eigenvalue by these factors.

Fig. 6.11 plots the compression-shear wrinkling envelope computed for this example. Shown on the same graph is the envelope calculated when [B] matrix coupling was ignored, which illustrates the large overestimate for the full range of load combinations if these terms are neglected. The reduction factor as a result of [B] coupling was 41% under pure compression, falling off slightly to 36% as the compression component of the load falls to zero under pure shear.

Also plotted on the graph is an estimate of the wrinkling envelope calculated using the specially orthotropic formula. This envelope was constructed using the recommendations of reference [35] for calculating wrinkling strengths under combined loading. This suggests applying the compression wrinkling formula (equation (6.1)) in the principal compression direction. This then becomes :

$$\frac{1}{2} N_x \left(1 + \sqrt{1 + 4K_s^2}\right) = 1.633 \left(\frac{E_f t^3 E_c}{h}\right)^{\frac{1}{2}} \qquad \text{(eq. 6.16)}$$

where, K_s (loading ratio) $= \dfrac{N_{xy}}{N_x}$

E_f = Effective Modulus in principal compression direction, θ

$$\theta = \frac{1}{2} \text{Tan}^{-1} (2K_s)$$

The envelope so constructed agrees with the program calculations with [B] = 0 at $N_x = 0$ and $N_{xy} = 0$, but over predicts at intermediate load ratios. The reason for the discrepancy is that the use of E_f in the principal compression direction is not valid at angles away from 0° and 45° because D_{13} and D_{23} terms are then generated. These are not included in the specially orthotropic formula but their presence is implicit in the program, which hence predicts slightly lower loads. The outermost envelope of fig. 6.11 can therfore be thought of as ignoring all facesheet coupling effects. The middle envelope ignores membrane-bending coupling (B_{11} and B_{22}) but does include implicit bending-twisting coupling at intermediate load ratios; and the innermost curve includes all coupling effects. Viewed this way, the coupling reduction effect can be seen to be dominated by B_{11}, B_{22} coupling for [0/90] facesheet lay-ups.

Plotted in fig. 6.12 is the wrinkled waveform nodal line slope against the shear/compression load ratio. It is interesting to compare this with the slope of the principal compression plane. This shows the principal compression plane slope lags behind nodal line slope at low shear load ratios before they both approach 45° at high shear ratios. This illustrates the inherent coupling effects for the [0/90] facesheet lay-up under combined loads which do not occur when the loads are applied separately.

6.7.2 Bending and Shear

The combined bending and shear wrinkling envelope differs somewhat from the smooth envelope for combined compression and shear, as shown by fig. 6.13 for the case of a [+30/90/-30] HM-S CYCOM 985 faced panel. The envelope is characterised by a sharp knee at a certain critical load ratio as the wrinkling mode switches from a symmetric one to an asymmetric one.

At lower shear loads, region I of the curve, wrinkling is dominated by instability in the compression facesheet. Tension in the other facesheet has a stabilising effect which results in an asymmetric mode shape. As the proportion of shear increases, this adds to the destabilising principal compression in both of the facesheets. At a certain critical ratio (region II) the stabilising effect in the tension facesheet due to flexure is offset by the principal compression in this facesheet due to shear. This facesheet then no longer stabilises the other, and the mode shape becomes like that of classical symmetric wrinkling. As the proportion of shear increases further, in region III, the mode shape becomes more symmetric in nature as the principal compression shear resultants in each facesheet become closer to each other in magnitude and direction. Shear then dominates the wrinkling behaviour.

The abrupt change in the wrinkling failure mode is also shown in fig. 6.14 which is a plot of the nodal line slope (or skew angle) against the load ratio. At the critical load ratio, 0.50 in this case, there is an instantaneous change in the nodal line slope as shear takes over from flexure as the dominating load component. Below the critical load ratio there is a small increase in the slope up to about 8°, this then changes suddenly to about 48° at the critical load ratio, and increase steadily once more to about 54° as the flexure load component becomes zero. This final skew angle under pure shear, agrees with that found in section 6.6.1.2 for the same facesheet lay-up but different material and core depth. This implies it is the relative magnitudes of the various coupling terms which dictate the wrinkling mode shape.

The shape of the combined bending and shear envelope has important consequences for wrinkling failure analysis. At load ratios close to the knee of the curve the interaction between the two loads should be taken into account. If the wrong load is assumed to dominate, and the analysis is performed using a simple estimation which ignores the other load, the estimate will be seriously under-conservative.

6.8 DIMPLING INSTABILITY

Dimpling instability can occur when one or both facesheets of a honeycomb sandwich panel are loaded under compression. Buckling of the compressed facesheet occurs within the honeycomb cell cavities; the mode is shown in fig. 6.15.

The dimpling analysis of isotropic faced honeycomb panels usually considers the buckling of a simply supported square facesheet element with dimensions of the honeycomb cell size. The actual hexagonal shape of the honeycomb cells and additional support provided by adhesive fillets at the edges of the 'plate' are ignored. When unbalanced composite facesheets are considered an effective analysis is further complicated by the presence of coupling terms in the facesheet constitutive matrix. These coupling terms prevent simple shape functions for the buckled mode (even assuming the plate boundary is square) from being used in conjunction with the equilibrium equations and assumed boundary conditions.

The critical facesheet dimpling stress for an isotropic faced honeycomb panel is normally estimated by the following equation, assuming that the facesheets are initially flat :

$$\sigma_d = \frac{3.29}{(1-\nu^2)} E \left(\frac{t}{d_c}\right)^2 \qquad \text{(eq. 6.17)}$$

where σ_d = single facesheet critical dimpling stress

E = facesheet modulus

ν = facesheet poisson's ratio

t = facesheet thickness

d_c = honeycomb cell size

Using the same approach for specially orthotropic composite facesheets, assuming a buckled waveform of a single half-wave in both directions of a square plate of side d_c, the dimpling equation is modified to :

$$N_{xd} = \left\{ 20\ (D_{11}\ D_{22})^{\frac{1}{2}} + 2\pi^2\ (D_{12} + 2D_{33}) \right\} \frac{1}{d_c{}^2} \qquad \text{(eq. 6.18)}$$

where, Nx_d = single facesheet dimpling stress resultant

D_{ij} refer to the flexural rigidity matrix of the facesheet, the 1 direction being parallel to the applied compression.

Because the buckled mode shape is symmetric with regard to the x and y directions (parallel and perpendicular to the applied compression) the D_{11} and D_{22} terms have an equal importance in the determination of the critical dimpling load. The D_{12} and D_{33} also play an important role in determining the dimpling strength. A facesheet lay-up which is pseudo-isotropic will therefore have a higher dimpling resistance than one which is highly directional, for the same thickness. This contrasts with wrinkling behaviour, in which it is desirable to orientate the fibres to give a high D_{11}, because this instability mode is characterised by buckles in the load direction only.

Experimental evidence[42] suggests that the simple estimation of dimpling, even for unbalanced facesheet lay-ups tends to be over-conservative, and that dimpling itself is not a catastrophic failure mode. Load is carried beyond the onset of dimpling, although dimpling can lead to a reduction in stiffness and a possible interaction with other modes of failure.

Dimpling is only significant for very thin facesheets if core cell sizes of 3/16 " or less are used. Aluminium honeycomb cores down to 2.0 lb/cu ft are available without having to resort to larger cell sizes. These densities are of sufficiently low weight for most applications. Table 6.8 gives the critical facesheet compression resultants for several unidirectional (0.10 mm ply) and woven (0.23 mm ply) T-300/CYCOM 985 lay-ups on a 3/16 " cell core using equation (6.18). Note that only the single ply woven lay-ups are specifically orthotropic.

TABLE 6.8

DIMPLING STRENGTHS OF T-300/985 LAY-UPS ON 3/16" CELL CORE

LAY-UP	DIMPLING LOAD PER FACESHEET (N/mm)
[0/90] UD	46
[0] WOVEN	61
[+45/-45] UD	78
[45] WOVEN	101
[+60/0/-60] UD	217
[+30/90/-30] UD	217
[0/+45/-45/90] UD	403
[+45/0/90/-45] UD	590
[0/+45] WOVEN	647

This table shows that for these bi-directional and pseudo-isotropic lay-ups, dimpling strengths for facesheets thicker than about 0.2 mm are quite high even with such a low modulus carbon fibre system. It is quite likely that panels with these faces will fail by other modes before dimpling occurs. For facesheets thinner than 0.2 mm dimpling may occur prior to failure. It is interesting to note from Table 6.8 that dimpling resistance is higher for [±45] lay-ups than [0/90]. By contrast wrinkling and material strength are higher for the latter. This is a consequence of the relative importance of the D_{12} and D_{33} terms in equation (6.18).

6.9 LOCAL INSTABILITY TESTS ON CO-CURED SANDWICH CONSTRUCTIONS

In order to test the local instability theories, composite faced sandwich specimens were manufactured for testing under pure compression. These specimens were manufactured using the co-cure process with typical spacecraft panel facesheet lay-ups containing [B] coupling terms in their constitutive matrices. This enabled the coupling effect predicted by the wrinkling theory to be compared with experimental results. Testing was limited to pure compression, since this load condition was the simplest to attain experimentally.

6.9.1 Panel Construction

Two flat sandwich panels were manufactured using the co-cure method described in Chapter 4. The facesheets were preconsolidated at 80 psi and room temperature, and the co-cure of the complete sandwich was carried out at 30psi and 180°C. Each panel was divided into two with a different facesheet lay-up in each half. There were a total of four different facesheet lay-ups altogether, these are given in Table 6.9. A common core of 2.0-3/16"-0.0007" perforated 5056 aluminium honeycomb with a thickness of 1¼" was used in all the panel constructions. FM 300M film adhesive of 150 g/m^2 was used to bond core and facesheets together.

TABLE 6.9 PANEL CONSTRUCTIONS

PANEL	FACESHEETS		CORE
	Material	Lay-Up	
1A	UD HM-S/CYCOM 985	[+30/90/-30]	
1B	UD HM-S/CYCOM 985	[-60/0/+60]	2.0-3/16"-0.0007"
2A	UD HM-S/CYCOM 985	[0/90]	h = 31.25 mm
2B	Woven T-300/CYCOM 985	[0]	

Note: Facesheet lay-ups specified with outermost ply first.

The first three facesheet lay-ups were of unidirectional HM-S/CYCOM 985, for which material property data had been previously generated (Chapter 5), and the fourth was a single ply of plain woven T-300/CYCOM 985 which enabled a comparison with the [0/90] UD to be made, and for which some limited test coupon data was available.

6.9.2 Compression Specimens

Six specimens with nominal dimensions of 140 mm L x 90 mm W were cut from each panel half with the honeycomb ribbon direction aligned longitudinally. Aluminium tags were bonded to the loaded ends in a manner similar to the smaller sandwich compression specimens described in section 5.5.2. The cavity was filled with epoxy and machined flat to provide end reinforcement and ensure uniform load introduction, fig. 6.16.

6.9.3 Specimen Constitutive Matrices

The prediction of instability modes was based on facesheet constitutive matrices computed using material property test data. For unidirectional HM-S/CYCOM 985 the properties found from tests on 30 psi cured coupons, and given in Table 5.6, were used. For woven T-300/CYCOM 985 test data from coupons cured at 80 psi, and given in Table 6.1, were used since no low pressure cure test data was available for this system. The effect of cure pressure on E_1, the important property as regards instability behaviour, was not expected to be great however.

In reference [40] the facesheet to core adhesive layer was considered to be an important factor in the determination of wrinkling behaviour because of its effect on the facesheet constitutive matrix. Fig. 6.17 shows photographs (magnification x 5) of the facesheet-core interface for the 3-ply faced sandwich constructions. The light coloured layer is the film adhesive. Away from the cell walls where it forms fillets, the adhesive layer has a fairly uniform thickness which is comparable with the prepreg thickness. Measurements from such photographs gave an average thickness of 0.135 mm.

Constitutive matrices for the panel facesheets were computed both including and excluding the adhesive layer. The adhesive was included by assuming it to be a 0.135 mm uniform layer with the following isotropic stiffness properties :

E = 2.8 GPa
G = 1.0 GPa
v = 0.39

These properties were taken from reference [25] for a typical epoxy in compression. The computed facesheet constitutive matrices for the different lay-ups with and without the adhesive layer are given in Table 6.10.

The constitutive matrices which neglect the adhesive layer (Table 6.10a) show the [B] matrix coupling inherent in the unbalanced facesheet lay-ups. For the 3-ply quasi-isotropic lay-ups, [+30/90/-30] & [-60/0/+60], the coupling is between direct membrane and twist behaviour (B_{13} & B_{23} non-zero). For the [0/90] lay-up the coupling effect is between direct membrane and bending behaviour (B_{11} & B_{22} non-zero). When the adhesive layer is included (Table 6.10b) the prepreg plies are displaced away from the facesheet mid-plane such that the D_{11} flexural stiffness terms are substantially increased. At the same time, the one sidedness of the reinforcement leads to increased coupling behaviour. B_{11}, B_{12}, B_{22} and B_{33} coupling terms are added to the matrices. For the 3-ply facesheet lay-ups, bending-twisting coupling (D_{13} & D_{23} non-zero) is also induced.

6.9.4 Specimen Failure Load Predictions

Critical loads for the specimens were predicted for material compression failure, overall (Euler) instability, wrinkling and dimpling local instability modes. Overall instability loads were computed using the wrinkling program (Appendix C) with the critical half-wavelength, m, set to 1. In all cases the calculated critical load assuming simply supported ends was greater than 2000 N/mm. Ideally, the material compression strength of the facesheets should be high to ensure the specimens failed through local instability. However, because the prepreg and core were determined by availibility, although the average calculated compression strengths were higher than the wrinkling strengths, the minimum 'A' allowables were not. There was therefore a possibility of failure as a result of facesheet compression rather than through local instability. Nonetheless, compression

tests described in section 5.5, found that the computed 'A' allowable for co-cured sandwich was more than 50% over-conservative compared to the value found from tests.

Wrinkling loads were calculated using four different idealisations in order to assesss their effectiveness at predicting this instability mode. These were :

1. Using the Specially Orthotropic Formula, equation (6.1), and neglecting the adhesive layer.

2. Using the Specially Orthotropic Formula and including the effect of the adhesive layer on D_{11}.

3. Using the generalised theory (computer program) to account for facesheet coupling, but ignoring the adhesive layer.

4. Using the generalised theory including the adhesive layer and all coupling effects.

The core was assumed to have the following properties :

E_c = 310 MPa
G_{xz} = 186 MPa
G_{yz} = 90 MPa
h = 31.25 mm

Critical dimpling loads were calculated using the approximate method of equation (6.18). Two loads were calculated, one neglecting the adhesive layer and one in which its effect on the facesheet [D] matrix was included.

The specimen critical load predictions are summarised in Table 6.11. The large disparities between the different wrinkling and dimpling predictions is evident, particularly where there is significant facesheet coupling.

6.9.5 Compression Tests

The compression test set-up is illustrated in fig. 6.18. The specimens were placed between the platens of an Instron 1195 machine, with load cell and self-aligning lower table. Only one specimen of each construction was strain gauged to give longitudinal stiffness data which was recorded on a data-logger.

A major problem in the experimental evaluation of wrinkling instability is ascertaining when, or even if, the instability occurs. Because of the short wavelength of this mode the use of strain gauges to determine the onset of instability is inpractical because this could be initiated at any point on the specimen. The critical wrinkling load is often equated to the failure load since any further load carying capability is lost once wrinkling has occured. The characteristics of a wrinkling failure are a sharp trough in the facesheet accompanied by local crushing of the core, or facesheet separation/delamination from the core. Hence the determination of wrinkling is very much dependent on visual inspection of the failed specimen.

Dimpling is generally not considered to result in immediate failure, although it can lead to a loss of stiffness and subsequent interaction and premature failure through other modes. Again, the use of strain gauges to detect the onset of this instability is inpractical, and visual observation of the specimen is necessary.

The [0/90] UD and single ply woven faced specimens exhibited the following behaviour up to failure. At about 70% of the ultimate load dimpling occured at one or two inter-cell sites along the unloaded edge of the specimen. As the load increased the number of edge dimples and their amplitude increased. This effect is shown in fig. 6.19, which is a photograph of [0/90] faced specimen no.3 at 92 N/mm (82% of its ultimate load). As the load increased further, certain edge dimples grew in preference to the others. These dimples became more pronounced and fewer in number as they 'fed' from the others. Failure finally occured at the position of the largest dimple, across the full specimen width. In all cases this consisted of a trough in the facesheet, on one or both sides, with slight

crushing of the honeycomb core. On some specimens the facesheets tended to collapse into the cells along the line of the trough, splitting the fibres at the facesheet-cell wall interfaces, see fig. 6.20. This was believed to indicate a wrinkling failure mode.

The [+30/90-30] and [-60/0/+60] specimens behaved in a different manner. There was no evidence of any dimpling at any position on the specimens prior to failure. This occured as a fracture across the full facesheet width on one or both sides. In some specimens the site of this fracture was close to the end tags. Determining the mode of failure was more difficult for these specimens. In one instance, [+30/90/-30] specimen no.1, there was good evidence to support a wrinkling failure with a trough in one facesheet accompanied by core crushing, and a delamination crease across the other facesheet. For many of the other specimens the mode of failure was obscured by damage which occured during collapse. For example, in fig. 6.18 of [+30/90/-30] specimen no.5, a failure accompanied by lifting and delamination of the outer plies is evident. It cannot be said with absolute certainty whether this was initiated by wrinkling, or whether a low facesheet compression failure occured which caused delamination as the fractured plies attempted to ride up over one another.

6.9.6 Comparison of Test Results and Predictions

The ultimate loads for the sandwich specimens are given in Table 6.12. The consistency from specimen to specimen is quite good, with coefficients of variation within 12% for all construction types.

In fig. 6.21 the experimental failure loads are plotted against the four different wrinkling predictions for all of the construction types. Fig. 6.21a compares the experimental loads with the predictions made using the specially orthotropic formula neglecting the adhesive layer. The general trend for the different facesheet types is reasonably well predicted, but a large strength increase for the [+30/90/-30] facesheet lay-up over the specimens with [-60/0/+60] facesheets predicted by this method was not reflected in the test results. Generally, the predictions were higher than

the experimental failure loads. In fig. 6.21b, the predictions are again based on the specially orthotropic formula but with the effect of the adhesive on D_{11} included. Inclusion of the adhesive is a more realistic representation but it results in a larger discrepency with the experimental failure loads, the test results being considerably higher than the specially orthotropic prediction in all cases. It is interesting to note that much better agreement is obtained if the 40% knock-down factor as recommended by references [25] and [35] is applied to the prediction.

Figs. 6.21c and 6.21d compare the experimental failure loads with predictions using the generalised theory which takes full account of facesheet coupling effects. These give a better correlation than the specially orthotropic formula, particularly when the adhesive layer is included. The agreement between test and theory is very good for the unidirectional prepreg faced specimens and slightly less than predicted for the woven faced specimens.

The dimpling effect which was observed at about 70% of the ultimate load for the [0/90] UD and [0] woven faced specimens occured at a much lower load than predicted, even if the adhesive layer was ignored, although the approximate dimpling formula is normally considered to be on the conservative side. The reason for this apparent contradiction is that the prediction refers to a facesheet element supported around its entire periphery, whereas the observed dimpling was confined to the edges only. Here the facesheet element is unsupported along one side and consequently buckles at a lower load.

Fig. 6.22 shows load-strain plots for the strain gauged specimens. The [+30/90/-30] and [-60/0/+60] faced specimens exhibit linear behaviour up to failure. The slope of these curves is in close agreement with the prediction of laminate theory based on 30 psi coupon test data. The slopes of the two curves are almost identical as the theory predicts for this quasi-isotropic type of lay-up. Agreement between test and prediction for the stiffness of the [0/90] UD and [0] woven faced specimens is not so good. The measured stiffnesses in both cases are lower than predicted. The [0] woven faced specimen initially had a tangent modulus close to that

predicted, but subsequently deformed non-linearly as load increased. Buckling in the vicinity of the strain gauge was not suspected because the non-linearity began from the outset. A possible explanation was the age of the prepreg which had past its expiry date when used to manufacture the sandwich specimens.

6.9.7 Discussion

Prior to assessing the performance of the theory in the light of the observed correlation with experimental failure loads, it is important to put forward some justification for equating failure loads with wrinkling. Tests reported in reference [40] on carbon-epoxy faced sandwich columns showed a similar behaviour to those found in this work. That is, a sudden failure, with no evidence of prior instability, which consisted of facesheet fracture and core crushing. Wrinkling in aluminium faced sandwich tends to show the more distinct classical failure of a facesheet trough and core crushing, or facesheet disbonding, because of the higher material ductility. This behaviour has been observed in carbon-epoxy faced sandwich in a few instances, as reported in reference [42]. How wrinkling actually manifests itself is probably a complex inter-dependence between the facesheet material (strain to failure, inter-laminar shear strength), the lay-up, the adhesive (facesheet-core bond strength) and the core type (crush strength, cell size for facesheet bond area). This can vary from specimen to specimen of the same construction, suggesting the failure mode is sensitive to variations in these parameters. In all experimental work however, it is quite clear that wrinkling in carbon-fibre faced sandwich does result in instantaneous failure of the panel. Other low strain fibre composite material systems would be expected to behave similarly.

In the experimental programme reported here, there is a possibility that failure in the [+30/90/-30] and [-60/0/+60] faced specimens was a consequence of material compression rather than wrinkling. It is believed that wrinkling initiated failure was observed. There are several reasons to support this. Firstly, the theoretical predictions for material compression failure showed average loads in excess of the observed failures. Although the calculated 'A' allowable stengths using 30 psi cured coupon data were

lower, the probability of such low compression failures is quite low, and compression testing of co-cured sandwich described in section 5.5 indicated that the strength allowable calculated in this way was considerably over-conservative. Secondly, the observed specimen failures were different to the compression specimens described in section 5.5. In addition to fracture of the facesheets across the width there was also a delaminated zone adjacent to the fracture. Thirdly, the consistency of failure loads with specimens which showed clearer signs of wrinkling suggest that this is the likely cause of failure in all cases.

A further consideration when attempting to compare theoretical and experimental wrinkling loads is the possibility of dimpling-wrinkling interaction. This may occur if the wrinkling mode has a short wavelength comparable with the honeycomb cell dimensions. There appears to be no published literature on this specific interaction problem although one would expect any interaction effect to reduce the critical wrinkling load and precipitate a premature failure. In the tests reported here, the only evidence of dimpling was confined to the unsupported edges of the [0/90] UD and [0] woven faced specimens. There was no dimpling over the remainder of the specimen area, which was in agreement with the approximate prediction if the adhesive layer was included. Because the final wrinkling failure for these specimens tended to spread across the width from an edge dimpling site, it is possible that this may have induced a premature failure, particularly since the computed critical wrinkling wavelengths were found to be comparable to the cell size. However, because the dimpling was confined to only the edges, it is unlikely that this would have had a sufficiently destabilising effect across the full width to cause premature wrinkling.

If the observed failure in the specimens is due to wrinkling, as is believed, the correlation between experiment and theory is remarkably good. This then supports the suggestion made in reference [40] that the adhesive layer and facesheet coupling play a significant part in wrinkling prediction since both of these effects are accomodated in the most accurate of the theoretical predictions. The largest difference between test and theory was for the woven faced specimens which had an average failure load

25% less than predicted, the discrepencies for the others were within 12% which can easily be accounted for by material property variations. The discrepency for the woven specimens can probably be accounted for by the apparent stiffness non linearity observed. The inherent initial waviness in the fibre reinforcement due to the under-and-over weave style may also have an effect. The lower than predicted membrane stiffness for the [0/90] faced strain gauged specimen does not appear to reduce the wrinkling failure load in this case.

The apparently good experimental and theoretical correlation has not been the case for many other composite sandwich panel wrinkling studies. In most investigations (eg. refs. [25],[36],[42],[43]) the observed wrinkling failure loads were found to be considerably less, usually by about a half, than the theoretical predictions made using a specially orthotropic formula. Work carried out in refs. [39] & [40], on the other hand found experimental loads to be greater than predictions based on the specially orthotropic formula.

In references [25] and [36] tests carried out on typical spacecraft panel facesheet lay-ups were used to derive the knock-down factors to apply to the specially orthotropic formula given in section 6.1.1. These are typically about 0.4 to 0.5 for lower bound predictions and are alleged to account for initial imperfections in the facesheets. However, the test specimen facesheets used to derive these factors consisted of [0/90], [+45/-45] and quasi-isotropic lay-ups, which exhibit coupling and have been shown in the current analysis to result in over-predictions of typically 25-50% if the specially orthotropic formula is used. It is possible that some of the discrepency between test and theory can be accounted for by the neglect of coupling effects. Not enough detail of the test panel constructions was given in these references, in particular regarding the adhesive thickness, to calculate the magnitude of the discrepency accurately however. If the adhesive was omitted from the calculation of D_{11} in the specially orthotropic theory then the discrepencies between the two theories would not be as large, and this would suggest that initial waviness was playing a part in giving lower-than-predicted loads.

The results reported in references [39] and [40], and also those found in this study, contradict the explanation of test & specially orthotropic theory discrepency as due to initial waviness. Experimental wrinkling loads found in reference [39] were higher than predicted using the specially orthotropic formula. The discrepency was attributed to the adhesive layer, and in reference [40] the theory was extended to include the adhesive and coupling in [0/90] faced columns. This resulted in a much better theoretical and experimental correlation. The findings of this study also suggest that inclusion of coupling and the adhesive layer are sufficient to give good correlation, and therefore initial imperfections either do not lead to large reductions in wrinkling loads, or the imperfections in these test specimens were small.

In reference [43] the wrinkling test method of reference [39] was repeated using the same type of test rig on $[0_2]$, $[\pm 45]_s$ and [0/90/-45/+45] E-glass epoxy faced panels. In all cases the test results were only about half the predictions using the column wrinkling theory (eq. (6.11)). The over-prediction was even greater if allowance was made for the adhesive layer. Although the theory was not strictly applicable to panels with significant Poissons effect and did not include D_{13} & D_{23} coupling, these effects would not be sufficient in themselves to account fully for the observed lower-than-predicted critical loads. The theory is 'exact' for the truly specially orthotropic $[0_2]$ faced panels in any case. Application of design formulae to account for initial waviness was found to result in reductions of about 35% in the $[0_2]$ panels, which still did not fully account for the low experimental loads recorded.

It is very difficult to come to any firm conclusions regarding the apparent contradictions arising from different test programmes. Although the findings of this study support the idea that wrinkling loads can be confidently predicted by inclusion of adhesive and coupling terms in the theory, the low wrinkling loads found by many of the test programmes cannot be easily reconciled. Unfortunately many of the references cited do not give sufficient information to enable the generalised wrinkling analysis program to be used to investigate whether better correlation could be achieved. However, it is not thought that the large reductions necessary to

improve the correlations would be achieved simply by allowing for facesheet coupling. Neither does initial waviness seem to fully account for the observed discrepencies. In the specimens tested in this study there was no detectable facesheet surface waviness, only overall thickness variations arising from differences in the honeycomb thickness. There was an undulating fibre distortion within the facesheets, as evidenced by the photographs of fig. 6.17, but this did not lead to a wrinkling load reduction. Although different test methods were used in the experimental investigations, this does not in itself appear to be an explanation. The method used in this study was comparable to that used in reference [42] yet the latter found the test results to be lower than predicted; the methods used in references [39] and [43] were also comparable yet the former under-predicted the failure loads and the latter over-predicted. Materials, manufacturing methods and sandwich configurations tested have also been quite diverse but there appears to be no connection between these and the theoretical-experimental correlations achieved.

As regards the use of the theoretical prediction method for design, although the testing performed here would suggest only a modest knock-down factor to encompass the variability observed, until the contradictory results of other test programmes can properly be explained, the use of the large knock-down factors of 0.4 to 0.5 are still recommended with the generalised theory. This should guarantee conservative results yet still enable the coupling and combined loading effects to be included. The method is therefore useful for relative comparisons of alternative lay-ups, providing an insight into which give better wrinkling resistance. The ability to predict the behaviour under combined loading is also useful.

6.10 CONCLUSIONS

The investigation of composite faced sandwich local instability has led to an extension of the current wrinkling theory to enable unbalanced facesheet lay-ups (such as incorporated in many co-cured constructions) to be analysed. This theory was incorporated in a computer program. Numerical examples calculated for typical spacecraft composite sandwich panels

highlighted a reduction effect due to facesheet coupling which could typically amount to 25%-50%. This effect was also found for panels analysed in shear and bending. The flexural wrinkling analysis showed that the tension facesheet of the panel had a stabilising effect and resulted in critical wrinkling loads that exceeded that of the panel loaded in compression. The importance of correctly analysing wrinkling under combined loading was also highlighted.

The inclusion of facesheet coupling into the wrinkling theory was achieved by assuming skew-sinusoidal shape functions which were admissable given the small effect of the violated boundary conditions. This approach could not be extended to dimpling instability analysis because of the significant effect of the boundary conditions (the honeycomb cell walls) in this case. An accurate analytical solution to this problem would be extremely difficult given the hexagonal geometry. Analysis was therefore limited to an approximate approach which ignored coupling and considered the facesheet element to be square and simply supported.

Co-cured sandwich specimens with different coupled facesheet lay-ups were tested in compression. The failure loads, which were equated to wrinkling instability loads, were found to agree well with theoretical predictions if coupling and the film adhesive layer were taken into account. These findings were in agreement with some other investigations but contradictory to others. It was not possible to ascertain how much the over-predictions of some of these other investigations was due to ignoring coupling in the analysis, and how much to initial waviness or material variability. Since the contradictory evidence could not be satisfactorily explained, it was recommended to apply currently adopted wrinkling knock-down factors to the generalised theory in design, which guarantees results on the conservative side but takes due consideration of coupling and combined loading.

TABLE 6.1 PANEL MATERIAL PROPERTIES

(a) Facesheet Materials

UD T-300/CYCOM 985	WOVEN T-300/CYCOM 985
E_1 = 124 GPa	E_1 = 56 GPa
E_2 = 8.2 GPa	E_2 = 56 GPa
$_{12}$ = 0.34	$_{12}$ = 0.12
G_{12} = 4.8 GPa	G_{12} = 2.3 GPa
t_{ply} = 0.10mm	t_{ply} = 0.23mm

(b) 2.0 - 3/16" - 0.0007" 5056 Honeycomb

E_c = 310 MPa
G_{xz} = 186 MPa
G_{yz} = 90 MPa

h = 20mm

TABLE 6.2 BI-DIRECTIONAL FACESHEET LAY-UPS

	[A] (N/mm)			[B] (N)			[D] (N-mm)		
[0/90] UD T300/985	13320	562	0	-584	0	0	44.4	1.9	0
		13320	0		584	0		44.4	0
			960			0			3.2
[0] WOVEN T300/985	13070	1568	0	0	0	0	57.6	6.9	0
		13070	0		0	0		57.6	0
			529			0			2.3
[+45/-45] UD T300/985	7902	5982	0	0	0	-292	26.3	19.9	0
		7902	0		0	-292		26.3	0
			6380			0			21.3
[45] WOVEN T300/985	7847	6789	0	0	0	0	34.6	30.0	0
		7847	0		0	0		34.6	0
			5750			0			25.3

TABLE 6.3 3-FIBRE DIRECTION QUASI ISOTROPIC LAY-UPS

	[A] (N/mm)			[B] (N)			[D] (N/mm)		
[0/+60/-60]	15920	4908	0	-1078	203	-135	155.3	30.0	-13.5
UD T300/985		15920	0		672	-370		97.0	-37.0
			5505			203			34.5
[+60/0/-60]	15920	4908	0	0	0	-271	47.5	50.4	0
UD T300/985		15920	0		0	-740		164.2	0
			5505			0			54.8
[90/+30/-30]	15920	4908	0	672	203	-370	97.0	30.0	-37.0
UD T300/985		15920	0		-1078	-135		155.3	-13.5
			5505			203			34.5
[+30/90/-30]	15920	4908	0	0	0	-740	164.2	50.4	0
UD T300/985		15920	0		0	-271		47.5	0
			5505			0			54.8

TABLE 6.4 4-FIBRE DIRECTION QUASI ISOTROPIC LAY-UPS

	[A] (N/mm)	[B] (N)	[D] (N-mm)
[0/+45/-45/90] UD T300/985	21220 6544 0 21220 0 7340	-1750 -1114 -292 1750 -292 0	337.2 33.1 0 337.2 0 43.7
[+45/0/90/-45] UD T300/985	21220 6544 0 21220 0 7340	-584 0 -875 584 -875 0	228.8 141.4 0 228.8 0 152.1
[0/+45] WOVEN T300/ 985	20920 8357 0 20290 0 6279	-600 600 0 -600 0 600	368.8 147.4 0 368.8 0 110.7

TABLE 6.5 WRINKLING OF BI-DIRECTIONAL FACED PANELS

FACESHEET LAY-UP	COMPRESSION N_x (N/mm)	ϕ (degs)	l^* (mm)	SHEAR N_{xy} (N/mm)	ϕ (degs)	l^* (mm)	FLEXURAL N_x (N/mm)	ϕ (degs)	l^* (mm)
[0/90] UD T300/985	48 (74)	0 (0)	2.8 (3.4)	40 (57)	45 (45)	2.5 (3.0)	65 (74)	0 (0)	2.5 (3.4)
[0] WOVEN T300/985	85 (85)	0 (0)	3.7 (3.7)	66 (66)	45 (45)	3.2 (3.2)	114 (85)	0 (0)	3.3 (3.7)
[+45/-45] UD T300/985	40 (57)	0 (0)	2.5 (3.0)	48 (74)	45 (45)	2.8 (3.4)	54 (57)	0 (0)	2.2 (3.0)
[+45] WOVEN T300/985	66 (66)	0 (0)	3.2 (3.2)	85 (85)	45 (45)	3.7 (3.7)	88 (66)	0 (0)	2.9 (3.2)

TABLE 6.6 WRINKLING OF 3-FIBRE DIRECTION FACE PANELS

FACESHEET LAY-UP	COMPRESSION N_x (N/mm)	O (degs)	1* (mm)	+VE SHEAR N_{xy} (N/mm)	O (degs)	1* (mm)	-VE SHEAR N_{xy} (N/mm)	O (degs)	1* (mm)	FLEXURAL N_x (N/mm)	O (degs)	1* (mm)
[0/+60/-60] UD T300/985	91 (139)	-18 (0)	3.7 (4.7)	95 (142)	+40 (+45)	3.8 (4.8)	-68 (-88)	-49 (-45)	3.3 (3.7)	122 (139)	-18 (0)	3.3 (4.7)
[+60/0/-60] UD T300/985	65 (77)	0 (0)	3.2 (3.5)	81 (128)	+36 (+45)	3.4 (4.5)	-81 (-128)	-36 (-45)	3.4 (4.5)	88 (77)	0 (0)	2.9 (3.5)
[90/+30/-30] UD T300/985	72 (110)	-7 (0)	3.4 (4.2)	95 (142)	+51 (+45)	3.9 (4.8)	-68 (-88)	-41 (-45)	3.8 (3.7)	97 (110)	-7 (0)	3.0 (4.2)
[+30/90/-30] UD T300/985	90 (143)	0 (0)	3.8 (4.8)	81 (128)	+54 (+45)	3.6 (4.5)	-81 (-128)	-54 (-45)	3.6 (4.5)	120 (143)	0 (0)	3.4 (4.8)

TABLE 6.7 WRINKLING OF 4-FIBRE DIRECTION FACE PANELS

FACESHEET LAY-UP	COMPRESSION N_x (N/mm)	O (degs)	1* (mm)	+VE SHEAR N_{xy} (N/mm)	O (degs)	1* (mm)	-VE SHEAR N_{xy} (N/mm)	O (degs)	1* (mm)	FLEXURAL N_x (N/mm)	O (degs)	1* (mm)
[0/+45/-45/ 90] UD	147 (205)	-13 (0)	4.8 (5.7)	+116 (+168)	+48 (+45)	4.3 (5.2)	-116 (-168)	-42 (-45)	4.3 (5.2)	194 (205)	-13 (0)	4.3 (5.7)
[+45/0/90/ -45] UD	115 (168)	-3 (0)	4.2 (5.2)	+149 (+205)	+48 (+45)	4.8 (5.7)	-149 (-205)	-42 (-45)	4.8 (5.7)	154 (168)	-3 (0)	3.8 (5.2)
[0/45] WOVEN T300/985	209 (214)	0 (0)	5.8 (5.8)	+209 (214)	+45 (+45)	5.8 (5.8)	-209 (-214)	+45 (-45)	5.8 (5.8)	274 (214)	0 (0)	5.2 (5.8)

TABLE 6.10

FACESHEET CONSTITUTIVE MATRICES FOR LOCAL INSTABILITY SPECIMENS

(a) NEGLECTING ADHESIVE LAYER

FACESHEET LAY-UP	[A] (N/mm)	[B] (N)	[D] (N-mm)
[+30/90/-30]	22090 7009 0	0 0 1173	251.2 79.8 0
UD HM-S/985	22090 0	0 408	61.3 0
	7540	0	84.1
[-60/0/+60]	22090 7009 0	0 0 -408	61.3 79.8 0
UD HM-S/985	22090 0	0 -1173	251.2 0
	7540	0	84.1
[0/90]	18970 426 0	913 0 0	68.4 1.5 0
UD HM-S/985	18970 0	0 -913 0	68.4 0
	780	0	2.8
[0] WOVEN	12720 1527 0	0 0 0	51.3 6.2 0
T-300/985	12720 0	0 0	51.3 0
	506	0	2.0

(b) INCLUDING ADHESIVE LAYER

FACESHEET LAY-UP	[A] (N/mm)	[B] (N)	[D] (N/mm)
[+30/90/-30]	22540 7183 0	1422 446 1173	363.3 116.3 158.4
UD HM-S/985	22540 0	1422 408	173.5 55.1
	7675	488	122.0
[-60/0/+60]	22540 7183 0	1422 446 -408	173.5 116.3 -55.1
UD HM-S/985	22540 0	1422 -1173	363.3 -158.4
	7675	488	122.0
[0/90]	19420 600 0	2147 11 0	283.6 5.6 0
UD HM-S/985	19420 0	322 0	37.1 0
	915	39	8.0
[0] WOVEN	12950 1674 0	795 82 0	113.4 15.3 0
T-300/985	12950 0	795 0	113.4 0
	641	19	6.2

TABLE 6.11 FAILURE MODE PREDICTIONS FOR LOCAL INSTABILITY SPECIMENS

FAILURE MODE	CRITICAL LOAD (N/mm)			
	[+30/90/-30]	[-60/0/+60]	[0/90]	[0] Woven
Mtl. Compression				
(1) Average	266	191	218	226
(2) 'A' Allowable	89	75	80	-
Wrinkling				
(1)	282	139	147	128
(2)	340	235	300	190
(3)	148	112	88	126
(4)	173	140	121	143
Dimpling				
(1) w/o adhesive	651	651	133	108
(2) incl. adhesive	1070	1070	218	248

For all constructions core is 2.0-3/16"-0.0007" 5056 aluminium, 1¼" thick.

Wrinkling idealisations:

(1) Specially orthotropic formula, adhesive neglected.

(2) Specially orthotropic formula, effect of adhesive on D_{11} included.

(3) Generalised theory, adhesive neglected.

(4) Generalised theory, adhesive included.

TABLE 6.12 ULTIMATE LOADS FOR SANDWICH LOCAL INSTABILITY SPECIMENS

SPECIMEN NO.	ULTIMATE LOAD (N/mm)			
	[+30/90/-30]	[-60/0/+60]	[0/90]	[0] Woven
1	165	167	140	u/s
2	162	u/s	104	106
3	u/s	u/s	112	114
4	u/s	167	116	u/s
5	164	132	101	103
6	179	163	125	110
Mean	167.5	157.25	116.3	108.25
S.D	6.7	14.7	13.2	4.2
C.o.V	4.0%	9.3%	11.3%	3.9%

Fig. 6.1 SYMMETRIC & ANTI-SYMMETRIC WRINKLING MODES

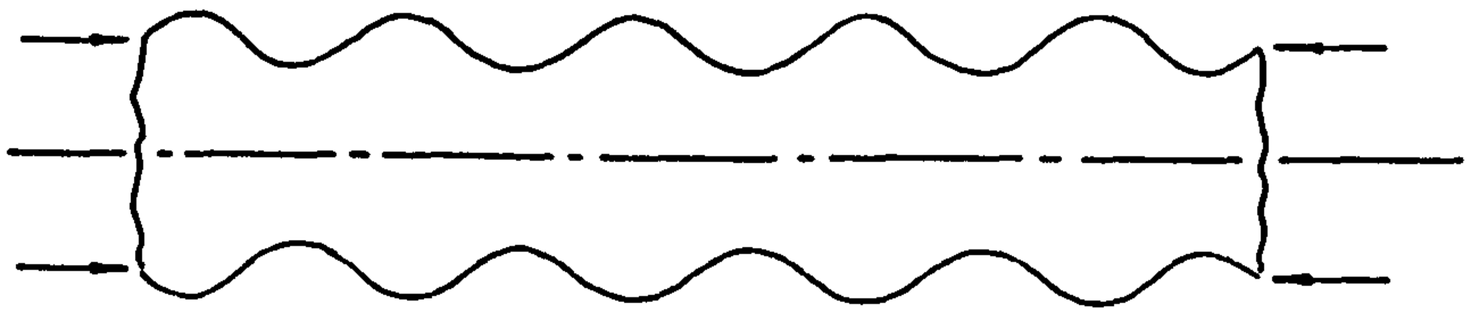

(a) SYMMETRIC

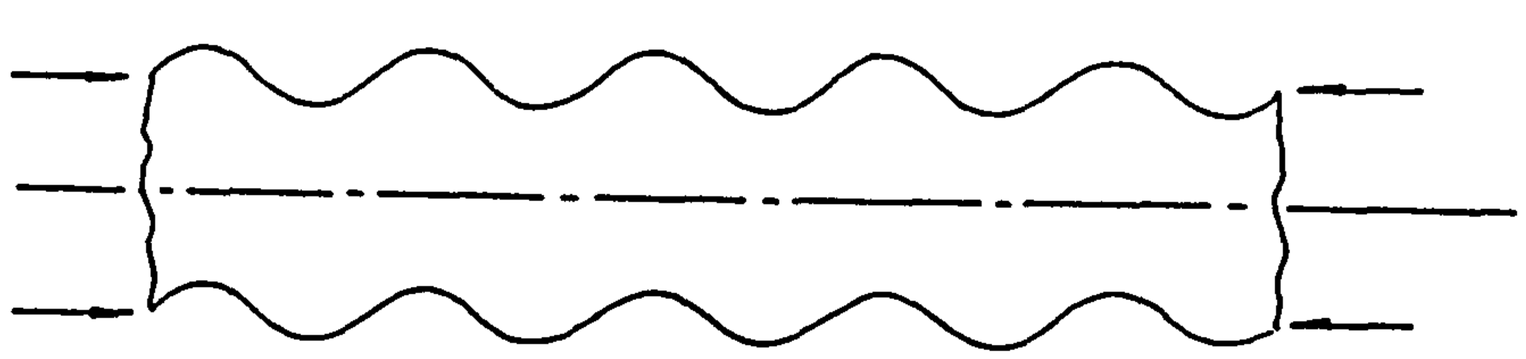

(b) ANTI-SYMMETRIC

Fig. 6.2 SIGN CONVENTION FOR GENERAL WRINKLING THEORY

FACESHEET STRESS AND MOMENT RESULTANT SIGN CONVENTION

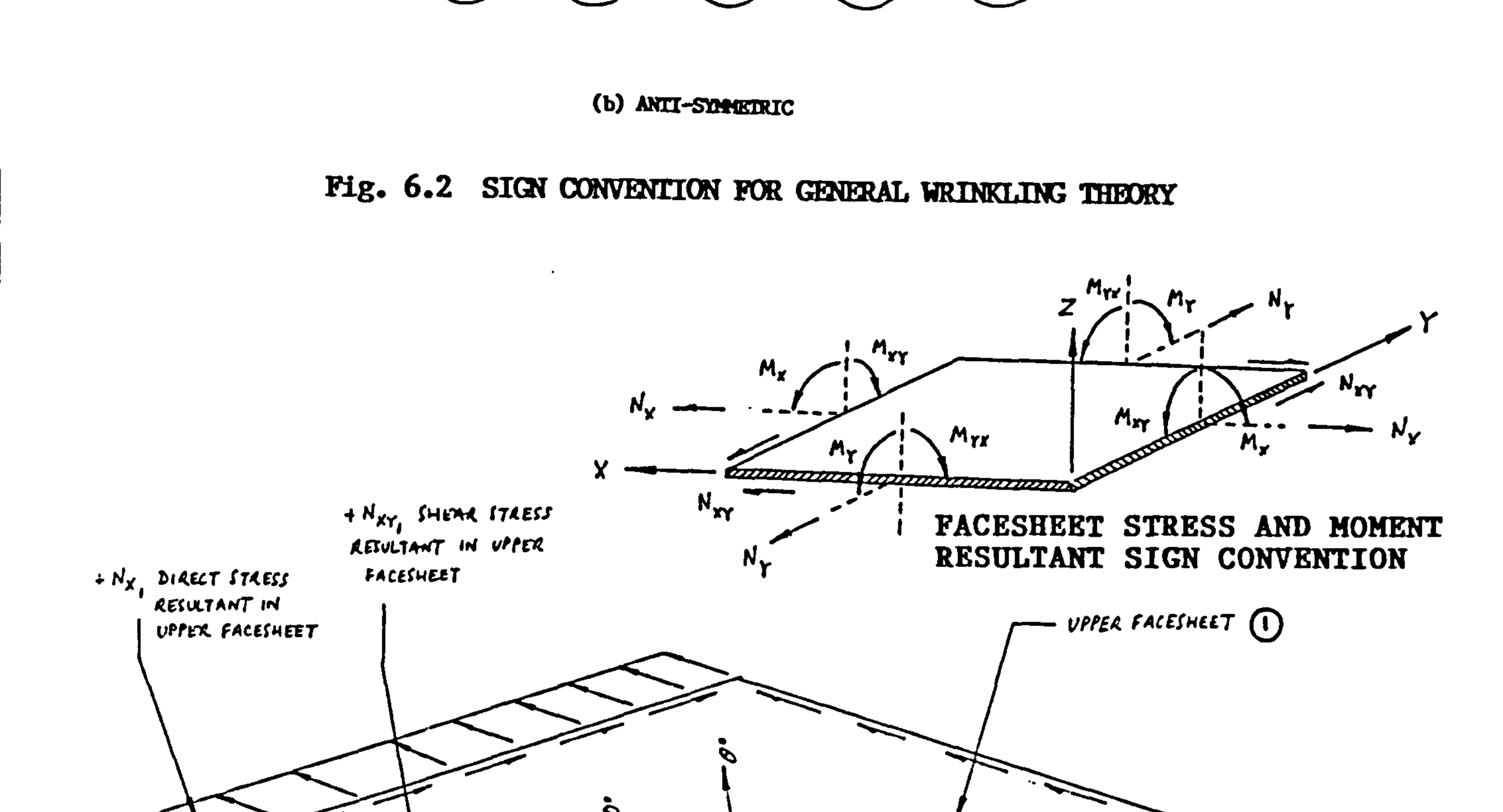

Fig. 6.3 ASSUMED SKEW-SINUSOIDAL BUCKLED SHAPE FUNCTION

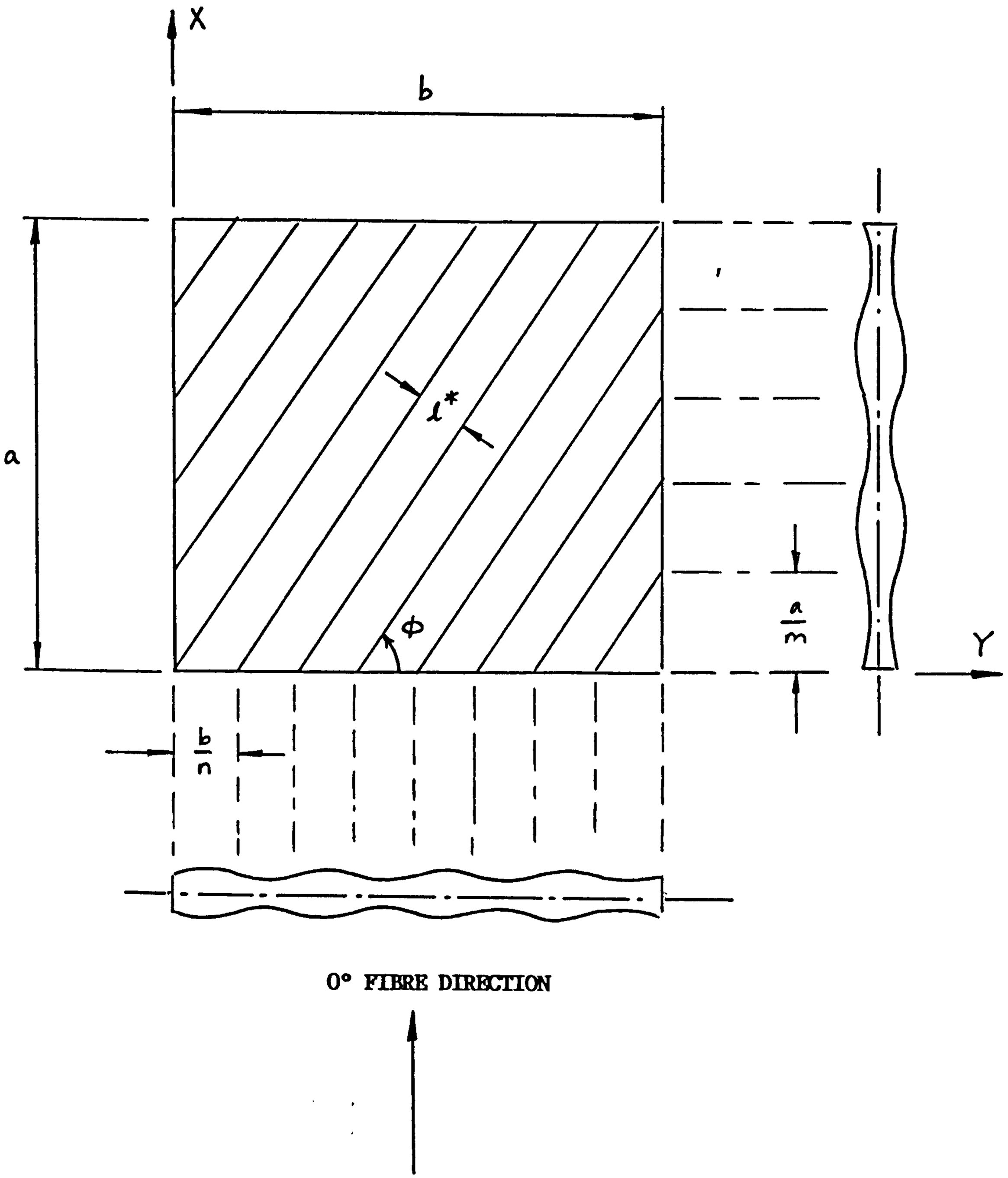

Fig. 6.4 COMPRESSIVE BUCKLING OF [0/90] CFRP FACED SANDWICH PANEL

FACESHEETS

$E_1 = 142$ GPa
$E_2 = 9.8$ GPa
$G_{12} = 4.3$ GPa
$\nu_{12} = 0.34$

CORE

$E_c = 109$ MPa
$G_{xz} = 26.6$ MPa
$G_{yz} = 15.5$ MPa

$h = 10$ mm

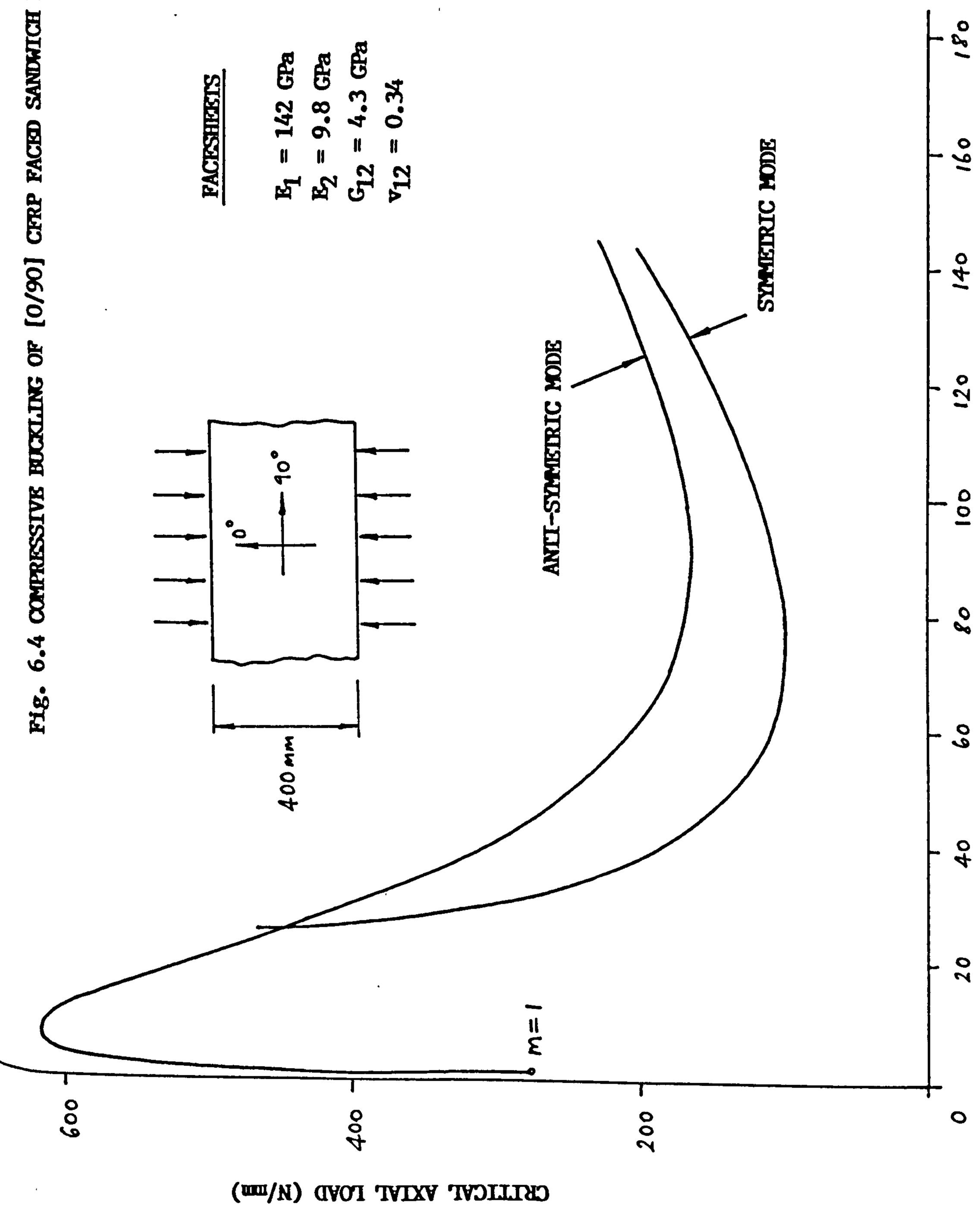

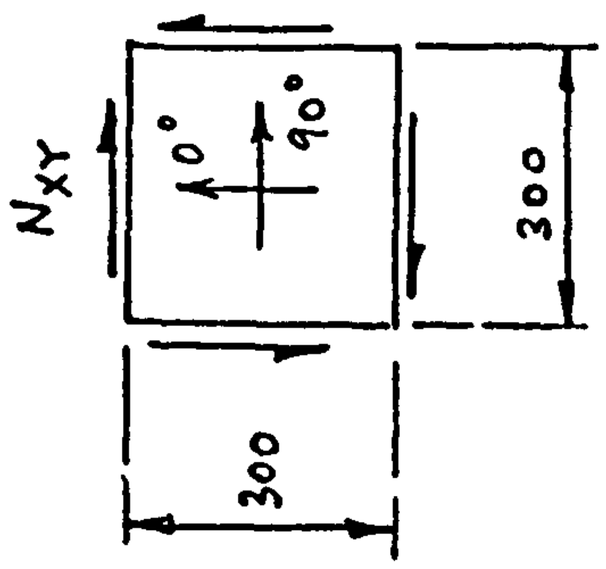

FACESHEETS

E_1 = 175 GPa
E_2 = 6.8 GPa
G_{12} = 3.75 GPa
ν_{12} = 0.30

t_{ply} = 0.10 mm

CORE

E_c = 310 MPa
G_{xz} = 186 MPa
G_{yz} = 90 MPa

h = 10 mm

NUMBER OF AXIAL WAVELENGTHS

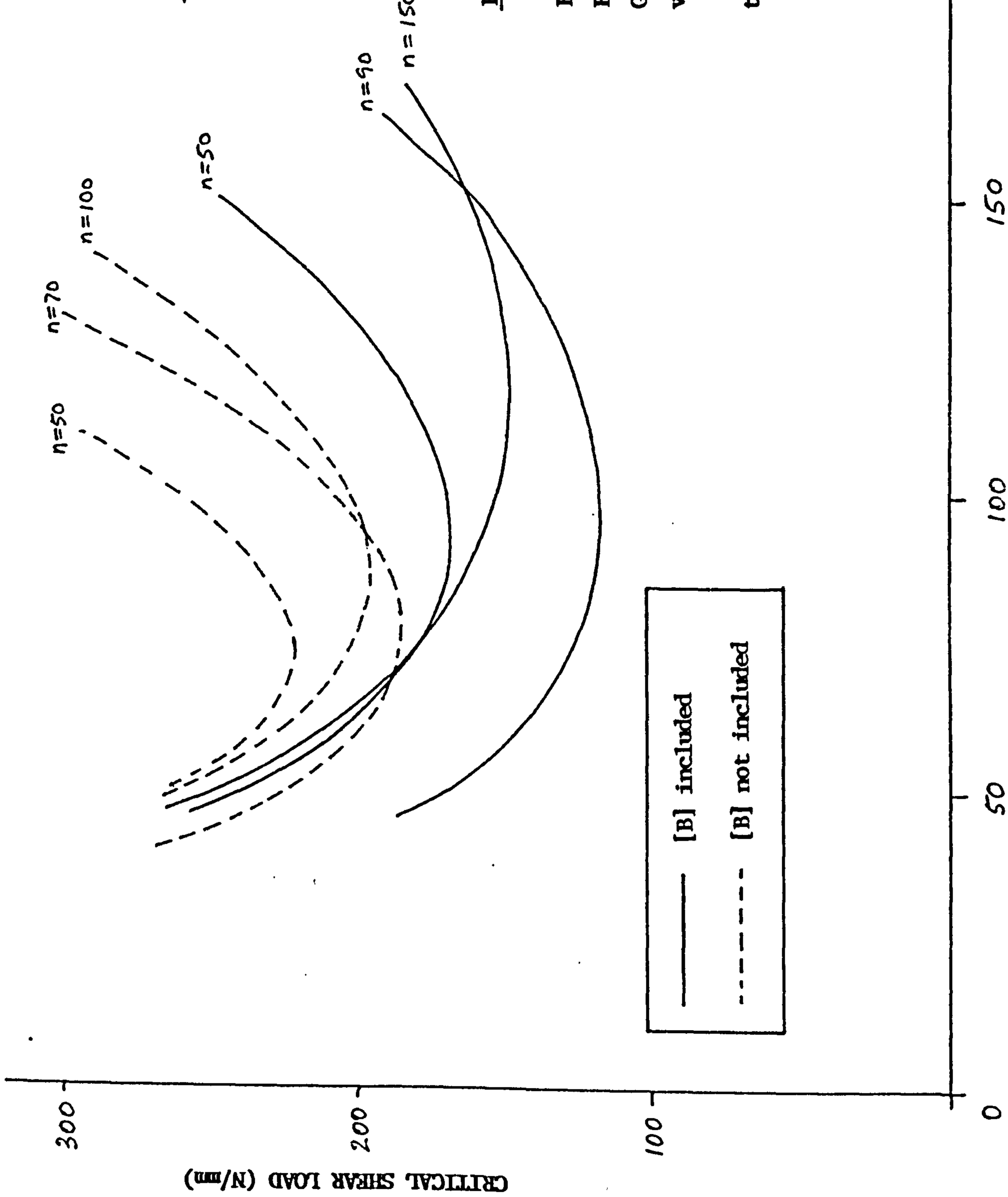

Fig. 6.5 SHEAR WRINKLING OF [0/90] HM-S/EPOXY FACED SANDWICH PANEL

Fig. 6.6 HONEYCOMB SUPPORT FOR SHORT WAVELENGTH WRINKLING MODE

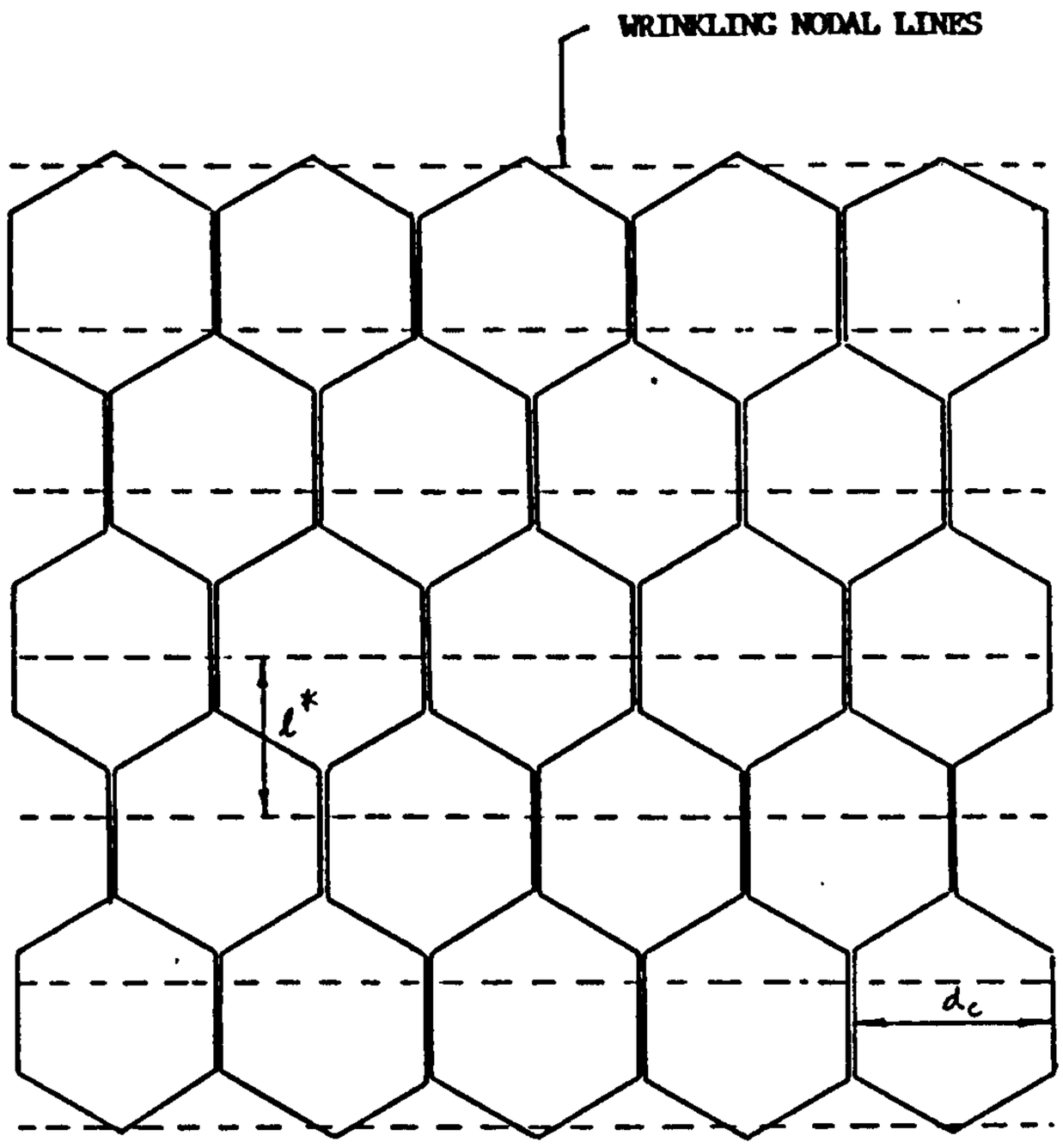

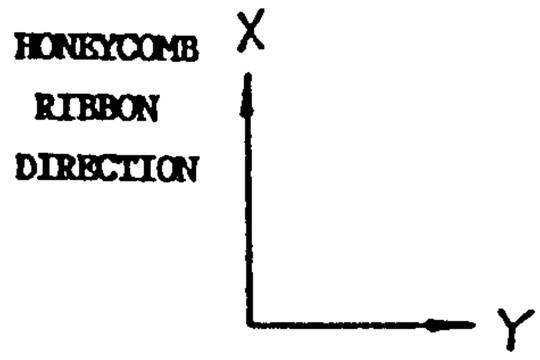

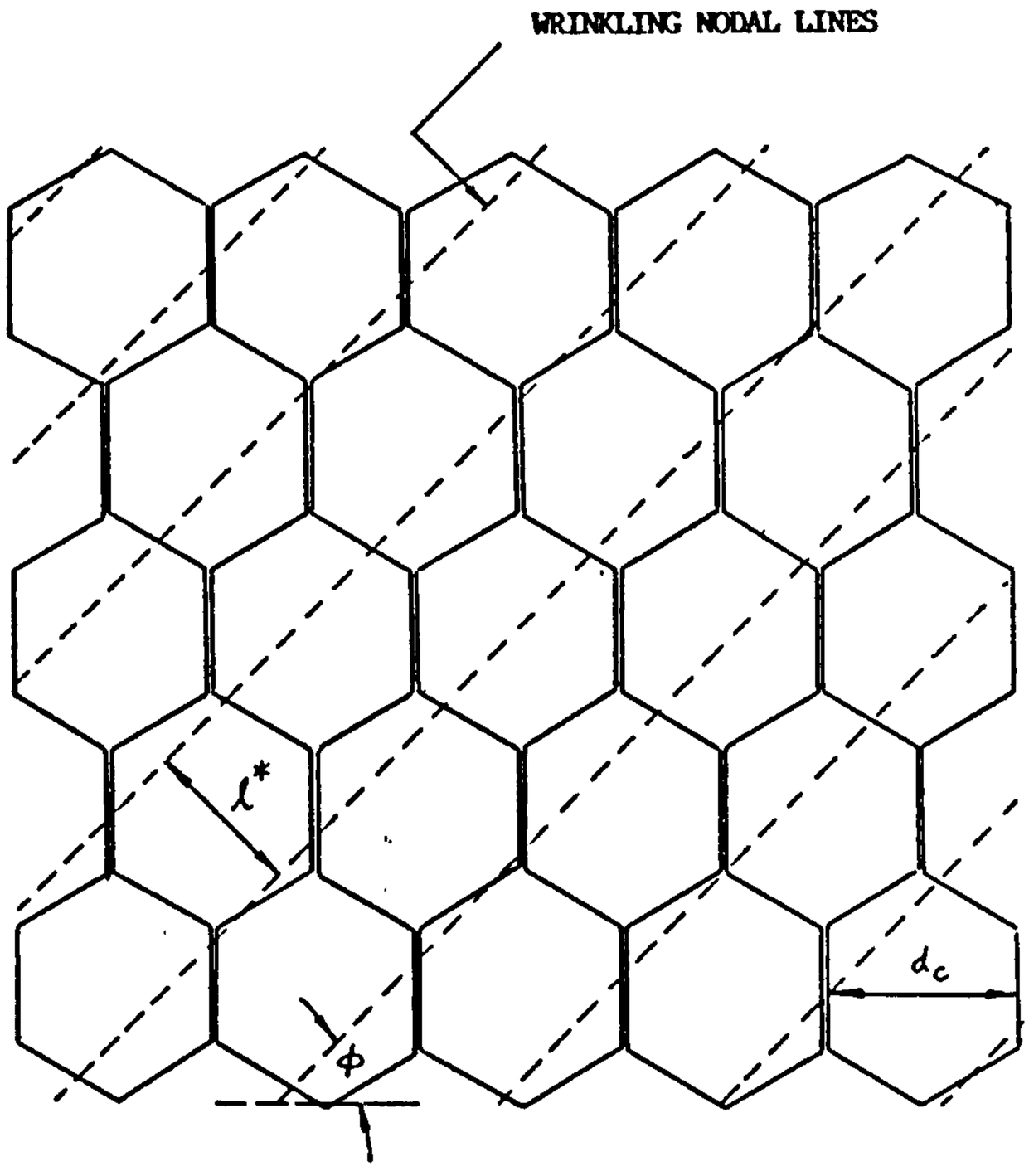

Fig. 6.7 COMPRESSION AND FLEXURAL WRINKLING OF [0/90] FACED SANDWICH PANEL

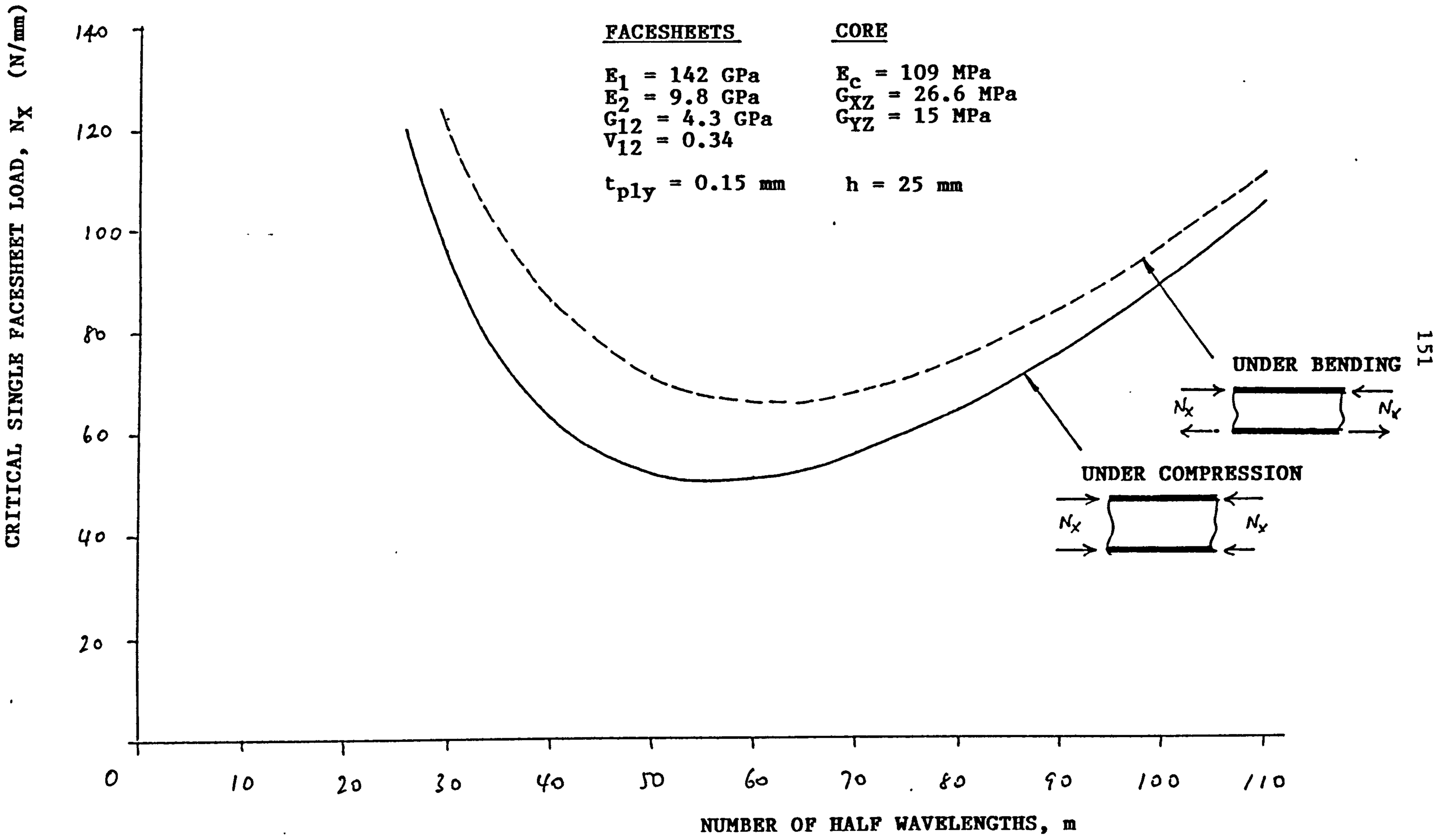

Fig. 6.9 EFFECT OF CORE DEPTH ON THE COMPRESSION WRINKLING STRENGTH OF [0/+45/-45/90] HM-S/CYCOM 985 FACED SANDWICH PANELS

FACESHEETS

E_1 = 175 GPa
E_2 = 6.8 GPa
G_{12} = 3.75 GPa
ν_{12} = 0.30

t_{ply} = 0.10 mm

CORE

E_c = 310 MPa
G_{xz} = 186 MPa
G_{yz} = 90 MPa

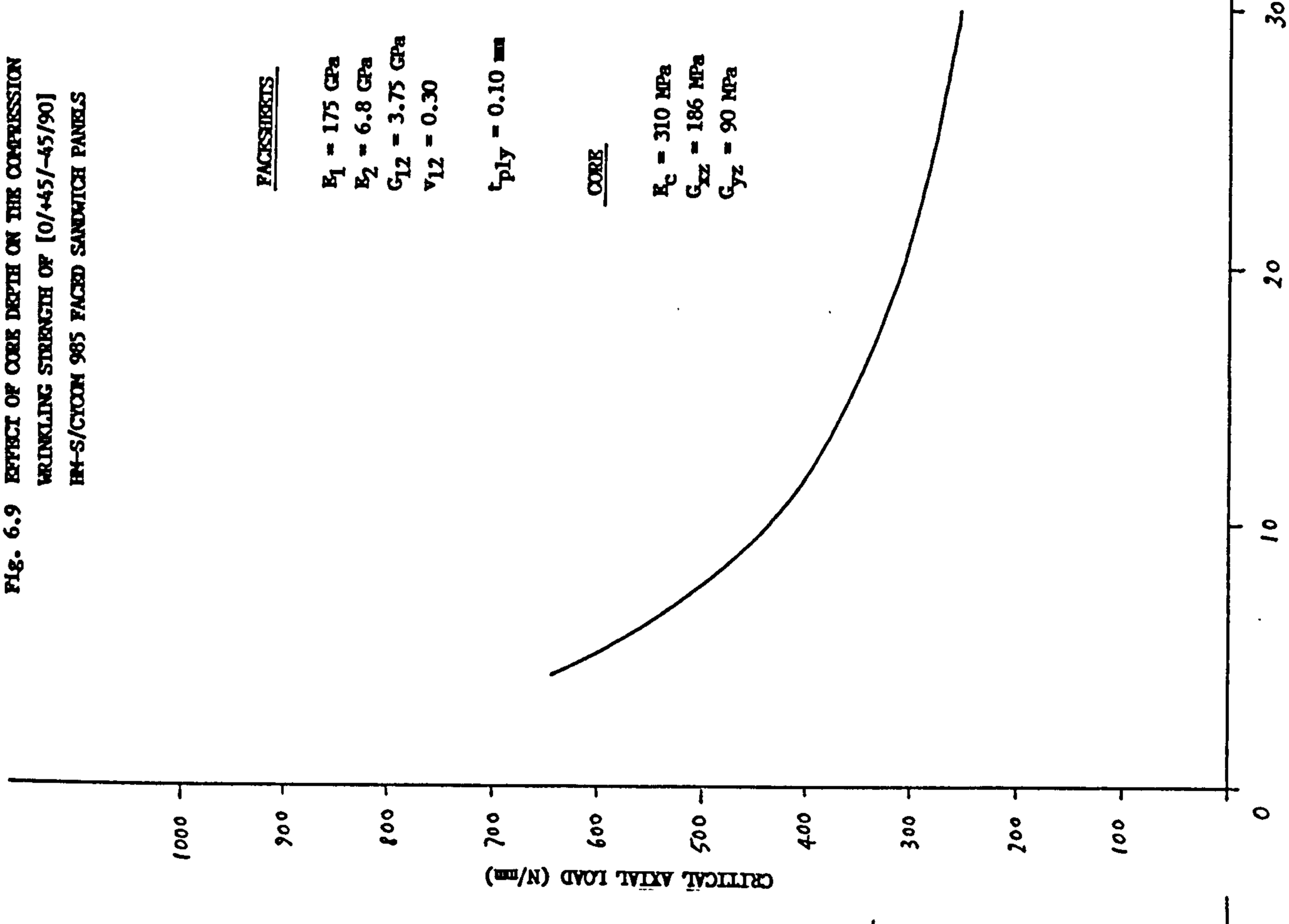

Fig. 6.8 EFFECT OF CORE DEPTH ON AXIAL COMPRESSION WRINKLING STRENGTH OF [0/90] HM-S/CYCOM 985 FACED SANDWICH PANEL

FACESHEETS

E_1 = 175 GPa
E_2 = 6.8 GPa
G_{12} = 3.75 GPa
ν_{12} = 0.30

t_{ply} = 0.10 mm

CORE

E_c = 310 MPa
G_{xz} = 186 MPa
G_{yz} = 90 MPa

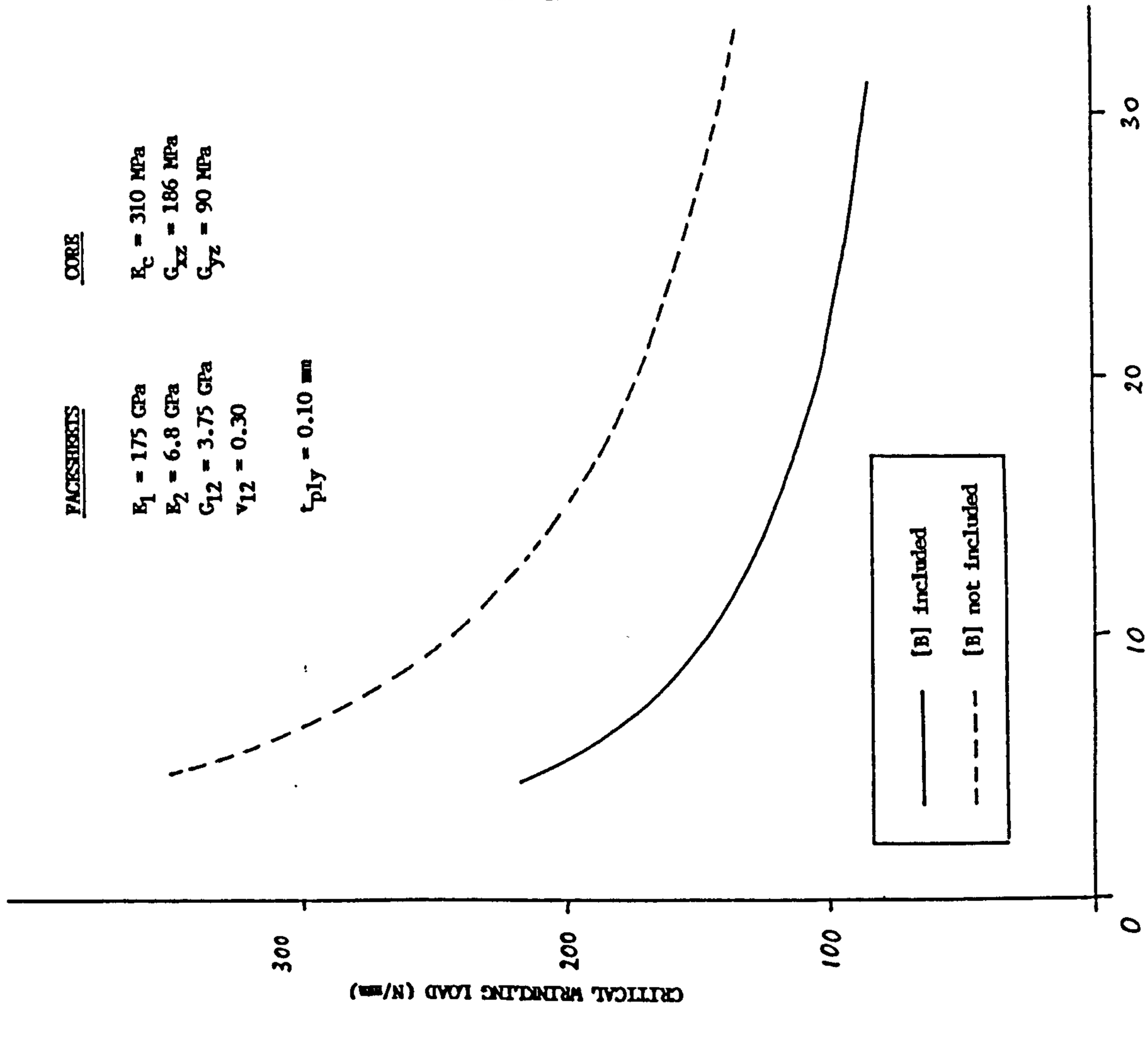

Fig. 6.10 EFFECT OF CORE DEPTH ON FLEXURAL WRINKLING STRENGTH OF [0/90] HM-S/CYCOM 985 FACED SANDWICH PANEL

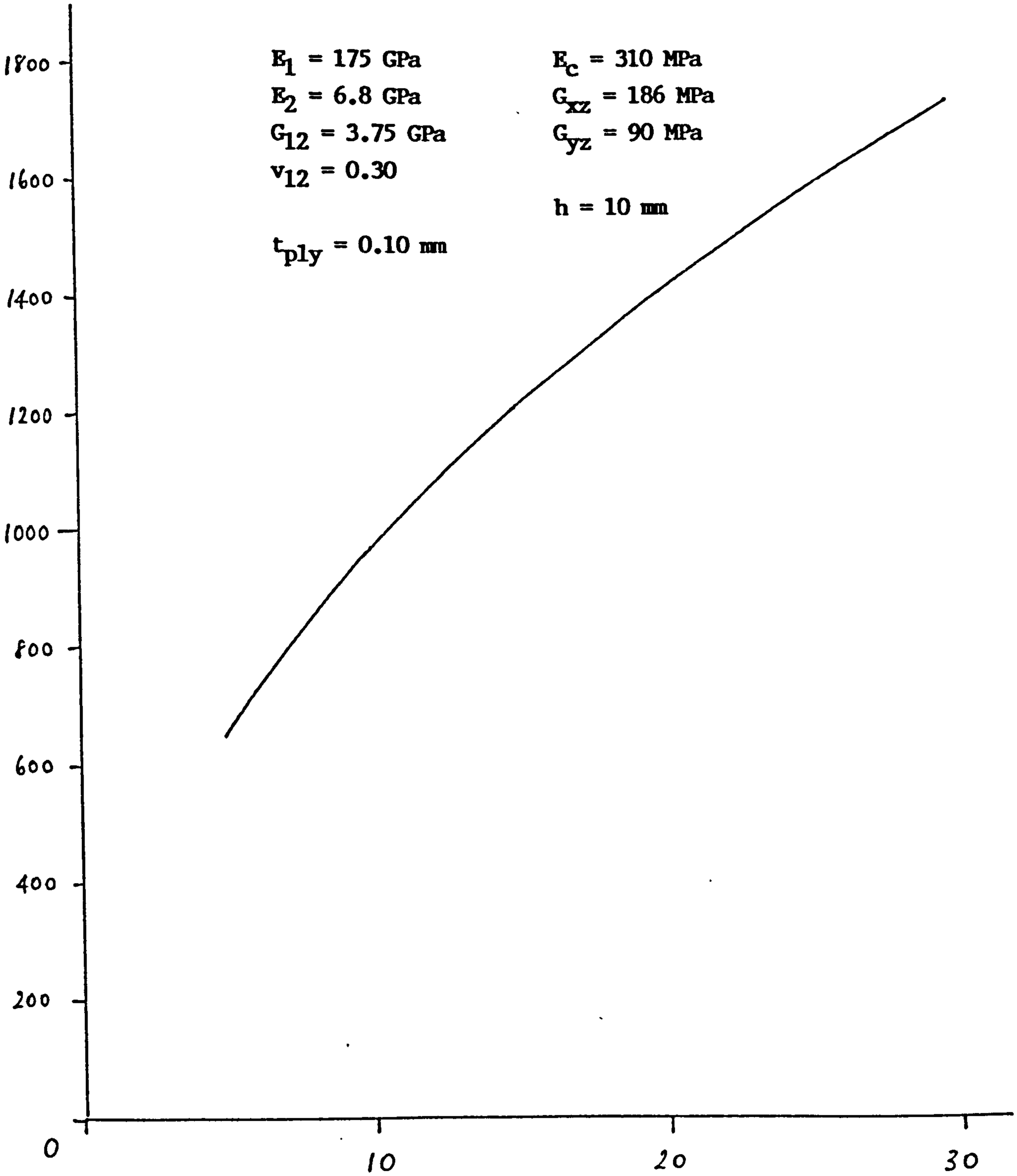

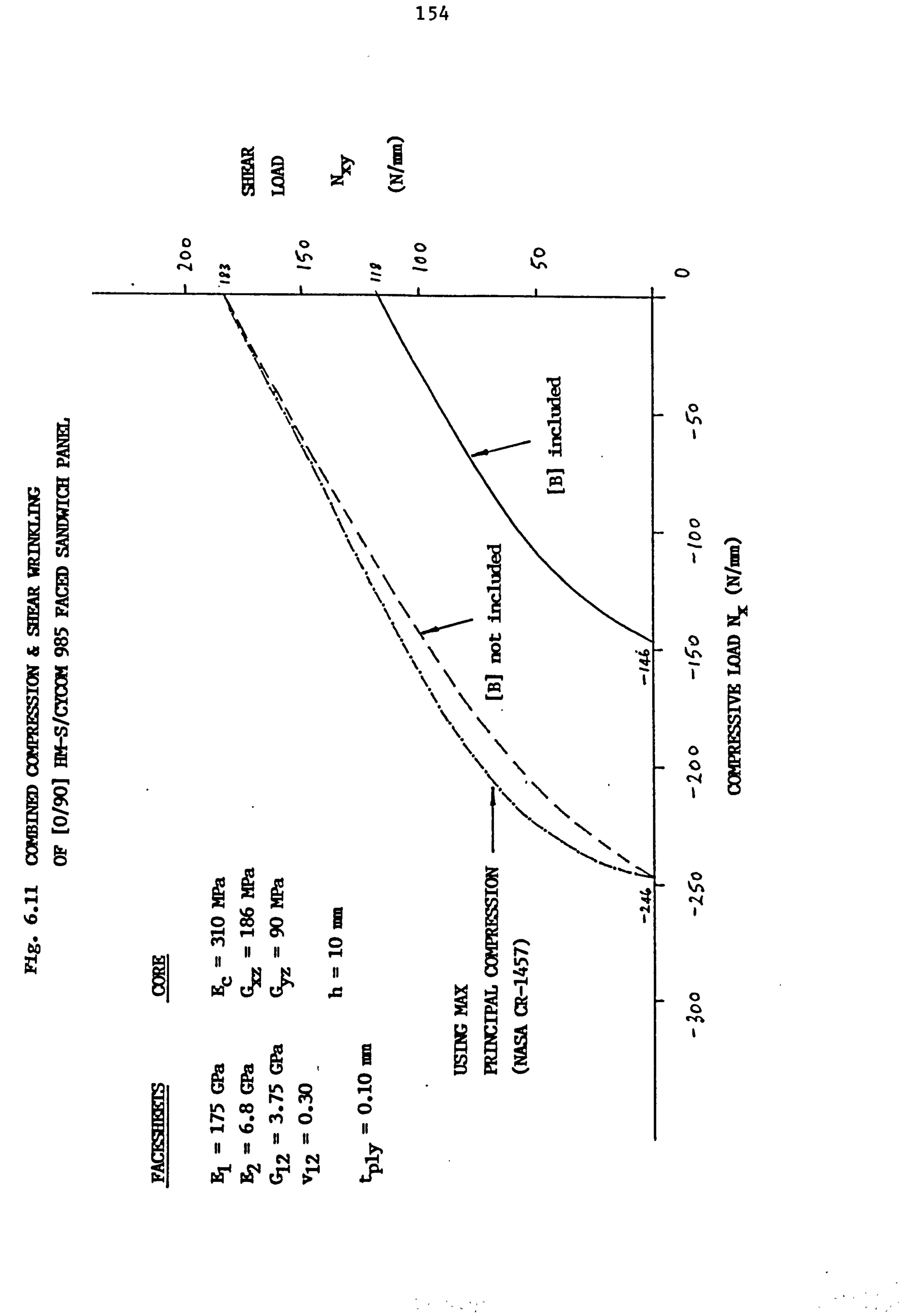

Fig. 6.11 COMBINED COMPRESSION & SHEAR WRINKLING OF [0/90] HM-S/CYCOM 985 FACED SANDWICH PANEL

CORE

E_c = 310 MPa
G_{xz} = 186 MPa
G_{yz} = 90 MPa

h = 10 mm

FACESHEETS

E_1 = 175 GPa
E_2 = 6.8 GPa
G_{12} = 3.75 GPa
ν_{12} = 0.30

t_{ply} = 0.10 mm

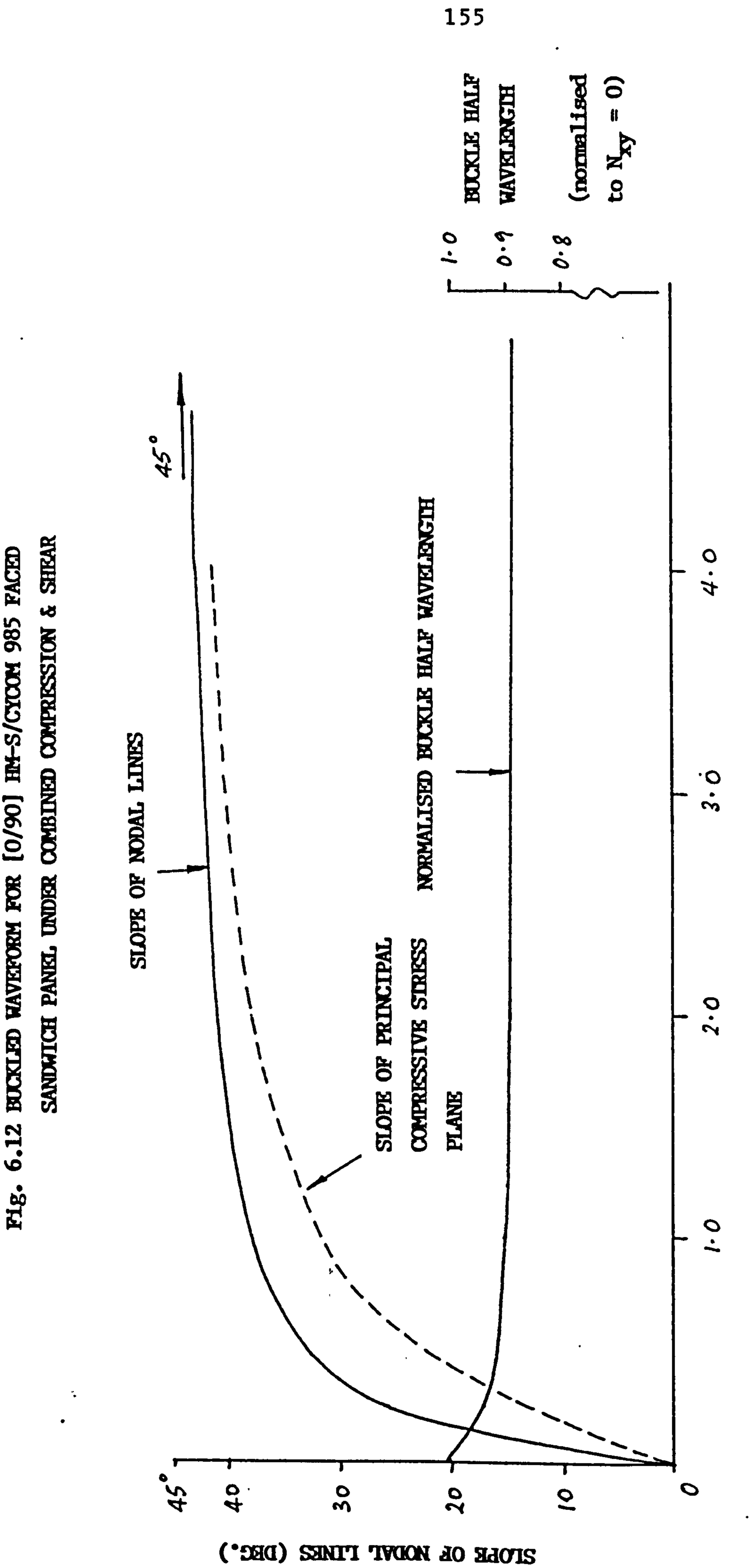

Fig. 6.12 BUCKLED WAVEFORM FOR [0/90] HM-S/CYCOM 985 FACED SANDWICH PANEL UNDER COMBINED COMPRESSION & SHEAR

Fig. 6.13 COMBINED BENDING & SHEAR WRINKLING OF [+30/90/-30] HM-S/CYCOM 985 FACED SANDWICH PANEL

FACESHEETS

E_1 = 175 GPa
E_2 = 6.8 GPa
G_{12} = 3.75 GPa
ν_{12} = 0.30

t_{ply} = 0.10 mm

CORE

E_c = 310 MPa
G_{xz} = 186 MPa
G_{yz} = 90 MPa

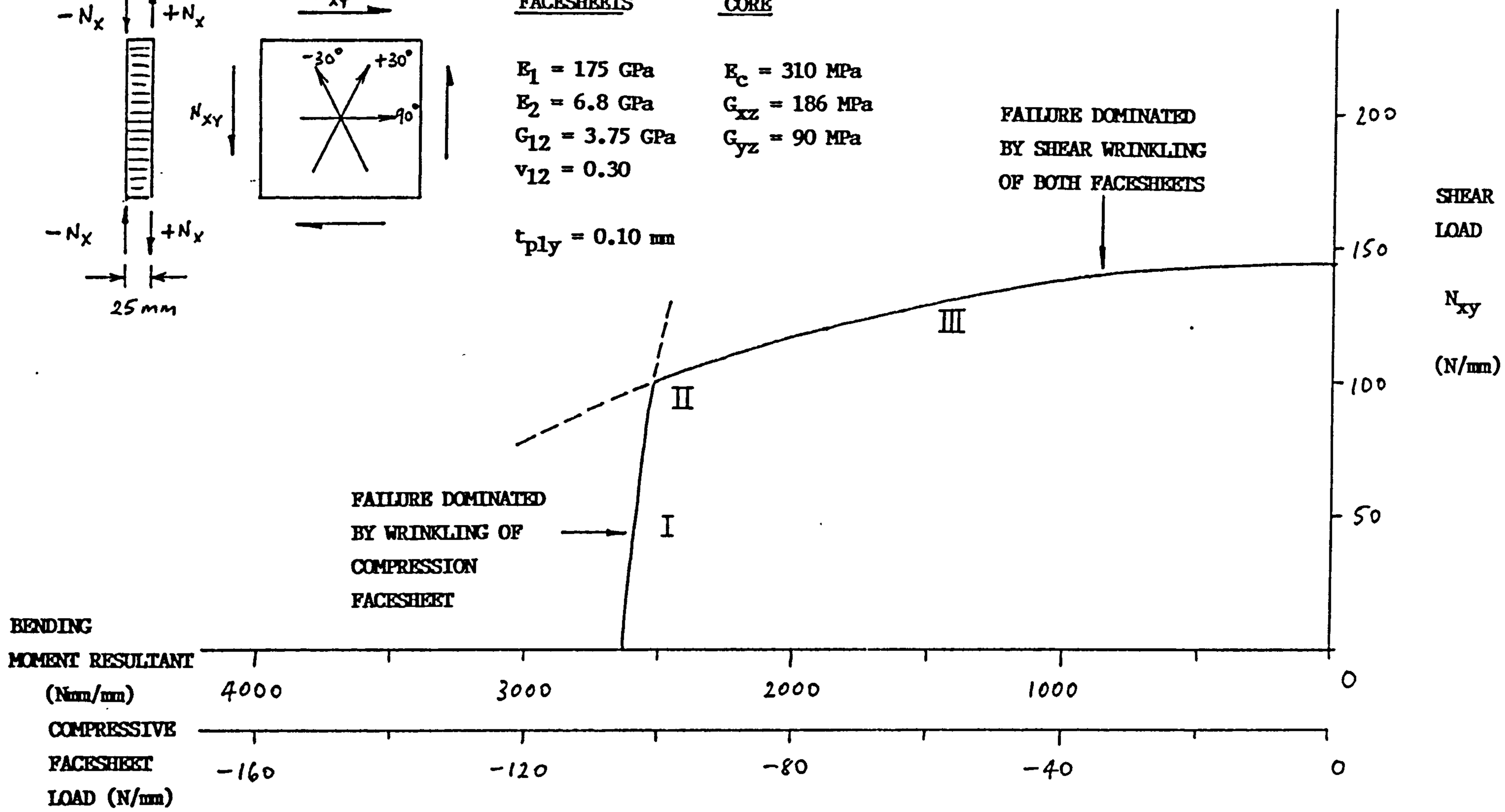

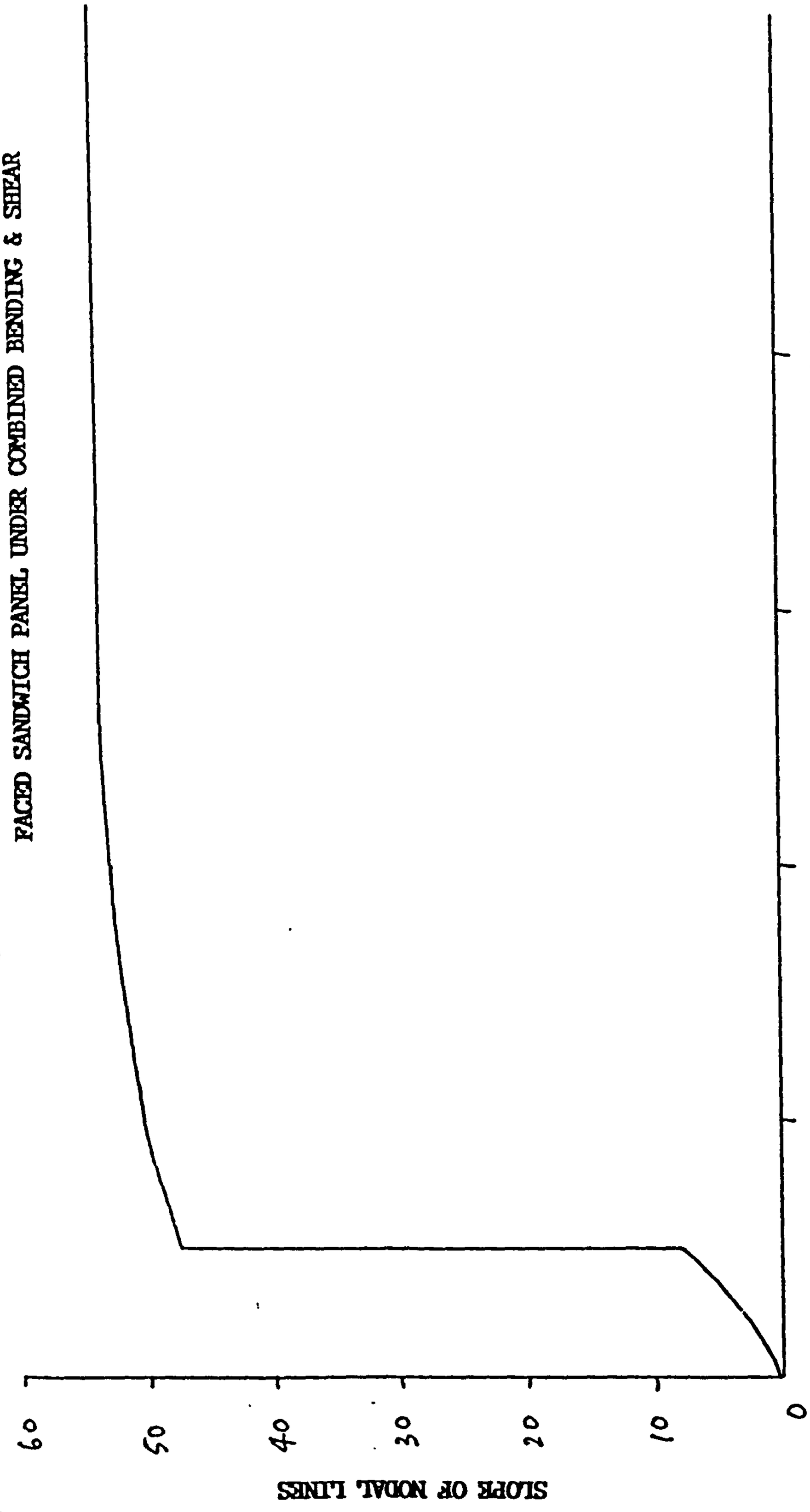

Fig. 6.14 BUCKLED WAVEFORM FOR [+30/90/-30] HM-S/CYCOM 985
FACED SANDWICH PANEL UNDER COMBINED BENDING & SHEAR

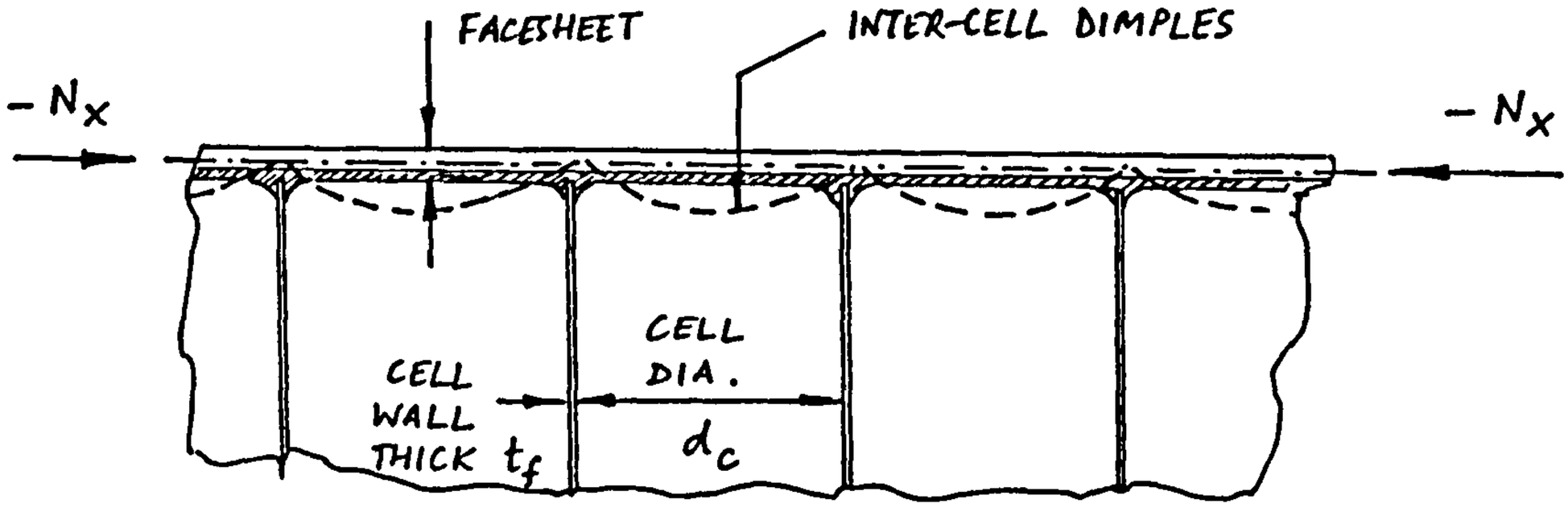

Fig. 6.15 DIMPLING LOCAL INSTABILITY MODE

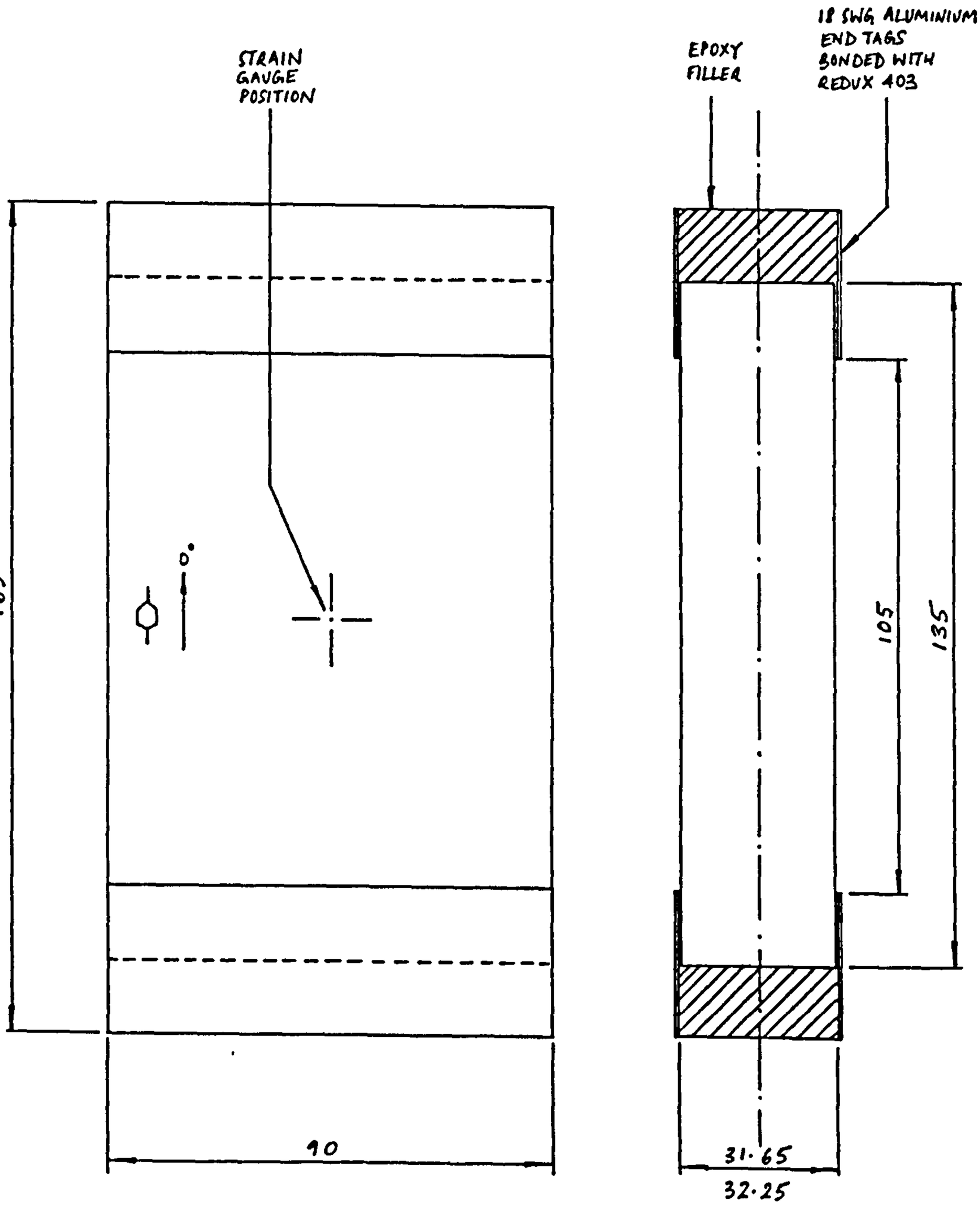

Fig. 6.16 SANDWICH LOCAL INSTABILITY COMPRESSION SPECIMEN

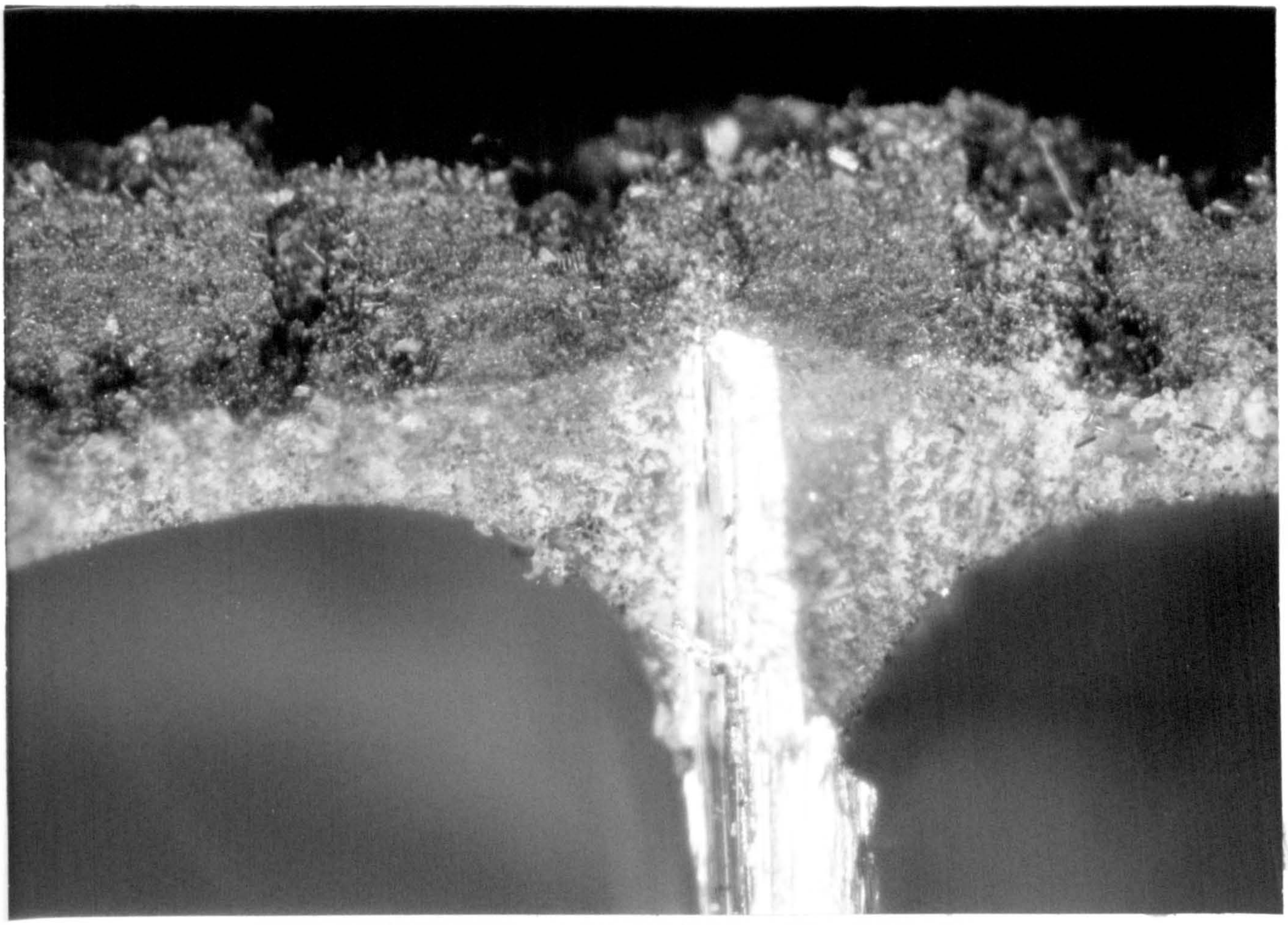

Fig. 6.17 CO-CURED SANDWICH: ADHESIVE THICKNESS

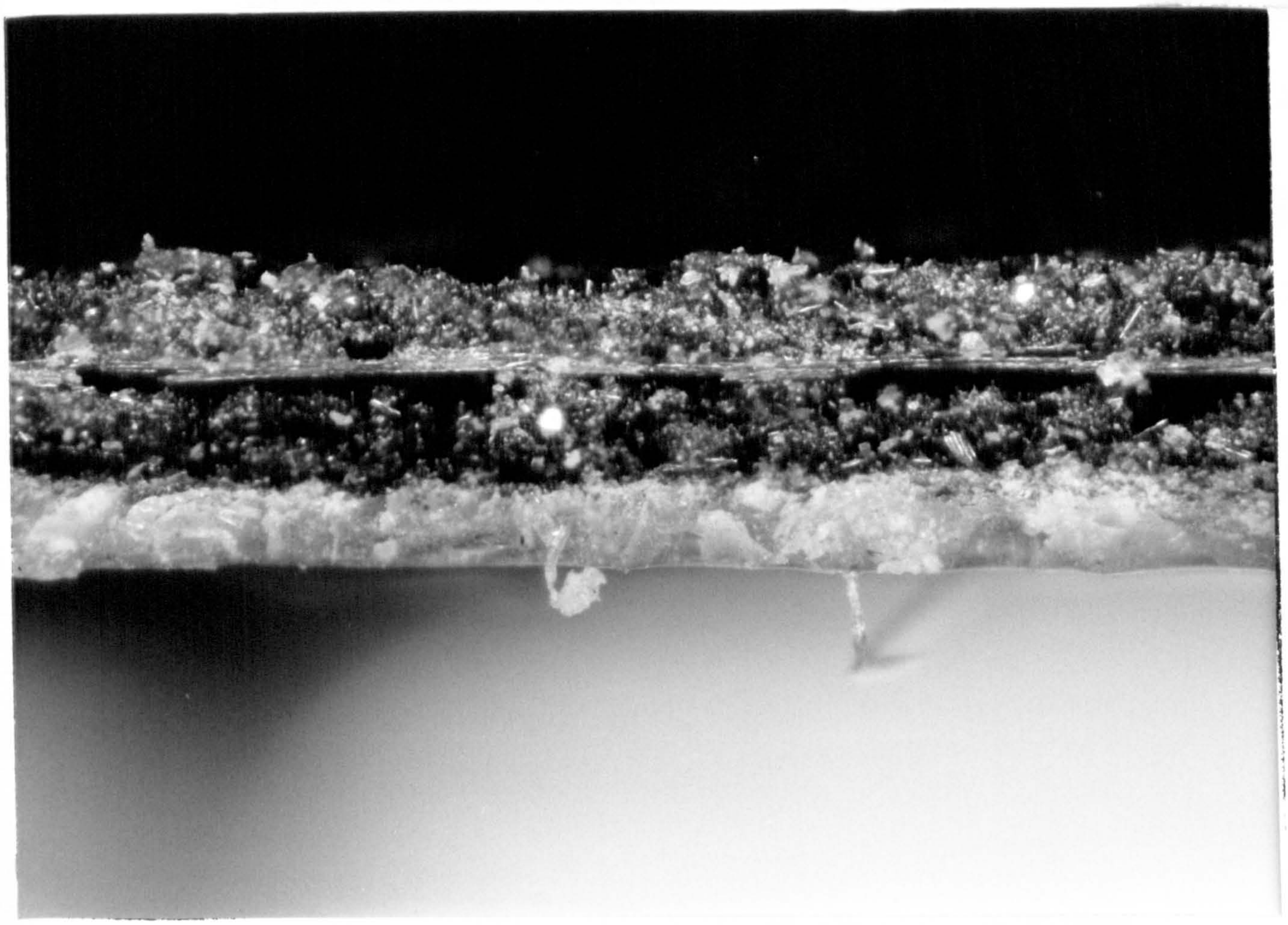

Fig. 6.18 SANDWICH LOCAL INSTABILITY COMPRESSION SPECIMEN IN TEST M/C
([+30/90/-30] FACED SPECIMEN No. 5)

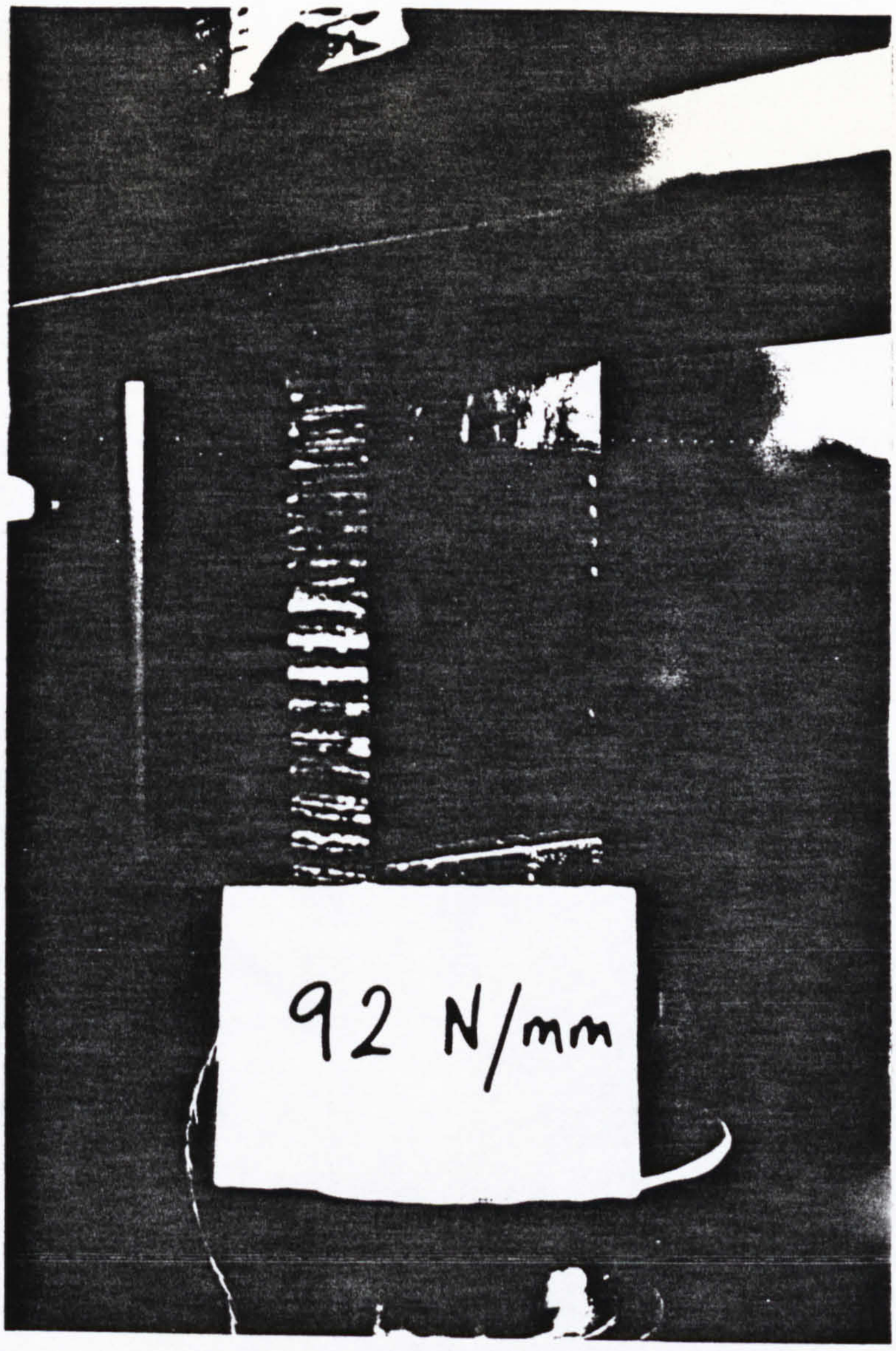

Fig. 6.19 EDGE DIMPLING ON [0/90] FACED SPECIMEN No. 3 AT 92 N/mm

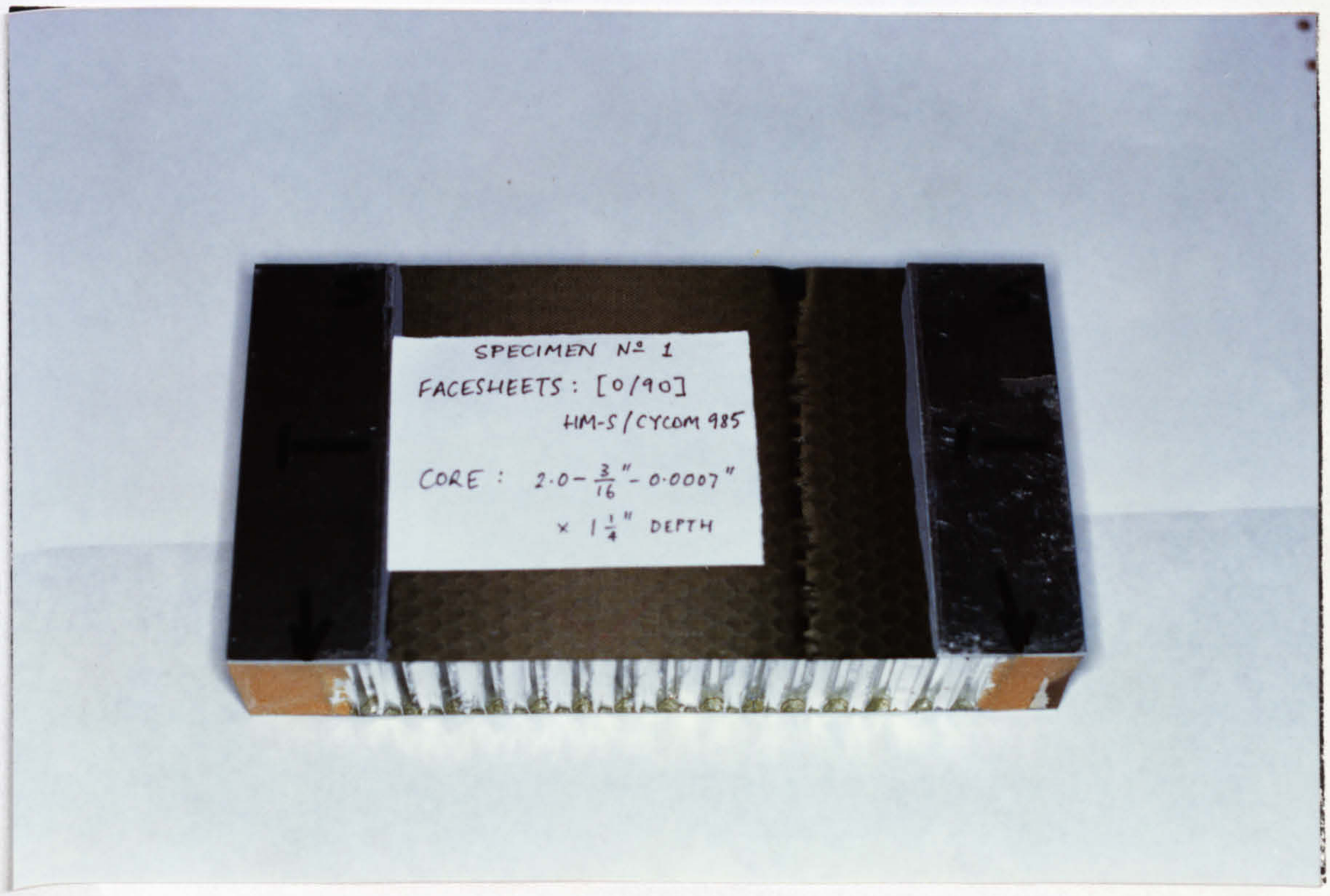

Fig. 6.20 [0/90] FACED SPECIMEN No. 1 FAILURE MODE

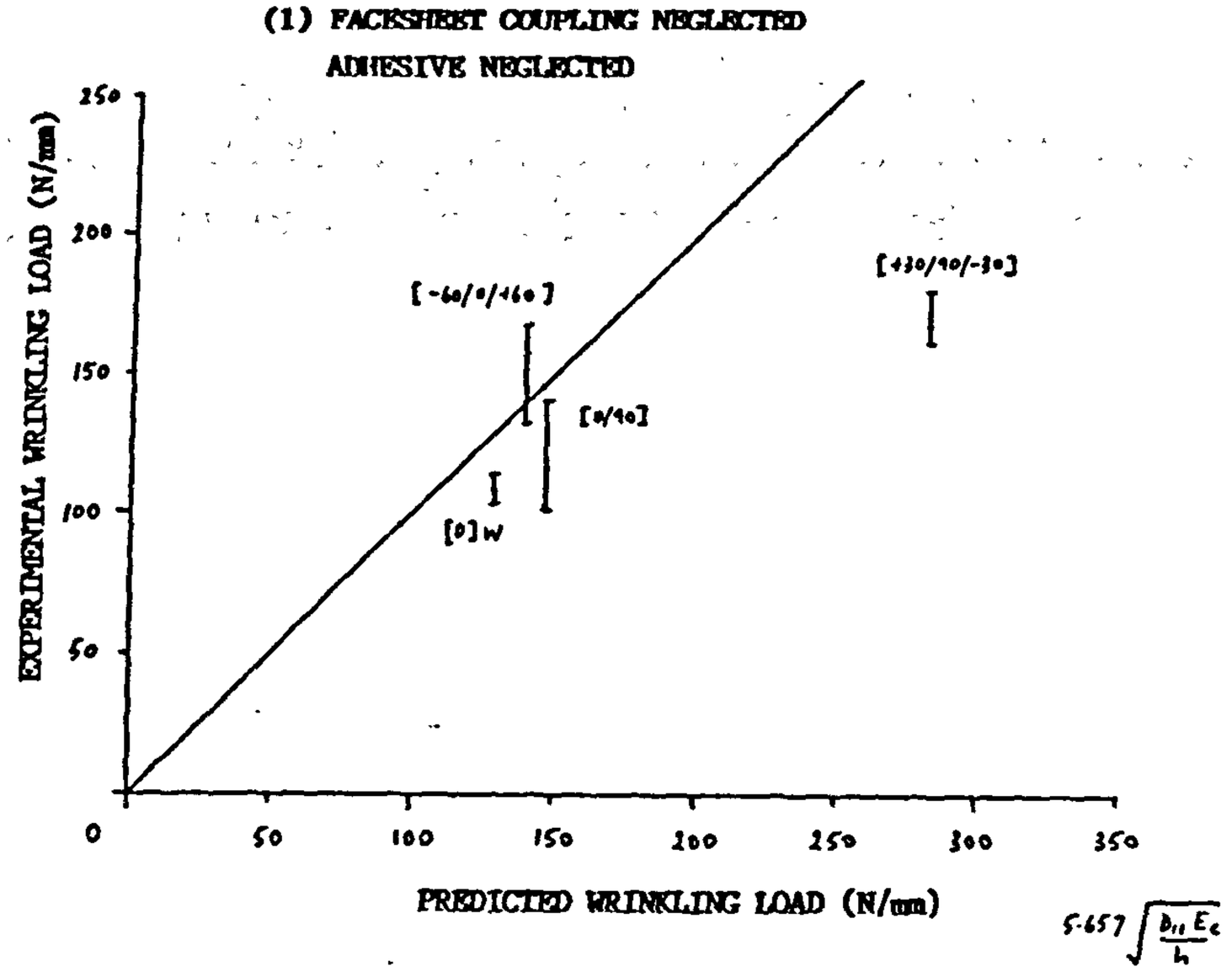

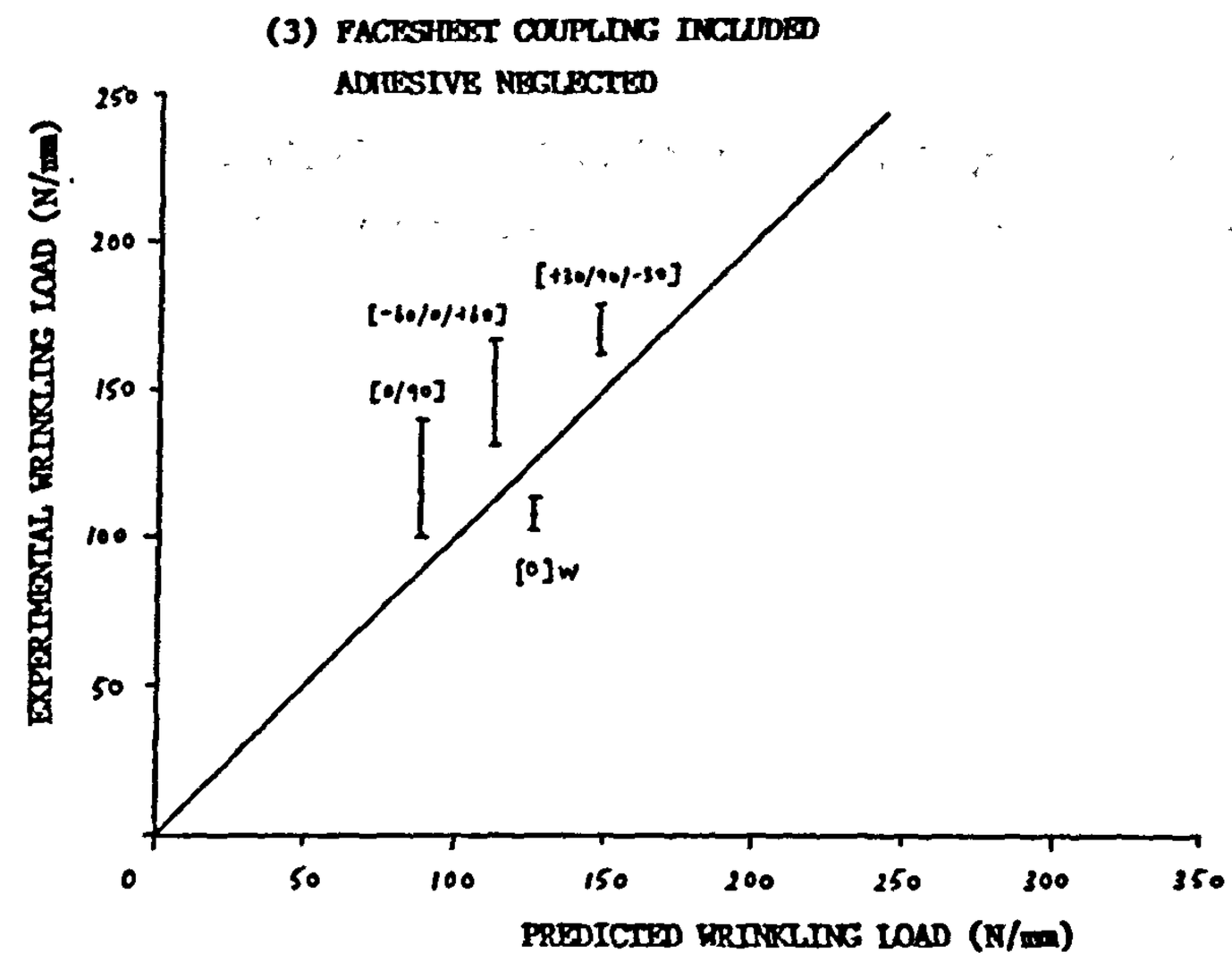

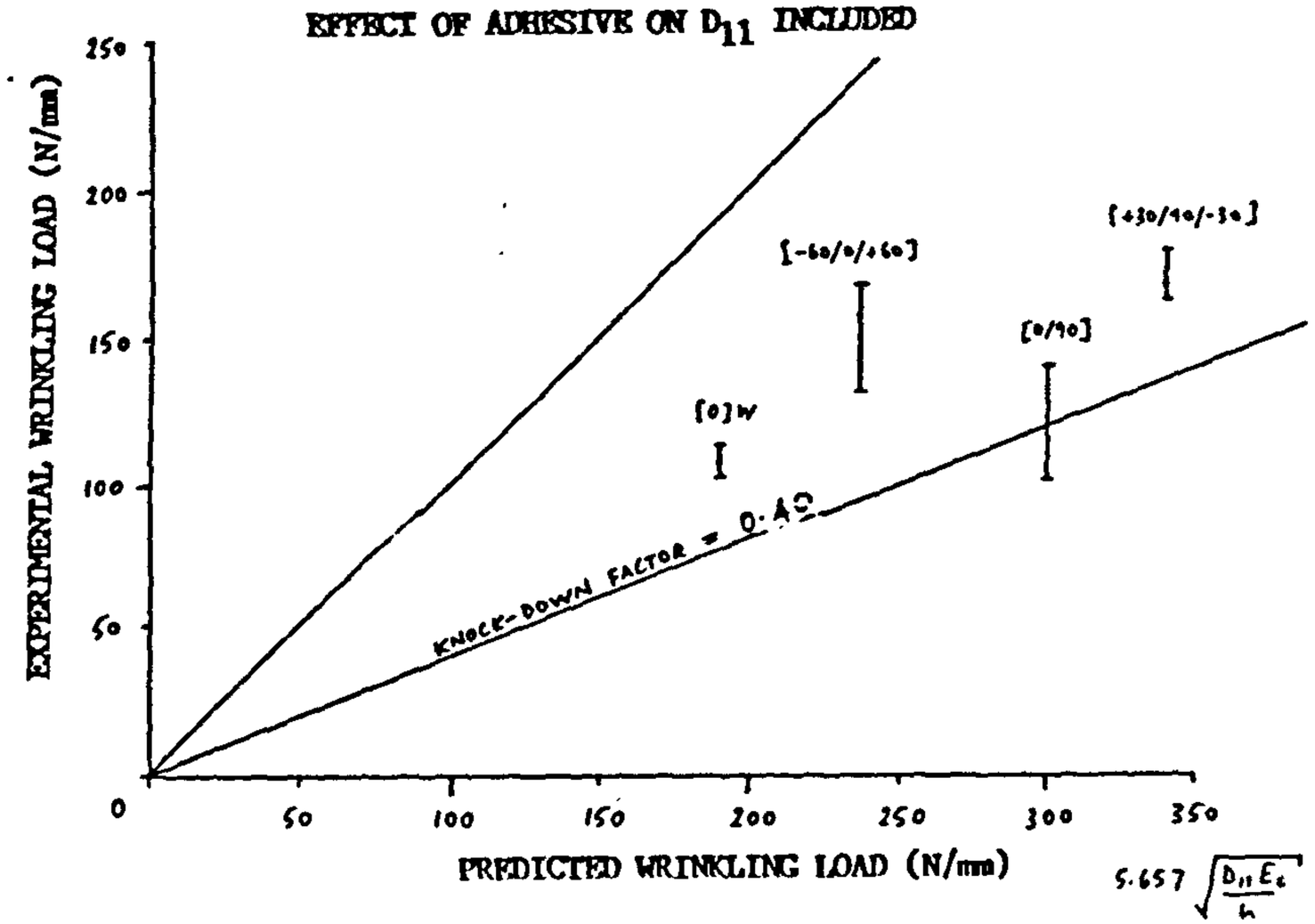

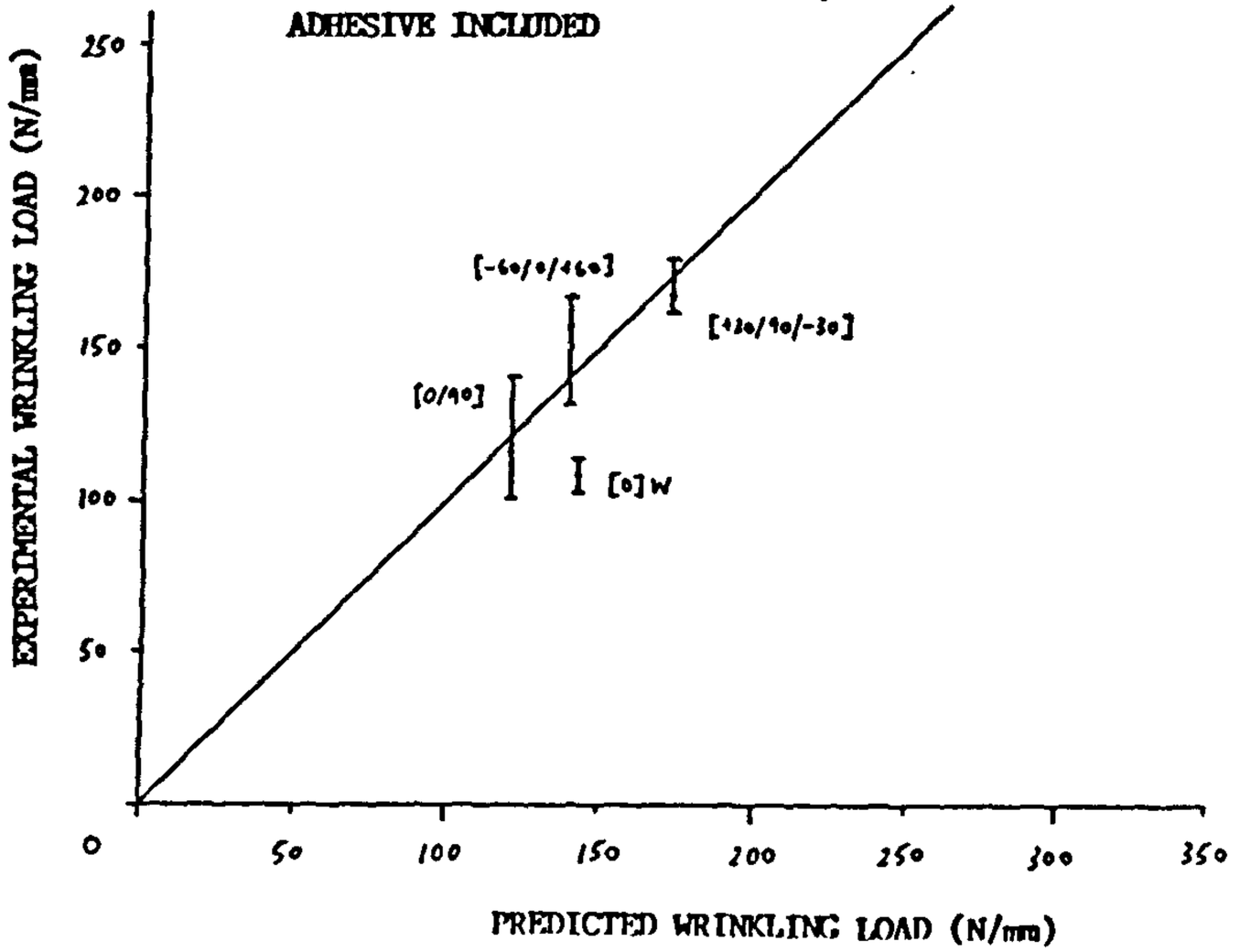

Fig. 6.21 EXPERIMENTAL Vs PREDICTED WRINKLING LOADS

Fig. 6.22

LONGITUDINAL COMPRESSION LOAD Vs. LONGITUDINAL STRAIN FOR 3-PLY QUASI-ISOTROPIC HM-S/CYCOM 985 FACED SANDWICH

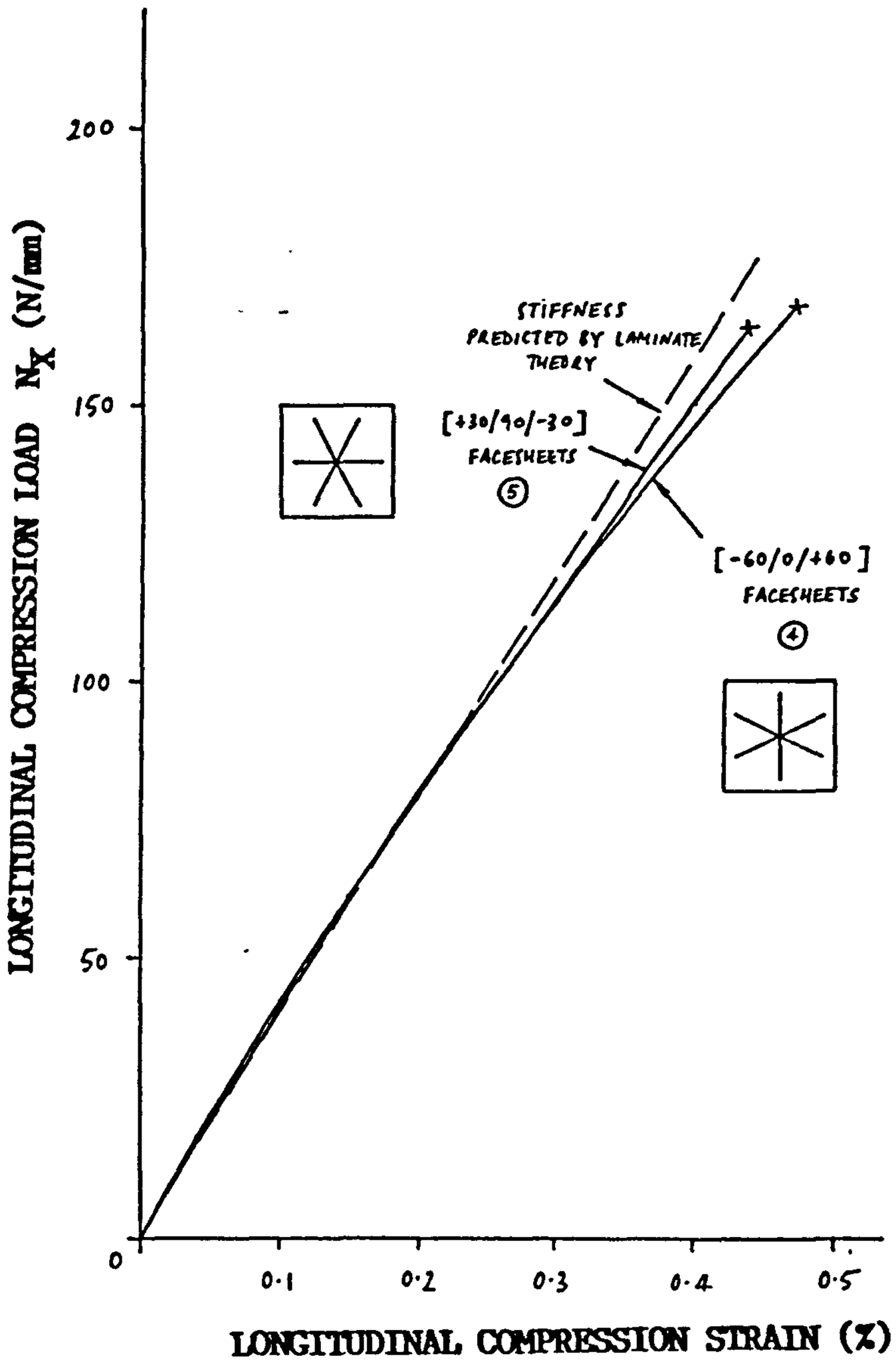

LONGITUDINAL COMPRESSION LOAD Vs. LONGITUDINAL STRAIN FOR [0/90] HM-S/CYCOM 985 AND WOVEN T-300/CYCOM 985 FACED SANDWICH

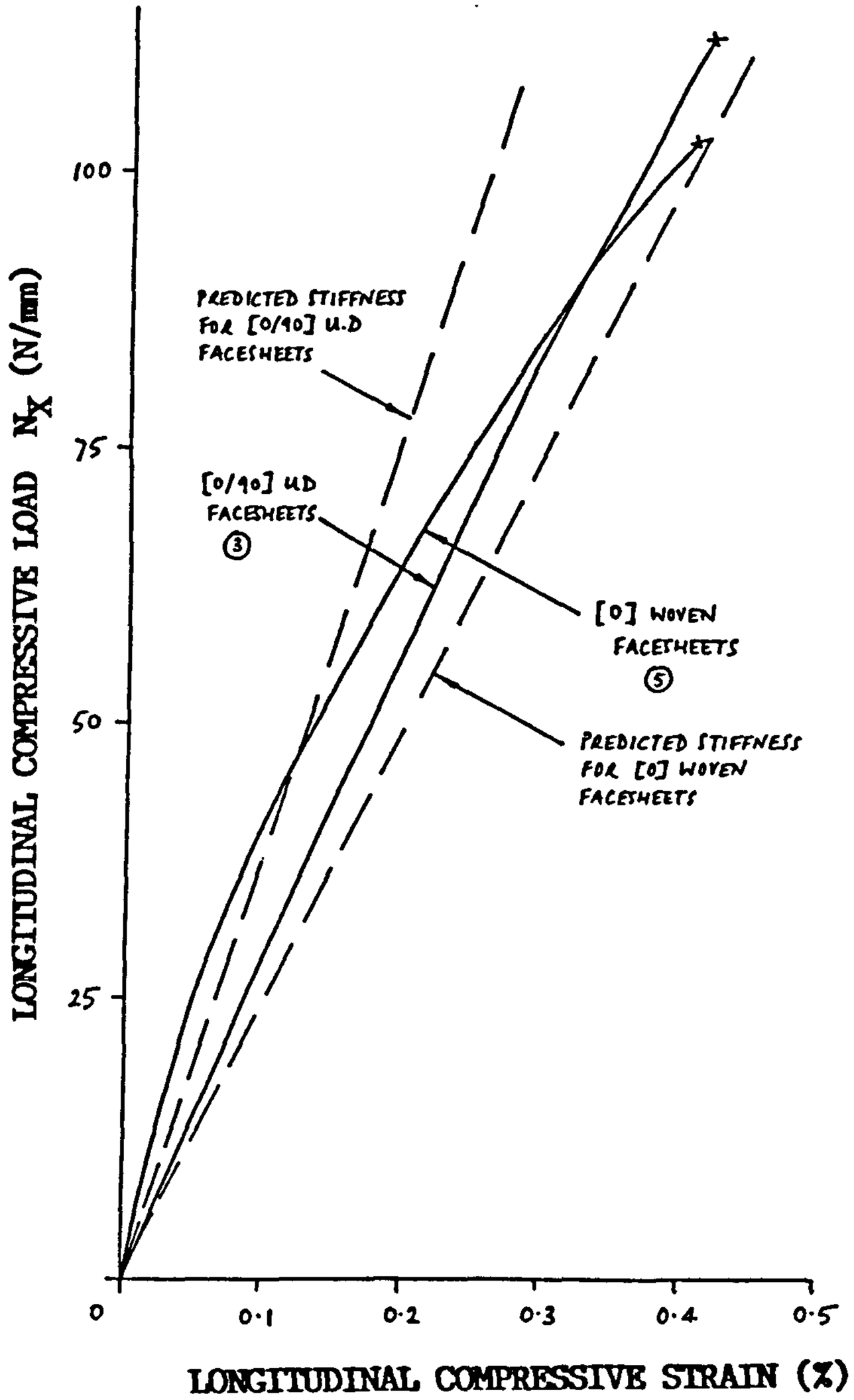

CHAPTER 7 SANDWICH PANEL OPTIMISATION

7.1 INTRODUCTION

Sandwich panels make up a large part of many spacecraft structures as platforms, equipment mounting panels, shear webs, sidewalls and access panels. Components of this type are designed to meet stiffness and strength requirements for low structure mass, and as such, composite materials can in some cases offer advantages over metallic counterparts. The potential mass savings through the use of composites in the facesheets of flat sandwich panels is not as great as thrust tube and strut components however, because the multi-axial loading of most panel components does not favour the orthotopic nature of the material. The major role played by the core in determining panel bending stiffness and strength, dictates thin facesheets for high structural efficiency, which conflicts with the requirement to include several differently orientated plies for multi-axial loading. Consequently it is not immediately apparent whether composites can save weight in any given sandwich component. For this reason it is important to be able to establish the savings, if any, that can be made through the use of composites at an early stage in the design evolution. This chapter describes a simple optimisation procedure, embodied in a computer program, which draws on the composite sandwich analysis methods outlined in the previous chapters to enable alternative minimum weight sandwich panel design solutions to be generated. The program is illustrated by two design examples of sandwich panel components which formed part of the T-Sat spacecraft primary structure.

The major structural design constraints on panels of this type are a stiffness constraint, normally specified in terms of a minimum first resonant freqeuncy, and a requirement to demonstrate positive margins of safety on all likely failure modes. The modes of failure generally considered are material failure of the facesheets, general panel instability, wrinkling instability and dimpling. Although the latter does not necessarily constitute a failure of the panel, it is often a requirement that the critical dimpling load exceeds the design loads to prevent any destabilising effect on other modes of failure. Other

constraints can also affect the design, such as thermal conductivity and thermal expansion, but these are usually either over-riding considerations which determine whether composites are employed at all, or only of secondary importance.

The optimsation scheme is intended for use at the feasibility/preliminary design (phase A) stage. At this stage a panel design specification will define the panel geometry, a design natural frequency target and internal design load cases derived from a preliminary FE model of the structure. The FE model is assumed to be a reasonable description of the structure stiffness distribution so that the component internal loads are representative for a range of possible constructions. The actual internal loads will depend on the relative stiffnesses of the structure components, but provided the initial assumptions are reasonable, these will not be affected greatly by small component stiffness changes. The internal loads will, in the case of platforms and sidewalls, be dominated by bending, although other loads, shear for example, must also be considered to ensure adequate reinforcement in all the necessary directions.

In this work the optimisation was limited to rectangular panels with zero or single curvature loaded in bending, since this type form the largest class to be found in spacecraft structures. Extending the procedure to other loading actions and load combinations could be readily accomplished based on the analysis methods described in previous chapters. Extending it to incorporate more complex geometry would be limited by the analytical solutions available for the prediction of resonant frequency, and for most components likely to be encountered in a spacecraft structure that could not be analysed as rectangular panelsit would be necessary to resort to an FE model. For some panel components (eg. platforms) the stiffness requirement may be specified in terms of a minimum frequency for an overall spacecraft mode (eg. spacecraft axial mode) rather than a local panel mode, so a stiffness analysis must consider an assembly of several components rather than the panel in isolation. Nevertheless, the panel optimisation can still be performed with respect to the strength constraints, since these are independent of the geometry (unless overall panel instability is

critical) once the internal design loads are specified, and a reduced set of possible designs subsequently checked for stiffness by an FE model.

There are several design variables that can be adjusted to meet the constraints for a minimum weight design. Broadly speaking these are :

1. Facesheet Material
2. Facesheet Lay-up
3. Honeycomb type
4. Honeycomb depth

Under the category of facesheet material are included variations in the fibre reinforcement type, resin system and whether the fibres are in unidirectional or woven form. Facesheet lay-up includes the ply angles, stacking sequence and ply thickness. Honeycomb type is specified by the material, foil thickness and cell size. There is also a choice of panel manufacturing method (pre-cured or co-cured facesheets) which will influence the facesheet lay-up (balanced or unbalanced) and determine material properties. None of these variables are particularly suited to incorporation into a formal numerical optimisation scheme since they are specific and non-continuous. For example, honeycombs are commercially available only in certain combinations of foil thickness and cell size, prepregs are available in usually one or two thicknesses only and material properties are specific to the particular fibre/matrix system. Facesheet lay-up angles are continuous variables, but for most panel components the loading requirements limit lay-ups to cross-ply [±45], [0/90] or quasi-isotropic [+60/0/-60], [0/+45/-45/90] which can be specified from the outset, with little variation as regards intermediate angles possible. Only the core depth can be regarded as a truly free design variable. The optimisation method therfore involves pre-selecting the other variables and reducing the problem to a simple one-dimensional minimisation with respect to the core depth.

The procedure adopted is to locate the minimum core depth, and hence panel mass for several facesheet material & lay-up and core type constructions. Practical constraints will limit the possibilities to a fairly small number

of design options. The minimum panel weights to meet the design constraints for the different constructions can be rapidly calculated using the program and these can then be compared. Selection of the best design solution can then proceed based on the panel weights and by taking in to consideration cost and fabrication implications.

7.2 NATURAL FREQUENCIES OF RECTANGULAR COMPOSITE FACED SANDWICH PANELS

This section describes the analysis method for the prediction of natural frequencies of rectangular sandwich panels with composite facesheets which is incorporated within the optimisation program. The panel is idealised as having simply supported edges and a uniform mass distribution consisting of mounted equipment and the panel structure mass. Such an idealisation is reasonable at the preliminary design stage since simply supported edges are a closer representation of typical edge connections than clamped edges, and detail of the actual equipment mass distribution will be unknown. In reality the panel will be connected by brackets to other non-rigid structure, and the equipment mass will be non-uniform and have inertia associated with its out-of-plane distribution. The omission of the out-of-plane mass distribution will be more than compensated for by the omission of the stiffening effect of the equipment boxes themselves.

The analysis is based on the following assumptions. Firstly, that the sandwich panel has an uncoupled constitutive relationship. For facesheets which are symmetric about the core, which includes co-cured constructions, [B] coupling will be zero, and D_{13}, D_{23} bending-flexural coupling terms will be near zero for facesheets which are thin compared to the core. Such an assumption simplifies the analysis without invalidating it for almost all practical constructions. Secondly, the facesheets are considered to take only in-plane loads and the core to take only through-thickness shear. Direct through-thickness deformation in the core is neglected since this will have little contribution to the low frequency modes of the panel. Thirdly, that out-of-plane deformations dominate the low frequency modes, so in-plane displacements u and v are not included. Fourthly, rotary inertia of the uniform mass distribution is not included since this is

unlikely to be known with any certainty at the preliminary design stage, and the effect will be small.

7.2.1 Theory

The three equilibrium equations for forces in the z-direction and moments in the x and y-directions for a curved panel of radius R, with uniform mass distribution of ρ per unit area are :

$$\frac{\partial Q_x}{\partial x} + \frac{\partial Q_y}{\partial y} + \frac{N_y}{R} = \rho \omega^2 w$$

$$\frac{\partial M_x}{\partial x} + \frac{\partial M_{xy}}{\partial y} - Q_x = 0 \qquad \text{(eqs. 7.1)}$$

$$\frac{\partial M_y}{\partial y} + \frac{\partial M_{xy}}{\partial x} - Q_y = 0$$

where ω is the cyclic frequency in rad/s

For thin plates, transverse shear can be neglected and the three equations can be combined to give a single equation in terms of the transverse displacement w, only. However, for sandwich panels, the shear rigidity of the core is low so all three equations are retained.

The strain-displacement relationships for the panel mid-surface are :

$$\epsilon_x = \frac{\partial u}{\partial x} \qquad \epsilon_y = \frac{\partial v}{\partial y} - \frac{w}{R} \qquad \gamma_{xy} = \frac{\partial u}{\partial y} + \frac{\partial v}{\partial x}$$

(eqs. 7.2)

$$k_x = \frac{\partial \beta_x}{\partial x} \qquad k_y = \frac{\partial \beta_y}{\partial y} \qquad k_{xy} = \frac{\partial \beta_x}{\partial y} + \frac{\partial \beta_y}{\partial x}$$

where β_x and β_y are the x and y components of the slopes to the normal of the panel mid-surface, including core shear. These are given by :

$$\beta_x = \gamma_{xz} - \frac{\partial w}{\partial x}$$

$$\beta_y = \gamma_{yz} - \frac{v}{R} - \frac{\partial w}{\partial y} \qquad \text{(eq. 7.3)}$$

By employing the constitutive relationship for the complete panel (equation 5.1 of chapter 5) and the panel shear stress resultant - strain relationship :

$$Q_x = S_{xz}.\gamma_{xz}$$

$$Q_y = S_{yz}.\gamma_{yz} \qquad \text{(eqs. 7.4)}$$

where,

$$S_{xz} = G_{xz}(t + h)$$
$$S_{yz} = G_{yz}(t + h)$$

and substituting these and equations (7.2) into the equilibrium equations (7.1) results in three differential equations in terms of w, β_x and β_y.

These equations are solved by assuming modal shape functions of the following form :

$$w = W \sin \frac{m\pi x}{a} \sin \frac{n\pi y}{b}$$

$$\beta_x = \bar{\beta}_x \cos \frac{m\pi x}{a} \sin \frac{n\pi y}{b} \qquad \text{(eqs. 7.5)}$$

$$\beta_y = \bar{\beta}_y \sin \frac{m\pi x}{a} \cos \frac{n\pi y}{b}$$

where m and n are the number of sinusoidal half-waves in the x and y directions respectively. These functions satisfy the simply supported edge conditions of zero edge moments and w displacements.

Differentiating these functions and substituting into the differential equilibrium equations, results in the following matrix equation in terms of the displacement and slope amplitudes W, $\bar{\beta}_x$ and $\bar{\beta}_y$:

$$([K] - \lambda[M])\begin{Bmatrix} W \\ \bar{\beta}_x \\ \bar{\beta}_y \end{Bmatrix} = 0 \qquad \text{(eq. 7.6)}$$

where, [K] is a 3 x 3 stiffness matrix

[M] is a 3 x 3 mass matrix

λ is the natural frequency eigenvalue = ω^2

The stiffness matrix elements are :

$$K_{11} = \frac{A_{22}}{R^2} + S_{xz}\alpha^2 + S_{yz}\beta^2$$

$$K_{12} = S_{xz}\alpha$$

$$K_{13} = S_{yz}\beta$$

$$K_{21} = K_{12}$$

$$K_{22} = D_{11}\alpha^2 + D_{33}\beta^2 + S_{xz}$$

$$K_{23} = (D_{12} + D_{33})\alpha\beta$$

$$K_{31} = K_{13}$$

$$K_{32} = K_{23}$$

$$K_{33} = D_{22}\beta^2 + D_{33}\alpha^2 + S_{yz}$$

where, $\alpha = \frac{m\pi}{a}$ and $\beta = \frac{n\pi}{b}$

All the mass matrix elements are zero except for M_{11}.

$M_{11} = \rho$ (total panel mass per unit area)

The eigenproblem, equation (7.6), can be solved by setting the determinant to zero :

$$\left| [K] - \lambda[M] \right| = 0 \qquad \text{(eq. 7.7)}$$

Since the matrices are only third order, the single finite eigenvalue can be relatively easily found. The solution is :

$$\lambda = \frac{K_{11}(K_{22}K_{33} - K_{23}^2) - K_{12}(K_{12}K_{33} - K_{13}K_{23}) + K_{13}(K_{12}K_{23} - K_{13}K_{22})}{M_{11}\,(K_{22}K_{33} - K_{23}^2)} \qquad \text{(eq. 7.8)}$$

and the natural frequency is then :

$$f = \frac{\sqrt{\lambda}}{2\pi} \text{ Hz} \qquad \text{(eq. 7.9)}$$

The first mode natural frequency can be found by varying m & n until the frequency is minimised. In most cases where the panel shape is near-square with a fairly large radius of curvature and the facesheet lay-up has an even distribution of fibre directions, the lowest mode will occur for (m = 1, n = 1). For very narrow panels and/or highly directional lay-ups the lowest mode shape may consist of 2 half waves in the longest/least stiff direction ie. (m = 2, n = 1), or (m = 1, n = 2).

7.2.2 Effect of Design Parameters on Natural Frequency

The stiffness matrix elements, K_{ij}, show that panel natural frequency is determined by the panel's flexural rigidity [D] matrix, the core shear rigidities S_{xz}, S_{yz}, and if the panel is curved, the membrane stiffness in

the direction of curvature, A_{22}. An insight into the relative importance of these terms can be gained by considering the case of a flat panel with infinitely rigid core. The (m = 1, n = 1) mode natural frequency is then reduced to the simple expression :

$$f = \frac{\pi}{2\sqrt{\rho}}\sqrt{\frac{D_{11}}{a^4} + \frac{2(D_{12} + 2D_{33})}{a^2\, b^2} + \frac{D_{22}}{b^4}} \qquad \text{(eq. 7.10)}$$

where D_{ij} refer the flexural stiffness of the constitutive matrix for the complete panel. These can be approximated by:

$$D_{ij}^{S/W} \simeq \frac{1}{2}\, h^2\, A_{ij}^{F/S} \qquad \text{(eq. 7.11)}$$

for thin facesheets on a thick core. Therefore the frequency is almost directly proportional to the core depth, provided core shear is neglected. Another interesting feature shown by equation (7.10) is that frequency can most effectively be increased by arranging the fibres in the short span direction (ie. $D_{11} > D_{22}$ if a < b) for rectangular panels. This is illustrated in fig 7.1 which plots first natural frequency (normalised to the maximum) for a rectangular panel with aspect ratio 3, constant depth infinitely rigid core, and facesheet lay-ups of $[+\theta/-\theta]$ against the fibre angle, θ. The first natural frequency is maximised for fibre angles of approximately [±15]. At higher angles the stiffening is less effective because D_{11} is reduced in the short span direction. But below this angle, the frequency reduces because shear stiffness D_{33} is lost and D_{22} becomes so low that the first mode switches to two half-waves in the longest span direction, (m = 1, n = 2).

The effect of the honeycomb shear rigidity can be demonstrated by comparing the results of equation (7.10) with those of equation (7.8) which includes the core shear effects. Consider the example of a [0/ 60] HMS-CYCOM 985 faced panel with a 20 mm deep 2.0lb/cu.ft aluminium core of aspect ratio 2. Table 7.1 gives the predicted first mode natural frequencies using both equations for the panel when it has dimensions of 1.0 m x 0.5 m, and when these dimensions are halved to 0.5 m x 0.25 m.

TABLE 7.1 **Effect of Core Shear on Natural Frequency of Rectangular Panel**

PANEL DIMENSIONS (m)	1SI MODE FREQUENCY (Hz)	
	Neglecting Core Shear (eq. 7.10)	Including Core Shear (eq. 7.8)
1.0 x 0.5	73.5	71.0
0.5 x 0.25	293.9	259.9

As one would expect, the effect of core shear is larger for the smaller panel because the linear dependence on dimensions of shear deformation is more significant. In the larger panel bending deformation, dependent on the cube of dimensions, dominates. The effect of core shear for the larger, 1.0 x 0.5 m, panel results in only a 2% reduction even for this low honeycomb density. This suggests the selection of honeycomb density will have little bearing on the frequencies of panels this size, which is typical of sidewalls and cover panels of medium to large sized spacecraft. The reduction effect becomes more significant, 12% in this case, when the panel area is reduced to a quarter, as for example in a side panel divided into quadrants by supporting shear webs.

7.3 PANEL STRENGTH AND STABILITY UNDER BENDING

The analytical techniques described in the previous two chapters for predicting material failure and local instability are incorporated in the panel optimisation scheme. These prediction methods were shown to give quite good agreement with experimental results, although these were for compression rather than bending which is the loading condition considered in this chapter.

Facesheet material failure was analysed by converting the applied bending moment to an equivalent stress resultant couple acting on the upper and lower faces, inverting the facesheet [A] matrix, calculating the ply stresses (equation (5.9)) and applying the Tsai-Wu failure criterion. In the majority of cases failure was dominated by the compression facesheet because fibre-direction compression strength is lower than the tension strength in most composite systems.

Panel wrinkling under flexure was analysed by the method described in chapter 6, and included the effect of coupling in co-cured facesheets and the stabilising effect of the tension facesheet. The program given in Appendix C was included as a subroutine of the optimisation program to compute critical flexural wrinkling loads. To minimise wrinkling loads with respect to the wave parameters m and n, initial estimates from specially orthotropic compression wrinkling theory were used.

Dimpling was analysed using the approximate method of section 6.8 which considered a simply supported square element of the compression facesheet the size of a honeycomb cell, and assumed special orthotropy. This method was approximate since any facesheet coupling effects were ignored, although it is generally accepted to yield conservative results.

7.4 PANEL OPTIMISATION PROGRAM

The panel optimisation program is illustrated by the flow chart of fig. 7.2. The problem is specified by the following parameters :

1. Panel dimensions and curvature.
2. Uniform panel mass per unit area.
3. Design frequency requirement.
4. Design M_x bending moment resultant.

The user selects the facesheet material and lay-up, and the core type by supplying strength, stiffness and density data. Starting from a minimum core depth (supplied by the user) the program first calculates the panel

mass and the constitutive matrices for the individual facesheets and the complete sandwich. These are used to calculate the four constraint functions (frequency, material failure, wrinkling and dimpling) defined below :

Natural Frequency

$$g_1 = \frac{f - f_D}{f} \qquad \text{(eq. 7.12)}$$

where,

f = Calculated first resonant frequency.

f_D= Design frequency requirement.

Material Strength

$$g_2 = 1 - TW \qquad \text{(eq. 7.13)}$$

where,

TW = Maximum Ply Tsai-Wu Index

Wrinkling

$$g_3 = \frac{Nx_{wr} - Nx}{Nx_{wr}} \qquad \text{(eq. 7.14)}$$

where,

Nx_{wr} = Calculated critical wrinkling equivalent stress resultant

Nx = Applied equivalent stress resultant

Dimpling

$$g_4 = \frac{Nx_d - Nx}{Nx_d} \qquad \text{(eq. 7.15)}$$

where,

Nx_d = Calculated critical dimpling equivalent stress resultant
Nx = Applied equivalent stress resultant

The calculated values of natural frequency, material strength and local stability include knock-down factors to the theoretical predictions which can be specified to account for uncertainties and modelling idealisations. For natural frequency, a reduction factor might be applied if it is known that equipment mass is likely to be concentrated at the centre of the panel area, or if the panel is connected to other low stiffness structure at the edges, for example. If high confidence design allowable strengths are used no knock-down factor is necessary for the computed failure indices to account for material variability. For wrinkling and dimpling, factors can be applied to correlate with minimum test results.

The calculated constraint functions are violated if they have a value less than zero. If any are violated then the core depth is simply increased by a user specified increment and the analysis repeated until all are a positive. The core depth is always increased (ie. there is no necessity to establish an optimum search direction for h) because all the constraint function gradients with respect to core depth have the same sign for all h. In other words, increasing core depth always increases natural frequency, panel strength against facesheet failure and wrinkling & dimpling strengths under applied bending. Material and dimpling strengths are not affected by the core depth as such, but an increase for a given applied moment reduces the equivalent stress resultant couple applied to the facesheets so the corresponding constraint functions are reduced. Panel natural frequency increases almost linearly with core depth, as shown in section 7.2.2. Critical wrinkling moment capacity increases approximately with the square root of h, as illustrated in fig. 6.10.

A point worth remarking on is that if the optimising program is extended to include applied design membrane and shear loads in addition to bending, the optimum search direction (whether to increase or decrease h) must be assessed. Increasing core depth may not tend towards a feasible design if membrane compression loads are high and wrinkling is critical because compression and shear wrinkling capacities decrease with core depth (inversely proportional to the square root of h). See figs. 6.8 and 6.9 for example.

The increase in core depth is a fixed quantity for each iteration defined by the user (1 mm is practical). It was not considered worthwhile to attempt to optimise the step length by estimating the necessary increase in h to reach a feasible design by fitting functions to the constraints. Since there was only a single variable and the search direction was known, the time taken to locate the optimum core depth was found to be sufficiently fast simply by stepping through with constant increments from the first estimate.

The program terminates by outputting the minimum core depth for a feasible design, the panel weight and values of the design constraints. Appendix D gives a description of the program and examples of input and output files.

7.5 EXAMPLE 1 : STIFFNESS CRITICAL PANEL (T-SAT REAR PANEL)

7.5.1 Panel Configuration and Design Requirements

The following example is a typical lightly-loaded stiffness-critical spacecraft panel which demonstrates the optimisation program. It is representative of a rear closure panel on the T-SAT spacecraft. The basic panel dimensions and design bending moments are shown in fig 7.3. Most electronic equipment on this spacecraft is mounted to the sidewalls for heat dissipation, so that the rear panel serves only to form the enclosed centrebody of the structure. Fixed to the external periphery of the rear face from brackets is a flat phased array antenna. Because this is mounted around the edges, the only mass on the panel is the weight of thermal

control surfaces, electrical wiring and the panel's own mass. Because it is relatively light, a design target frequency of 100Hz was specified. Bending moments resulting from lateral excitation of the antenna are induced at the panel edges. At the factored static design load levels, the maximum moment resultant found from a FE model of the structure was 150 Nm/m along the upper edge. In addition, the maximum vertical edge moment resultant was found to be 50 Nm/m. The panel had no appreciable shear loading under any load cases.

7.5.2 Design Optimisation

Composite facesheets containing only 0° and 90° orientated fibres were considered, with the 0° direction taken parallel to the vertical edges. Possible facesheet lay-ups were [0/90] and [0/90/0]. The former minimises the number of plies and the latter attempts to improve structural efficiency by biasing extra fibres in the major bending moment direction. Several different carbon fibre types, prepreg thicknesses and honeycomb densities were considered. Also the effect of the manufacturing process, whether pre- or co-cured facesheets were used, was investigated. Facesheet material properties were taken from the design allowables listed in Table 3.3, and the factors of Table 5.9 were applied to estimate the degradation effect of a reduced pressure co-cure. The minimum necessary core depths and the corresponding panel weights found by the program are given in Table 7.2. A knock-down factor of 0.4 was applied to the computed wrinkling strengths and no knock-down factors for the other constraints. The film adhesive was taken to have a weight of 150 g/m^2, and the core density was assumed to be uniform over the full panel area.

Construction 1 consisted of the minimum possible facesheet thickness, with 2 x 0.05 mm [0/90] plies of ultra high modulus GY-70/Code 92 on a 2.0 lb/cu.ft 5056 aluminium core. Because this facesheet lay-up was unbalanced the sandwich must be co-cured to prevent distortion. The optimum core depth was found to be 15 mm (to the nearest millimetre), yielding a panel weight of 1.120 kg/m^2 with the critical constraint being dimpling. The dimpling strength was improved by moving to the next lowest available honeycomb cell size : 5/32 " (construction 2), which although having an increased density

enabled the core depth to be reduced to 12 mm and yielded a small net weight saving.

Construction 3 incorporated [0/90/0] x 0.05 mm co-cured GY-70/Code 92 facesheets, which were thicker but better tailored to the bi-directional design loading. A core of 2.6 lb/cu.ft with a thickness of 7 mm was found to minimise mass, with both dimpling and natural frequency being the critical constraints. (The failure mode constraints for this biased lay-up under the vertical edge design bending moment resultant of 50 Nm/m, were checked by considering the panel rotated through 90°, and were lower in all cases). This design had a weight of 1.104 kg/m^2, which made a slight saving over the 2-ply facesheet constructions. Because the 3-ply lay-up was symmetric it is possible to pre-cure the facesheets. Construction 4 considered the same facesheets and core, but with the facesheets pre-cured. The minimum core thickness was found to be the same, since pre-curing results in only a very small improvement in longitudinal modulus over co-curing, and this property largely determines the critical dimpling behaviour and panel stiffness. There were small increases in the margins of safety on these constraints, and a large improvement on the facesheet material strength constraint because of the much higher longitudinal compression strength.

Construction 5 considered [0/90] co-cured GY-70/Code 69 facesheets with thicker 0.10 mm prepreg. The extra facesheet thickness gave a much improved margin on dimpling, but although thicker, the additional 90° fibres in the long span direction did not significantly improve the panel stiffness over [0/90/0] x 0.05 mm facesheets, so the same thickness core was required to meet the over-riding stiffness constraint. Because of the additional 'unworked' facesheet thickness, this construction was heavier than the [0/90/0] faced constructions. It was possible to obtain a similar facesheet lay-up by pre-curing [0/90/90/0] x 0.05 mm GY-70/Code 69 prepreg (construction 6). The small improvement in stiffness properties did not yield any weight saving over co-cured [0/90] x 0.10 mm facesheets, with only an improved material failure margin to compensate for the additional cost of the thinner prepreg and lengthier manufacturing cycle.

High modulus carbon fibres offer a cheaper alternative to ultra high modulus fibres for a drop in stiffness performance. The weight penalty incurred through the use of HM-S/985 facesheets is indicated by constructions 7 to 10. The reduced stiffness of [0/90] x 0.05 mm co-cured facesheets in construction 7 resulted in a low dimpling strength, which forced a small cell size honeycomb for structural efficiency. The lowest weight panel had a core of 3.1 lb/cu.ft and a thickness of 11 mm which was dictated by the overall stiffness requirement. The weight penalty was only 0.050 kg/m^2 over its GY-70/92 faced counterpart. The structural efficiency was improved, as with ultra high modulus facesheets, by adopting a biased [0/90/0] x 0.05 mm lay-up (construction 8), and there was no advantage in pre-curing the facesheets (construction 9). The designs for these constructions had only a 1 mm core thickness penalty over GY-70/92, this being determined by the panel overall stiffness and dimpling requirements. There was no advantage in going to thicker facesheets (construction 10). The lowest weight HM-S fibre reinforced panels (constructions 8 & 9) were only 1% heavier than the lowest weight GY-70 reinforced panels (constructions 3 & 4).

Constructions 11 & 12 have high strength T-300/69 facesheets. The relatively low stiffness of these fibres precluded thin facesheets because of the dimpling constraint. Construction 11 had [0/90/0] x 0.05 mm co-cured facesheets with a 10 mm 2.6 lb/cu.ft core dictated by the panel stiffness and dimpling requirement. The thicker [0/90] x 0.10 mm facesheets of construction 12 improved dimpling resistance and enabled a lower density honeycomb to be employed, but this did not offset the additional facesheet weight. The optimum T-300/69 faced design (construction 11) was 8% heavier than the lowest weight GY-70/92 faced design.

The lightest 2024-T81 alloy faced construction had 0.10 mm faces on a 2.0lb/cu ft core with a weight of 1.304 kg/m^2. The relative weight savings by replacement of this design with carbon composites for GY-70, HM-S and T-300 UD fibres were 15%, 14% and 8% respectively. For the full rear panel area which is 3 bays of 1.6m x 0.55m, these translate into savings of 0.53 kg, 0.50 kg and 0.29 kg. The preferred design solution was [0/90/0] x 0.05 mm co-cured HM-S/985 facesheets on an 8 mm deep 2.6 lb/cu.ft. core, since

this represented the best compromise between weight and cost. The cost saving through the use of HM-S fibres offset the 1% weight penalty compared to GY-70 reinforcement, and also conferred advantages in terms of easier handling and lower susceptibility to damage. Use of a co-cure method of manufacture enabled lay-up and curing time to be reduced to make cost savings over a pre-cured facesheets, whilst still yielding a sufficient margin om material failure under the design loading.

All the facesheet materials given in Table 7.2 are unidirectional since no design allowable data was available for high and ultra high modulus woven materials. Because all of the constructions considered were either frequency or dimpling critical, single ply plain woven faced panels would be expected to have a performance roughly comparable with their [0/90] UD faced counterparts. They would therefore not be as efficient as the [0/90/0] UD facesheet lay-ups, unless a 2:1 bias weave material was available. Such a material could offer practical advantages such as a greater robustness, a lower stress concentration effect, improved drilling and machining properties and a saving in lay-up time.

7.6 EXAMPLE 2 : STRENGTH CRITICAL PANEL (T-SAT SM PLATFORM)

7.6.1 Platform Configuration and Design Requirements

This example is typical of a more highly loaded panel, again from the T-SAT structure. It is the service module platfrom, shown in fig. 7.4, which stiffens the spacecraft sidewalls and transmits load to the thrust cylinder. The cylinder attachment is around the circumference of a central circular cut-out. No heavy equipment is fitted to this platform and local panel vibration modes are not critical, but it provides stiffness to overall axial spacecraft modes. As such, it cannot be treated as a simple panel in isolation for stiffness analysis within the optimisation program. It was therefore only possible to optimise the design for strength under the predominant design bending loading, and stiffness had to be subsequently checked through the spacecraft FE model. The design bending moment was found from a static FE model for an initial platform

construction. Fig. 7.4 illustrates bending momemts in the platform under the critical load case of highest axial acceleration. Highest moments were situated around the thrust cylinder attachment in the radial direction. Because the moments were high around the complete circumference, it was necessary to provide strength in all directions which suggested a pseudo-isotropic type facesheet lay-up. The maximum moment resultant was 450 Nm/m at the -X cylinder attachment position and this was specified as the selected design moment for optimisation.

7.6.2 Design Optimisation

Pseudo-isotropic co- and pre-cured facesheet lay-ups of the form [+30/90/-30] and [0/+45/-45/90] with different material systems were considered. The 0° direction was taken parallel to the design moment, ie. in the spacecraft X direction. [±30/90] lay-ups were considered in preference to [0/±60] because material and wrinkling strengths are then maximised in the highest moment direction. Results of the core depth optimisation are given in Table 7.3.

Construction numbers 1 and 2 considered co-cured facesheets consisting of 0.05 mm plies of GY-70/Code 92 in [90/±30] type lay-ups. The only difference between the two was in the stacking sequence. Both had lightweight 2.0 lb/cu ft cores. Wrinkling was the primary design criterion because of the thin facesheets and very thick cores that were necessary. By arranging the stacking sequence as in construction 2 with the 90° ply central, the wrinkling performance was greatly improved because facesheet coupling effects were minimised and D_{11} was maximised (see discussion of section 6.6.1.2). Consequently the core depth and panel mass were significantly reduced over construction 1. A further reduction in panel mass was achieved in construction 3 by employing a denser honeycomb which improved wrinkling performance further. The core depth was limited by bothmaterial strength and wrinkling instability considerations and the panel mass was 1.860 kg/m^2.

More weight was saved by employing thicker 4 x 0.05 mm ply [0/±45/90] type co-cured facesheet lay-ups (constructions 4 and 5). Again, judicious selection of the stacking sequence led to improved wrinkling performance, with the [0/+45/-45/90] lay-up of construction 5 being superior to [+45/0/90/-45] of construction 4. Both designs were of equal weight however, because the minimum core depth was limited by the material strength constraint. The low wrinkling margin of construction 4 was nevertheless improved by the alternative stacking sequence of construction 5. The panel mass was 1.780 kg/m^2.

The lowest weight designs utilising GY-70 fibre reinforcement had thicker 0.3 mm facesheets with [+30/90/-30] lay-ups. At this thickness it was possible to consider balanced pre-cured facesheets of [+30/-30/90/90/-30/+30] x 0.05 mm (construction 7) in addition to co-cured [+30/90/-30] x 0.10 mm facesheets (construction 6). Both gave high wrinkling resistance, enabling low density 2.0 lb/cu.ft cores to be employed, but the superior longitudinal compression strength of the pre-cured facesheets resulted in a lower core depth, since this was determined by the material strength constraint. The pre-cured facesheet design had a weight of 1.544 kg/m^2, which saved 8% over the co-cured design.

Constructions 8, 9, 10 and 11 had HM-S/985 facesheets. The higher longitudinal compression strength of this material led to lower weight designs than with GY-70 reinforcement despite its reduced modulus, because of the dominant material strength constraint. The thin [+30/90/-30] x 0.05 mm co-cured facesheets of construction 8 required a relatively thick core to confer sufficient wrinkling strength. The thicker [0/+45/-45/90] x 0.05 mm co-cured facesheets of construction 9 were more efficient, with the core depth limited by compression strength. There was no advantage in going to still thicker [+30/90/-30] x 0.10 mm co-cured facesheets (construction 10) because the reduction in core depth that this allowed did not offset the additional facesheet mass. The lightest HM-S/985 design employed pre-cured facesheets of [+30/-30/90/90/-30/+30] x 0.05 mm (construction 11), with a weight of 1.516 kg/m^2. This was as a result of the improved longitudinal compression strength due to pre-curing, which saved 6% over the lowest weight co-cured construction.

The lightest composite designs considered were those that employed high strength T-300 carbon fibre reinforcement. Construction 12 employed co-cured [0/+45/-45/90] x 0.05 mm facesheets, which required a 15 mm thick 2.0 lb/cu.ft core to meet both material strength and wrinkling requirements. Thicker [+30/90/-30] x 0.10 mm co-cured facesheets improved the compression strength (construction 13), but the low stiffness of the T-300 reinforcement required a core depth of 7 mm to meet the wrinkling constraint and the saving in core thickness did not offset the additional facesheet mass. However, by pre-curing balanced [+30/-30/90/90/-30/+30] x 0.05 mm facesheets (construction 14), the wrinkling strength was improved sufficiently to enable the core depth to be reduced to 5 mm and yield the lightest design of 1.408 kg/m^2.

Construction 15 considered co-cured woven [0/45] x 0.10 mm T-300/F263 facesheets. It was assumed the reduction of compression strength due to co-curing applied to unidirectional materials also applied to woven material (in both warp and weft directions). Based on this assumption, the woven faced design was found to require a core of 18 mm to meet the material strength constraint. Use of woven material gave a good margin on wrinkling instability. At a panel weight of 1.476 kg/m^2 it was competitive with the lightest of the UD material alternatives and had attendant practical advantages over these.

The lightest aluminium alloy design had 0.15 mm facesheets on a 14 mm deep 2.0 lb/cu.ft core, with a weight of 1.582 kg/m^2. The lightest composite design, construction 14, with pre-cured [+30/-30/90/90/-30/+30] x 0.05 mm T-300/69 facesheets on a 5 mm deep 2.0 lb/cu.ft core, saved 11% in comparison, but this was not considered to be a practical alternative. The thin core resulted in a low overall panel stiffness and was considered to be insufficient for the potting of inserts for structural attachments. The prefered composite design was therefore construction 12, with co-cured [0/+45/-45/90] x 0.05 mm T-300/69 facesheets on a 15 mm core. This made a weight saving of about the same as construction 14, just under 11% or 0.275 kg over the full panel area, but the thicker core gave improved platform stiffness (which the spacecraft FE model showed to be sufficient for overall axial modes) and adequate depth for inserts. The co-cure technique

also enables manufacturing cost to be reduced. There was no advantage in going to higher modulus materials because of increased raw material cost and no reduction in weight. The lowest weight designs utilising HM-S and GY-70 reinforcement were the pre-cured options because of the lower inherent compression strengths of these materials. These made weight savings of 4% and 2.5% respectively compared to the lightest aluminium faced design.

7.7 CONCLUSIONS

The possible mass savings in spacecraft sandwich panel components through the use of composite facesheets are recognised as being relatively modest, and in some cases no savings are possible at all. This fact, combined with the additional design variables of ply angles and stacking sequences, and the extra complexity of analysis, makes the simple optimisation program described here a useful design aid, enabling optimum composite designs to be generated. This allows alternative materials, prepreg thicknesses, lay-ups and manufacturing methods to be rapidly evaluated and compared. The method is applicable at the early design stage since it is based on preliminary internal design loads and stiffness requirements. This is particularly useful since it enables candidate composite material systems to be evaluated on a component by component basis and particular systems to be selected in the context of the whole structure. The pros and cons of co-curing and pre-curing can be assessed and the estimates of panel weights are useful for calculating the all important mass budget and evaluating the cost effectiveness of the mass savings.

The optimisation program provides a cheaper and quicker alternative to several design iterations and modifications of an FE model. Designs sized by the optimisation program can be incorporated into the FE model allowing iterations to be skipped. In its present form, the panel optimisation program is restricted to a single bending moment design loading condition. Such a design condition is not unrepresentative for many spacecraft panels, but the program could be readily extended to include multiaxial moments and membrane stress resultants based on the analysis techniques described in

previous chapters. Several quasi-static load cases and the corresponding internal loads at several panel positions could also be incorporated. This would require all the strength and stability constraints to be calculated for each load case and position, the optimum being found when all constraints are satisfied and weight is minimised. As mentioned in section 7.3, the inclusion of applied membrane stress resultants would require a search direction assessment routine (increase or decrease h) to be incorporated, because the wrinkling constraint function slope may be positive or negative. Membrane compression and shear loads would also require the additional design constraints of overall buckling to be calculated. Overall buckling for a simply-supported panel or column could be readily analysed using the wrinkling analysis subroutine. The overall buckling load is the anti-symmetric eigenvalue for m = 1 and n = 1 (simply supported panel) or m= 1 and n = 0 (simply supported column). Analysis of shear buckling would require a different approach because of the sloped nodal lines of the buckled mode shape, which are in conflict with the boundary conditions and the assumed shape functions.

The two typical spacecraft panel examples given, loaded primarily in bending, illustrated how all four basic design constraints influence the optimum construction. For the stiffness-critical panel, dimpling and natural frequency were the primary constraints whereas for the strength-critical panel, wrinkling and material compression strength were the major design drivers. As expected, the lightly loaded stiffness-critical panel favoured the use of ultra high modulus carbon fibre reinforcement. Co-curing was also shown to be a cost-effective method of manufacture because the reduction in compression strength as a result of the low pressure cure did not inhibit the optimum designs, which were determined by stiffness considerations. In this example, the tailorability of composite properties, through the selection of fibre angles, was used to advantage by biased [0/90/0] lay-ups which increased the panel frequency without incurring unecessary mass. A saving of 15% over aluminum alloy was possible. The strength-critical panel favoured high strength carbon fibre reinforcement, although stiffness was still important to meet the wrinkling constraint. Despite lower compression strength, a co-cured design was still found to

offer the maximum weight saving because of the stiffness requirement dictated by wrinkling. The saving over aluminium alloy was 11%.

These examples suggest that co-curing is an acceptable method of manufacture for spacecraft panels because many of these are designed largely to meet stiffness (natural frequency) requirements, and those under higher loading will often have designs determined by instability failure modes. Since these are dependent mainly on the longitudinal modulus, E_1, rather than compression strength, X_T, the degradation of compression strength (which is the principal drop in performance as a result of co-curing) will not handicap efficient design.

TABLE 7.2 ALTERNATIVE DESIGNS FOR T-SAT REAR PANEL

No.	FACESHEETS			CORE		CO/PRE	DESIGN CONSTRAINT FUNCTIONS				MASS
	Mat'l	t_p (mm)	LAY-UP	TYPE	h (mm)	CURE	Freq'y	Mat'l. Str.	Wrink.	Dimpl.	(kg/m^2)
1	GY-70/92	0.05	[0/90]	2.0-3/16-0.0007	15	CO	0.408	0.348	0.211	0.002	1.120
2	GY-70/92	0.05	[0/90]	2.6-5/32-0.0007	12	CO	0.289	0.109	0.292	0.147	1.144
3	GY-70/92	0.05	[0/90/0]	2.6-5/32-0.0007	7	CO	0.118	0.272	0.784	0.091	1.104
4	GY-70/92	0.05	[0/90/0]	2.6-5/32-0.0007	7	PRE	0.126	0.699	0.786	0.104	1.104
5	GY-70/92	0.10	[0/90]	2.0-3/16-0.0007	7	CO	0.088	0.283	0.570	0.733	1.204
6	GY-70/92	0.05	[0/90/90/0]	2.0-3/16-0.0007	7	PRE	0.108	0.704	0.811	0.627	1.204
7	HM-S/985	0.05	[0/90]	3.1-1/8 -0.0007	11	CO	0.027	0.464	0.307	0.181	1.170
8	HM-S/985	0.05	[0/90/0]	2.6-5/32-0.0007	8	CO	0.068	0.688	0.761	0.070	1.116
9	HM-S/985	0.05	[0/90/0]	2.6-5/32-0.0007	8	PRE	0.078	0.916	0.764	0.082	1.116
10	HM-S/985	0.10	[0/90]	2.0-3/16-0.0007	8	CO	0.051	0.699	0.563	0.678	1.196
11	T300/69	0.05	[0/90/0]	2.6-5/32-0.0007	10	CO	0.056	0.782	0.741	0.064	1.194
12	T300/69	0.10	[0/90]	2.0-3/16-0.0007	10	CO	0.055	0.792	0.561	0.632	1.252
13	2024-T81	0.10	-	2.0-3/16-0.0007	14	-	0.201	0.911	0.409	0.016	1.304
14	2024-T81	0.10	-	2.6-3/16-0.0007	12	-	0.055	0.880	0.487	0.215	1.360

TABLE 7.3 ALTERNATIVE DESIGNS FOR T-SAT SM PLATFORM

No.	FACESHEETS			CORE		CO/PRE	DESIGN CONSTRAINT FNS.			MASS
	Mat'l	t_{ply} (mm)	LAY-UP	TYPE	h (mm)	CURE	Mat'l. Str.	Wrink.	Dimpl.	(kg/m^2)
1	GY-70/92	0.05	[90/+30/-30]	2.0-3/16-0.0007	51	CO	0.701	0.005	0.798	2.410
2	GY-70/92	0.05	[+30/90/-30]	2.0-3/16-0.0007	39	CO	0.587	0.008	0.770	2.058
3	GY-70/92	0.05	[+30/90/-30]	3.1-1/8 -0.0007	21	CO	0.019	0.077	0.813	1.860
4	GY-70/92	0.05	[+45/0/90/-45]	2.0-3/16-0.0007	25	CO	0.004	0.053	0.873	1.780
5	GY-70/92	0.05	[0/+45/-45/90]	2.0-3/16-0.0007	25	CO	0.004	0.351	0.798	1.780
6	GY-70/92	0.10	[+30/90/-30]	2.0-3/16-0.0007	11	CO	0.083	0.315	0.898	1.672
7	GY-70/92	0.05	$[\pm 30/90_2/\mp 30]$	2.0-3/16-0.0007	7	PRE	0.073	0.569	0.843	1.544
8	HM-S/985	0.05	[+30/90/-30]	2.6-5/32-0.0007	24	CO	0.262	0.018	0.640	1.788
9	HM-S/985	0.05	[0/+45/-45/90]	2.0-3/16-0.0007	19	CO	0.074	0.215	0.631	1.548
10	HM-S/985	0.10	[+30/90/-30]	2.0-3/16-0.0007	11	CO	0.140	0.336	0.856	1.612
11	HM-S/985	0.05	$[\pm 30/90_2/\mp 30]$	2.0-3/16-0/0007	8	PRE	0.083	0.540	0.807	1.516
12	T-300/69	0.05	[0/+45/-45/90]	2.0-3/16-0.0007	15	CO	0.077	0.083	0.323	1.412
13	T-300/69	0.10	[+30/90/-30]	2.0-3/16-0.0007	7	CO	0.148	0.098	0.667	1.472
14	T-300/69	0.05	$[\pm 30/90_2/\mp 30]$	2.0-3/16-0.0007	5	PRE	0.108	0.102	0.645	1.408
15	T300/F263 WOVEN	0.10	[0/45]	2.0-3/16-0.0007	18	CO	0.005	0.265	0.521	1.476
16	2024-T81	0.10	-	2.0-3/16-0.0007	44	-	0.919	0.007	0.061	2.264
17	2024-T81	0.15	-	2.0-3/16-0.0007	14	-	0.646	0.027	0.126	1.582
18	2024-T81	0.20	-	2.0-3/16-0.0007	7	-	0.203	0.056	0.262	1.636

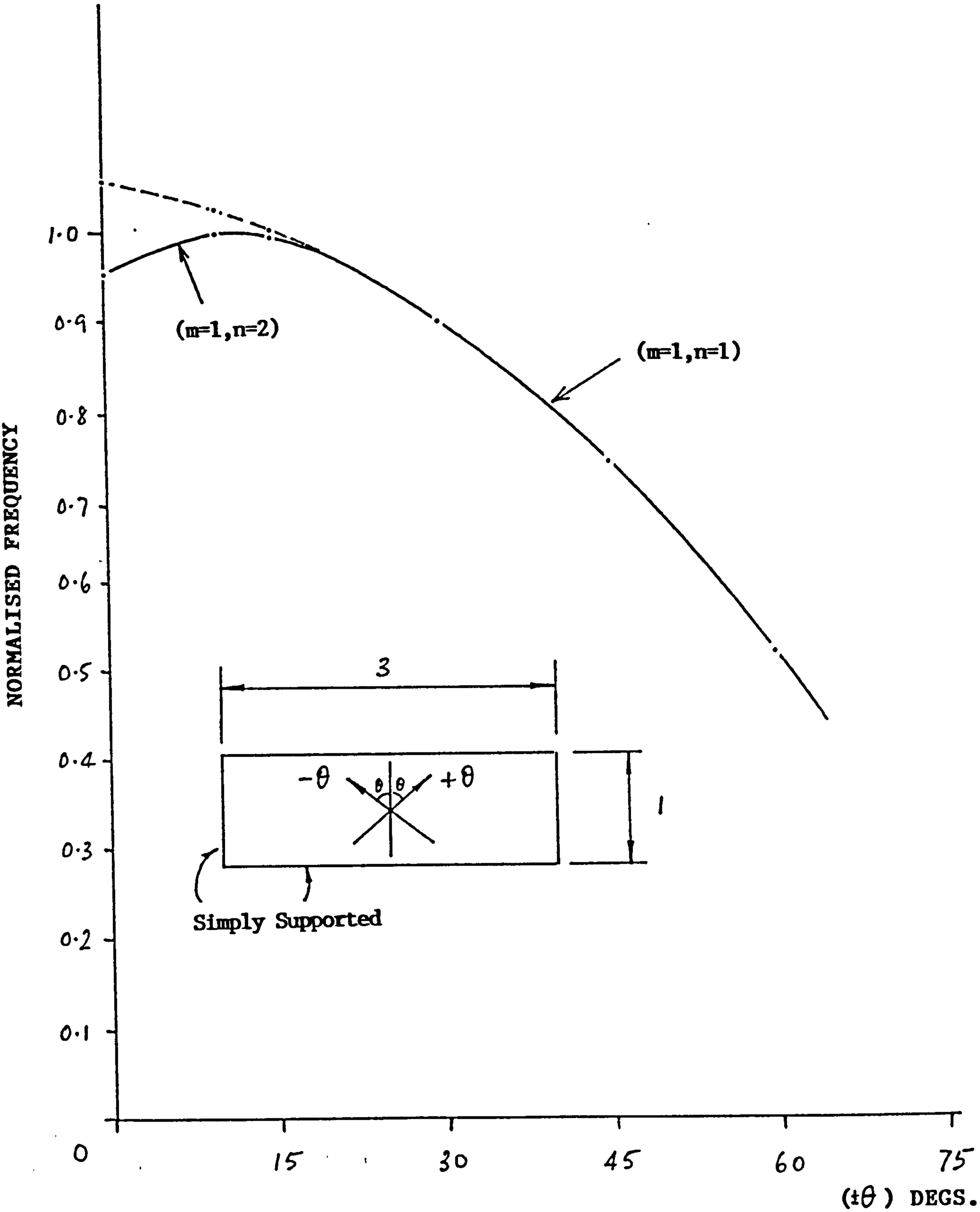

Fig. 7.1 FIRST NATURAL FREQUENCY VS. LAY-UP FOR ANGLED PLY FACED RECTANGULAR SANDWICH PANEL

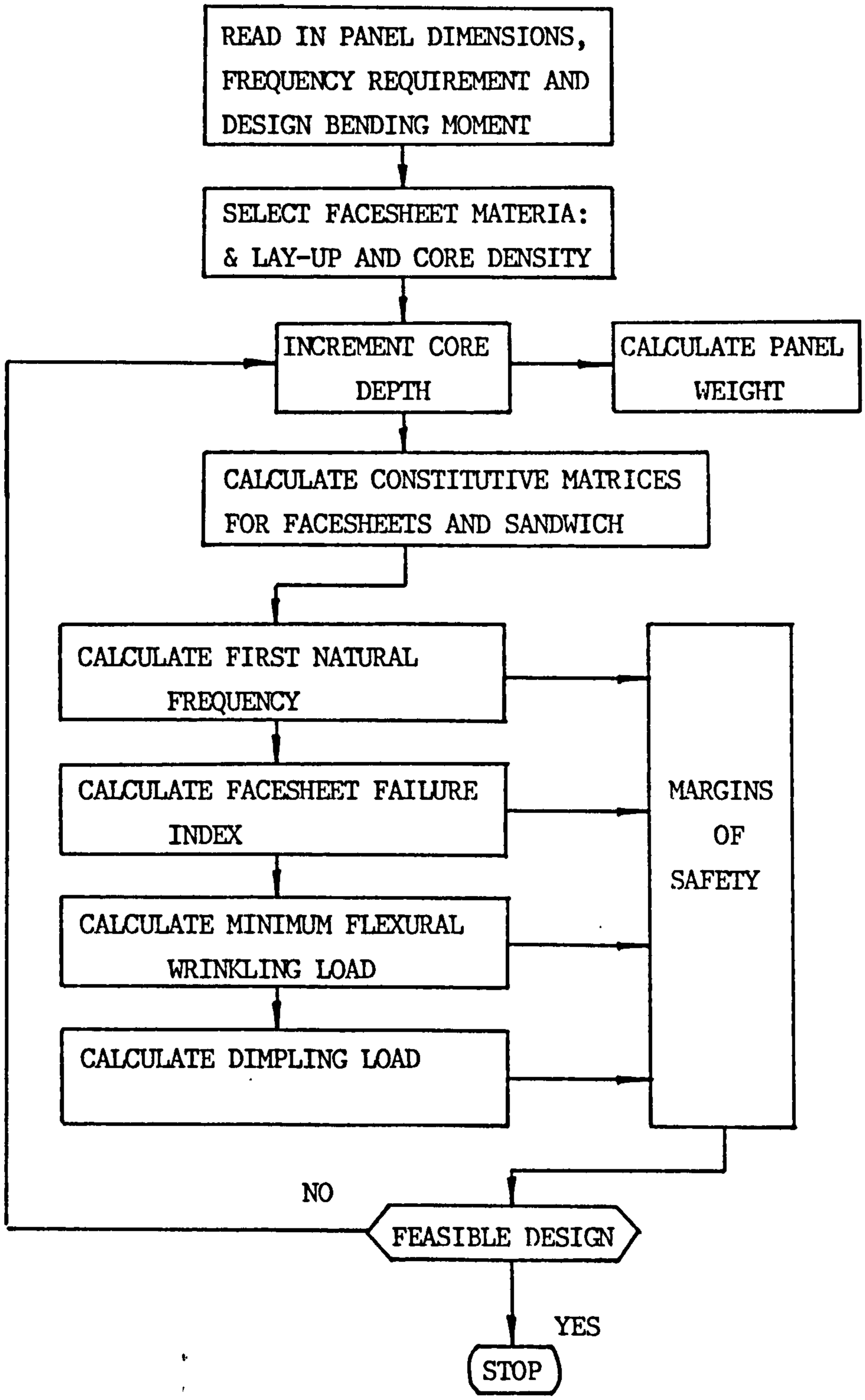

Fig. 7.2 SANDWICH PANEL OPTIMISATION PROGRAM

Fig. 7.3 T-SAT REAR PANEL

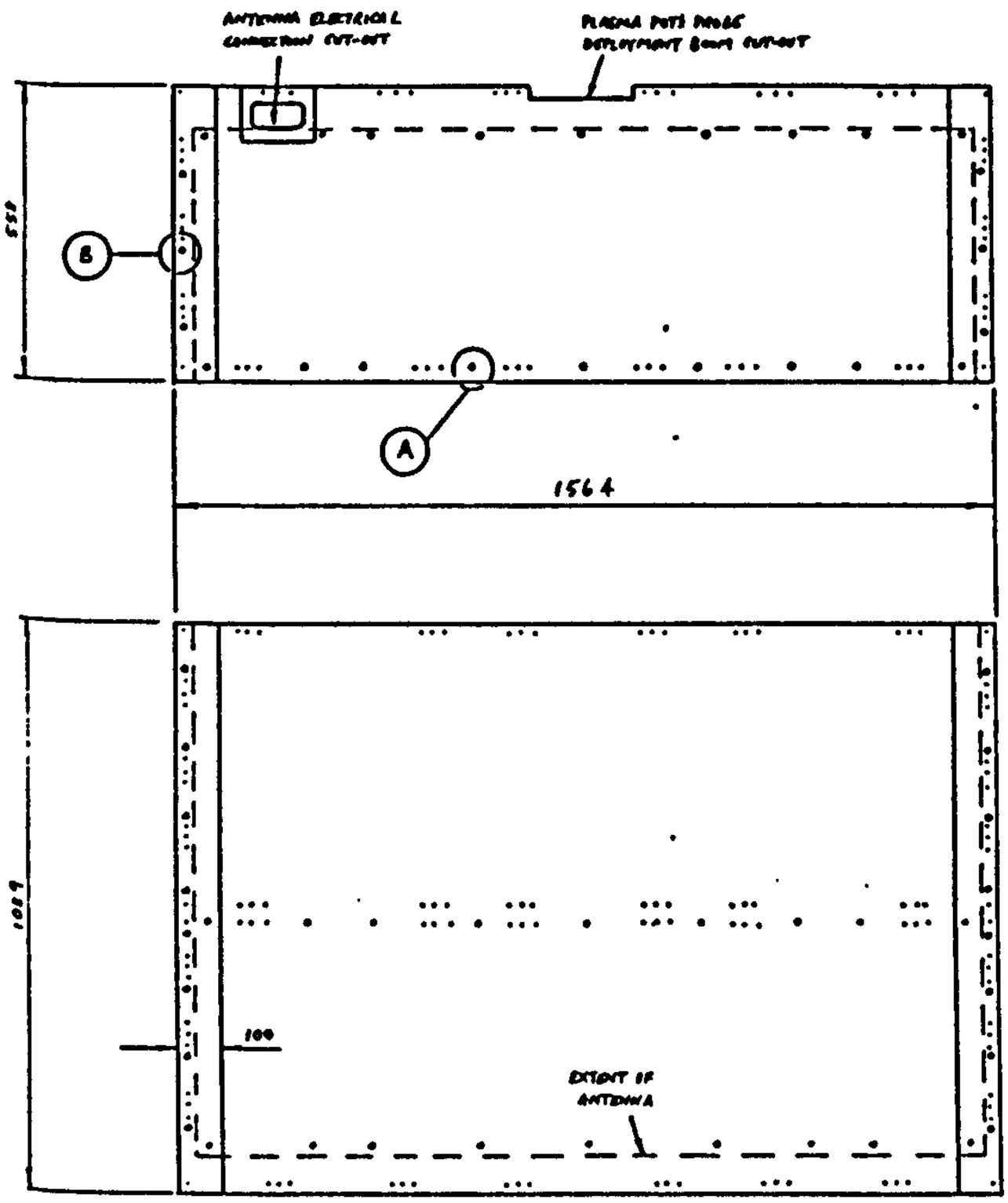

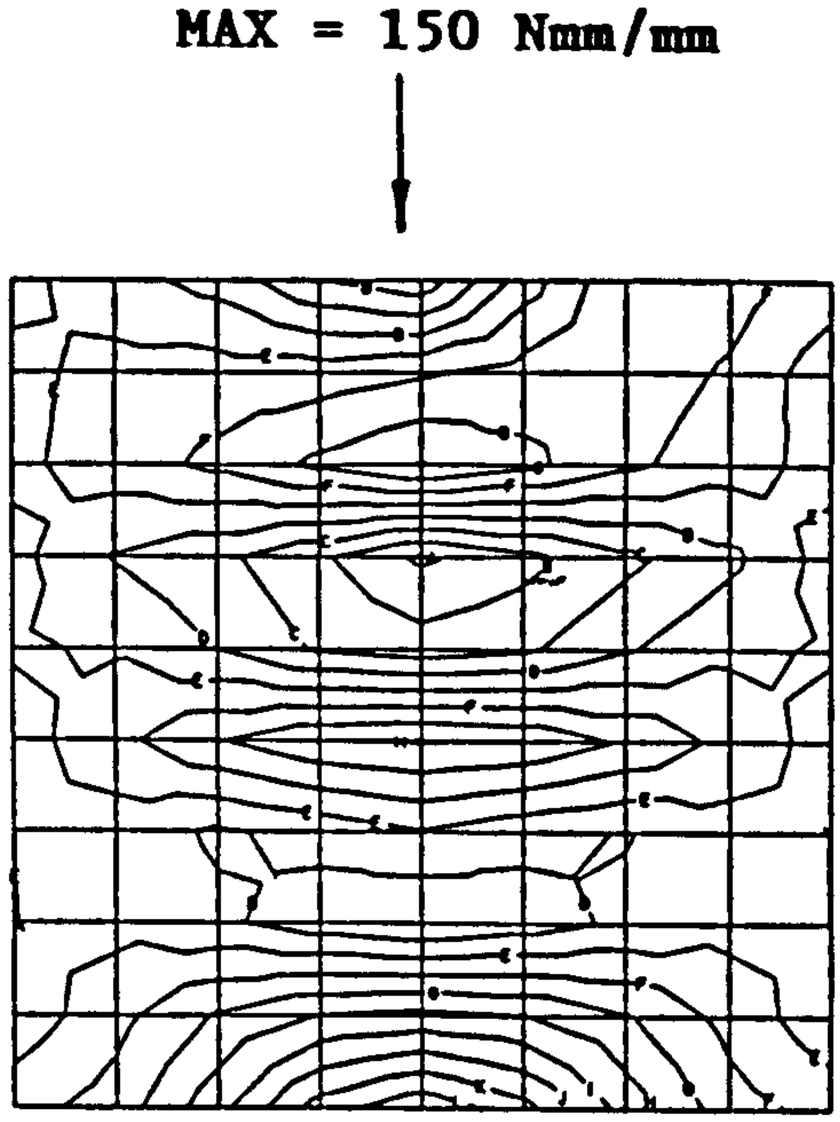

REAR PANEL

MY MOMENTS

STIFFNESS TARGET = 100 Hz

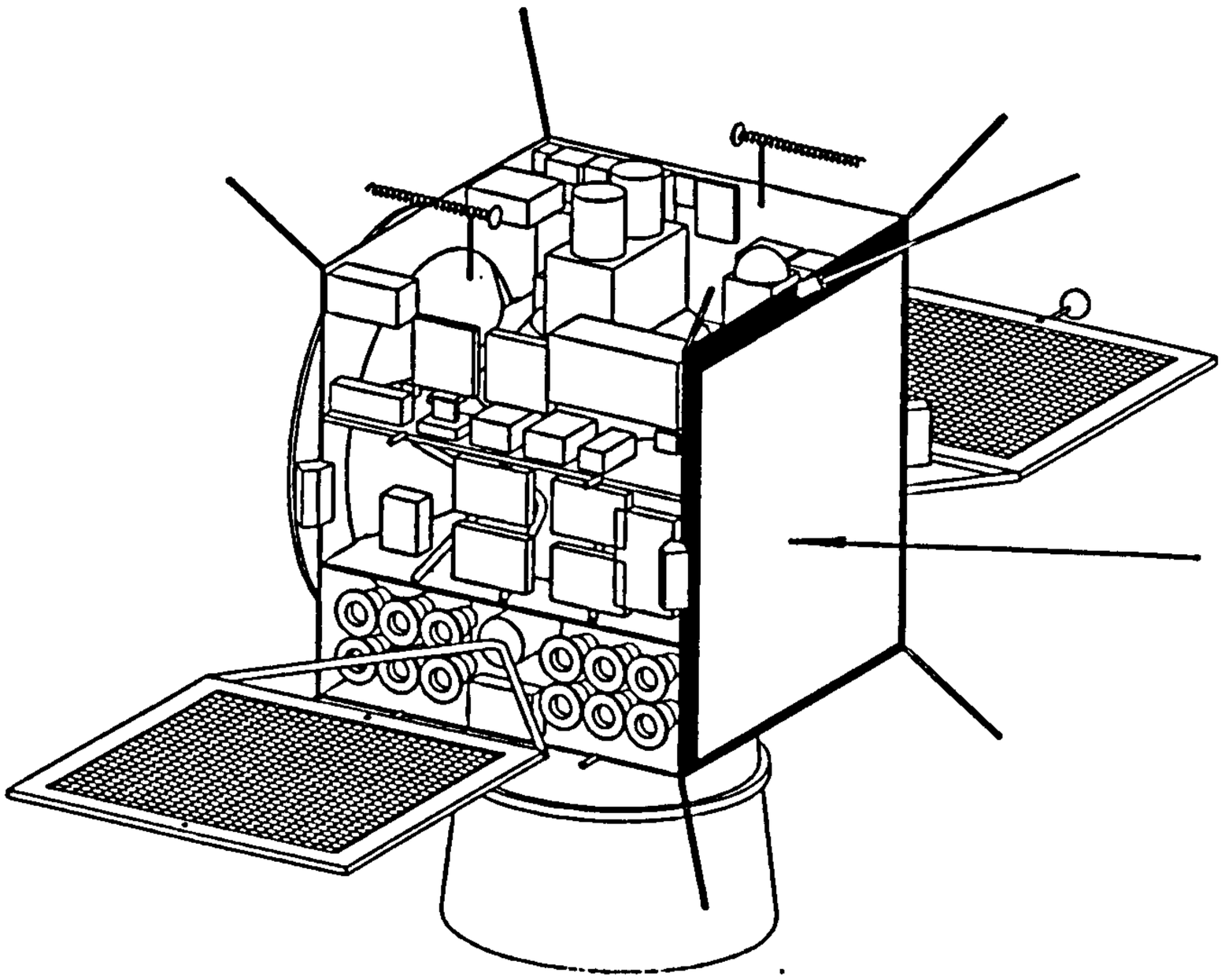

POSITION OF REAR PANEL AND PATCH ANTENNA ON SPACECRAFT

Fig. 7.4 T-SAT SERVICE MODULE PLATFORM

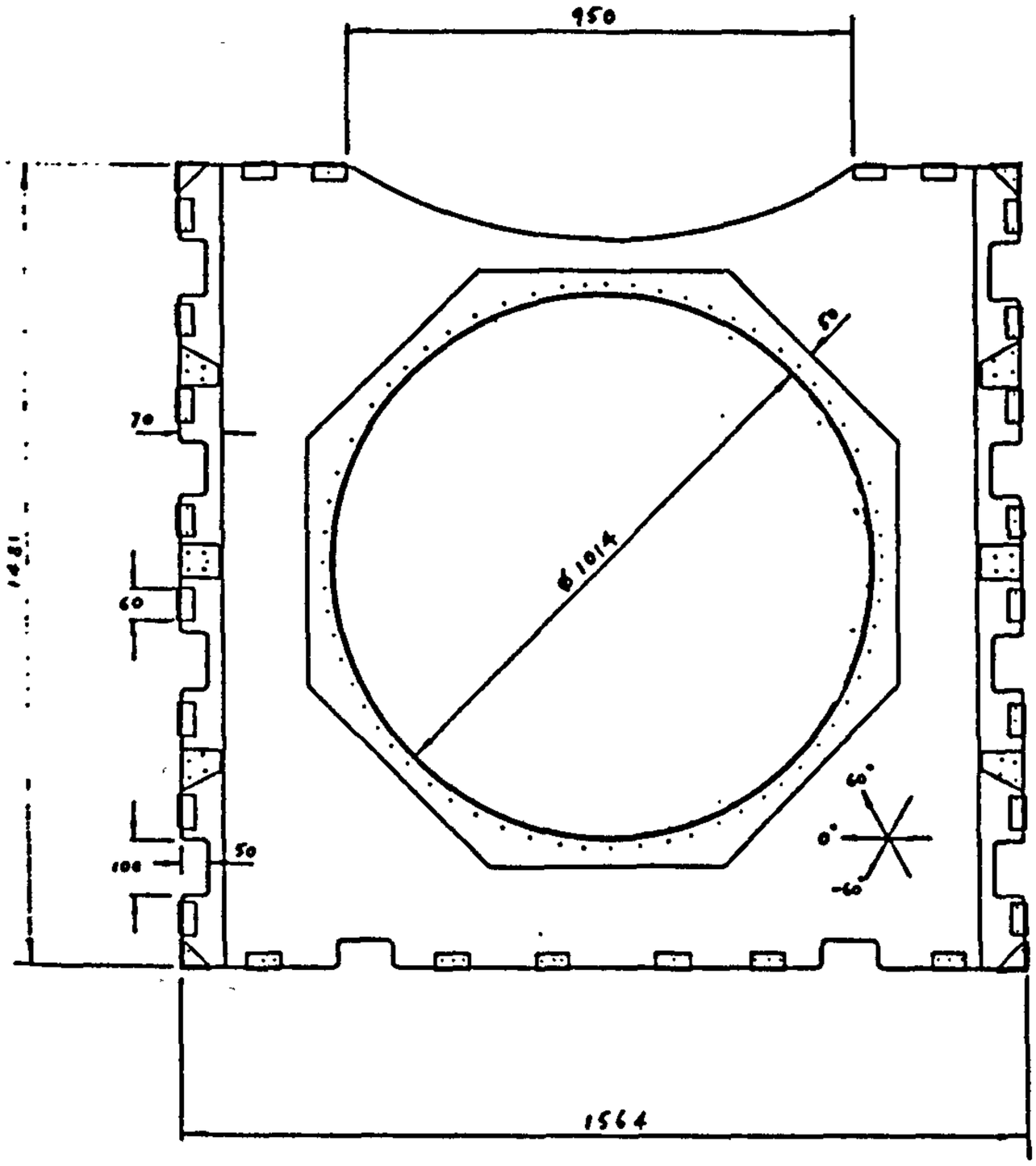

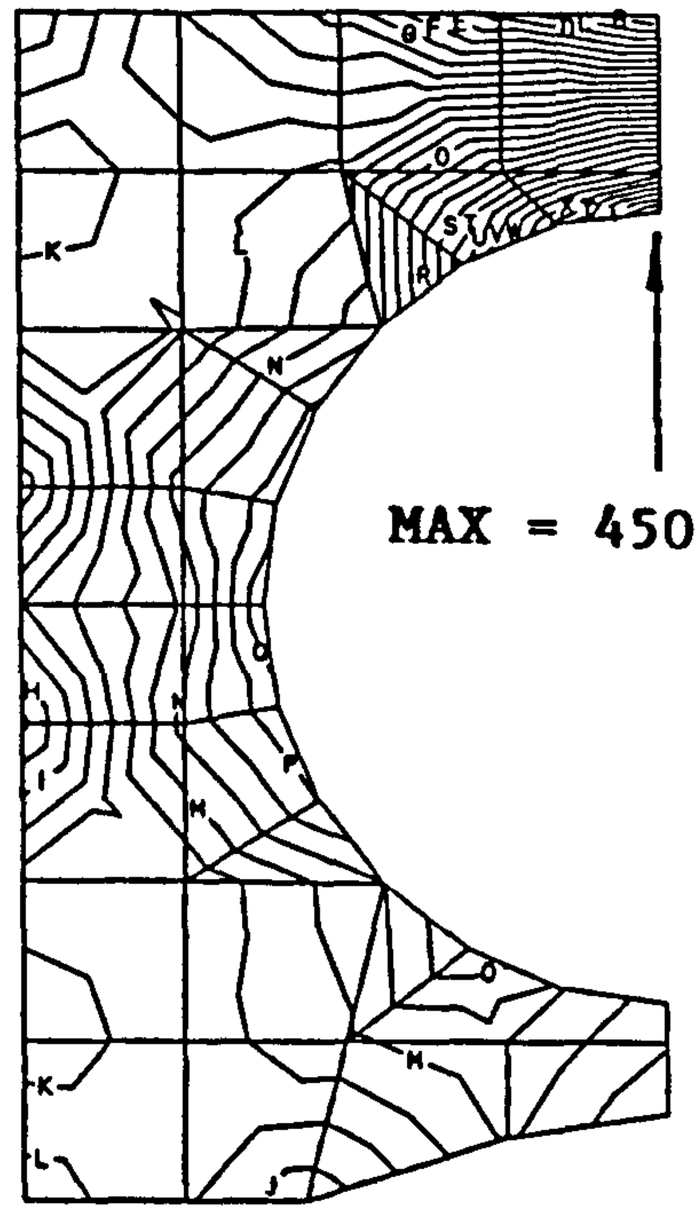

SM PLATFORM

MY MOMENTS

POSITION OF SM PLATFORM ON SPACECRAFT

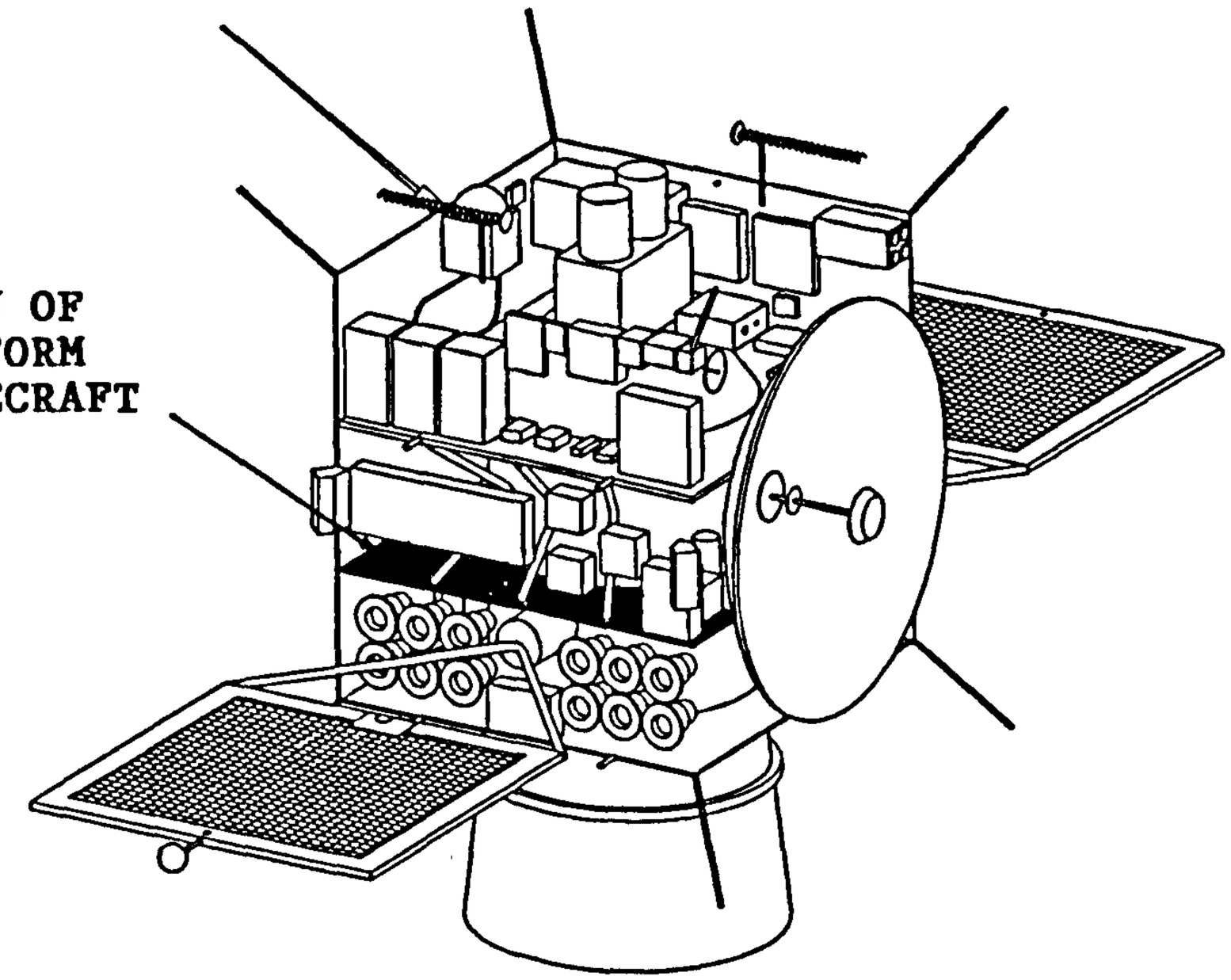

CHAPTER 8 THRUST TUBE DESIGN

8.1 DESIGN REQUIREMENTS

A central thrust tube is the primary structural member in the majority of spacecraft structure configurations. It provides the interface with the launcher and the load path for all the inertia loads. The geometric form of the thrust tube is determined by the overall configuration of the spacecraft, and generally consists of one or more cylindrical or conical sections. The lower diameter of the thrust tube provides the interface with the launcher adapter or spin-table. The lower diameter is therefore fixed to one of the interfaces which are standard for most expendable launchers : 37" (937 mm), 47" (1194 mm), and 59" (1497 mm). The length of the thrust tube and changes in diameter up the length depend on the dimensions of the satellite and overall configuration constraints. In many spacecraft configurations, the thrust tube is sized to accommodate a solid motor or liquid propellant tanks. From the structural viewpoint, the thrust tube diameter should be maximised to increase stiffness and reduce load intensity, but the requirement to maximise the spacecraft's internal volume compromises this ideal. A common arrangement is an upper cylindrical section with a truncated cone below tapering out to the interface diameter.

8.1.1 Launcher Imposed Requirements

The requirements on the thrust tube design are determined by the launcher, since the launch phase imposes the highest loads on the spacecraft. As far as strength constraints on the design are concerned, these consist of static inertia loads due to the launcher accelerations, with superimposed dynamic accelerations. The dynamic loads in the structure are dependent on the stiffness, mass and damping properties. Analysis of the dynamic response of the structure requires some form of coupled analysis of the spacecraft and launcher dynamic FE models. The spacecraft model in turn is generally validated by a modal survey test which also determines the damping properties. Damping properties can only be reliably found from testing and it is these which determine the levels of the dynamic internal loads. In order to begin the structure design process it is therefore

necessary to use acceleration levels for a typical spacecraft as preliminary structure dimensioning loads. These are normally provided by the launcher authority as quasi-static flight limit accelerations for different flight events. These are then factored to give ultimate acceleration levels for preliminary design. Flight loads for Ariane, and Long March 2F launchers are given in Table 8.1. Typical factored quasi-static dimensioning loads are given in Table 8.2.

Highest axial accelerations generally occur at engine burn-out/stage separation and highest lateral accelerations at maximum dynamic pressure. For Shuttle launch, where payloads are mounted with the thrust tube axis perpendicular to the shuttle thrust axis, the lateral accelerations on the spacecraft are highest. This results in high bending moments on the spacecraft thrust tube if no lateral restraint is provided. Modern spacecraft are often designed to be compatible with a number of alternative launchers to maximise the possible launch opportunities. The spacecraft structure must therefore be designed for all launcher load cases. Also included in the load cases are the accelerations imposed on the spacecraft during transfer to its final orbit. High orbiting spacecraft carry an apogee boost motor which when fired imposes high axial static acceleration. Spacecraft are generally spin-stabilised during the transfer orbit (at 30-60 rpm) which results in additional centrifugal accelerations.

To prevent dynamic coupling between the launch vehicle and the spacecraft, mimimum frequency requirements are specified by the launcher authority. The first lateral mode frequency for the spacecraft, assumed to be rigidly clamped at the launcher interface, must be greater than 10-20 Hz, (depending on the launcher) to prevent coupling with the launcher fundamental bending modes. A first longitudinal mode is generally specified as being greater than 35 Hz to prevent coupling with launcher 'pogo' modes. These minimum frequency requirements, particularly on the first lateral mode imposes a stiffness constraint on the design of the spacecraft thrust tube.

8.1.2 Thrust Tube Design Constraints

The longitudinal and lateral accelerations acting on the spacecraft are transfered to the thrust tube assembly via platfrom ring attachments, shear webs and/or struts. The thrust tube behaves like a beam-column under axial compression and shear and bending loads (fig. 8.1). These loads are carried by the thrust tube predominantly as membrane axial and shear stresses. An idealisation of these stresses around the circumference is shown in fig. 8.2. Hoop stresses and shell bending moments are confined to localised areas around the load introduction points and launcher interface frame. These are diffused into the shell over a short distance as membrane stresses. Local reinforcement around the load introduction areas is sufficient for withstanding these additional stresses.

The basic design of the thrust tube is dictated by the possible failure mode constraints under the applied membrane stress distribution, in addition to a stiffness constraint imposed by the minimum spacecraft lateral frequency requirement. The four major design constraints are:

1. Stiffness.
   The thrust tube must provide sufficient stiffness to meet the minimum spacecraft lateral frequency requirement specified by the launcher authority.

2. Material Failure.
   The thrust tube must be designed to provide an adequate margin of safety against material failure under the applied membrane stresses. For a composite thrust tube, failure is equally likely due to shear in the shell wall as the much higher axial compressive stresses.

3. General Instability.
   The thrust tube must be designed to withstand collapse through general instability. This constraint is of primary importance for thin walled monocoque constructions. The analysis of general buckling must account for the destabilising effect of the membrane shear in addition to axial compression.

4. Local Instability.
   The local instability failure modes depend on the particular form of thrust tube construction adopted. For stiffened shells local instability can occur as buckling of the stiffeners or buckling of the skin between stiffeners in a number of possible modes. For sandwich construction, wrinkling and dimpling are the local instability modes which must be accounted for in the design.

8.2 TYPES OF CONSTRUCTION

A number of possible types of composite thrust tube constructions can be utilised to meet the design constraints. The most commonly adopted construction types are :

1. Monocoque shell
2. Stiffened shell
3. Sandwich stiffened shell

The stiffened shell category includes stringer-frame, corrugated and waffle constructions. Examples of the construction types are illustrated in fig. 8.3.

8.2.1 Monocoque Shell

The monocoque composite shell is the simplest form of construction. Examples of this type of composite thrust tube are the Japanese CS-3 satellite thrust cone and the thrust cone-cylinder for the ACESM (Navstar composite replacement structure). The main advantage of this form of construction is in its manufacturing simplicity, using either hand lay-up or filament winding techniques. The lay-up must be symmetric to prevent curing distortion.

The disadvantage of this type of construction is that the thrust tube is invariably stabilty critical. Designs of this type rely on the plain shell

itself and high modulus fibres to withstand buckling under compressive launch loads. The buckling requirement can constrain some of the fibres to be orientated in the hoop (90°) or near-hoop directions, since buckling reistance is improved with a large A_{22} term in the shell constitutive matrix. This is not an efficient use of the material because hoop fibres do not contribute to the material strength under axial and shear loading, or to the lateral stiffness of the thrust tube. For example, the CS-3 thrust cone has a lay-up containing 20° and 70° plies to maximise buckling strength and the ACESM cone has a lay-up which varies from $[0/\ 53/90_2/0]_s$ to $[0/\ 39/\ 52/0]_s$ which also suggests overall buckling is a major design criterion. It is more mass-efficient to adopt external stiffners or a sandwich construction to confer the necessary buckling strength rather than introduce hoop reinforcement. A further disadvantage with buckling critical designs is the prediction of buckling strength since this is very sensitive to initial imperfections, particularly for monocoque shells. It is therefore necessary to adopt conservative safety factors to ensure high confidence in the design.

8.2.2 Stiffened Shell

The stiffened shell form of construction is the most popular for metallic thrust tubes. The shell skin is either corrugated with intermediate rings or has longitudinal stiffeners and circumferential frames which are rivetted and/or bonded on. Although this method of construction is amenable to sheet metal forming, manufacture in thermosetting composites can be quite involved. This is because of complex tooling and additional secondary bonding operations. The cost of manufacturing can therefore be high for short production runs when compared with monocoque and sandwich constructions.

A number of alternative forms of stiffeners are possible. Of these, the closed top-hat section is generally recognised as being one of the most efficient because of its higher local buckling strength. Fig. 8.4, taken from ref [44] shows the improved efficiency over J and blade stiffener configurations. The manufacture of top-hat stiffeners is more difficult

than the open section types, however, requiring collapsable or elastomeric inner mandrels.

Tooling design can also be complicated for the open stiffener types if these are co-cured with the shell skin. Co-curing can nevertheless be advantageous because the additional jigging and assembly time of secondary bonding operations can be avoided. Mass can also be saved because the size of the 'foot' of the stiffener is then no longer dictated by bonding requirements. The price paid is in increased tooling cost. To minimise tooling complexity, co-cured blade stiffeners or an open corrugated section offer good compromises.

Further design options for stiffened shells are the possibility of incorporating the stiffeners on the inside or outside surface, and the use of a non-orthogonal stiffener arrangement. Generally, external stiffeners offer improved buckling resistance over inside stiffeners, typically having 30% higher theoretical compression buckling strengths. Non-orthogonal stiffener arrangements include the so-called 'isogrid' type which have stiffeners orientated at 0°, +60° and -60°. Another stiffener arrangement which is sometimes adopted for shell structures are the +/- 45° type. Any angles could be used, although the stiffener type is then limited to simple blade stiffeners if tooling is not to become excessively complicated. One advantage of a non-orthogonal stiffener arrangement is that it is possible to increase panel local instability modes. However, the inherent tailorability of composites offered to the designer through the use of variable fibre angles will generally render stiffener angle a redundant variable.

Examples of composite stiffened shell structures are the Ariane 2nd/3rd inter-stage skirt and the thrust tube of the DFS Kopernikus class of communications satellites. The former is an external, integral blade stiffened type, and the latter a corrugated design. The corrugated design for the DFS Kopernikus thrust tube was selected because of the provision of hard points for attachments and better reliability and inspectability over sandwich designs, although of both forms of construction were recognised as having comparable efficiency.

8.2.3 Sandwich Shell

Sandwich construction has proved the most popular for composite thrust designs. Examples are INTELSAT V, Skynet IV, Arabsat, the Olympus Propulsion Module Replacement thrust cylinder and the thrust tube for the proposed 580 kg future Japanese GEO satellite. Other examples of this form of construction in space vehicles are to be found in the SPELDA dual launch system structure and payload adaptors in the Ariane 4 launcher. The major attraction of sandwich construction is that shell stability can be provided by the lightweight core whilst the facesheet lay-ups can be tailored to meet strength and stiffness constraints. The directional properties of composite materials can therfore be best exploited to the full. The diversity of lay-ups, selected to best meet particular design constraints, is shown by the examples given in Table 8.3.

The INTELSAT V composite thrust tube[8] was designed as a replacement to the corrugated aluminium tube used in the earlier batches of spacecraft. This example is unusual for sandwich construction thrust tubes in that the sandwich is unsymmetric (ie. the facesheets are of unequal thickness). The design is illustrated in fig. 8.5a. In addition to the shell itself, all rings other than the Marman ring and ABM ring were made of carbon-epoxy composite. The selection of an unsymmetric sandwich configuration was based on weight considerations, although these are not detailed in reference [8]. The uneven distribution of load in the two face-sheets would not be expected to yield an inherently more efficient design solution, but mass savings over a symmetric sandwich are probably attributable to the ring attachment interfaces. Here, the two facesheets are 'panned' together which obviates the necessity for heavy inserts and densified honeycomb at these local load introduction areas. The cost of production of this thrust tube will be significantly greater than a symmetric configuration because of the additional geometric complexity of the inner facesheet and the honeycomb profiling required. This can be appreciated in fig. 8.6, which illustrates the complicated manufacturing sequence.

The thrust tubes for Skynet 4[11], Arabsat[12] and the Olympus lower propulsion module[13] have symmetric sandwich configurations. The Arabsat

thrust tube is illustrated in fig. 8.5b. The manufacture of these tubes follows basically the same pattern as that for the Intelsat V tube. That is, the facesheets are cured separately and then bonded to the honeycomb with film adhesive in a subsequent operation. Aerospatiale (Intelsat V and Arabsat thrust tubes) favour the production of the outer facesheet on a female mould and the inner facesheet on a male mandrel. The inner facesheet is cut after curing amd positioned on the honeycomb and outer facesheet, along with longitudinal splices. The complete sandwich is then bonded together on the female mould. B.Ae. (Skynet 4) and Fokker (Olympus LPM) manufacture both facesheets in third or half segments on male moulds. The facesheets are bonded to the core in segments and the segments are then assembled to the end rings in a jig with longitudinal splices. These methods of manufacture are less costly than the fabrication of an unsymmetric 'panned' sandwich or a corrugated construction because of the simplicity of the tooling. The cost savings are greater still if both facesheets are cured on the same mould. The tooling cost is then comparable to a monocoque construction. Fokker estimated an additional cost penalty of only 6% over a corrugated aluminium construction for the composite sandwich Olympus central tube. The cost of a corrugated composite design was estimated to be 54% greater than the composite sandwich.

Aerospatiale performed a study to investigate the possibility of co-curing both facesheets and honeycomb for the Arabsat thrust tube[12]. The main aim was to reduce recurrent costs. A further advantage of co-curing is that the constraint on balancing facesheet lay-ups is lifted. Only the complete sandwich needs to be balanced. This was not exploited in the Arabsat study because only the fabrication of the existing (balanced facesheet lay-up) Arabsat design was investigated. If co-curing is adopted from the outset, the extra design freedom offered can enable mass to be saved, or thicker less expensive prepreg to be used. The Arabsat study used a female mould to co-cure the sandwich. The conclusion reached was that significant cost savings could be made over the traditional manufacturing method.

Sandwich construction is hence an attractive thrust tube design solution because of a cost which is less than stiffened construction, and which can approach that of a monocoque design if a co-cure method is used. As will be

discussed in the next section, the structural efficiency is comparable to optimum externally stiffened designs and superior to monocoque construction.

8.2.4 Structural Efficiency of Shell Construction Types

The relative structural efficiencies of the different forms of construction are discussed with reference to references [13] and [45]. The latter studied the efficiency of optimised composite cylinder configurations under compression loading. The former included a detailed mass trade-off analysis for different constructions for the Olympus composite central tube.

Reference [45] performed numerical optimisation of monocoque, top-hat stiffened and symmetric sandwich high strength carbon-epoxy cylinders under uniform axial compression. The design constraints were material failure (maximum strain theory), overall buckling and local stiffener buckling. No stiffness constraint or local sandwich buckling constraint (dimpling and wrinkling) were included. For the monocoque and sandwich constructions the design variables were 3 ply angles and corresponding thicknesses. Core density was fixed at 3.0 lb/cu ft. For the top-hat stiffened construction five additional variables were allowed : stiffener width and height, and the stiffener element thicknesses, which were assumed to be built up from 0° and 45° plies.

Fig. 8.7a compares the weight of the different constructions in aluminium and high strength carbon-epoxy against the compression load parameter N_x/R. The range of values spans that of typical spacecraft thrust tubes. This demonstrates a structural efficiency ranking of :

1. Honeycomb construction
2. Externally stiffened
3. Internally stiffened
4. Monocoque

for both carbon-epoxy and aluminium cylinders. The continuous nature of these curves for the composite options is unrealistic because these reflect the continuously variable ply thicknesses allowed in the optimisation. This is obviously not realised in practice, but nevertheless indicates the general trends. Plotted in fig. 8.7b are the optimised configurations when a minimum carbon-epoxy ply thickness of 0.14mm and minimum aluminium gauge thickness of 0.50 mm are applied as side constraints. A continuously variable carbon-epoxy thickness is still assumed. The general trends of the curves are the same as fig. 8.7a, but with the weight of honeycomb cylinders increased in the low loading range. The efficiency of externally stiffened constructions is similar in this load range. Other than aluminium faced honeycomb in the medium to high load range where this construction is lighter than carbon-epoxy monocoques, the carbon-epoxy constructions are lighter for all construction types.

The above study demonstrated the relative efficiencies of the different construction types for cylinders under pure compression, but a more thorough comparison for application to thrust tubes must account for shear loading in addition to compression, the lateral stiffness constraint, discrete ply thicknesses and reinforcements at load introduction areas. The study of reference [13] compared the efficiency of blade stiffened, corrugated and sandwich composite design alternatives for the Olympus Lower Propulsion Module thrust tube. Several designs for each construction type utilising 0.05mm ply T-300/Code 92 UD prepreg were derived.

Neglecting the reinforcements at load introduction points, the relative weights of the best designs for each construction type were :

Blade stiffened	1.64
Corrugated	1.00
Sandwich	1.23

with the corrugated option being the lightest. However the additional load offset at the end rings associated with the corrugated design incurs a greater weight penalty over the sandwich construction because of the

necessary reinforcement at the connections. When these were taken into consideration the relative weights became :

Corrugated	1.18
Sandwich (bonded end rings)	1.00
Sandwich (bolted end rings)	1.14

with the sandwich construction providing the lowest weight design solution.

This example illustrates the importance of the reinforcement/end ring design in determining the lightest construction option. The Olympus LPM tube has only a ring at each end which can be bonded on. Intermediate level rings which are found in most thrust tube configurations will invariably require a bolted and bonded connection to prevent peel failure of the joint. As shown above, the use of inserts and fasteners in a sandwich construction can result in a severe weight penalty. In certain instances this may be such that a stiffened construction becomes the lowest weight solution.

At the preliminary design stage it may not be readily apparent whether a sandwich or corrugated construction offers the lowest weight alternative since these will require a detailed design trade off. Such a trade off must include the connection element design and composite reinforcements for localised bending moments and hoop stresses. These in turn will be dependent on the particular thrust tube. Nonetheless, the following generalised conclusions can be drawn from these studies:

1. All forms of composite construction offer significant weight savings over their aluminium counterparts.

2. Corrugated and sandwich constructions utilising composites yield designs of comparable weight.

3. Corrugated designs offer better provision for hard points which can be advantageous if loads are introduced discretely at many points. Inspectability is also an advantage for this form of construction.

4. Composite faced sandwich constructions provide the best combination of high efficiency coupled with low cost.

The remainder of this chapter is concerned with the optimisation of composite faced sandwich thrust tube designs since this is identified as one of the most promising forms of construction and is currently the most widely adopted. The follwing sections outline the analysis of the major design criteria for composite sandwich shells and these are then combined to form an optimisation method for the preliminary design of spacecraft thrust tubes.

8.3 ANALYSIS OF COMPOSITE THRUST TUBE STIFFNESS

8.3.1 Method of Analysis

Analysis of the low frequency vibration modes of a spacecraft is commonly carried out through the use of a dynamic FE model, both for the development of the structural design and during the validation process. Often the dynamic model is reduced from the full static model by a method such as Guyan reduction to give a reasonable solution time. Although the use of such a model can give accurate results for a relatively large number of modes, the time taken for solution makes the use of the full spacecraft FE model uneconomic for the design optimisation of the thrust tube in which only the first one or two lateral modes are of interest and a large number of design iterations may be required. An effective analysis requires that the magnitude of the problem be reduced to include only the essential stiffness properties of the thrust tube itself, the pertinent mass properties of the spacecraft, and only lateral degrees of freedom.

The idealisation adopted for the analysis of spacecraft lateral vibration behaviour was a simple beam and lumped mass model, an example of which is shown in fig. 8.8. Using beam finite elements to represent the thrust tube and lumped mass and inertia at the nodes to represent the spacecraft, the size of the problem is reduced considerably from perhaps a few thousand degrees of freedom in a full dynamic FE model to maybe a dozen or less in a

beam and mass model. Such a reduction enables various thrust tube design possibilities to be rapidly analysed for stiffness.

In order to ensure that a model of this type is a realistic representation, a number of features must be included. Firstly, because of the relatively small length to diameter ratio of many thrust tube configurations and the possibility of composite lay-ups with low shear stiffness, shear deformation can be of a magnitude comparable with bending deformation. Therefore the effects of shear must be included in the beam element formulation. Secondly, rotational inertia must be included at the element nodes to account for the spacecraft mass distribution which is idealised as being centered at a point. Selection of the centres of mass with their corresponding inertia properties plays an important part in determining the validity of the model representation. The spacecraft mass should be broken down only as far as the major structural units, with the centre of mass and inertia about that centre lumped at a node. Breaking down the mass and increasing the number of nodes further, although increasing the number of degrees of freedom, does not increase the accuracy of the model. This is perhaps best illustrated by an example. Fig. 8.9 shows three FE representations of the T-Sat spacecraft, fig. 8.9a is the first lateral mode as computed by a full dynamic FE model (1727 d.o.f) and figs. 8.9b & 8.9c are lumped mass and beam models. In fig. 8.9b the launch mass of the spacecraft is divided into the boost motor mass lumped at its vertical mounting position, and the orbiting part of the spacecraft lumped at its centre of mass. The inertias are those of the corresponding masses about the nodal points. In fig. 8.9c the spacecraft mass is divided further by lumping masses of the constituent spacecraft modules at their individual centres of mass. A feature of the lateral mode shape is that the main body of the spacecraft remains essentially rigid, provided its local modes are sufficiently separated from the overall lateral mode. Hence lumping the spacecraft mass and inertia at its C.G. position, about which it displaces and rotates as a rigid body, as in fig. 8.9b, is a better representation than the model of fig. 8.9c in which the masses and inertias are unconstrained and their displacements and rotations depend on their positions on the beam.

The beam element formulation used (which includes transverse shear deformation) was based on reference [46]. For a single beam element, as shown in fig. 8.8, with freedoms v_1, θ_1, v_2, θ_2 respectively the stiffness matrix is given by :

$$[K] = \begin{bmatrix} \frac{12EI}{(1+\zeta)L^3} & \frac{-6E}{(1+\zeta)L2} & \frac{-12EI}{(1+\zeta)L^3} & \frac{-6EI}{(1+\zeta)L^2} \\ & \frac{(4+\zeta)EI}{(1+\zeta)L} & \frac{6EI}{(1+\zeta)L^2} & \frac{(2-\zeta)EI}{(1+\zeta)L} \\ & & \frac{12EI}{(1+\zeta)L^3} & \frac{6EI}{(1+\zeta)L^2} \\ \text{SYM} & & & \frac{(4+\zeta)EI}{(1+\zeta)L} \end{bmatrix} \qquad \text{(eq. 8.1)}$$

where :

$$\zeta = \frac{12EI}{L^3} \Big/ \frac{GA_s}{L}$$

which accounts for the stiffness reduction due to shear deformation. EI and GA_s are the beam bending and shear rigidities respectively. For a thin walled circular section, such as a thrust tube beam element:

$$I = \pi R^3 t \qquad A_s = \pi R t$$

where, R = radius

t = wall thickness

For a composite beam, the bending and shear rigidity terms can be substituted by elements of the sandwich shell constitutive matrix. If the laminate X-axis is aligned with the beam, these become :

$$EI = A_{11} \pi R^3$$

$$GA_s = A_{33}\,\pi\,R$$

A_{11} and A_{33} refer to the membrane coefficients for the shell wall. For a symmetric sandwich construction, these terms are simply the summed effects of both facesheets. Because only A_{11} and A_{33} terms appear in the element stiffness matrix, it is clear only the membrane axial and shear stiffnesses of a thrust tube lay-up are significant in determining lateral vibration behaviour. Hence the incorporation of hoop direction (90°) fibres will have little effect on lateral frequency since these will only have a significant effect on the A_{22} membrane stiffness term. In fig. 8.10 A_{11} & A_{33} terms are plotted for a range of 4-ply faced HM carbon-epoxy sandwich constructions of the form $[\pm\theta/\pm\phi/\text{core}/\mp\phi/\mp\theta]$. Clearly the lay-ups that maximise lateral frequency will have large A_{11} & A_{33} which are those indicated by the band to the right of the graph. The lay-up on this band which actually maximises frequency will depend on the particular spacecraft thrust tube geometry and mass distribution.

The corresponding lumped mass matrix for the elements is :

$$[M] = \begin{bmatrix} M_1 & 0 & 0 & 0 \\ & I_1 & 0 & 0 \\ & & M_2 & 0 \\ & & & I_2 \end{bmatrix} \qquad \text{(eq. 8.2)}$$

where, M_i and I_i refer to the lumped mass and inertia centred at the ith node.

The global stiffness and mass matrices for the complete model can be assembled in the usual way, the equations relating to the freedoms at the fully fixed base eliminated and the free vibration problem solved by the eigenvalues of :-

$$\left| [K] - \lambda[M] \right| = 0 \qquad \text{(eq. 8.3)}$$

where,

[K] = Global Stiffness Matrix

[M] = Global Mass Matrix

λ = Eigenvalue

The above beam & lumped mass FE method for spacecraft lateral frequency prediction was incorporated in a FORTRAN program which is described in detail in Appendix E.

8.3.2 Beam & Mass Model Validation

The beam & lumped mass model idealisation for the T-Sat spacecraft was compared with a much more sophisticated full dynamic model of the structure in order to assess the validity of this method of representation. The two models were those depicted in fig. 8.9. The full model was generated and analysed using the LUSAS (London University Structural Analysis System) FE system and had 1727 d.o.f (fig. 8.9a), and the beam model was analysed using the program described in Appendix E and had 6 d.o.f. (fig. 8.9b). The particular thrust tube design examined in this case consisted of $[0_4/(\pm 30)_2]$ facesheets in the lower conical section (Orbit Transfer Module) and $[\pm 15/\pm 45]$ facesheets in the upper cylindrical section, of HM carbon-epoxy on a honeycomb core. The spacecraft inertia used in the beam & mass model refered to its I_{XX} value since this was slightly higher than the I_{YY} value and so yielded the lower of the two orthogonal first lateral modes.

The calculated values of the first and second lateral mode frequencies from the two models are compared in Table 8.4. The beam & lumped mass idealisation was found to give good agreement with the much larger FE model for both of the first two lateral modes. For the first mode the beam model was within 1½% and for the second was within 3%. The stiffness description of the thrust tube in the full FE model was later validated by a modal survey test (described in Chapter 9), which by implication supported the beam & lumped mass representation. This approach was therefore adopted to describe lateral vibration behaviour and optimise thrust tube designs.

8.4 ANALYSIS OF COMPOSITE THRUST TUBE MATERIAL STRENGTH

The analysis of material strength margins for composite faced sandwich thrust tubes follows the laminate and failure theories outlined in Chapter 5. A FORTRAN program for the analysis of composite thrust tube constructions using the Tsai-Wu failure criterion is described in Appendix F. The required load input information are pairs of N_x and N_{xy} axial and shear stress resultants at various points in the thrust tube shell under the design load cases. These can be derived from a preliminary static FE model of the structure. For composite construction it is important to analyse positions of high shear in addition to high axial stress resultants.

8.5 ANALYSIS OF COMPOSITE FACED SANDWICH THRUST TUBE GENERAL INSTABILITY

8.5.1 Method of Analysis

An effective general instability or buckling analysis for composite faced sandwich thrust tubes is complicated by the following factors:

1. The state of combined axial and shear stress and the distribution of these stresses in the thrust tube shell wall are complex, due to a non-uniformity of load introduction into the shell from various structural attachments. Although it is possible to simplify the loading on the thrust tube by considering the applied loads as uniform axial and shear forces and bending moments, even this combined loading is a formidible problem for any analysis. In many instances where load introduction is highly localised, the use of assumed uniform loading actions is inappropriate.

2. The low density honeycomb cores used in sandwich thrust tube construction have a low through-thickness shear stiffness. This tends to reduce the buckling capacity over an equivalent monocoque shell. Any analysis must therefore include this effect by incorporating core shear strains in addition to bending and membrane strains in the face-

sheets. The core direct through-thickness stiffness is also low, but this is only siginificant for local wrinkling instability.

3. The range of dimensions for thrust tubes and shell wall stiffness properties if composites are employed, mean that the simplifying assumptions which are often adopted to reduce small deflection buckling theories to closed form solutions (eg. that the cylinder be "moderately long") cannot be applied. A numerical minimisation procedure is therefore necessary to calculate critical buckling loads if a method of this type is used.

4. The buckling analysis must include truncated conical geometry in addition to cylinders.

It is clear that a rigourous theoretical approach to buckling analysis which takes into account all of these factors would, even if possible, be extremely complicated and not amenable to preliminary design optimisation. The method adopted was therefore firstly to calculate critical buckling loads using existing small deflection theories for orthotropic faced sandwich cylinders under the separate conditions of uniform compression and uniform shear. These critical loads were calculated for each section of the thrust tube, between frames or changes in geometry/stiffness, and each section was considered to have simply supported ends. For conical sections an effective cylindrical radius was used. The separate loading actions were then combined by using a semi-empirical interaction formula to describe a buckling failure envelope. Comparison of this envelope with the applied axial and shear loads indicated whether buckling failure was likely or not.

In this approach the conservative assumption made is that the buckling strength of the shell under a non-uniform state of stress is equal to the buckling strength of the shell under the maximum stress acting uniformly around the complete circumference. One would expect the buckling strength under the non-uniform stress field to be higher than that of the shell under uniform stress at the maximum level, although the degree of this conservatism is not perhaps as great as might be expected.

Under an applied bending moment an axial stress gradient is set up around the shell circumference, with tension stresses in the one half and compressive stresses in the other. Despite this non-uniform state of stress, for an isotropic homogeneous cylinder under pure bending the theoretical buckling maximum fibre compression stress is found to be equal to the critical buckling stress under uniform compression[47]. In reference [48], for orthogonally stiffened cylinders, the theoretical buckling maximum bending stress was found to be only slightly higher than the uniform compressive buckling stress (by a factor of 1.075 for the particular example considered). Hence for a circumferentially varying axial stress, such as under cylinder bending, there is little conservatism from the theoretical point of view at least, in taking the maximum applied stress as an equivalent uniform load. Experimental evidence[49] suggests the degree of conservatism in this approach is slightly greater than the theory predicts because the knock-down effect of initial imperfections has less of an effect statistically since less of the shell wall is under the maximum compression.

The lateral loads acting on the thrust tube result in shear stresses in the shell wall which are distributed in an approximately sinusoidal manner around the circumference (although this ideal is departed from in reality by non-uniform load introduction), as shown in fig. 8.2. Theoretical work on the instability of shells under transverse shear is somewhat scarce so it is necessary to resort to the case of pure applied torsion, with a uniform state of shear stress around the circumference, to obtain a solution. By assuming a uniform torsional shear stress, design guidelines such as reference [50] suggest multiplying the critical stress by 1.25 to give the critical stress under transverse shear. In this current work, no factor was applied to account for non-uniformity in the shell wall shear stress, which introduced a degree of conservatism.

In order to combine the effects of axial compression, bending and torsion on shell buckling, the following interaction formula is often used[49,51] as a criteria for failure (given here in terms of stress resultants):

$$\frac{(N_x)_b}{(N_x)_{b,cr}} + \frac{(N_x)_c}{(N_x)_{c,cr}} + \left(\frac{(N_{xy})_t}{(N_{xy})_{t,cr}}\right)^2 = 1 \qquad \text{(eq. 8.4)}$$

where,

$(N_x)b$ = Applied max. fibre axial compression stress resultant due to bending.

$(N_x)_c$ = Applied axial stress resultant due to compression.

$(N_{xy})_t$ = Applied shear stress resultant due to torsion.

$(N_x)_{b,cr}$ = Critical axial stress resultant under applied bending only.

$(N_x)_{c,cr}$ = Critical axial stress resultant under compression only.

$(N_{xy})_{t,cr}$ = Critical shear stress resultant under torsion only.

An alternative interaction equation suggested in reference [52] contains the axial stress resultant ratios raised to the power of 1.5 rather than 1.0 as in equation (8.4). Experimental evidence of reference [53] in which a large number of combined torsion and compression tests were carried out on conical Mylar shells, and of reference [54] in which similar tests were carried out on carbon and boron-epoxy cylinders, support a relationship nearer to that of equation (8.4). This expression was therefore adopted in this work.

By equating the uniform applied stress resultants due to compression, torsion and bending with actual values of the non-uniform stress resultants in the shell wall, and by making no differentiation between the axial stress resultants due to compression and bending, it is possible to modify the interaction formula to :

$$\frac{N_x}{(N_x)_{cr}} + \left(\frac{N_{xy}}{(N_{xy})_{cr}}\right)^2 = 1 \qquad \text{(eq. 8.5)}$$

where,

N_x = Applied axial stress resultant at a given location.

N_{xy} = Applied shear stress resultant at a given location.

$(N_x)_{cr}$ = Critical axial stress resultant under compression only.

$(N_{xy})_{cr}$ = Critical shear stress resultant under torsion only.

The interaction equation defines a failure envelope for buckling on the N_x-N_{xy} stress resultant plane, shown for a typical thrust cylinder geometry and lay-up in fig. 8.11. The format of this envelope makes it compatible with similar envelopes on the N_x-N_{xy} plane generated by the Tsai-Wu index for facesheet material failure (section 5.3.3 and fig. 5.1), and by the interactive wrinkling theory of Chapter 6 (fig. 6.11). The use of these envelopes enables 'worst case' stress resultant combinations and the likely mode of failure to be ascertained.

The interaction index given by the left hand side of equation (8.5) can be applied at various locations in the cylinder wall, each with a pair of stress resultant values (N_x, N_{xy}), and a buckling failure is deemed to occur if it exceeds unity. The interaction formula will tend to give conservative results since the inherent assumption is that the worst case pair of values N_x and N_{xy} are acting uniformly over the entire shell area. In reality the stress resultants are non-uniform at levels below the worst case combination, both around the circumference and along the length.

Application of this interaction equation requires two buckling loads to be evaluated: the critical axial compression load and the critical torsional load. The following sections outline the linear small deflection theories used to calculate these loads for orthotropic faced sandwich shells.

8.5.2 Buckling of Composite Faced Sandwich Cylinders under Axial Compression

8.5.2.1 Theory

The method used to analyse the compressive buckling of composite faced sandwich cylinders is based on that of Teichmann, Wang & Gerard[55]. This is a small deflection approach in which an assumed buckled waveform is substituted into the cylindrical shell equilibrium equations, and in which core shear deformation is included. The method is reworked here by expressing the equations in terms of the shell constitutive matrix elements and writing them in matrix form. The critical axial load is found by

solving the eigen problem which is then minimised with respect to the buckled waveform parameters.

The shell constitutive matrix coupling terms B_{11}, B_{12}, B_{22}, B_{33} are included in the analysis described here since these are allowed by the buckled waveform shape functions used. Although these terms are zero in a symmetric sandwich lay-up, they are included to enable unsymmetric sandwich configurations to be analysed (provided B_{13}, B_{23} are zero). Stiffened shells with smeared stiffness properties can also be analysed in this way taking into account stiffener eccentricity. The D_{13} and D_{23} bending-twisting terms, which are generally non-zero for a symmetric sandwich with arbitary facesheet lay-ups, are assumed to be zero to allow simple shape functions to be employed. These terms are very small for thin faced sandwich (see 5.2.2) so such an assumption is reasonable.

The theoretical development is described fully in Appendix G. The assumed buckled waveform shape functions were :

$$u = U \sin n\theta \cos \frac{m\pi x}{L}$$

$$v = V \cos n\theta \sin \frac{m\pi x}{L}$$

$$w = W \sin n\theta \sin \frac{m\pi x}{L} \qquad \text{(eq. 8.6)}$$

$$\beta_x = \bar{\beta}_x \sin n\theta \cos \frac{m\pi x}{L}$$

$$\beta_\theta = \bar{\beta}_\theta \cos n\theta \sin \frac{m\pi x}{L}$$

where, u, v & w refer to displacements of the shell mid-plane and β_x & β_θ refer to components of the slope of the normal to the shell mid-plane, and

n = No. of full waves around the circumference.

m = No. of half-waves along the length.

By substituting these into the equilibrium equations the following matrix equation to describe the onset of buckling in terms of the displacement amplitudes is obtained :

$$([C] - \lambda[P])\{U\} = 0 \qquad \text{(eq. 8.7)}$$

where, [C] is a 5 x 5 symmetric matrix of stiffness coefficients

[P] is a 5 x 5 sparse diagonal matix of load coefficients

$\{U\}$ is the 5 degree of freedom vector of displacement amplitudes

λ is the buckling eigenvalue (= critical stress resultant)

The terms of these matrices are given in full in Appendix F.

Calculation of the buckling load requires the eigenvalue problem of equation (8.7) to be solved and minimised with respect to the waveform parameters m & n. Generation of the matrix coefficients, solution of the eigen problem and minimisation with respect to m & nis carried out in a FORTRAN program, described in Appendix H, which performs various buckling analyses for composite sandwich thrust tubes.

8.5.2.2 Conical Geometry

The above formulation is based on a cylindrical geometry. In order to analyse compressive buckling in conical shells, an equivalent cylinder radius and equivalent cylinder length were used. These are given by[49]:-

$$R_e = \frac{R_1}{\cos \alpha_{1/2}}$$

$$L_e = \frac{L}{\cos \alpha_{1/2}} \qquad \text{(eqs. 8.8)}$$

where,

R_1 = Smaller radius of truncated cone

L = Height of truncated cone

$\alpha_{1/2}$ = Semi-Cone angle ($\alpha_{1/2} < 75°$)

8.5.2.3 Axisymmetric Buckling Solution

A common technique used to simplify axial buckling analysis[47] which was adopted by Teichmann, Wang & Gerard, is to assume an axisymmetric buckled waveform ie. no circumferential waves. Such an assumption is valid for "moderately long" isotropic cylinders, and was also found to be valid by Teichmann, Wang & Gerard for the aluminium faced honeycomb core sandwich cylinders they considered. The use of this assumption results in a considerable simplification to the problem. The 5 equilibrium equations can be reduced to 3 (by setting v = 0 and $\beta_\theta = 0$) and these can be combined to yield a single expression for the axial buckling stress resultant, which can then be minimised with respect to the one waveform parameter, m. The details of this simplification are given in Appendix G. The simplified expression for the case of a symmetric sandwich shell is :

$$N_{x(crit)} = \frac{D_{11}\left(\frac{\mu}{R}\right)^2 + \frac{A_{22}}{R^2}\left(1 - \frac{A_{12}^2}{A_{11}A_{22}}\right)\left[\left(\frac{R}{\mu}\right)^2 + \frac{D_{11}}{S_{xz}}\right]}{\left[1 + \frac{D_{11}}{S_{xz}}\left(\frac{\mu}{R}\right)^2\right]} \qquad \text{(eq. 8.9)}$$

where,

$$\mu = \frac{m\pi R}{L}$$

By setting the longitudinal through-thickness shear rigidity to infinity, as for a monocoque construction with transverse shear ignored, the equation can be reduced further and minimised with respect to m (provided it can be considered to be continuous) to give the familiar orthotropic cylinder axial buckling expression :

$$N_{x(crit)} = \frac{2}{R}\left\{A_{22}\left(1 - \frac{A_{12}^2}{A_{11}A_{22}}\right)D_{11}\right\}^{\frac{1}{2}} \qquad \text{(eq. 8.10)}$$

It is interesting to note that the critical buckling load is not dependent on the cylinder length. Equation (8.9) for sandwich cylinders and equation (8.10) for monocoques are useful in that they provide an insight into the relative importance of the stiffness terms which govern compression buckling. Lay-ups with good buckling strength are those which provide high membrane hoop stiffness (A_{22}) and high axial bending stiffness (D_{11}). Buckling capability can be seen to be reduced for lay-ups with large Poissons ratios (ie. large A_{12} such as ± 45 lay-ups), and as core shear stiffness (S_{xz}) is reduced. Since only the S_{xz} core stiffness term appears in the equation, it is advantageous from the point of view of improving compressive buckling performance, to orientate the honeycomb ribbon direction with the cylinder axis.

Unfortunately the range of applicability of these expressions does not fully encompass the range of possible composite thrust tube elements that might be encountered in a spacecraft structure. In order for the assumptions of axisymmetric buckling to hold, firstly the cylinder must fall into the "moderately long" range. For simply supported orthotropic cylinders, this condition is met if the following inequality is satisfied[49] :

$$\frac{A_{22}}{12D_{11}}\left(1 - \frac{A_{12}^2}{A_{11}A_{22}}\right)\frac{L^2}{R} > 25 \qquad \text{(eq. 8.11)}$$

where, L = Cylinder length

R = Cylinder radius

Although the majority of practical thrust tube elements would fall into this range, in order to apply the axisymmetric formula the shell wall stiffness properties must also be proportioned in an allowable range. For thrust tube lay-ups with a relatively high proportion of near-axial fibres, the stiffness properties are too biased for the buckling mode to be axisymmetric. In such instances the shell wall is relatively weak in the

hoop direction so that buckles form around the circumference in addition to down the length. The assumption of an axisymmetric buckling mode can then no longer be applied and it is necessary to revert to the more general solution given by equation (8.7). This point can be illustrated by the following example. Consider the case of a cylindrical tube of length 1.0m and radius 0.5m with a shell wall consisting of equal 4-ply HM carbon-epoxy facesheets and a 10mm 2.0lb/cu.ft. honeycomb core. The facesheet lay-up is $[(\pm\theta)_2]$, where θ is a variable angle measured relative to the cylinder axis.

In fig. 8.12 the theoretical axial buckling load for the cylinder is plotted against the fibre angle, θ, for the general solution found from equation (8.7) and for the axisymmetric solution (ignoring core shear) given by equation (8.10). For low values of θ, ie. fibres aligned close to the longitudinal direction, the minimum buckling load solutions found from equation (8.7) are for buckled modes where m=1 and n=4. This means the buckled mode shape is dominated by circumferential waves because the shell stiffness is low in this direction. The axisymmetric solution is seen to be vastly unconservative in this region. As the fibre angle opens up, the mode shape becomes axisymmetric with an increasing number of axial buckles as increases (ie. axial stiffness decreases), as shown by the series of festoon curves in fig. 8.12. The axisymmetric solution then follows the trend of the general solution. The discrepency between the two solutions is due to the presence of core shear and the assumption of a continuously valued m in the axisymmetric solution of equation (8.10). Neglect of core shear in this particular example, which is typical of a thrust tube configuration, leads to an over-prediction in the buckling load of 5%-7%.

For the purposes of computing a value for the critical axial compression stress resultant, for use in the buckling interaction equation (eq. 8.8), the general solution was adopted. This enabled a comprehensive range of facesheet lay-ups and core shear to be included making the method suitable for incorporation into an optimisation scheme.

8.5.3 Buckling of Composite Faced Sandwich Cylinders under Torsion

8.5.3.1 Theory

The method adopted for the prediction of torsional buckling of sandwich cylinders was that due to March & Kuenzi[56]. This is an energy method in which the extensional and flexural strain energy of the shell, minimised for an assumed buckled shape function, is equated to the work done by the applied torsional couple. The method is outlined here with the original equations (given in terms of effective moduli and rigidities) rewritten in terms of the shell constitutive matrix elements, for consistency with the rest of this chapter. It is assumed that the shell constitutive matrix is uncoupled, such that $B_{ij}=0$, A_{13}, A_{23}, D_{13} & $D_{23}=0$.

The following shape function (written in a consistent format here) was used to describe the buckled surface :

$$w = W \sin\left(\frac{m\pi x}{L} - n\theta \right) \sin \frac{\pi x}{L} \qquad \text{(eq. 8.12)}$$

where,

m = No. of axial half waves

n = No. of circumferential full waves

The first trigonometric factor in the equation refers to skewed sinusoidal buckles which spiral around the cylinder, similar to those assumed for wrinkling of a flat plate (shown in fig. 6.3). The second factor is introduced to ensure zero deflection at the ends of the cylinder. Equation (8.12) can be re-expressed in the form :

$$w = W \left(\cos\left(\delta x - n\theta\right) - \cos\left(\epsilon x - n\theta\right)\right) \qquad \text{(eq. 8.13)}$$

where,

$$\delta = (m+1)\frac{\pi}{L}$$

$$\epsilon = (m-1)\frac{\pi}{L}$$

also, it is convenient to write :

$$\alpha = n/R$$

$$\gamma = m\pi R/nL \quad \text{(nodal line slope)}$$

The extensional strain energy is given by :

$$W_1 = \frac{\pi RLW^2}{8}\left(\frac{\delta^4}{K_1} + \frac{\epsilon^4}{K_2}\right) \qquad \text{(eq. 8.14)}$$

where,

$$K_1 = A_1\alpha^4 + A_3\alpha^2\delta^2 + A_2\delta^4$$
$$K_2 = A_1\alpha^4 + A_3\alpha^2\delta^2 + A_2\epsilon^4$$

and,

$$A_1 = 1 \Big/ A_{11}\left(1 - \frac{A_{12}^2}{A_{11}A_{22}}\right)$$

$$A_2 = 1 \Big/ A_{22}\left(1 - \frac{A_{12}^2}{A_{11}A_{22}}\right)$$

$$A_3 = 1 \Big/ A_{33} - 2A_{12} \Big/ A_{11}A_{22}\left(1 - \frac{A_{12}^2}{A_{11}A_{22}}\right)$$

The minimum flexural strain energy, including the effect of core shear, is found to be :

$$W_2 = \frac{\pi R^3 LW^2}{8} \frac{\left(D_1 + 2D3 + D_2 + (D_1D_2 - D_3^2)(1/S_1 + 1/S_2)\right)}{\left(1 + D_1/S_1 + D_2/S_2 + (D_1D_2 - D_3^2)/S_1S_2\right)} \qquad \text{(eq. 8.15)}$$

where,

$$D_1 = D_{11}(\delta^4 + \epsilon^4) + D_{33}\alpha^2(\delta^2 + \epsilon^2)$$

$$D_2 = 2D_{22}\alpha^4 + D_{33}\alpha^2(\delta^2 + \epsilon^2)$$

$$D_3 = (D_{12} + D_{33})\alpha^2(\delta^2 + \epsilon^2)$$

$$S_1 = S_{xz}(\delta^2 + \epsilon^2)$$

$$S_2 = 2S_{\theta z}\alpha^2$$

The work done by the applied torsion couple is :

$$W_3 = N_{x\theta}\frac{\pi R^3 L W^2 \alpha^2 \gamma}{2} \qquad \text{(eq. 8.16)}$$

where $N_{x\theta}$ is the uniform shear stress resultant due to torsion.

The critical shear stress resultant is determined by equating the strain energy and work done :

$$W_3 = W_1 + W_2 \qquad \text{(eq. 8.17)}$$

Substituting for W_1, W_2 & W_3 from equations (8.14) to (8.16) and solving for $N_{x\theta}$ results in the equation :

$$N_{x\theta} = \frac{1}{4R^2\alpha^2\gamma}\left(\frac{\delta^4}{K_1} + \frac{\epsilon^4}{K_2}\right) +$$

$$\frac{1}{4\alpha^2\gamma}\ \frac{(D_1 + 2D_3 + D_2 + (D_1D_2 - D_3^2)(1/S_1 + 1/S_2))}{(1 + D_1/S_1 + D_2/S_2 + (D_1D_2 - D_3^2)/S_1S_2)} \qquad \text{(eq. 8.18)}$$

The critical torsional buckling stress resultant is then found by minimising equation (8.18) with respect to the parameters α, γ, δ & ϵ, which in turn are dependent on the waveform parameters m & n. The above

equation was included in a FORTRAN buckling analysis program (described in Appendix H) which also performs the necessary minimisation.

8.5.3.2 Conical Geometry

To analyse torsional buckling in conical shells the same approach used for compression buckling was adopted by substituting an effective radius and length into the equations. These effective cylinder dimensions are not the same as those used for compression buckling. For isotropic and orthotropic cones, the effective dimensions can be found from[49,53,57] :

$$R_e = (1 + \chi - \chi^{-1}) R_1 \cos \alpha_{1/2}$$

$$L_e = L \qquad \text{(eqs. 8.19)}$$

where,

$$\chi = \left(\frac{1 + R_2/R_1}{2} \right)^{\frac{1}{2}}$$

R_1 = Smaller radius of truncated cone
R_2 = Larger radius of truncated cone
L = Height of truncated cone
$\alpha_{1/2}$ = Semi-cone angle ($\alpha_{1/2} < 60°$)

These expressions are assumed to be valid for orthotropic faced sandwich shells also.

8.5.3.3 Solution for Moderately Long Cylinders

As with buckling of cylinders under compression, a closed form solution[58,59] can be obtained for orthotropic shells which fall into a "moderately long" range. This solution can be written using shell constitutive matrix notation as :

$$N_x\,(\text{crit}) = k_T \left(A_{11}\left(1 - \frac{A_{12}^2}{A_{11}A_{22}} \right) \right)^{3/8} D_{22}^{5/8} \cdot \frac{1}{L^{\frac{1}{2}}R^{\frac{3}{4}}} \qquad \text{(eq. 8.20)}$$

where, k_T is a constant coefficient dependent on the cylinder end conditions. For simply supported ends,

$k_T = 3.459$ (ref[58])

$k_T = 3.595$ (ref[59])

The latter of these two coefficients is the more accurate, since the simpler shape function assumed in the estimation of the former does not completely satisfy simply supported boundary conditions.

Equation (8.20) shows that torsional buckling of moderate length cylinders, unlike axial compression buckling, is length dependent. An increase in cylinder length results in a decrease in the critical buckling load. The equation is useful in that it suggests torsional buckling resistance is best built into the shell lay-up by arranging for a high axial in-plane stiffness (A_{11}) and a high hoop bending stiffness (D_{22}). Note that this is the converse to the requirement for high compression buckling strength in which A_{22} & D_{11} are the terms to maximise. Torsional buckling is decreased by Poissons effects, and core shear (not included in eq.(8.20)) would also be expected to reduce buckling capacity.

Because of a greater sensitivity to end conditions, the "moderately long" range over which equation (8.20) becomes applicable begins at a much greater length than the "moderately long" defined by equation (8.11) for axisymmetric compression buckling. This condition can be expressed in terms of the cylinder dimensions and shell constitutive matrix terms by the approximate inequality[58]:

$$\frac{A_{22}}{12D_{11}} \left(1 - \frac{A_{12}^2}{A_{11}A_{22}} \right)^{\frac{1}{2}} \left(\frac{A_{11}}{A_{22}}\right)^{1/2} \left(\frac{D_{22}}{D_{11}}\right)^{5/6} \frac{L^2}{R} > 1000 \qquad \text{(eq. 8.21)}$$

The actual value of the length parameter on the left hand side of equation (8.21) at which the "moderately long" solution can be confidently applied

depends on the shell construction. The value tends to be highest for highly orthotropic configurations and lowest for near isotropic configurations. For values of about 1000 equation (8.20) will give sufficiently accurate solutions for most configurations, and at a value of 10000 will give complete convergence with the full solution. For the majority of typical thrust tube configurations the length parameter will not be large enough to yield sufficiently accurate estimates of torsional buckling strength through the use of equation (8.20).

This can be illustrated by the example cited in the previous section for compression buckling, of a 0.5m radius 1.0m long cylinder, typical of a section of thrust tube. The walls are a sandwich construction with 4-ply $[(\pm\theta)_2]$ HM carbon-epoxy facesheets on a 2.0lb/cu.ft. honeycomb core. In fig. 8.13a the critical torsional buckling shear stress resultant is plotted against the lay-up angle, θ , for the general orthotropic sandwich solution from equation (8.18), and the "moderately long" orthotropic solution given by equation (8.20). There is a large discrepency between the two solutions which is attributable to the fact that the cylinder does not fall into the "moderately long" range defined by equation (8.21) for any fibre angle θ. Although core shear is included in only the general sandwich solution, by setting the core stiffness to infinity this can be shown to account for only about 1%-6% of the discrepency. The "moderately long" solution does not even follow the same general trend with fibre angle, θ which suggests that the relative importance of the constitutive matrix terms inferred from equation (8.20) does not strictly hold for short cylinders. The March & Kuenzi general solution predicts torsional buckling strength to be maximised at a fibre angle of $\pm 35°$ which is not predicted by the "moderately long" solution.

As the cylinder length is increased, the two solutions begin to converge as shown by fig. 8.13b, which depicts the torsional buckling loads against fibre angle for the same cylinder, but with length increased to 10m and 25m. At a length of 25m the two solutions follow approximately the same trend and give critical loads within +/- 10%. Some of the difference can be accounted for by the assumption of continuously variable, rather than discrete valued, m & n in the "moderately long" solution.

This example demonstrates the inapplicability of the closed form "moderately long" cylinder solution for the torsional buckling analysis of spacecraft thrust tubes. The method of March & Kuenzi, requiring the minimisation of equation (8.18), was therefore adopted for incorporation in the buckling analysis of composite faced sandwich thrust tube constructions. This method also includes the effect of core shear. Fig. 8.14 shows the error in neglecting core shear for a [0/0/+45/-45] HM carbon-epoxy faced sandwich construction with 2.0lb/cu.ft core, for a cylinder of 1m length and 0.5m radius. The overestimate of torsional buckling strength increases from 8% for a 5mm core to 12% for a 15mm core if shear is neglected.

8.5.4 Effect of Initial Imperfections

The effect of initial imperfections or irregularities in thin-walled shells is known to lead to large reductions in buckling strength compared to predictions made by small deflection theories. In order to account for the effect of imperfections the possible approaches are to apply a suitable "knock-down factor" to small deflection theory predictions in order to give better correlation with test results, or to use a more sophisticated large deflection theory which makes some attempt to include the initial imperfections. The former approach is the most commonly adopted since it is the simplest and more amenable for design purposes. Effective use of a large deflection theory requires knowledge of the actual shell wall imperfections and often leads to over-conservative results. The small deflection theory coupled with a knock-down factor was therefore the approach adopted here for initial design optimisation.

The effect of initial imperfections is known to increase with increasing radius/thickness ratios for monocoque shells. One would hence intuitively expect the effect of imperfections to be less for sandwich shells. Figs. 8.15 and 8.16 (from reference [49]), plot knock-down factors against R/ρ ratios for cylinders subjected to axial compression and torsion, where for orthotropic cylinders :

$$\text{radius of gyration, } \rho = \left(\frac{D_{11}D_{22}}{A_{11}A_{22}}\right)^{\frac{1}{4}} \qquad \text{(eq. 8.22)}$$

For sandwich shell constructions it is suggested that this expression be used in conjunction with figs. 8.15 & 8.16 unless the core shear stiffness is very low. If the core shear stiffness is low, the effect of initial imperfections is known to be less than predicted by these figures, but for typical thrust tube configurations the core stiffness is not sufficiently low enough to warrant an increase in the predicted factor. For facesheets which are thin compared to the core it is possible to make the approximations:

$$D_{11} \doteq \frac{1}{2} A_{11}\, h^2 \qquad \& \qquad D_{22} \doteq \frac{1}{2} A_{22}\, h^2$$

where,

h = dist. between facesheets, $\simeq$ core thickness

so that

$$\rho = \tfrac{1}{2}h$$

Thrust tube constructions typically have a radius of 0.4-0.8m and core thicknesses of 8-15mm, giving a range of R/ρ ratios of 50-200. From figs. 8.15 and 8.16, this in turn results in a range of knock-down factors of 0.81-0.66 for axial compression, and 0.84-0.72 for torsion. The knock-down factors for torsion are a little higher than those for axial compression, as one might expect, because of the stablising effect of the principal tension field. Some authors[53,54,56] suggest that there is little imperfection sensitivity for shells loaded by pure torsion, but that a knock-down factor is necessary to correlate test and small deflection theory if even small axial compression load component is present.

The knock-down factors given by figs. 8.15 and 8.16 are generated primarily from test data for monocoque and orthotropic stiffened cylinders. Published test data on sandwich cylinders is considerably more limited. Reference [57] contains test data on glass-epoxy sandwich cylinders and cones, loaded

under compression and torsion, which were similar to thrust tube configuarations. For a cylinder loaded in compression the knock-down factor required to correlate test and theory was 0.53, and the factor for pure torsion was 0.64. For a truncated cone, the factors were 0.95 for pure bending and 0.73 for pure torsion. The low factors for the cylinder (below those predicted from figs. 8.15 & 8.16) were attributed to the manufacturing process, which was improved for the production of the cones. In the light of these data, and insufficient justification for adopting the higher orthotropic cylinder factors of figs. 8.15 & 8.16, the following conservative knock-down factors were adopted for the prediction of buckling loads for all sandwich shell constructions:

Pure Compression	0.50
Pure Torsion	0.60

These were considered sufficient to define a lower bound on buckling loads. By applying these factors to the theoretical buckling stress resultants for compression and torsion and including these in the interaction equation (eq.(8.5)) an allowable buckling envelope can be generated, such as that shown in fig. 8.11.

8.6 ANALYSIS OF COMPOSITE FACED SANDWICH THRUST TUBE LOCAL INSTABILITY

The possible local instability modes in sandwich shells are wrinkling and dimpling. Of these, wrinkling is the most critical since it results in collapse, whereas dimpling does not necessarily constitute failure. The analysis of wrinkling under combined axial and shear stress resultants is covered in detail in Chapter 6. However, both of these instability modes are limited to sandwich constructions with thin facesheets and/or thick cores. Because of the primarily membrane loading on thrust tubes, the facesheets are of necessity relatively thick (compared to the majority of flat spacecraft panels) and these instability modes are therefore not commonly critical.

8.7 COMPOSITE FACED SANDWICH THRUST TUBE DESIGN OPTIMISATION

8.7.1 Introduction

The primary objective in the optimisation of thrust tube design is to minimise the weight of the structure whilst satisfying all the failure mode and stiffness constraints. With fibre reinforced composite materials it is also possible to widen the objectives of optimisation to maximise margins of safety on certain modes of failure and to include manufacturing and cost implications. This is because the fibre orientations in a composite lay-up can be varied to significantly change the structural properties without altering the structure weight. The composite lay-up can therefore be selected both to minimise weight, maximise safety margins and also take into consideration ease of manufacture and hence cost.

This section discusses the optimisation problem and rigourous solution methods using numerical programming techniques. The drawbacks of applying these techniques to composite sandwich thrust tube optimisation are highlighted. A less automatic approach is proposed as an alternative which avoids the limitations of numerical optimisation techniques and allows the designer more freedom in the decision making process.

The constraints are evaluated using the analytical methods described earlier in this chapter, which allow optimised design solutions to be generated from only limited information such as spacecraft mass properties, thrust tube overall dimensions and given design loads. The optimisation method is therefore useful from the feasibility/preliminary design (phase A) stage onwards. Optimum composite sandwich designs found in this way can be compared with other materials and methods of construction in trade off studies.

8.7.2 The Optimisation Problem

The classical structural design optimisation problem can normally be stated mathematically by a constrained minimisation of the form :

$$\text{Minimise} \quad f(x) \qquad \text{(eq. 8.23)}$$

$$\text{subject to} \quad g_j(x) \geq 0 \quad j = 1, \text{NIC} \qquad \text{(eq. 8.24)}$$

where, x refers to a vector of design variables, f(x) is the objective function which is usually the structure weight, and $g_j(x)$ refer to the NIC inequality constraints such as allowable stresses, displacements etc. and limits on the design constraints such as minimum gauge thicknesses. Solution of the problem can be carried out by several methods including various numerical optimisation techniques.

For the composite sandwich thrust tube optimisation problem, the set of design variables, x, may include :

1. Ply lay-up angles	α , β , γ ... etc.
2. Number of plies of a given angle	n_α , n_β , n_γ ... etc.
3. Honeycomb type (foil thickness & cell size)	t_f, d_c
4. Honeycomb thickness	h

It is assumed that the facesheet material, the number of ply angle variables and some arrangement of the ply stacking sequence are fixed. If the thrust tube is split into a number of sections, or bays, up its length (at changes in geometry or where there is a step change in loading) there will be a set of independent variables like this to be optimised for each bay, see fig. 8.17. The aim of the optimisation process is to find the set of design variables which meets the requirements of equations (8.23) and (8.24). The magnitude of the problem can be reduced by fixing some of the variables. For example, the core variables could be fixed by practical considerations (to the minimum practical density) and local design considerations (sufficient thickness for shear strength at load introduction points).

The inequality constraints, $g_j(x)$, refer to the spacecraft minimum lateral frequency requirement and to the possible failure modes of facesheet material failure, general instability and local instability discussed previously. The actual constraint functions can be defined such that they

have values between 0 and 1 if feasible, and values less than 0 if the constraint is violated. They can therefore be considered as a measure of the margin of safety. For the principal thrust tube design constraints these can be expressed by :

Stiffness

$$g(x) = \frac{f_1 - f_D}{f_1} \qquad \text{(eq. 8.25)}$$

where, f_1 = Calculated first s/c lateral frequency
f_D = Lateral frequency design target

Material Strength

$$g(x) = 1 - TW \qquad \text{(eq. 8.26)}$$

where, TW = Maximum ply Tsai-Wu index

General Instability

$$g(x) = 1 - BI \qquad \text{(eq. 8.27)}$$

where, BI = Buckling interaction index (defined by the LHS of eq.(8.5))

Wrinkling

$$g(x) = 1 - \frac{(N_x^2 + N_{x\theta}^2)}{(N_{xwr}^2 + N_{x\theta wr}^2)} \qquad \text{(eq. 8.28)}$$

where, N_x & $N_{x\theta}$ = Applied axial & shear stress resultants
N_{xwr} & $N_{x\theta wr}$ = Critical wrinkling stress resultants at the particular ratio of $N_x/N_{x\theta}$.

In other words, this is the fraction of the unit vector distance to the wrinkling envelope on the N_x-$N_{x\theta}$ plane (eg. fig.6.11) from the point defined by the applied stress resultant vector (N_x, $N_{x\theta}$).

Dimpling

$$g(x) = \frac{N_{Id} - N_I}{N_{Id}} \qquad \text{(eq. 8.29)}$$

where, N_I = Applied principal compression stress resultant
N_{Id} = Critical dimpling stress resultant in direction of applied principal compression.

There is a single stiffness constraint governing the overall thrust tube design and several constraint functions for material strength, buckling, wrinkling and dimpling for each bay and each load case within the bay.

The first difficulty encountered in applying established numerical optimisation procedures to this problem is the mix of continuous and discrete design variables. The ply fibre angles and core thickness can be regarded as continuous, whereas the number of plies or thickness of each fibre orientation and the core type represent discrete variables. Although the core type can be fixed through practical considerations, the discrete ply thickness variables must be included since these obviously play a large part in determining the structure weight.

The majority of numerical optimisation schemes are directed towards problems with continuous variables, since most problems can be represented in this way. Where the number of plies in a composite structure is anticipated to be quite large it is possible to use a method of this type by smoothing thickness into a continuous variable and then rounding the optimised design to the nearest integer number of plies. This is similar to metal structure optimisation since it is still probable that the theoretical optimum must be rounded to a practical design by considerations such as available gauge thicknesses. A popular established method for numerical optimisation of continuous variables is the Method of Feasible

Directions (MFD)[60]. This method has been used to perform the optimisation of preliminary composite aircraft wing design[61] and the design of stiffened composite shells and panels[62] where the skin and stiffeners are relatively thick. In both of these cases, the composite lay-ups were considered to be built up of 0°, ±45° & 90° plies in given sequences, with the total thickness of each particular ply orientation as a continuous variable.

An attempt at applying an optimisation technique of this type to the minimum weight design of composite faced sandwich cylinders was described in reference [63]. The problem described was similar to that of spacecraft thrust tube design optimisation, but was aimed at application to the upper stages of launchers and contained no lateral stiffness (natural frequency) constraint. The design variables specified were two ply angles (θ and ϕ), the ply thickness and core thickness. The facesheet lay-up was presupposed to consist of 4 plies of $[+\theta/+\phi/-\phi/-\theta]$ and the total facesheet thickness was allowed to vary only through changes in the single ply thickness. The ply thickness was considered to be a continuous variable, but in reality will normally be limited to a choice of 0.05 mm, 0.10 mm or 0.125 mm. The assumptions made about the variables did not reflect the real choices confronting the designer. Increasing facesheet thickness would be achieved in reality by adding extra plies rather than retaining just the four and increasing the single ply thickness.

An alternative approach to preserve the discretely varying thicknesses, which is more realistic for the sandwich constuction problem, is to adopt an optimisation method for discrete variables. Some methods of this type are discussed in reference [64]. These methods consider all the design variables to be discretely valued members of a set of possible values. The problem must therefore be converted to one in which all the variables are discretised, so that in addition to an integer number of plies, only unique values of ply angles and core thickness are allowed. This does not particularly constrain the optimisation since the fibre angles can be specified in 5° intervals and the honeycomb depth in 1 mm intervals, for example. These methods are loosely associated with the family of "branch and bound" algorithms in which the basic strategy is to continuously

partition the full set of variables until a single optimum is found. A discrete variable optimisation method is therefore more promising for the composite faced sandwich thrust tube problem.

However, all numerical optimisation methods aim to solve the constrained minimisation problem defined by equations (8.23) and (8.24). They are hence limited to an optimisation based on the mathematical definition of the objective function. The commonly used objective function for structural optimisation is weight, but as stated previously, for composite materials this is rather limiting. Once weight has been minimised it is still possible to use the fibre angle variables to tailor the structure to optimise for other design criteria. This problem was highlighted by numerical examples performed in reference [63] for the optimisation of composite faced sandwich cylinders. It was found that the optimisation process terminated once the ply and core thicknesses (which determine weight) had stabilised, and the optimum ply angles found depended only on the initial starting design. Alternative designs of equal weight but different fibre angles, and hence structural properties, could be found by using different starting points.

Other concepts of an optimum design, such as one which minimises weight and maximises certain failure mode constraint functions could be envisaged. These could possibly be incorporated in existing optimisation methods by redefining the objective function, once weight had been minimised, as some other figure of merit, and allowing only the fibre angle variables to remain free. The optimisation process would then become a two step operation. Firstly to minimise weight subject to simply satisfying the constraints, and secondly to maximise the constraint functions expressed in terms of the figure of merit. The major drawback of this approach is that other concepts of an optimum design such as a prefered ranking of failure modes, or cost and ease of manufacture cannot be expressed as a simple mathematical function. Also, there is little flexibility once the objective function has been defined.

A further limitation of all numerical optimisation methods is that only a single optimum design is generated from a given initial starting point.

Even by using a more elaborate definition of the objective function, the tailorability of composite properties through the use of fibre angles will generally mean there a several optimum design solutions possible. Some of these could be missed by a 'black-box' automatic optimisation process, and the reasons behind a particular optimum solution are hidden from the designer.

Certain practical difficulties are also inherent in the application of standard numerical optimisation techniques to the composite sandwich thrust tube problem. Most methods require gradients of the objective and constraint functions to be evaluated with respect to the design variables and curves to be fitted to the functions. The nature of some constraints will make accurate estimates of these functions difficult without resort to high order polynomials and a consequent increase in the necessary solution time.

Summarising, composite sandwich thrust tube optimisation can be seen to contain several inherent problems if established numerical programming methods are to be used. These are :

1. The presence of continuous and discrete variables.
   An assumption that all the variables can be regarded as continuous is not valid for the case of thin-faced sandwich construction. A better approach is to consider all the variables to be discrete.

2. The difficulty in defining the objective function.
   Although the over-riding aim is to minimise the structure weight, the tailoring of properties through the variation in ply angles makes it possible to consider other optimising criteria. These may be difficult to define mathematically.

3. Only a single optimum is found from a given starting point.
   There may be several optima (particularly if weight is the only objective function) which can only be found by re-starting the procedure from different initial designs.

4. Practical difficulties.
   Some of the constraints cannot be easily represented as simple functions of the design variables, with a consequent increase in solution complexity and time.

8.7.3 Proposed Optimisation Scheme

The approach adopted for optimisation was to narrow down the possible set of design variables, and instead of formally optimising this set with respect to a particular objective function, to analyse all the constraints as functions of lay-up angles. Superimposing the feasible regions for each constraint then defined a feasible design region. The process was repeated with different total numbers of plies per facesheet until a feasible region that satsfies all the constraints was obtained for the minimum structure weight. The designer then selects a single design from the set of feasible designs by applying some selection criteria, which can include ease of manufacture in addition to quantifiable criteria such as safety margins on various failure modes.

Although this method is less automatic than a numerical programming approach and hence slower, it does avoid the difficulties described above, allowing realistic designs to be produced without sacrificing practicality for ease of stating the problem mathematically. The optimisation can still be carried out fairly rapidly through the use of constraint evaluation programs based on the analytical techniques described earlier in this chapter. By narrowing down the design options to the full feasible set there is no necessity to carry out repeated runs, as with a numerical optimisation method, to ensure all possible minimum weight feasible designs are obtained. By presenting the constraint functions in graphical form the designer gains a better understanding of the merits of one lay-up compared to another and participates in the decision making process.

For the method to be successful it was first necessary to reduce the number of variables to a manageable size. This was accomplished by practical considerations. Firstly, the core design variables (material, foil

thickness, cell size and thickness) are determined to a large extent by secondary detail design considerations rather than the overall constraints discussed here. For example, the core density for the majority of thrust tubes would normally be specified as the practical minimum available, since the core is essentially unstressed away from load introduction areas. The core at the load introduction areas would be selected to give sufficient shear strength and localised bending strength to the shell, with its thickness then defining the thickness for the complete shell area. The core design parameters can therefore be specified at the outset and held fixed for optimisation. The core density only has a significant effect on local instability behaviour (wrinkling and dimpling) and these constraints are not the prime design drivers for the majority of thrust tubes. The core thickness plays an important role in determining overall stability (the core stiffness plays a lesser role), but a core thickness selected to meet local strength criteria will often satisfy stability considerations. This was checked once a core thickness had been assumed.

The remaining variables are those pertaining to the sandwich facesheets : the ply angles and the number of plies of a given angle. It was possible to limit the number of different ply orientations to two +/- angle pairs per bay since this gave a reasonable compromise between the range of properties attainable and manufacturing complexity. Where there were an odd number of plies, the centre ply was specified to be 0° to retain balanced membrane properties (A_{13} & A_{23} = 0). For separately cured facesheets it was necessary to ensure that the lay-up was symmetric such that [B] = 0 also. This resriction did not apply to co-cured facesheets assuming one facesheet was symmetric with respect to the other. There were therefore two fibre angle variables per bay of the thrust tube. It was reasonable to restrict the range of these angles to between 0° and ±45° since the predominant axial and shear stresses mean there is no neccesity to incorporate fibres at angles greater than 45° to improve facesheet material strength. This restriction was not detrimental to stiffness behaviour either, since this is dependent on only the A_{11} and A_{33} shell constitutive terms. Ply angles of greater than 45° are only beneficial in improving buckling performance and dimpling strength. However, buckling performance is dominated by the core thickness which far overrides the effect of limiting the facesheet ply

angles, and dimpling is not a primary design consideration for most thrust tube configurations.

In order to establish a sufficiently accurate picture of the constraints with respect to the two angle variables, the calculation of the constraints over a 10 x 10 grid of points defined by the intersection of the angle variables at 5° intervals (ie. 0°, 5°, 10°, ... 35°, 40°, 45°) was specified. This density of points was sufficient for the values of the constraints at intermediate angles to be determined by interpolation if a better resolution of optimum angles was required.

The ply thicknesses were considered to be fixed variables which were initially specified. These were then adjusted in the light of the constraint analysis to ensure there was a range of lay-up angles at which the design was feasible for all constraints, and with the total number of plies kept to a minimum to minimise weight. Once the minimum number of plies was found, the thrust tube weight was fixed and it was only necessary to select the values of the ply angles to optimise the design.

The adopted optimisation approach was therefore :

1. Split the thrust tube into a number of 'bays' and select the core type and thickness for each bay.

2. Select an initial total facesheet thickness for each bay and specify the lay-up sequences, which must contain only two +/- angle variable pairs, plus a single central 0° ply if there are an odd number.

3. Perform an analysis of material failure, general instability and local instability for each bay in turn for the design load cases over a 10 x 10 grid of angle combinations.

4. Adjust the total number of facesheet plies per bay and core thickness if necessary to give a set of strength-feasible designs for each bay, for the least weight.

5. Evaluate the complete thrust tube stiffness for a reduced set of ply angle variables.

6. Adjust the total number of facesheet plies if necessary to give a set of stiffness-feasible designs for the complete thrust tube, for the least weight.

7. From the final set of feasible designs select an optimum.

The analysis of the constraints over a 10 x 10 grid of ply angle combinations for specified lay-up sequences was performed by options included in FORTRAN programs described in Appendices E, F and H. These contained subroutines (using GINO) which enabled the results to be presented as isoparametric plots and interpolated contour plots of the constraints against the two ply angle variables.

The method is best illustrated by example so the optimisation of two composite faced thrust tube designs using this method are described in the following sections.

8.8 THRUST TUBE DESIGN EXAMPLE 1 : T-SAT SPACECRAFT

8.8.1 Thrust Tube Configuration

The T-Sat spacecraft is described in Appendix A.

The thrust tube was composed of two separate parts (fig. 8.18). The lower part was a truncated cone which formed the Orbit Transfer Module (OTM), housing a large solid kick motor for injecting the spacecraft into a Molniya orbit. Once on orbit, the OTM was separated from the rest of the spacecraft. The lower frame of the OTM provided the interface with a $\emptyset$ 47" adaptor on the Long March 2 launcher, and its upper frame formed the separable interface with the orbiting part of the spacecraft. An intermediate internal frame provided the mounting flange for the boost

motor. A box section belt around the exterior was proposed to take the high local bending moments at the boost motor flange.

The upper part was cylindrical, with a Ø 1 m inner diameter. This part formed the backbone of the orbiting part of the spacecraft. In addition to a lower interface frame with the OTM, two additional external frames were located on the cylinder which provided attachments for the payload and service module platforms. An internal frame at the same level as the service module provided the mounting for a conical support structure which housed liquid propellant tanks, reaction wheels and gyropack of the attitude control system. Three pairs of struts on opposite sides of the spacecraft between the equipment ±Y panels and the cylinder performed a stiffening role and were the primary load path for the sidewall equipment loads into the cylinder.

8.8.2 Materials & Manufacture

A symmetric honeycomb sandwich construction was specified for both parts of the thrust tube. Each part of the tube was to be manufactured separately. For an initial design trade-off, high modulus HM-S and high strength T-300 unidirectional carbon fibre reinforced epoxy prepreg tapes in 0.05 mm and 0.10 mm thicknesses were considered for the facesheet material. The effect of manufacturing method - whether the facesheets were separately pre-cured and bonded to the core, or whether the complete sandwich was co-cured was also investigated. Design allowable data for pre-cured HM-S and T-300 prepregs assumed were those with code 69 epoxy given in Table 3.5. Design allowable data for co-cured HM-S/Cycom 985 was based on 30 psi laminate data generated in this current work and tabulated in Table 5.6. No actual data was available for low pressure cured T-300/code 69 so these were reduced from the standard pressure cured data by applying the factors given in Table 5.9. Aluminium alloy (7075-T6) was also investigated as a facesheet material.

The honeycomb material was specified as 5056 aluminium alloy and a film adhesive with a weight of 150 g/m^2 was assumed for the facesheet to core

bonds. A core density of 2.0 lb/cu.ft.-3/16"-0.0007" was selected for the majority of the thrust tube surface area because it was the minimum practical density available, with a sufficiently small cell size to prevent dimpling or handling damage. A more substantial core of 5.7 lb/cuft.-3/16"-0.0020" was specified at the load introduction points. At a thickness of 10 mm this gave the required shear strength and was anticipated to give the required bending strength at these locations. The core was therefore initially considered to have a thickness of 10 mm in both parts of the thrust tube.

8.8.3 Stiffness Requirements & Design Loads

The T-Sat spacecraft was configured for a dedicated launch by Long March 2. The Chinese launch authority specify a minimum first lateral spacecraft frequency of 20 Hz for Long March 2 payloads - a somewhat more stringent requirement than the 10 Hz minimum for Ariane. To account for modelling idealisations and assumptions in the preliminary analysis, a design target for the first lateral mode of 25 Hz was therefore specified.

The Spacecraft-OTM preliminary finite element model (see Appendix A, fig. A.6a) was used to define internal design loads in the thrust tube under the ultimate quasi-static load cases. Typical stress and moment resultant contour plots for the thrust tube cylinder are shown in fig. 8.19. These illustrate the localisation of moments and hoop stresses around the attachment points. For the optimisation of the thrust tube design over the majority of the shell area, a number of 'worst case' axial and shear stress resultant internal load combinations were derived from the FE model. Although these apply specifically to the particular thrust tube lay-up used in the model, the general internal membrane load pattern will remain unchanged for other lay-ups. Four 'worst cases' were identified, two for the cylinder and two for the OTM, corresponding to the maximum axial and maximum shear stress resultants. These were:

O.T.M.	Max. Axial	N_x = -250 N/mm	N_{xy} = 0 N/mm
	Max. Shear	N_x = - 77 N/mm	N_{xy} = 37 N/mm

Cylinder	Max. Axial	N_x = - 96 N/mm	Nxy = 14 N/mm
	Max. Shear	N_x = - 32 N/mm	N_{xy} = 20 N/mm

Their locations on the thrust tube are shown in fig. 8.20.

8.8.4 Design Optimisation

The design optimisation method was used to generate optimum designs for the thrust tube utilising the different facesheet materials and manufacturing techniques.

8.8.4.1 Co-cured HM-S/Cycom 985 Facesheets

The facesheet material strength constraints (Tsai-Wu) for the cylindrical section of the thrust tube under the design load cases indicated that at least 4 x 0.10 mm plies would be required per facesheet. Lay-ups with the following configuration were therefore considered :

Cylinder $[+\theta/-\phi/+\phi/-\theta]$ x t_{ply} = 0.10 mm

Because the facesheets were co-cured it was permissible to adopt this unbalanced configuration. The maximum ply Tsai-Wu indices under the maximum axial and maximum shear resultant load cases were computed and plotted against the two fibre angle variables, θ & ϕ, using the program described in Appendix F. These are shown in figs. 8.21a & 8.21b. The maximum value of the Tsai-Wu index plotted on these graphs is 1.50 to give a reasonable scaling over the range of results, the graphs hence show plateaux in regions where the computed value exceeds 1.50. The plots are symmetric because the two angle varaibles are interchangeable.

For the maximum compression load case, fig. 8.21a, there is a belt of feasible designs (Tsai-Wu index less than 1.00) running diagonally across the middle of the graph from top left to bottom right. Near 0° angles in the bottom left corner are precluded due to the shear component of the load, and near 45° angles in the top right are precluded due to the axial

component. Because of the dominant axial loading, the unfeasible region of near 45° angles is the larger of the two. In fig. 8.21b, for the maximum shear load case, the magnitude of the shear stress resultant is only slightly larger than for the maximum compression case, so the size of the unfeasible region for near 0° angles in the bottom left corner is only extended slightly. The axial component of the load is much smaller than the maximum compression case, so the unfeasible region in the upper right hand corner of the graph is not as large. By combining the feasible regions under the two design load cases the feasible region for material strength in the cylinder is defined, as shown in fig. 8.22. The upper boundary is dictated by the maximum axial load case and the lower boundary by the maximum shear load case. This illustrates the importance of including both load cases in the optimisation analysis.

A similar process was carried out for the OTM part of the thrust tube under its design load cases. A minimum of 8 plies x 0.10 mm were found to be necessary and the following lay-up configurations were considered :

O.T.M. $[+\alpha/-\beta/+\beta/-\alpha/-\alpha/+\beta/-\beta/+\alpha]$ x t_{ply} = 0.10 mm

The resulting material failure feasible region is shown in fig. 8.23. The high maximum axial compression load case precludes large fibre angles and results in a smaller feasible region than for the cylinder.

The general instability of the cylinder and OTM with 2.0-3/16"-0.0007" 10 mm thick core and 4 and 8 x 0.10 mm ply facesheets respectively was checked using the program described in Appendix H. Fig. 8.24a shows the computed theoretical axial buckling stress resultant as a function of θ & ϕ for the cylinder. The axial buckling strength can be seen to be maximised towards the upper left and lower right hand corners of the graph where the lay-ups are of the form [0/+45/-45/0]. There is a trough of low buckling strength lay-ups running diagonally across the graph from the origin to the upper right hand corner where the two variable angles are equal. This suggests buckling performance under axial compression is best enhanced by arranging a wide separation in fibre angles. The depressed region of low buckling strength lay-ups in the left hand corner, near the origin, is due to a non-

axisymmetric buckling mode which arises as a result of the poor hoop stiffness of lay-ups of this type. This is comparable with the low buckling strength region for near-axial fibre lay-ups shown in fig. 8.12 and discussed in section 8.5.2.3. (Note that the interpolation process that produced the contour plots smoothes over the discontinuities arising from a change in the whole number of half-waves in the buckling mode which are shown in fig. 8.12).

The shape of the torsional buckling graph for the cylinder as a function of fibre angles, given in fig. 8.24b, shows a gradual increase in buckling loads moving from the origin towards the upper right hand corner. The torsional buckling strength is maximised at a lay-up of about [+40/-40/-40/+40] before starting to flatten off.

The computed theoretical buckling loads were reduced to allow for initial imperfections and combined under the applied load cases to give a buckling interaction index (LHS of eq.(8.5)). A knock-down factor of 0.50 was applied to the calculated axial buckling load, and a factor of 0.60 was applied to the torsional buckling load. The most severe load case regarding buckling for the cylinder was maximum axial compression. The combined buckling interaction index for this case is plotted against fibre angle variables in fig. 8.25. The interaction index was dominated by the axial component of the load, so the shape of the surface resembles a plaster cast of fig. 8.24a. The index is highest for the low hoop stiffness lay-ups in the bottom left corner and lowest for lay-ups of the form [0/ 45/ 45/0]. The index is less than 1.00 over the whole region making any of these angle combinations feasible for buckling strength. Similarly, for the OTM, all the 8 ply lay-up combinations were found to be feasible with a 10 mm 2.0-3/16"-0.0007" core.

The local instability modes of wrinkling and dimpling were found to exhibit large margins of safety for this core and all lay-up combinations in both the cylinder and OTM due to the relatively thick facesheets. The 10mm thick 2.0lb/cu.ft. was therefore found to confer sufficient stability to the thrust tube for all modes.

The stiffness of the OTM-cylinder thrust tube configuration, in terms of the spacecraft first lateral frequency, was analysed using the simple beam and lumped mass finite element approach described in section 8.3 and embodied the program described in Appendix E. The model idealisation of the spacecraft in its launch configuration was described previously in section 8.3.2 and illustrated by fig. 8.9b.

The stiffness analysis of the overall thrust tube was more complex than the previous failure mode analysis of the individual parts because all 4 angle variables had to be considered simultaneously. To analyse all the angle combinations, spaced at 5° intervals, would have required 10 x 10 x 10 x 10 calculations and it would not have been possible to display the results in the same convenient contour plot format as previously. It was hence desirable to reduce the number of free fibre angle variables. The OTM facesheet lay-ups were therefore restricted to $[0_4/\pm\alpha_2]$ by setting $\beta = 0°$, and the cylinder facesheet lay-ups were restricted to $[0_2/\pm\theta]$ by setting $\phi = 0°$. The justification for this was that lay-ups of this type (which lie along the vertical or horizontal axes of the contour plots) include those which give minimum Tsai-Wu and buckling indices. Also, the use of 0° plies aligned with the thrust tube axis offer advantages in terms of manufacturing simplicity. It is worth noting that the converse might be true (ie. larger angles prefered) if filament winding had been the intended method of manufacture.

By considering OTM facesheet lay-ups of the form $[0_4/\pm\alpha_2]$ and cylinder lay-ups of the form $[0_2/\pm\theta]$, the plot of spacecraft first lateral frequency against the angle variables α & θ given in fig. 8.26a was obtained. Because of the fairly squat spacecraft configuration and the inclusion of fixed 0° fibres in the lay-ups, the spacecraft frequency can be seen to be maximised as α & θ approach 45°. The contour value at the design frequency target of 25 Hz defines the lower limit for the angles at which the design is stiffness-feasible. Although not of prime interest from the point of view of initial design optimisation, it is interesting to compare the plot of the second spacecraft lateral frequency predicted by the model, shown in fig. 8.26b. The high second mode frequencies are for lay-ups which provide high axial stiffness in the cylinder and high shear stiffness in the OTM.

This is because the second mode is dominated by displacement of the high boost motor mass concentrated low down in the OTM. The maximum occurs for a cylinder lay-up of $[0_2/\pm 12.5]$ and OTM lay-up of $[0_4/\pm 42.5]$.

The feasible design space which satisfied all the constraints was obtained by superimposing the strength feasible limits with the stiffness feasible region defined by the 25 Hz boundary, as shown in fig. 8.27. The strength constraint boundaries were reduced to straight lines on this graph because one of the ply angle variables in each part of the thrust tube was held constant at 0°. The feasible region obtained was bounded by the stiffness constraint, the OTM facesheet failure constraint under maximum compression, and by the maximum allowable ply angle of 45° in the cylinder. All of the designs bounded by these constraints were possible minimum weight solutions. The particular design point chosen from the feasible set was an OTM facesheet lay-up of $[0_4/(\pm 20)_2]$ and a cylinder facesheet lay-up of $[0_2/\pm 45]$ since these maximised the margins of safety on the facesheet failure modes which are most susceptible to material property degradation.

8.8.4.2 Pre-cured HM-S/Code 69 Facesheets

Pre-cured HM-S carbon epoxy was considered as an alternative to co-cured facesheets to investigate the effect on the optimised design of the superior fibre direction compression strength, X_c, of the higher pressure cured material. Code 69 resin was considered as the matrix material because design allowable data for this composite system was available (Table 3.5). Stiffness properties of co-cured HM-S/Cycom 985 and pre-cured HM-S/Code 69 are essentially the same (E_1= 175GPa for the former, E_1 = 179GPa for the latter) and the only significant differences in strength allowable properties are longitudinal compression strength (X_c = 546MPa versus X_c = 344MPa) and in-plane shear strength (S= 45MPa versus S= 15MPa). The low shear strength allowable for co-cured HM-S/Cycom 985 is more a consequence of the small number of data points used to generate the allowable rather than intrinsically inferior properties.

Although the pre-cured material has superior compression strength it constrains the individual facesheet lay-ups to be symmetric about the mid-plane to avoid curing distortion. To exploit the improved compression performance, yet ensure symmetry in the lay-up, it is necessary to use thinner (and more expensive) 0.05 mm prepreg to build in sufficient plies. A minimum of 4 plies is required for a symmetric lay-up with a single angle variable, with the form : $[+\theta/-\theta/-\theta/+\theta]$. For the T-Sat thrust cylinder it was found that 5 x 0.05 mm plies of co-cured HM-S/code 69 with lay-ups of $[+\theta/-\theta/0/-\theta/+\theta]$ were necessary to give strength feasible designs under the two load cases. However, these thin facesheets (0.25 mm) meant that dimpling instability was a problem which forced a move to either thicker facesheets or a smaller honeycomb cell size. Adding an extra 0.05 mm ply was found to be a lighter alternative than going to 1/8" cell honeycomb. This also had the additional benefit of improving strength and stiffness of the shell wall. Facesheet lay-ups for the cylinder with the following configurations were considered :

$$\text{Cylinder} \qquad [+\theta/-\theta/+\phi/-\phi/-\theta/+\theta] \quad \text{x } t_{ply} = 0.05 \text{ mm}$$

Note that this lay-up configuration is not strictly symmetric unless $\phi = 0$ because coupling arises from the asymmetry of the $+\phi$ and $-\phi$ plies. By arranging these plies to be adjacent to the mid-plane the coupling effect can be minimised and it is possible to manufacture such lay-ups without excessive distortion. The pre-cured facesheets for the Skynet 4 thrust tube had a lay-up of [+10/-10/-50/+50/-10/+10] for example.

Fig. 8.28 depicts the maximum ply Tsai-Wu index against the angle variables for the above lay-ups under the cylinder maximum axial load case. The Tsai-Wu index = 1.00 contour defines a feasible region in the left hand portion of the graph, ie. where θ = 0° to 15° approximately. This suggests a large proportion of near axial fibres are required to sustain the high axial compression load. Lay-ups of this type were not precluded by the maximum shear load case because the in-plane shear strength of the unidirectional material was found to be sufficient to ensure that the complete design region was feasible.

For the OTM it was found that 6 x 0.10 mm plies with lay-ups of the form [+α /-α /+β /-β /-α /+α] gave a material strength feasible design region, but that the ply angles that fulfilled this constraint did not overlap with those necessary to confer sufficient stiffness. The same was also true for 7 plies with the central one orientated at 0°. It was necessary to increase the number of plies to 8 and consider lay-ups of the form :

O.T.M. [+α /-α /+β /-β /-β /+β /-α /+α] x 0.10 mm

The feasible region for material strength under the maximum axial load case is shown in fig. 8.29. The full region was found to be feasible under maximum shear conditions.

To reduce the number of ply angle variables for the analysis of the complete thrust tube lateral stiffness, the cylinder facesheet lay-ups were restricted to $[0_4/\pm\phi]$ x 0.05 mm, and the OTM facesheet lay-ups to $[0_4/\pm\alpha_2]$. These lay-ups gave large margins of safety on material failure and allowed a wide range for the free angle variables (α , ϕ = 0° to 45°) hence ensuring a wide range of stiffness properties. The spacecraft first lateral frequency as a function of these ply angle variables is given in fig. 8.30. The frequency is increased as both angles tend to 45°. The stiffness feasible region, bounded by the 25 Hz contour, can be seen to be somewhat smaller than the corresponding region for co-cured HM-S material, shown in fig. 8.26a, because of the thinner facesheets in the cylinder section. The selected optimum design was an OTM facesheet lay-up of $[0_4/\pm45_2]$ x 0.10 mm, and a cylinder facesheet lay-up of $[0_4/\pm45]$ x 0.05mm to maximise stiffness and minimise Tsai-Wu indices om material failure. These lay-ups combined with a 10 mm 2.0lb/cu.ft core met general and local instability constraints.

Use of precured facesheets with thinner 0.05 mm plies resulted in a thickness saving of 0.1 mm per facesheet in the cylinder over a co-cured design. There was no saving in the OTM despite the improved compression strength because of the over-riding stiffness requirement.

8.8.4.3 Pre-cured T-300/Code 69 Facesheets

Pre-cured facesheets of T-300 high strength carbon-epoxy prepreg offer the highest compression strength of the material options considered. The optimisation technique was applied to see whether such a facesheet material could offer any weight savings as a result. Allowable data for T-300/Code 69 listed in Table 3.5 was assumed.

The higher strength of this material system meant that fewer plies were required to meet the material failure constraint in the facesheets of the cylinder and OTM, but dimpling and overall stiffness considerations pushed up the minimum thicknesses to 8 x 0.05mm for the cylinder and 8 x 0.10 mm for the OTM. By reducing the number of angle variables from two to one in the cylinder it was possible to consider cheaper 0.10 mm prepreg with a symmetric lay-up of $[+\theta/-\theta/-\theta/+\theta]$.

Similarly, by considering lay-ups of $[+\alpha/-\alpha/+\alpha/-\alpha/-\alpha/+\alpha/-\alpha/+\alpha]$ x 0.10 mm for the OTM, the plot of first lateral frequency against α and θ shown in fig. 8.31 was obtained. This shows the small stiffness feasible region which exceeds the 25 Hz design target. A facesheet lay-up of $[\pm 25_4]$ x 0.10 mm was selected for the OTM and one of $[\pm 30_2]$ for the cylinder, to give a central position in the stiffness feasible region.

The use of pre-cured T-300 reinforced material resulted in the same facesheet thicknesses as co-cured HM-S, with only a small mass saving arising from its slightly lower density, because of the over-riding stiffness constraint.

8.8.4.4 Aluminium Alloy Facesheets

High strength 7075-T6 aluminium alloy was considered as a facesheet material for the T-Sat thrust tube as a yardstick for assessing the optimised carbon-epoxy designs described above. The design in aluminium was dominated by the stiffness requirement with the facesheet thicknesses in the two parts of the tube as design variables. It was therefore possible to

locate an optimum design from the graph shown in fig. 8.32, which is a carpet plot of the spacecraft first lateral frequency against total facesheet mass for different cylinder and OTM facesheet thicknesses. This was obtained using the same FE beam and mass model as for the composite tube optimisation, but with isotropic thrust tube properties substituted in the program data. The best compromise between the facesheet thicknesses in the two parts of the thrust tube was t = 0.7 mm for the OTM and t = 0.4 mm for the cylinder. The ease of locating this optimum, with only two design variables, contrasts with the steps necessary to locate an optimum for a composite design.

8.8.5 Discussion of Optimum Designs

The optimum thrust tube designs for the different materials/manufacturing methods are summarised in Table 8.5. The lightest of these had pre-cured high modulus HM-S/Code 69 facesheets making a weight saving of 34% compared to the optimum aluminium faced design. Using the same material but a less costly co-cure method of manufacture resulted in a slightly higher weight design, but still made a saving of 29% compared with aluminium alloy. The additional weight arose from extra thickness required in the facesheets of the cylinder to compensate for a reduction in compression strength. The full saving in facesheet thickness with higher strength pre-cured facesheets could not be fully realised however, because of local instability considerations with thinner facesheets. There was no extra material in the OTM facesheets because the design was stiffness critical. The optimum OTM facesheet lay-up when pre-cured was $[0_4/\pm 45_2]$ because the lateral frequency constraint forced a high shear stiffness, whereas when co-cured the optimum lay-up was $[0_4/\pm 20_2]$ to give additional axial strength. The use of pre-cured material offered higher safety margins on material failure but with co-cured facesheets the optimum design was stiffer.

The use of pre-cured T-300/Code 69 facesheets resulted in a bare structure weight between the two alternative HM-S designs, and made a saving of 32% over aluminium. The lateral stiffness constraint dictated the selection of

the optimum fibre angles at $[\pm 25_4]$ for the OTM and $[\pm 30_2]$ for the cylinder. These angles were unfavourable for confering high strength under the design loading, so the maximum ply Tsai-Wu indices using this higher strength material were comparable with the intrinsically lower strength HM-S reinforced system. For a pre-cure method of manufacture, HM-S reinforced material would therefore be preferable to T-300 because of the saving in weight for little reduction in margins of safety on material failure.

The favoured option was co-cured HM-S/Cycom 985 because it was the lowest cost alternative using composites, for reasonably low weight. The use of a pre-cured facesheet method was not considered to be worth the additional cost of manufacture to make only a further 5% weight saving. The 5% saving was due to the use of low thickness 0.05 mm prepreg which would also add to the cost. The basic T-Sat thrust tube shell construction was therefore chosen as :

O.T.M.	Facesheets:		Co-cured HM-S/Cycom 985
			[0/+20/-20/0/0/-20/+20/0] x 0.10 mm
	Core	:	5056 2.0-3/16"-0.0007" x 10 mm
Cylinder	Facesheets:		Co-cured HM-S/Cycom 985
			[0/+45/-45/0] x 0.10 mm
	Core	:	5056 2.0-3/16"-0.0007" x 10 mm

8.8.6 Attachments and Reinforcements

To the bare shell design must be added the mass of attachment rings and brackets, facesheet reinforcements, denser honeycomb, secondary bonding adhesive, inserts and fasteners. The attachments constitute the majority of the additional mass, which for the T-Sat thrust tube were aluminium alloy, and are largely independent of the basic shell design. Similarly, denser honeycomb of 5.7 lb/cu.ft at the attachments was chosen to confer the necessary local shear strength and insert load capability for a 10 mm thickness, and was hence independent of the optimum design chosen.

The facesheet reinforcements in the vicinity of the attachments serve a dual role. They carry the localised hoop stresses and bending moments where load is introduced to the shell, and equalise the stiffnesses between the shell and aluminium frame adherends to maximise bond strength. As such they are to an extent dependent on the chosen basic facesheet lay-up. Reinforcements of 4 x 0.10 mm ply UD HM-S/Cycom 985 with a lay-up of [0/0/90/0] were incorporated at all the ring attachments within the basic facesheet lay-ups selected. The 0° reinforcement gave additional axial bending moment capacity and improved stiffness for equalisation with the thicker aluminium frame adherends. The 90° reinforcement added the necessary extra hoop strength. The reinfocement lay-up was unbalanced and as such was designed to be co-cured with the basic thrust cylinder and OTM shells.

Pre-cured designs would be forced to adopt a balanced lay-up for the reinforcements, which would offset the possible saving in the number of plies due to improved compressive strength. The adherend stiffness requirement may also prevent any reduction in the thickness of reinforcements. In some cases the requirement to achieve symmetry may add unwanted plies if the number of necessary plies is small.

Tables 8.6 and 8.7 give the estimated mass breakdowns for the two parts of the thrust tube. The total mass of the cylinder was calculated to be 18.2 kg and the total mass of the OTM 27.3 kg. More than half the total mass in each case consisted of the attachments. The final cylinder and OTM designs and attachment details are shown in figs. 8.33 and 8.34.

Assuming all but the facesheets and facesheet reinforcements are identical for an aluminium sandwich construction, the selected composite thrust tube design saves a total of 10.1 kg, or 22%.

8.9 EXAMPLE 2 : PRIMUS SPACECRAFT

8.9.1 Thrust Tube Configuration

The PRIMUS (Primevial Sample Return Mission) spacecraft was a conceptual study of a spacecraft designed to rendezvous with a comet nucleus and return a core sample to earth. The spacecraft configured to fly the mission is described in Appendix I. It consisted of three modules : a Main Propulsion Stage (MPS), a Lander (LDR) and a Re-entry Capsule, and was designed for launch on Ariane 5.

A thrust tube structure provided the backbone of the spacecraft in its launch configuration. This was divided into two parts by the LDR-MPS separation plane, as in shown in fig. 8.35[65]. The lower part, within the MPS, consisted of a truncated cone which interfaced at its lower circumference with the Ø 2624 mm Ariane 5 equipment bay, and tapered to a Ø 1900 mm upper cylindrical section. The main propellant tanks were mounted around this cylinder and the liquid engines within it. The thrust tube within the Lander also had a lower conical section and an upper cylinder. The lower diameter of the cone interfaced with the Ø 1900 mm cylinder in the MPS module, and tapered to the cylinder diameter of Ø 1200 mm. The Re-entry capsule was located within the conical part of the thrust tube of the Lander but was attached to the upper diameter of the MPS cylinder.

8.9.2 Materials & Manufacture

As with the T-Sat spacecraft, both high strength (T-300) and high modulus (HM-S) unidirectional carbon fibre reinforced epoxy prepregs were considered as candidate materials for a symmetric sandwich shell construction. Ply thicknesses of 0.05 mm and 0.10 mm were considered, and the effect of pre-curing the facesheets or co-curing them with the core was investigated. The LDR and MPS parts of the thrust tube were considered to be manufactured separately, allowing the shell construction in each of these two parts to be optimised independently. Because of the large size of the lower MPS thrust tube, this would have to be manufactured in segments

(facesheet segments if pre-cured, sandwich shell segments if co-cured) and bonded together with splices. Design allowables assumed, were those given in Table 3.5, with the appropriate knock-down factors of Table 5.9 applied for co-cured facesheets.

A honeycomb of 5056 2.0-3/16"-0.0007" was assumed for the majority of the thrust tube area. A minimum thickness of 10 mm in the MPS and 8 mm in the LDR was considered to be sufficient for insert pull out strength with a denser honeycomb at attachments, and to confer a reasonable local bending moment capacity. A film adhesive of 150 g/m^2 was assumed for the facesheet to honeycomb bonds.

8.9.3 Stiffness Requirements & Design Loads

The overall thrust tube stiffness requirement dictated by the launcher was a minimum lateral frequency of 10 Hz. A stiffness design target of 15 Hz was proposed.

The spacecraft configuration was not known in sufficient detail to enable an FE model of the structure to be generated, and hence the axial and shear membrane loads in the thrust tube shell walls were not known with any certainty. In order to begin preliminary design optimisation of the thrust tube design, it was proposed to use factored quasi-static loads combined with a simple beam representation of the thrust tube, and then to simply multiply the calculated stress resultants by a factor of 2 to allow for uneven load introduction (this ratio of maximum to average load intensity was typical on the T-Sat spacecraft). The highest loading on the structure occured during launch, when all fuel tanks were full, a single enveloped design quasi-static acceleration case of -8.75g vertically and 4.375g horizontally was used. Applying these to a simple point loaded beam model of the thrust tube and factoring by 2 resulted in the following 'worst case' internal loads :

MPS	Max. Axial	N_x = -360 N/mm	N_{xy} = 0 N/mm
	Max. Shear	N_x = -190 N/mm	N_{xy} = 190 N/mm

LDR	Max. Axial	N_x = - 54 N/mm	N_{xy} = 0 N/mm
	Max. Shear	N_x = - 30 N/mm	N_{xy} = 28 N/mm

The loads in the Main Propulsion Stage were considerably higher than in the Lander due to the large fuel load and higher bending moments on this lower module.

8.9.4 Design Optimisation

The design optimisation was carried out using the previously described procedure for different facesheet materials and manufacturing processes. Two fibre angle variables were considered for each part of the thrust tube.

8.9.4.1 Pre-cured T-300/Code 69 Facesheets

The wide base and low cenre of mass of the fuel tanks, yet high membrane loading in the thrust tube walls suggested that the design would be determined mainly by strength rather than stiffness considerations. Pre-cured T-300/epoxy offered the highest compressive strength of the composite systems short-listed, so was investigated initially.

The Lander section was relatively lightly loaded, and it was found that 4 x 0.05 mm plies were sufficient to meet the strength constraints. Fewer than 4 plies was not possible because of the manufacturing constraint that requires a balanced lay-up. (Only $[0_3]$ would be a balanced 3-ply lay-up, but this has insufficient shear strength and dimpling stiffness). The lay-up possibilities were limited to lay-ups of the form :

LDR $[+\theta/-\theta/-\theta/+\theta]$ x 0.05 mm

with only a single fibre angle variable, θ. Fig. 8.36 plots the maximum ply Tsai-Wu index against the angle θ for the two design load cases. The curves define a feasible region (Tsai-Wu index less than 1.0) for angles between

about 5° and 40°, with minimum indices at about 25°. Such a lay-up was found to confer sufficient dimpling stiffness.

The much higher loaded MPS section was found to require a minimum of 10 x 0.10 mm plies for facesheet strength. Lay-ups of the form :

$$\text{MPS} \qquad [+\alpha/-\alpha/+\beta/-\beta/+\alpha/-\alpha/-\beta/+\beta/-\alpha/+\alpha] \quad \text{x } 0.10 \text{ mm}$$

were investigated. This lay-up exhibits slighty asymmetry in the centre plies but would not preclude pre-curing the facesheets separately. Figs. 8.37a and 8.37b are plots of the maximum ply Tsai-Wu index as a function of the angle variables, α and β , for the maximum axial and maximum shear load cases respectively. Because the facesheet lay-up is biased (there are more plies at α than at β), these plots are not symmetric about the diagonal. The two load cases define upper and lower bounds for the allowable ply angles to meet the facesheet strength requirement.

Because of the concentration of mass in the MPS module of the spacecraft and the thicker facesheets of the thrust tube in this part, the LDR facesheet lay-up had only a small effect on the overall lateral stiffness of the spacecraft. A facesheet lay-up of $[\pm 25_2]$ x 0.05 mm was therefore considered for the LDR to maximise the margin of safety on strength, and the MPS fibre angles were allowed to vary to meet the 15 Hz stiffness constraint. This resulted in lay-ups which gave lateral frequencies close to 15 Hz, but none which exceeded it. The shear stiffness of the LDR thrust tube was therefore increased by going to a $[\pm 30_2]$ lay-up which gave the necessary small increase in lateral frequency for only a slight degradation in predicted strength and for no extra mass. The resulting plot of first lateral frequency as a function of the MPS fibre angles, α and β , is given in fig. 8.38. There is a small stiffness feasible region for fairly high shear stiffness MPS facesheet lay-ups, with the first lateral frequency maximised for lay-ups of about $[\pm 30_5]$. By superimposing the facesheet strength constraints on the MPS lay-up, from figs. 8.37a & b, on that of the stiffness constraint results in an overall feasible region as shown in fig. 8.39. The overlap of the constraints results in only a small feasible

region. A lay-up of $[\pm 25_3/\pm 30_2]$ was selected from this region to give the best compromise between strength and stiffness.

Because of the confined feasible design region, the lay-ups were forced to contain similar angles (ie. lay-ups close to the diagonal of the graphs) which resulted in a poorer buckling strength than if the angles had a wide separation. It was found that the selected lay-ups for both the MPS and LDR combined with the minimum core thicknesses of 10 mm and 8 mm were insufficient to confer the required buckling capability. The lowest weight solution to this inadequacy was to increase the core thicknesses, rather than add additional facesheet plies. The MPS core was increased to 14 mm and the LDR core to 10 mm to give positive safety margins on buckling.

8.9.4.2 Co-cured T-300/Code 69 Facesheets

The effect of co-curing T-300/Code 69 facesheets was studied to determine the weight penalty, if any, incurred for a simplification of the manufacturing process. The co-cured material was assumed to exhibit a reduction in compression strength (as per Table 5.9) resulting from the lower cure pressure, but gave additional freedom in the choice of facesheet lay-ups since they were not constrained to be symmetric.

The additional freedom was exploited in the LDR thrust tube. At least 4 plies were required for strength, but these could have unbalanced lay-ups of the form :

$$\text{LDR} \quad [+\theta/-\phi/+\phi/-\theta] \times 0.05 \text{ mm}$$

The maximum ply Tsai-Wu indices calculated for the range of possible lay-ups under the two design load cases defined the feasible region shown in fig. 8.40. Along the diagonal ($\theta = \phi$), the feasible region extends from about $\theta = \phi = 15°$ to $30°$, which is somewhat less than the range of $5°$ to $40°$ found for pre-cured facesheets, and the lowest Tsai-Wu index is higher. But the extra freedom allowed by a second angle variable extends the feasible region to the upper left and lower right corners of the graph.

Here, at a strength optimum lay-up of [±10/±45], the highest Tsai-Wu index is 0.655 (under the maximum shear load case) which is comparable with an index of 0.549 for the optimum pre-cured lay-up, despite the much superior longitudinal compression strength of the latter.

The additional freedom of lay-up design could not be exploited in the MPS thrust tube because the larger number of plies meant it was possible to achieve symmetry in pre-cured facesheets without any constraints on the choice of angles. The lower compression strength of co-cured material dictated that a minimum of 12 x 0.10 mm plies, an extra 2 over pre-cured material, were required. Lay-ups of the form :

$$\text{MPS} \qquad [+\alpha/-\alpha/+\beta/-\beta/+\alpha/-\beta/+\beta/-\alpha/-\beta/+\beta/-\alpha/+\alpha] \quad \text{x } 0.10 \text{ mm}$$

were considered. A fairly narrow band of feasible lay-ups, as shown in fig. 8.41, was defined by the material strength constraints under the two design load cases.

General Instability was investigated using the program described in Appendix H. The LDR thrust tube was found to have sufficient buckling strength in both cylindrical and conical sections under the applied loading conditions for the range of possible facesheet lay-ups on an 8 mm core. The MPS cone, with its large diameter, on the other hand, was found to be susceptible to buckling with a 10 mm core. By considering the full range of lay-ups, plots of the interactive buckling index under the two design load cases were obtained, figs. 8.42a and 8.42b. These defined a buckling feasible design region which further limited the choice of fibre angles. Because of the additional thickness of the facesheets, it was not necessary to increase the core thickness, as with the pre-cured material, so long as the lay-up was in this region. The buckling indices can be seen to be minimised for lay-ups close to $[0_6/\pm 45_3]$.

By fixing the LDR facesheet lay-up at [±10/±45] x 0.05 mm to maximise strength, the stiffness constraint on $[\pm\alpha_3/\pm\beta_3]$ x 0.10 mm MPS facesheet lay-ups was investigated. This is shown by the 15 Hz contour in fig. 8.43 which plots the spacecraft lateral frequency against the angle variables α

and β . By superimposing all the design constraints on the range of possible α and β fibre angle combinations for the MPS, the feasible region which satisfies all the constraints was constructed. This is shown in fig. 8.44. Only two small feasible regions (which are the same since α and β are interchangeable) in the top left and bottom right corners were found. These are bounded mainly by the buckling and material strength (max. axial load case) constraints. An MPS facesheet lay-up of $[0_6/\pm45]$ x 0.10 mm was selected from the feasible region because it gave the best compromise of maximising the safety margins on the various failure modes.

8.9.4.3 HM-S/Code 69 Facesheets

Because of the over-riding strength constraint, high modulus reinforced facesheets, both in pre-cured and co-cured form were found to be uncompetitive with T-300 fibre reinforcement. More than 12 x 0.10 mm plies were required in the MPS thrust tube facesheets for sufficient strength. This material was therefore not investigated any further.

8.9.4.4 Aluminium Alloy Facesheets

7075-T6 high strength aluminium alloy facesheets were considered for the PRIMUS thrust tube to enable the mass savings through the use of composites to be evaluated.

As with the T-Sat thrust tube, the major design driver for aluminium faced sandwich construction was the overall lateral stiffness. Fig. 8.45 shows a plot of the spacecraft first lateral frequency against total thrust tube facesheet mass for different MPS and LDR facesheet thicknesses. The minimum facesheet thicknesses were limited to 0.15 mm in the LDR to avoid dimpling, and to 0.65 mm in the MPS by material yielding. The lowest weight solution which exceeded the 15 Hz stiffness target had MPS facesheets of 0.90 mm and LDR facesheets of 0.20 mm. General instability calculations showed that the nominal core thicknesses of 10 mm in the MPS and 8 mm in the LDR were sufficient to give the necessary buckling resistance.

8.9.5 Discussion of Optimum Designs

The optimised designs for the PRIMUS thrust tube with pre-cured and co-cured T-300/Code 69 and aluminium alloy facesheets are summarised in Table 8.8. The heaviest of these was the aluminium design with a total bare mass of 113.7 kg. The optimised pre-cured T-300/Code 69 facesheets saved 31% of this mass, and the co-cured facesheets made a saving of 23%.

The optimum fibre angles for the pre-cured T-300/Code 69 facesheets were dictated largely by the spacecraft lateral frequency requirement, and buckling requirements determined the core thicknesses. The additional core thickness required in the LDR thrust tube over the co-cured facesheet design, in which the unsymmetric lay-up gave better buckling resistance, resulted in a slightly higher weight for this part of the tube. This was more than compensated for however, by the saving of 2 plies per facesheet in the much larger MPS part of the thrust tube. Co-cured facesheets were not competitive in the MPS because there was no advantage in being able to utilise unsymmetric lay-ups with large numbers of plies, and the reduction in compressive strength was disadvantageous in this particular case.

One design solution is a hybrid configuration utilising co-cured T-300/Code 69 facesheets in the upper LDR part of the thrust tube and pre-cured facesheets in the MPS. These were the lowest weight options for the two parts, and combined they meet the 15 Hz stiffness target. Use of co-cured facesheets in the LDR gives an extra 0.5 kg saving over a pre-cured design plus a cost saving in manufacture. For the large diameter MPS it is likely that pre-curing the facesheets, rather than attempting the co-cure of large sandwich segments, will be the preferable method of production and the weight saving of 8.9 kg justified this. The prefered design was therefore :

MPS	Facesheets:	Pre-cured T-300/Code 69	
		[+25/-25/+30/-30/+25/-25/-30/+30/-25/+25] x 0.10 mm	
	Core :	5056 2.0-3/16"-0.0007" x 14 mm	

LDR	Facesheets:	Co-cured T-300/Code 69	
		[+10/+45/-45/-10] x 0.05 mm	
	Core	:	5056 2.0-3/16"-0.0007" x 8 mm

8.10 CONCLUSIONS

Thrust tubes are the most common primary members in spacecraft structures and composite faced sandwich shell construction offers one of lowest weight and lowest cost design solutions for these components. In this chapter the analysis of the major constraints on thrust tube design, in terms of stiffness and modes of failure, have been described for composite faced sandwich construction. These analysis methods were incorporated in computer programs and these were used in a scheme for thrust tube design optimisation.

For the analysis of stiffness, a simple but effective FE approach was adopted in which the thrust tube was modelled as a beam and the spacecraft as lumped masses. Spacecraft lateral mode frequencies were obtained and found to correlate well (for the first 2 modes) with much more complex plate & shell FE models, provided that thrust tube shear stiffness and spacecraft rotational inertia were included. A plate & shell model of the T-Sat spacecraft was later found to correlate with a modal survey test (Chapter 9) suggesting in turn that the beam & mass formulation gives a good representation of the actual spacecraft mass distributionand thrust tube stiffness.

For the analysis of general instability, an interactive buckling expression using theoretical buckling loads under pure compression and pure torsion was adopted. It was assumed that the torsional buckling load was equal to the maximum lateral shear buckling load. Equivalent radii and lengths were assumed for conical geometry. Existing small deflection theories for orthotropic faced sandwich cylinder buckling under these loading actions were modified and re-expressed in terms of the shell constitutive matrices for more general composite constructions. Numerical examples showed large errors if simplifying assumptions were used to reduce the problems to

closed form solutions. The often adopted axisymmetric solution for axial buckling of metallic cylinders was found to be inappropriate for composite constructions with low hoop stiffness. The use of more complex general solutions was therefore found to be necessary. The effect of core shear for both axial and torsional buckling was found to be of the order of 10% for typical thrust tube constructions.

The application of an established numerical optimisation scheme to composite faced sandwich thrust tubes was found to have several drawbacks. These arose from the presence of discrete and continuous design variables, and the definition of a suitable objective function. The structure weight was not in itself a sufficient definition of the optimisation objective because the variation in fibre orientation allows several 'optima' of the same weight but with different properties to be found. A less automatic method which gave the designer more control and insight into the optimisation process was found to be more appropriate. This approach was made feasible by making some practical assumptions which reduced the number of design variables.

The optimisation method was described with reference to two thrust tube examples. Optimum designs were found for different composite material systems. The optimum designs both minimised weight and maximised safety margins on failure modes, and took into consideration manufacturing requirements. The effect of a co-cured manufacturing technique was investigated by assuming reduced material properties and allowing greater freedom in facesheet lay-ups. This showed that the co-cured technique, with lower attendant costs, was advantageous where the number of facesheet plies was small (greater lay-up freedom) and where the design was stiffness dominated (little stiffness degradation due to low pressure cure). Where the number of plies was large and where facesheet material strength was the dominant constraint, pre-cured facesheets resulted in lighter designs. In these instances, co-cured designs still made large savings over aluminium alternatives and the saving in manufacturing cost may justify the small mass penalty over pre-cured designs.

TABLE 8.1 QUASI-STATIC LAUNCHER LOADS

ARIANE 4

Flight event	Loads	Acceleration (g)	
		Longitudinal	Lateral axis
Maximum dynamic pressure	QSL	- 3.0	± 1.5
	S + D	- 2 ± 1.0 (5 to 100Hz)	± 0.2 ± 0.4 (5 to 100 Hz)
Before thrust termination	QSL	- 7.0	± 1.0
	S + D	- 4.5 ± 1.0 (5 to 100 Hz)	± 0.8 (5 to 18 Hz) ± 0.6 (18 to 100 Hz)
During thrust tail-off	QSL	+ 2.5	± 1.0
	S + D	± 1.0 (5 to 100 Hz)	± 0.8 (5 to 18 Hz) ± 0.6 (18 to 100 Hz)

The minus sign with longitudinal axis values indicates compression.

Lateral loads may act in any direction simultaneously with longitudinal loads.

The Quasi-Static Loads (QSL) apply uniformly all over to spacecraft.

The Static (S) loads combined with the Dynamic (D) loads (sinusoidal vibrations) are induced at the base of the spacecraft.

These loads apply for spacecraft complying with :
- the frequency requirements of para. 4.5.3.
- the static moments of para. 4.5.1.

LONG MARCH 2F

LOAD CASE	LONGITUDINAL			LATERAL
	STATIC	DYNAMIC	TOTAL	TOTAL
Max. Dynamic Pressure	-2.3	0.6	-1.7 -2.9	1.0
FECO	-6.4	+0.5 -0.7	-5.9 -7.1	0.6
$1^{st}/2^{nd}$ Stage Separation	-1.4	7.0	+5.6 -8.4	0.3

TABLE 8.2 PRELIMINARY QUASI STATIC DESIGN ACCELERATIONS

LAUNCHER	LOAD CASE	FACTORED FLIGHT LOADS (G)	
		AXIAL	LATERAL
SKYNET 4 PRELIMINARY STATIC ANALYSIS			
SHUTTLE/ PAM-D (1)	MAX LONG (COMP)	-7.7	5.9
	MAX LONG (TENS)	+5.6	8.0
	MAX LATERAL	-5.1	8.0
DELTA (2)		-13.5	2.5
ARIANE	SECO	-12.6	3.6
	MAX DYN PRESSURE	-6.6	7.0
	ABM BURN	-8.4	66 RPM
ARABSAT PRELIMINARY STATIC ANALYSIS			
SHUTTLE/ PAM-D	MAX LONG (COMP)	-7.5	5.25
	MAX LONG (TENS)	+4.95	7.65
	MAX LATERAL	-4.95	7.65
	PAM-D BURN	-9.0	0
	EMERGENCY LANDING	+20.0	4.5
		-4.5	
ARIANE 4	MAX LONG (COMP)	-10.5	1.5
	MAX LONG (TENS)	+3.75	1.5
	MAX LATERAL	-4.5	2.25
CS-3 PRELIMINARY STATIC ANALYSIS			
H-I (3)	LIFT OFF	+3.6	3.0
		-1.5	
	MECO-POGO	-14.7	1.5
INTELSAT V PRELIMINARY STATIC ANALYSIS			
ARIANE	FECO	+1.2	0.3
		-7.8	
	SECO	-8.6	0.2
	MAX DYN PRESSURE	-4.0	1.6
	ABM BURN	-7.0	0
ATLAS CENTAUR	BECO	-9.0	2.2
	MECO	+2.3	0.6
		-6.8	
	ABM BURN	-7.0	0

NOTES:

(1) Factor by 1.4 for Ultimate
(2) Factor by 1.5 for Ultimate
(3) Factor by 1.25 for Ultimate

TABLE 8.3 COMPOSITE SANDWICH THRUST TUBE DESIGNS

SPACECRAFT	MATERIAL SYSTEM	CORE	FACESHEET LAY-UP
INTELSAT V	HYBRID T-300 Woven HM-UD	2.0-3/16"-0.0007" 5 mm - 7 mm	Inner Facesheet = 0.3 mm Outer Facesheet = 0.6 mm, 0.7 mm
ARABSAT	HYBRID HM/G837 Woven HM/V108 UD	10 mm	$[45_W/0_{UD}/45]$ to $[45_W/0_{3UD}/45_W]$ (0.3 mm to 0.5 mm)
ARABSAT (Co-cured Version)	HM/914 UD	10 mm	[+45/0/-45] to $[+45/0_3/-45]$ (0.3 mm to 0.5 mm)
SKYNET IV	HMS/Code 87 UD	2.0-3/16"-0.0007"	[+10/-10/-50/+50/-10/+10] (0.6 mm)
OLYMPUS (LPM)	T-300/Code 92 UD	2.0-3/16"-0.0007" 10 mm	[+25/-25/0/-25/+25] (0.25 mm)

TABLE 8.4 COMPUTED LATERAL MODE FREQUENCIES FOR 6 DOF AND 1727 DOF MODELS

OTM : $[0_4/(\pm 30)_2]$ HM-S/985 Facesheets
CYLINDER : [±15/±45] HM-S/985 Facesheets

MODEL	FIRST LATERAL (Hz)	SECOND LATERAL (Hz)
Full Dynamic 1727 d.o.f.	30.54	50.07
Lumped Mass 6 d.o.f.	30.09	51.44

TABLE 8.5 OPTIMUM DESIGNS FOR T-SAT THRUST TUBE

MATERIAL SYSTEM	BAY	t_{ply} (mm)	LAY-UP	CORE[1] DEPTH (mm)	TSAI-WU INDEX MAX. AXIAL	TSAI-WU INDEX MAX. SHEAR	BUCKLING INDEX MAX. AXIAL	BUCKLING INDEX MAX. SHEAR	FIRST FREQY (Hz)	BARE MASS[2] (kg)		%
HM-S/985	CYL	0.10	$[0_2/\pm45]$	10	0.714	0.272	0.253	0.092	27.6	6.635	16.187	71
CO-CURED	OTM	0.10	$[0_4/\pm20_2]$	10	0.714	0.454	0.488	0.169		9.552		
HM-S/69	CYL	0.05	$[0_4/\pm45]$	10	0.387	0.316	0.364	0.145	25.5	5.506	15.058	66
PRE-CURED	OTM	0.10	$[0_4/\pm45_2]$	10	0.622	0.089	0.348	0.114		9.552		
T-300/69	CYL	0.10	$[\pm30_2]$	10	0.641	0.215	0.507	0.185	25.6	6.389	15.420	68
PRE-CURED	OTM	0.10	$[\pm25_4]$	10	0.626	0.210	0.634	0.208		9.031		
7075-T6	CYL	-	t = 0.4mm	10	0.340(3)	0.113(3)	0.277	0.103	25.7	9.672	22.810	100
AL. ALLOY	OTM	-	t = 0.7mm	10	0.434(3)	0.154(3)	0.311	0.101		13.138		

(1) Core type for all designs is 5056 2.0lb/cu.ft-3/16"-0.0007"

(2) Bare Mass is Facesheets + Core + Film Adhesive, neglecting reinforcements, frames etc.

Assumed densities : HM-S/epoxy = 1650 kg/m^3

T-300/epoxy = 1560 kg/m^3

7075-T6 alloy = 2760 kg/m^3

Film adhesive = 150 g/m^2

Area of Cylinder = 3.42 m^2 Area of OTM = 2.93 m^2

(3) Based on Maximum Principal stress

TABLE 8.6 T-SAT THRUST CYLINDER ESTIMATED MASS BREAKDOWN

COMPONENT		MASS (kg)
FACE-SHEETS	$[0_2/\pm45]$ x 0.10 mm	4.51
	REINFORCEMENTS	0.80
FILM ADHESIVE 150 g/m^2		1.03
HONEY-COMB	2.0 lb/cu.ft x 10 mm	0.83
	5.7 lb/cu.ft x 10 mm	0.77
ATTACH-MENTS	OTM INTERFACE	2.97
	BOTTOM COVER	0.66
	SM & AOCS PLATFORMS	4.13
	PAYLOAD MODULE	1.14
	STRUT BRACKETS (6 off)	0.52
INSERTS, FASTENERS etc.		0.80
TOTAL		18.16

TABLE 8.7 T-SAT OTM ESTIMATED MASS BREAKDOWN

COMPONENT		MASS (kg)
FACE-SHEETS	$[0_4/\pm 20_2]$ x 0.10 mm	7.74
	REINFORCEMENTS	0.61
	FILM ADHESIVE 150 g/m^2	0.88
HONEY-COMB	2.0 lb/cu.ft x 10 mm	0.62
	5.7 lb/cu.ft x 10 mm	0.65
ATTACH-MENTS	CZ-2 INTERFACE	6.91
	STAR 37XFP MOTOR	2.76
	BOX SECTION BELT	2.68
	T-SAT INTERFACE	3.85
	INSERTS, FASTENERS etc.	0.61
	TOTAL	27.31

TABLE 8.8 OPTIMUM DESIGNS FOR PRIMUS S/C THRUST TUBE

MATERIAL SYSTEM	BAY	t_{ply} (mm)	LAY-UP	CORE(1) DEPTH (mm)	TSAI-WU INDEX MAX. AXIAL	TSAI-WU INDEX MAX. SHEAR	BUCKLING INDEX MAX. AXIAL	BUCKLING INDEX MAX. SHEAR	FIRST FREQY (Hz)	BARE MASS(2) (kg)		%
T-300/69	MPS	0.10	$[\pm 25_2/\pm 30_2]$	14	0.893	0.785	0.977	0.803	15.0	69.04	78.97	69
PRE-CURED	LDR	0.05	$[\pm 20_2]$	10	0.364	0.549	0.547	0.755		9.93		
T-300/69	MPS	0.10	$[0_6/\pm 45_3]$	10	0.674	0.845	0.503	0.678	15.0	77.90	87.31	77
CO-CURED	LDR	0.05	[±10/±45]	8	0.636	0.655	0.796	0.855		9.41		
7075-T6	MPS	-	t = 0.9mm	10	0.556(3)	0.474(3)	0.610	0.274	15.3	100.39	113.70	100
AL. ALLOY	LDR	-	t = 0.2mm	8	0.389(3)	0.325(3)	0.265	0.122		13.31		

(1) Core type for all designs is 5056 2.0lb/cu.ft-3/16"-0.0007"

(2) Bare Mass is Facesheets + Core + Film Adhesive, neglecting reinforcements, frames etc.
Assumed densities : T-300/epoxy = 1560 kg/m^3
7075-T6 alloy = 2760 kg/m^3
Film adhesive = 150 g/m^2
Area of MPS = 17.850 m^2 Area of LDR = 7.979 m^2

(3) Based on Maximum Principal stress

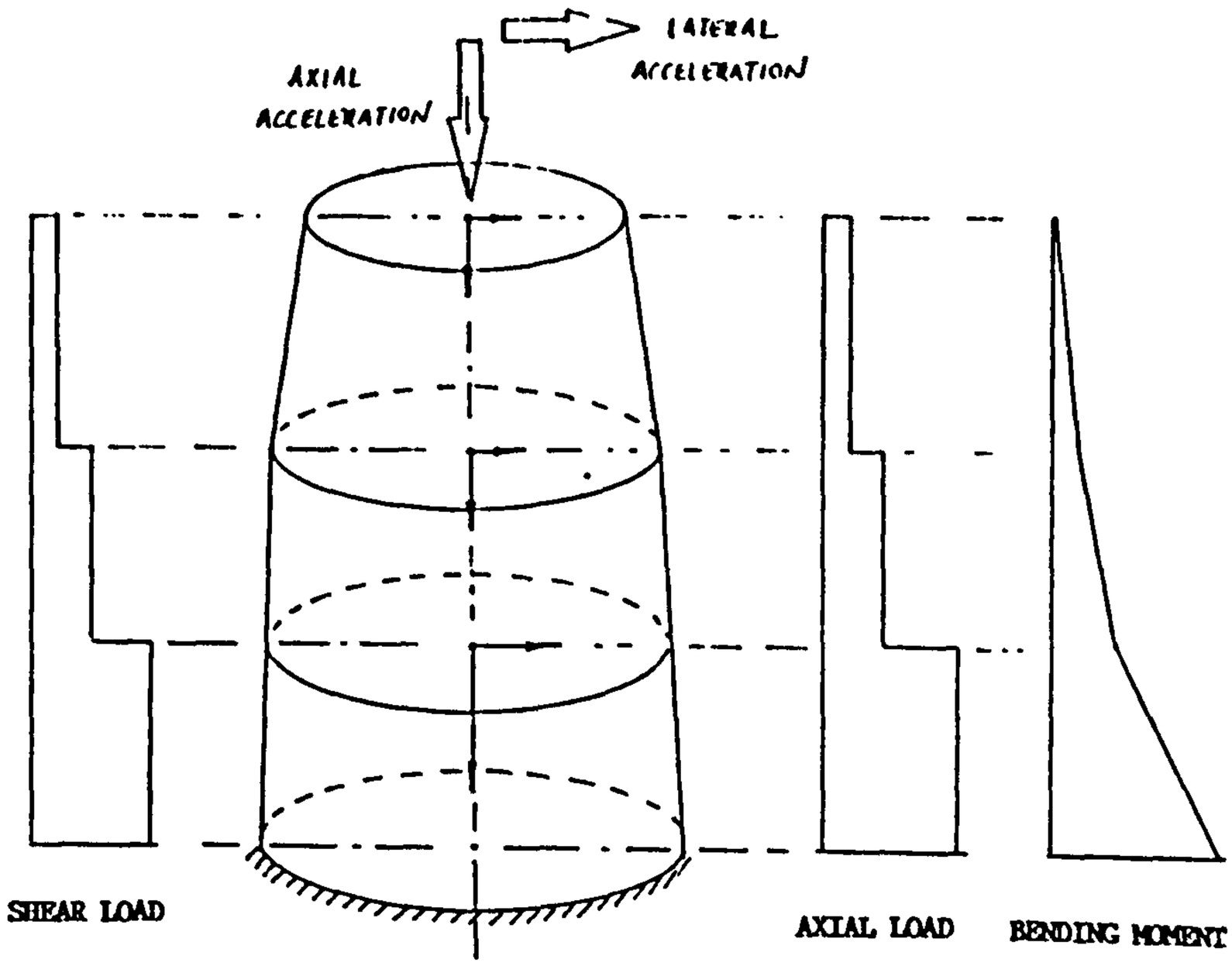

Fig. 8.1 TYPICAL LOADING IDEALISATION ON THRUST TUBE

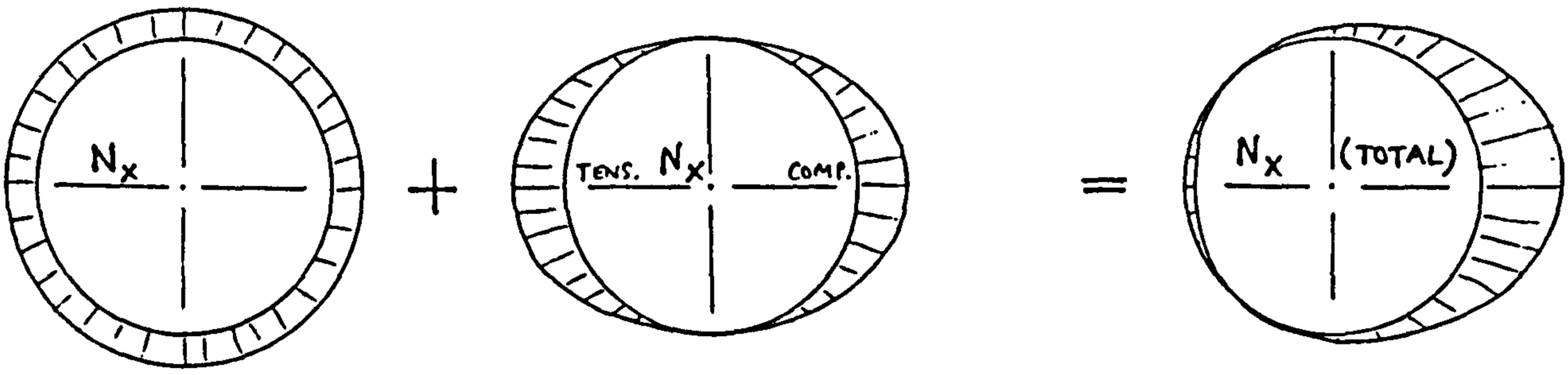

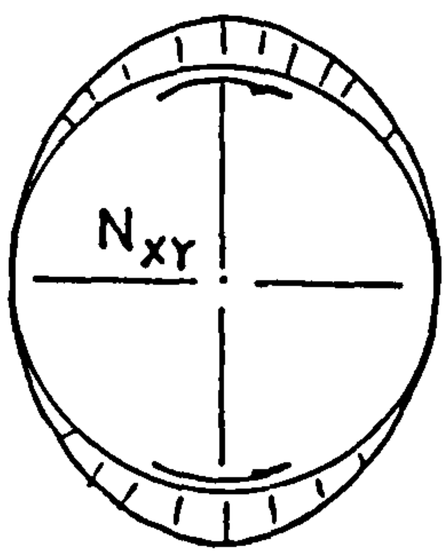

Fig. 8.2 INTERNAL THRUST TUBE LOADS

Fig. 8.3 THRUST TUBE CONSTRUCTION TYPES

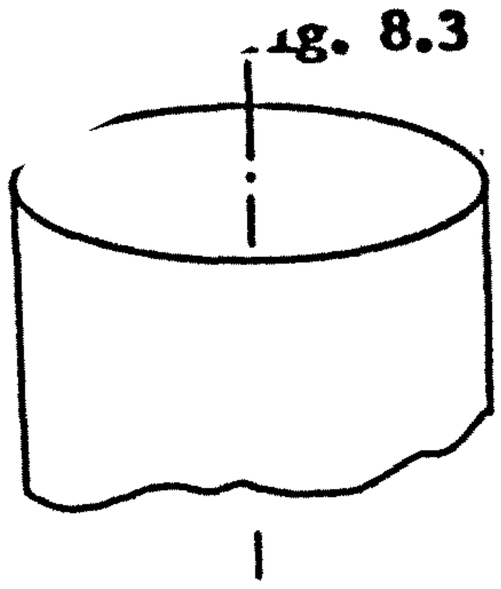

MONOCOQUE/PLAIN SHELL

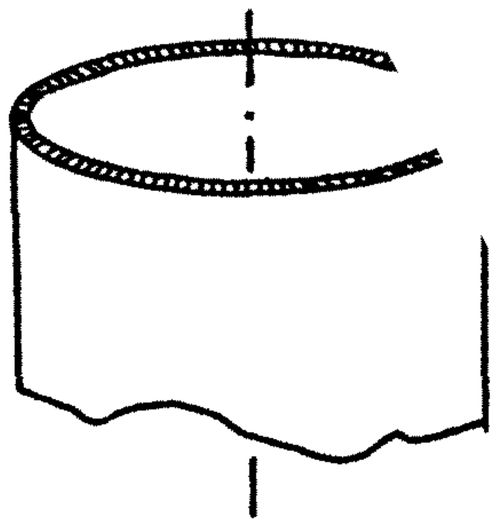

SANDWICH

(SYMMETRIC OR UNSYMMETRIC)

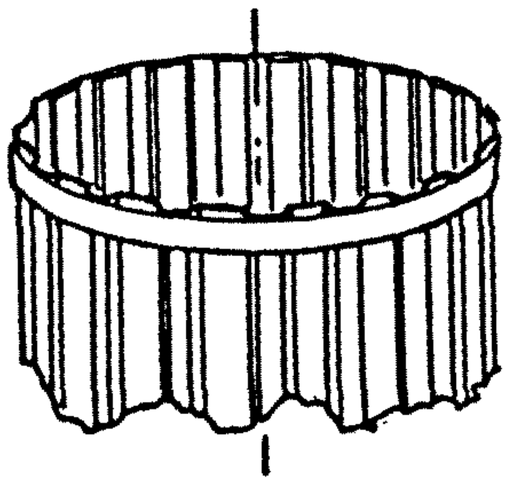

CORRUGATED (WITH BELTS)

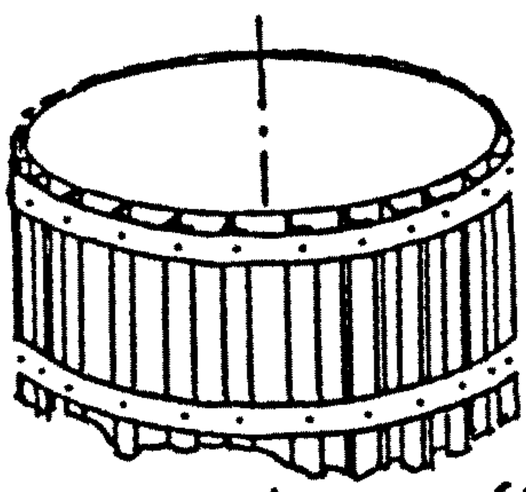

EXTERNALLY STIFFENED

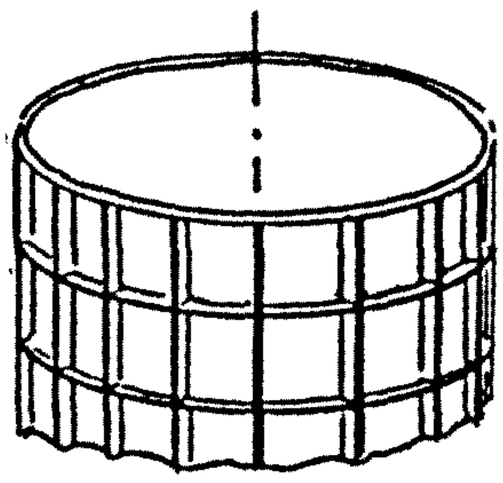

(ALSO INTERNAL STIFFENERS)

BLADE, TOP HAT, J, Z STIFFENERS

INTEGRALLY STIFFENED WAFFLE

(ALSO ISOGRID, ANGLED STIFFENERS)

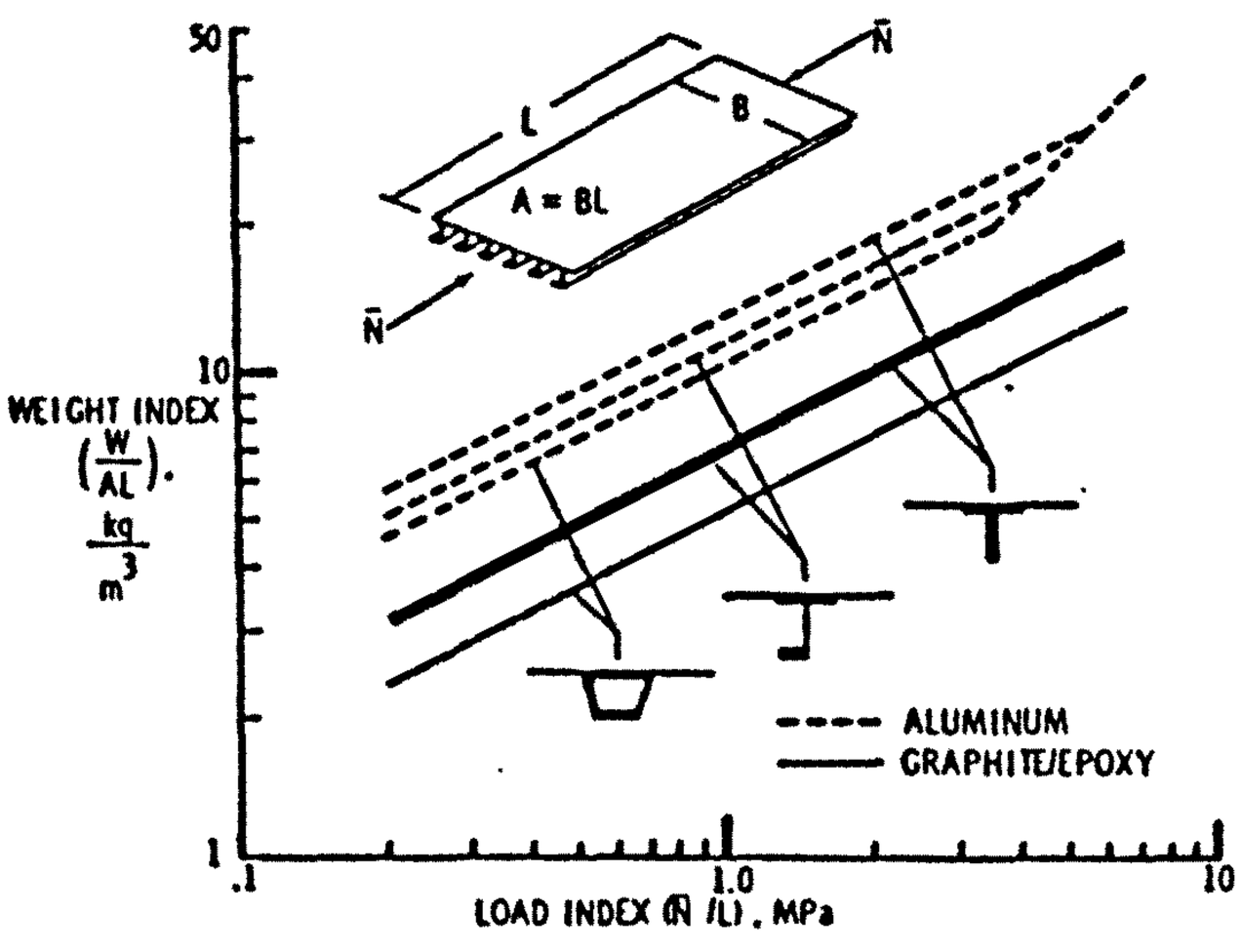

8.4 STRUCTURAL EFFICIENCY OF STIFFENER TYPES

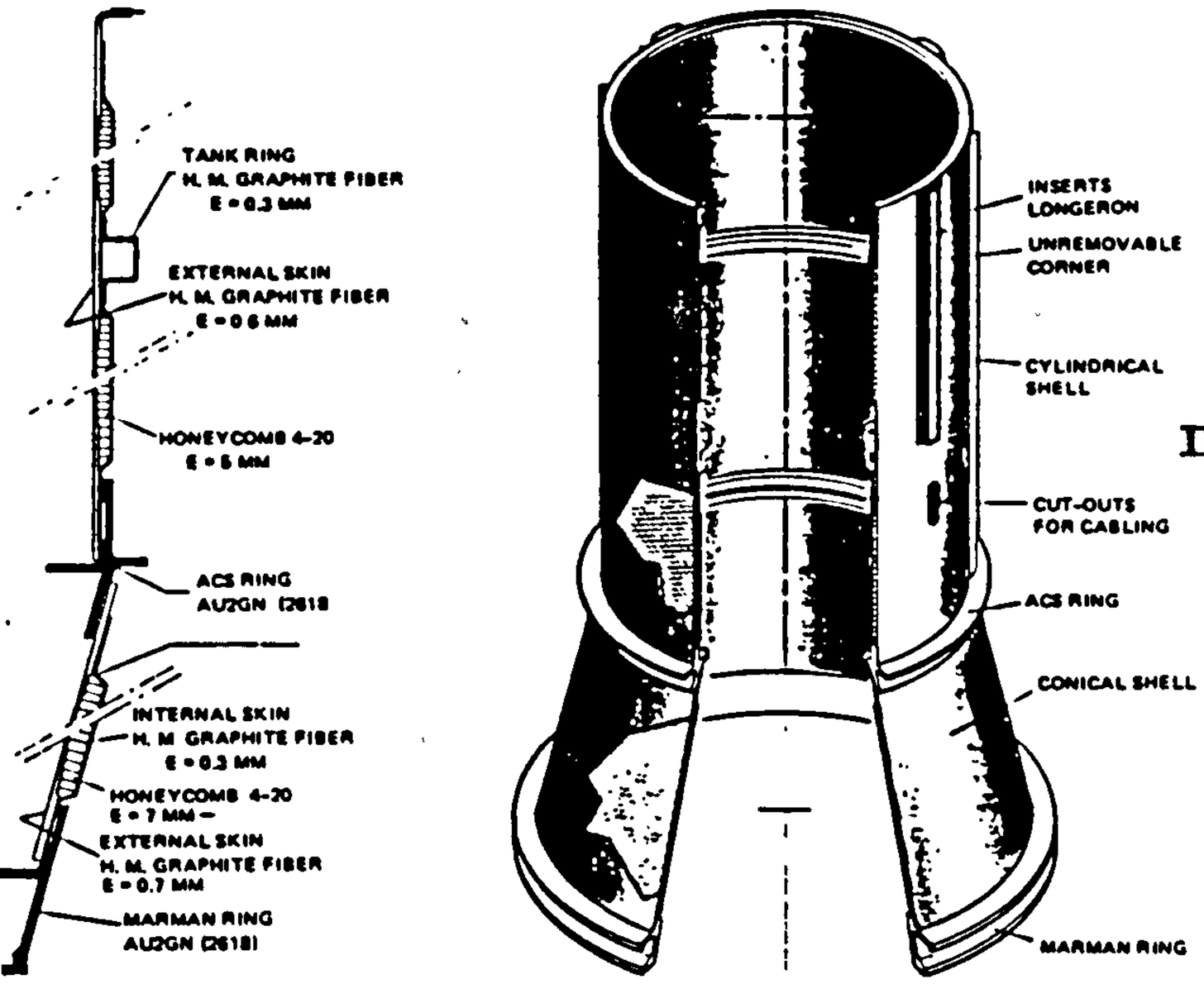

Fig. 8.5a

INTELSAT V THRUST TUBE

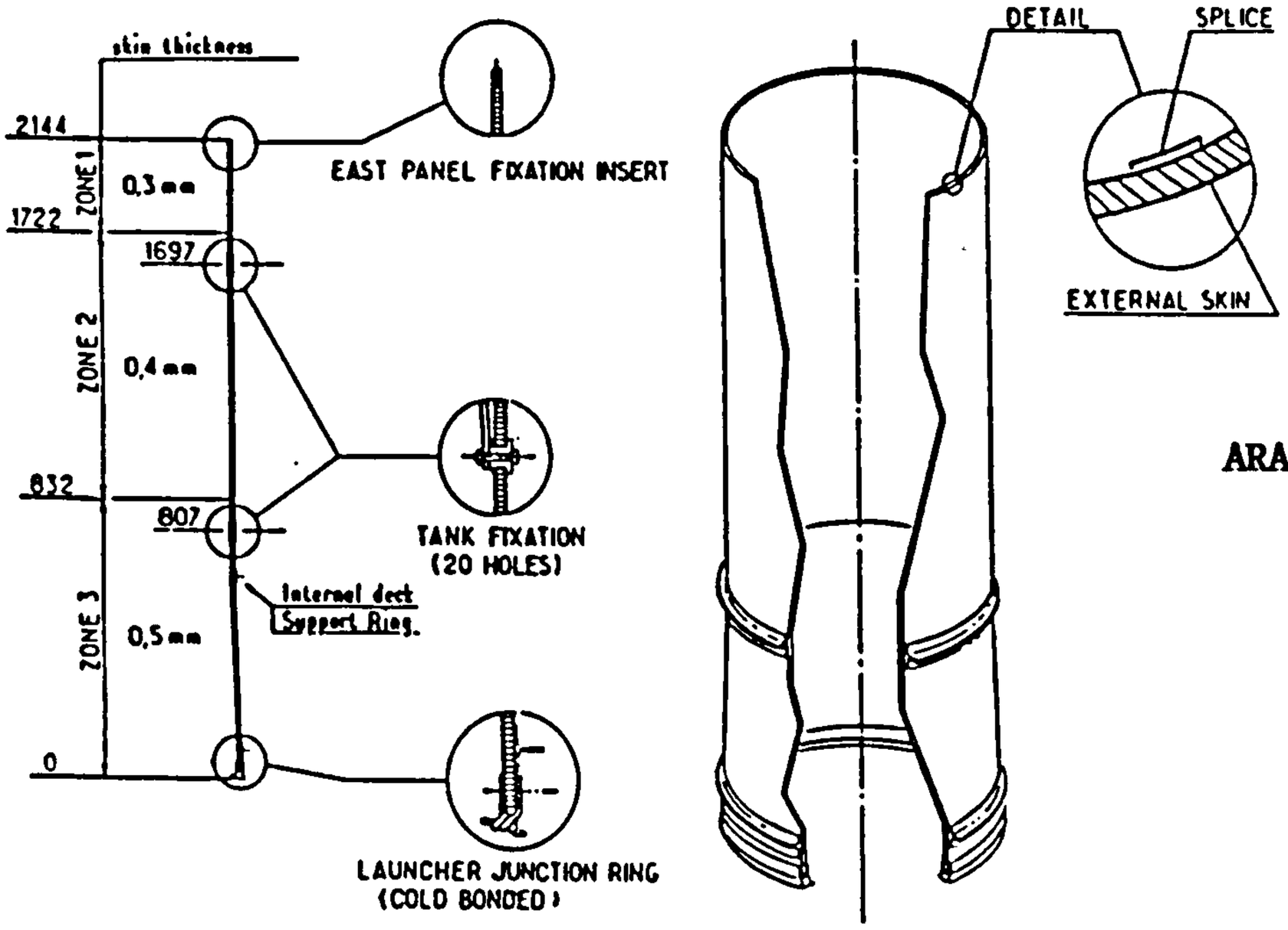

Fig. 8.5b

ARAB SAT THRUST TUBE

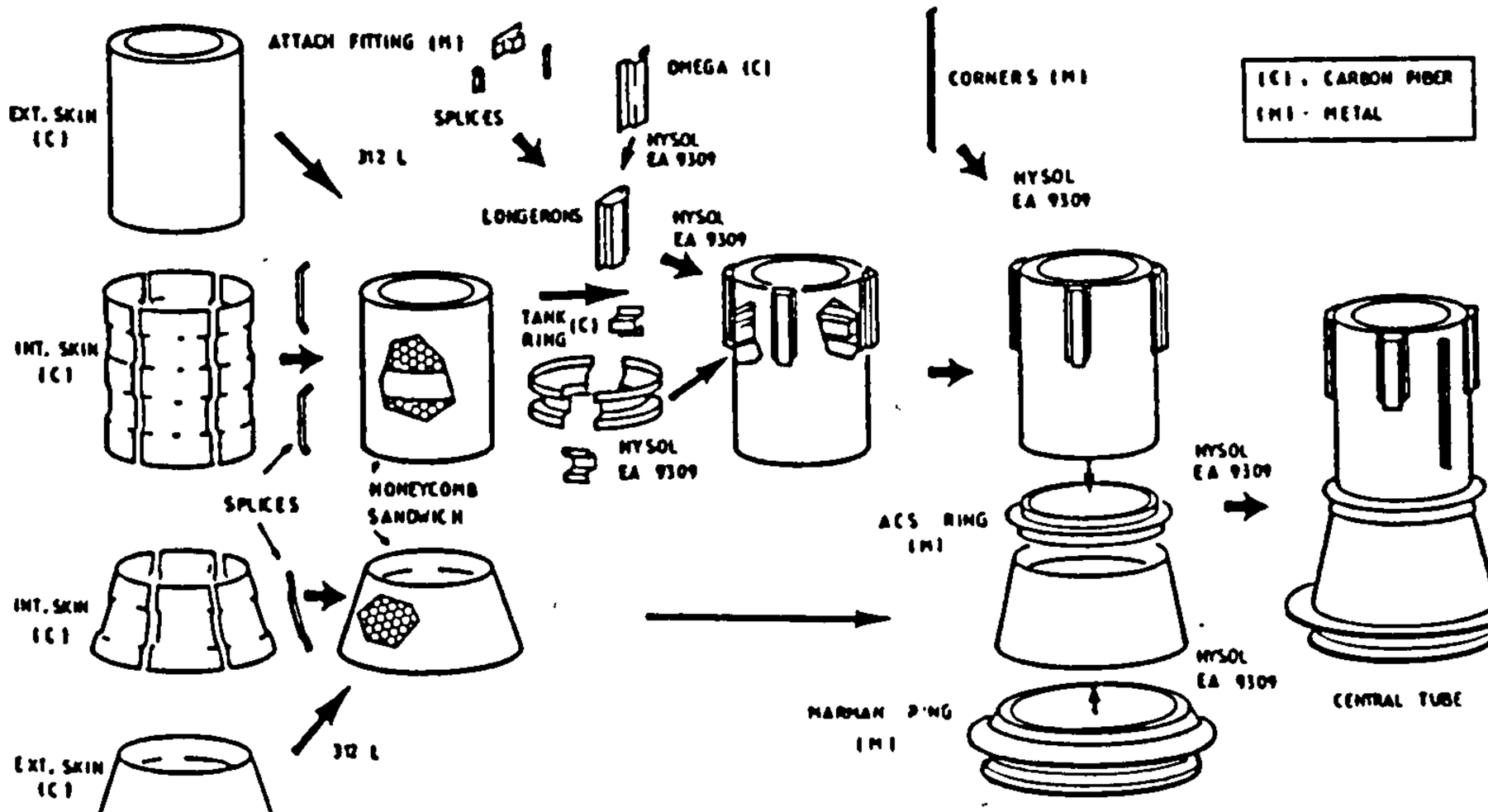

Fig. 8.6 ASSEMBLY SEQUENCE FOR INTELSAT V THRUST TUBE

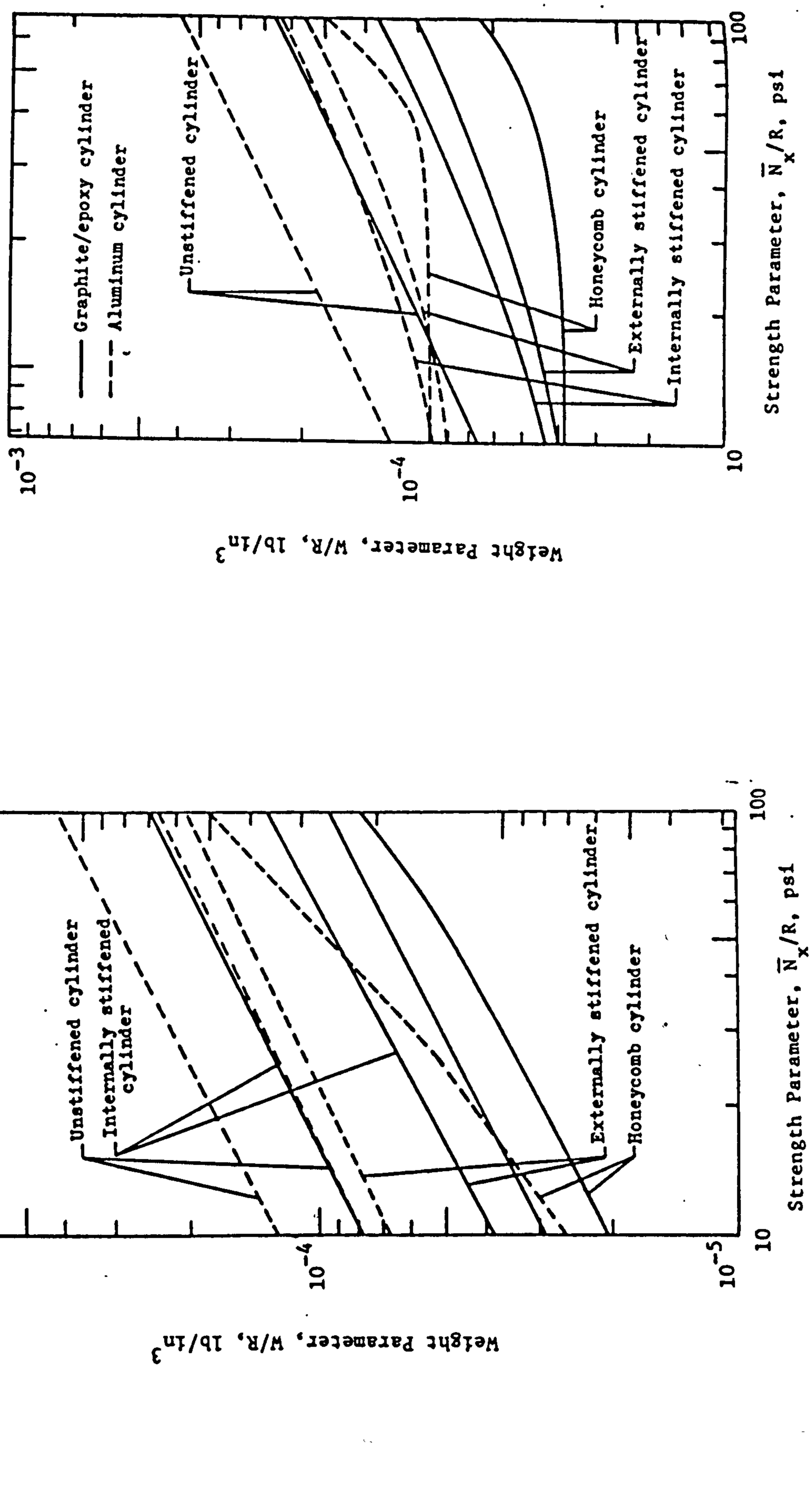

Fig. 8.7 EFFICIENCY OF CYLINDER CONSTRUCTION TYPES UNDER UNIFORM COMPRESSION LOAD

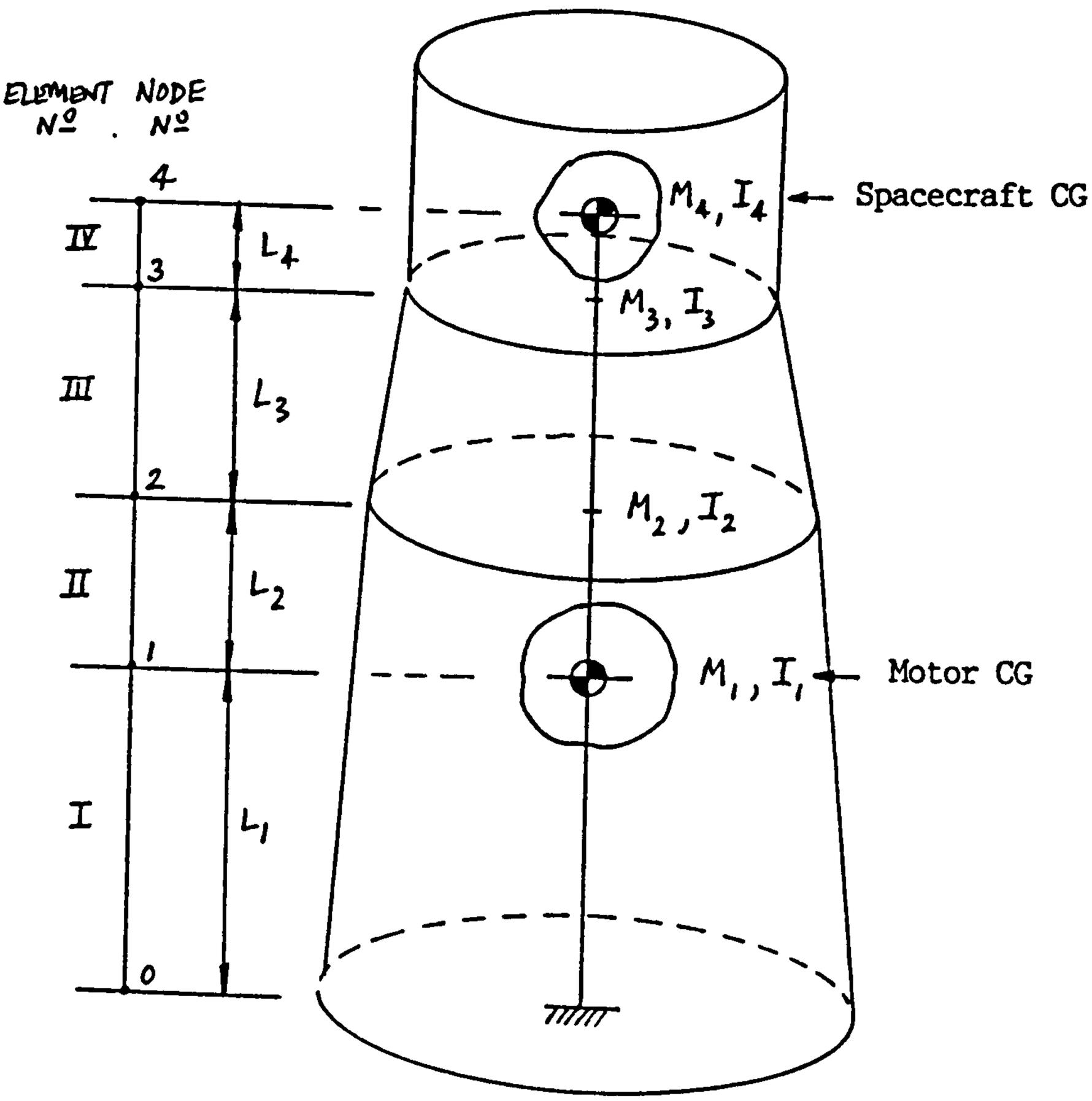

Fig. 8.8 BEAM AND LUMPED MASS FE REPRESENTATION OF SPACECRAFT

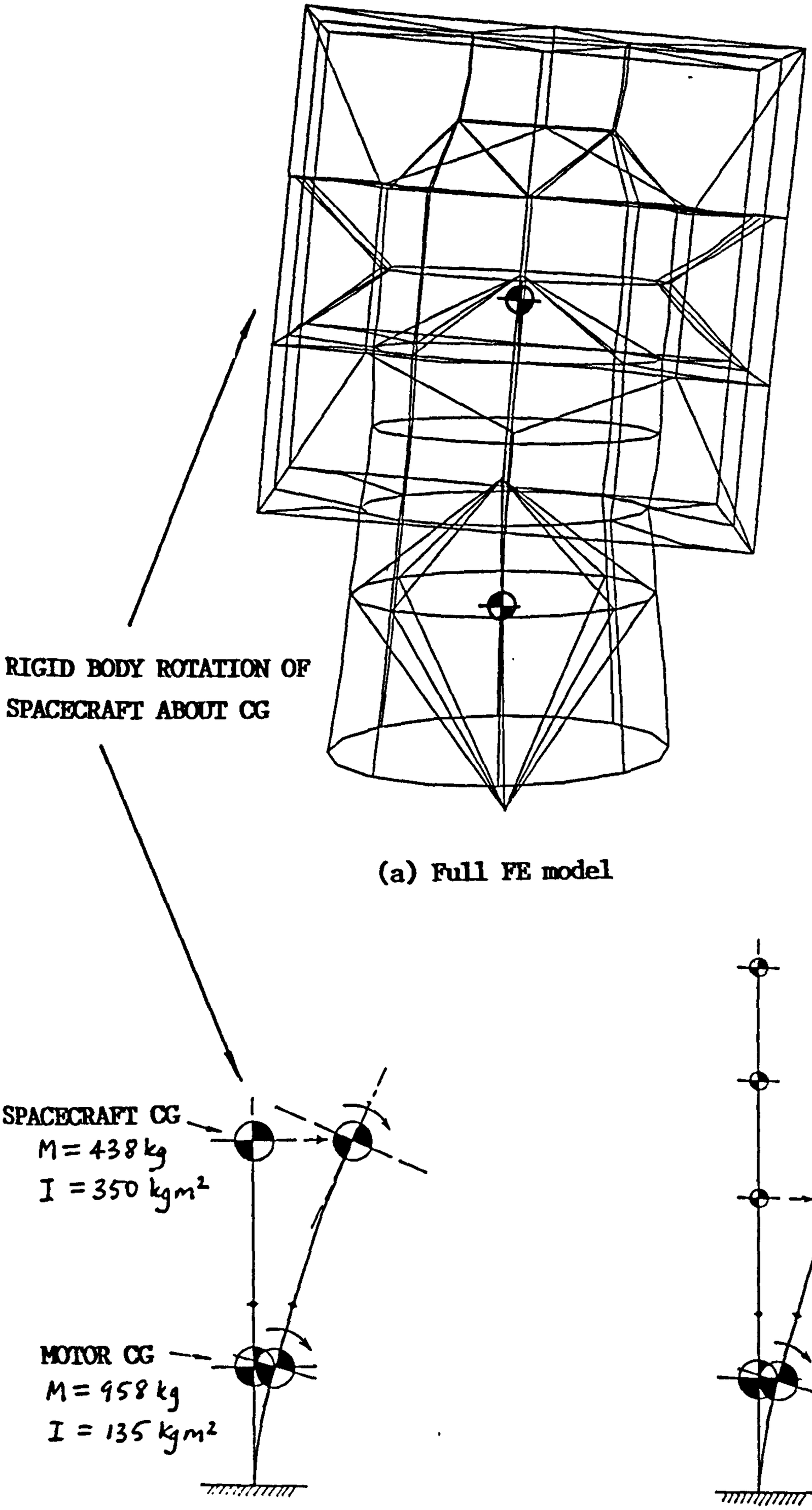

(a) Full FE model

(b) Lumped spacecraft mass at CG

(c) Distributed spacecraft mass

Fig. 8.9 FIRST LATERAL MODE IDEALISED BY DIFFERENT FE MODELS

Fig. 8.10 A_{33} vs A_{11} FOR HM-S/985 FACED SANDWICH WITH LAY-UPS OF THE FORM $[\pm\theta/\pm\phi/CORE/\mp\phi/\mp\theta]$

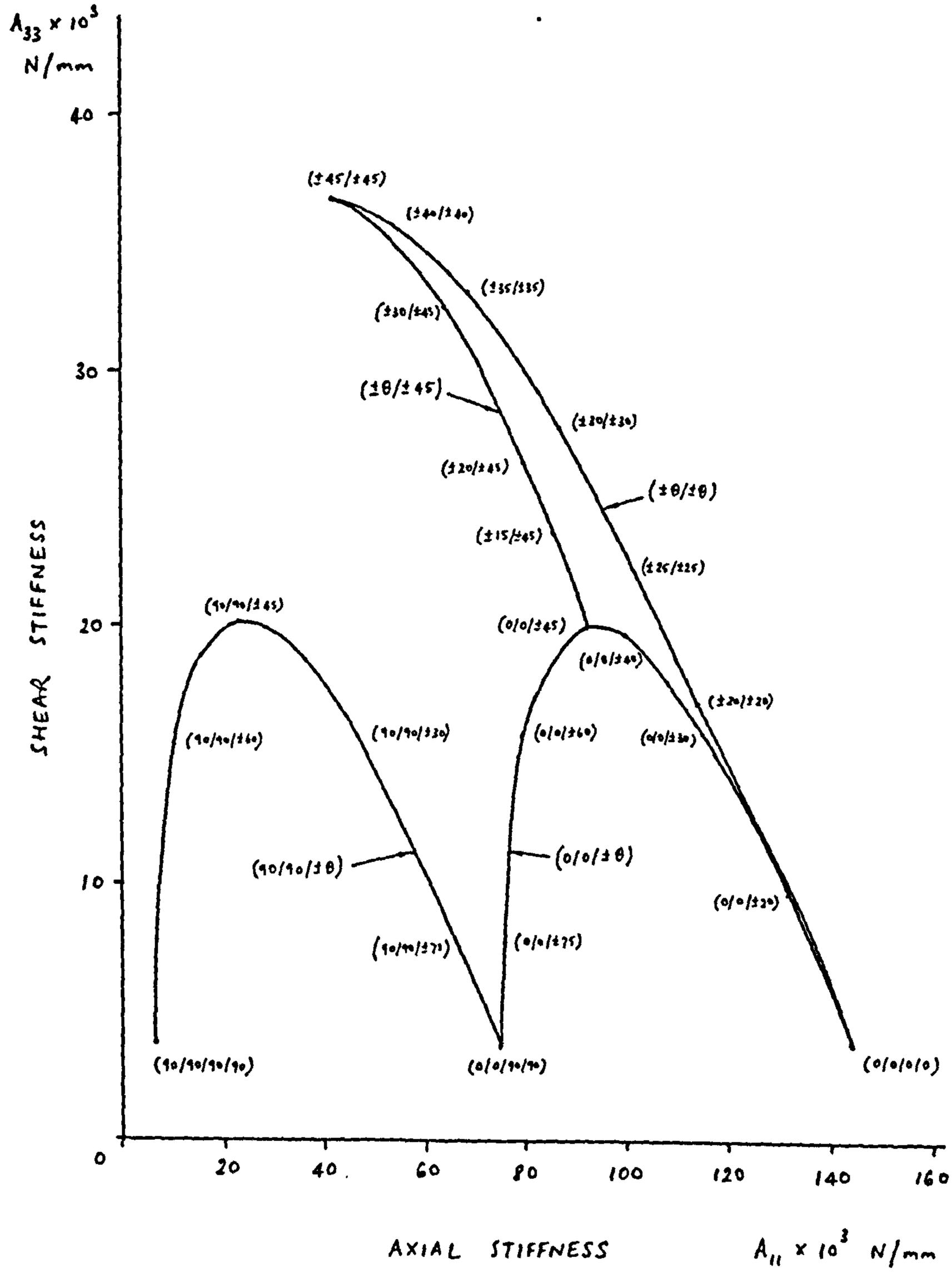

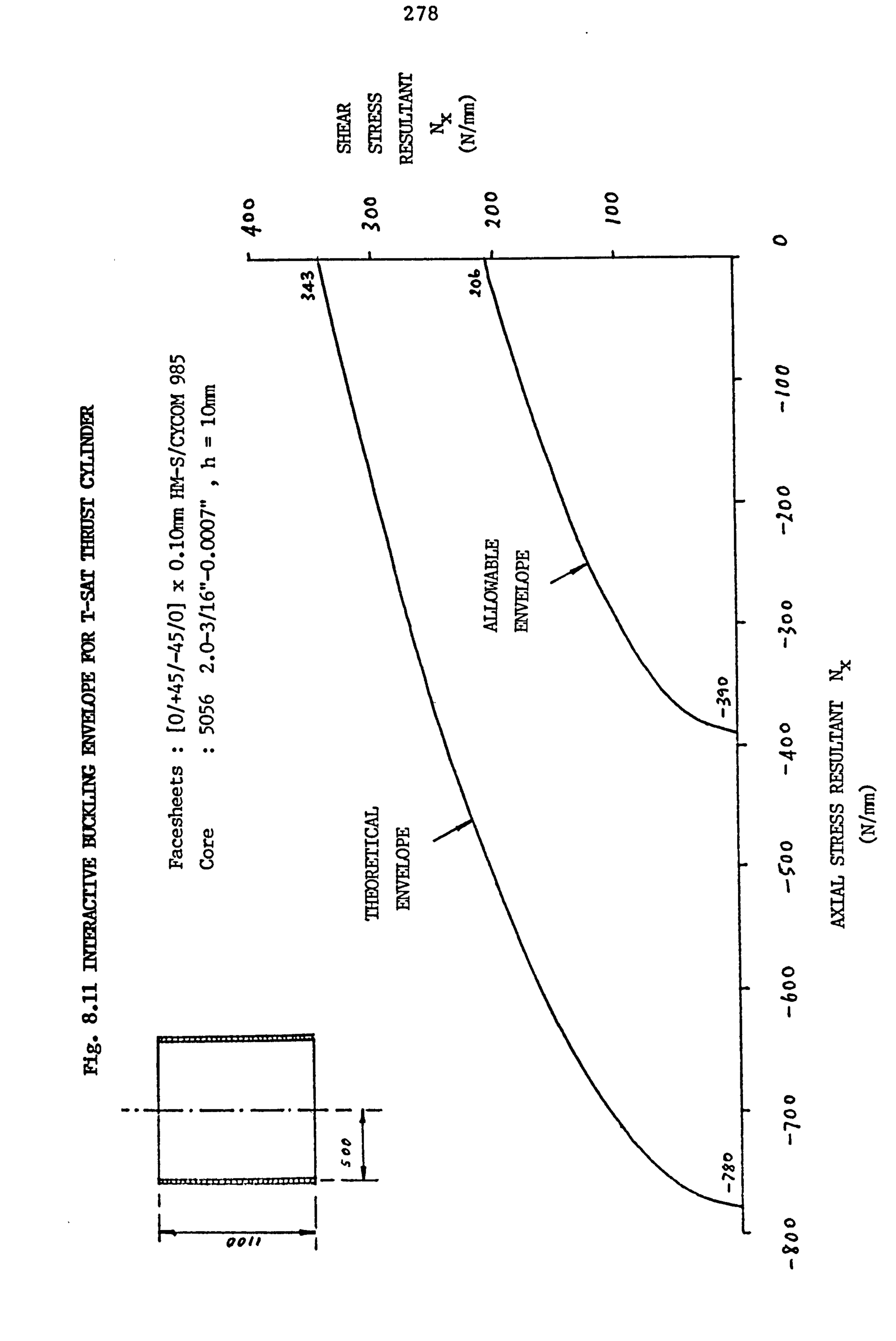

Fig. 8.11 INTERACTIVE BUCKLING ENVELOPE FOR T-SAT THRUST CYLINDER

Fig. 8.12 AXIAL COMPRESSIVE BUCKLING OF $[\pm\theta_2]$ FACED SANDWICH CYLINDER

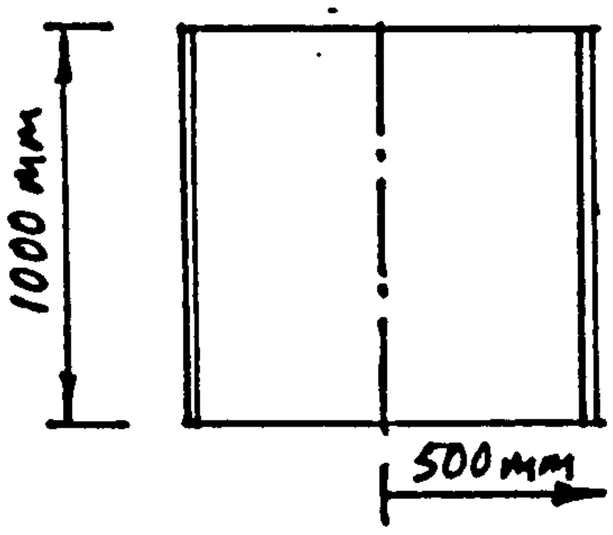

Facesheets : HM-S/CYCOM 985 t_{ply} = 0.10mm
Core : 5056 2.0-3/16"-0.0007" h = 10mm

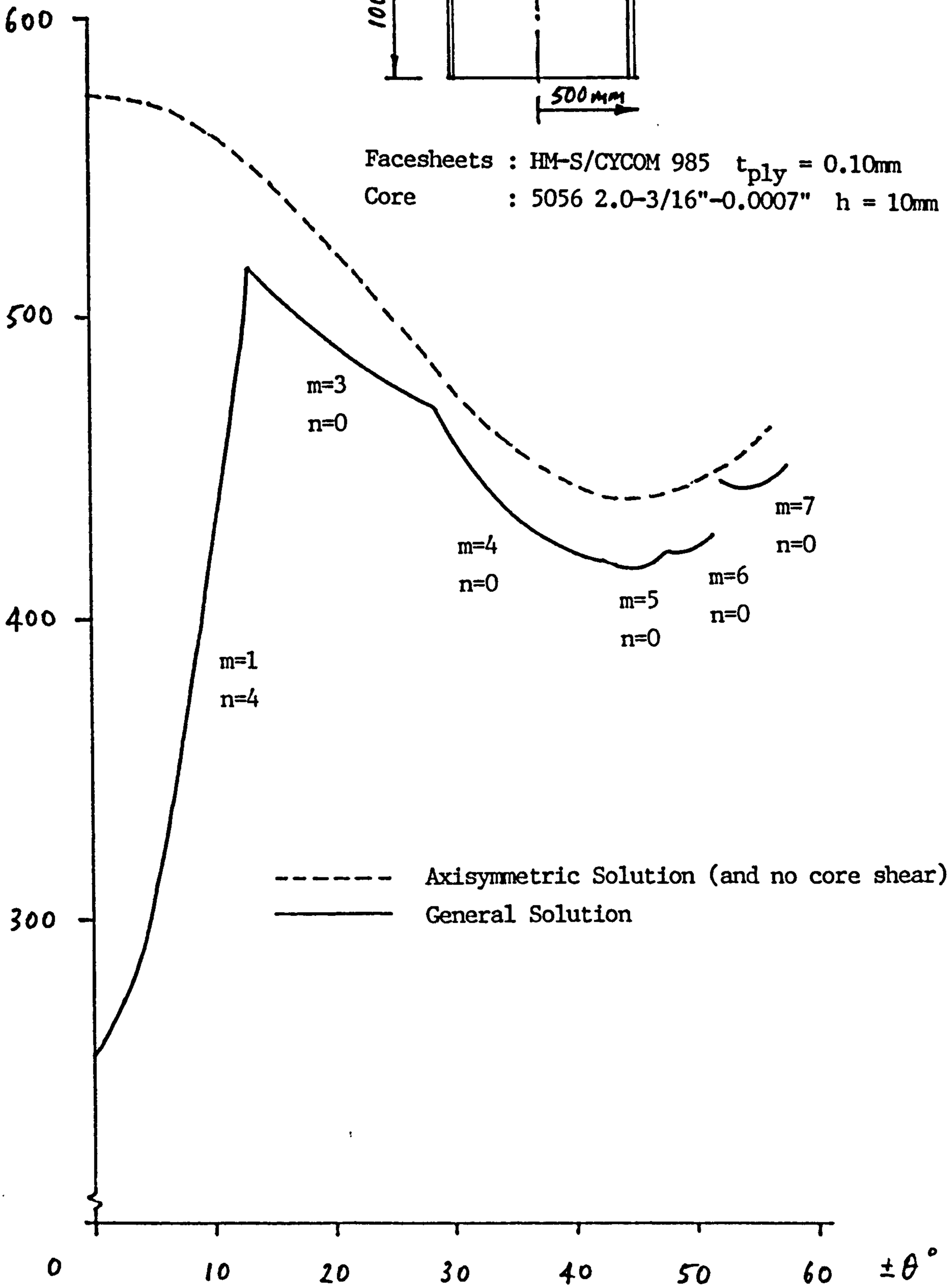

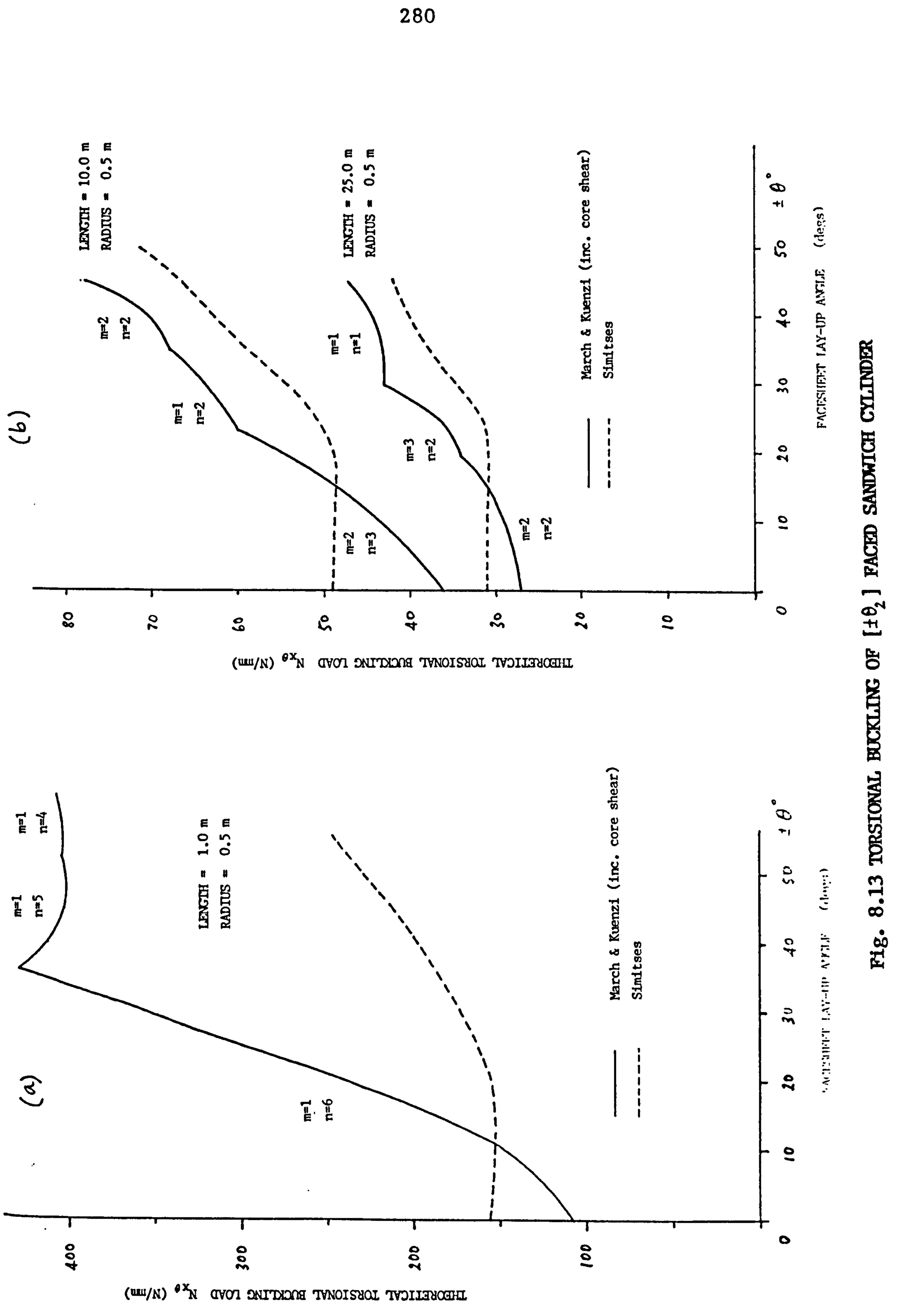

Fig. 8.13 TORSIONAL BUCKLING OF $[\pm\theta_2]$ FACED SANDWICH CYLINDER

Fig. 8.14 EFFECT OF CORE SHEAR ON SANDWICH CYLINDER TORSIONAL INSTABILITY

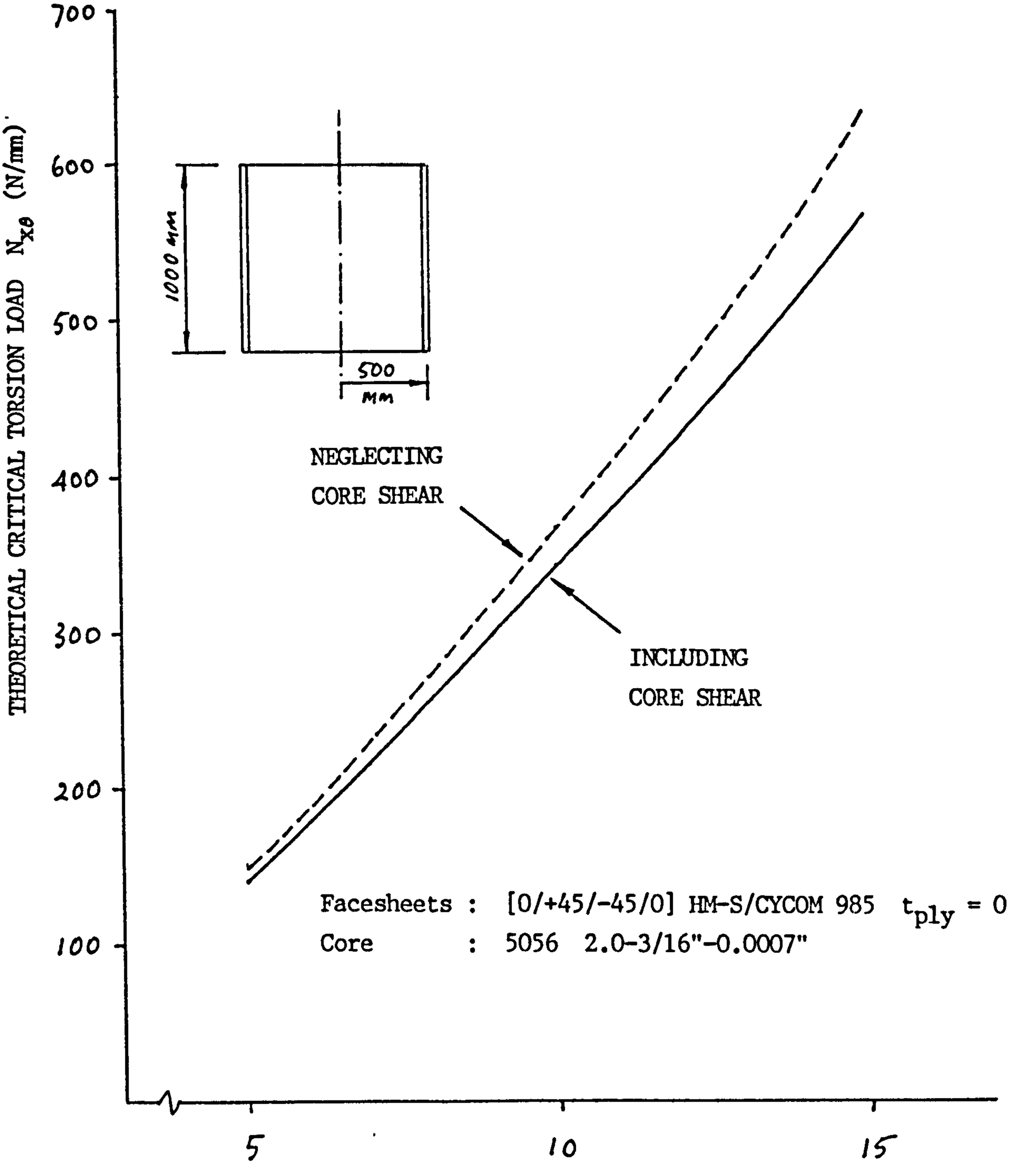

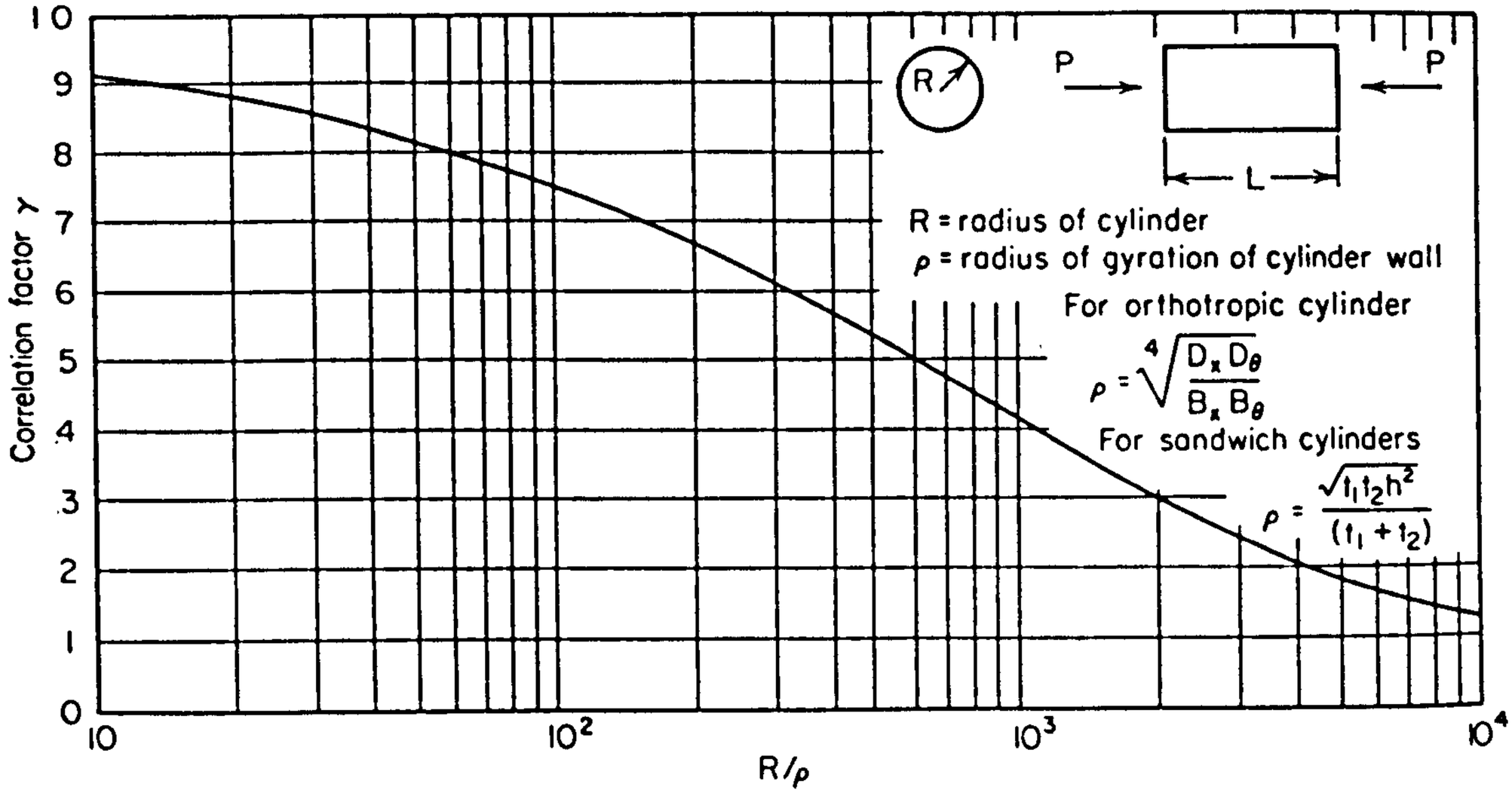

Fig. 8.15 KNOCK-DOWN FACTORS FOR AXIAL COMPRESSION BUCKLING

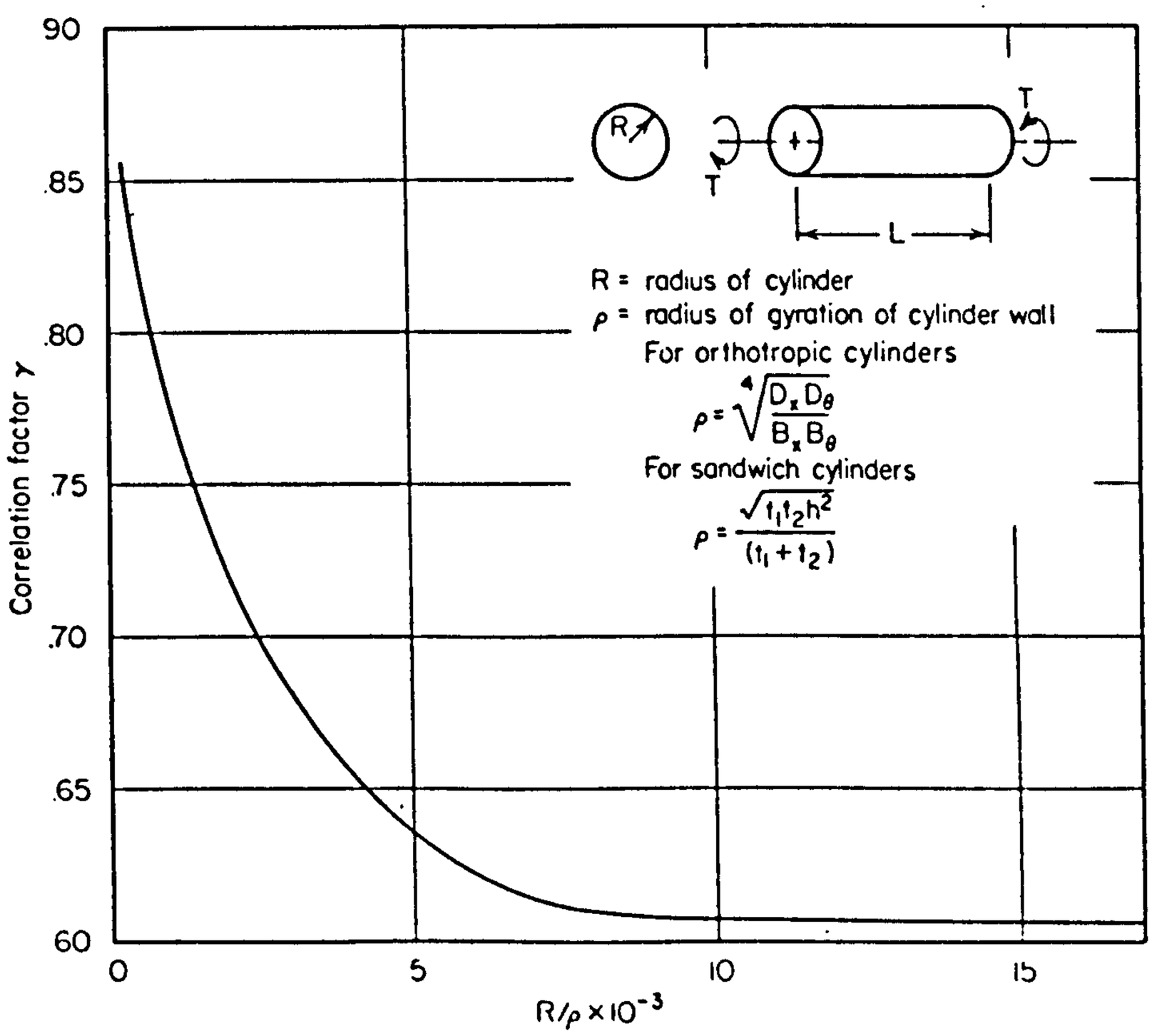

Fig. 8.16 KNOCK-DOWN FACTORS FOR TORSIONAL BUCKLING

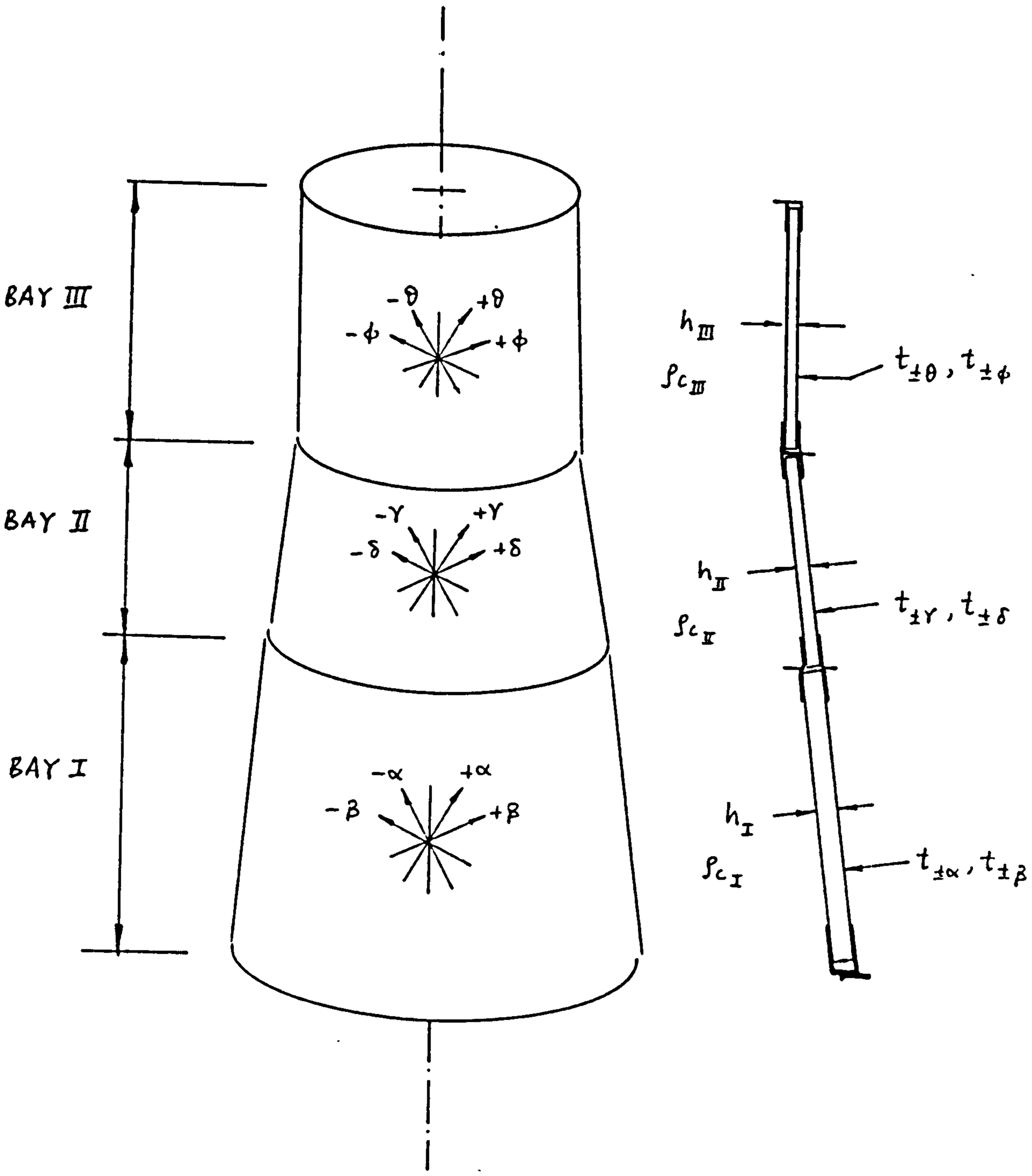

Fig. 8.17 DESIGN VARIABLES FOR A MULTI-BAY SPACECRAFT COMPOSITE FACED SANDWICH THRUST TUBE

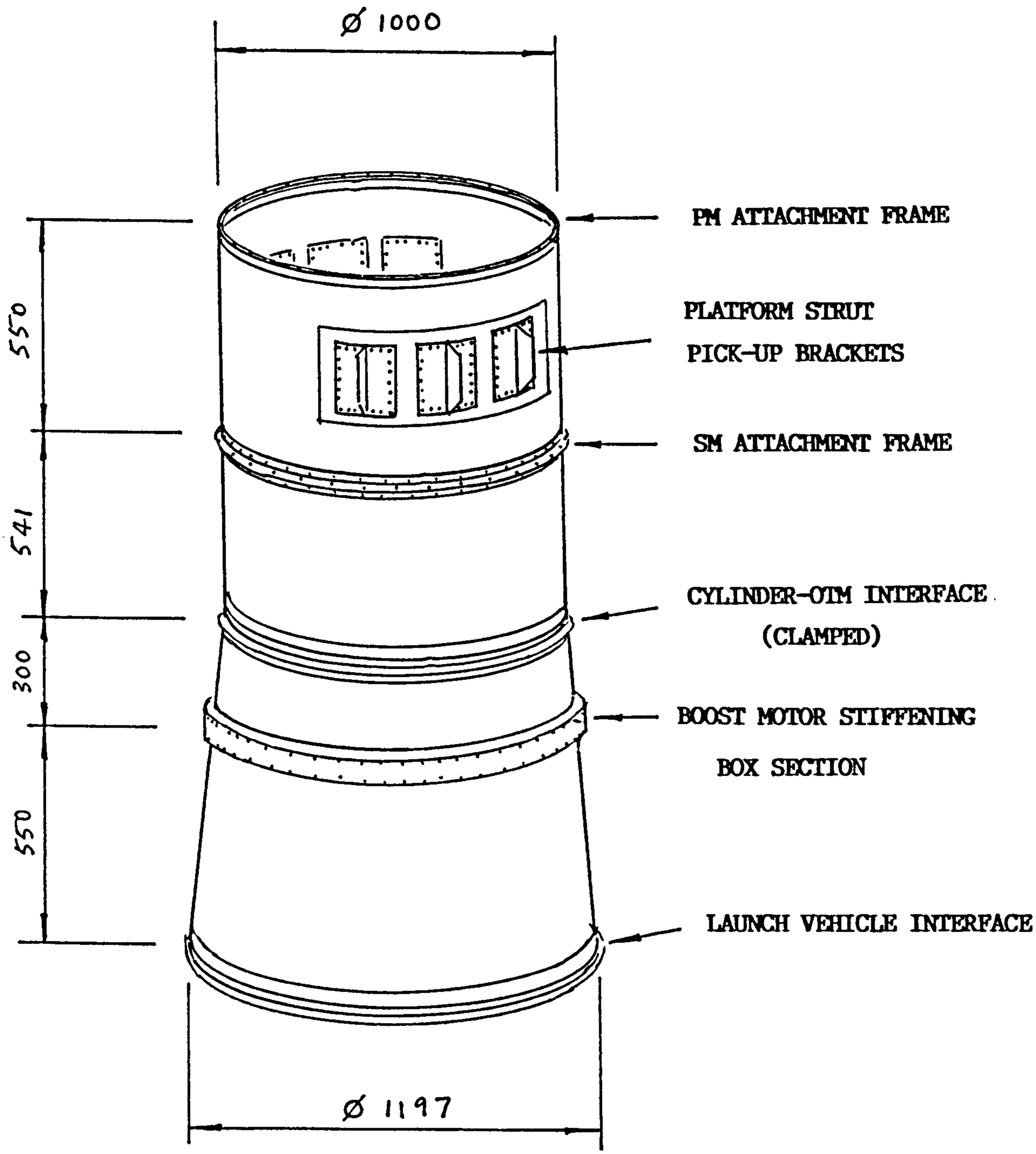

Fig. 8.18 T-SAT SPACECRAFT THRUST TUBE

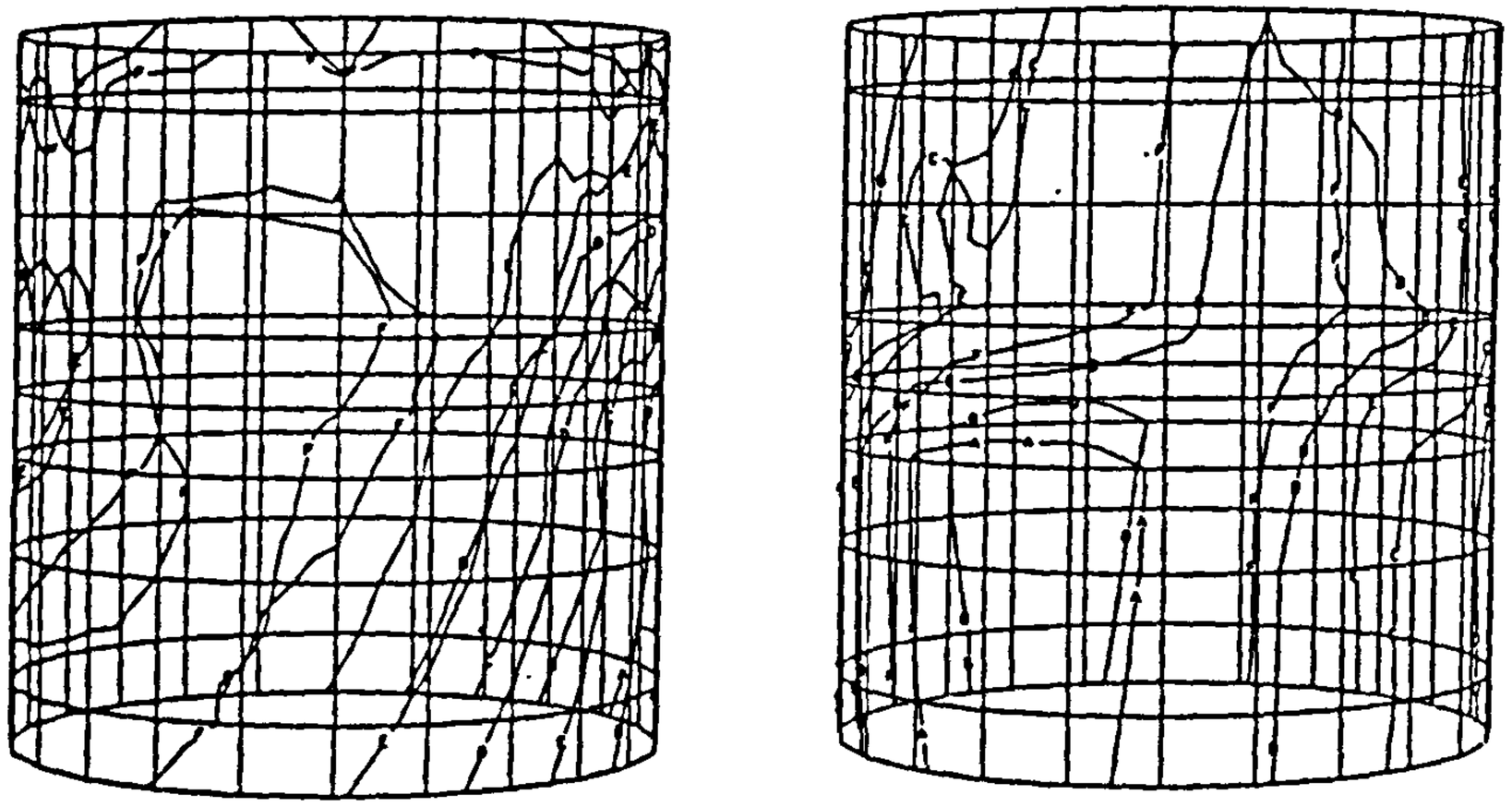

AXIAL STRESS
MAX DYN PRESS

SHEAR STRESS
MAX DYN PRESS

HOOP STRESS
ORBIT T/FER

AXIAL MOMENTS
ORBIT T/FER

Fig. 8.19 INTERNAL STRESS RESULTANTS IN T-SAT THRUST CYLINDER

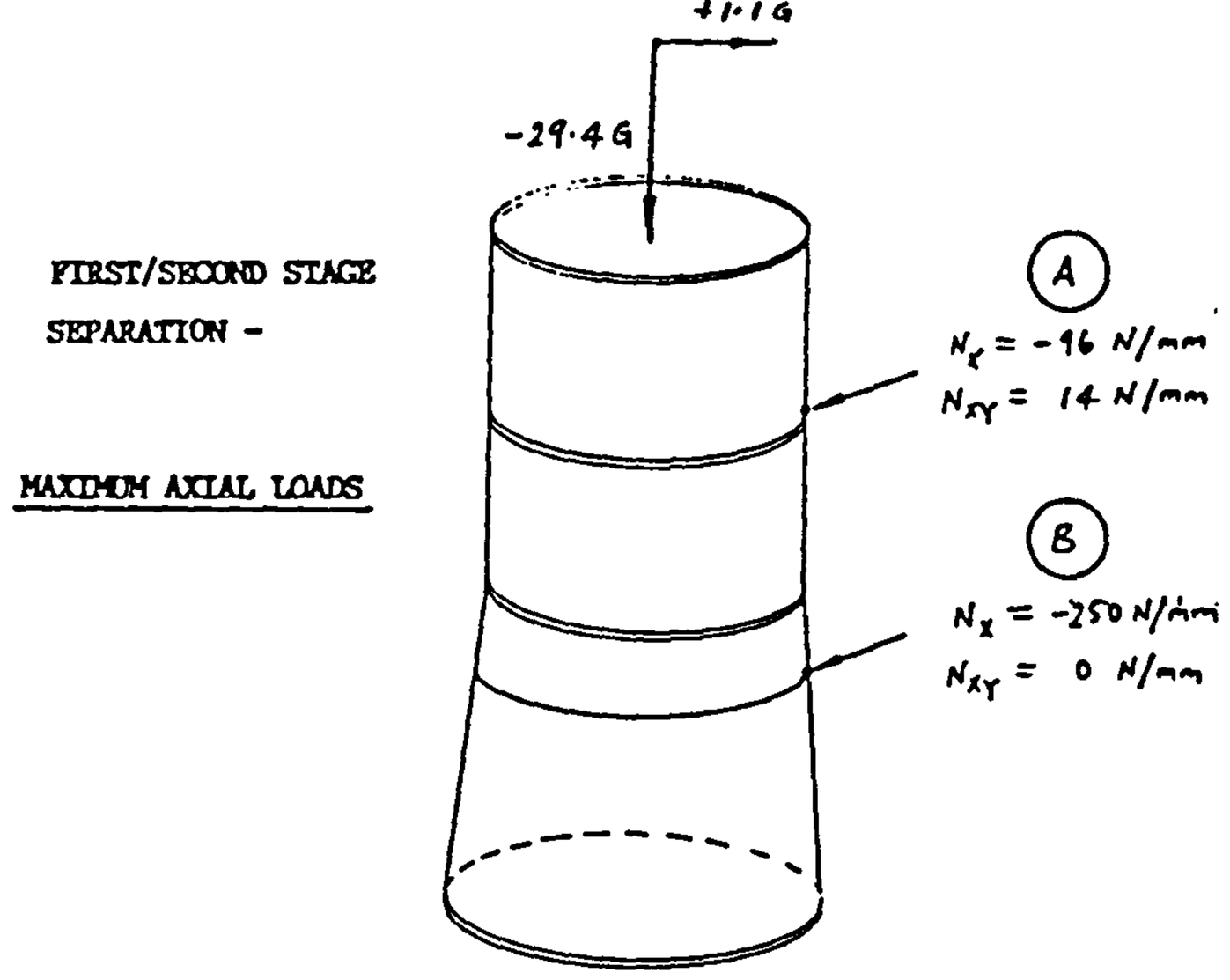

Fig. 8.20 T-SAT THRUST TUBE DESIGN LOAD CASES :

Fig. 8.21 T-SAT CYLINDER TSAI-WU INDEX Co-cured HM-S/985

SPACECRAFT THRUST TUBE	T-SAT CYLINDER
Material System	HM-S/CYCOM 985 (CO-CURED) 0.10 mm
Facesheet Lay-Up	$[\pm\theta/\pm\phi]$
PLOT	MAX. PLY TSAI-WU INDEX
Load Case N_x =	-96 N/mm
N_{xy} =	14 N/mm

(a) MAX. AXIAL LOAD CASE

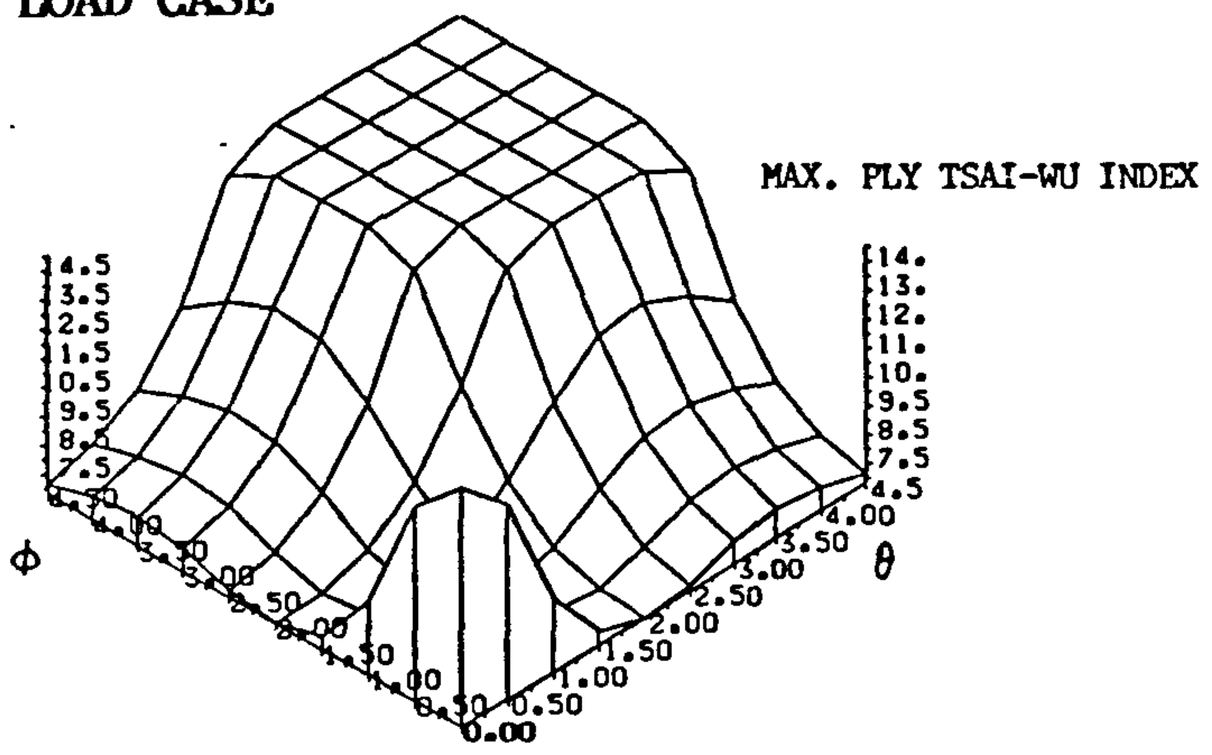

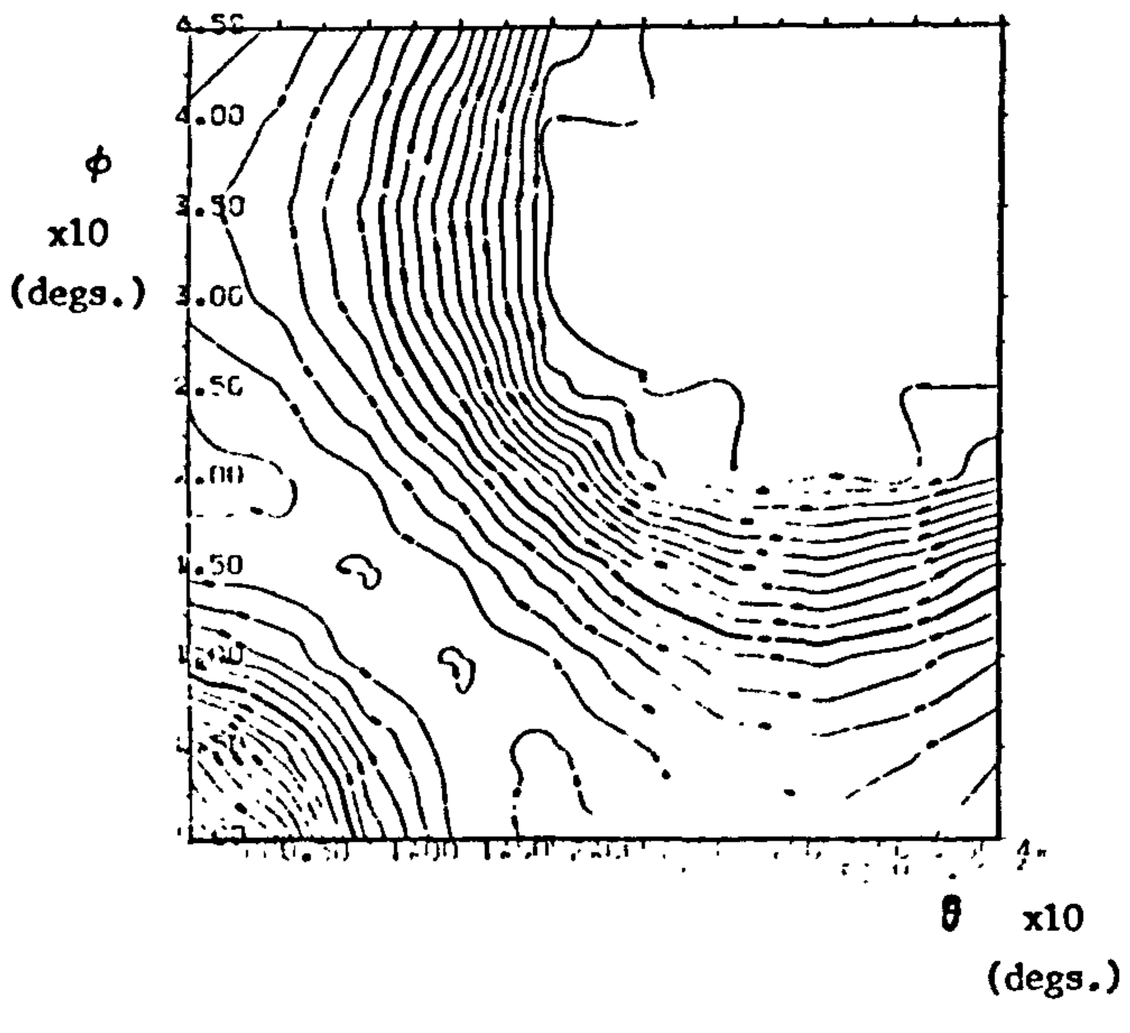

SPACECRAFT THRUST TUBE	T-SAT CYLINDER
Material System	HM-S/CYCOM 985 (CO-CURED) 0.10 mm
Facesheet Lay-Up	$[\pm\theta/\pm\phi]$
PLOT	MAX. PLY TSAI-WU INDEX
Load Case N_x =	-32 N/mm
N_{xy} =	20 N/mm

(b) MAX. SHEAR LOAD CASE

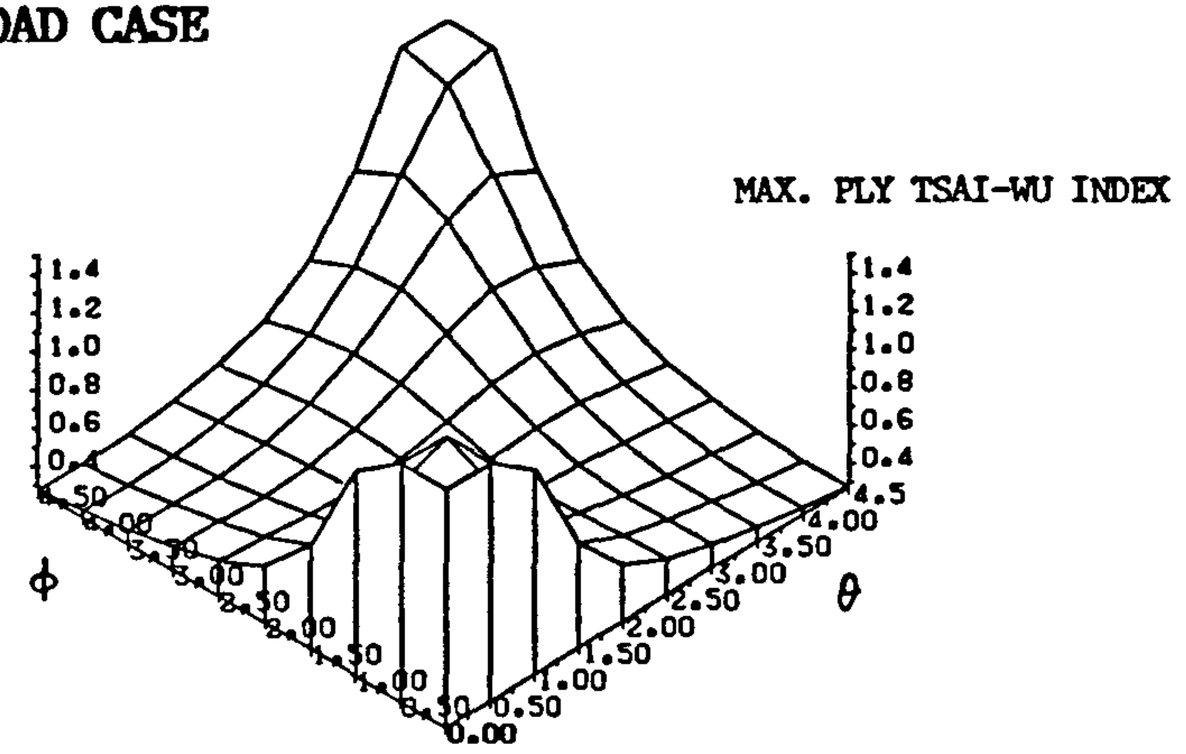

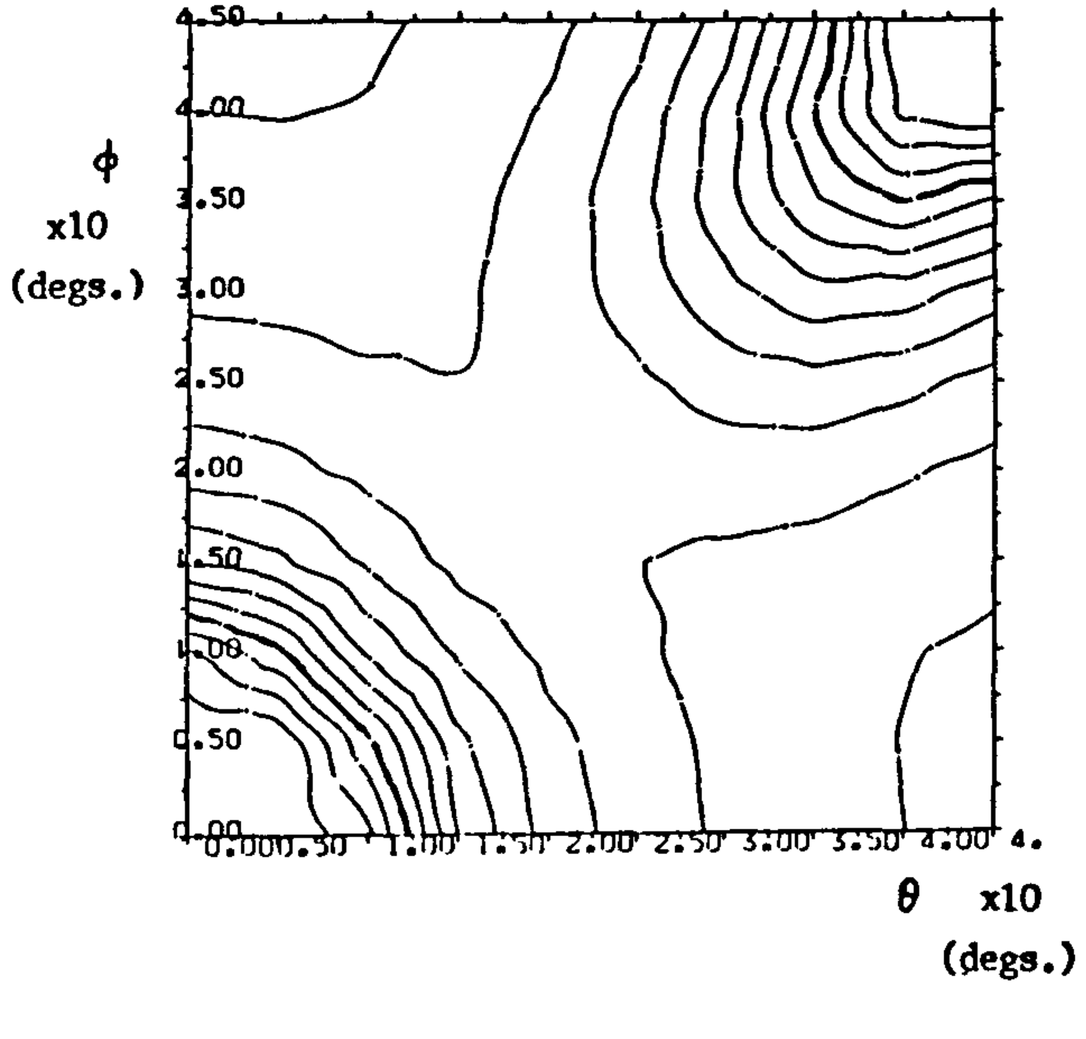

Fig. 8.22 CYLINDER: STRENGTH FEASIBLE REGION Co-cured HM-S/985

SPACECRAFT THRUST TUBE	T-SAT CYLINDER
Material System	HM-S/CYCOM 985 (CO-CURED) 0·10mm
Facesheet Lay-Up	$[\pm\theta/\pm\phi]$
PLOT	FEASIBLE REGION FOR MATERIAL STRENGTH
Load Case N_x =	−96 N/mm −32 N/mm
N_{xy} =	14 N/mm 20 N/mm

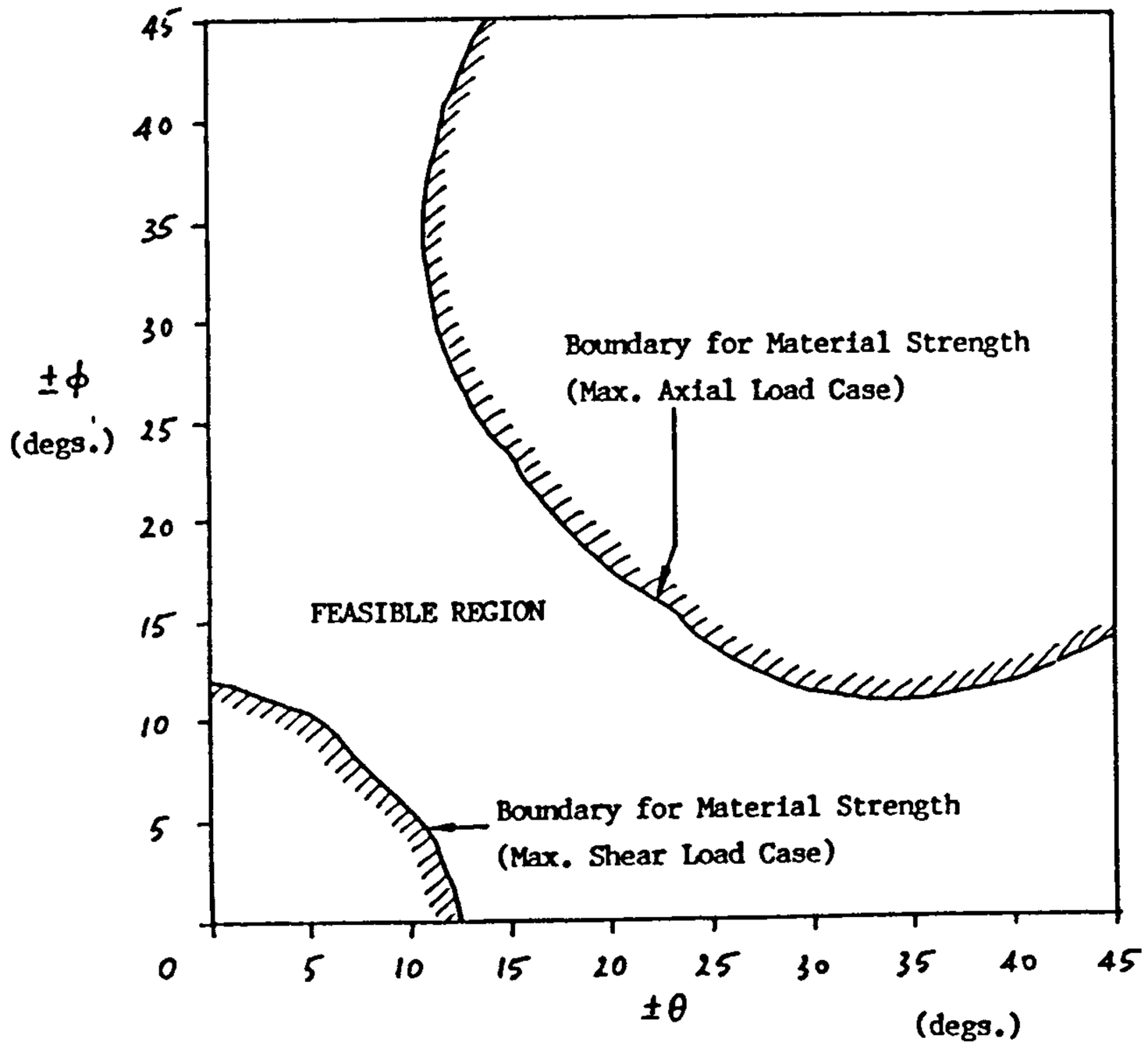

Fig. 8.23 O.T.M: STRENGTH FEASIBLE REGION Co-cured HM-S/985

SPACECRAFT THRUST TUBE	T-SAT OTM
Material System	HM-S/CYCOM 985 (CO-CURED) 0·10mm
Facesheet Lay-Up	$[\pm\alpha_2/\pm\beta_2]$
PLOT	FEASIBLE REGION FOR MATERIAL STRENGTH
Load Case N_x =	−250 N/mm −77 N/mm
N_{xy} =	0 N/mm 32 N/mm

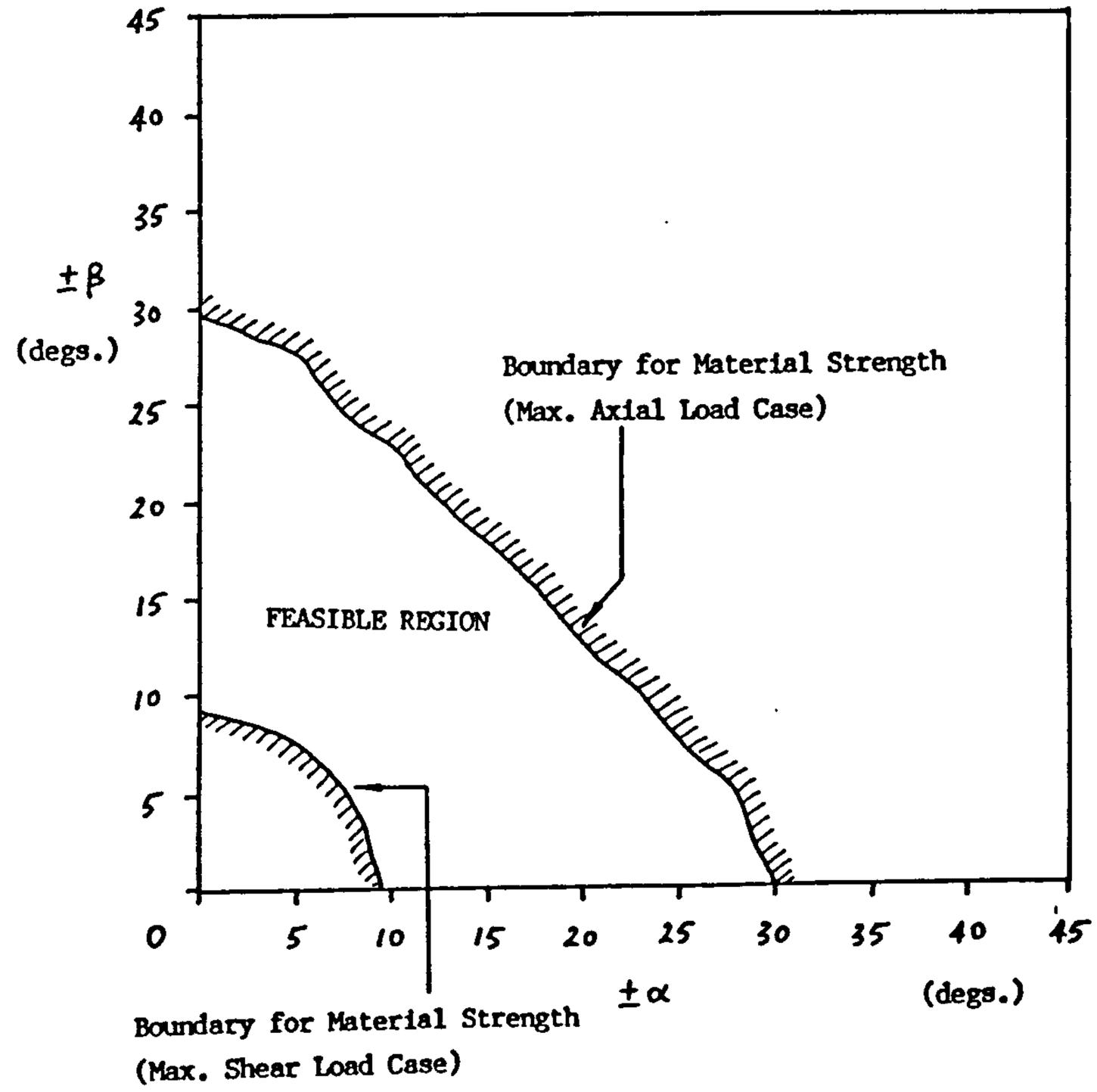

Fig. 8.24 T-SAT CRITICAL BUCKLING LOADS Co-cured HM-S/985

SPACECRAFT THRUST TUBE	T-SAT CYLINDER
Material System	HM-S/CYCOM 985 (CO-CURED) 0·10mm
Facesheet Lay-Up	$[\pm\theta/\pm\phi]$
PLOT	CRITICAL AXIAL BUCKLING LOAD $N_{x_{CRIT}}$ (N/mm)
Load Case N_x =	
N_{xy} =	

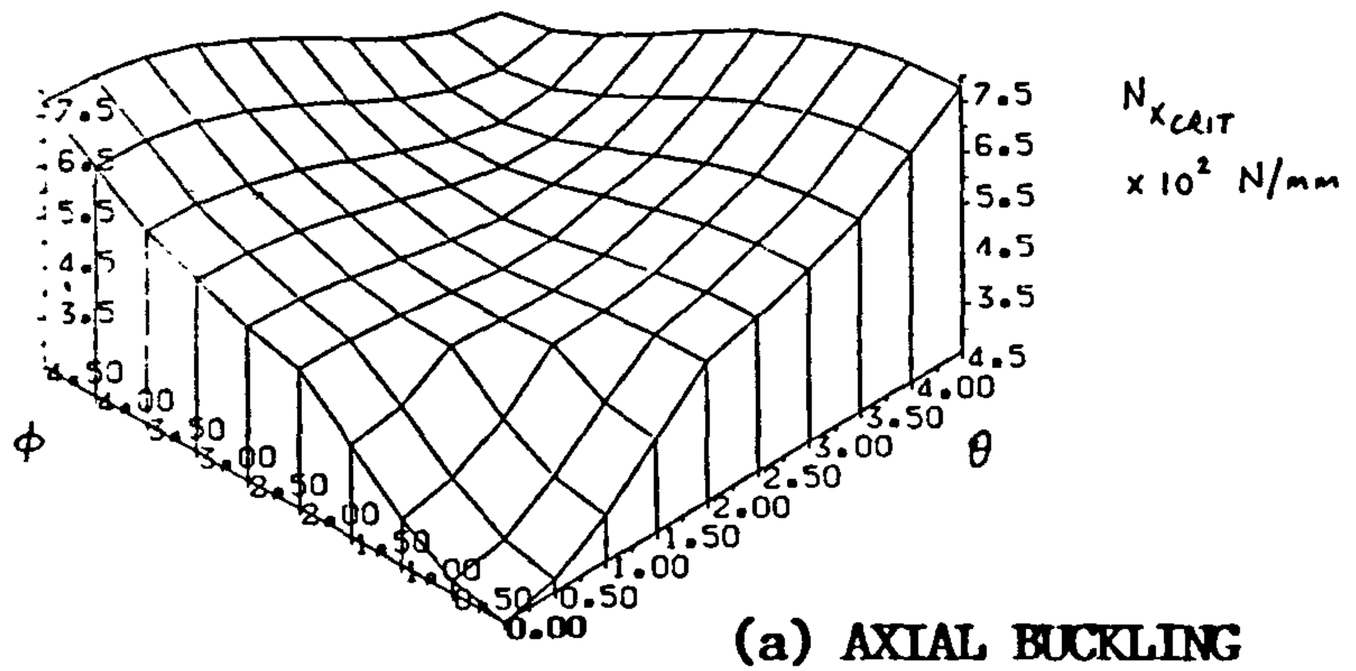

(a) AXIAL BUCKLING

SPACECRAFT THRUST TUBE	T-SAT CYLINDER
Material System	HM-S/CYCOM 985 (CO-CURED) 0·10mm
Facesheet Lay-Up	$[\pm\theta/\pm\phi]$
PLOT	CRITICAL TORSIONAL BUCKLING LOAD $N_{x\theta_{CRIT}}$ (N/mm)
Load Case N_x =	
N_{xy} =	

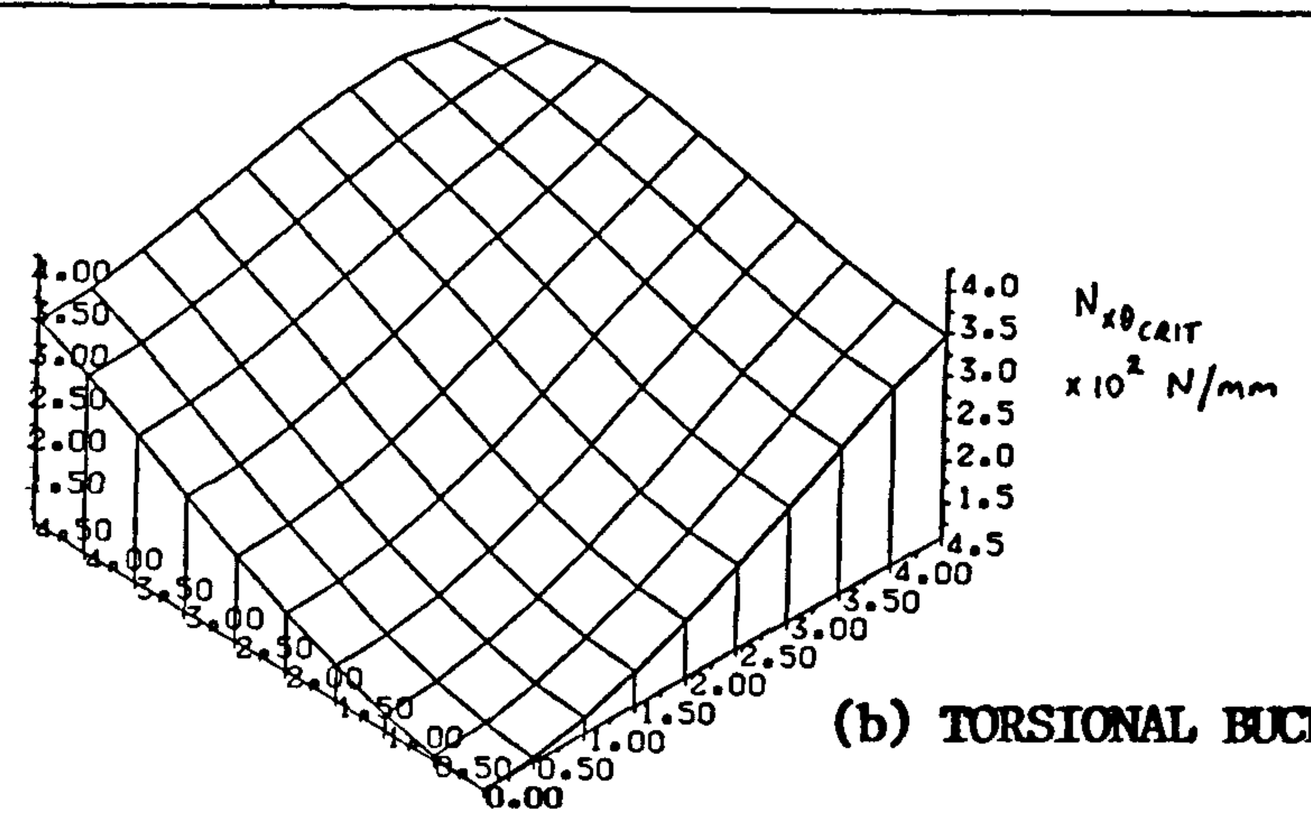

(b) TORSIONAL BUCKLING

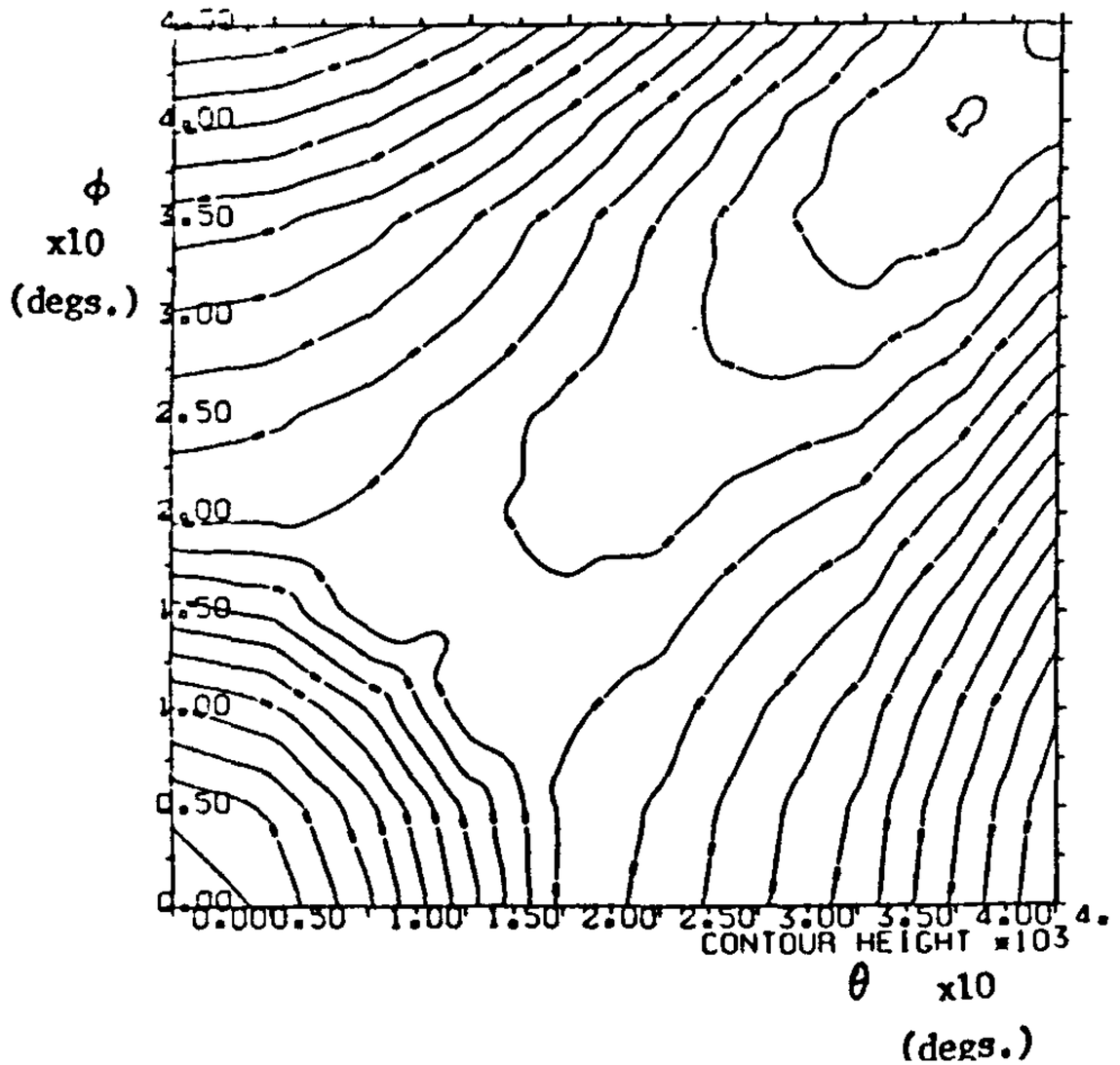

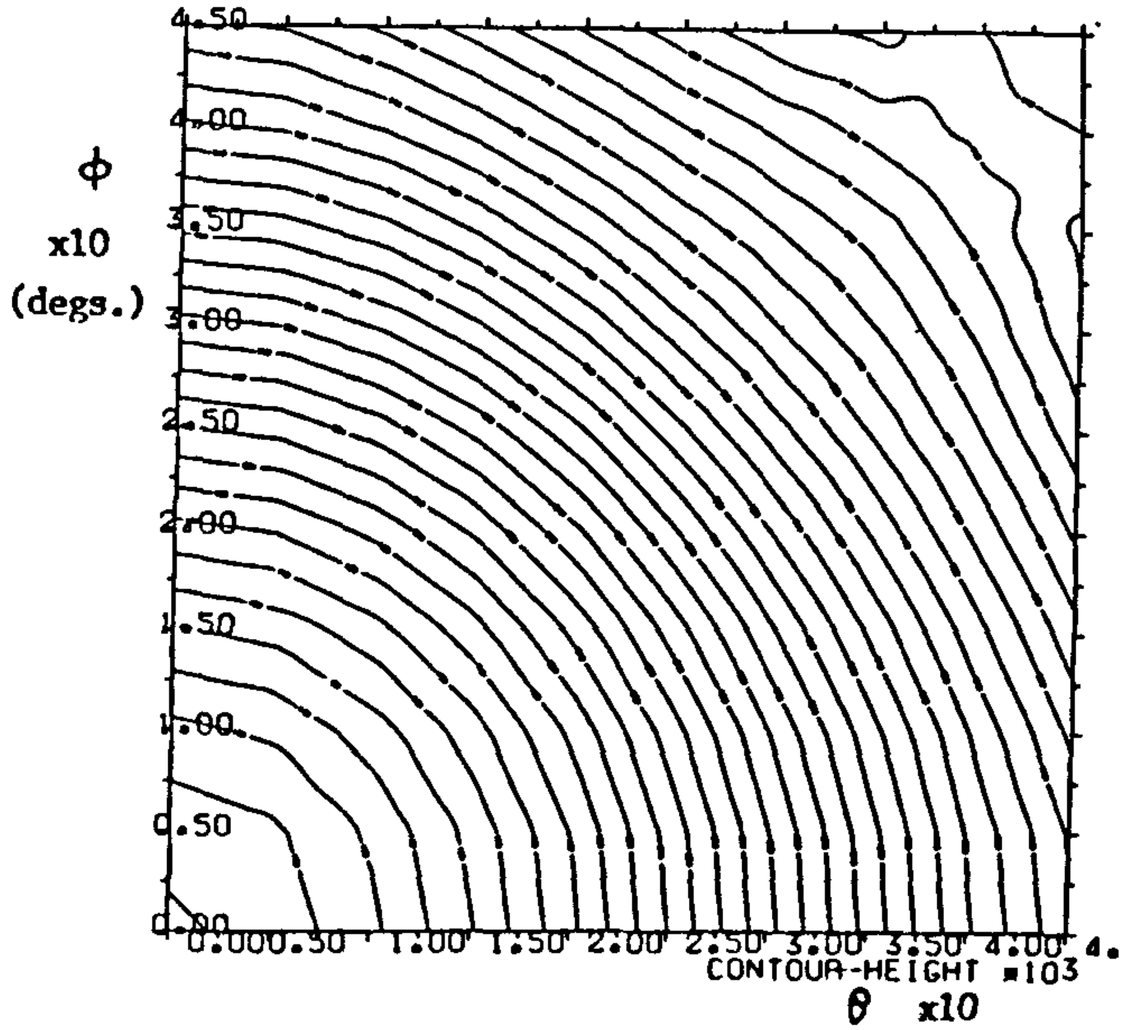

Fig. 8.25 T-SAT CYLINDER BUCKLING INTERACTION INDEX Co-cured HM-S/985

SPACECRAFT THRUST TUBE	T-SAT CYLINDER	
Material System	HM-S/CYCOM 985 (CO-CURED) 0·10mm	
Facesheet Lay-Up	$[\pm\theta/\pm\phi]$	
PLOT	BUCKLING INTERACTION INDEX	
Load Case N_x =	-96 N/mm	Max. Axial Load Case
N_{xy} =	14 N/mm	

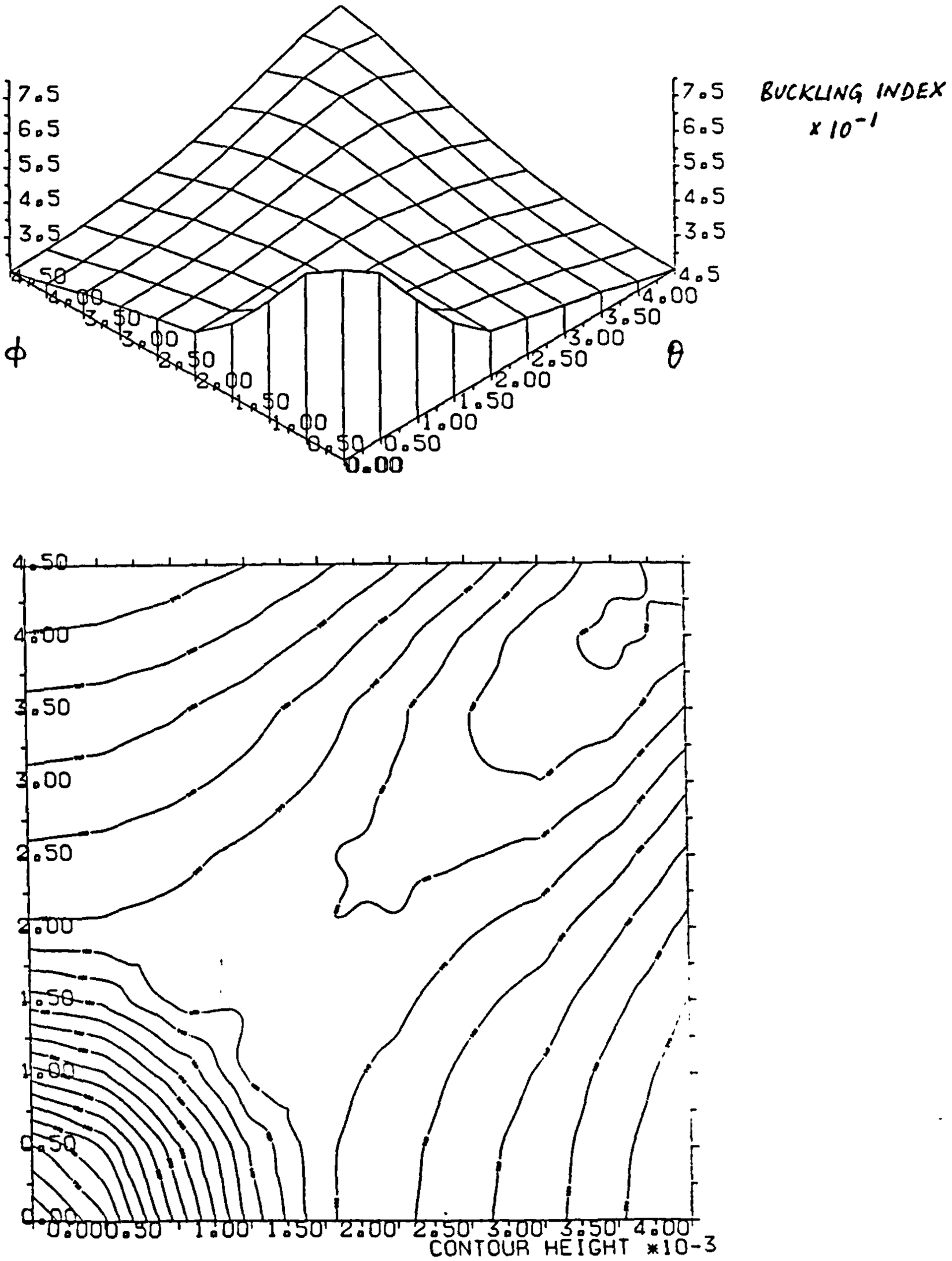

Fig. 8.26 (a) T-SAT FIRST LATERAL FREQUENCY *(b) T-SAT SECOND LATERAL FREQUENCY* **Co-cured HM-S/985**

SPACECRAFT THRUST TUBE	T-SAT
Material System Facesheet Lay-Up	HM-S/CYCOM 985 (CO-CURED) 0.10 mm OTM: $[0_4/\pm\alpha_2]$ CYLINDER: $[0_2/\pm\theta]$
PLOT	FIRST LATERAL FREQUENCY
Load Case N_x = N_{xy} =	

SPACECRAFT THRUST TUBE	T-SAT
Material System Facesheet Lay-Up	HM-S/CYCOM 985 (CO-CURED) 0.10 mm OTM: $[0_4/\pm\alpha_2]$ CYLINDER: $[0_2/\pm\theta]$
PLOT	SECOND LATERAL FREQUENCY (Hz).
Load Case N_x = N_{xy} =	

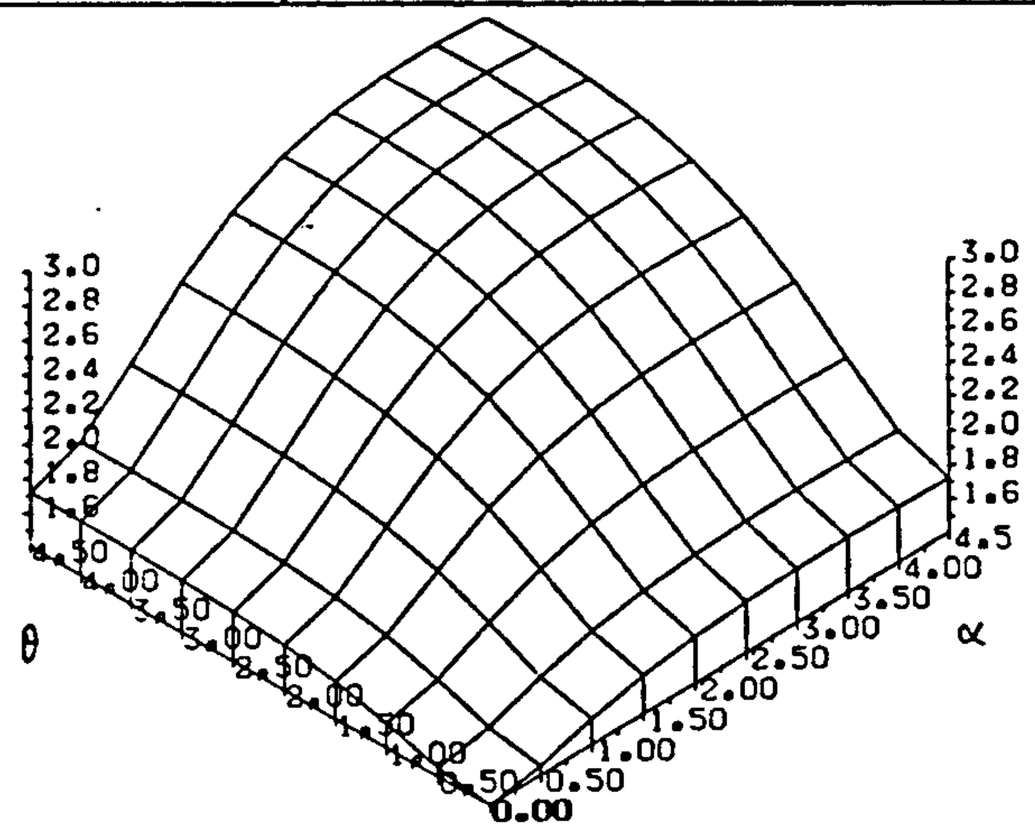

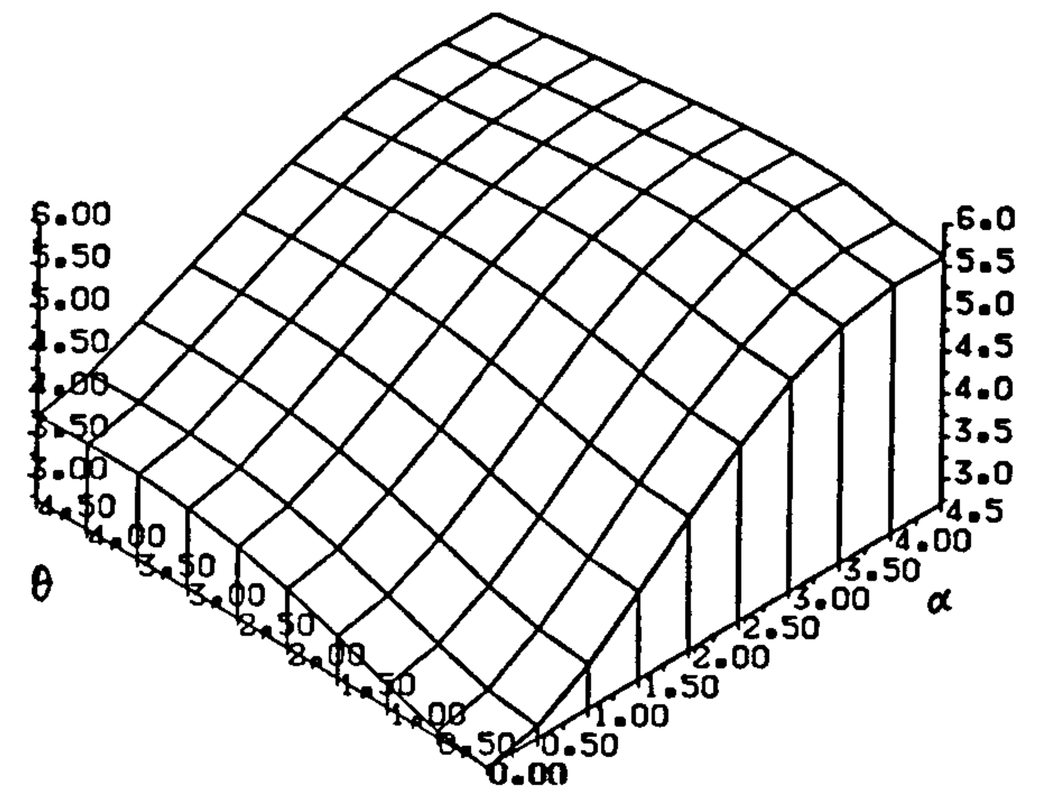

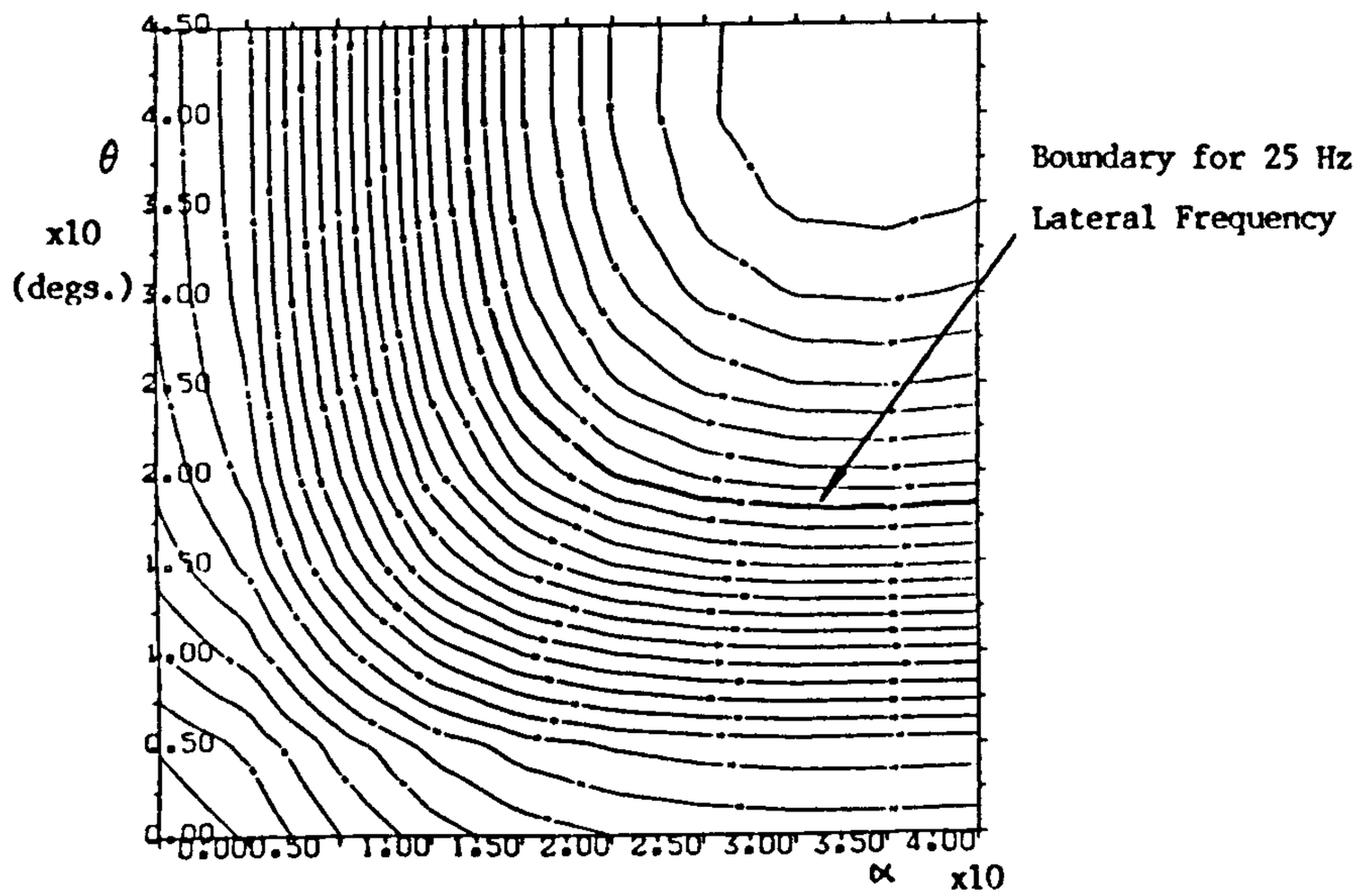

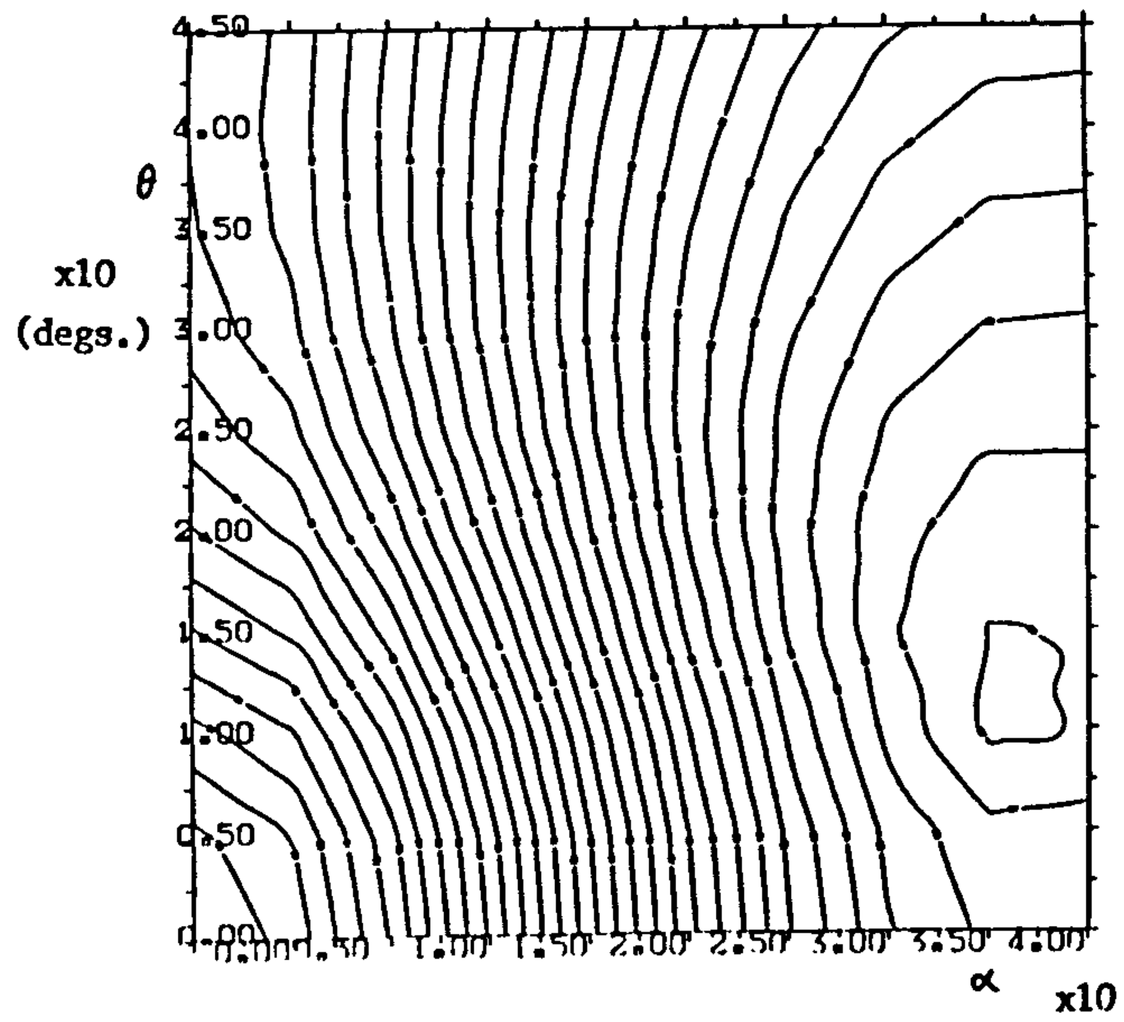

Fig. 8.27 FEASIBLE DESIGN REGION Co-cured HM-S/985

SPACECRAFT THRUST TUBE	T-SAT
Material System	HM-S/CYCOM 985 (CO-CURED) 0·10 mm
Facesheet Lay-Up	OTM : $[0_4/\pm\alpha_2]$ CYLINDER $[0_2/\pm\theta]$
PLOT	FEASIBLE DESIGN REGION
Load Case N_x = N_{xy} =	

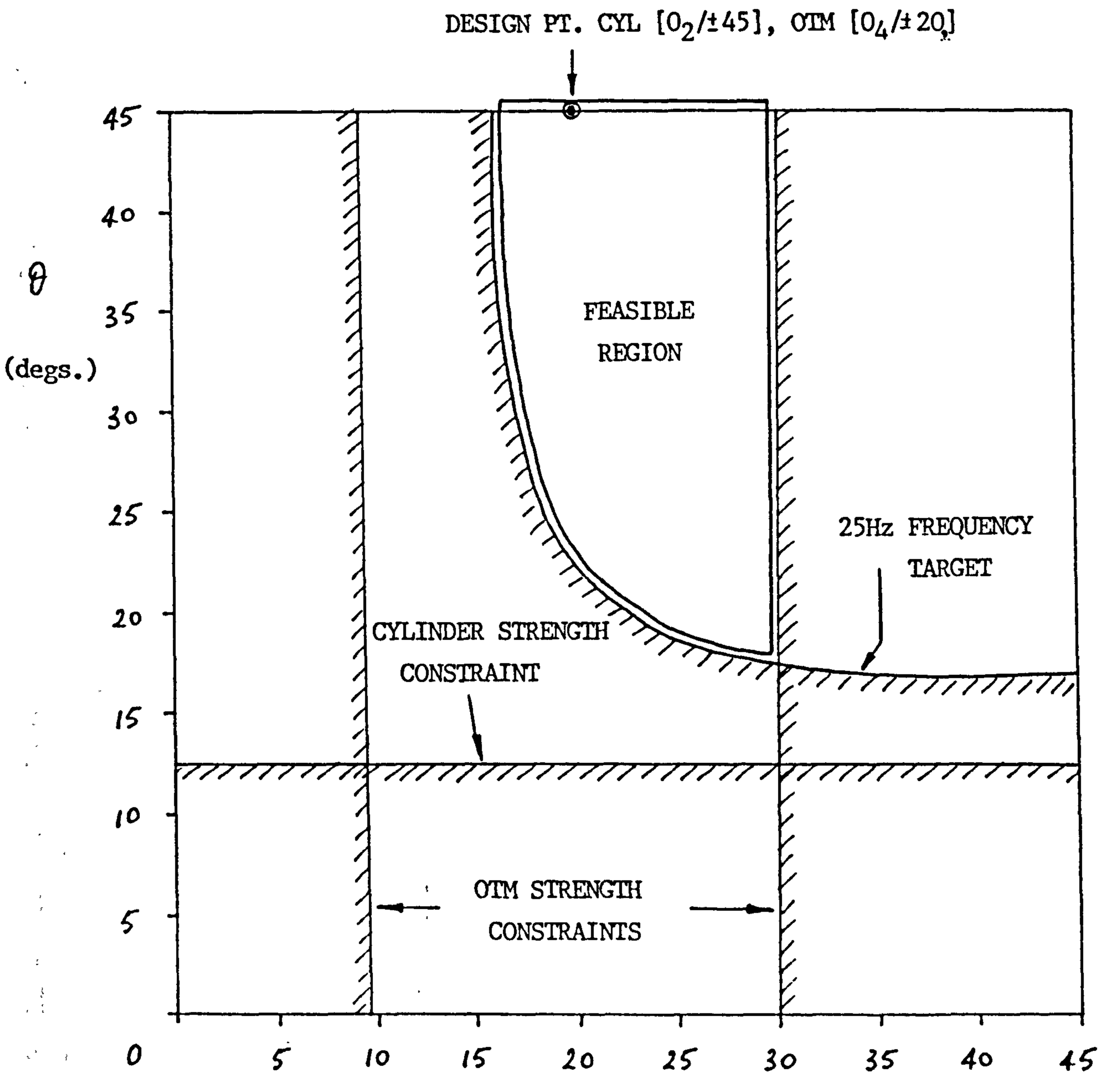

Fig. 8.28 TSAI-WU INDEX : CYLINDER (MAX. AXIAL LOAD CASE)

SPACECRAFT THRUST TUBE	T-SAT CYLINDER
Material System	HM-S/CODE 69 (PRE-CURED) 0·05mm
Facesheet Lay-Up	$[+\theta/-\theta/+\phi/-\phi/-\theta/+\theta]$
PLOT	MAX. PLY TSAI-WU INDEX
Load Case N_x =	-96 N/mm
N_{xy} =	14 N/mm

Fig. 8.29 TSAI-WU INDEX : OTM (MAX. AXIAL LOAD CASE)

SPACECRAFT THRUST TUBE	T-SAT OTM
Material System	HM-S/CODE 69 (PRE-CURED) 0·10 mm
Facesheet Lay-Up	$[\pm\alpha_2/\pm\beta_2]$
PLOT	MAX. PLY TSAI-WU INDEX
Load Case N_x =	-250 N/mm
N_{xy} =	0 N/mm

Pre-cured HM-S/69

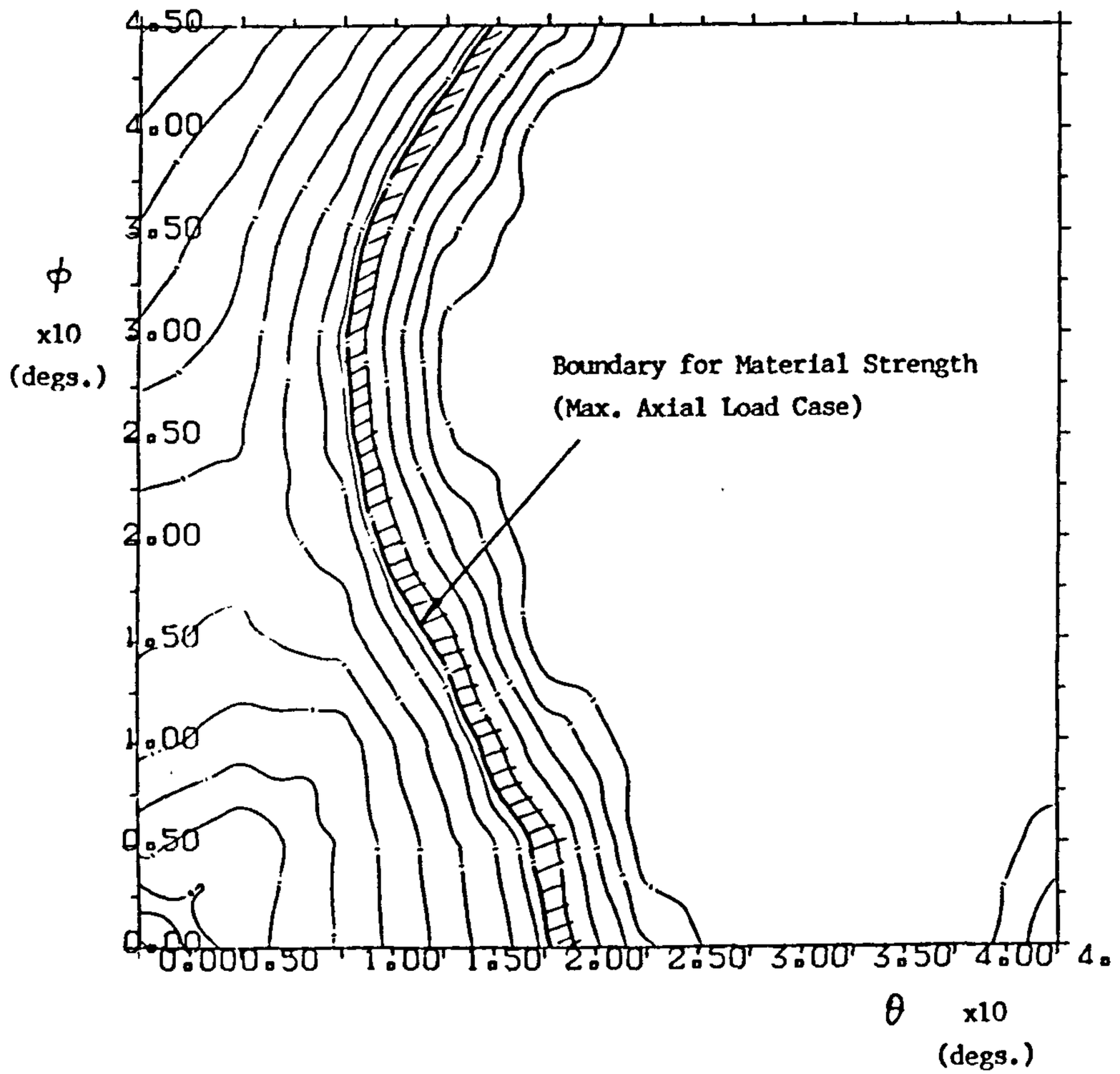

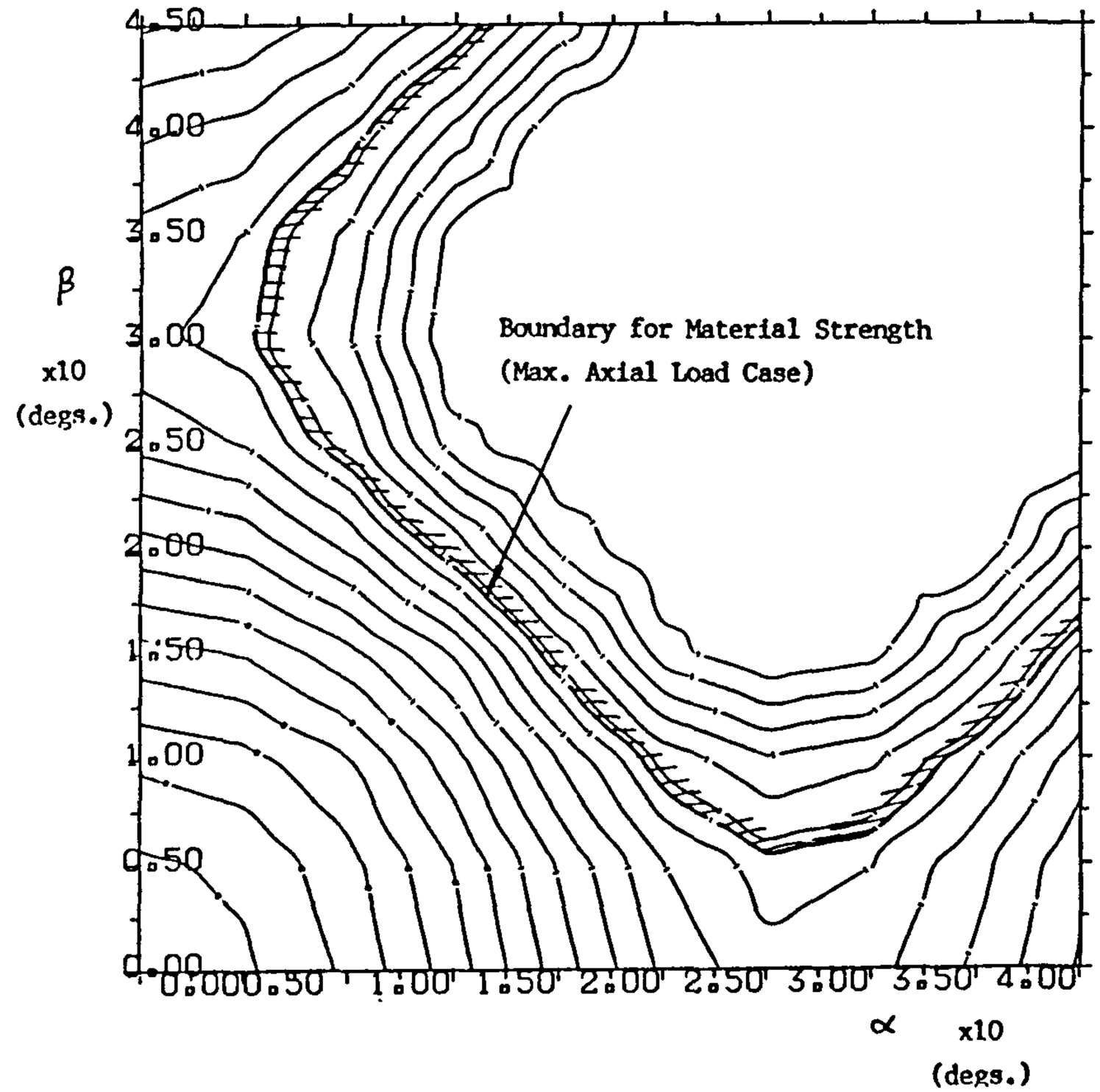

Fig. 8.30 T-SAT FIRST LATERAL FREQUENCY Pre-cured HM-S/69

SPACECRAFT THRUST TUBE	T-SAT
Material System	HM-S / CODE 69 (PRE-CURED) 0·05 & 0·10 mm
Facesheet Lay-Up	OTM: $[0_4/\pm\alpha_2]$ x 0·10mm CYL: $[0_4/\pm\Phi]$ x 0·05 mm
PLOT	FIRST LATERAL FREQUENCY (Hz)
Load Case N_x =	
N_{xy} =	

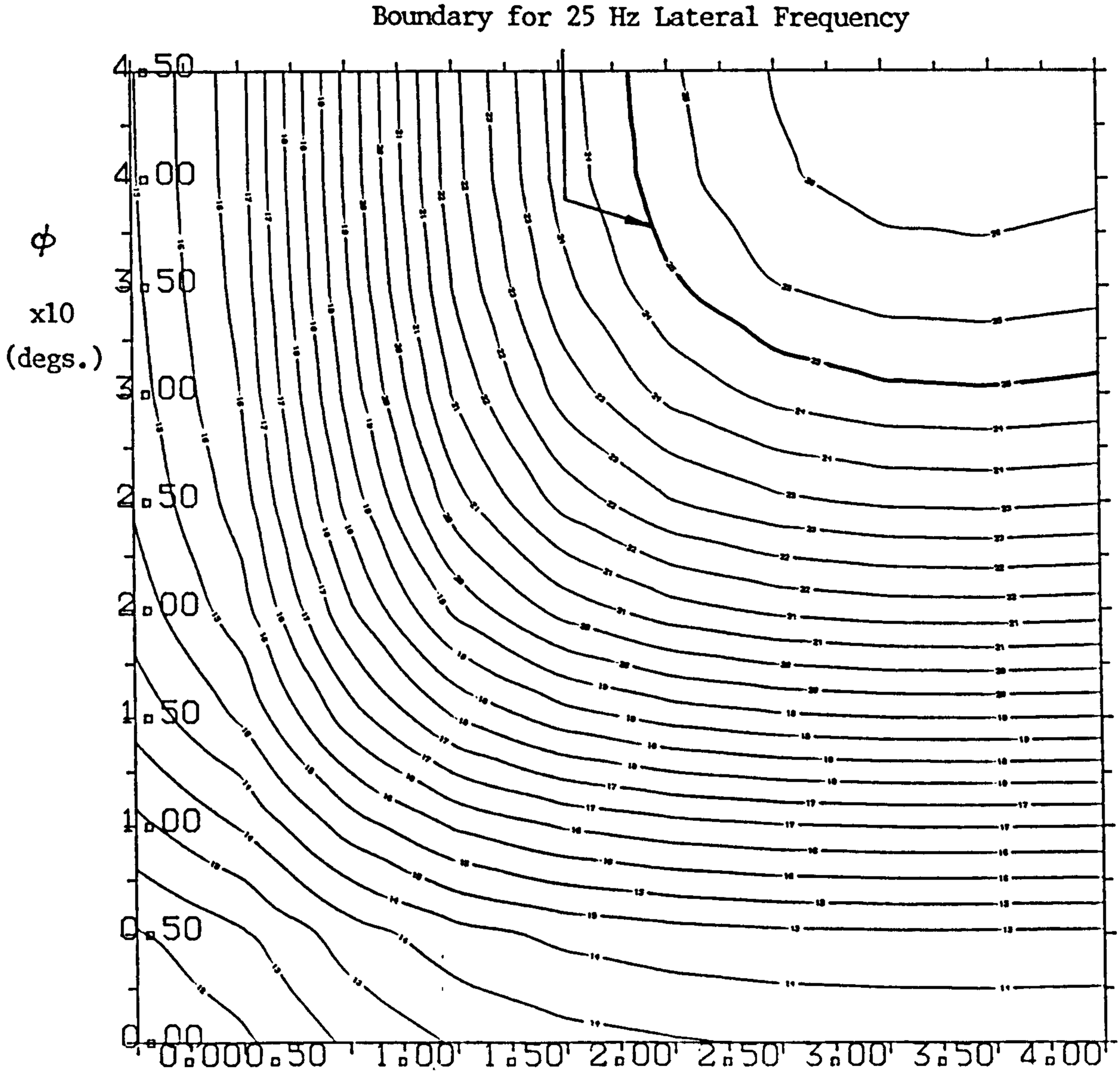

Fig. 8.31 T-SAT FIRST LATERAL FREQUENCY Pre-cured T-300/69

SPACECRAFT THRUST TUBE	T-SAT
Material System Facesheet Lay-Up	T-300 / CODE 69 (PRE-CURED) 0·10 mm OTM: $[(\pm\alpha)_4]$ CYLINDER: $[(\pm\theta)_2]$
PLOT	FIRST LATERAL FREQUENCY (Hz)
Load Case N_x = N_{xy} =	

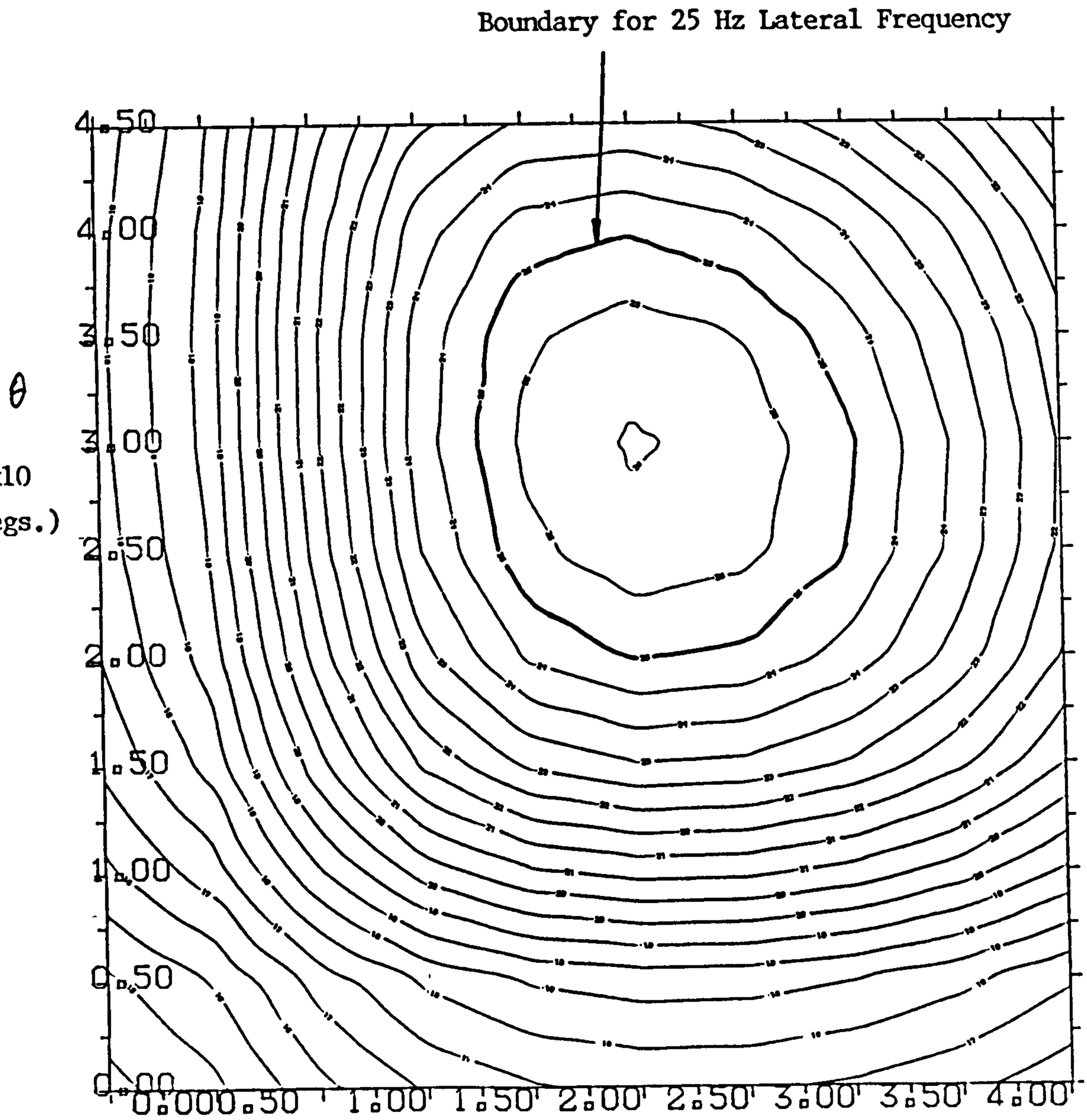

Fig. 8.32 FIRST LATERAL FREQUENCY vs. ALUMINIUM FACESHEET MASS FOR T-SAT THRUST TUBE

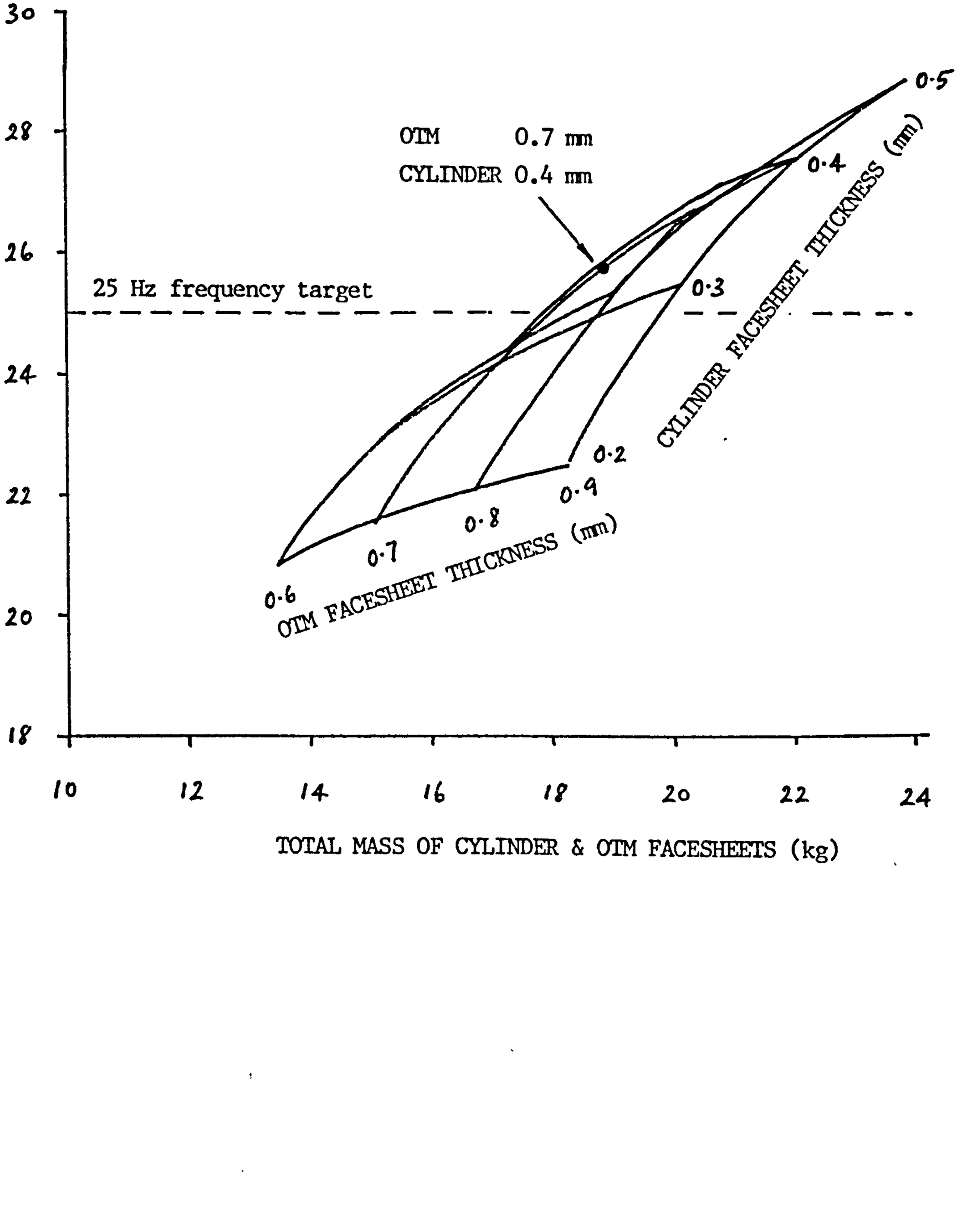

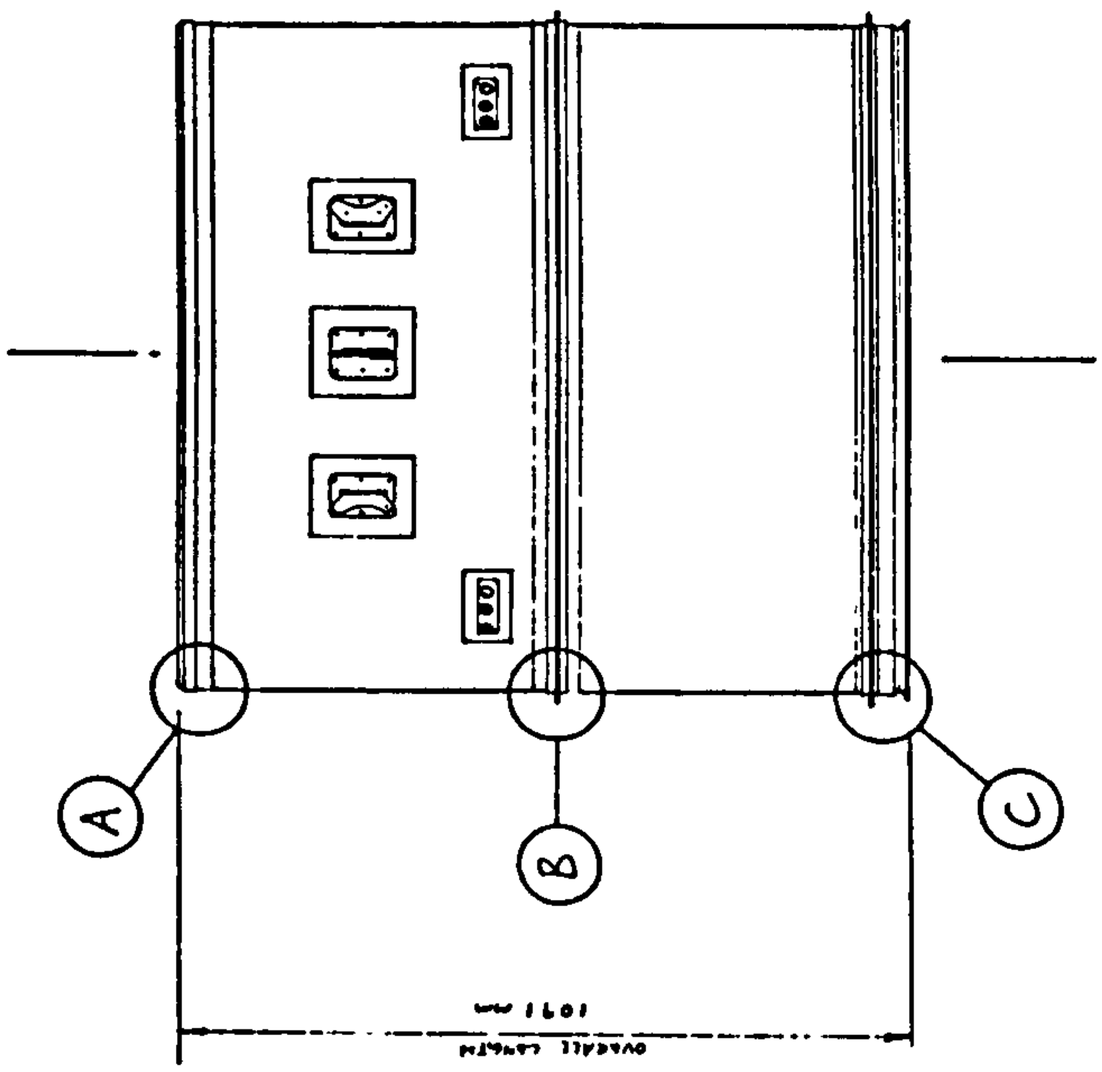

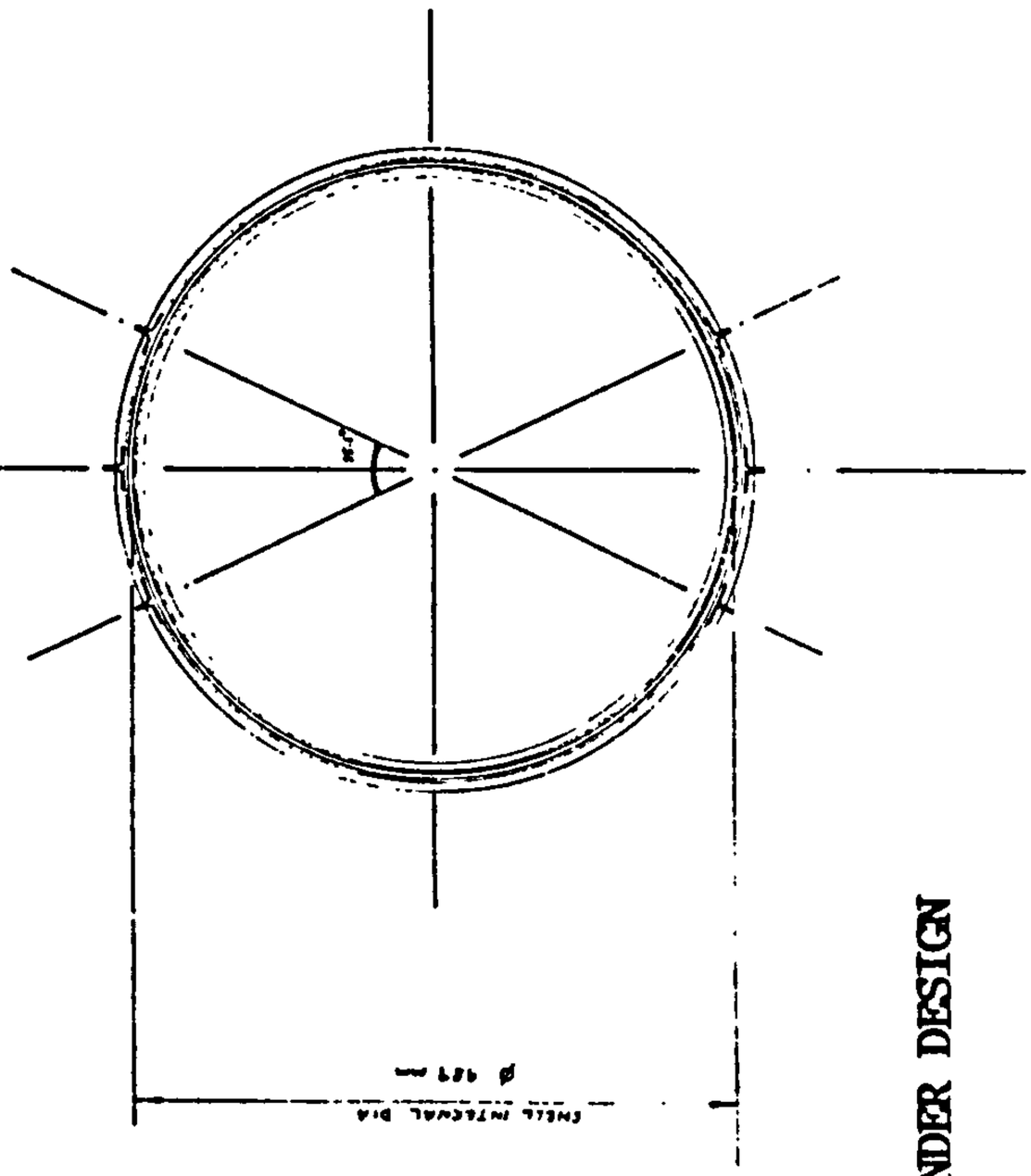

THRUST CYLINDER DESIGN

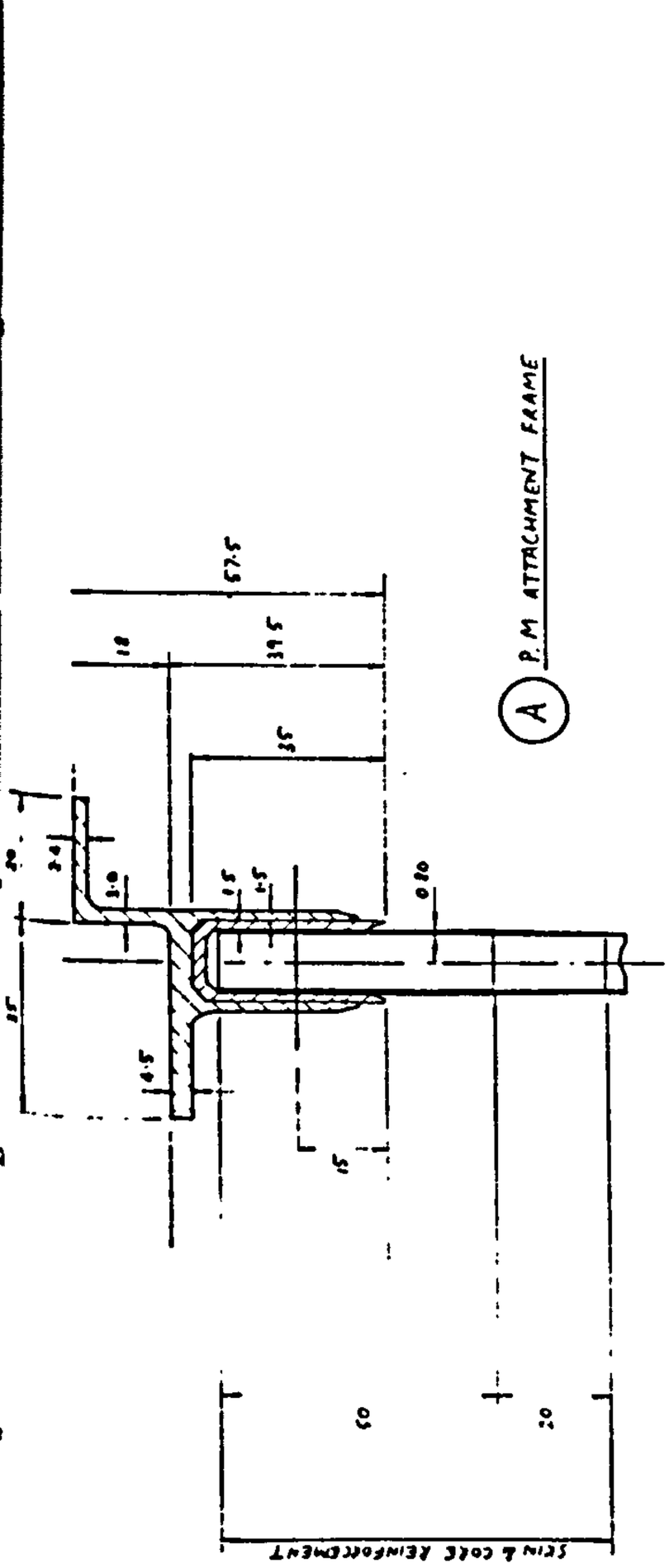

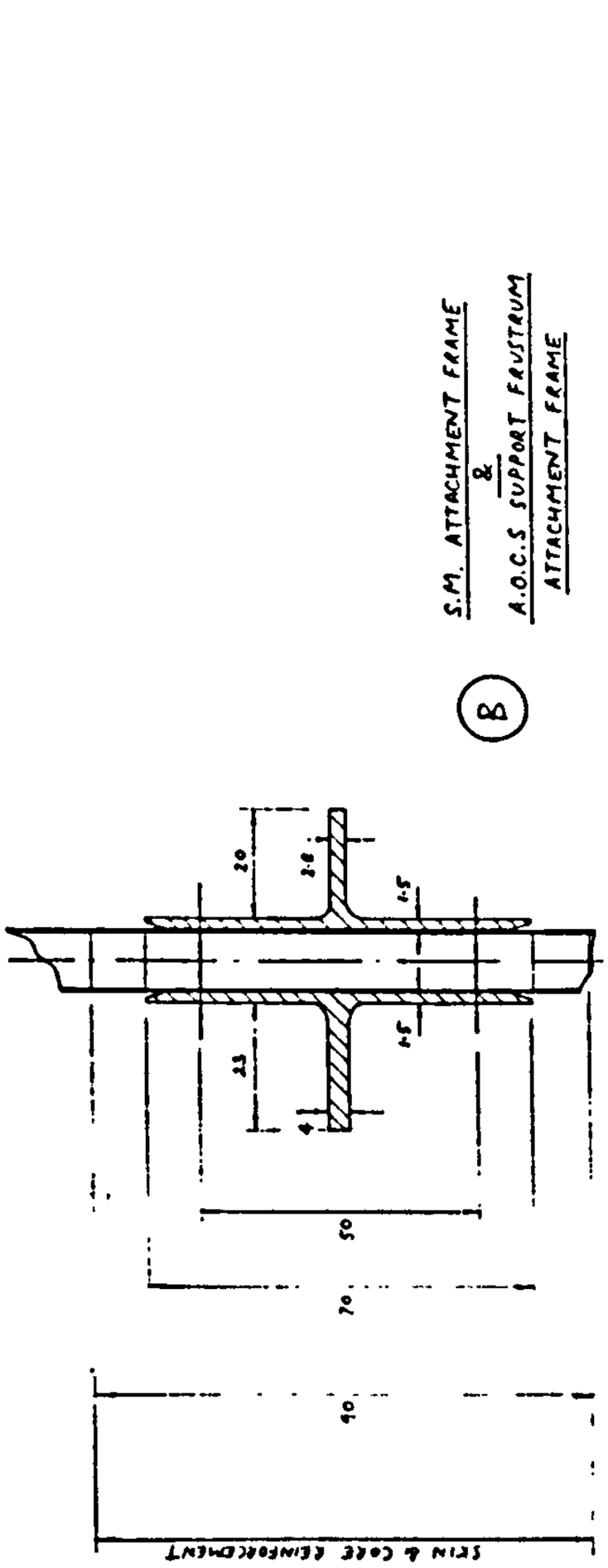

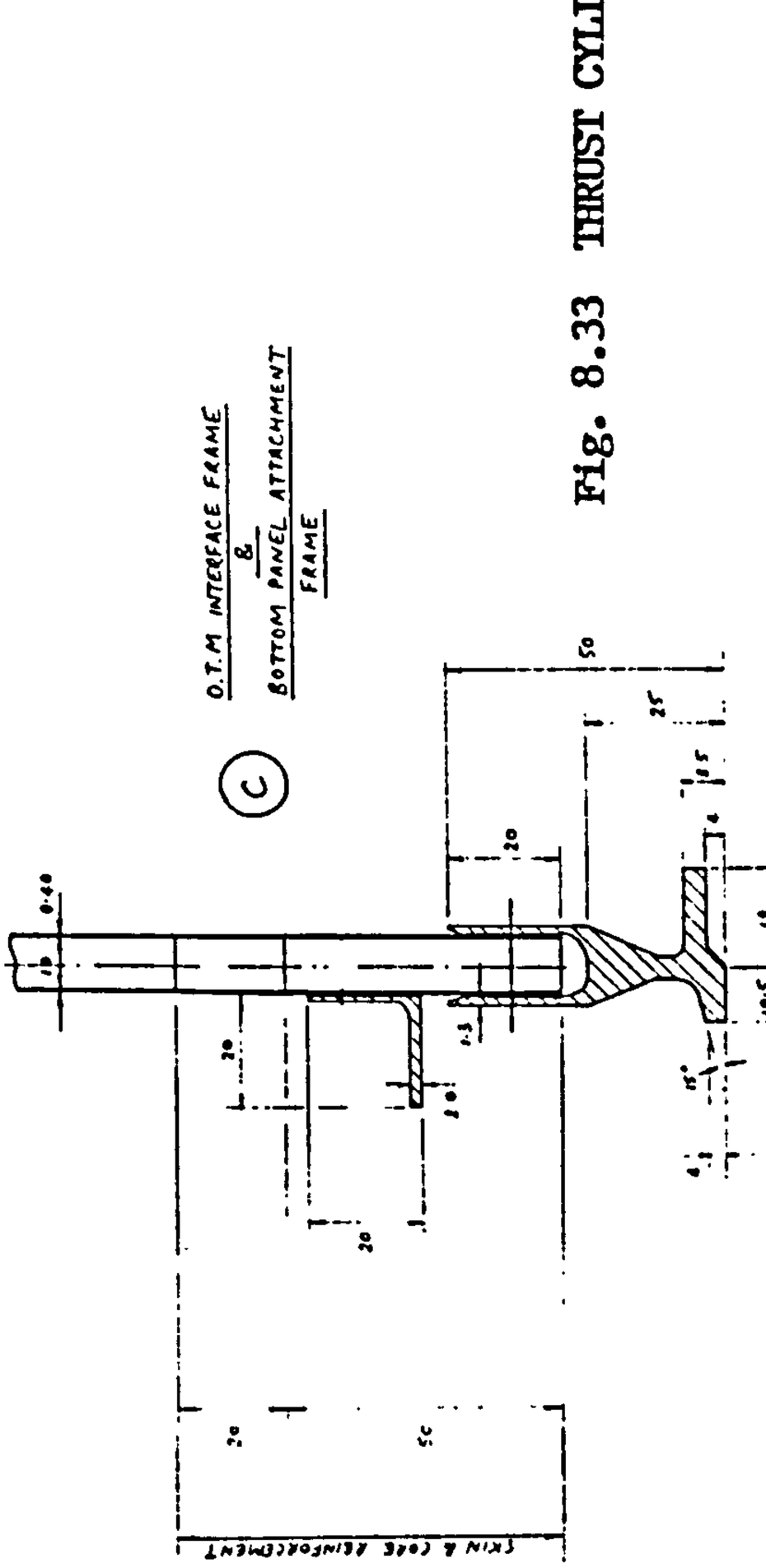

Fig. 8.33 T

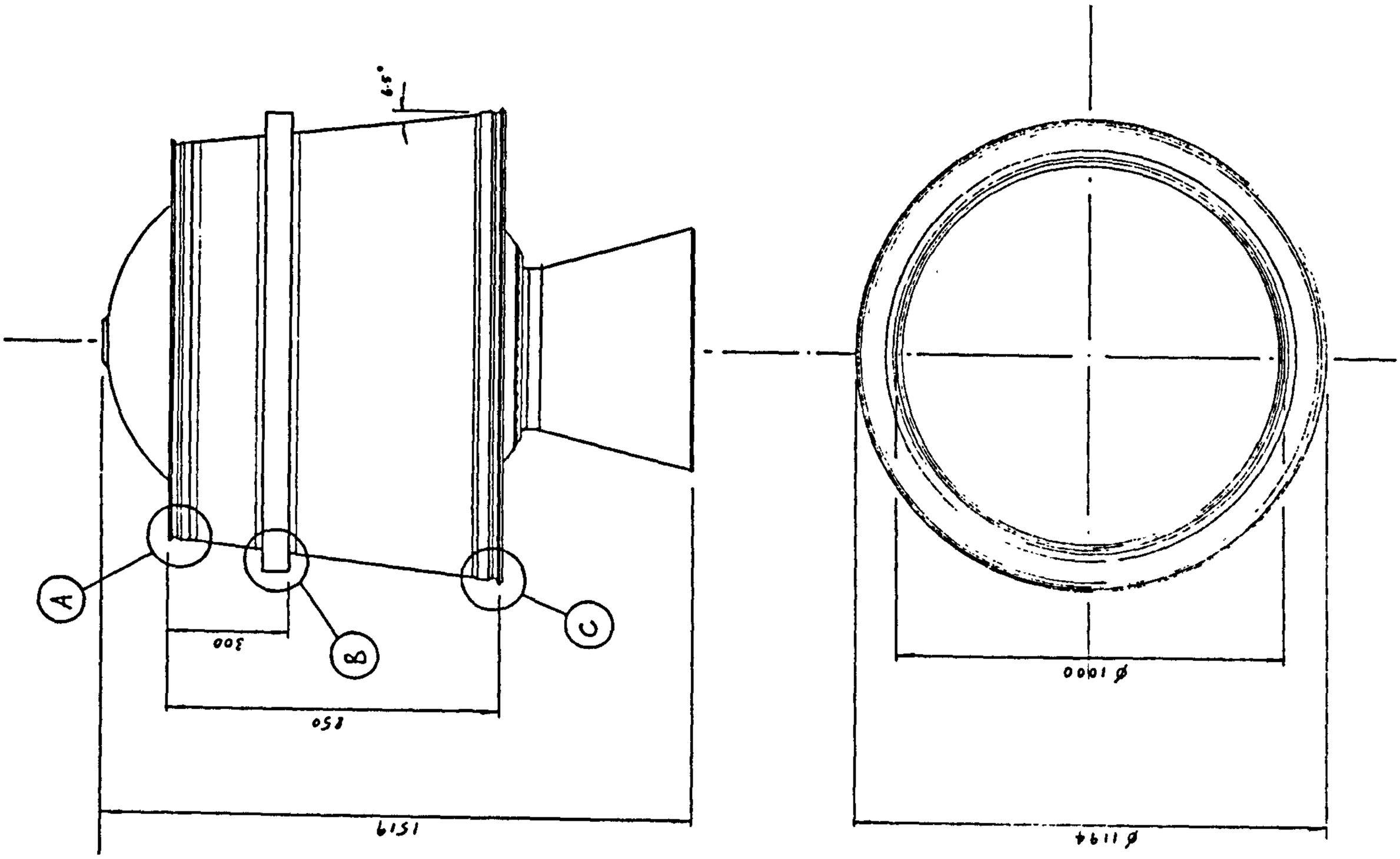

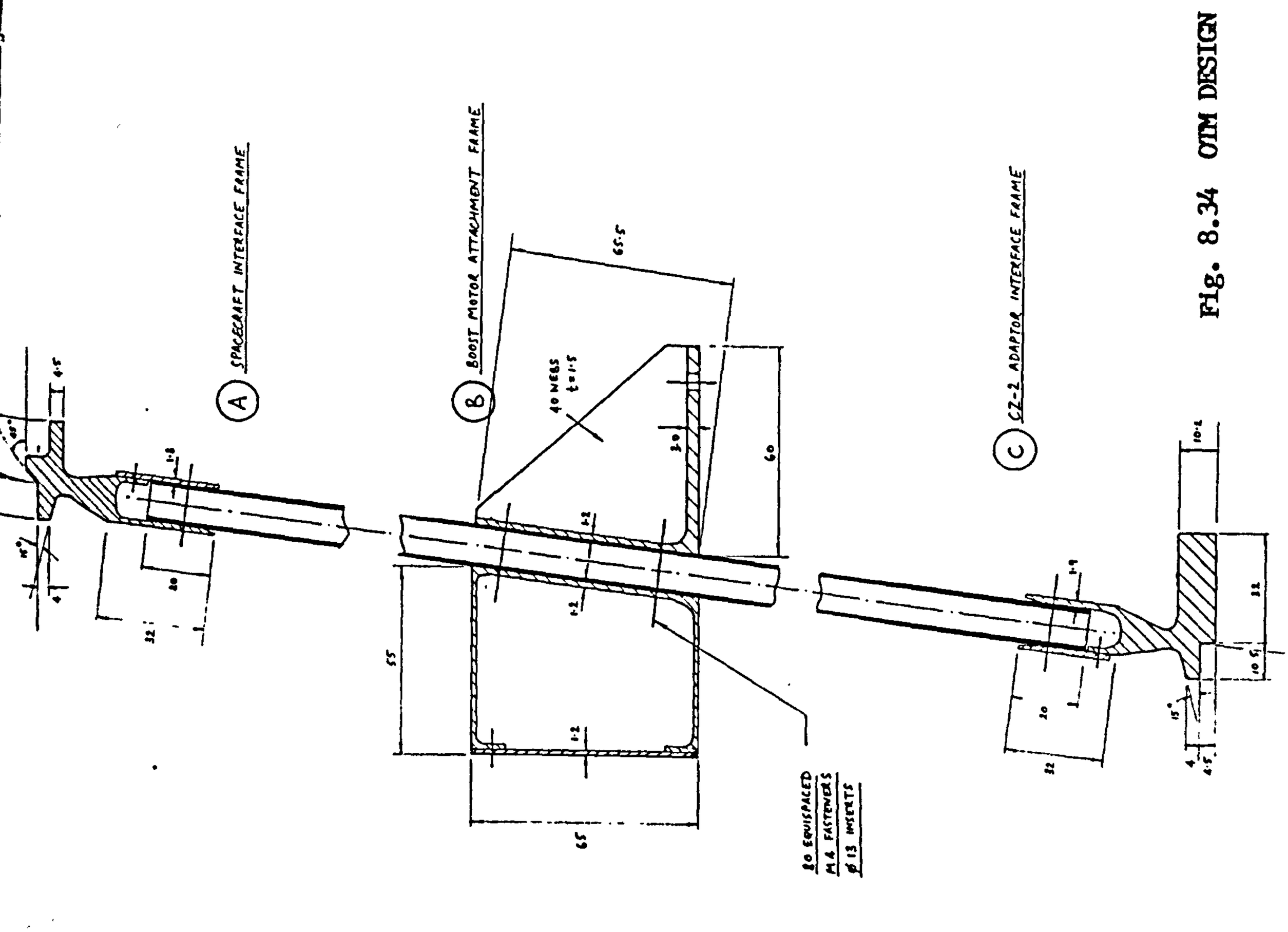

Fig. 8.34 OTM DESIGN

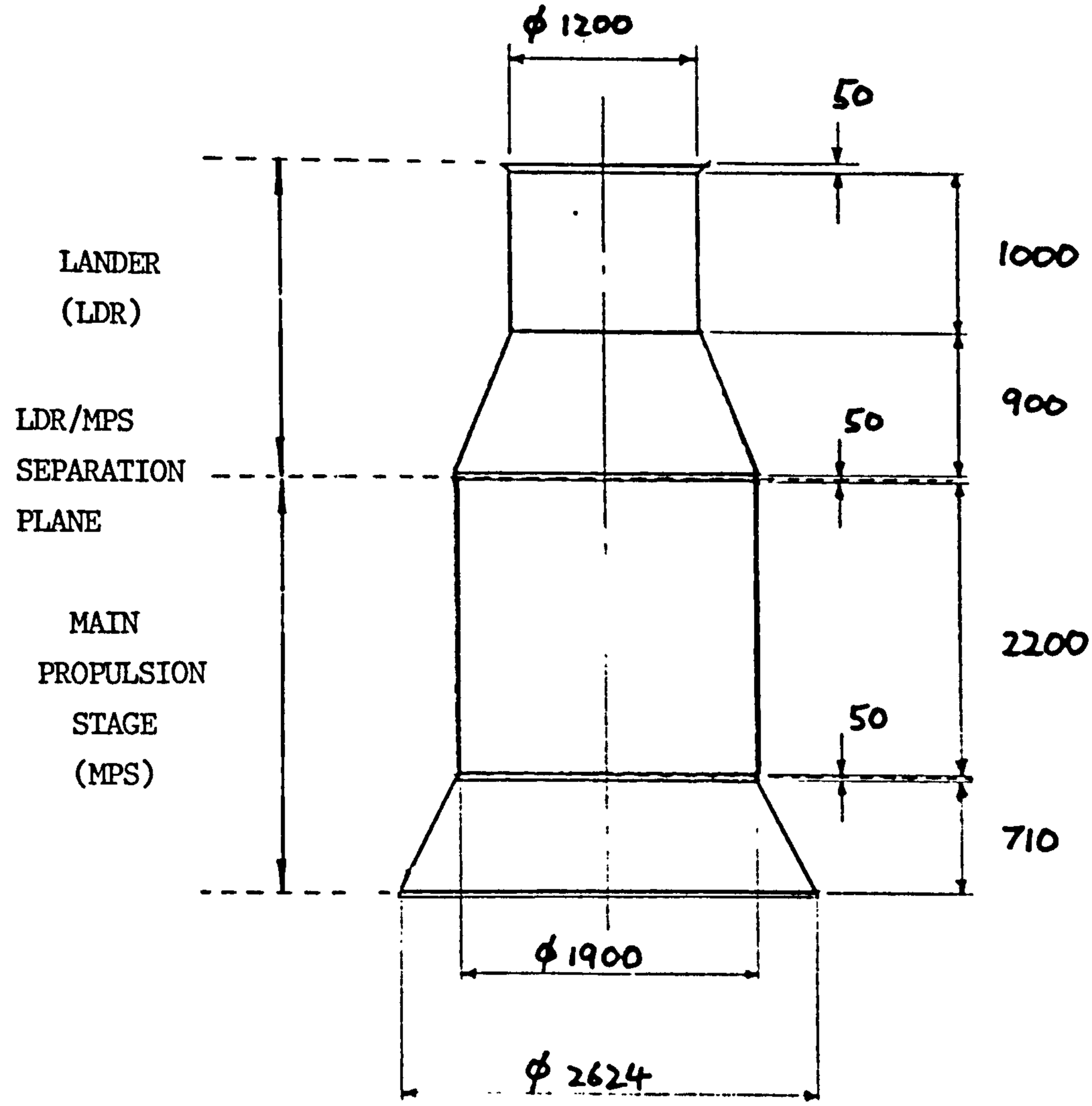

Fig. 8.35 PRIMUS THRUST TUBE CONFIGURATION

Fig. 8.36 TSAI-WU INDEX vs. FIBRE ANGLE FOR PRIMUS LDR
[+θ/-θ/-θ/+θ] x 0.05 mm pre-cured T-300/69 FACESHEETS

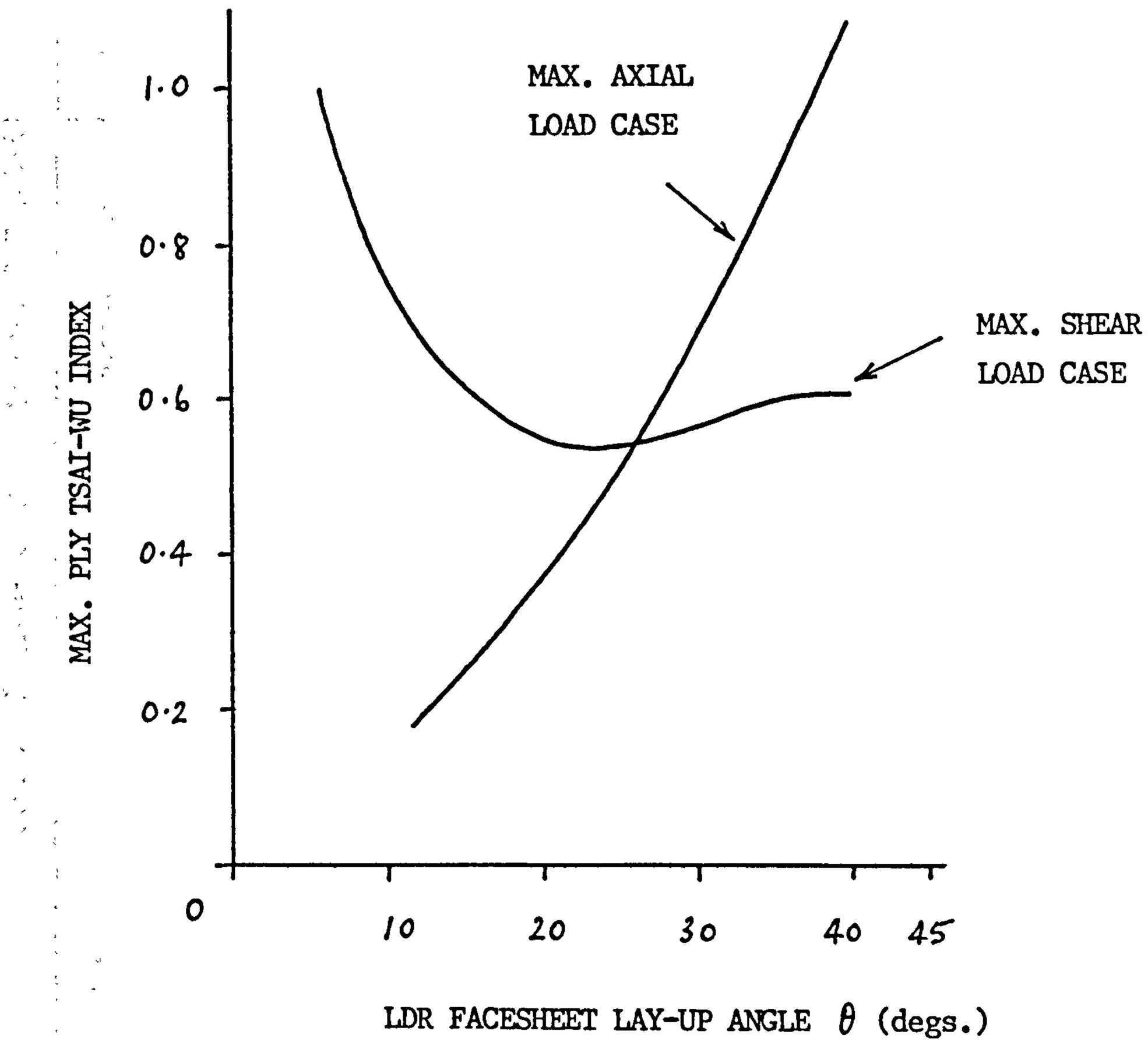

Fig. 8.37 TSAI-WU INDEX Pre-cured T-300/69

SPACECRAFT THRUST TUBE	PRIMUS MPS
Material System	T-300/CODE 69 (PRE-CURED) 0·10 mm
Facesheet Lay-Up	$[\pm\alpha_3/\pm\beta_2]$
PLOT	MAX. PLY TSAI-WU INDEX
Load Case N_x =	−360 N/mm
N_{xy} =	0 N/mm

(a) MAX. AXIAL

SPACECRAFT THRUST TUBE	PRIMUS MPS
Material System	T-300/CODE 69 (PRECURED) 0·10 mm
Facesheet Lay-Up	$[\pm\alpha_3/\pm\beta_2]$
PLOT	MAX. PLY TSAI-WU INDEX
Load Case N_x =	−190 N/mm
N_{xy} =	190 N/mm

(b) MAX. SHEAR

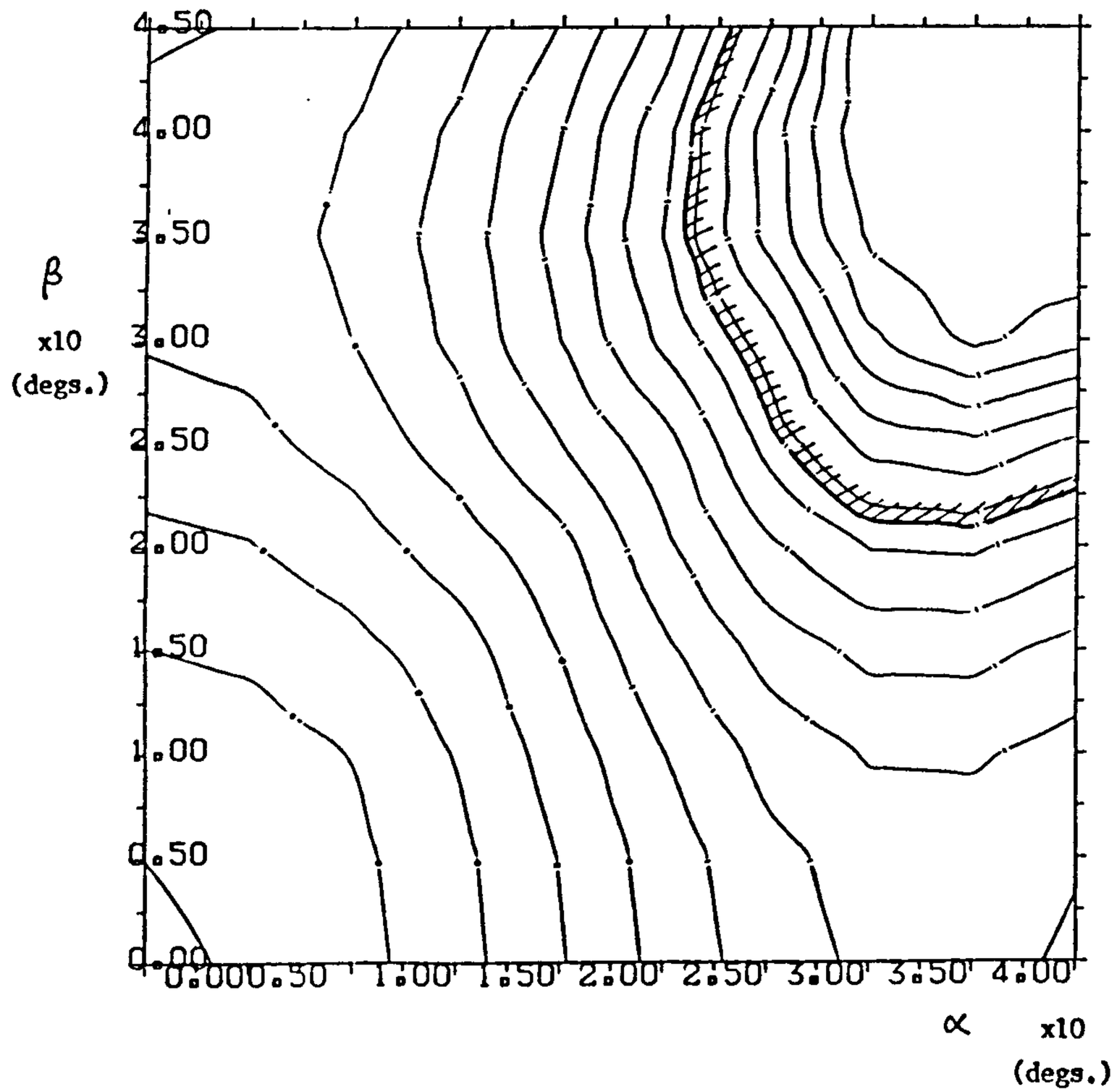

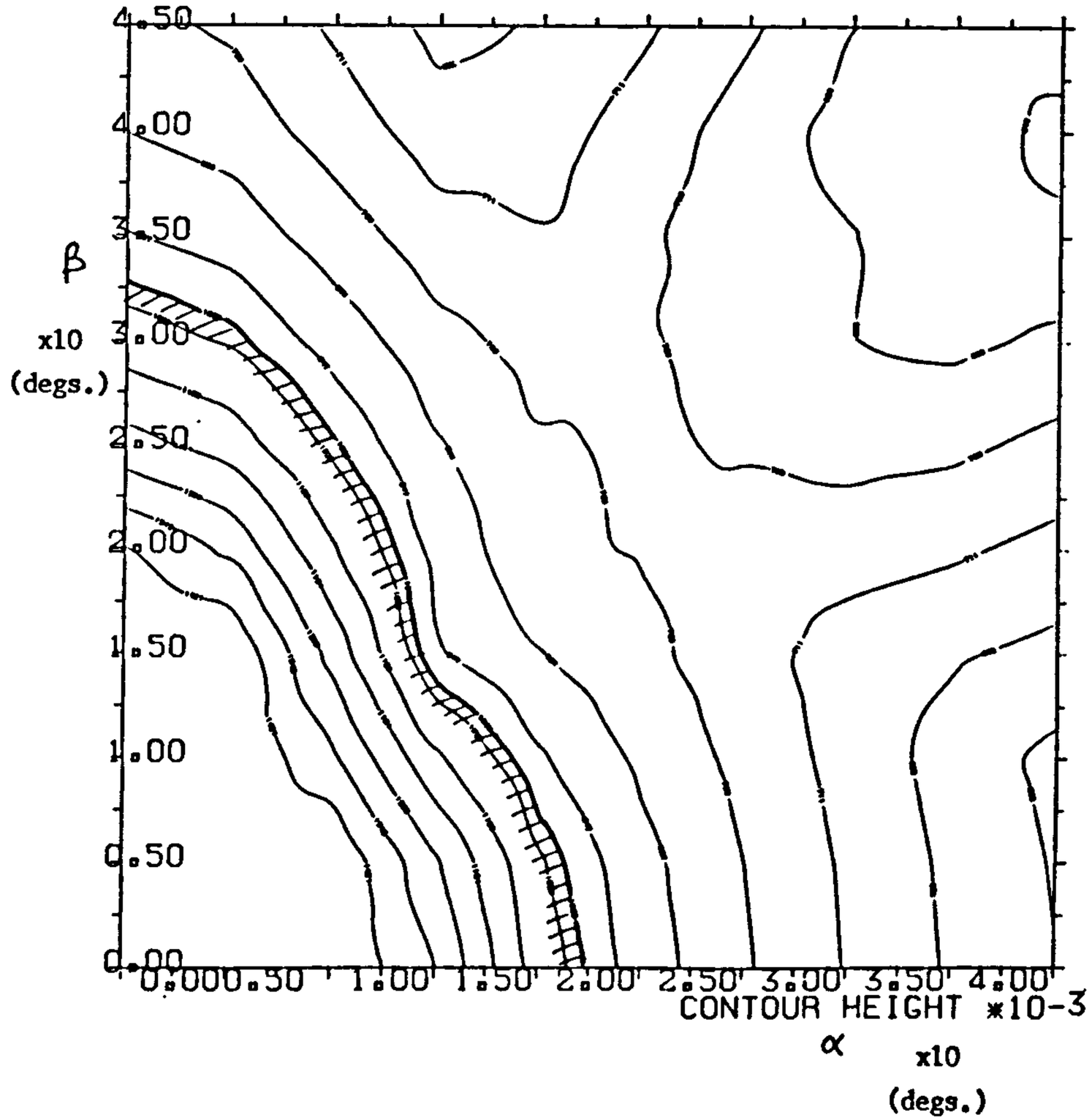

Fig. 8.38 PRIMUS FIRST LATERAL FREQUENCY Pre-cured T-300/69

SPACECRAFT THRUST TUBE	PRIMUS
Material System Facesheet Lay-Up	T-300/CODE 69 (PRE-CURED) 0·05mm & 0·10mm MPS: $[\pm\alpha_3/\pm\beta_2] \times 0{\cdot}10mm$ LDR: $[\pm 30_2] \times 0{\cdot}05mm$
PLOT	FIRST LATERAL FREQUENCY (Hz)
Load Case N_x = N_{xy} =	

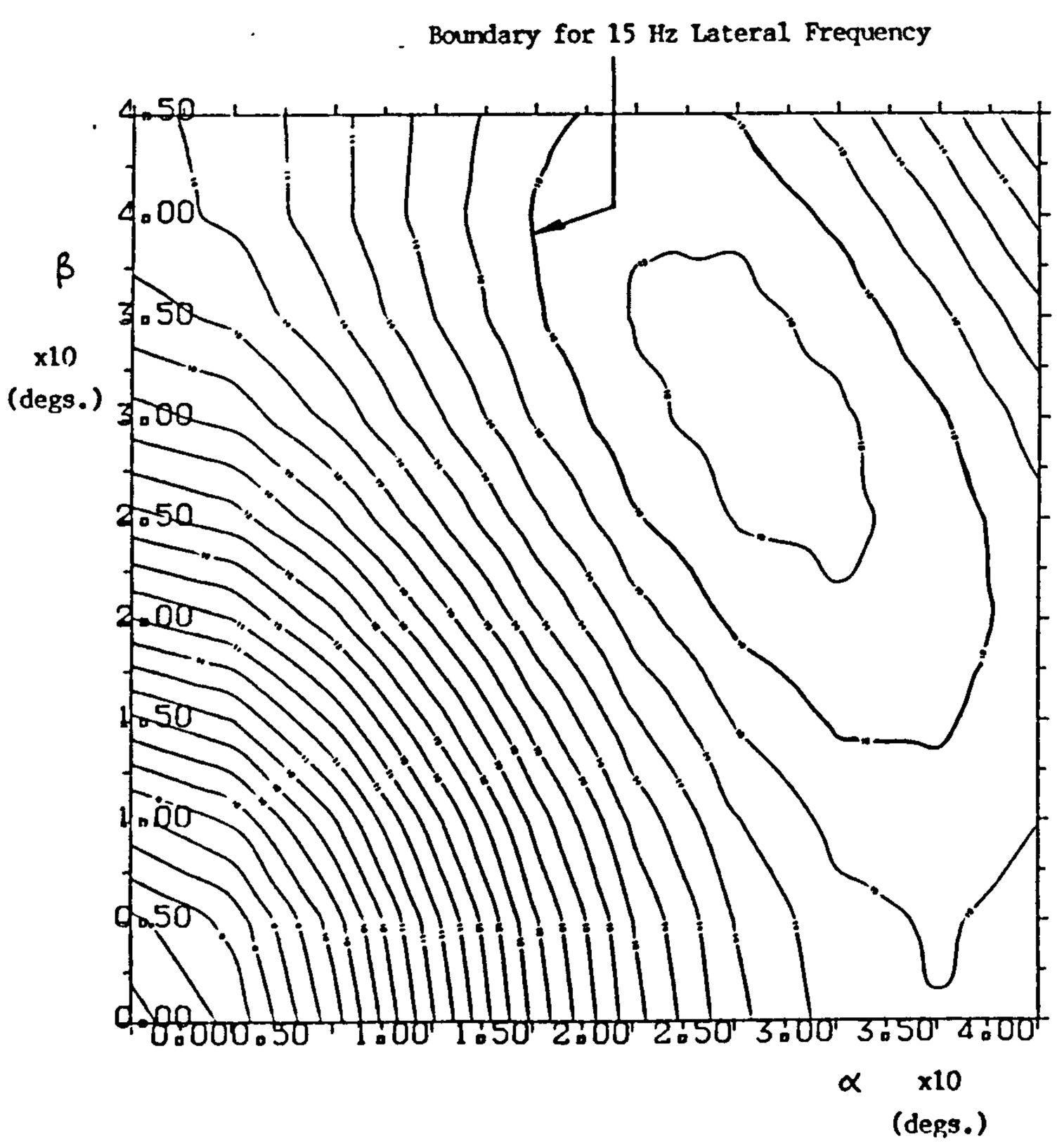

Fig. 8.39 FEASIBLE DESIGN REGION Pre-cured T-300/69

SPACECRAFT THRUST TUBE	PRIMUS
Material System Facesheet Lay-Up	T-300/CODE 69 (PRE-CURED) 0·05mm & 0·10mm MPS: $[\pm\alpha_3/\pm\beta_2] \times 0{\cdot}10mm$ LDR: $[\pm 30_2] \times 0{\cdot}05mm$
PLOT	FEASIBLE DESIGN REGION
Load Case N_x = N_{xy} =	

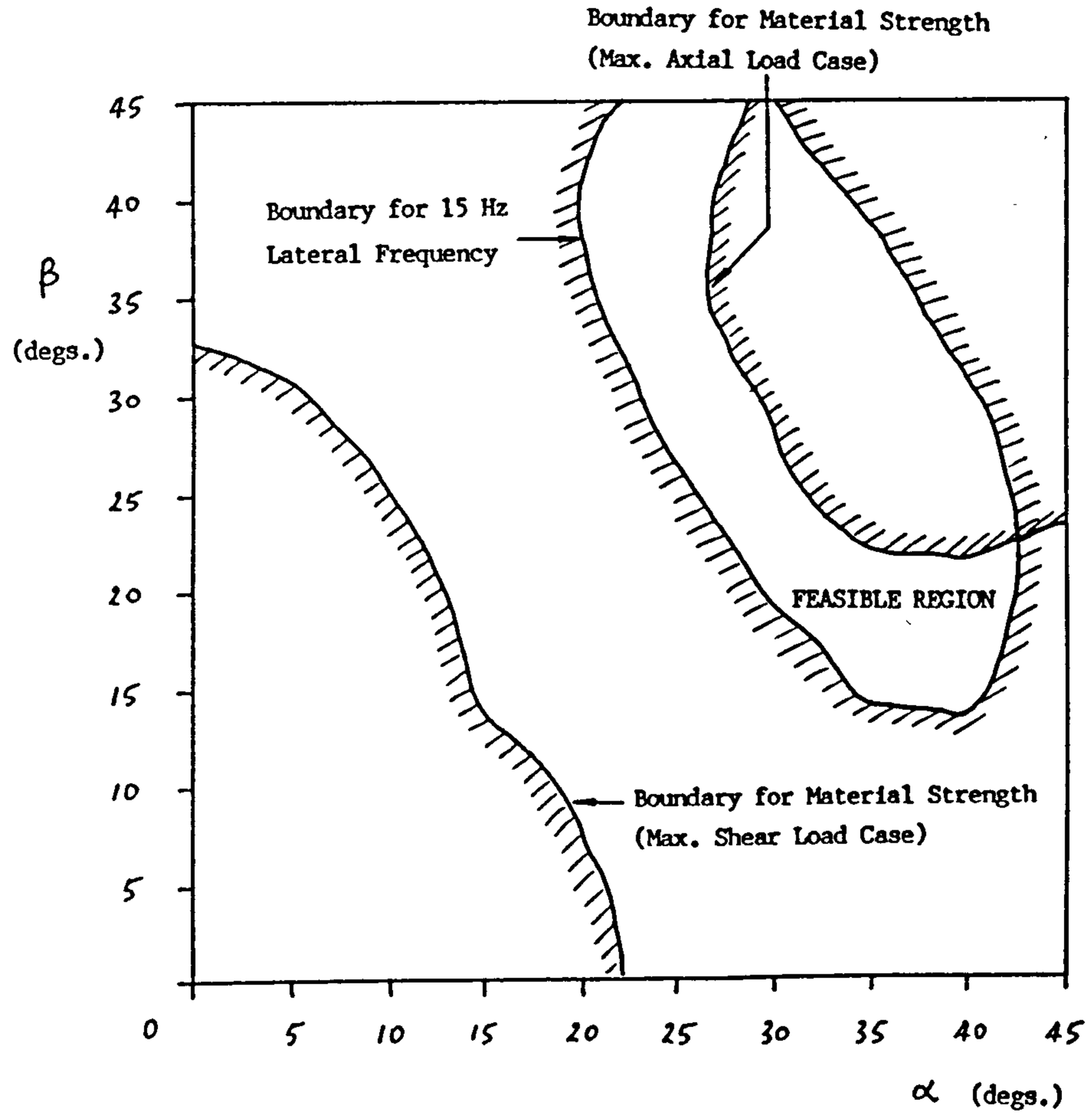

Fig. 8.40 LDR : STRENGTH FEASIBLE REGION Co-cured T-300/69

SPACECRAFT THRUST TUBE	PRIMUS LDR
Material System Facesheet Lay-Up	T-300/CODE 69 (CO-CURED) 0·05 mm $[+\theta/-\phi/+\phi/-\theta]$
PLOT	FEASIBLE REGION FOR MATERIAL STRENGTH
Load Case N_x = N_{xy} =	−54 N/mm & −30 N/mm 0 N/mm & 28 N/mm

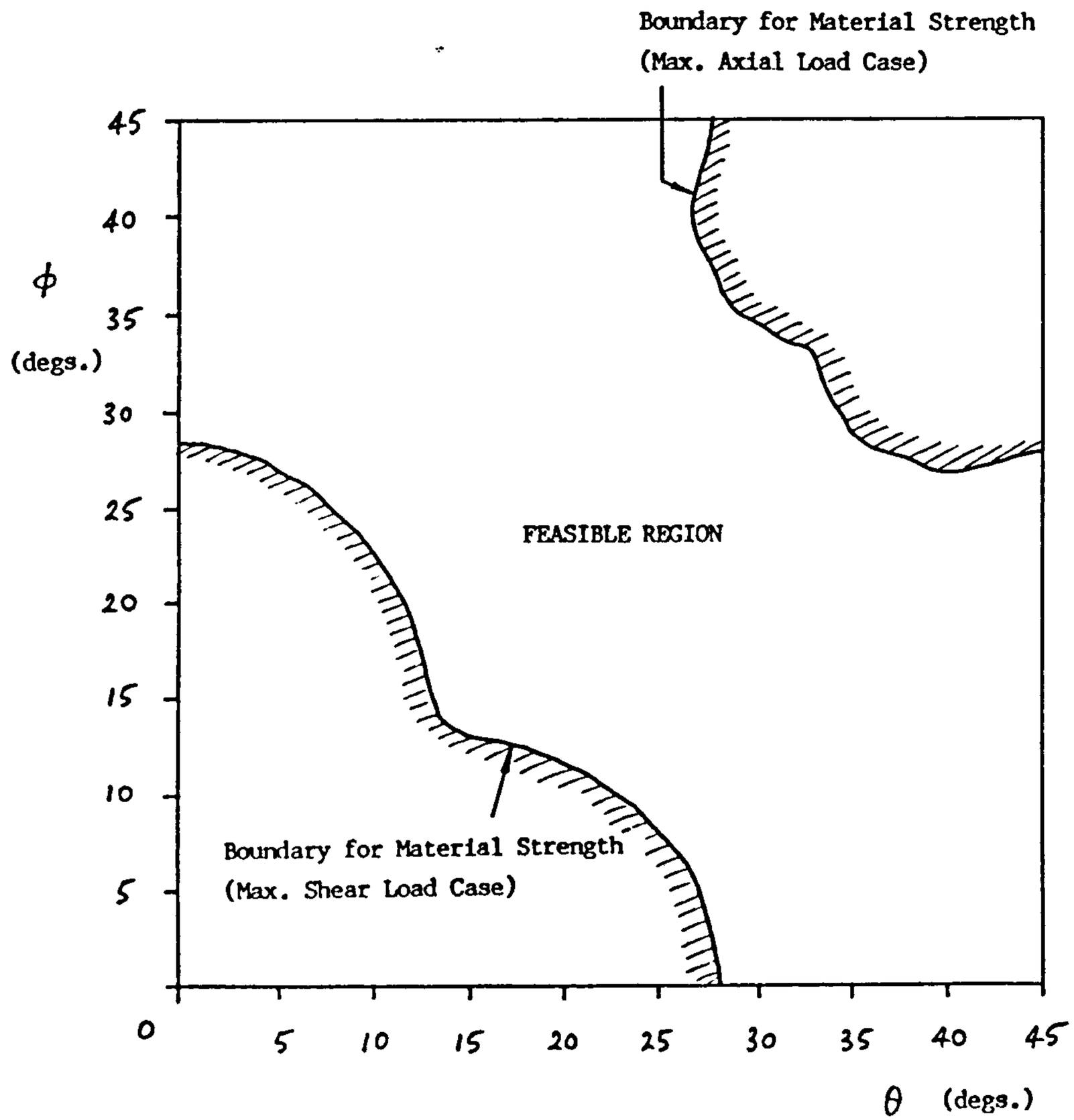

Fig. 8.41 MPS : STRENGTH FEASIBLE REGION Co-cured T-300/69

SPACECRAFT THRUST TUBE	PRIMUS MPS
Material System Facesheet Lay-Up	T-300/CODE 69 (CO-CURED) 0·10 mm $[\pm\alpha_3/\pm\beta_3]$
PLOT	FEASIBLE REGION FOR MATERIAL STRENGTH
Load Case N_x = N_{xy} =	−360 N/mm & −190 N/mm 0 N/mm & 190 N/mm

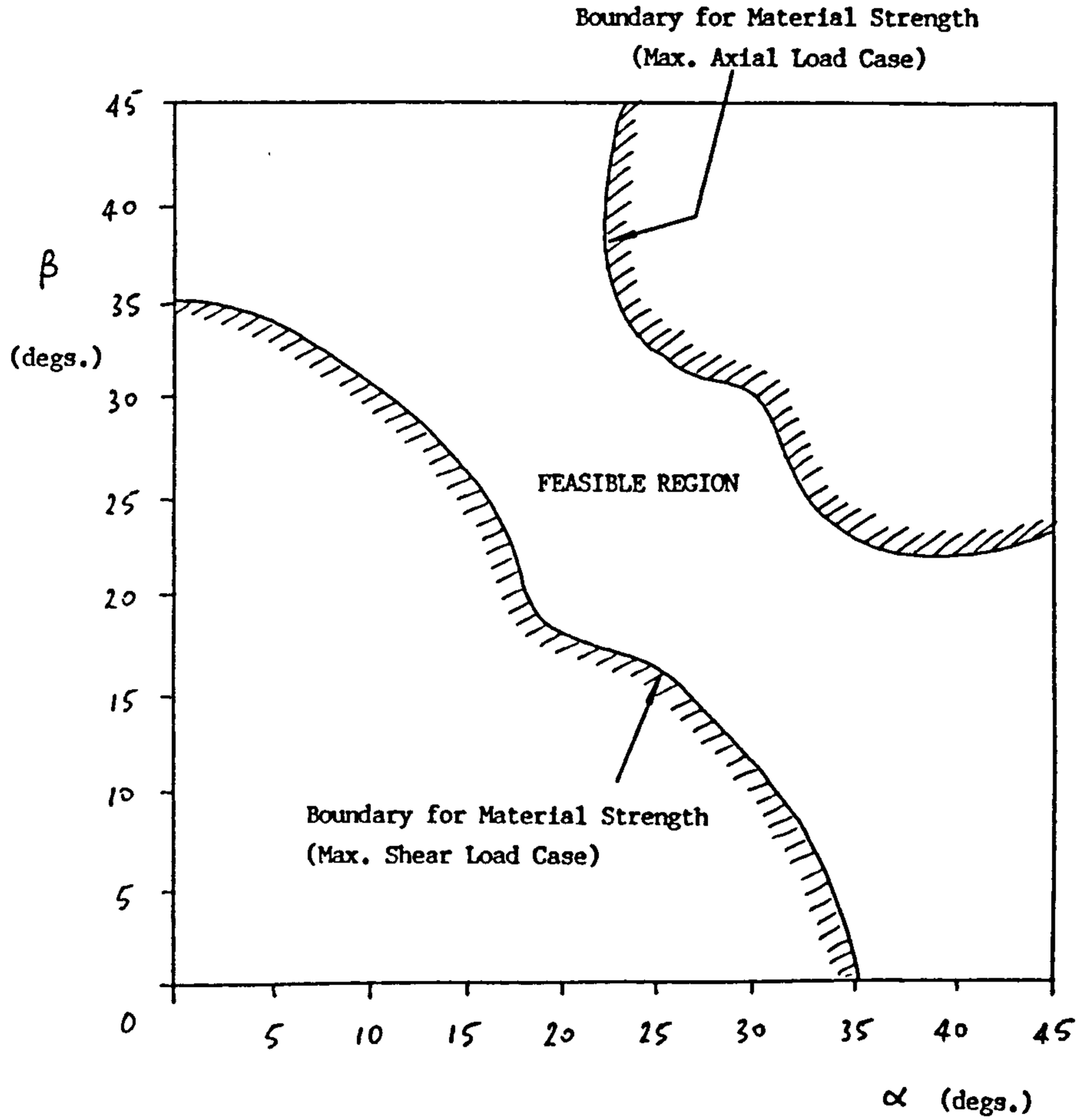

Fig. 8.42 MPS BUCKLING INTERACTION INDEX Co-cured T-300/69

SPACECRAFT THRUST TUBE	PRIMUS MPS	SPACECRAFT THRUST TUBE	PRIMUS MPS
Material System Facesheet Lay-Up	T-300/CODE 69 (CO-CURED) 0·10 mm $[\pm\alpha_3/\pm\beta_3]$	Material System Facesheet Lay-Up	T-300/CODE 69 (CO-CURED) 0·10 mm $[\pm\alpha_3/\pm\beta_3]$
PLOT	BUCKLING INTERACTION INDEX	PLOT	BUCKLING INTERACTION INDEX
Load Case N_x = N_{xy} =	−360 N/mm 0 N/mm	Load Case N_x = N_{xy} =	−190 N/mm 190 N/mm

(a) MAX. AXIAL

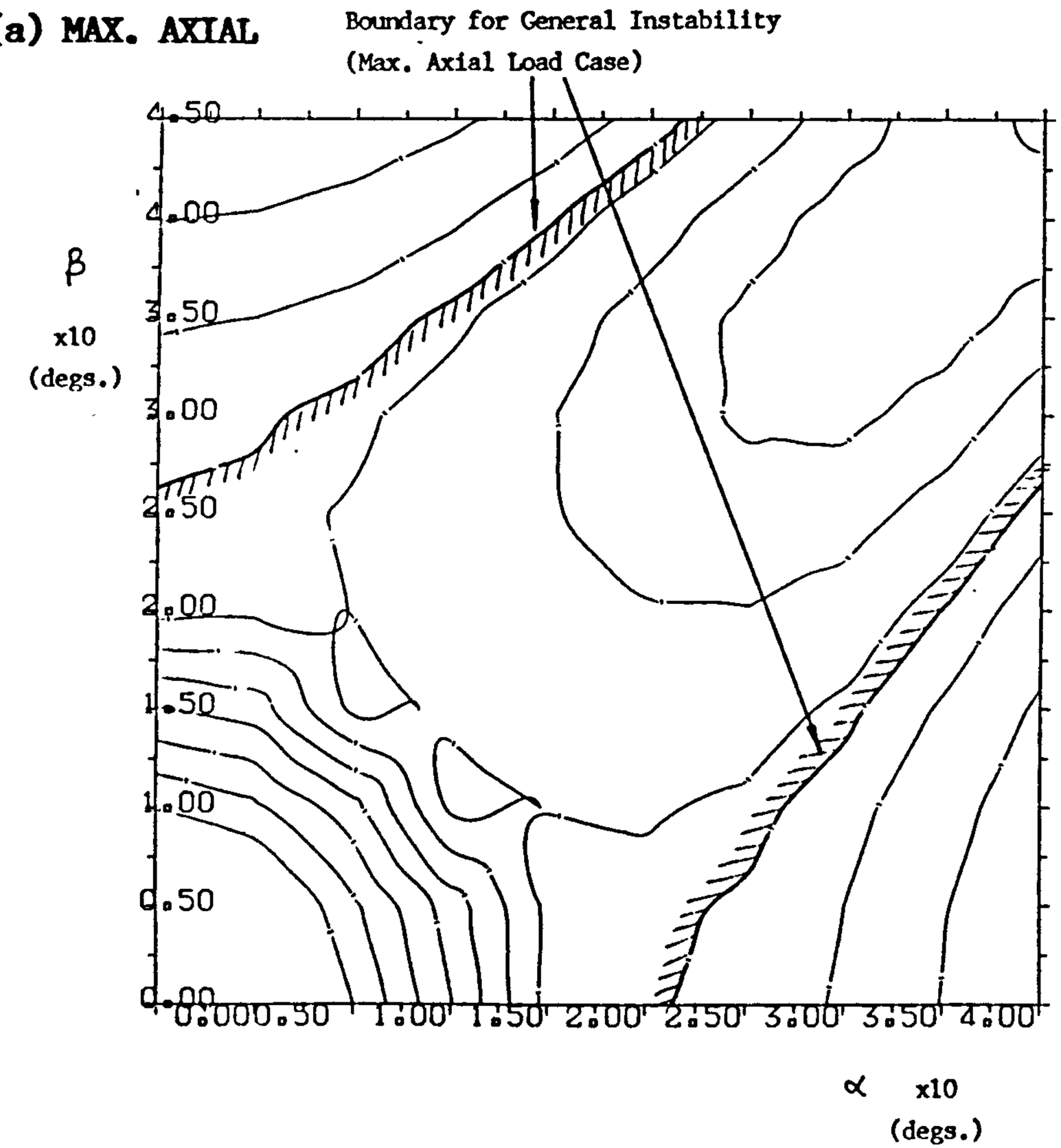

(b) MAX. SHEAR

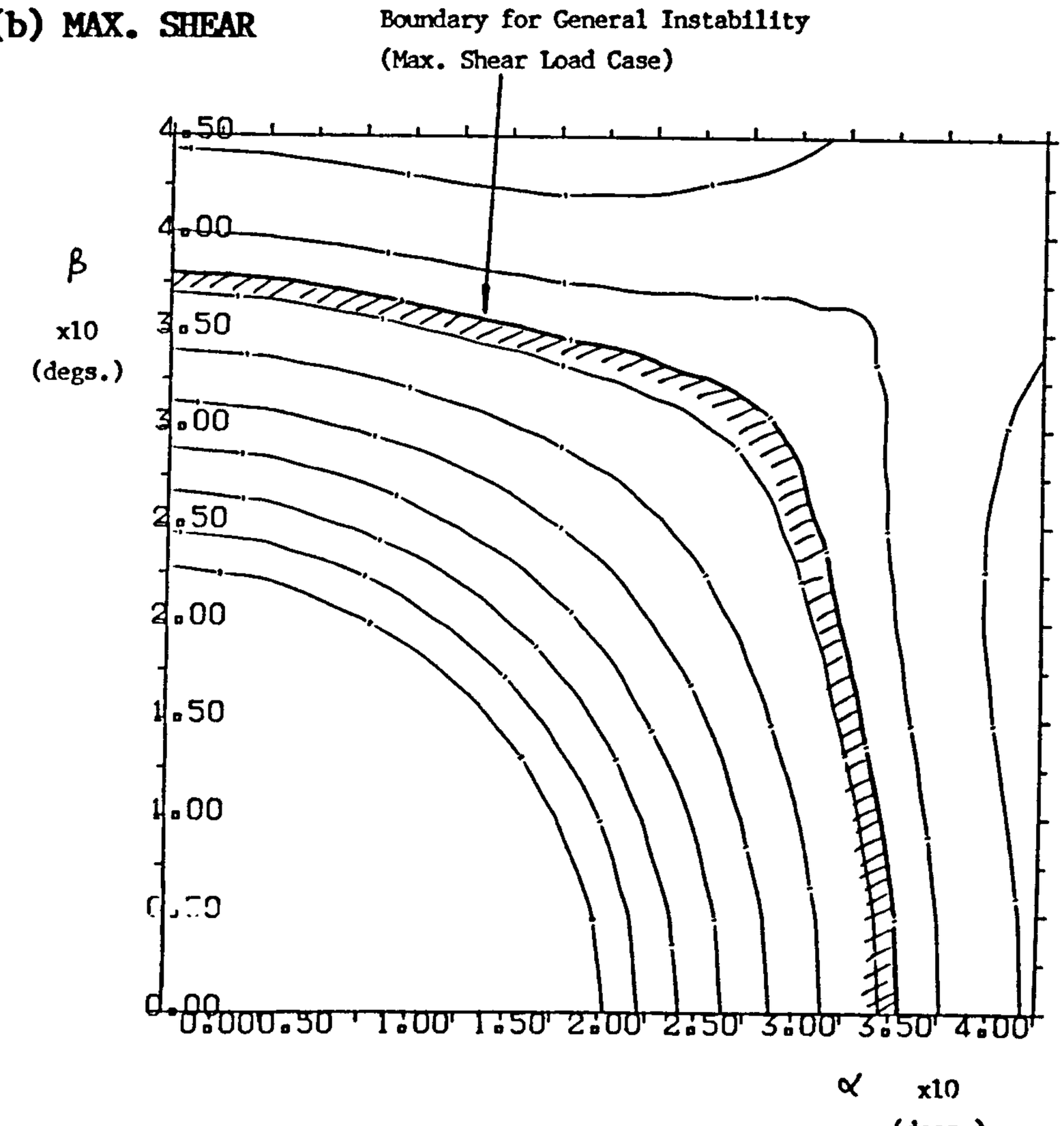

Fig. 8.43 PRIMUS FIRST LATERAL FREQUENCY Co-cured T-300/69

SPACECRAFT THRUST TUBE	PRIMUS
Material System Facesheet Lay-Up	T-300/CODE 69 (CO-CURED) 0·05mm & 0·10mm MPS: $[\pm\alpha_3/\pm\beta_3] \times 0{\cdot}10$mm LDR: $[\pm 10/\pm 45] \times 0{\cdot}05$mm
PLOT	FIRST LATERAL FREQUENCY
Load Case N_x = N_{xy} =	

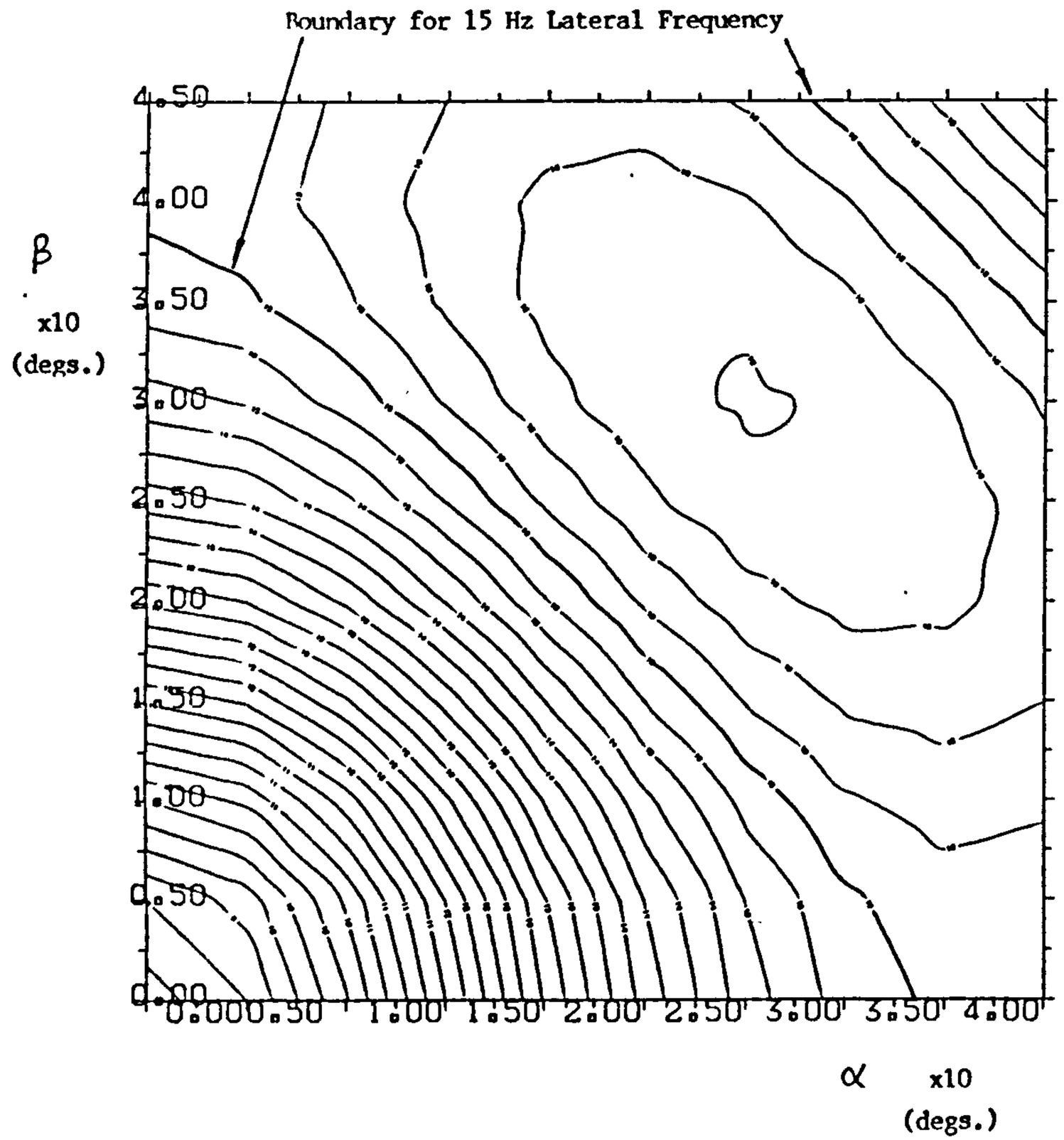

Fig. 8.44 FEASIBLE DESIGN REGION Co-cured T-300/69

SPACECRAFT THRUST TUBE	PRIMUS
Material System Facesheet Lay-Up	T-300/CODE 69 (CO-CURED) 0·05mm & 0·10mm MPS: $[\pm\alpha_3/\pm\beta_3] \times 0{\cdot}10$mm LDR: $[\pm 10/\pm 45] \times 0{\cdot}05$mm
PLOT	FEASIBLE DESIGN REGION
Load Case N_x = N_{xy} =	

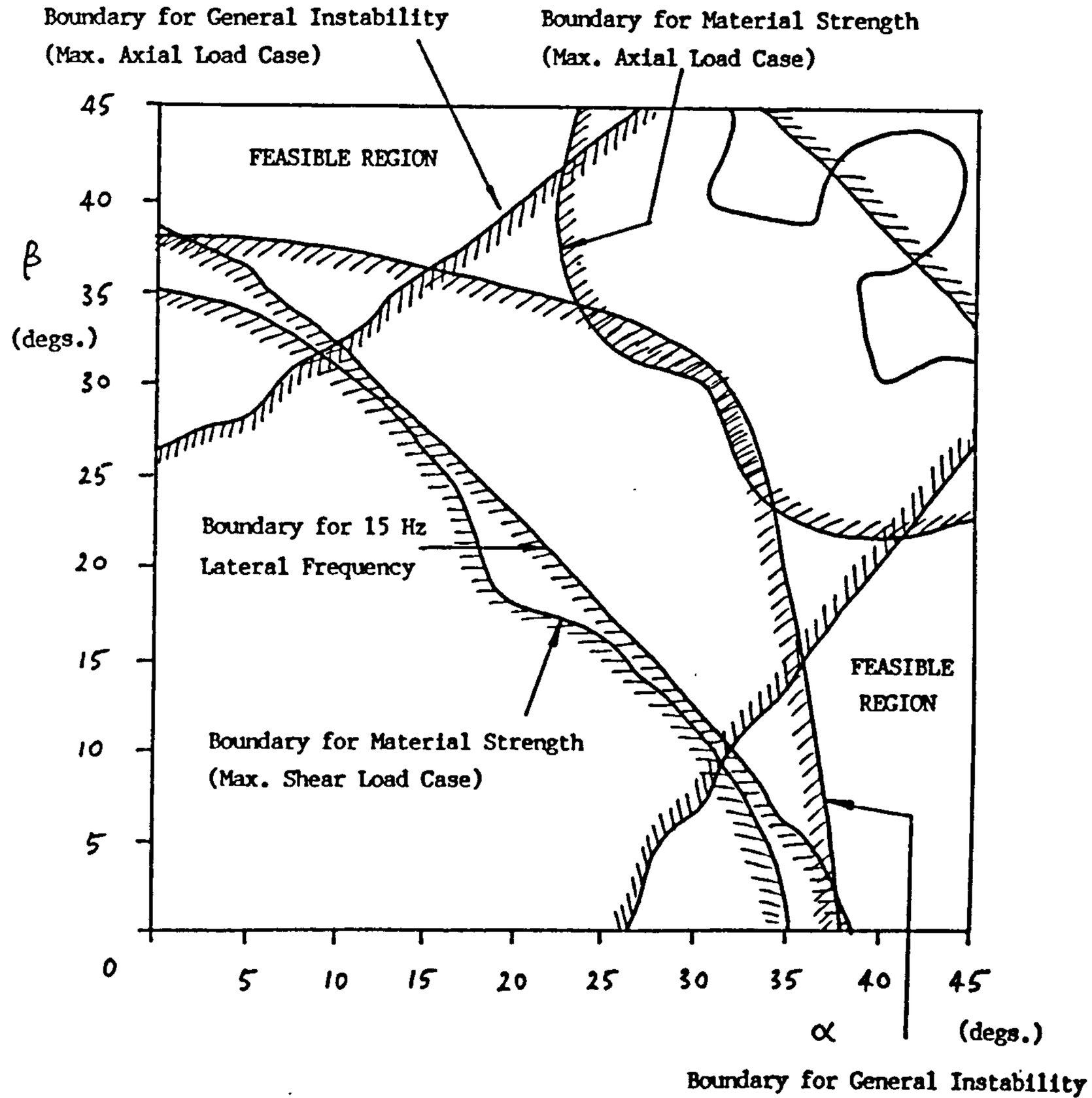

Fig. 8.45 FIRST LATERAL FREQUENCY vs. ALUMINIUM FACESHEET MASS FOR PRIMUS SPACECRAFT

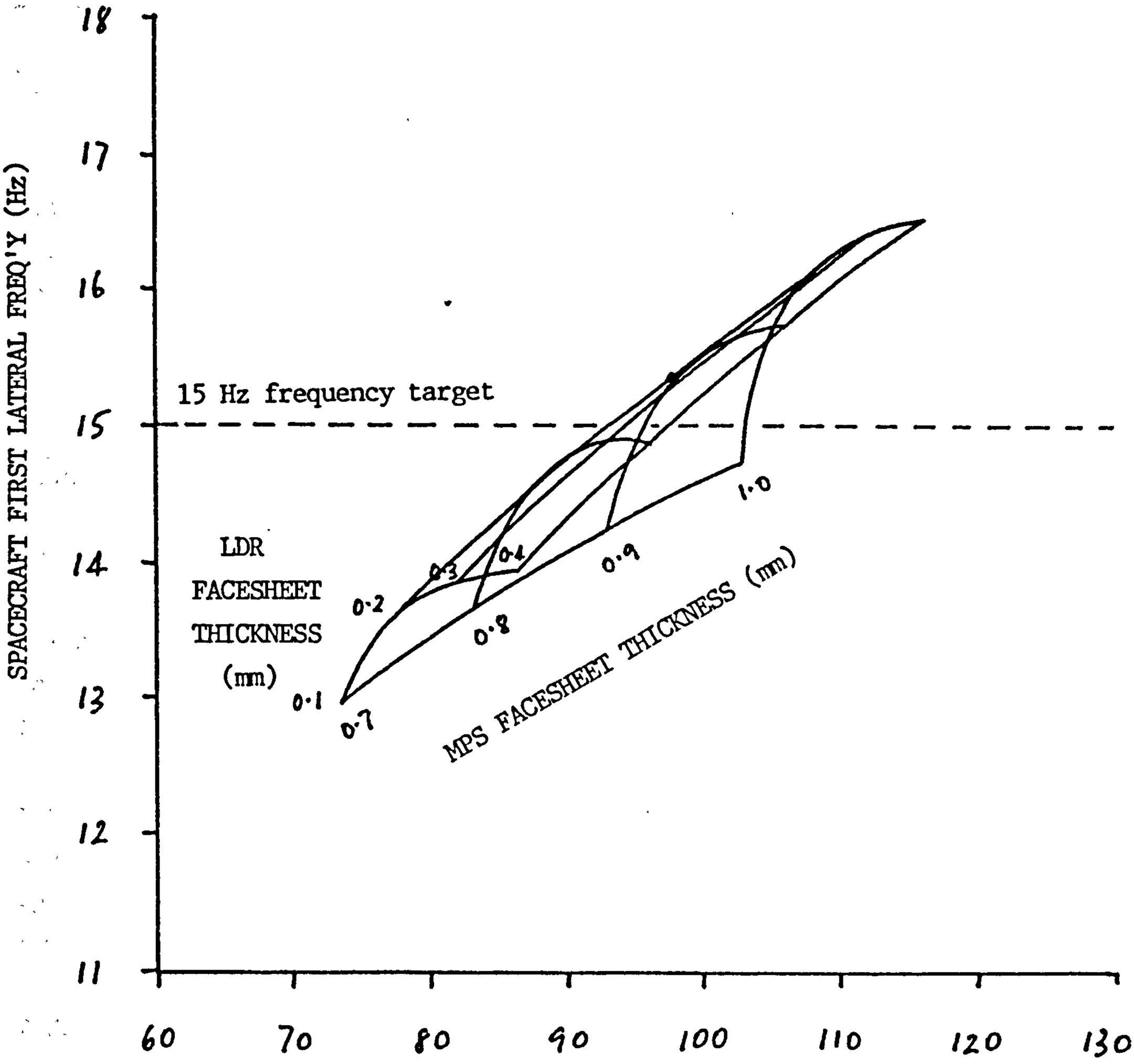

CHAPTER 9 THRUST CYLINDER MANUFACTURE AND TEST

9.1 MANUFACTURE OF T-SAT THRUST CYLINDER

In order to demonstrate the co-cured manufacturing method for a complex component, and to provide a means for validating thrust tube design optimisation, a full scale thrust tube was manufactured. This was based on the design of the upper, cylindrical part of the T-Sat thrust tube, with some simplifications to attachment details to reduce production cost.

9.1.1 Tooling

The tooling concept selected for manufacturing the cylinder is shown in fig. 9.1. This was a complete circumference male mould to enable the full cylinder to be produced in a single operation. A male mould was chosen to facilitate easy access for the lay-up of prepreg and honeycomb onto the tool surface. The positioning of material onto the inside surface of a female mould was considered to be too difficult, although this would have simplified part removal and given a better exterior finish. For longer and/or smaller diameter tubes, an inside surface lay-up of a complete cylinder would not be possible. Lay-up on a male mould was therefore considered to have a wider applicability to other thrust tube designs.

Budget constraints dictated that the tooling be fabricated from sheet steel. This compromised the accuracy of the surface form, so that the best achievable tolerance on circularity was ±1 mm (on a diameter of 1000 mm). Although this was sufficient for the purposes of this study, the production of a flight item would require a machined thick-walled cylindrical tool to achieve the neccesary tolerances on bonded joints. The sheet steel tool was fabricated in four quadrants, held together by two circular end plates. The four quadrants were designed to collapse inwards after removal of the end plates, to release the thrust tube after curing. Small gaps at the longitudinal quadrant joints were filled with a polyester based compound which was cut back to a circular profile. Two ½" thick rings built up from laminations of aluminium sheet were bolted to the tool cylinder around each

end. These acted as end dams to prevent the honeycomb collapsing at exposed edges, and as reference points for material positioning during the lay-up. They were positioned to allow for 15 mm trimming at each end.

The completed cylinder tool was sealed with mastick along the inside of the longitudinal separation joints, and at the end ring fastener holes. A vacuum bag was sealed to the outer surface to test for air-tightness and a pressure differential of 23" Hg was achieved.

9.1.2 Prepreg Cutting and Consolidation

The main facesheet and reinforcment plies were cut, layed up and consolidated under pressure in sections prior to placement on the cylinder tooling. The main facesheet plies were layed up in 1085 mm x 1085 mm squares which corresponded to 1/3 circumference segments after trimming. The prereg squares were built up from strips of 300 mm wide prepreg tape cut to the correct lengths. A 5 mm overlap was allowed between adjacent strips. Six squares were produced consisting of two 0° plies and six consisting of +45° & -45° plies and a layer of FM300M film adhesive. Together these formed the $[0_2/ 45]$ lay-up of the two facesheets. The squares were preconsolidated at a pressure of 85 psi and then sealed and stored in a freezer prior to positioning on the tool. Reinforcing belts with a [0/0/90/0] lay-up were built up and consolidated in a similar manner.

9.1.3 Honeycomb Cutting and Forming

The 2.0 lb/cu ft and 5.7 lb/cu ft aluminium honeycomb was cut into sections using a carbide disc cutter. These were then formed to the correct cylindrical curvature by passing through rollers. The honeycomb panels were degreased in an acetone bath and sealed in bags prior to lay-up on the cylinder.

9.1.4 Thrust Cylinder Lay-Up

The steel tool surface was prepared for laying-up by spraying with a release agent and attaching a layer of porous release cloth which was taped in position at each end around the circumference. Such a release system had previously been shown to be adequate for the low flow CYCOM 985 resin, and the porous release cloth gave a rougher surface finish for secondary bonding. The tool was orientated vertically for the lay-up.

The three $[0_2]$ preconsolidated panels of the inner facesheet were positioned on the cylinder first. In order to hold them (and the subsequent layers) in position release tape around the upper and lower ends was used. This tape which was built into the lay-up at the ends was trimmed away after curing. Fig 9.2 shows the first 0° layers on the tool after removal of the backing paper. The three belts of reinforcing plies were added next, fig 9.3, so that they were sandwiched between the main facesheet plies. The reinforcing plies were stepped in width so the change in thickness was gradual. Tapering the change in thickness and positioning the reinforcements between the main facesheet plies gave a smoother profile which overcame possible bridging problems at the facesheet surface or honeycomb interface. The three [±45] preconsolidated panels with film adhesive facing outwards were positioned on top of the $[0_2]$ and reinforcing layers to complete the inner facesheet, fig. 9.4. As with the $[0_2]$ panels, these were overlapped by 5 mm.

The preformed honeycomb panels were positioned on the film adhesive starting at the bottom of the cylinder and working upwards, fig. 9.5. In order to hold the honeycomb in position and prevent it from springing off the cylinder, a hair-dryer was used to locally warm the adhesive under the honeycomb to make it sufficiently tacky. Adjacent honeycomb panels were butted together with strips of REDUX 208NA foaming adhesive. These joints were staggered in a brickwork fashion. Fig. 9.6 shows the cylinder with the honeycomb lay-up almost completed. The open rectangular area threequarters of the way up the length in this photograph was for a 5.7 lb/cu ft honeycomb panel which provided the reinforcement behond the strut pick-up brackets.

Lay-up of the outer facesheet followed a reverse pattern to the inner facesheet to give a balanced sandwich. The [±45°] preconsolidated panels were positioned on the honeycomb first with the film adhesive inwards. Some slight heating with a hair-dryer was sufficient to stick these panels to the honeycomb. Fig. 9.7 shows the first of these panels on the cylinder. The reinforcing belts for the outer facesheet at the upper, middle and lower positions were layed up onto the [±45°] plies. The sandwich was completed with the $[0_2]$ preconsolidated panels. The lay-up stack is depicted in fig. 9.8.

A layer of porous release cloth was placed over the lay-up to prevent adhesion to the caul plate and vac stack. The caul plate was of 28 swg L73 aluminium alloy in two halves, this was included to ensure an even pressure distribution over the sandwich lay-up, as discussed in chapter 4, during the cure. The caul plate was initially placed directly onto the outer release cloth layer but this was found to cause problems when a vacuum was applied. Because of the curved geometry, the caul plate was unable to deform to follow the change in the lay-up thickness at the reinforced areas. This thickness change amounted to 0.8 mm. Caul plate deformation had been sufficient for following changes in the lay-up thickness on flat panels, but with curvature the caul plate formed buckles over its unsupported areas, as shown in fig. 9.9, under applied pressure. To overcome this problem, 3 plies of woven prepreg and an release cloth layer were cut to size and added in the unreinforced areas to build the stack up to a uniform thickness.

A further problem with the caul plate was at the longitudinal joints between the two halves. The original joint adopted is shown in fig. 9.10a, this included cork spacers to enable the joint to close up when pressure was applied. This joint was unsuccessful because the cork proved insufficiently flexible, causing the caul plate to bow and lift away, rather than close up when a vacuum was applied. On removal of the caul plate severe creasing of the outer facesheet was discovered under the joint. This was attributed to slack in the lay-up finding its way to the joint gap. This creasing was repaired by slitting down the crease and overlapping the affected region with a splice of [0/45] woven prepreg

plies. The caul plate joint design was modified to that shown in fig. 9.10b, the cork spacers were removed, and a gap of 5 mm was left to allow the caul plate to close up. 40 mm wide chamfered strips of 28 swg L73 were placed under the gap to spread load to the lay-up underneath and prevent it riding up at the opening. A gap of 5 mm was selected based on the observed close up of the gaps at the first attempt. Too large a gap would result in an incomplete closure of the joint and possible creasing, whereas too small a gap would cause the two caul plate halves to butt up and lift away under pressure. Figs. 9.11 and 9.12 show the final caul plate system, with the woven prepreg spacer plies being posiitoned and the cylinder enclosed in its aluminium caul plate jacket.

The caul plate jacket was covered by a layer of glass breather cloth followed by a Kapron vacuum bag which was sealed to the tool surface with mastick. Although initial vacuum testing had demonstrated the tooling could hold a vacuum of 23" Hg, this could no longer be achieved once the lay-up was complete. This was attributed to breakage of the filler and mastick seals along the longitudinal tooling joints while the tool was moved about. Because these joints were no longer accessible for repair, a second vac bag was installed on the inside of the cylinder. With the two vac bags it was possible to achieve a vcauum of 19" Hg. This improved slightly to 20" Hg in the autoclave when the warmed mastick sealed better. Fig. 9.13 shows the cylinder rotated to the horizontal, bagged up and under vacuum. The cylinder was mounted on a cradle and placed horizontally in the College of Aeronautics autoclave, as shown in fig. 9.14. Thermocouples were attached to the caul plate surface under the vac bag at four different positions.

9.1.5 Cure Cycle

The thrust cylinder was cured using the same cycle that had been used for previous flat co-cured honeycomb panels. This was essentially the standard CYCOM 985 cure schedule, modified by a maximum positive autoclave pressure of 30 psi to prevent collapse of the honeycomb core. The cure was

controlled manually, the recorded pressure and temperature traces are shown in fig. 9.15. The nominal cure cycle is given below :

TIME (hrs:mins)

0.00	Raise to 50°C under vacuum
0.20	Dwell for 30 mins @ 50°C
0.50	Raise to 120°C under vacuum
1.50	Dwell for 60 mins @ 120°C
2.50	Apply positive pressure to 30 psi. Vent vacuum at 20 psi
3.10	Raise to 180°C under 30 psi
4.10	Stabilise @ 180°C. Begin 2 hr cure
6.10	Switch off. Natural cool down. Vent pressure.

The vacuum stack was removed and the tooling segments collapsed inwards to release the cured thrust cylinder. A visual inspection indicated a generally satisfactory finish, although some creasing of the outer facesheet was evident under the two longitudinal caul plate joins. These were caused by the remaining slack in the lay-up migrating to these circumferential positions. There was no creasing at changes in lay-up thickness, at the reinforcing belts. The inside surface was very good, with no apparent creases or blemishes.

9.1.6 Possible Improvements to the Manufacturing Method

The basic concept of co-curing a cylindrical composite sandwich component with integral reinforcements was satisfactorily demonstrated. The major problem highlighted, if this method is to be extended to production items, results from slack in the lay-up. Slack in the system builds up as the number of layers is increased. The inner facesheet can be applied with sufficient tension by hand, but slack in the outer facesheet is compounded by the honeycomb core. Once pressure is applied, settling of the honeycomb takes place and the slack manifests itself as creasing in the outer facesheet. One possible remedy is to apply a vacuum to the lay-up as each

successive layer is applied. This technique could not be used for the T-Sat thrust cylinder because of the difficulty in achieving a satisfactory vacuum on the tooling. With a machined and properly sealed tool, the quick application of a vacuum to compact down each layer may be possible. Alternatively, it may be more expedient to employ some form of tensioning system to wind on the prepreg layers. Some care would have to be applied to the design of such a system, because of the danger of splitting 0°, or near 0°, orientated prepreg along the fibres under transverse tension. The prepreg backing must be retained to help prevent this.

A further possibility for overcoming the slack problem may be through the use of a female rather than a male mould. Applying internal pressure to a curved lay-up stack will tend to push it onto the tool without forming creases so readily. A female mould was used by Aerospatiale for the co-cure feasability study of the Arabsat thrust tube. However as noted previously, the use of a female mould can create its own problems arising from poor accessibility, and where the thrust tube is long and narrow this approach is no longer feasible.

As an intermediate step between the full circumference cylinder co-cure method proposed and the fabrication methods currently employed, the cylinder could be bonded together from co-cured segments. Since each segment is only a part of the full circumference there will be no slack problem. The use of bonded splices and additional tooling or cure time would however incur weight and cost penalties.

9.1.7 Bonding and Bolting of Attachments

The ends of the cured cylinder were trimmed square using a diamond edged wheel. Two [45/0_2/45] woven T-300/CYCOM 985 patches measuring approximately 650 mm x 200 mm, which had previously been cured on a segment of the cylinder tooling, were bonded to the cylinder using REDUX 410NA two-part room temperature curing adhesive. These acted as facesheet reinforcements at the strut attachments. The cylinder was then marked up for drilling. 10 mm diameter holes were drilled around the circumference at the attachment

frame positions and for the strut pick-up brackets. These holes were subsequently potted with epoxy and redrilled to 5 mm, to act as 'inserts' for through bolts. Special carbon fibre tungsten carbide cutters were used for drilling, although problems with delamination on the break-out side were experienced. A curved wooden back support was used to try and prevent this but was not particularly successful. No problems were experienced when drilling through the woven prepreg reinforced patches. Use of woven prepreg reinforcements or glass cloth locally in areas to be drilled may be a way of avoiding this problem.

The two end frames were machined from HE30 aluminium alloy plate. These were simplified from the original thrust tube design to reduce cost for the purposes of the study. Separately formed lap plates of rolled aluminium sheet connected the frames to the sandwich shell. These were bolted to the frames with standard metric M5 fasteners (in the original design, the lap plates were integrally machined with the frames). The lap plates were bonded to the shell using REDUX 410NA. Small fasteners through the predrilled holes in the lap plates and shell wall were used to apply pressure to the bonded joints. The inner and outer lap plates were bonded on separately, each in two halves. Once the adhesive had cured, the small fasteners were removed and the 10 mm diameter hole cavities in the shell wall were injected with araldite 2005 two-part epoxy. The potted holes were then drilled out to 5 mm for fasteners.

Because of the achievable tolerance on the cylinder diameter with the sheet metal tooling used, it was not possible to retain the machined SM attachment and inner AOCS support structure frames of the original design. Instead, discrete T section aluminium brackets were used. These were bonded and bolted (to prevent peeling) in the same manner as the end rings. Inner and outer brackets were fixed in a back to back fashion. Finally, six strut pick-up brackets formed from aluminium sheet were bonded and bolted to the woven reinforcement patches. The completed cylinder is depicted in fig. 9.16.

The weight of the bare cylinder, prior to the attachment of frames, brackets and fasteners but including reinforcements was 8.78 kg. On

completion, the final weight was 18.31 kg. The weight of the attachments in this case was somewhat unrepresentative of flight hardware however, because of the crude bolting and bonding system adopted.

9.2 T-SAT THRUST CYLINDER STIFFNESS VALIDATION BY MODAL SURVEY TESTING

9.2.1 Validation Philosophy

A modal survey test was carried out on the manufactured thrust tube, loaded with dummy masses representing the rest of the spacecraft. The purpose of this test was to assess the integrity of the manufactured tube and to validate finite element models used in the analysis and optimisation. It was not feasible to simulate the true mass and stiffness distribution of the complete spacecraft and to include the OTM stage, so a simplified test configuration was adopted which attempted only to approximate the vertical mass distribution and inertia of the spacecraft itself, since it is these properties which essentially govern the lateral frequency. In the actual spacecraft, mass is concentrated on the equipment sidewalls, but to simulate this accurately would have required a much more sophisticated test structure. The test configuration adopted with dummy masses representing the Service Module, Payload Module and AOCS Module is shown in fig. 9.17.

The modal survey of the test configuration was compared with a plate and shell FE model which was formulated using the same principles as the full spacecraft FE model (fig. A.6b, Appendix A), with the same elements, material stiffness description and eigenvalue solving routine. A correlation of the test configuration model by the modal survey results would validate the basis of the full spacecraft model. This in turn would support the simple beam and lumped mass FE model used in the thrust tube lay-up stiffness optimisation, since this model was shown to be in good agreement with the full spacecraft model.

9.2.2 Test Configuration

The test configuration shown in fig. 9.17 consisted of two octagonal shaped 10 mm steel plates, with bolted angle stiffeners, to represent the Service Module and Payload Module, and a circular stiffened 10 mm plate to represent the AOCS equipment and fuel tanks. These were bolted to the thrust cylinder at the top attachment frame and intermediate brackets. The 12 inter-platform struts of the actual spacecraft configuration were included, but were fabricated from aluminium alloy rather than carbon-epoxy. The mass breakdown for the test structure was :

PM Platform	201 kg
SM Platform	135 kg
AOCS Platform	69 kg
Cylinder	18 kg
Struts/Bkts. etc.	2 kg
TOTAL	405 kg

The original intention for testing the structure was to enforce clamped conditions at the lower attachment frame. This was in keeping with common spacecraft modal survey practice, since this condition most closely represents the clamped configuration on the launcher. Some preliminary tests were carried out with the structure clamped to a steel surface table of approximately 2 tons, but this was shown to be totally inadequate. The weight and stiffness of the base were insufficient to prevent the structure and base behaving as a coupled system. Calculatiions suggested a base with a weight at least an order of magnitude greater was required. These were borne out by reference [66] which considered the effect of the weight of the seismic block on the accuracy of the first 'clamped' vibration mode of a spacecraft using a simple FE approach. This showed that 40 tonnes of concrete were required to give a first mode frequency within 1 Hz of the true clamped first mode for a typical 2 tonne-class spacecraft. Attempting to simulate clamped conditions was therefore ruled out since a seismic block of this mass was not available. Neither was it considered practical to include the surface table in the FE model since this would have added

additional complexities and uncertainties since the true stiffness and mass properties of the table were unknown.

The structure was consequently tested in a near free-free condition. this was achieved by suspending the structure from a single point at the centre of the PM platform. A rope and chain rather than a soft elastic suspension was used because of the weight of the structure. This introduced an axial stiffness constraint at its attachment to the PM platform when in tension, but there were no significant constraints on the other 5 degrees of freedom. Although the suspension attachment affected the local modes of the PM Platform under free-free conditions, the axial constraint at this point was not expected to affect the lateral modes of the thrust tube.

The major disadvantage of a free-free test configuration was that the first lateral fixed-base cantilever mode of the thrust tube, which was the mode of primary interest, was no longer excited. The suspended first lateral thrust tube mode was instead analogous to free-free bending of a beam (but with significant shear distortion also). This mode is dependent on the thrust tube lateral stiffness, just as the clamped-free mode was, but was expected to have a frequency about 4 times higher. Consequently this increased the likelihood of possible coupling with local high frequency thrust tube modes (such as shell bending modes) which could not be resolved by the relatively coarse FE model and would therefore invalidate a comparison of the test and analysis results. The higher frequency of the lateral mode also resulted in a lengthier solution time for the FE model. This was because the eigenvalue solution was limited to an inverse power method which solves for the lowest eigenvalue upwards. The error, or possibility of missing eigenvalues, was also increased as more modes were extracted in the solution process.

9.2.3 FE Model of the Test Structure

The initial FE model for analysing the test structure was developed using the LUSAS FE system and is shown in fig. 9.18a. This consisted of 8 noded quadrilateral semi-loof shell elements (for the thrust tube and platforms)

and compatible 3 noded beam elements (for the struts and frames). Material properties for the cylinder were specified in terms of the sandwich shell [A] and [D] constitutive matrices, and a consistent mass formulation was used for mass property modelling. The thin shell elements excluded through-thickness shear of the cylinder core. This omission only affects shell modes which were not of interest here. This model was used for predicting the originally proposed clamped base test configuration. The first two modes predicted with this model were the lateral cantilever modes in the X and Y directions, with frequencies of 44.2 Hz. However, once a free-free configuration was adopted for the structure, this model was uneconomic for predicting the free-free thrust cylinder behaviour because of the higher frequency of the first lateral mode which required a larger number of eigenvalues to be extracted. The model was therefore simplified to that depicted in fig. 9.18b. The same elements, stiffness and mass modelling was adopted, but the element mesh for both the platforms and thrust cylinder was made coarser. The thrust cylinder elements were curved, although these are shown flat in the figure because of the linear interpolation incorporated in the FE system plotting routine. The thrust cylinder element density in the vertical (Z) direction was retained the same as the finer mesh model and the overall density for the thrust tube was the same as the T-Sat dynamic model. This allowed sufficient freedom for a good description of the first lateral mode.

To simulate the test structure support condition, a single point constraint against vertical displacement was specified at the centre node of the PM Platform. In the real case this constraint was 'one-way', in that the rope attachment only constituted a constraint when in tension. Also, the real support had finite stiffness. In order to prevent poor conditioning in the solution process (small or negative pivots) a shift on the inverse power method extraction procedure was specified. Experimentation with a smaller FE model indicated a shift of 1×10^5 $(rad/s)^2$, which corresponded to a frequency of about 50 Hz, gave a good compromise between ill-conditioning and a lengthy solution time.

The FE model results are discussed in comparison with the modal survey test results later.

9.2.4 Modal Survey Test

The modal survey test of the suspended test structure was carried out with the aid of a Cranfield Data Systems Vibration Analyser. The structure was excited by a hammer incorporating a force transducer. The spectrum of the impulse force was essentially flat over the frequency range of interest (0 to 250 Hz). The response was measured by an accelerometer fixed to the structure with beeswax. To derive the Frequency Response Functions (FRF) between different points on the structure, the accelerometer was moved in turn to different locations. The accelerometer positions corresponded to nodes on the FE model. These are indicated by positions 1 to 31 on fig. 9.19. The other nodes shown in this figure were added to give clarity to the geometry of the mode shapes and do not refer to acceleration/ displacement measurement points. The accelerometer was orientated to measure acceleration perpendicular to the mounting surface, ie. the measured cylinder accelerations (positions 1 to 18) were horizontal, and the PM Platform accelerations (positions 20 to 31) were vertical. These positions were selected to enable thrust tube lateral modes and platform local bending modes to be differentiated. The impulse was applied horizontally at position 24 because this was known to have significant horizontal displacement in the first free-free lateral mode.

Measured impulse and acceleration response data was reduced by the FFT analyser built into the system which enabled FRFs to be derived for each measurement point. Examples are illustrated in fig. 9.20. These are given in terms of inertance (acceleration response/force excitation) and phase shift against frequency. In order to get an overall appreciation of all the modes excited, the indicator function shown in fig. 9.21 was used. This performs a summing technique of the individual FRFs to highlight all the resonant peaks on a single plot. The resonant mode frequencies and modal damping properties were derived from the FRF data by a curve fitting technique which was centered at each peak of the indicator function. Integration of the acceleration response at the measurement positions enabled animated mode shapes to be obtained corresponding to the resonant frequencies.

9.2.5 Comparison of FE and Test Results

The first 35 modes were extracted from the FE model to ensure that the first free-free lateral mode was found. The solution time was 5 cpu hours on a VAX 11/750. The first 30 of these converged to within a tolerance of ½% on successive eigenvalue iterations, by the specified maximum of ten iterations. The first five eigenvalues were zero, corresponding to the 5 rigid body modes. The sixth, which should have also been zero for genuine free-free conditions, was at 17.7 Hz as a result of the single point axial constraint at the suspension position. This mode was almost a rigid axial displacement of the structure, but with local deformation in the vicinity of the constraint. The eigenvectors for each mode were plotted out for comparison with the mode shapes found by test.

14 modes below 210 Hz (the highest frequency of the FE model modes) were located by the modal survey test, and stills of the mode shapes plotted. The smaller number of modes found from the test was attributable to the position and direction of the excitation impulse, which was a nodal point for many of the modes. In particular, there was little lateral excitation for the large number of platform bending and twisting modes which were characterised principally by vertical displacements. The horizontal impulse was sufficient to positively locate the first thrust tube lateral mode however, which was the primary interest.

A mode by mode comparison of the analysis and test results is given in Table 9.1 which includes all modes other than the rigid body modes up to 210 Hz. Correlation of analysed and tested modes was by inspection of the mode shapes. The lower frequency modes corresponded to bending, twisting and tipping of the steel dummy platforms. Many of these modes found by the FE model were not excited during the test. Those that were excited gave fairly good agreement, being within 8% of the FE model predictions.

The principal overall modes of the structure predicted by the FE model were torsion (136.7 Hz), first ±Y lateral (160.4 Hz), first ±X lateral (165.2 Hz) and first ±Z axial (182.5 Hz). Of these, the position and direction of the impulse was insufficient to excite the torsion and ±X lateral modes.

The latter was orthoganal to the first ±Y lateral mode which the test was designed to locate. This lateral mode was found at 166.5 Hz in the test. The predicted frequency from the FE model was 160.4 Hz, an error of 3.7%. Fig. 9.22 shows the test and analysis mode shapes. The overall ±Z axial mode predicted by the FE model at 182.5 Hz was found at 183.2 Hz in the test. This mode was governed primarily by platform axial displacement with hoop deformation in the cylinder at the strut attachments and lower frame, which enabled it to be picked up by the thrust tube mounted accelerometers.

Higher frequency modes found from the test seemd to indicate shell deformation in the cylinder walls, primarily at the lower frame opening. These correspond well with shell type modes predicted by the FE model. This seemingly good correlation (within 1%) was a little surprising bearing in mind the relatively low mesh density of the model and the neglect of core shear. However these modes were probably determined largely by the hoop stiffness and mass of the lower attachment frame, which were included in the model.

9.2.6 Conclusions

For the vibration modes detected by the test, agreement was in all cases within 8% of the FE model predictions, and in most cases within 5%. The discrepency between prediction and test of 3.7% for the first free-free lateral mode was particularly good. Such a discrepency can easily be accounted for by the idealisation of the mass distribution and eigenvalue extraction error in the FE model; by non-uniformity and variation in stiffness properties of the as-manufactured cylinder; and by measurement and data reduction error in the modal survey test. The agreement between prediction and test results for lateral behaviour of the thrust cylinder was sufficient to conclude that :

1. Laminate analysis of the co-cured cylinder sandwich construction, based on test coupon data, gives an accurate stiffness characterisation for a large and complex stucture of this type.

2. The FE model of the test structure was successfully validated.

3. By inference, the laminate analysis and FE models used in the thrust tube lay-up optimisation were also validated.

This final point makes it reasonable to adopt the simple beam & lumped mass FE model approach, as outlined in section 8.3, for the stiffness optimisation of thrust tube lay-ups in general.

9.3 T-SAT THRUST CYLINDER STRENGTH VALIDATION

The manufactured thrust cylinder was not statically tested because of the cost and limited value of such a test in this case. Failure was considered to be more likely at a joint rather than the composite shell wall itself, because the design tolerance on bonded joints could not be achieved with the sheet metal tooling used to manufacture the tube. Validation of the thrust tube design strength was therefore accomplished by compression testing of flat sandwich specimens with the same lay-up cured under the same conditions. An advantage of this approach was the ability to perform a series of tests and so give an indication of the variability of strength for sandwich manufactured using the co-cure process, rather than a single data point. These tests have been described in detail in chapter 5. The results indicated that the thrust cylinder sandwich lay-up exceeded the laminate failure analysis predictions (based on 30 psi cured coupon tests) by 11% and the coefficient of variation was reduced. The calculated 'A' design allowable compression strength was 194 N/mm giving a large margin of safety over the ultimate design compression load. Although shear is also present in the cylinder shell wall under the design load cases, the case of maximum compression represented a worst case for the $[0_2/\pm 45]$ cylinder facesheet lay-up. It was hence possible to conclude that the cylinder sandwich design was sufficient to meet the strength requirements.

9.4 CONCLUSIONS

The optimised co-cured composite faced sandwich design for the T-Sat thrust cylinder was manufactured to assess the feasibility of producing a large and complex component of this type as a single part. Although only low cost fabricated sheet metal tooling was used to produce the cylinder, the manufacturing technique was relatively successful. The major problem with the method related to slack in the lay-up which resulted in outer facesheet creasing. Possible improvements to avoid this defect were noted. Generally the quality of the finished thrust tube was good enough to demonstrate the practicality of the method for producing mass and cost efficient spacecraft thrust tube structures.

The manufactured cylinder was loaded with dummy masses to represent the rest of the spacecraft and a modal survey test carried out. The results of this test were found to be in good agreement with predictions made through the use of laminate analysis and an FE model. It was therefore concluded that the co-cured sandwich thrust tube structure demonstrated predictable stiffness properties. Also, validation of the FE model by test implied that the stiffness optimisation method, based on a simpler FE formulation but which correlated well with the more complex model, was a good representation of the real structure. Hence, the method can be reasonably applied to other spacecraft configurations for thrust tube stiffness optimisation as outlined in Chapter 8.

Compression tests on cylinder sandwich lay-up samples were found to comfortably exceed the design requirements on strength.

TABLE 9.1 COMPARISON OF FE AND MODAL SURVEY TEST RESULTS

FE MODEL		MODAL SURVEY			ANALYSIS	MODE SHAPE DESCRIPTION
MODE	FREQ'Y (Hz)	MODE	FREQ'Y (Hz)	DAMPING RATIO %	TEST	
7	53.9	NOT EXCITED			-	Opposed platform bending (±X)
8	57.3	1	60.4	0.640	0.95	Opposed platform twisting
9	58.8	NOT EXCITED			-	Opposed platform tipping (±X)
10	60.9	NOT EXCITED			-	Platform edge local bending
11	64.2	1	60.4	0.640	1.06	In phase platform twisting
12	70.4	2	70.9	0.304	0.99	Platform edge local bending
13	72.1	NOT EXCITED			-	PM Platform ±X bending
14	77.8	3	80.3	0.284	0.97	In phase platform bending (±X)
15	90.0	NOT EXCITED			-	Opposed Platform bending (±Y)
16	94.8	NOT EXCITED			-	Platform edge local bending
17	96.1	4	104.9	1.175	0.92	Opposed platform tipping (±Y)
18	110.2	5	106.9	0.499	1.03	Platform edge local bending
19	122.5	6	113.3	0.304	1.08	Opposed ±X/±Y platform bending
20	136.7	NOT EXCITED			-	Cylinder Torsion
21	155.9	7	152.2	2.409	1.02	Platform bending & tipping
22	160.4	8	166.5	0.105	0.96	First Overall Lateral (±Y)
23	165.2	NOT EXCITED			-	First Overall Lateral (±X)
24	166.8	NOT EXCITED			-	Platform local / Shell
25	175.3	9	175.7	0.255	1.00	Platform local /Shell /Torsion
26	182.5	10	183.2	0.358	1.00	First Overall Axial (±Z)
-	-	11	189.0	0.447	-	Cylinder shell mode ?
27	198.4	12	199.4	0.303	0.99	Platform local / Shell
28	203.1	NOT EXCITED			-	Platform edge local bending
29	206.0	13	208.3	0.067	0.99	Platform local / Shell
30	210.0	14	208.4	0.336	1.01	Platform local / Shell

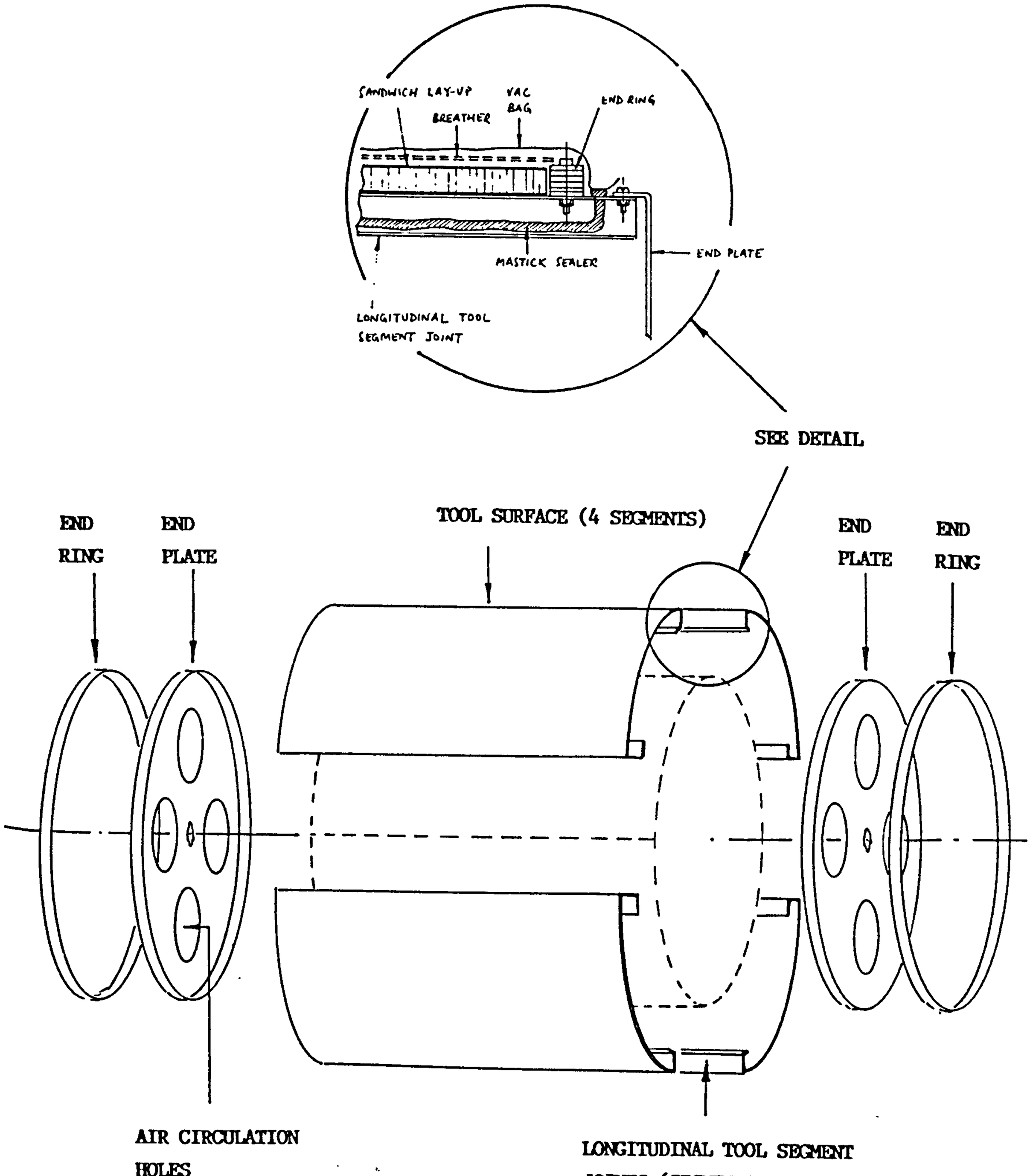

Fig. 9.1 TOOLING FOR T-SAT THRUST CYLINDER

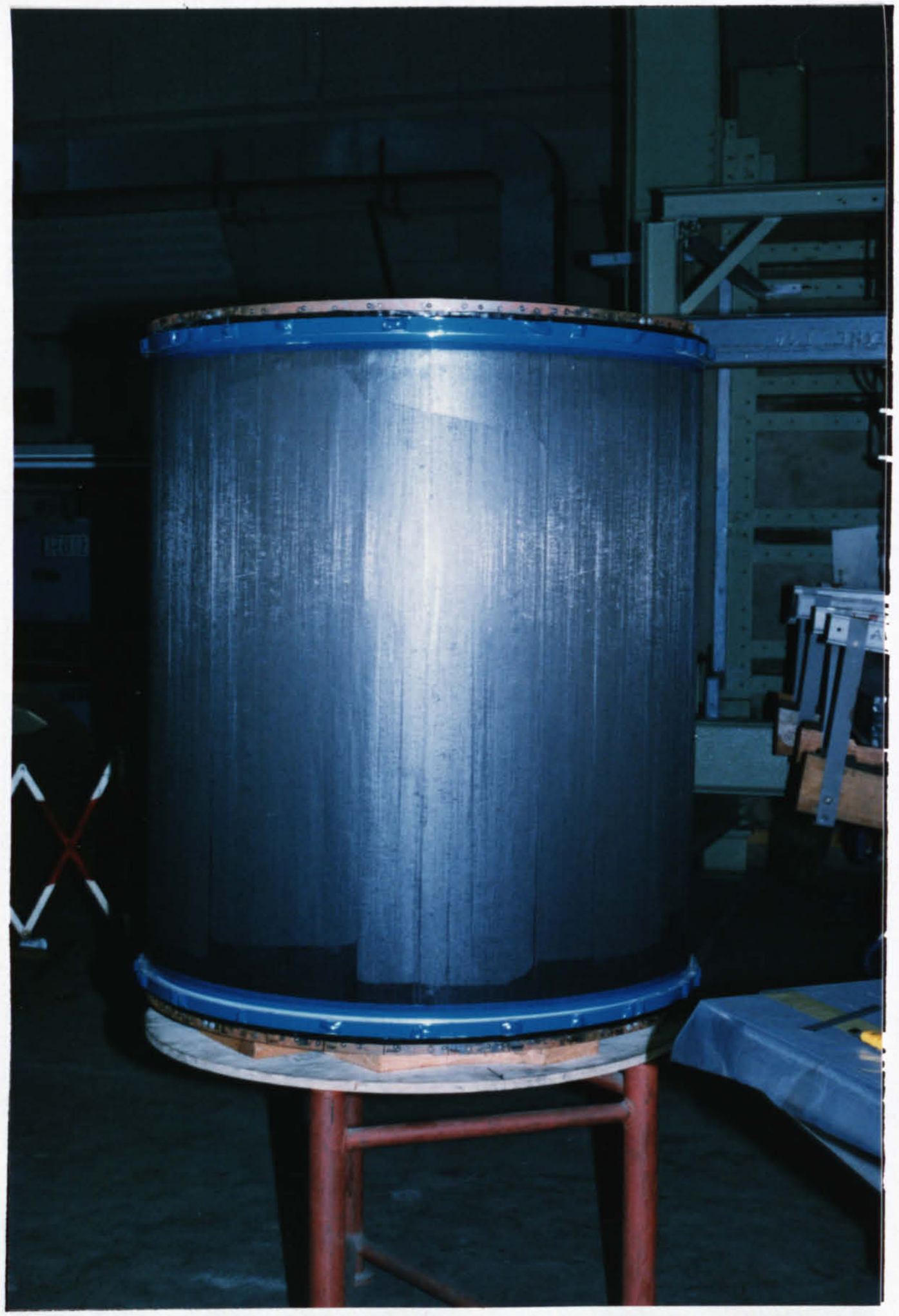

Fig. 9.2 0° PLIES, INNER FACESHEET

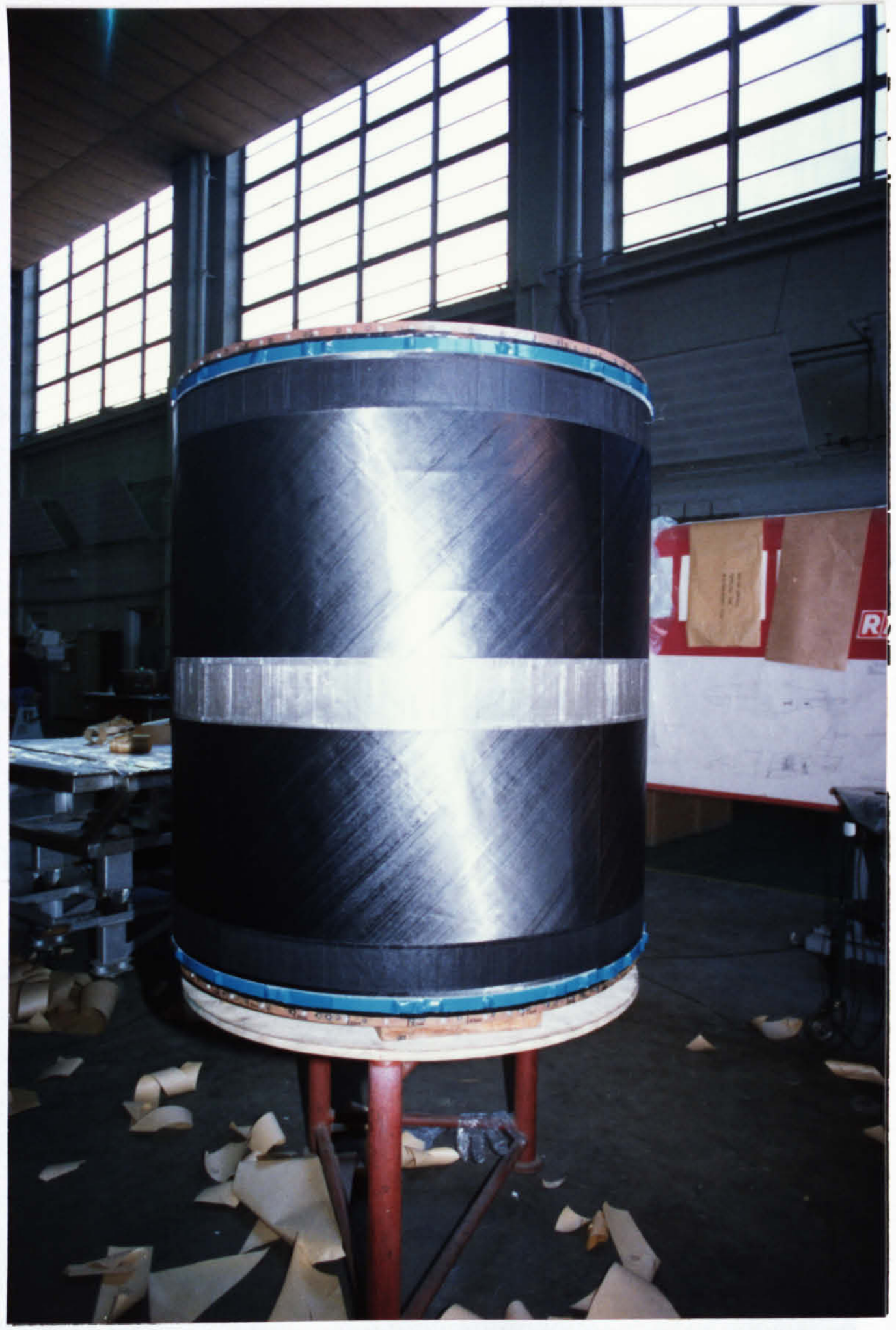

Fig. 9.3 REINFORCEMENT PLIES, INNER FACESHEET

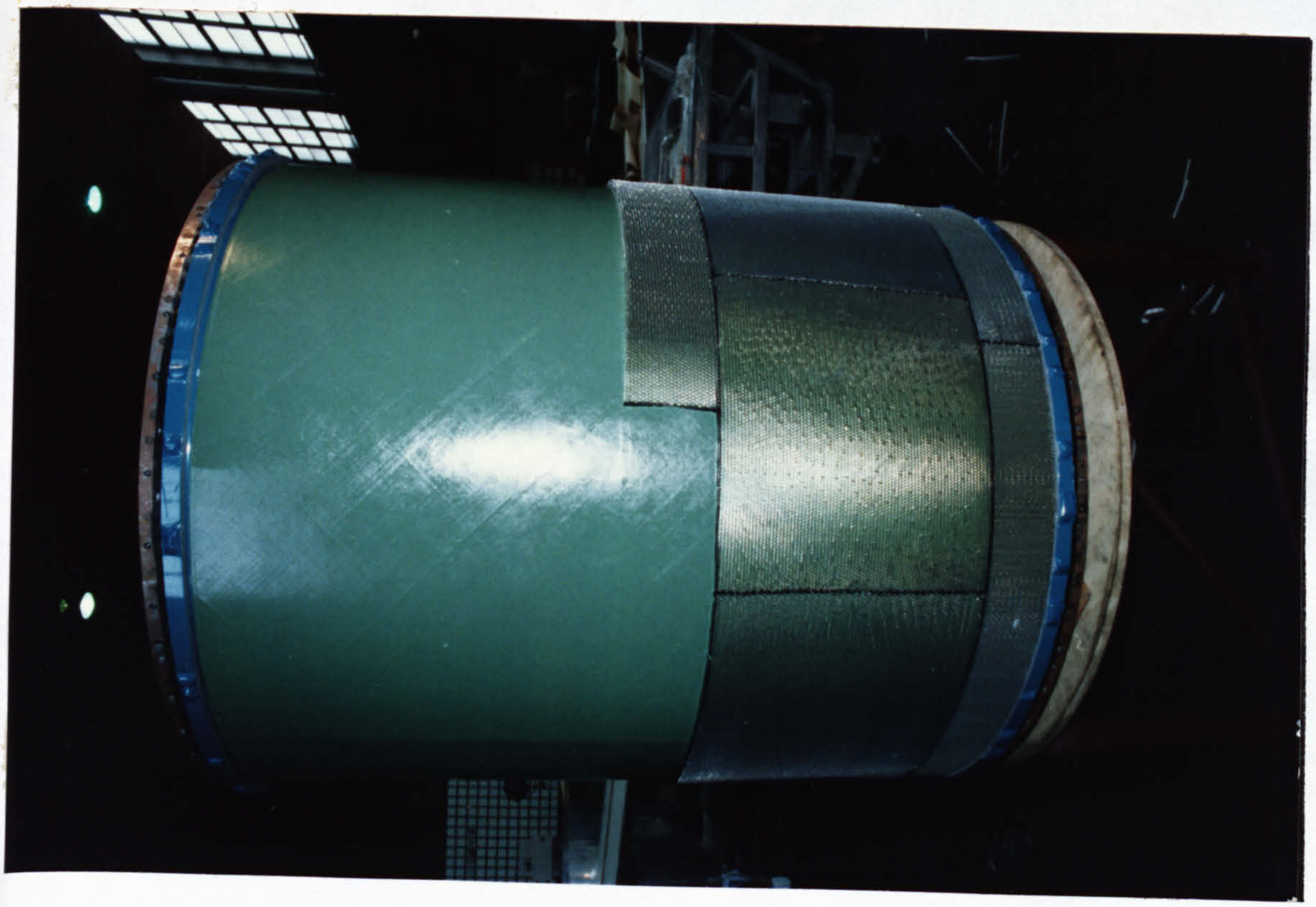

Fig. 9.5 LAY-UP OF HONEYCOMB PANELS

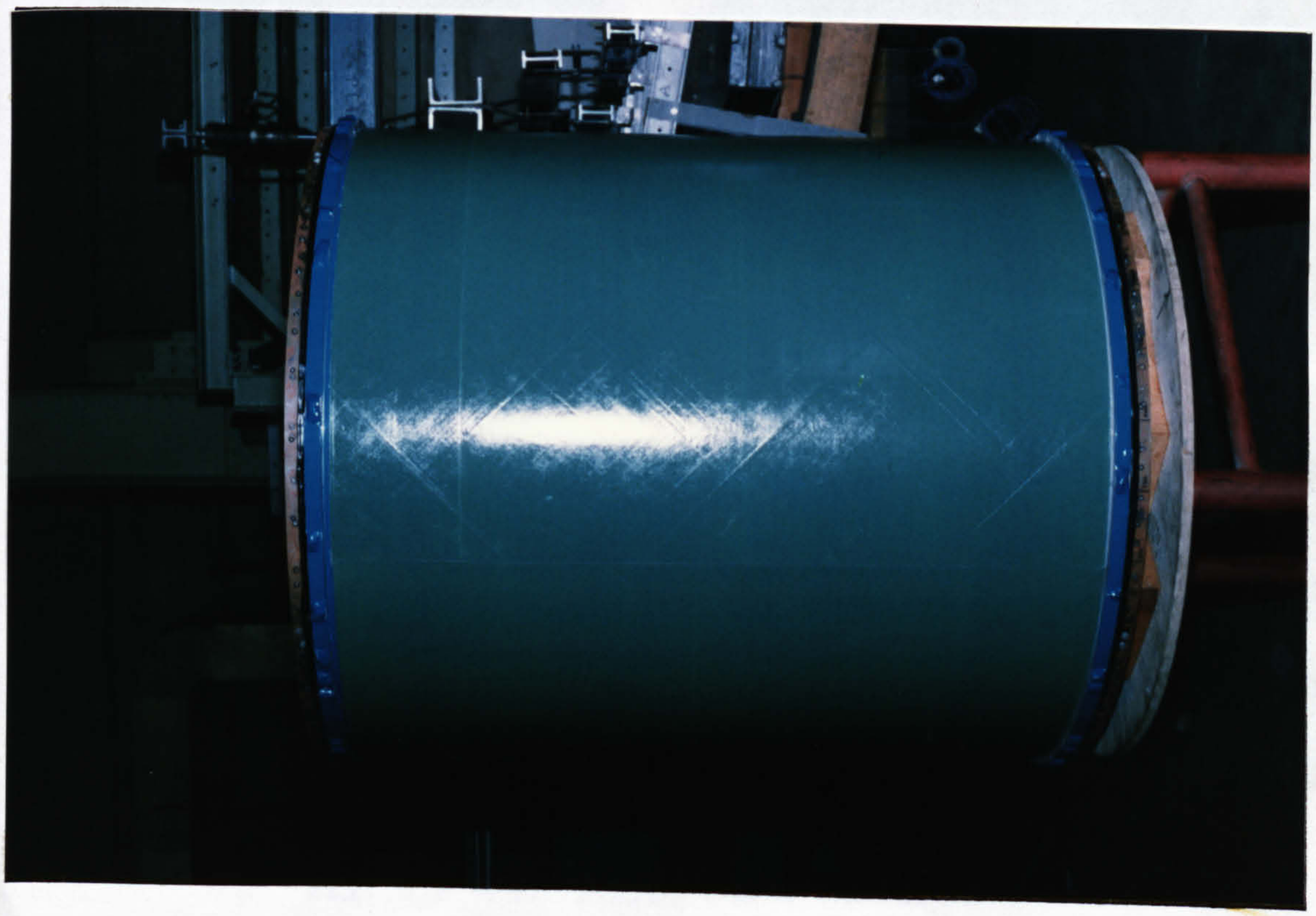

Fig. 9.4 FILM ADHESIVE ON ±45° PLIES

Fig. 9.6 HONEYCOMB LAY-UP ALMOST COMPLETED

Fig. 9.7 ±45° PLIES, OUTER FACESHEET

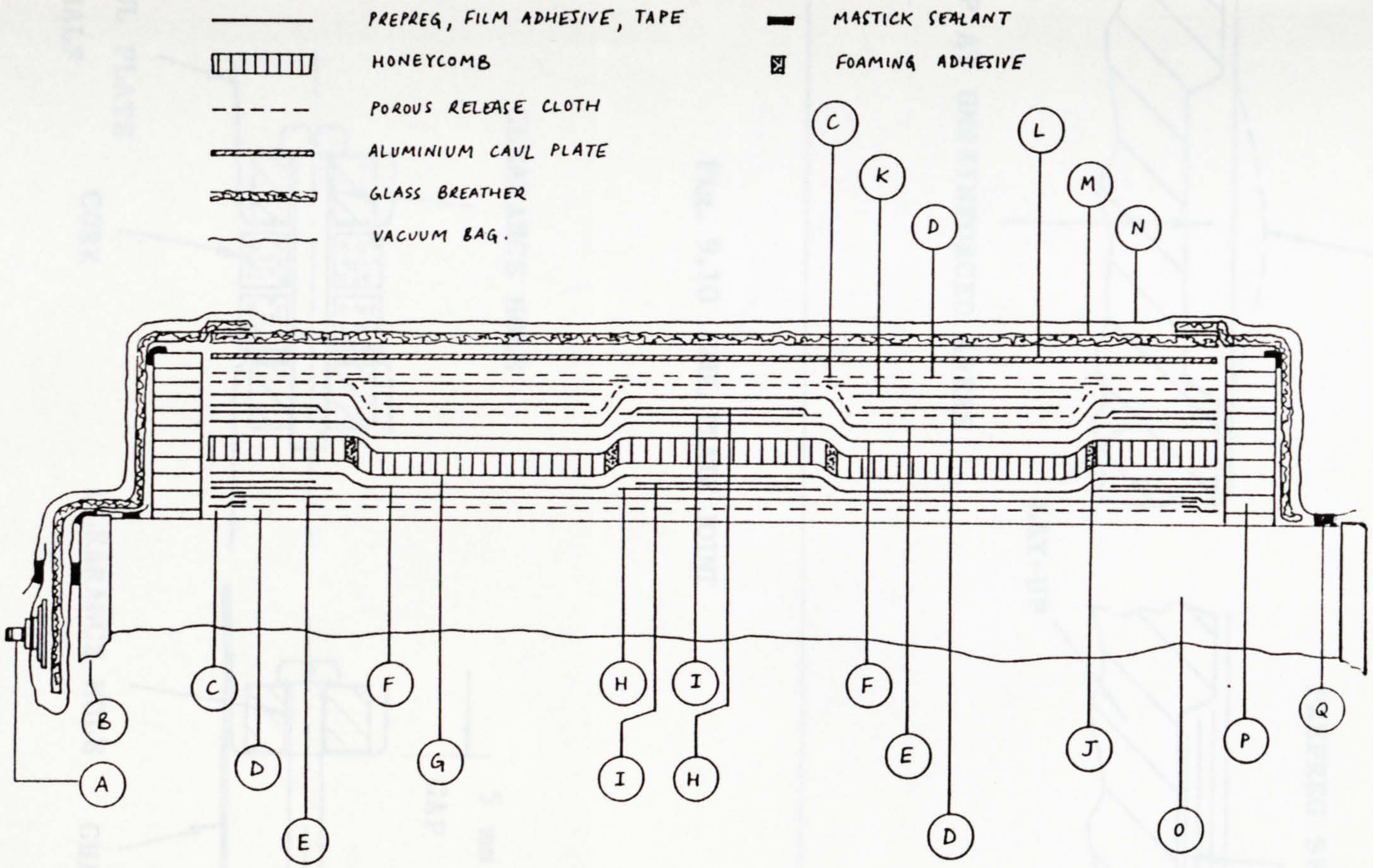

Fig. 9.8 THRUST CYLINDER LAY-UP (SCHEMATIC)

KEY

A Vacuum Take-Off Port
B Tool End Plate
C High Temperature Release Tape
D Porous Release Cloth
E $[0_2]$ Preconsolidated Prepreg
F $[\pm 45]$ Preconsolidated Prepreg & Film Adhesive
G Aluminium Honeycomb
H [0/90] Reinforcing Plies
I $[0_2]$ Reinforcing Plies
J Foaming Adhesive
K Woven Prepreg Spacer Plies
L 28SWG Aluminium Caul Plate
M Glass Breather Cloth
N Kapron Vacuum Bag
O Tool Surface
P Tool End Ring/Dam
Q Mastick Sealant

Fig. 9.9 CAUL PLATE BUCKLING

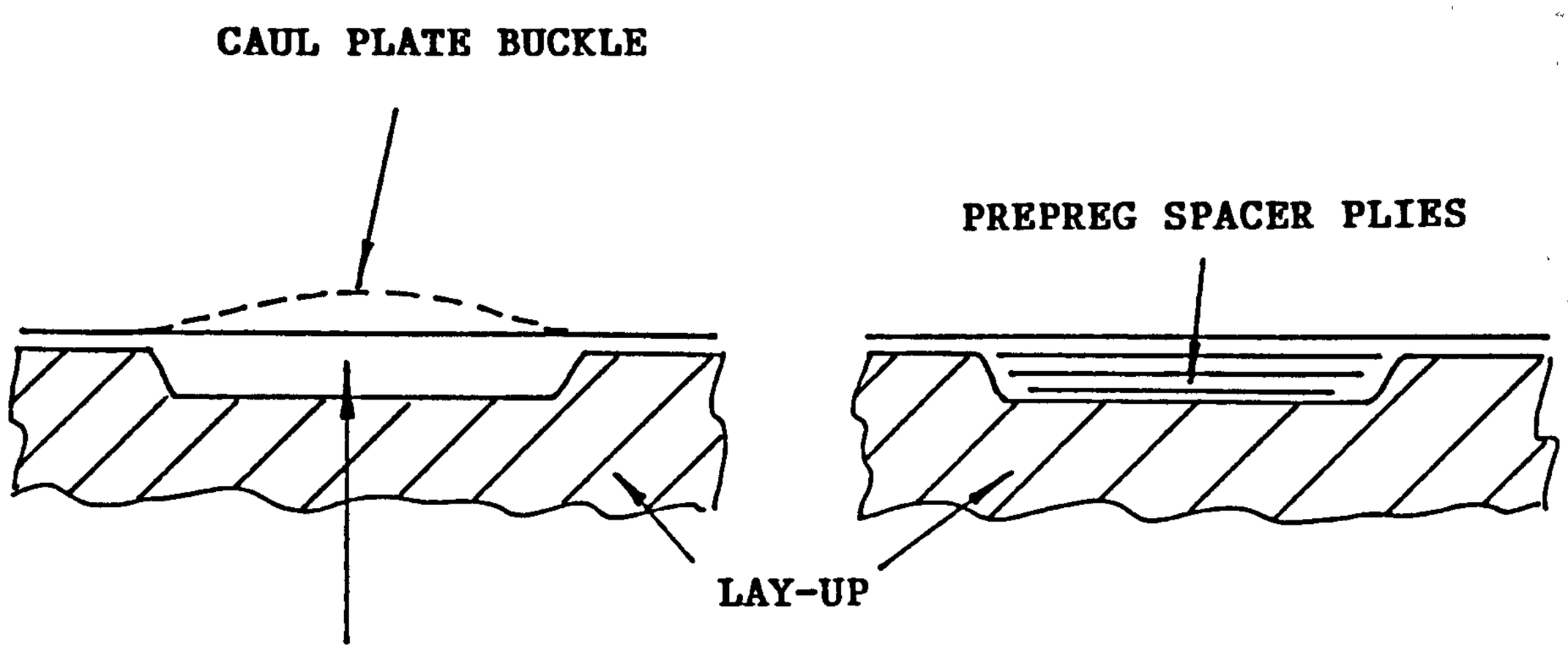

Fig. 9.10 CAUL PLATE JOINT

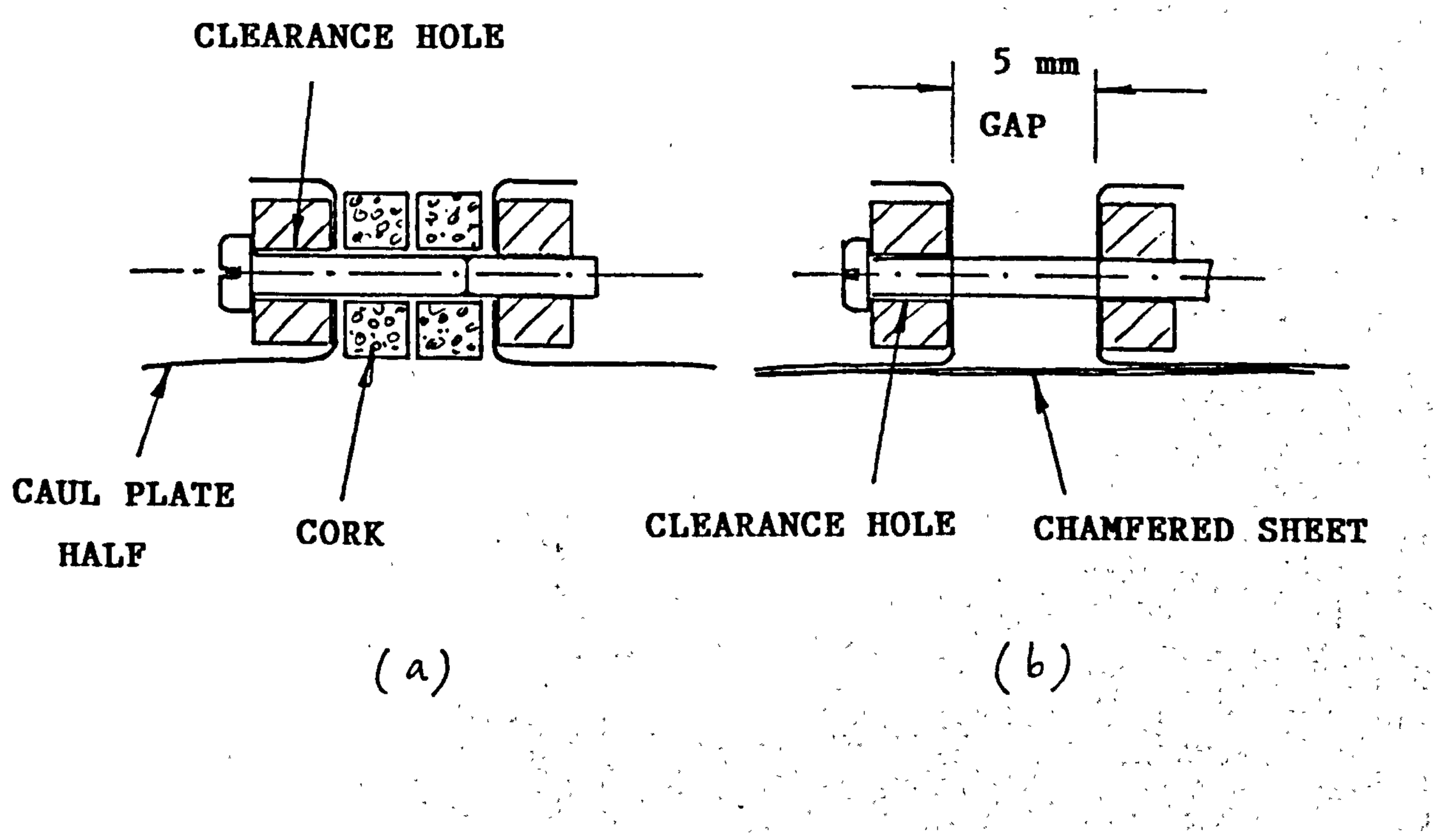

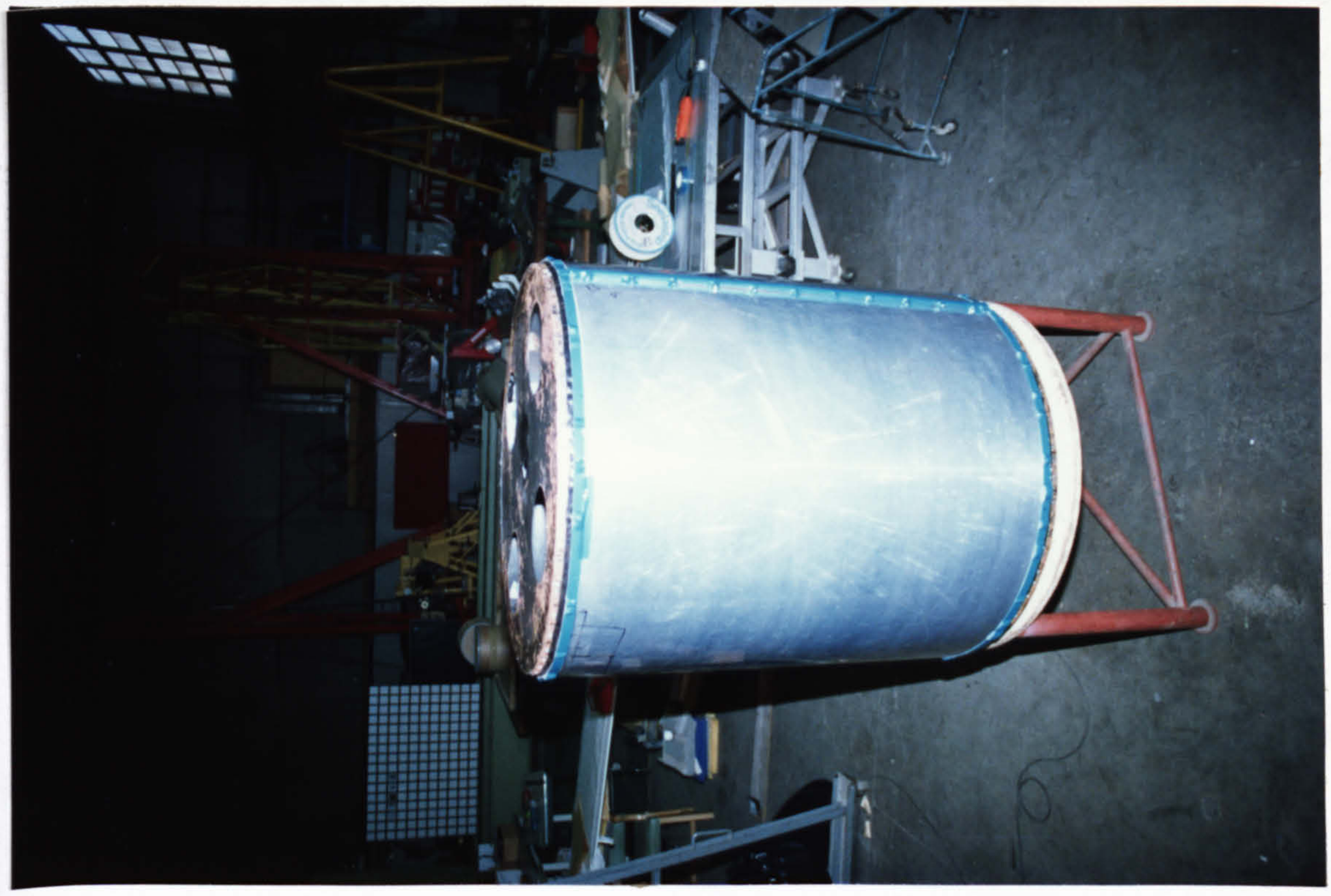

Fig. 9.12 ALUMINIUM CAUL PLATE IN POSITION

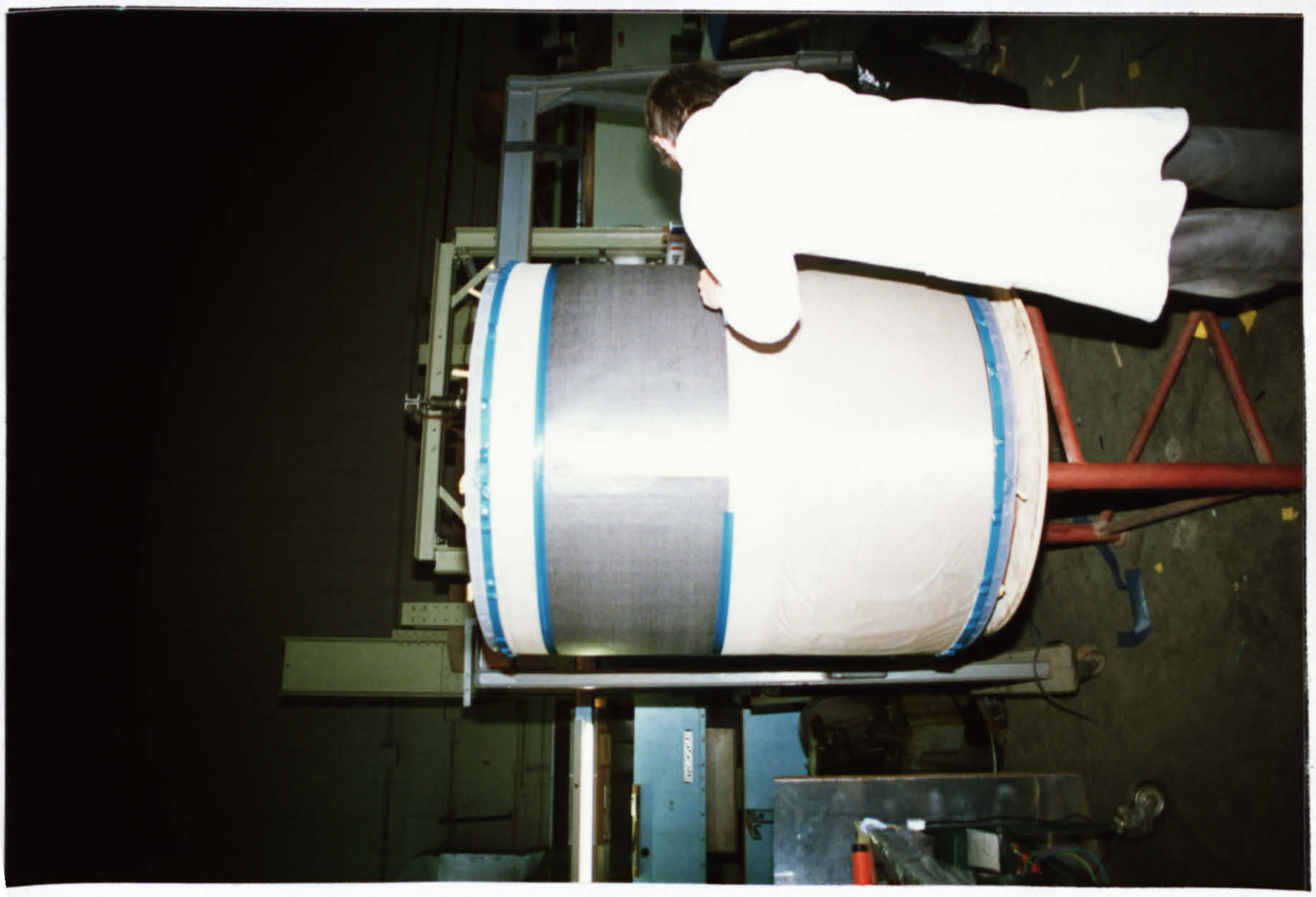

Fig. 9.11 WOVEN PREPREG SPACER PLIES

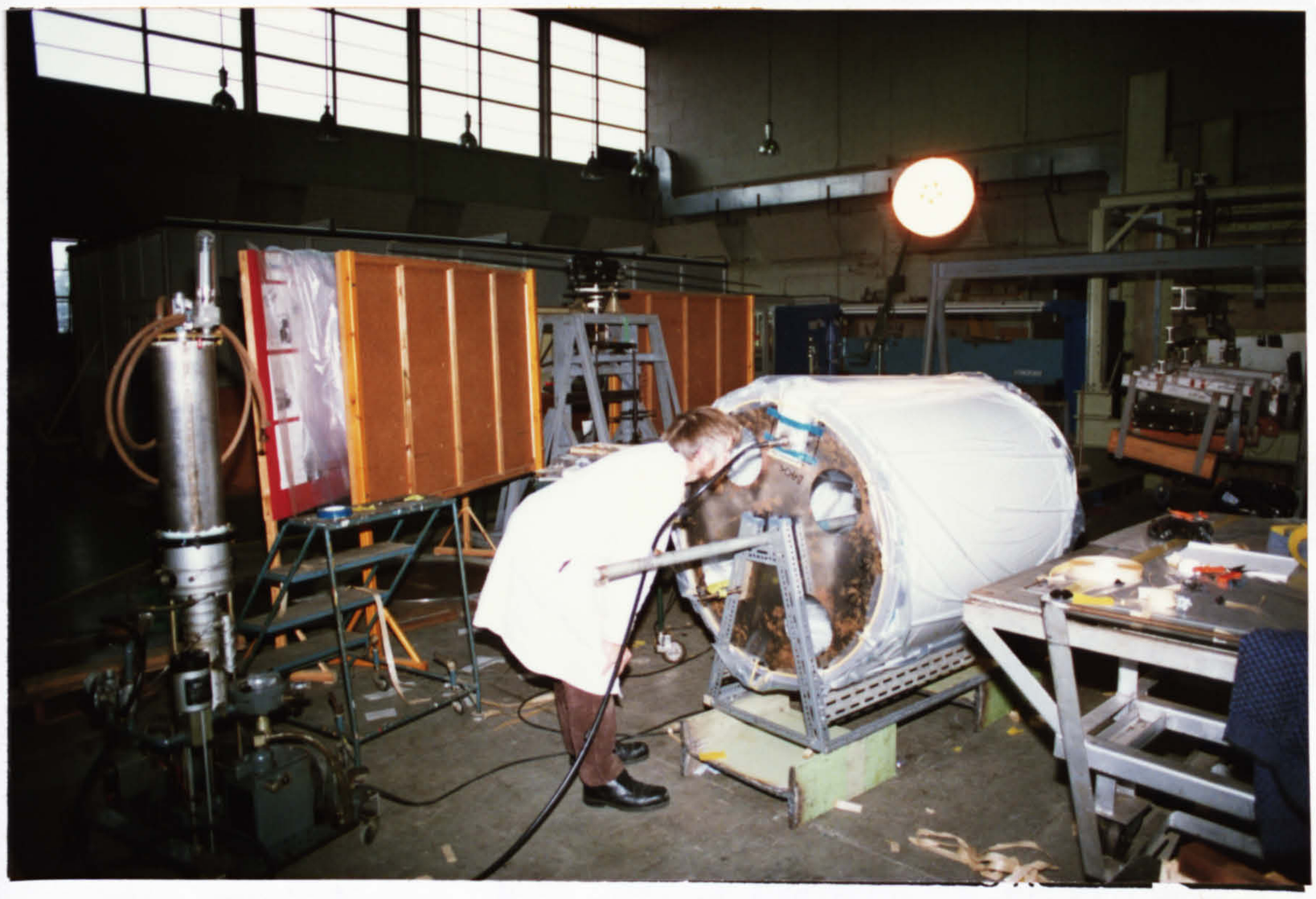

Fig. 9.13 APPLYING A VACUUM

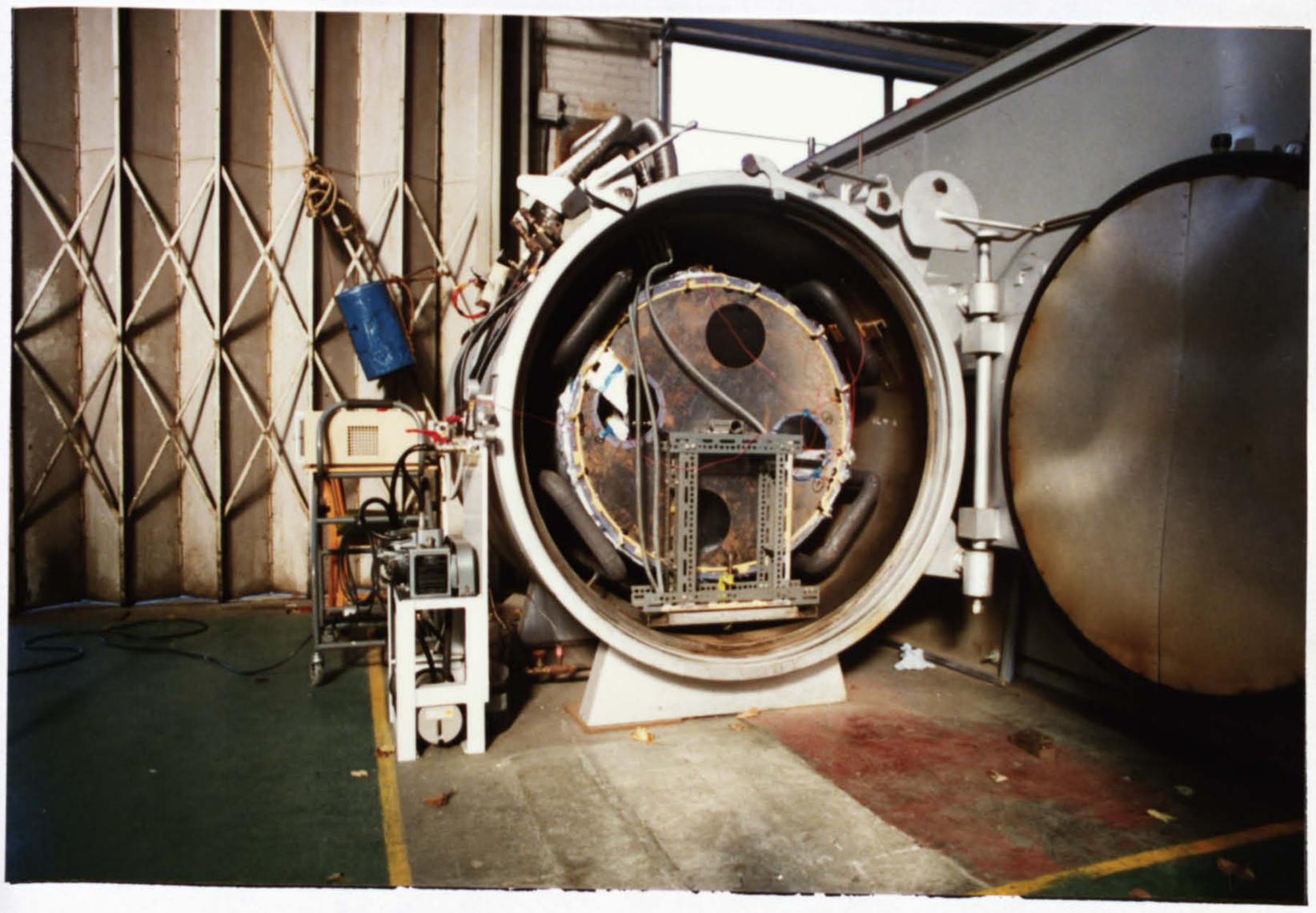

Fig. 9.14 IN THE AUTOCLAVE PRIOR TO CURING

Fig. 9.15 THRUST TUBE CURE CYCLE

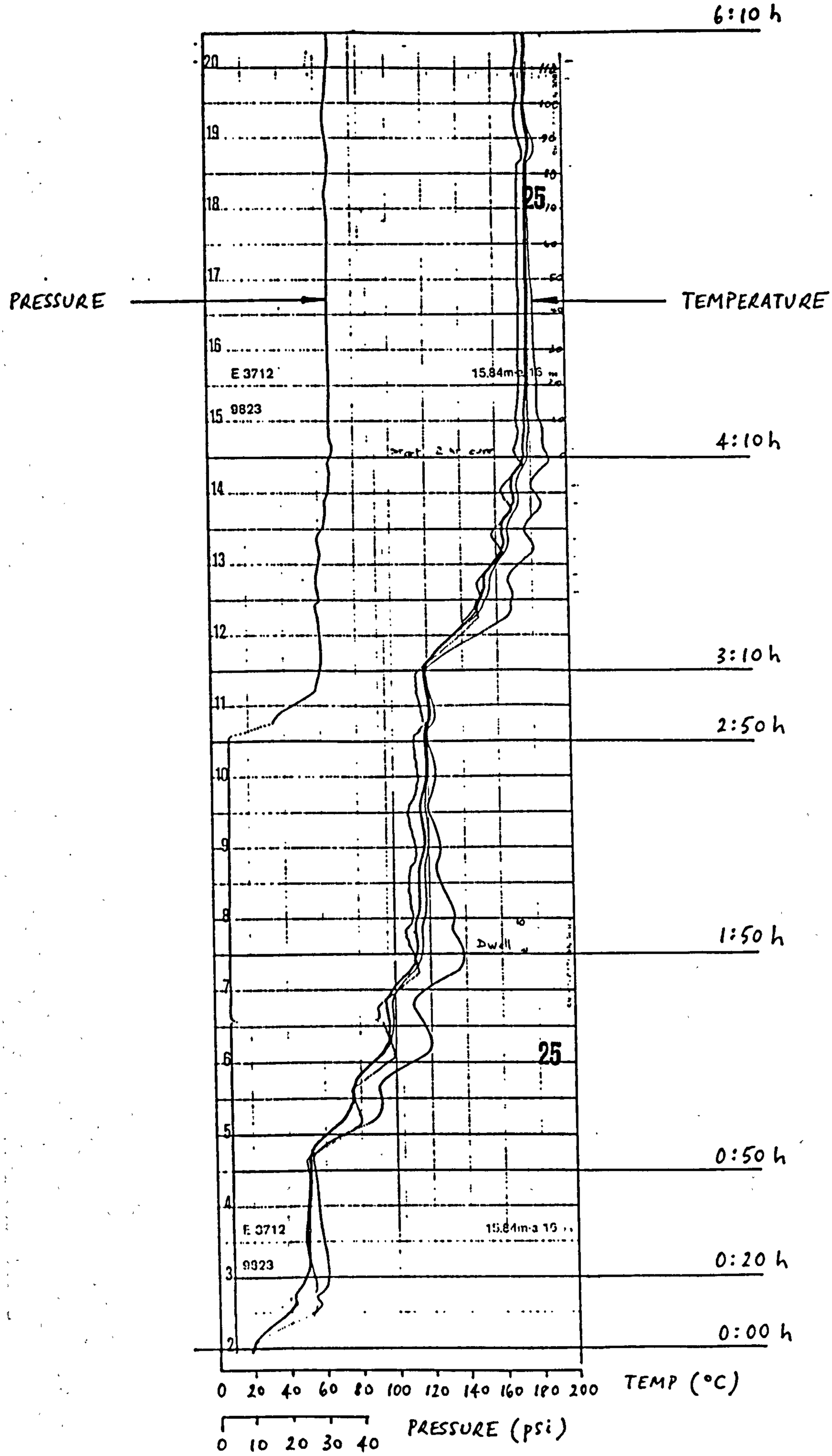

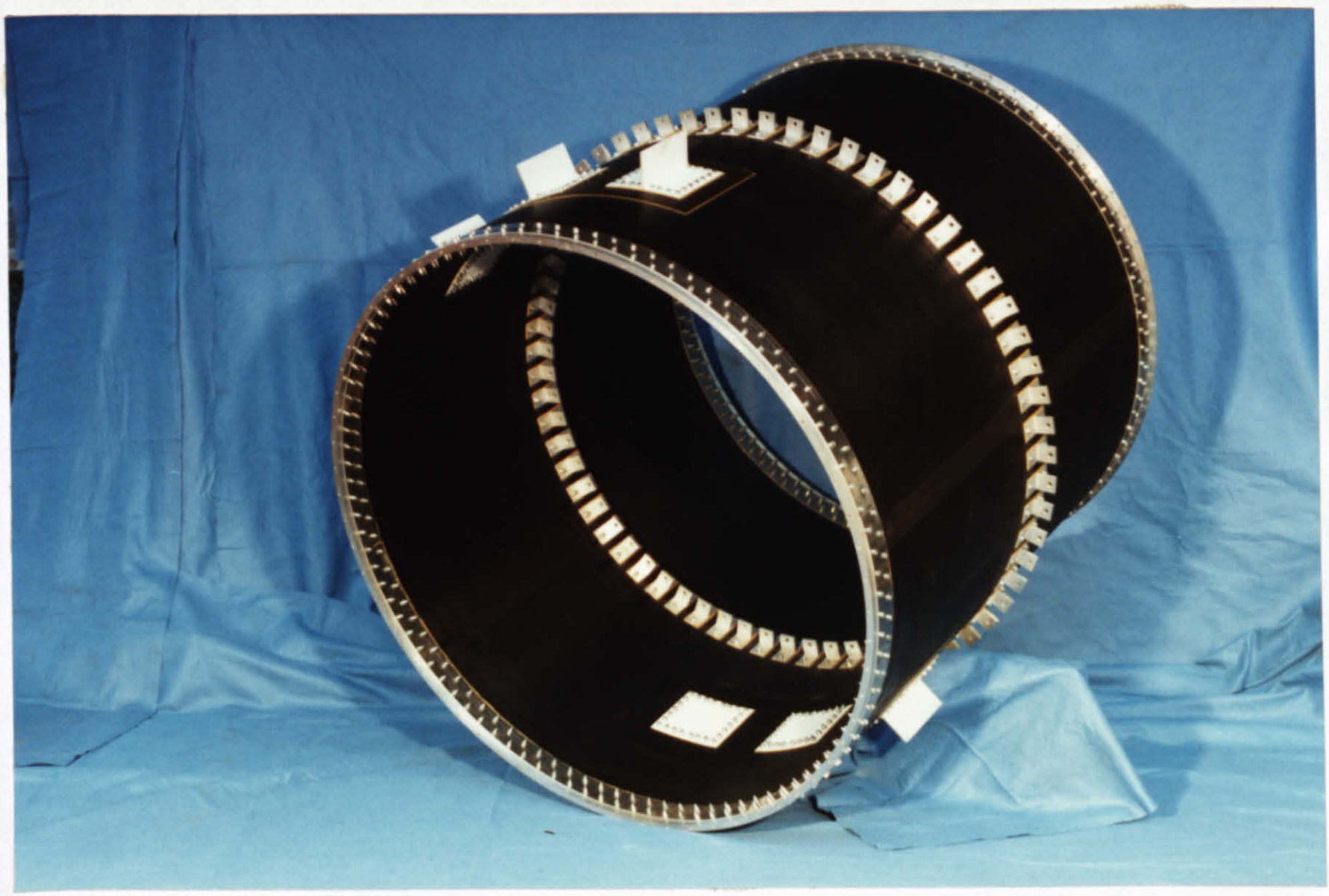

Fig. 9.16 THE COMPLETED CYLINDER

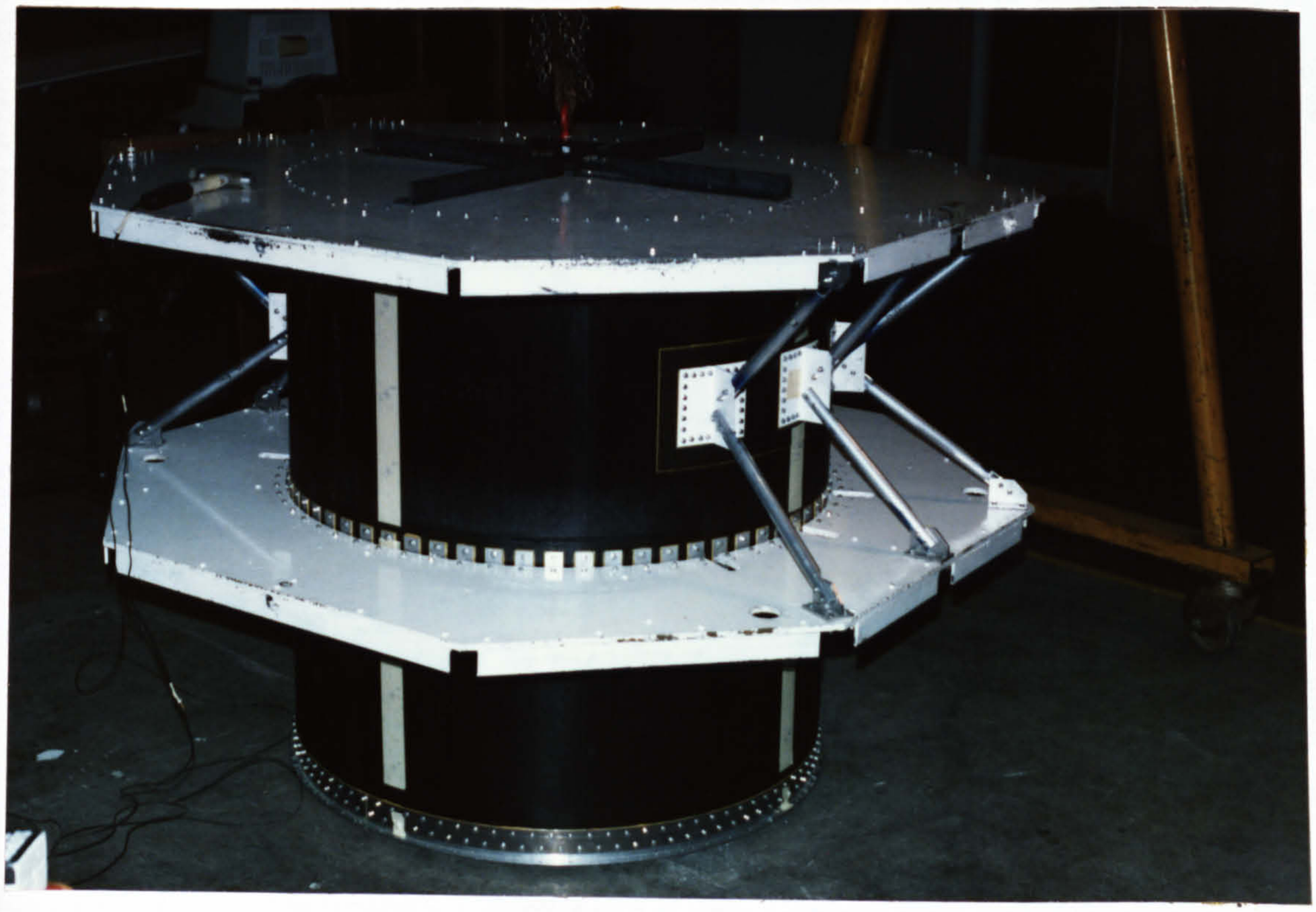

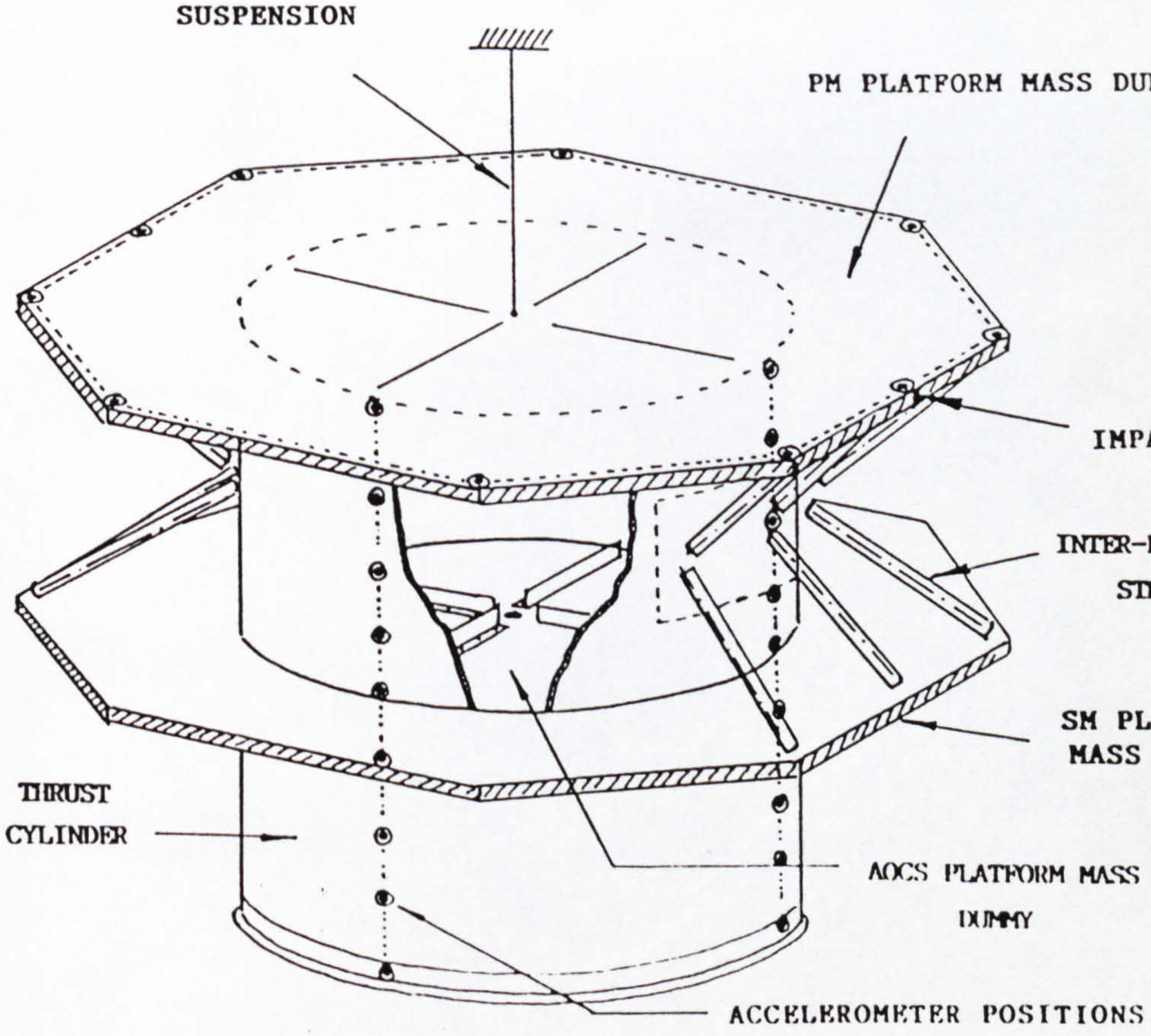

Fig. 9.17 MODAL SURVEY TEST CONFIGURATION

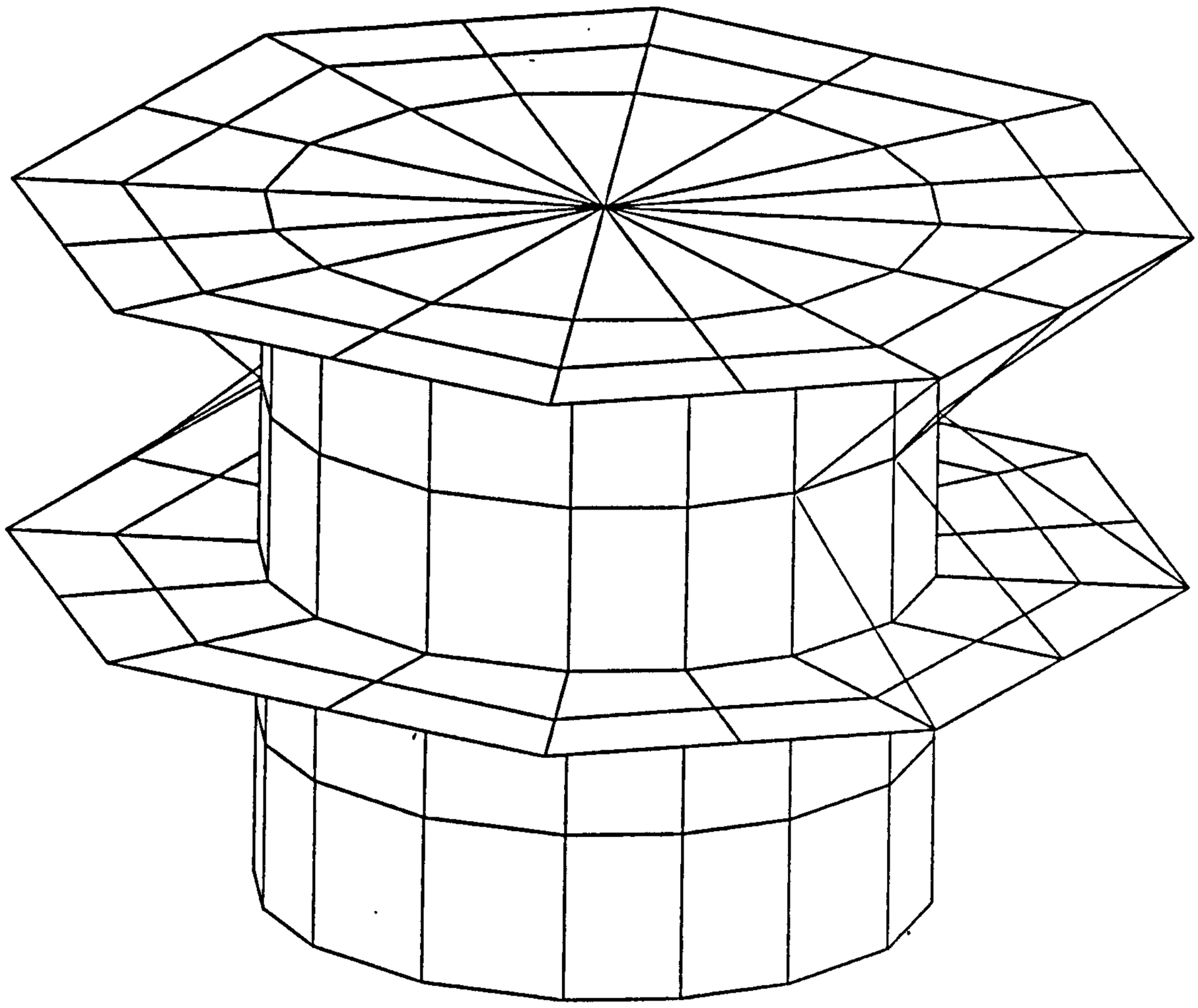

(a) ORIGINAL FE MODEL

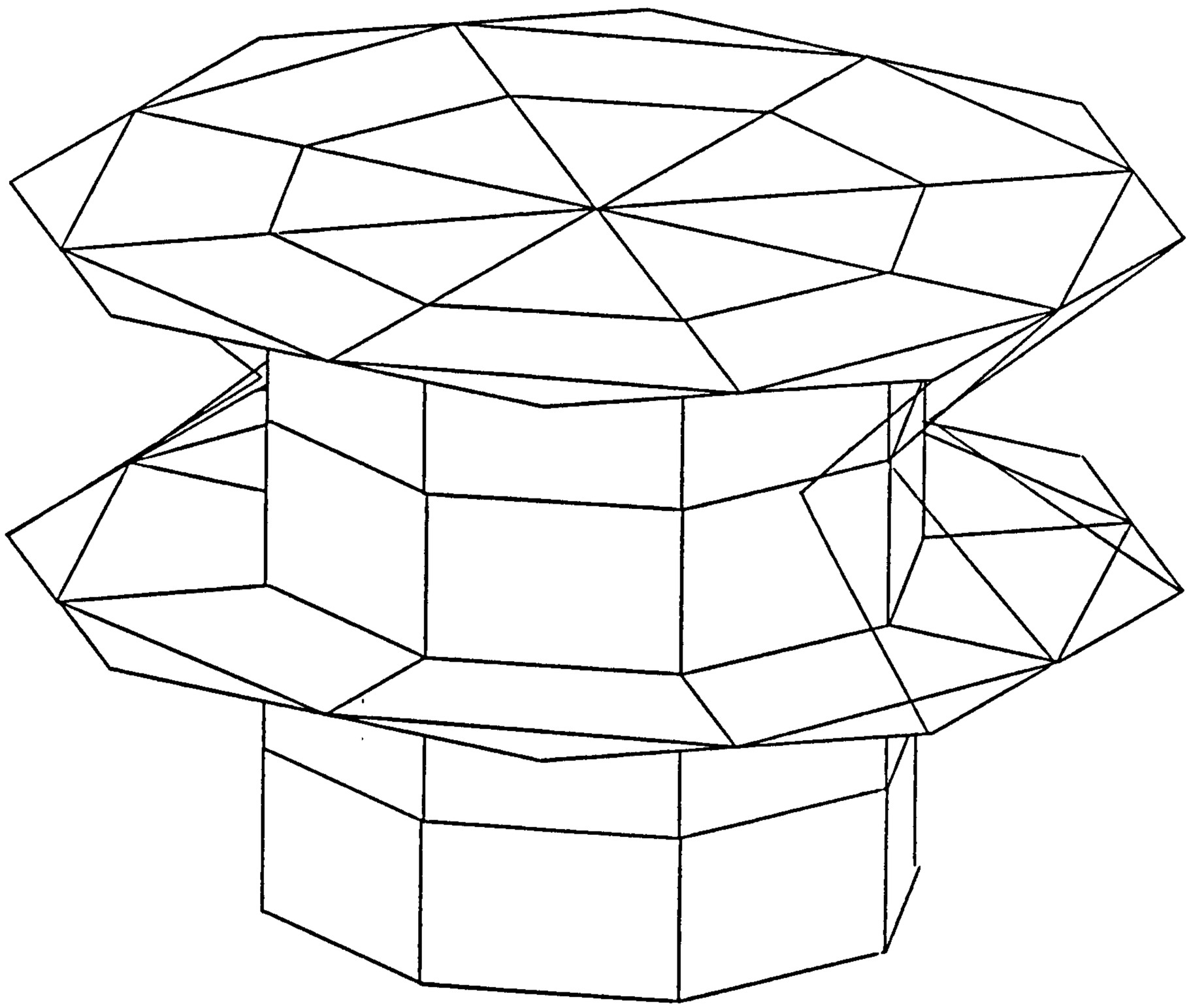

(b) COARSE FE MODEL

Fig. 9.18 TEST STRUCTURE FE MODELS

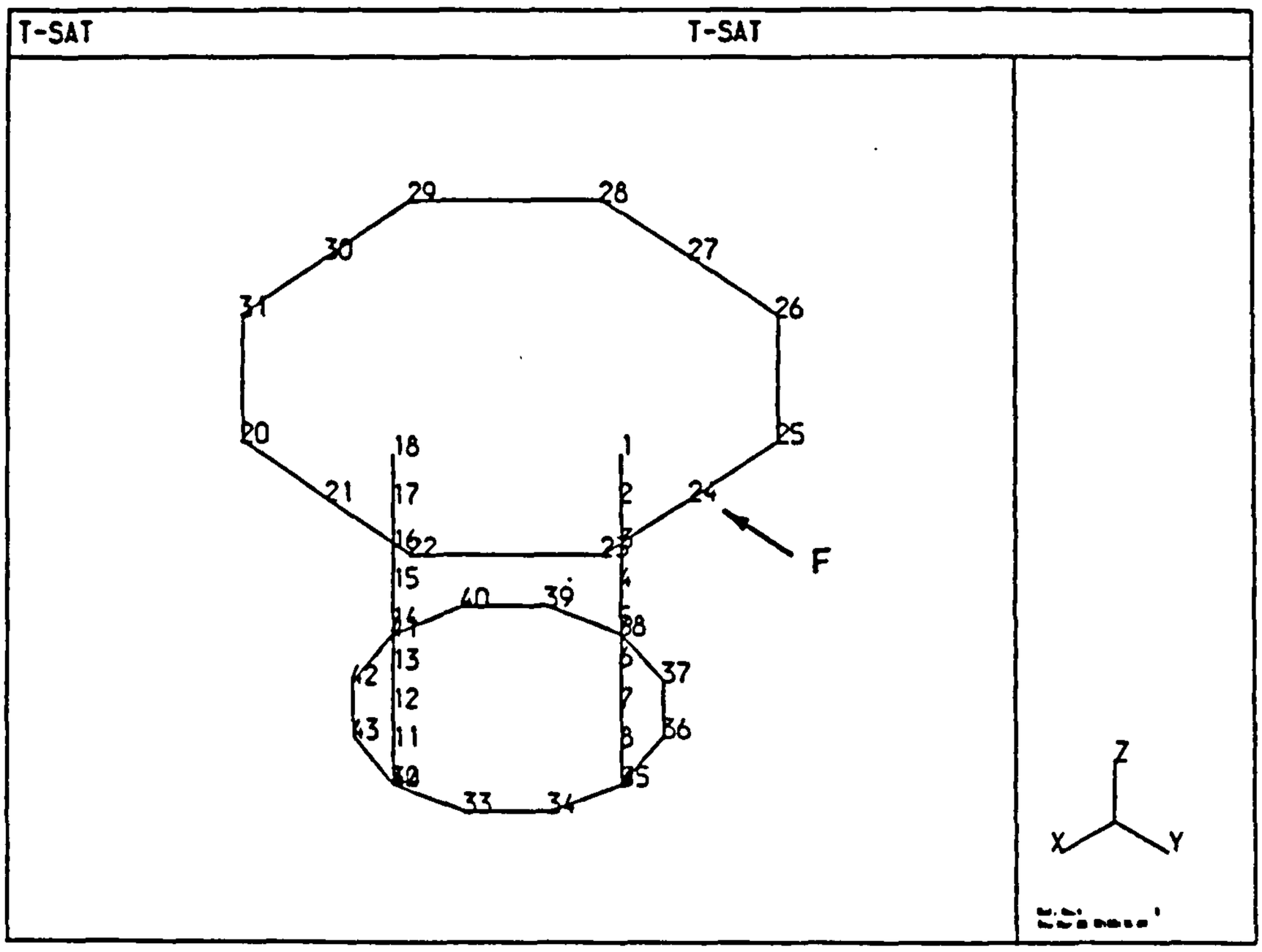

Fig. 9.19 ACCELEROMETER POSITIONS ON TEST STRUCTURE

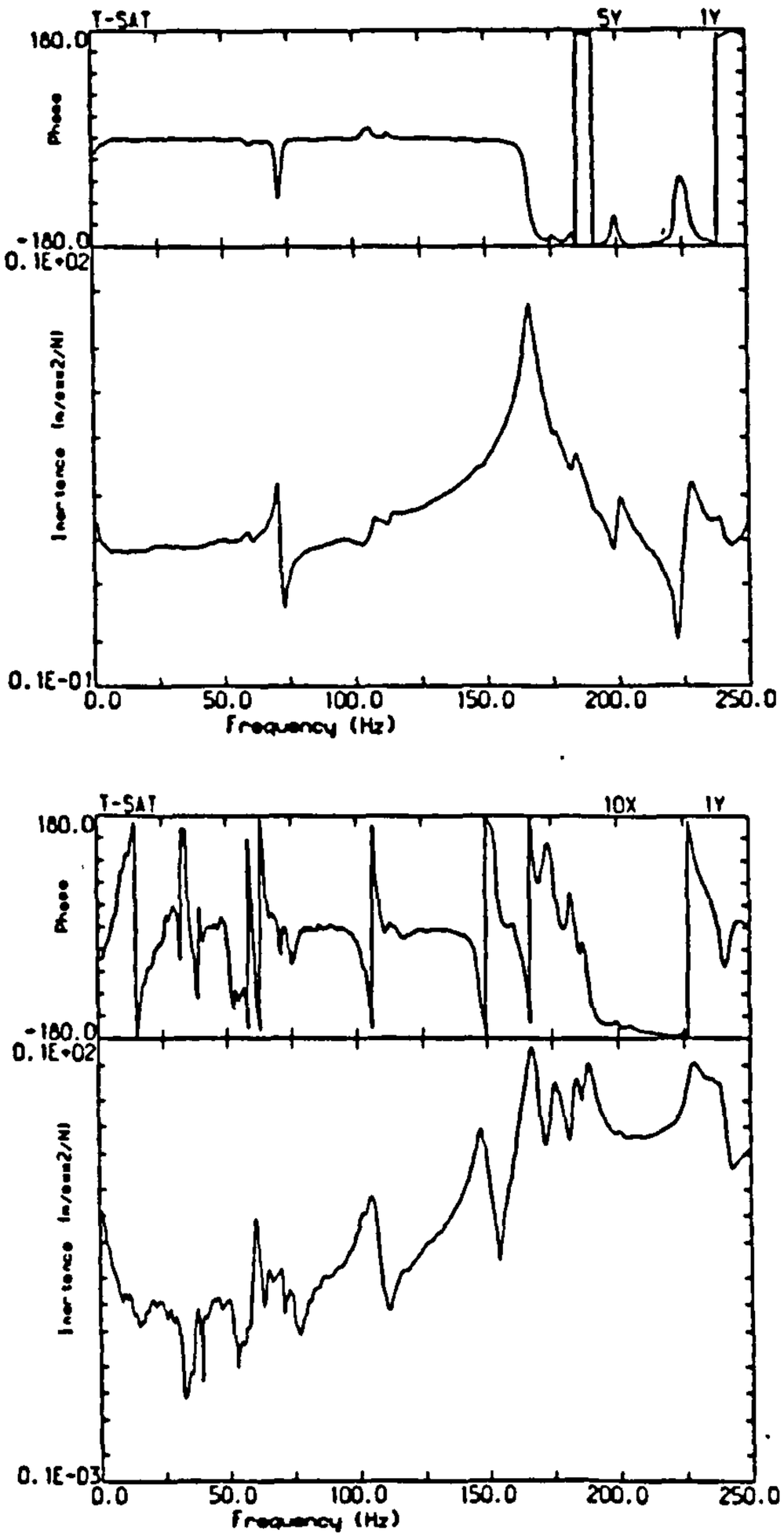

Fig. 9.20 EXAMPLE FRF PLOTS

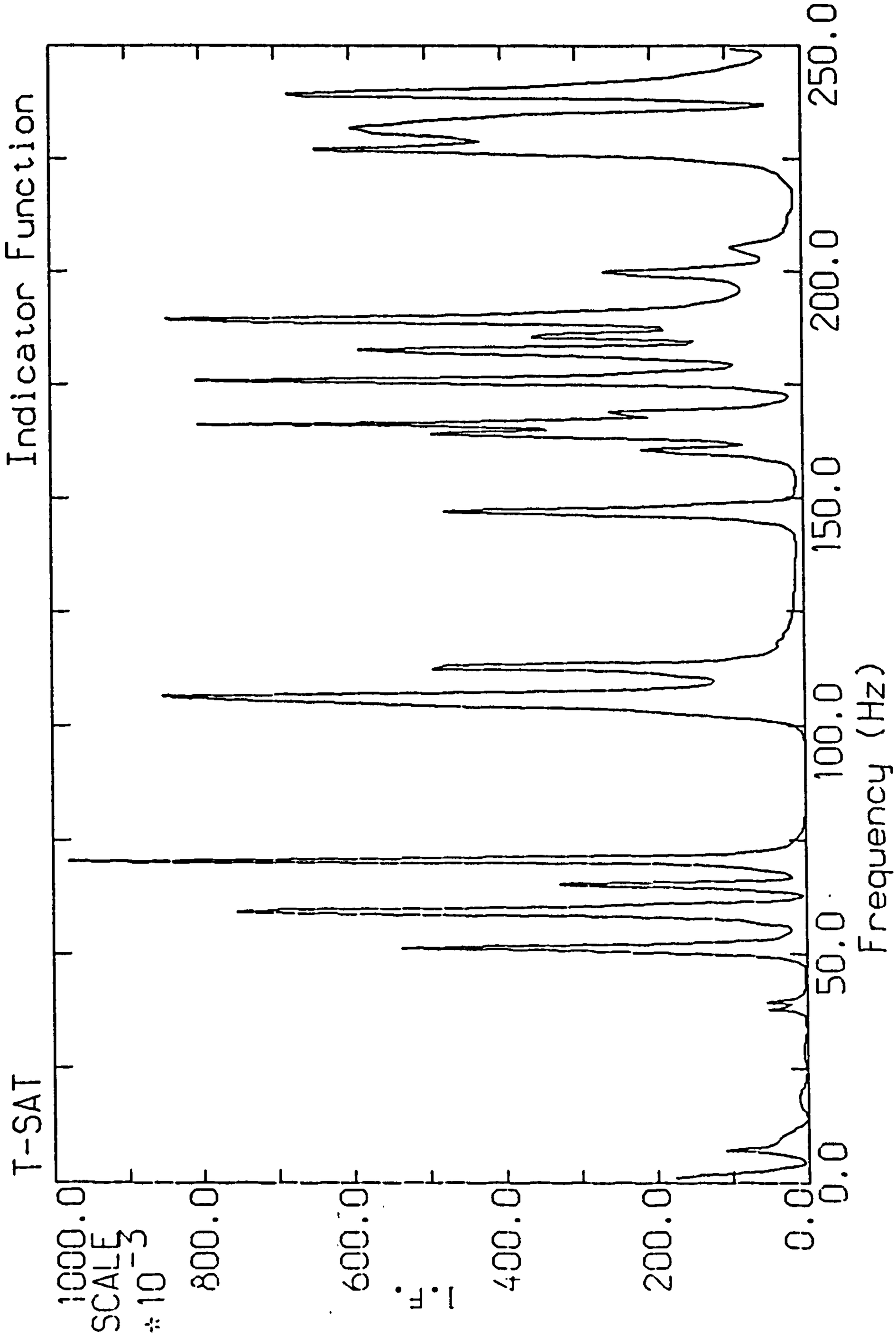

Fig. 9.21 INDICATOR FUNCTION

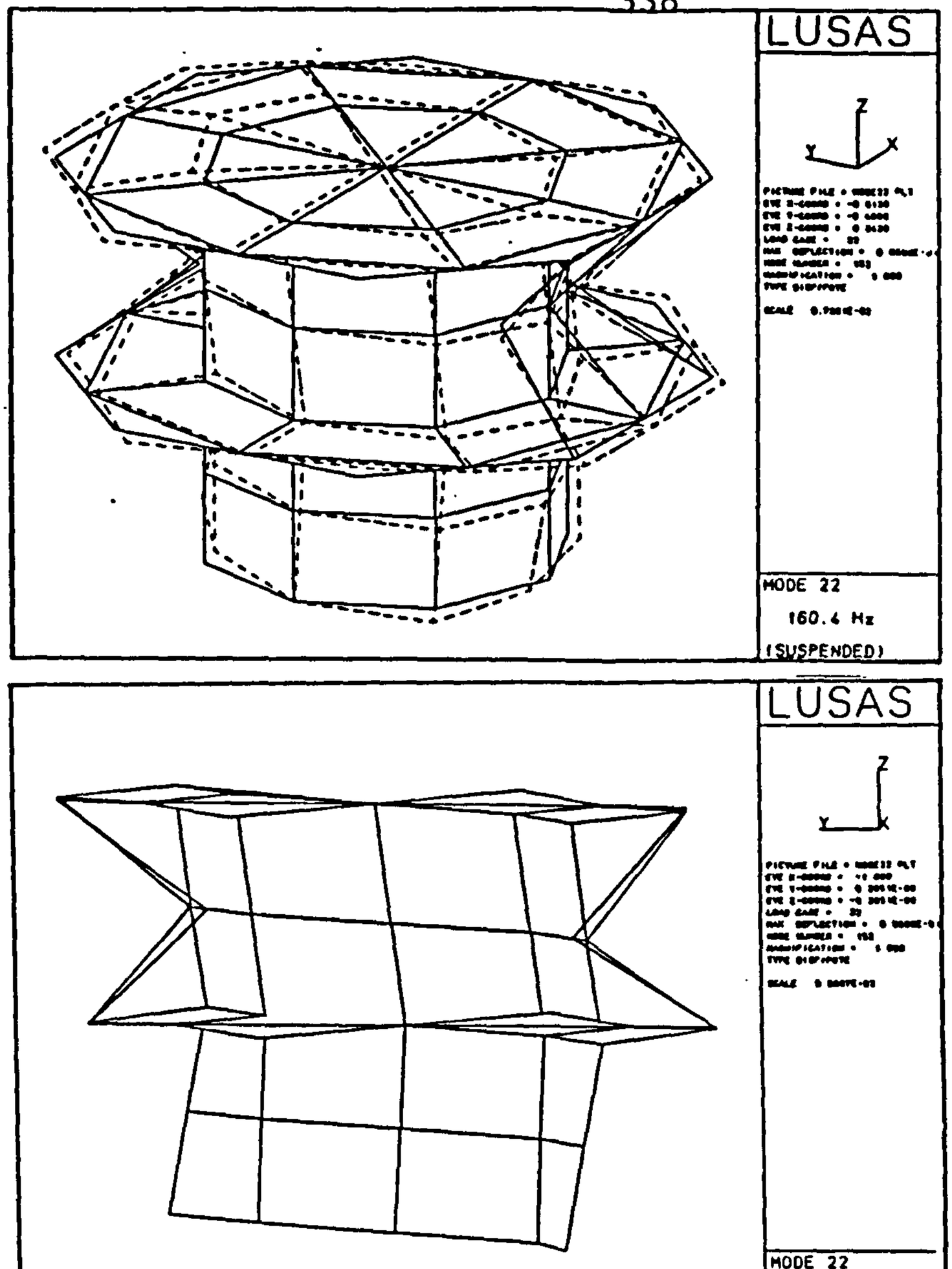

(a) FE MODEL

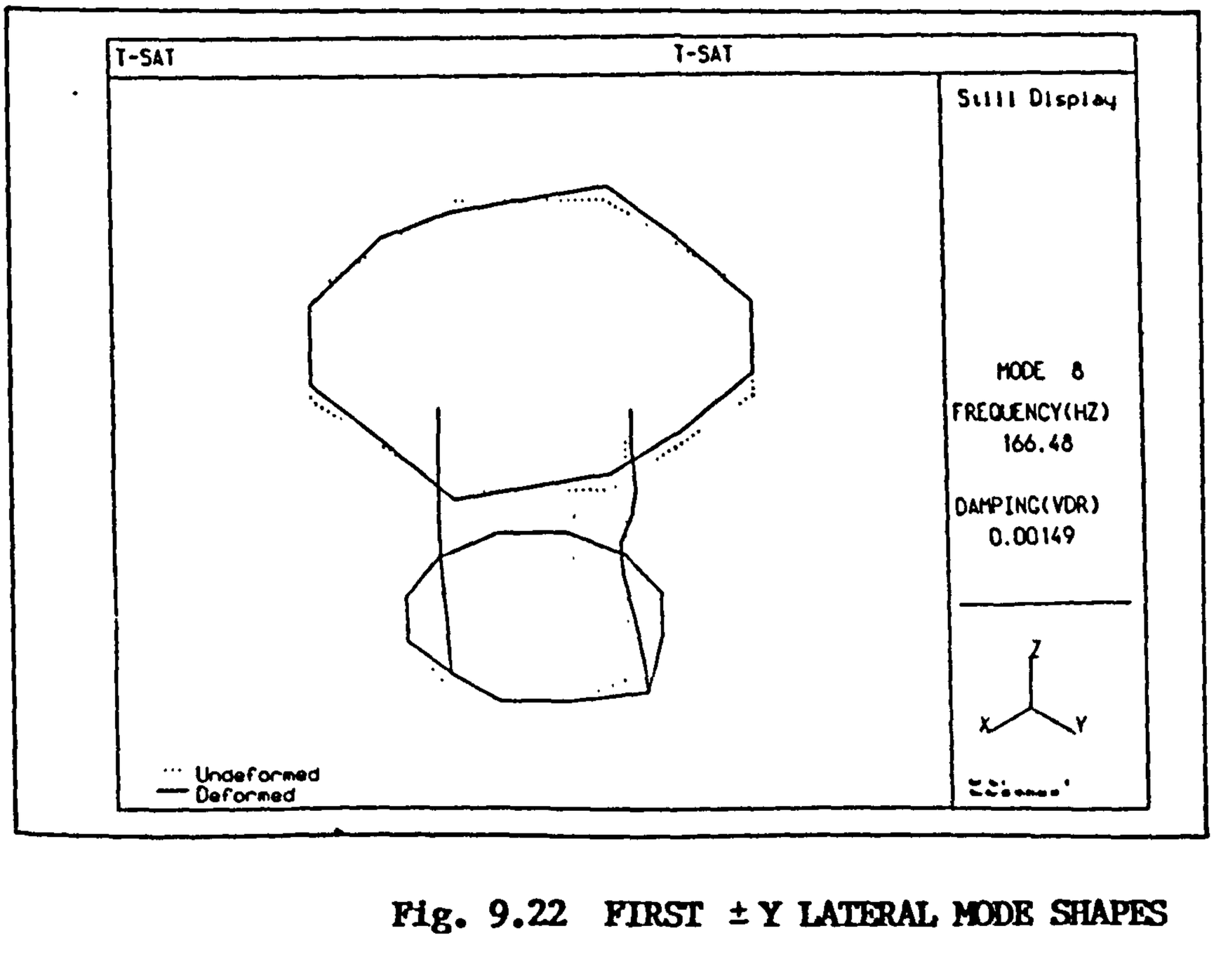

(b) MODAL SURVEY TEST

Fig. 9.22 FIRST ± Y LATERAL MODE SHAPES

CHAPTER 10 CONCLUSIONS

The focus of the research work was an investigation into the efficient usage of fibre-reinforced plastic composite materials for the facesheets of primary spacecraft sandwich structures. Efficiency was considered both in terms of minimising the mass of such structures and in reducing the cost of fabrication. The areas of investigation included the development of co-cure methods of manufacture, the extension of existing theory for the prediction of sandwich construction behaviour, the validation of theoretical predictions by test and the incorporation of the prediction methods in schemes for the optimisation of typical spacecraft sandwich components.

The following are the main conclusions drawn from the investigation.

(1) Manufacturing trials indicated that the co-cure method was practical for typical composite faced spacecraft sandwich components.

Both flat panel and cylindrical components were satisfactorily produced using a low pressure autoclave co-cure method. The method was developed sufficiently to enable curved geometry, integral facesheet doublers and core reinforcement to be successfully incorporated. This culminated in the manufacture of a full size thrust cylinder, designed for the T-Sat spacecraft, which was co-cured in a single piece on a full circumference mould. The principal features of the technique found to be necessary were:

(a) Low autoclave pressure. 30 psi was found to be satisfactory for a wide range of sandwich constructions with low density cores up to 1¼" thick. The pressure could be increased for thinner sandwich.

(b) Pre-consolidation of the facesheet plies. This enabled the plies to be compacted prior to cure to help make up for the low cure pressure.

(c) A caul plate. This was to spread the pressure load over the component surface and prevent inter-cell dimpling. For complete circumference curved components special attention is required at the caul plate joint(s).

(d) The main problem encountered in the production of the thrust tube stemmed from slack in the lay-up which manifested itself as creasing in the outer facesheet of the finished item. Vacuum de-bulking of each layer as it is applied, or a tensioning system were suggested as possible solutions in light of this.

(2) Laminate Analysis techniques were reasonably successful for the prediction of co-cured sandwich stiffness and strength.

The prediction of co-cured sandwich stiffness and strength, with a construction based on the T-Sat thrust cylinder shell, was made using laminate analysis and the Tsai-Wu failure theory. These were based on data from low pressure cured unidirectional laminates. The predictions were compared with tests performed on a series of co-cured samples under compression. The observations made were :

(a) The low pressure (30 psi) cured unidirectional laminates exhibited comparable average properties to standard pressure cured material. Greater scatter in the data however, resulted in an 'A' allowable longitudinal compression strength which was 63% of that for the standard cure pressure material. The other properties were less affected, notably longitudinal modulus.

(b) The predicted compression strength of the co-cured sandwich was 11% lower than the average test value. The data scatter was considerably less than for the low pressure cured laminates, which resulted in an 'A' allowable value 50% higher than predicted from the laminate data. It was suggested that the uneven pressure distribution in the facesheets of co-cured sandwich improves resin flow, reduces void content and improves strength over low pressure cured solid laminates.

(c) Stiffness prediction and test for the co-cured sandwich were found to be in good agreement.

(3) Successful prediction of composite faced sandwich wrinkling instability requires facesheet coupling effects to be incorporated.

Currently used methods for the prediction of wrinkling instability neglect the effect of coupling in the facesheets, which results from unbalanced lay-ups (permitted if a co-cure method of manufacture is used), and/or due to the displacement effect of the film adhesive used to bond the facesheets and core. The method proposed by Pearce & Webber[37] was modified by including skew-sinusoidal shape functions to comprehensively include all coupling effects. Combined loading actions of axial, shear and bending loads were also included. The theory was incorporated in a program which allowed numerical examples to be calculated. The theoretical results for a number of different sandwich constructions were compared with compression tests performed on samples. The wrinkling investigation resulted in the following conclusions :

(a) Calculations of numerical examples for typical spacecraft sandwich constructions indicated that the inclusion of facesheet coupling in the analysis led to reductions in critical wrinkling loads of typically 30%, but which could be as high as 50%. The reduction effect was largely due to [B] coupling, although there was no simple way of estimating the reduction based on the magnitude of these terms.

(b) Careful attention to facesheet ply stacking sequence can lead to large improvements in wrinkling strength by minimising coupling. Woven material can be benficial because the coupling effect can be less than an equivalent UD material lay-up.

(b) Under shear loading the wrinkling waveform was not necessarily perpendicular to the principal compression direction. This was contrary to the recommended assumption for analysing wrinkling under shear using simple design formulae.

(c) Lay-ups with D_{13}, D_{23} coupling were found to have a shear wrinkling strength which was dependent on the direction of the applied shear.

(d) Critical wrinkling loads under bending were calculated to be higher than the equivalent wrinkling load under pure compression. This was believed to be due to a stabilising effect of the tension facesheet.

(e) The critical wrinkling mode was dependent on the ratio of the applied load components. Under pure compression and pure shear, the critical mode was always found to be symmetric, but with bending present the critical mode became a combination of the classical symmetric and anti-symmetric modes.

(f) A comparison of test results for co-cured sandwich constructions with unbalanced facesheets showed that the best correlation with theoretical predictions was achieved if both the coupling effect and the adhesive thickness were taken into consideration. Agreement for sandwich panels with cross-ply and quasi-isotropic lay-ups of UD material was within 9%.

(g) It was believed that the generally accepted knock-down factor of 0.40 applied to simple design formulae to account for initial imperfections, which has been derived from tests on sandwich with unbalanced facesheets, could be partly due to coupling effects. However, further test-theory correlation work is necessary to sort out the existing contradictory results of various test programmes before a reduction in the design knock-down factors can be justified.

(4) The use of carbon fibre composites as the facesheets of flat sandwich panel spacecraft components can make modest weight savings over aluminium alloy.

A computer program based on the analysis of panel vibration, material failure, wrinkling and dimpling instability was written to enable minmium weight designs to be generated for certain classes of spacecraft sandwich panel. The program was limited to flat or singly curved rectangular panels loaded primarily by bending. This covered a large number of spacecraft panels and enabled optimum designs for a rear closure panel and Service

Module platform on the T-Sat spacecraft to be produced. Conclusions drawn from this area of investigation were :

(a) The program provided a useful design aid for design optimisation. Optimum designs for sandwich constructions with different material systems, prepreg thicknesses, facesheet lay-ups and methods of manufacture could be rapidly evaluated in trade off studies.

(b) For the stiffness-critical rear panel of the T-Sat spacecraft, high modulus carbon fibre reinforcement was the preferred solution, with considerably more costly ultra-high modulus material yielding only a slightly improved weight saving. A 14% saving was made over aluminium due largely to the exploitation of tailorability in a [0/90/0] face-sheet lay-up. The co-cure method of manufacture was found to be beneficial for this type of panel because material strength was only a secondary consideration.

(c) For the strength-critical SM platform, high strength carbon prepreg was found to offer the lightest solution. A quasi-isotropic lay-up for the facesheets resulted in a weight saving of just under 11% over aluminium alloy. Despite the lower compression strength of co-cured facesheets, this method of manufacture still yielded competitive designs because of the stiffness requirement dictated by wrinkling instability.

(5) The use of carbon fibre composites in the facesheets of sandwich shell thrust tubes is both a mass-efficient and cost-effective design solution.

Previous studies had shown that composite sandwich and corrugated shell constructions were the most efficient forms of construction for thrust tubes. Small differences in the relative weights of the two were dependent on local connection design details. However, sandwich construction was recognised as being cheaper to manufacture, and the cost was expected to be reduced further if a co-cure technique was adopted. Methods for the design and analysis of thrust tube structural behaviour were developed, aimed at

the early design stages, and these where incorporated into a scheme for optimisation. Lateral stiffness, material strength, general instability, wrinkling and dimpling were included. The optimisation scheme was used in the design of the thrust tube for the T-Sat spacecraft and for the preliminary design of a thrust tube for a comet sample return spacecraft. The cylindrical part of the T-Sat spacecraft thrust tube was manufactured using a co-cure technique. It was subsequently loaded with dummy masses to represent the rest of the spacecraft and a modal survey test was performed to validate the lateral stiffness analysis. The following conclusions were drawn :

(a) The use of a simple lumped mass and beam finite element approach for the analysis of spacecraft lateral frequency, and hence thrust tube stiffness was found to be very effective. For the T-Sat spacecraft, the full dynamic FE model was reduced from 1727 d.o.f to 6 d.o.f to vastly reduce the solution time for only a 1½% loss in accuracy on the first lateral mode. The inclusion of shear stiffness, rotational inertia and careful lumping of mass were found to be essential for a realistic representation.

(b) An interactive buckling expression using theoretical buckling loads for cylinders under uniform compression and pure torsion was used to analyse general instability under combined axial and shear stresses. For the analysis of compression buckling it was inappropriate to assume an axisymmetric mode for lay-ups with low hoop stiffness, so it was therefore necessary to resort to a more general solution. Similarly, for the analysis of torsional buckling, the range of typical thrust tube dimensions and stiffnesses prevented a simple closed form solution from being employed.

(c) The application of established numerical optimisation methods to composite faced sandwich shell thrust tube design was found to have several drawbacks. These related to the presence of discrete design variables (ply thicknesses) and difficulty in defining a suitable objective function. A less automatic method was proposed, which

sacrificed some speed for better control and understanding over the optimisation process.

(d) The optimisation method was successfully used to locate optimum designs for the two thrust tube examples. Fibre angle variables were used to minimise weight and maximise safety margins on failure modes. The optimum composite faced designs were found to save 34% and 31% over alternative aluminium alloy designs (not including attachments and reinforcements). Use of a co-cure manufacturing technique was found to be advantageous where the number of facesheet plies was small or the thrust tube design was dominated by the stiffness requirement.

(e) The modal survey test performed on the manufactured T-Sat thrust cylinder was found to be in good agreement with predictions made through the use of laminate analysis and a plate & shell FE model. The first lateral mode frequency was predicted within 4% of its measured value. It was therefore inferred that the beam & lumped mass representation used for thrust tube optimisation, which correlated well with the plate & shell FE model, was a reasonable approach.

ACKNOWLEDGEMENTS

This work was sponsored by the Science and Engineering Research Council.

The author is indebted to the following staff of the College of Aeronautics who provided invaluable assistance during the course of this work:

Tom Bowling for countless helpful discussions and management of the project, Maurice Crook for composite lay-up expertise in the manufacture of test panels and the thrust cylinder, Martin Paul for his help in completion of the thrust tube and construction of the test structure, Trevor Backhurst for numerous machining jobs, Mike Jones for carrying out most of the testing, and Mark Williams for building the thrust cylinder tooling.

Many thanks also, to Denice Jaunzens for help with the typing, words of encouragement and much tea making.

REFERENCES

[1] WILSON D — Advanced Polymer Composites For High Temperature Applications. 15th Congress Intl. Council for the Aeronautical Sciences. London 1986.

[2] — Aerospatiale Prepares Composites for Orbit. Air & Cosmos Monthly. Sept. 1988 p 72.

[3] VANDERKLEY P S — Comparison of Satellite Thrust Cone of Monocoque and Sandwich Construction. 30th SAMPE Conf. Anaheim, Ca. 19-21 Mar. 1985 pp 129-134.

[4] DOMNIKOV L, SWITZ R J — An Application of Unsupported Film Adhesive to Fabricate Spacecraft Structures. 14th National SAMPE Tech. Conf. Atlanta Ga. 12-14 Oct 1982 pp 337-348

[5] — T-Sat Design Study. Final Report Vol. 1 Technical Study. March 1988. RAL-88-033

[6] QUALLS J P — Graphite Epoxy Satellite Structure Development Program. 14th National SAMPE Tech. Conf. Atlanta Ga. 12-14 Oct 1982 pp 513-520

[7] MAZZIO V F, BIXLER C H — Optimised Design and Fabrication Processes for Advanced Composite Spacecraft Structures 17th Aerospace Sci. Mtg, New Orleans La. 15-17 June 1979

[8] BARBERIS N
ZILIANI M
GABRIEL C
Design & Development of the Intelsat V Graphite-Epoxy Central Thrust Tube.
23rd Structures, Structural Dynamics & Mtls. Conf. May 1982 pp 594-602

[9] FRANZ J
LAUBE H
Strength of Carbon Fibre Composite/Titanium Bonded Joints as used for SPAS Type Structures
Proc. Workshop: Composites Design for Space Applications, ESTEC, 15-18 Oct. 1985 pp 301-308

[10] BRODSA D
On the Development of a Corrugated CFRP Central Cylinder for Satellites.
Proc. Workshop: Composites Design for Space Applications, ESTEC, 15-18 Oct. 1985 pp 285-290
1985 pp 285-290

[11] SHARKEY J T
NAYLER G H F
REYNOLDS J
Design & Development Testing of the Bonded Joint between a Typical LVA Ring and CFRP Thrust Cone
Proc. Workshop: Composites Design for Space Applications, ESTEC, 15-18 Oct. 1985 pp 275-284

[12] PETTEX J L
Comparison of Classical and Co-Curing Manufacturing Techniques for a CFRP Honeycomb Central Tube.
Proc. Workshop: Composites Design for Space Applications, ESTEC, 15-18 Oct. 1985 pp 291-294

[13] BLAAS C
ENSCHEDE G J
REKERS F
VAN ZELST R F P
Study of a CFRP Replacement for the Olympus Central Cylinder.
Proc. Workshop: Advanced Structural Materials, Design for Space Applications, ESTEC, 23-25 Mar. 1988 pp 219-225

[14] KAWASHIMA T
INOVE T
SEKO H
Design & Development of the Graphite Epoxy Structure for CS-3 Satellite.
Proc. Workshop: Composites Design for Space Applications, ESTEC, 15-18 Oct. 1985 pp 267-274

[15] KATOH T
YAMADA K
Development of the Graphite Epoxy Satellite Structure
ICCM V, San Diego Ca, July 1985

[16] THOMPSON H D
SMITH G B
BIXLER C H
Advanced Composites Satellite Equipment Support Module Study.
4th Conf. Fibrous Composites in Structural Design. San Diego Ca, 14-17 Nov. 1978.

[17] MICHNO M J
High Modulus Composite Properties.
Space Systems Technical Conf., San Diego Ca. 9-12 June 1986 pp 126-131.

[18] BERMAN L D
Reliability of Composite Zero-Expansion Structures for Use in Orbital Environment.
Comp. Reliability, ASTM STP 580, 1975, pp 288-297.

[19] PHELPS H R
Property Changes of a Graphite-Epoxy Composite Exposed to Non-Ionising Parameters.
Jl. Comp. Mtls., Vol. 14, Oct. 1980.

[20] NIEUWENHUIZEN M P
Reliability & Economics of Spacecraft Structure Development.
Proc. Conf: Spacecraft Structures. CNES, 3-6 Dec. 1985, ESA SP-238, pp 261-267

[21] CURRAN M J
The Application of Fibre-Reinforced Thermoplastic for Space.
Proc. Workshop: Advanced Structural Materials, Design for Space Applications. ESTEC, 23-25 Mar. 1988, pp 79-83

[22]
Cyanamid Aerospace Literature.

[23] LUBIN G (Ed.)
Handbook of Composites.
(Van Nostrund Reinhold, 1982).

[24] Ciba-Geigy Literature

[25] Composite Design Handbook Vol. 1,
ESA PSS-03-1101, issue 1 (1986)

[26] Westland Literature.

[27] Fiberite (AMOCO) Literature.

[28] THOMAS M G
OLIVER W T
The Development of the Ariane 4 SPELDA.
Proc. Workshop: Composites Design for Space Applications, ESTEC, 15-18 Oct. 1985, pp 251-263

[29] TANG J M
LEE W I
SPRINGER G S
Effect of Cure Pressure on Resin Flow, Voids and Mechanical Properties of Composites.
Jl. Composite Mtls. Vol. 21, May 1987, pp 421-440

[30] SUAREZ J A
Cost Effective Mechanical Property Characterization.
Symp. on Test Methods & Design Allowables for Fibrous Composites, Dearborn Mi. Oct. 2-3 1979
ASTM STP 734 1981 pp 208-228

[31] ROWLANDS R E
Strength Failure Theories and their Experimental Correlation.
in: Failure Mechanics of Composites, ed. Sih G C & Skudra A M, pub. North-Holland 1985

[32] TSAI S W
HAHN H T
Introduction to Composite Materials.
pub. Technomic, Westport Ca. 1980

[33] TENN L F
Statistical Analysis of Fibrous Composite Strength Data.
Test Methods & Design Allowables for Fibrous Composites, ASTM STP 734, 1979, pp 229-244

[34] ASTM
Metals Handbook 9th edition. 1978
vol. 8 Mechanical Testing, p 665

[35] SULLINS R T
SMITH G W
SPIER E E
Manual of Structural Stability Analysis of Sandwich Plates & Shells
NASA CR-1457 Dec. 1969

[36] BANSEMIR H
PFEIFER K
Local Stability of Sandwich Structures for Space Applications having Thin Fibre Reinforced Face Skins.
SAMPE: Engineering with Composites 1988, paper7

[37] PEARCE T R A
WEBBER J P H
Buckling of Sandwich Panels with Laminated Face Plates.
Aeronautical Quarterly, May 1972, pp 148-160

[38] HEMP W S
On a Theory of Sandwich Construction.
ARC R&M 2672 1952

[39] PEARCE T R A
WEBBER J P H
Experimental Buckling Loads of Sandwich Panels with Carbon Fibre Faceplates.
Aeronautical Quarterly, Nov. 1973, pp 295-312

[40] WEBBER J P H
KYRIAKADES S
LEE C T
On the Wrinkling of Honeycomb Sandwich Columns with Laminated Cross Ply Faces.
Aeronautical Jl. June 1976, pp 264-272

[41] GUTIERREZ A J
WEBBER J P H
Flexural Wrinkling of Honeycomb Sandwich Beams with Laminated Faces.
Jl. of Computers & Structures, Vol. 16, 1980
pp 645-651

[42] BANKS W M
CHAI G B
The Behaviour of CFRP Sandwich Panels under In Plane Compressive Loading.
Proc. Workshop: Advanced Structural Materials, Design for Space Applications, ESTEC, Mar. 23-25 1988,
pp 305-321

[43] JACKSON P
The Design of Sandwich Panels with Composite Face Skins.
College of Aeronautics M.Sc. Thesis Sept.1988

[44] WILLIAMS J G
MIKULAS M M
Analytical & Experimental Study of Structurally Efficient Hat-Stiffened Panels Loaded in Axial Compression.
AIAA paper 75-754, Denver Co 1975 (& NASA TM X-72813)

[45] AGARWAL B L
SOBEL L H
Weight Comparisons of Optimised Stiffened, Unstiffened and Sandwich Cylindrical Shells.
Jl. of Aircraft, Vol. 14, Oct. 1977 pp 1000-1008

[46] PRZEMIENIECKI J S
Theory of Matrix Structural Analysis. Chpt. 5.6
Pub. McGraw-Hill 1968

[47] TIMOSHENKO S P
GERE J M
Theory of Elastic Stability
Pub. McGraw-Hill 1961

[48] BAIG M I
YANG T Y
Buckling Analysis of Orthogonally Stiffened Waffle Cylinders.
Jl. of Spacecraft, Vol. 11, no. 12, Dec. 1974
pp 832-837

[49] BAKER E H
KOVALEVSKY L
RISH F L
Structural Analysis of Shells.
Pub. McGraw-Hill 1972. ISBN 0-07-003354-4

[50] JOHNSTON B G (Ed.)
Guide to Stability Design Criteria for Metal Structures. (3rd edition)
Pub. John Wiley & Sons 1976. p288

[51] WANG C T
VACCARO J R
DeSANTO D E
Buckling of Sandwich Cylinder under Combined Compression, Torsion and Bending Loads.
Jl. of Applied Mechanics, Vol. 22, 1955, p 324-328

[52] BRUHN E F
Analysis & Design of Flight Vehicle Structures.
Pub. Tri-State Offset Co. 1965. c.8.17, c.8.20

[53] MacCALDEN P B
MATTHIESON R B
Combination Torsion & Axial Compression Tests of Conical Shells.
AIAA Jl, Vol. 5, no. 2, Feb. 1967, pp 305-309

[54] WILKINS R J
LOVE T S
Combined Compression-Torsion Buckling Tests of Laminated Composite Cylindrical Shells.
Jl. Aircraft, Vol. 12, no. 11, 1975, pp 885-889

[55] TEICHMANN F K
WANG C H
GERARD G
Buckling of Sandwich Cylinders under Axial Compression.
Jl. of Aeronautical Sciences, June 1951, pp 398-406

[56] MARCH H W
KUENZI E W
Buckling of Sandwich Cylinders in Torsion.
FPL Report No. 1840, June 1953 (rev. Dec. 1957)

[57] BERT C W
CRISMAN W C
NORDBY G M
Buckling of Cylindrical & Conical Sandwich Shells with Orthotropic Facings.
AIAA Jl, Vol. 7, no. 2, Feb. 1969, pp 250-257

[58] BECKER H
GERARD G
Elastic Stability of Orthotropic Shells.
Jl. of Aerospace Science, Vol. 29, no. 5, May 1962, pp 505-522

[59] SIMITSES G J
Instability of Orthotropic Cylindrical Shells under Combined Torsion & Hydrostatic Pressure.
AIAA Jl, Vol. 5, no. 8, Aug. 1967, pp 1463-1469

[60] VANDERPLAATS G N
MOSES F
Structural Optimisation by Methods of Feasible Directions.
Computers & Structures, Vol. 3, 1973, pp 739-755

[61] STARNES J H
HAFTKA R T
Preliminary Design of Composite Wings for Buckling, Strength and Displacement Constraints.
Jl. of Aircraft, Aug. 1979, pp 564-570

[62] BUSHNELL D
PANDA - Interactive Program for Minimum Weight Design of Stiffened Cylindrical Panels & Shells.
Computers & Structures, Vol. 16, 1983, pp 167-185

[63] MIN K T
DeCHARENTENAY F X
Optimum Weight Design of Sandwich Cylinders with Orthotropic Facings and Core under Combined Loads.
Computers & Structures, Vol. 24, no. 2, 1986, pp 313-322

[64] CELL A
SOOSAR K
Discrete Variables in Structural Optimisation.
in : Optimum Structural Design- Theory & Applications
ed. Gallagher R H & Zienkiewicz O C. Chapter 11.
Pub. John Willey & Sons. 1972.

[65] WONG G
Configuration & Structure of Primordial Sample Return Mission Spacecraft.
College of Aeronautics M.Sc. Thesis, May 1989

[66] HUNERS H
Applying Modal Survey Test Results for Updating Dynamic Mathematical Models of Spacecraft Structures
Proc. Conf: Spacecraft Structures, CNES, Toulouse, 3-6 Dec. 1985 pp 195-201

APPENDIX A : T-SAT SPACECRAFT

Introduction

The T-Sat spacecraft formed the basis of a study initiated by the Engineering Board of the Science and Engineering Research Council to investigate the feasibility of a combined mobile communications and technology demonstrator satellite. This work was carried out by a consortium of university engineering groups led by the Rutherford-Appleton Laboratory. The structure of this spacecraft formed the focus for much of the research into composite faced sandwich described here.

Mission

The primary objectives of the T-Sat spacecraft were to fly a mobile communications payload and to provide flight opportunities for in-orbit testing of UK space technology items, either as payload or in the spacecraft bus itself.

A highly elliptical 12 hr. Molniya orbit, inclined at 63.4° (see fig. A.1), was selected to give the spacecraft a near-stationary position at its zenith over the UK for an 8 hr. period per day. The orbit is earth synchronous with alternate apogees over the UK and North Pacific. This orbit enables efficient communication between mobile units because there is no requirement for tracking antennas on the ground and the overhead position of the spacecraft allows good reception in built-up areas. The latter is a problem for spacecraft in the overcrowded geostationary orbit. The Molniya orbit also provided the opportunity to test components under harsh enviromental conditions because of the passage of the spacecraft through the Van-Allen belts four times a day, plus thermal cycling and large changes in altitude.

Technology demonstrator payloads proposed for flight on T-Sat included the following:

Microstrip Patch Antenna
Nickel Hydrogen Battery
Xenon Ion Thruster
Microwave Ring Gyro
Fluid Loop Gyro
Gallium Arsenide Solar Cells
Solar Concentrator
Cold Gas Propulsion Valves
Optical Data Bus
Plasma Diagnostics Package

As part of the technology demonstrator concept composite materials were proposed for use in as much of the primary structure as possible.

Configuration

The spacecraft configuration evolved through several proposed launch options and changes in the on-board systems. These included launches on Ariane 4, Shuttle, Delta and the Chinese Long March 2. Because of the difficulty in reaching Molniya orbit from the various launchers, several launch configurations were proposed each with a different (and in some cases two) solid kick motor stages. The launch options were finally reduced to just one : a dedicated launch on the Long March vehicle. This required the spacecraft to be suspended upside down below its boost motor stage in order to be accomodated within the small nose shroud. As the spacecraft grew an alternative fairing was proposed and this enabled the spacecraft to be launched in the more conventional orientation with the boost motor below the spacecraft.

The final spacecraft configuration is illustrated in fig. A.2 and its position in the Long March 2C launcher in fig. A.3. The spacecraft was 3-axis stabilised with a main body of dimensions 1.5m x 1.6m x 1.65m. The earth pointing face was occupied by a semi-recessed 1.5m diameter parabolic antenna of the communications payload. The opposite face provided the mounting for an experimental flat phased array antenna which could be

brought into operation by a 180° roll manoeuvre. The other two side faces were essentially non-earth and non-sun pointing and hence served as passive radiators for the rejection of waste heat. Most of the spacecraft electrical equipment was mounted directly to these two faces. They also supported the array drive mechanisms for two 1.2m x 1.6m rigid GaAs solar arrays. Twin nozzles of the xenon ion-motor, plasma potential probe and TT&C antennas were mounted to the top face. The antennas were to be errected after launch and the plasma probe deployed on a boom away from the spacecraft main body. Hydrazine thrusters of the attitude control system were positioned equatorially in groups of three on small extensions to clear the primary antenna. The fuel tanks, reaction wheels and gyropack of the AOCS were mounted internally close to the in-orbit CG position.

In its launch configuration the spacecraft was clamped by a Marman ring at its base to an Orbit Transfer Module (OTM) which housed a STAR 37XFP solid boost motor for injection into the final orbit. The OTM was a truncated conical structure, the lower circumference of which provided the interface with the launch vehicle. The OTM was to be ejected when on-orbit to prevent propellant residue contaminating experiments and to reduce moments of inertia.

The orbiting spacecraft had an estimated BOL mass of about 440kg and with the addition of the OTM this increased to about 1400kg at launch. The solar arrays were to provide 700W BOL (400W EOL) and the spacecraft power requirement during the 8 hr. operational phase was 360W.

Structure

An exploded view of the spacecraft structure is shown in fig. A.4. The basic concept was of the thrust-tube-and-platform type, or 'cakestand' arrangement. The spacecraft was broken down into three separate modules for ease of assembly and integration. These were a Payload Module (PM) and Service Module (SM) which make up the orbiting part of the spacecraft, and an Orbit Transfer Module (OTM) which housed the solid boost motor. The assembly sequence of these modules is illustrated in fig. A.5.

The thrust tube provided the stiff backbone to the spacecraft and acted as the primary load path for the launch loads. Its lower part comprised the conical OTM structure, and its upper part within the Service Module was cylindrical. The Payload Module consisted of a box-shaped structure of honeycomb sandwich panels which provided mounting points for equipment on the radiator sidewalls and on the platform which formed its base. A truncated conical structure within the PM formed the support for the ion motor. The PM was bolted to the top of the thrust cylinder.

The SM structure included two radiator panels divided in two by a platform mounted to the cylinder approximately halfway up its length. The platforms of the SM and PM were stiffened by struts (12 in total) which also provided the major load path for the radiator-mounted equipment loads into the cylinder. Struts were adopted in preference to shear webs to improve equipment access and internal radiative heat exchange. A conical structure was fixed inside the thrust cylinder at the same level as the SM platform for the mounting of fuel tanks and reaction wheels. The main body of the spacecraft was closed out by panels at front, rear, top and bottom. The front panel contained a large circular cut-out for the primary antenna and access panels. At launch the rigid solar arrays were folded up against the radiator faces by latches at the level of the PM platform and bottom cover panel.

The spacecraft structure was analysed with the aid of Finite Element models, shown in fig. A.6, developed using the LUSAS FE system. Preliminary sizing and design optimisation of the sandwich components was carried out using the analysis methods described in the main body of this report. For these purposes the ultimate factored quasi-static accelerations given in Table A.1 were used. The high acceleration levels used reflected uncertainties in the loading to be encountered on the Long March launcher. The hightest quasi-static axial load case was at 1st and 2nd stage separation due mainly to dynamic loading associated with the separation shock. The load case corresponding to orbit transfer consisted of an axial thrust acceleration plus centrifugal acceleration due to spin stabilisation.

TABLE A.1 T-SAT PRELIMINARY DESIGN LOADS

FLIGHT EVENT	ACCELERATION (g)	
	LONGITUDINAL	LATERAL
Max. Dynamic Pressure	-10.2	6.0
First Engine Cut Off	-21.3	2.1
$1^{st}/2^{nd}$ Stage Separation	-29.4	1.1
Orbit Transfer (STAR 37XFP)	-28.0	60 rpm

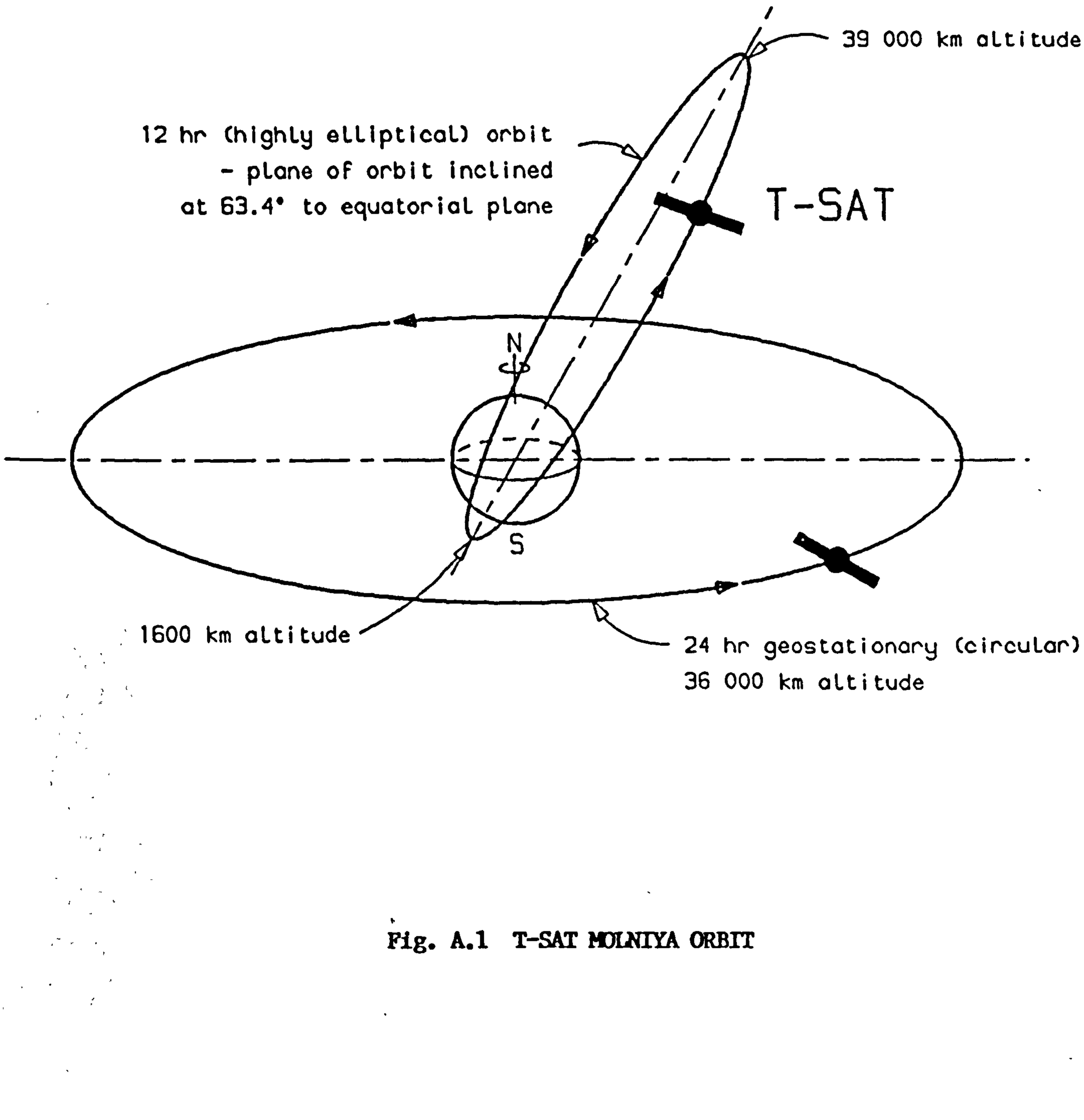

Fig. A.1 T-SAT MOLNIYA ORBIT

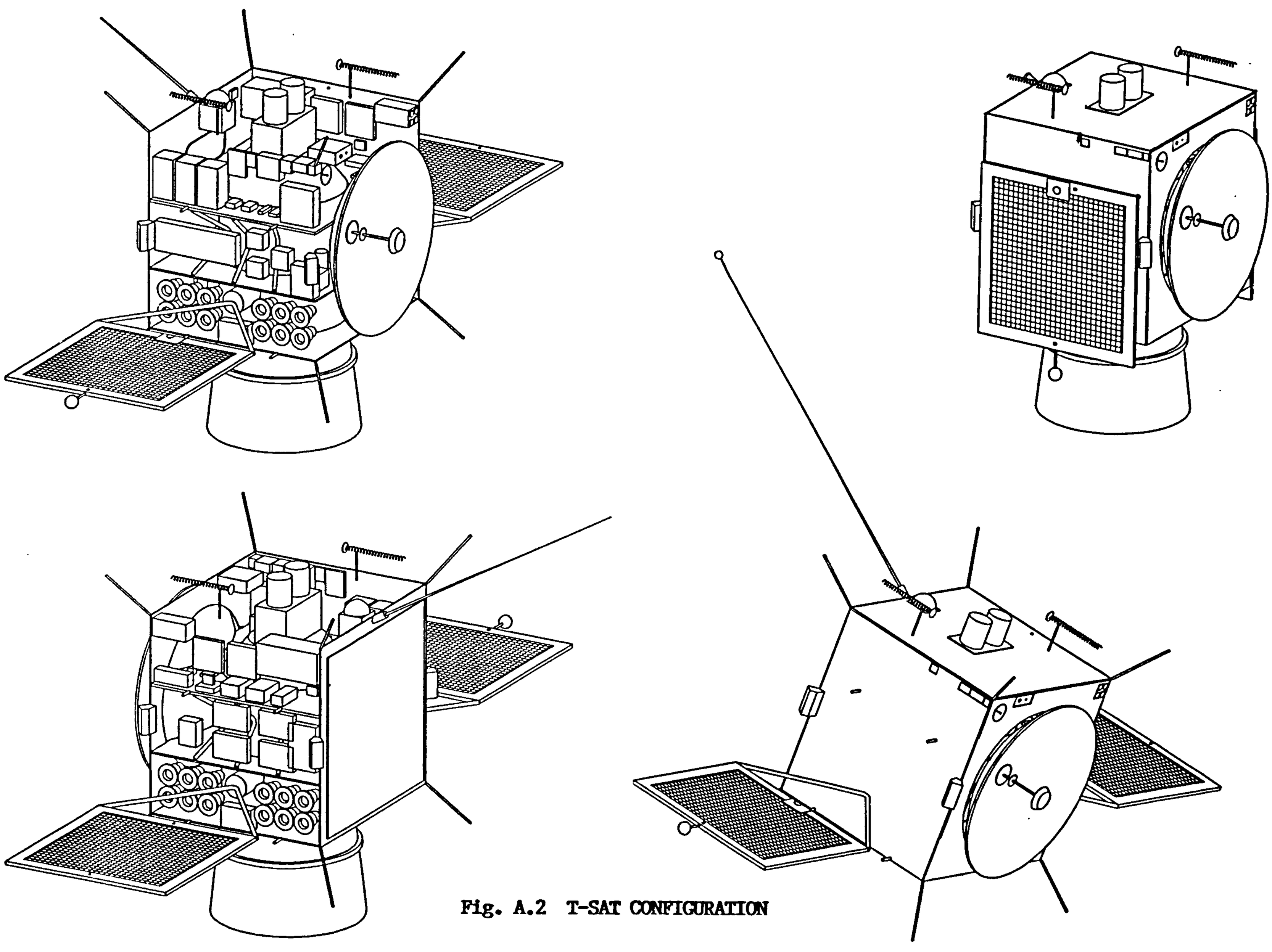

Fig. A.2 T-SAT CONFIGURATION

Fig. A.3 T-SAT - LONG MARCH 2
LAUNCH CONFIGURATION

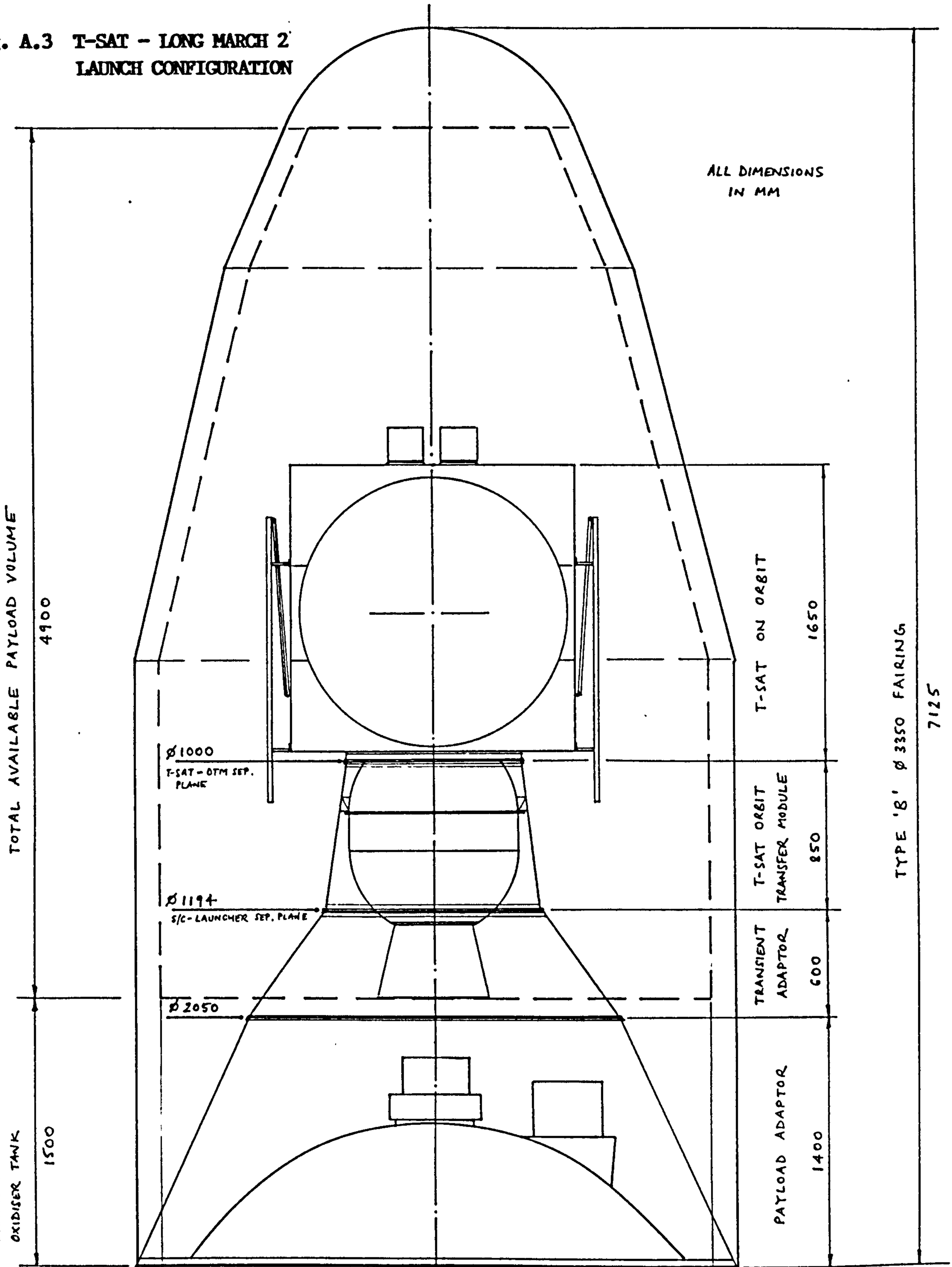

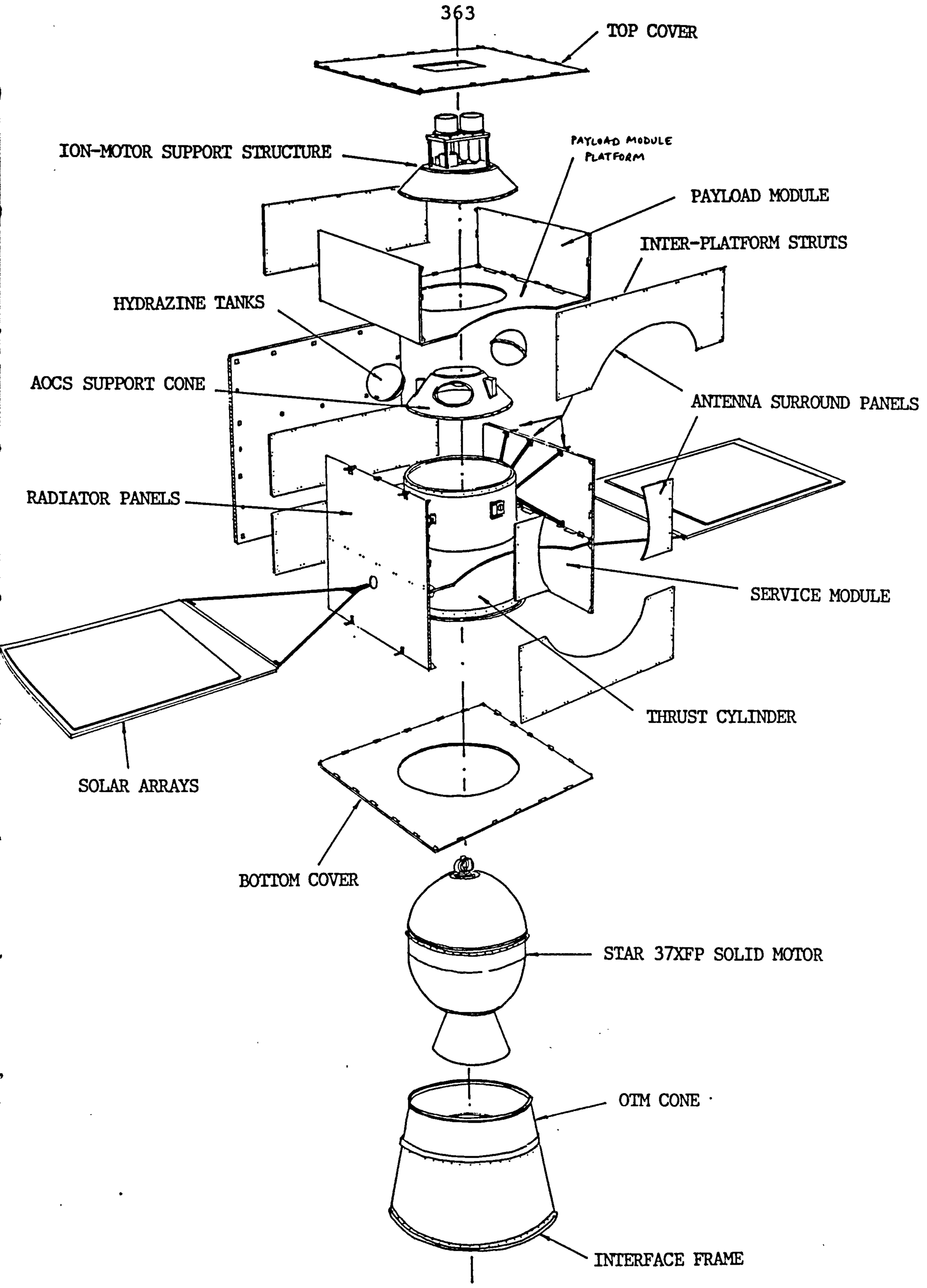

Fig. A.4 T-SAT PRIMARY STRUCTURAL COMPONENTS

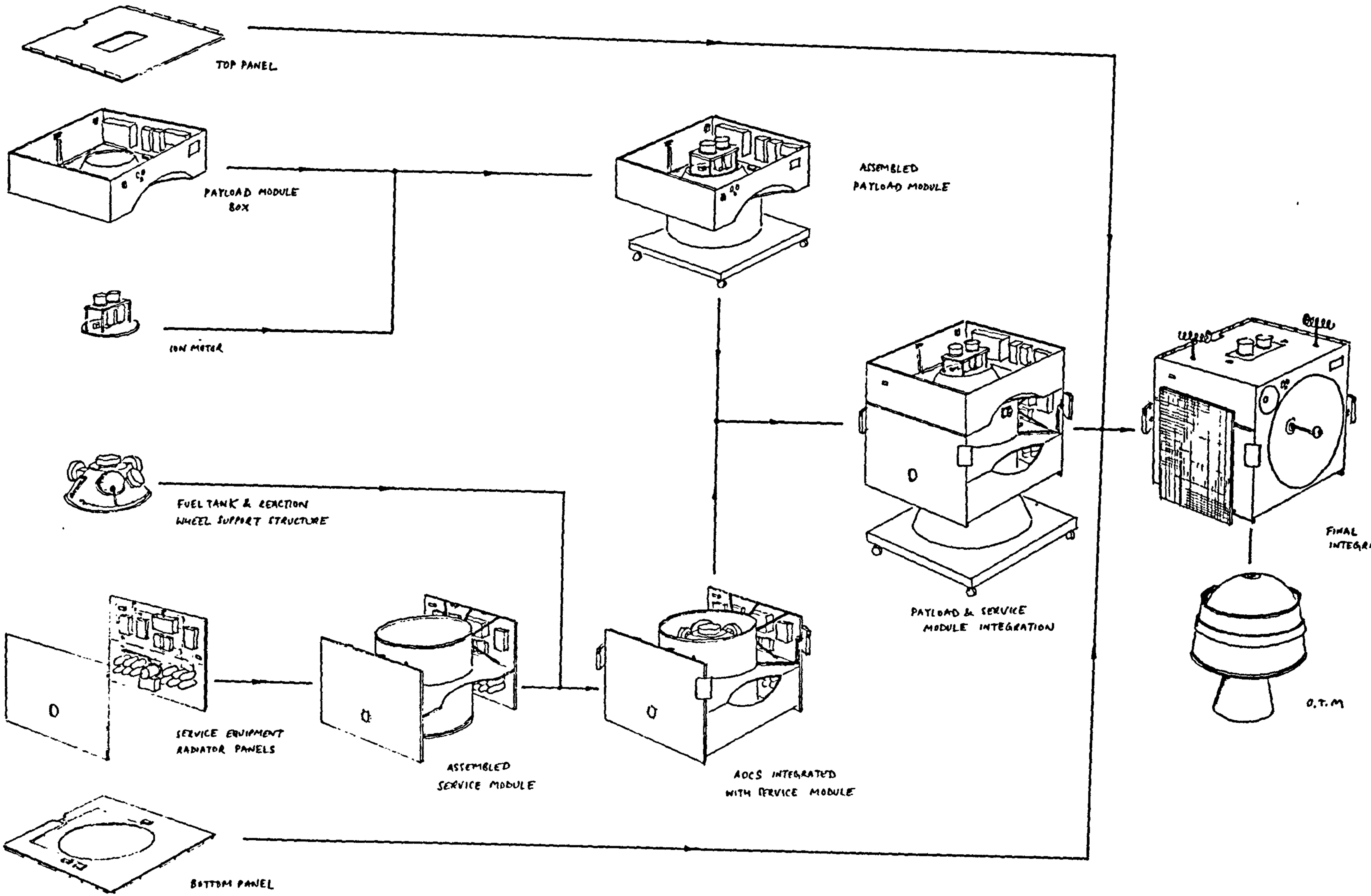

Fig. A.5 ASSEMBLY SEQUENCE

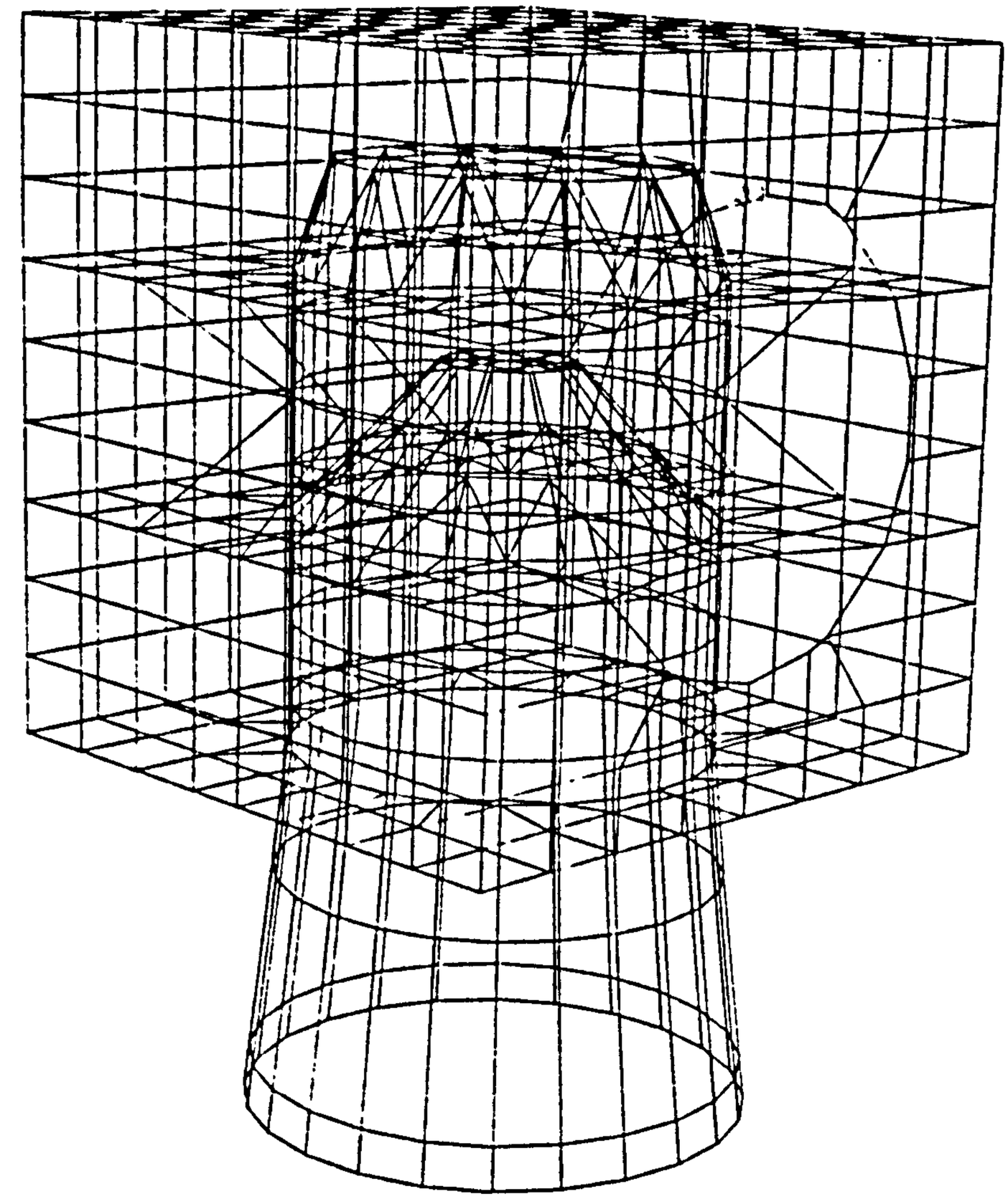

(a) STATIC

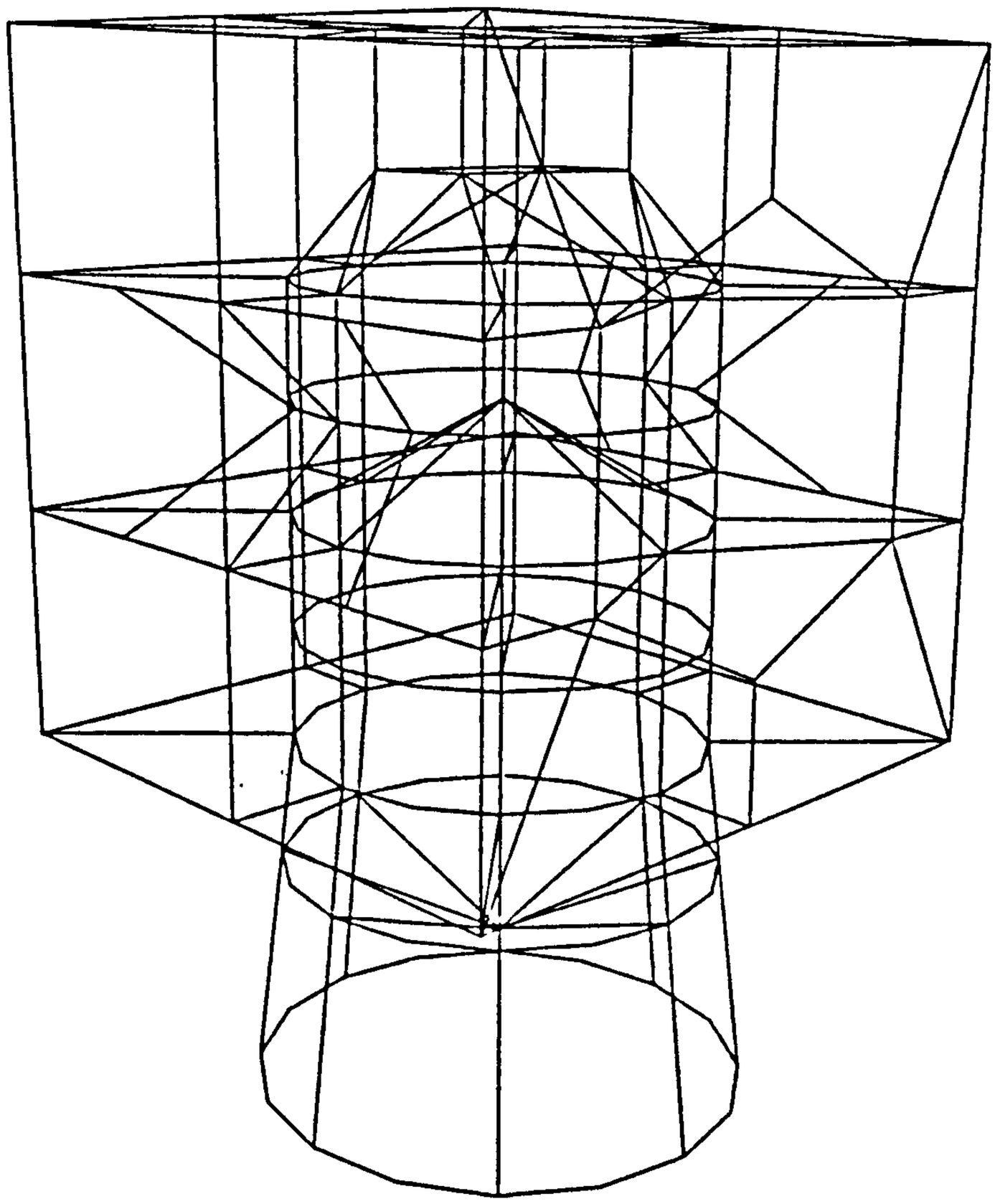

(b) DYNAMIC

Fig. A.6 LUSAS FE MODELS

APPENDIX B : WRINKLING THEORY

Introduction

This appendix develops the small deflection wrinkling theory for composite faced sandwich panels described in Chapter 6. The theory allows for coupled facesheet lay-ups ([B], D_{13}, D_{23} non-zero) and for combinations of applied axial, bending and shear loading actions.

The theory is developed for the general case of cylindrical geometry which reduces to a flat plate for $R \to \infty$. Although the effect of panel curvature is not expected to have a significant effect on wrinkling behaviour (for radii considerably larger than the wrinkle wavelength), curvature is included for completeness to allow overall buckling instability modes to be computed.

Fig. B.1 depicts an element of the panel showing the applied loads and directions of the core stresses and facesheet stress and moment resultants. The sandwich is assumed to have a neutral axis coincident with the mid-plane (ie. equal thickness facesheets), and the facesheets are assumed to be thin compared to the overall sandwich thickness.

Theory

The equilibrium equations for the facesheets loaded by uniform axial ($\bar{N}_x$) and shear ($\bar{N}_{xy}$) stress resultants at the onset of buckling are given by :

$$(a),(b) \quad \frac{\partial N_x}{\partial x} + \frac{\partial N_{xy}}{\partial y} + \bar{N}_{x_{1,2}} \left(\frac{\partial^2 u_f}{\partial x \partial y} - \frac{\partial^2 v_f}{\partial x^2} \right) = (\tau_{xz})_{\pm h/2}$$

$$(c),(d) \quad \frac{\partial N_y}{\partial y} + \frac{\partial N_{xy}}{\partial x} + \bar{N}_{x_{1,2}} \frac{\partial^2 v_f}{\partial x^2} + 2\bar{N}_{xy_{1,2}} \left(\frac{\partial^2 v_f}{\partial x \partial y} - \frac{1}{R} \frac{\partial w_f}{\partial x} \right)$$

$$- \frac{1}{R} \frac{\partial M_y}{\partial y} - \frac{1}{R} \frac{\partial M_{xy}}{\partial x} = (\tau_{yz})_{\pm h/2}$$

(e),(f) $$\frac{\partial^2 M_x}{\partial x^2} + 2\frac{\partial^2 M_{xy}}{\partial x \partial y} + \frac{\partial^2 M_y}{\partial y^2} + 2\bar{N}_{xy_{1,2}}\left(\frac{1}{R}\frac{\partial v_f}{\partial x} + \frac{\partial^2 w_f}{\partial x \partial y}\right)$$

$$+ \bar{N}_{x_{1,2}}\frac{\partial^2 w_f}{\partial x^2} + \frac{1}{R}N_y = \pm(\sigma_z)_{\pm h/2} \qquad \text{(eqs. B.1)}$$

There are three equations for each facesheet. Where terms appear, these refer to the upper and lower facesheets respectively. The applied stress resultants $N_{x_{1,2}}$ and $N_{xy_{1,2}}$ refer to the particular facesheet and need not be equal. In this way bending and twisting loading can be included.

τ_{xz}, τ_{yz} and σ_z are the equilibriating stresses arising at the facesheet-core interface. The assumption of thin facesheets enables the facesheet midplane to be considered coincident with the facesheet-core interface. Subscript f refers to displacements of the facesheets.

The facesheet strain-displacement relations (assuming small displacement theory and no through thickness strains) are :

$$\epsilon_x = \frac{\partial u_f}{\partial x} \qquad \epsilon_y = \frac{\partial v_f}{\partial y} - \frac{w_f}{R} \qquad \gamma_{xy} = \frac{\partial u_f}{\partial y} + \frac{\partial v_f}{\partial x} \qquad \text{(eqs. B.2)}$$

$$k_x = -\frac{\partial^2 w_f}{\partial x^2} \qquad k_y = -\frac{1}{R}\frac{\partial v_f}{\partial y} - \frac{\partial^2 w_f}{\partial y^2} \qquad k_{xy} = -\frac{1}{R}\frac{\partial v_f}{\partial x} - 2\frac{\partial^2 w_f}{\partial x \partial y}$$

The stress-strain relationship for the facesheets are given by the laminate constitutive matrix :

$$\begin{Bmatrix} N_x \\ N_y \\ N_{xy} \\ M_x \\ M_y \\ M_{xy} \end{Bmatrix} = \left[\begin{array}{ccc|ccc} A_{11} & A_{12} & 0 & B_{11} & B_{12} & B_{13} \\ & A_{22} & 0 & & B_{22} & B_{23} \\ \text{SYM} & & A_{33} & \text{SYM} & & B_{33} \\ \hline B_{11} & B_{12} & B_{13} & D_{11} & D_{12} & D_{13} \\ & B_{22} & B_{23} & & D_{22} & D_{23} \\ \text{SYM} & & B_{33} & \text{SYM} & & D_{33} \end{array}\right] \begin{Bmatrix} \epsilon_x \\ \epsilon_y \\ \gamma_{xy} \\ k_x \\ k_y \\ k_{xy} \end{Bmatrix} \qquad \text{(eq. B.3)}$$

where the matrix coefficients apply to the individual facesheets. These can be coupled, ie. [B], D_{13}, D_{23} not necessarily zero, but it is assumed that membrane shear coupling (A_{13} and A_{23} terms) is zero, as is the case for most practical lay-ups.

Equations (B.2) and (B.3) can be substituted into the equilibrium equations (B.1) :

(a),(b)
$$A_{11}\frac{\partial^2 u_f}{\partial x^2} + A_{33}\frac{\partial^2 u_f}{\partial y^2} - B_{13}\frac{1}{R}\frac{\partial^2 v_f}{\partial x^2} + \left(A_{12}+A_{33}-\frac{1}{R}\left(B_{12}+B_{33}\right)\right)\frac{\partial^2 v_f}{\partial x \partial y}$$
$$- B_{23}\frac{1}{R}\frac{\partial^2 v_f}{\partial y^2} - B_{11}\frac{\partial^3 w_f}{\partial x^3} - 3B_{13}\frac{\partial^2 w_f}{\partial x^2 \partial y} - \left(B_{12}+2B_{33}\right)\frac{\partial^3 w_f}{\partial x \partial y^2}$$
$$- B_{23}\frac{\partial^3 w_f}{\partial y^3} - A_{12}\frac{1}{R}\frac{\partial w_f}{\partial x} + \bar{N}_{xy_{1,2}}\left(\frac{\partial^2 u_f}{\partial x \partial y} - \frac{\partial^2 v_f}{\partial x^2}\right) = \pm \tau_{xz}$$

(c),(d)
$$- B_{13}\frac{1}{R}\frac{\partial^2 u_f}{\partial x^2} + \left(A_{12}+A_{33}-\frac{1}{R}\left(B_{12}+B_{33}\right)\right)\frac{\partial^2 u_f}{\partial x \partial y} - B_{23}\frac{1}{R}\frac{\partial^2 u_f}{\partial y^2}$$
$$+\left(A_{33}-\frac{2}{R}B_{33}+\frac{1}{R^2}D_{33}\right)\frac{\partial^2 v_f}{\partial x^2} + \left(-\frac{1}{R}B_{23}+\frac{2}{R^2}D_{23}\right)\frac{\partial^2 v_f}{\partial x \partial y}$$
$$+\left(A_{22}-\frac{2}{R}B_{22}+\frac{1}{R^2}D_{22}\right)\frac{\partial^2 v_f}{\partial y^2} - \left(B_{13}-\frac{1}{R}D_{13}\right)\frac{\partial^3 w_f}{\partial x^3}$$
$$+\left(-\left(B_{12}+2B_{33}\right)+\frac{1}{R}\left(D_{12}+2D_{33}\right)\right)\frac{\partial^3 w_f}{\partial x^2 \partial y} + 3\left(-B_{23}+\frac{1}{R}D_{23}\right)\frac{\partial^3 w_f}{\partial x \partial y^2}$$
$$+\left(-B_{22}+\frac{1}{R}D_{22}\right)\frac{\partial^3 w_f}{\partial y^3} + B_{23}\frac{1}{R^2}\frac{\partial w_f}{\partial x} + \left(-\frac{1}{R}A_{22}+\frac{1}{R^2}B_{22}\right)\frac{\partial w_f}{\partial y}$$
$$+ \bar{N}_{x_{1,2}}\frac{\partial^2 v_f}{\partial x^2} + 2\bar{N}_{xy_{1,2}}\left(\frac{\partial^2 v_f}{\partial x \partial y} - \frac{1}{R}\frac{\partial w_f}{\partial x}\right) = \pm \tau_{yz}$$

(e), (f)
$$B_{11}\frac{\partial^3 u_f}{\partial x^3} + 3B_{13}\frac{\partial^3 u_f}{\partial x^2 \partial y} + (B_{12}+2B_{33})\frac{\partial^3 u_f}{\partial x \partial y^2} + B_{23}\frac{\partial^3 u_f}{\partial y^3} + A_{12}\frac{1}{R}\frac{\partial u_f}{\partial x}$$

$$+\left(B_{13}-\frac{1}{R}D_{13}\right)\frac{\partial^3 v_f}{\partial x^3} + \left((B_{12}+2B_{33})-\frac{1}{R}(D_{12}+2D_{33})\right)\frac{\partial^3 v_f}{\partial x^2 \partial y}$$

$$+3\left(B_{23}-\frac{1}{R}D_{23}\right)\frac{\partial^3 v_f}{\partial x \partial y^2} + \left(B_{22}-\frac{1}{R}D_{22}\right)\frac{\partial^3 v_f}{\partial y^3} - B_{23}\frac{1}{R^2}\frac{\partial v_f}{\partial x}$$

$$+\left(\frac{1}{R}A_{22}-\frac{1}{R^2}B_{22}\right)\frac{\partial v_f}{\partial y} - D_{11}\frac{\partial^4 w_f}{\partial x^4} - 4D_{13}\frac{\partial^4 w_f}{\partial x^3 \partial y} - 2(D_{12}+2D_{33})\frac{\partial^4 w_f}{\partial x^2 \partial y^2}$$

$$-4D_{23}\frac{\partial^4 w_f}{\partial x \partial y^3} - D_{22}\frac{\partial^4 w_f}{\partial y^4} - 2B_{12}\frac{1}{R}\frac{\partial^2 w_f}{\partial x^2} - 4B_{23}\frac{1}{R}\frac{\partial^2 w_f}{\partial x \partial y} - 2B_{22}\frac{1}{R}\frac{\partial^2 w_f}{\partial y^2}$$

$$-\frac{A_{22}}{R^2}w_f + \bar{N}_{x_{1,2}}\frac{\partial^2 w_f}{\partial x^2} + 2\bar{N}_{xY_{1,2}}\left(\frac{1}{R}\frac{\partial v_f}{\partial x}+\frac{\partial^2 w_f}{\partial x \partial y}\right) = \pm(\sigma_z)_{\pm h/2}$$

(eqs. B.4)

The equilibrium equations for the core are given by :

$$\frac{\partial \tau_{xz}}{\partial z} = 0 \qquad \frac{\partial \tau_{yz}}{\partial z} = 0 \qquad \frac{\partial \tau_{xz}}{\partial x} + \frac{\partial \tau_{yz}}{\partial y} + \frac{\partial \sigma_z}{\partial z} = 0 \qquad \text{(eqs. B.5)}$$

in which it is assumed the core takes only direct and shear through-thickness stresses.

The core strain-displacement relations are :

$$\epsilon_z = \frac{\partial w}{\partial z} \qquad \gamma_{xz} = \frac{\partial u}{\partial z} + \frac{\partial w}{\partial x} \qquad \gamma_{yz} = \frac{\partial v}{\partial z} + \frac{\partial w}{\partial y} + \frac{v}{R} \qquad \text{(eqs. B.6)}$$

where u,v and w refer to the core displacements which are z-dependent.

The core stress-strain relationships are given by :

$$\sigma_z = E_c \epsilon_z$$

$$\tau_{xz} = G_{xz}\gamma_{xz} \qquad \text{(eqs. B.7)}$$

$$\tau_{yz} = G_{yz}\gamma_{yz}$$

It is possible to obtain expressions for the core displacements as fucntions of z-wise position in the following manner. Firstly by integration of equation (B.5c) :

$$\sigma_z(z) = \int_0^z -\left(\frac{\partial \tau_{xz}}{\partial x} + \frac{\partial \tau_{yz}}{\partial y}\right) dz$$

$$\sigma_z(z) = -z\left(\frac{\partial \tau_{xz}}{\partial x} + \frac{\partial \tau_{yz}}{\partial y}\right) + \sigma_{z_0} \qquad \text{(eq. B.8)}$$

and substituting the core stresses for strains using equations (B.7) :

$$\epsilon_z(z) = -\frac{z}{E_c}\left(G_{xz}\frac{\partial \gamma_{xz}}{\partial x} + G_{yz}\frac{\partial \gamma_{yz}}{\partial y}\right) + \epsilon_{z_0}$$

Then by integration of equations (B.6):

$$w(z) = \int_0^z \epsilon_z \, dz$$

$$w(z) = -\frac{z^2}{2E_c}\chi + z\epsilon_{z_0} + w_0 \qquad \text{(eq. B.9a)}$$

where,

$$\chi = G_{xz}\frac{\partial \gamma_{xz}}{\partial x} + G_{yz}\frac{\partial \gamma_{yz}}{\partial y}$$

$$u(z) = \int_0^z \left(\gamma_{xz} - \frac{\partial w}{\partial x}\right) dz$$

$$u(z) = \frac{z^3}{6E_c}\frac{\partial \chi}{\partial x} - \frac{z^2}{2}\frac{\partial \epsilon_{z_0}}{\partial x} + z\left(\gamma_{xz} - \frac{\partial w_0}{\partial x}\right) + u_0 \qquad \text{(eq. B.9b)}$$

$$v(z) = \int_0^z \left(\gamma_{yz} - \frac{\partial w}{\partial y} - \frac{v}{R}\right) dz$$

$$v(z) = \frac{z^3}{6E_c}\frac{\partial \chi}{\partial y} - \frac{z^2}{2}\frac{\partial \epsilon_{z_0}}{\partial y} + z\left(\gamma_{yz} - \frac{\partial w_0}{\partial y} - \frac{v}{R}\right) + v_0$$

$$v(z) = \frac{\frac{z^3}{6E_c}\frac{\partial \chi}{\partial y} - \frac{z^2}{2}\frac{\partial \epsilon_{z_0}}{\partial y} + z\left(\gamma_{yz} - \frac{\partial w_0}{\partial y}\right) + v_0}{(1 + z/R)}$$

For a large radius compared to the sandwich thickness, z/R→0, and :

$$v(z) = \frac{z^3}{6E_c}\frac{\partial \chi}{\partial y} - \frac{z^2}{2}\frac{\partial \epsilon_{z_0}}{\partial y} + z\left(\gamma_{yz} - \frac{\partial w_0}{\partial y}\right) + v_0 \qquad \text{(eq. B.9c)}$$

subscript 0 refers to the displacements/strain at the core mid-plane.

The facesheet displacements can therefore be given by substituting $z = \pm h/2$ into equations (B.9), where terms refer to the upper and lower facesheets respectively :

$$u_f = \frac{\pm h^3}{48E_c}\frac{\partial \chi}{\partial x} - \frac{h^2}{8}\frac{\partial \epsilon_{z_0}}{\partial x} \pm \frac{h}{2}\left(\gamma_{xz} - \frac{\partial w_0}{\partial x}\right) + u_0$$

$$v_f = \frac{\pm h^3}{48E_c}\frac{\partial \chi}{\partial y} - \frac{h^2}{8}\frac{\partial \epsilon_{z_0}}{\partial y} \pm \frac{h}{2}\left(\gamma_{yz} - \frac{\partial w_0}{\partial y}\right) + v_0 \qquad \text{(eqs. B.10)}$$

$$w_f = -\frac{h^2}{8E_c}\chi \pm \frac{h}{2}\epsilon_{z_0} + w_0$$

The facesheet displacements u_f, v_f and w_f appearing in the 6 facesheet equilibrium equations (B.4) are now therefore expressed in terms of 6 independent variables : u_0, v_0, w_0 , γ_{xz}, γ_{yz} and ϵ_{z_0} .

Solution of the facesheet equilibrium equations (B.4) requires admissable shape functions to be assumed for the 6 independent variables. In order to retain the facesheet coupling effects and applied shear loading it is necessary to assume skew-simusoidal shape functions as follows :

$$u_0 = U_0 \cos\left(\frac{m\pi x}{a} - \frac{n\pi y}{b}\right)$$

$$v_0 = V_0 \cos\left(\frac{m\pi x}{a} - \frac{n\pi y}{b}\right)$$

$$w_0 = W_0 \sin\left(\frac{m\pi x}{a} - \frac{n\pi y}{b}\right) \qquad \text{(eqs. B.11)}$$

$$\gamma_{xz} = \bar{\gamma}_{xz} \cos\left(\frac{m\pi x}{a} - \frac{n\pi y}{b}\right)$$

$$\gamma_{yz} = \bar{\gamma}_{yz} \cos\left(\frac{m\pi x}{a} - \frac{n\pi y}{b}\right)$$

$$\epsilon_{z_0} = \bar{\epsilon}_{z_0} \sin\left(\frac{m\pi x}{a} - \frac{n\pi y}{b}\right)$$

where, a & b are the panel length and width, and m & n refer to the number of half wave buckles along the length and across the width respectively. For cylindrical geometry, the term $n\pi y/b$ can be replaced by $n\theta$, where n is then the number of complete circumferential waves and θ the angular position.

These shape functions can alternatively be expressed in the form :

$$w_0 = W_0 \sin \frac{m\pi}{a}(x - \phi y) \qquad \text{(eq. B.12)}$$

where the sinusoidal buckles are skewed at an angle ϕ, see fig. B.2, and have a half-wavelength given by :

$$l^* = \frac{a}{m} \cos\phi \qquad \text{(eq. B.13)}$$

Although the use of these functions satisfies the facesheet equilibrium equations, in general boundary conditions (simply supported or fixed) will be violated. This limits the applicability of the method for the analysis of general instability, where the critical wavelengths are of the order of the panel/cylinder dimensions, to special cases where the boundary conditions are satisfied. For example, general buckling of a symmetric sandwich panel or cylinder under axial loading would satisfy the boundary conditions, whereas general buckling under shear or torsion would not.

However, for the analysis of wrinkling behaviour, where the critical buckle wavelengths are small compared to the overal dimensions, it is reasonable to apply these shape functions to all cases. This is because the distortion of the true edge conditions by the assumed buckling pattern has only a very small effect on the overall panel behaviour.

The shape functions, equations (B.11), can be substituted into the expressions for the facesheet displacements (B.10), and differentiated. By substituting the displacement derivatives obtained into the equilibrium equations (B.4), results in the following :

(using :- $\alpha = \frac{m\pi}{a}$, $\beta = \frac{n\pi}{b}$ (or, $\frac{n}{R}$ for cylinder)

$$Q_1 = \frac{G_{xz}}{E_c} \qquad Q_2 = \frac{G_{yz}}{E_c}$$

$$
\begin{aligned}
(a),(b)\ \Big\{ & \Big[-(A_{11}\alpha^2 + A_{33}\beta^2) + \bar{N}_{xY_{1,2}}\alpha\beta \Big] U_o + \Big[(A_{12}+A_{33})\alpha\beta \\
& + \frac{1}{R}\left(B_{13}\alpha^2 + B_{23}\beta^2 - (B_{12}+B_{33})\alpha\beta \right) + \bar{N}_{xY_{1,2}}\alpha^2 \Big] V_o \\
& + \Big[-\frac{A_{12}}{R}\alpha + \left(A_{11}\alpha^3 + (A_{12}+2A_{33})\alpha\beta^2 \right)\left(\pm\frac{h}{2}\right) + \left(B_{11}\alpha^3 - 3B_{13}\alpha^2\beta \right. \\
& + (B_{12}+2B_{33})\alpha\beta^2 - B_{23}\beta^3 \Big)\left(\pm\frac{h}{2}\right) + \frac{1}{R}\left(B_{13}\alpha^2\beta - (B_{12}+B_{33})\alpha\beta^2 + B_{23}\beta^3 \right)\left(\pm\frac{h}{2}\right) \\
& \Big] W_o + \Big[Q_1\left(A_{11}\alpha^4 + (A_{12}+2A_{33})\alpha^2\beta^2 \right)\left(\pm\frac{h^3}{48}\right) - \frac{A_{12}}{R} Q_1 \alpha^2 \left(\frac{h^2}{8}\right) \\
& - \left(A_{11}\alpha^2 + A_{33}\beta^2 \right)\left(\pm\frac{h}{2}\right) + \frac{Q_1}{R}\left(-(B_{12}+B_{33})\alpha^2\beta^2 + B_{23}\alpha\beta^3 \right. \\
& \left. + B_{13}\alpha^3\beta \right)\left(\pm\frac{h^3}{48}\right) + Q_1\left(B_{11}\alpha^4 - 3B_{13}\alpha^3\beta + (B_{12}+2B_{33})\alpha^2\beta^2 \right. \\
& \left. - B_{23}\alpha\beta^3 \right)\left(\frac{h^2}{8}\right) \mp G_{xz} + \bar{N}_{xY_{1,2}}\alpha\beta\left(\pm\frac{h}{2}\right) \Big] \bar{Y}_{xz} \\
& + \Big[Q_2\left(-A_{11}\alpha^3\beta - (A_{12}+2A_{33})\alpha\beta^3 \right)\left(\pm\frac{h^3}{48}\right) + \frac{A_{12}}{R} Q_2 \alpha\beta\left(\frac{h^2}{8}\right) \\
& + \left(A_{12}\alpha\beta + A_{33}\alpha\beta \right)\left(\pm\frac{h}{2}\right) + \frac{Q_2}{R}\left(-B_{13}\alpha^2\beta^2 + (B_{12}+B_{33})\alpha\beta^3 \right. \\
& \left. - B_{23}\beta^4 \right)\left(\pm\frac{h^3}{48}\right) - Q_2\left(B_{11}\alpha^3\beta - 3B_{13}\alpha^2\beta^2 + (B_{12}+2B_{33})\alpha\beta^3 \right. \\
& \left. - B_{23}\beta^4 \right)\left(\frac{h^2}{8}\right) + \frac{1}{R}\left(B_{13}\alpha^2 - (B_{12}+B_{33})\alpha\beta + B_{23}\beta^2 \right)\left(\pm\frac{h}{2}\right) \\
& + \bar{N}_{xY_{1,2}}\alpha^2\left(\pm\frac{h}{2}\right) \Big] \bar{Y}_{yz} + \Big[\left(A_{11}\alpha^3 + (A_{12}+2A_{33})\alpha\beta^2 \right)\left(\frac{h^2}{8}\right) \\
& + \frac{1}{R}\left(B_{13}\alpha^2\beta - (B_{12}+B_{33})\alpha\beta^2 + B_{23}\beta^3 \right)\left(\frac{h^2}{8}\right) - \frac{A_{12}}{R}\alpha\left(\pm\frac{h}{2}\right)
\end{aligned}
$$

$$+ \left(B_{11}\alpha^3 - 3\alpha^2\beta B_{13} + (B_{12}+2B_{33})\alpha\beta^2 - B_{23}\beta^3 \right)\left(\pm\frac{h}{2}\right)\Big]\,\bar{\epsilon}_{7_0}\Big\}$$

$$\times \cos(\alpha x - \beta y) \;=\; 0$$

(c), (d)
$$\Big\{\Big[(A_{12}+A_{33})\alpha\beta + \frac{1}{R}\left(B_{13}\alpha^2 - (B_{12}+B_{33})\alpha\beta + B_{23}\beta^2\right)\Big]u_0$$

$$+\Big[-(A_{22}\beta^2 + A_{33}\alpha^2) - \frac{1}{R}\left(D_{33}\alpha^2 - 2D_{23}\alpha\beta + D_{22}\beta^2\right) + 2\bar{N}_{xy_{1,2}}\alpha\beta$$

$$- \bar{N}_{x_{1,2}}\alpha^2 + \frac{1}{R}\left(2B_{33}\alpha^2 - 4B_{23}\alpha\beta + 2B_{22}\beta^2\right)\Big]V_0 + \Big[\frac{A_{22}\beta}{R}$$

$$+ \frac{1}{R^2}\left(-B_{22}\beta + B_{23}\alpha\right) + \left(B_{13}\alpha^3 - (B_{12}+2B_{33})\alpha^2\beta + 3B_{23}\alpha\beta^2 - B_{22}\beta^3\right)$$

$$- \frac{1}{R}\left(D_{13}\alpha^3 - (D_{12}+2D_{33})\alpha^2\beta + 3D_{23}\alpha\beta^2 - D_{22}\beta^3\right)$$

$$- \left(A_{22}\beta^3 + (A_{12}+2A_{33})\alpha^2\beta\right)\left(\pm\frac{h}{2}\right) - \frac{1}{R}\left(B_{13}\alpha^3 - (B_{12}+3B_{33})\alpha^2\beta\right.$$

$$\left. + 5B_{23}\alpha\beta^2 - 2B_{22}\beta^3\right)\left(\pm\frac{h}{2}\right) - \frac{1}{R^2}\left(D_{22}\beta^3 - 2D_{23}\alpha\beta^2 + D_{33}\alpha^2\beta\right.$$

$$\left. - 2D_{23}\alpha\beta^2\right)\left(\pm\frac{h}{2}\right) + 2\bar{N}_{xy_{1,2}}\alpha\beta^2\left(\pm\frac{h}{2}\right) - \bar{N}_{x_{1,2}}\alpha^2\beta\left(\pm\frac{h}{2}\right) - 2\frac{\bar{N}}{R}_{xy_{1,2}}\alpha\Big]W_0$$

$$+\Big[-Q_1\left((A_{12}+2A_{33})\alpha^3\beta + A_{22}\alpha\beta^3\right)\left(\pm\frac{h^3}{48}\right) + Q_1\frac{A_{22}}{R}\alpha\beta\left(\frac{h^2}{8}\right)$$

$$+ (A_{12}+A_{33})\alpha\beta\left(\pm\frac{h}{2}\right) - \frac{Q_1}{R}\left(B_{13}\alpha^4 - (B_{12}+3B_{33})\alpha^3\beta + 5B_{23}\alpha^2\beta^2\right.$$

$$\left. - 2B_{22}\alpha\beta^3\right)\left(\pm\frac{h^3}{48}\right) + \frac{Q_1}{R^2}\left(-B_{22}\alpha\beta + B_{23}\alpha^2\right)\left(\frac{h^2}{8}\right)$$

$$- Q_1\left(-B_{13}\alpha^4 + (B_{12}+2B_{33})\alpha^3\beta - 3B_{23}\alpha^2\beta^2 + B_{22}\alpha\beta^3\right)\left(\frac{h^2}{8}\right)$$

$$+\frac{1}{R}\left(B_{13}\alpha^2-(B_{12}+B_{33})\alpha\beta+B_{23}\beta^2\right)\left(\pm\frac{h}{2}\right)-\frac{Q_1}{R^2}\left(D_{33}\alpha^3\beta-2D_{23}\alpha^2\beta^2\right.$$

$$\left.+D_{22}\alpha\beta^3\right)\left(\pm\frac{h^3}{48}\right)-\frac{Q_1}{R}\left(D_{13}\alpha^4-(D_{12}+2D_{33})\alpha^3\beta+3D_{23}\alpha^2\beta^2\right.$$

$$\left.-D_{22}\alpha\beta^3\right)\left(\frac{h^2}{8}\right)+2\bar{N}_{xY_{1,2}}Q_1\alpha^2\beta^2\left(\pm\frac{h^3}{48}\right)-\frac{2\bar{N}_{xY_{1,2}}Q_1\alpha^2}{R}\left(\frac{h^2}{8}\right)$$

$$-\bar{N}_{x_{1,2}}Q_1\alpha^3\beta\left(\pm\frac{h^3}{48}\right)\Big]\bar{Y}_{xz}+\Big[Q_2\left((A_{12}+2A_{33})\alpha^2\beta^2\right.$$

$$\left.+A_{22}\beta^4\right)\left(\pm\frac{h^3}{48}\right)-Q_2\frac{A_{22}}{R}\beta^2\left(\frac{h^2}{8}\right)+\frac{Q_2}{R}\left(B_{13}\alpha^3\beta-(B_{12}+3B_{33})\alpha^2\beta^2\right.$$

$$\left.+5B_{23}\alpha\beta^3-2B_{22}\beta^4\right)\left(\pm\frac{h^3}{48}\right)+\frac{Q_2}{R^2}\left(-B_{23}\alpha\beta+B_{22}\beta^2\right)\left(\frac{h^2}{8}\right)$$

$$+Q_2\left(-B_{13}\alpha^3\beta+(B_{12}+2B_{33})\alpha^2\beta^2-3B_{23}\alpha\beta^3+B_{22}\beta^4\right)\left(\frac{h^2}{8}\right)$$

$$-\left(A_{33}\alpha^2+A_{22}\beta^2\right)\left(\pm\frac{h}{2}\right)+\frac{Q_2}{R^2}\left(D_{33}\alpha^2\beta^2-2D_{23}\alpha\beta^3+D_{22}\beta^4\right)\left(\pm\frac{h^3}{48}\right)$$

$$+\frac{Q_2}{R}\left(D_{13}\alpha^3\beta-(D_{12}+2D_{33})\alpha^2\beta^2+3D_{23}\alpha\beta^3-D_{22}\beta^4\right)\left(\frac{h^2}{8}\right)$$

$$-\frac{1}{R^2}\left(D_{33}\alpha^2-2D_{23}\alpha\beta+D_{22}\beta^2\right)\left(\pm\frac{h}{2}\right)+\bar{N}_{x_{1,2}}\left(Q_2\alpha^2\beta^2\left(\pm\frac{h^3}{48}\right)\right.$$

$$\left.-\alpha^2\left(\pm\frac{h}{2}\right)\right)+2\bar{N}_{xY_{1,2}}\left(-Q_2\alpha\beta^3\left(\pm\frac{h^3}{48}\right)+\frac{Q_2}{R}\alpha\beta\left(\frac{h^2}{8}\right)+\alpha\beta\left(\pm\frac{h}{2}\right)\right)$$

$$\pm G_{Yz}\Big]\bar{Y}_{Yz}+\Big[\left(-A_{22}\beta^3-(A_{12}+2A_{33})\alpha^2\beta\right)\left(\frac{h^2}{8}\right)+\frac{A_{22}}{R}\beta\left(\pm\frac{h}{2}\right)$$

$$-\frac{1}{R}\left(B_{13}\alpha^3-(B_{12}+3B_{33})\alpha^2\beta+5B_{23}\alpha\beta^2-2B_{22}\beta^3\right)\left(\frac{h^2}{8}\right)$$

$$+\frac{1}{R^2}\left(-B_{22}\beta+B_{23}\alpha\right)\left(\pm\frac{h}{2}\right)+\left(-B_{13}\alpha^3-(B_{12}+2B_{33})\alpha^2\beta+3B_{23}\alpha\beta^2\right.$$

$$- B_{22}\beta^3\Big)\Big(\pm\frac{h}{2}\Big) - \frac{1}{R^2}\Big(D_{33}\alpha^2\beta - 2D_{23}\alpha\beta^2 + D_{22}\beta^3\Big)\Big(\frac{h^2}{8}\Big)$$

$$- \frac{1}{R}\Big(D_{13}\alpha^3 - (D_{12}+2D_{33})\alpha^2\beta + 3D_{23}\alpha\beta^2 - D_{22}\beta^3\Big)\Big(\pm\frac{h}{2}\Big)$$

$$+ 2\bar{N}_{xy_{1,2}}\alpha\beta^2\Big(\frac{h^2}{8}\Big) - 2\frac{\bar{N}_{xy_{1,2}}}{R}\alpha\Big(\pm\frac{h}{2}\Big) - \bar{N}_{x_{1,2}}\beta\alpha^2\Big(\frac{h^2}{8}\Big)\Big]\bar{\epsilon}_{z_0}\Big\}$$

$$\times \cos(\alpha x - \beta y) = 0$$

(e), (f) $$\Big\{\Big[B_{11}\alpha^3 - 3B_{13}\alpha^2\beta + (B_{12}+2B_{33})\alpha\beta^2 - B_{23}\beta^3 - \frac{A_{12}}{R}\alpha\Big]U_0$$

$$+\Big[\frac{A_{22}}{R}\beta + \Big(B_{13}\alpha^3 - (B_{12}+2B_{33})\alpha^2\beta + 3B_{23}\alpha\beta^2 - B_{22}\beta^3\Big)$$

$$+ \frac{1}{R^2}(B_{23}\alpha - B_{22}\beta) - \frac{1}{R}\Big(D_{13}\alpha^3 - (D_{12}+2D_{33})\alpha^2\beta + 3D_{23}\alpha\beta^2$$

$$- D_{22}\beta^3\Big) - 2\frac{\bar{N}_{xy_{1,2}}}{R}\alpha\Big]V_0 + \Big[-\frac{A_{22}}{R^2} + \frac{1}{R}(A_{12}\alpha^2 + A_{22}\beta^2)\Big(\pm\frac{h}{2}\Big)$$

$$+\Big(-B_{11}\alpha^4 + 4B_{13}\alpha^3\beta - 2(B_{12}+2B_{33})\alpha^2\beta^2 + 4B_{23}\alpha\beta^3 - B_{22}\beta^4\Big)\Big(\pm\frac{h}{2}\Big)$$

$$+ \frac{1}{R^2}\Big(B_{23}\alpha\beta - B_{22}\beta^2\Big)\Big(\pm\frac{h}{2}\Big) + \frac{1}{R}\Big(2B_{12}\alpha^2 - 4B_{23}\alpha\beta + 2B_{22}\beta^2\Big)$$

$$+ \frac{1}{R}\Big(-D_{13}\alpha^3\beta + (D_{12}+2D_{33})\alpha^2\beta^2 - 3D_{23}\alpha\beta^3 + D_{22}\beta^4\Big)\Big(\pm\frac{h}{2}\Big)$$

$$- \Big(D_{11}\alpha^4 - 4D_{13}\alpha^3\beta + 2(D_{12}+2D_{33})\alpha^2\beta^2 - 4D_{23}\alpha\beta^3 + D_{22}\beta^4\Big)$$

$$- 2\frac{\bar{N}_{xy_{1,2}}}{R}\alpha\beta\Big(\pm\frac{h}{2}\Big) + 2\bar{N}_{xy_{1,2}}\alpha\beta - \bar{N}_{x_{1,2}}\alpha^2\Big]W_0$$

$$+\Big[\frac{Q_1}{R}(A_{12}\alpha^3 + A_{22}\alpha\beta^2)\Big(\pm\frac{h^3}{48}\Big) + Q_1(-B_{11}\alpha^5 + 4B_{13}\alpha^4\beta$$

$$- 2\left(B_{12}+2B_{33}\right)\alpha^3\beta^2 + 4B_{23}\alpha^2\beta^3 - B_{22}\alpha\beta^4\Big)\left(\pm\frac{h^3}{48}\right)$$

$$+ \frac{Q_1}{R^2}\left(B_{23}\alpha^2\beta - B_{22}\alpha\beta^2\right)\left(\pm\frac{h^3}{48}\right) - \frac{A_{12}}{R}\alpha\left(\pm\frac{h}{2}\right) + \Big(B_{11}\alpha^3 - 3B_{13}\alpha^2\beta$$

$$+ \left(B_{12}+2B_{33}\right)\alpha\beta^2 - B_{23}\beta^3\Big)\left(\pm\frac{h}{2}\right) - \frac{A_{22}}{R^2}Q_1\alpha\left(\frac{h^2}{8}\right)$$

$$+ \frac{Q_1}{R}\left(2B_{12}\alpha^3 - 4B_{23}\alpha^2\beta + 2B_{22}\alpha\beta^2\right)\left(\frac{h^2}{8}\right) + \frac{Q_1}{R}\Big(-D_{13}\alpha^4\beta$$

$$+ \left(D_{12}+2D_{33}\right)\alpha^3\beta^2 - 3D_{23}\alpha^2\beta^3 + D_{22}\alpha\beta^4\Big)\left(\pm\frac{h^3}{48}\right) + Q_1\Big(-D_{11}\alpha^5$$

$$+ 4D_{13}\alpha^4\beta - 2\left(D_{12}+2D_{33}\right)\alpha^3\beta^2 + 4D_{23}\alpha^2\beta^3 - D_{22}\alpha\beta^4\Big)\left(\frac{h^2}{8}\right)$$

$$- G_{xz}\alpha\left(\pm\frac{h}{2}\right) - 2\frac{\overline{N}_{xy_{1,2}}}{R}Q_1\alpha^2\beta\left(\pm\frac{h^3}{48}\right) + 2\overline{N}_{xy_{1,2}}Q_1\alpha^2\beta\left(\frac{h^2}{8}\right)$$

$$- \overline{N}_{x_{1,2}}Q_1\alpha^3\left(\frac{h^2}{8}\right)\Big]\overline{\gamma}_{xz} + \Big[\frac{Q_2}{R}\left(-A_{22}\beta^3 - A_{12}\alpha^2\beta\right)\left(\pm\frac{h^3}{48}\right)$$

$$+ Q_2\left(B_{11}\alpha^4\beta - 4B_{13}\alpha^3\beta^2 + 2\left(B_{12}+2B_{33}\right)\alpha^2\beta^3 - 4B_{23}\alpha\beta^4 + B_{22}\beta^5\right)\left(\frac{\pm h^3}{48}\right)$$

$$+ \frac{Q_2}{R^2}\left(-B_{23}\alpha\beta^2 + B_{22}\beta^3\right)\left(\pm\frac{h^3}{48}\right) + \frac{A_{22}}{R^2}Q_2\beta\left(\frac{h^2}{8}\right) + \frac{A_{22}}{R}\beta\left(\pm\frac{h}{2}\right)$$

$$+ \frac{Q_2}{R}\left(-2B_{12}\alpha^2\beta + 4B_{23}\alpha\beta^2 - 2B_{22}\beta^3\right)\left(\frac{h^2}{8}\right) + \frac{Q_2}{R}\Big(D_{13}\alpha^3\beta^2$$

$$- \left(D_{12}+2D_{33}\right)\alpha^2\beta^3 + 3D_{23}\alpha\beta^4 - D_{22}\beta^5\Big)\left(\pm\frac{h^3}{48}\right) + \frac{1}{R}\Big(-D_{13}\alpha^3$$

$$+ \left(D_{12}+2D_{33}\right)\alpha^2\beta - 3D_{23}\alpha\beta^2 + D_{22}\beta^3\Big)\left(\pm\frac{h}{2}\right) + Q_2\Big(D_{11}\alpha^4\beta$$

$$- 4D_{13}\alpha^3\beta^2 + 2\left(D_{12}+2D_{33}\right)\alpha^2\beta^3 - 4D_{23}\alpha\beta^4 + D_{22}\beta^5\Big)\left(\frac{h^2}{8}\right)$$

$$+ G_{YZ}\,\beta\left(\pm\frac{h}{2}\right) + 2\frac{\bar{N}}{R}_{XY_{1,2}}\left(Q_2\,\alpha\,\beta^2\left(\pm\frac{h^3}{48}\right) - \alpha\left(\pm\frac{h}{2}\right)\right)$$

$$- 2\,\bar{N}_{XY_{1,2}}\,Q_2\,\alpha\,\beta^2\left(\frac{h^2}{8}\right) + \bar{N}_{X_{1,2}}\,Q_2\,\alpha^2\,\beta\left(\frac{h^2}{8}\right)\Big]\,\bar{\gamma}_{YZ}$$

$$+ \Big[\left(-B_{11}\,\alpha^4 + 4B_{13}\,\alpha^3\beta - 2(B_{12}+2B_{33})\,\alpha^2\beta^2 + 4B_{23}\,\alpha\,\beta^3 - B_{22}\,\beta^4\right)\left(\frac{h^2}{8}\right)$$

$$+ \frac{1}{R^2}\left(B_{23}\,\alpha\beta - B_{22}\,\beta^2\right)\left(\frac{h^2}{8}\right) + \left(\frac{A_{22}}{R}\,\beta^2 + \frac{A_{12}}{R}\,\alpha^2\right)\left(\frac{h^2}{8}\right) - \frac{A_{22}}{R^2}\left(\pm\frac{h}{2}\right)$$

$$+ \frac{1}{R}\left(2B_{12}\alpha^2 - 4B_{23}\,\alpha\beta + 2B_{22}\,\beta^2\right)\left(\pm\frac{h}{2}\right) + \frac{1}{R}\left(-D_{13}\,\alpha^3\beta + (D_{12}+2D_{33})\,\alpha^2\beta^2\right.$$

$$\left. - 3D_{23}\,\alpha\,\beta^3 + D_{22}\,\beta^4\right)\left(\frac{h^2}{8}\right) + \left(-D_{11}\,\alpha^4 + 4D_{13}\,\alpha^3\beta - 2(D_{12}+2D_{33})\,\alpha^2\beta^2\right.$$

$$\left. + 4D_{23}\,\alpha\,\beta^3 - D_{22}\,\beta^4\right)\left(\pm\frac{h}{2}\right) + E_C - \frac{2\bar{N}}{R}_{XY_{1,2}}\,\alpha\,\beta\left(\frac{h^2}{8}\right)$$

$$\left.+ 2\bar{N}_{XY_{1,2}}\,\alpha\,\beta\left(\pm\frac{h}{2}\right) - \bar{N}_{X_{1,2}}\,\alpha^2\left(\pm\frac{h}{2}\right)\Big]\,\bar{\epsilon}_{z_0}\right\}\sin(\alpha x - \beta y) = 0$$

(eqs. B.14)

These equations can be more concisely expressed as an eigenvalue problem in matrix format :

$$\left\{\begin{bmatrix} C_{11} & C_{12} & C_{13} & C_{14} & C_{15} & C_{16} \\ C_{21} & C_{22} & C_{23} & C_{24} & C_{25} & C_{26} \\ C_{31} & C_{32} & C_{33} & C_{34} & C_{35} & C_{36} \\ C_{41} & C_{42} & C_{43} & C_{44} & C_{45} & C_{46} \\ C_{51} & C_{52} & C_{53} & C_{54} & C_{55} & C_{56} \\ C_{61} & C_{62} & C_{63} & C_{64} & C_{65} & C_{66} \end{bmatrix} - \lambda \begin{bmatrix} P_{11} & P_{12} & P_{13} & P_{14} & P_{15} & P_{16} \\ P_{21} & P_{22} & P_{23} & P_{24} & P_{25} & P_{26} \\ P_{31} & P_{32} & P_{33} & P_{34} & P_{35} & P_{36} \\ P_{41} & P_{42} & P_{43} & P_{44} & P_{45} & P_{46} \\ P_{51} & P_{52} & P_{53} & P_{54} & P_{55} & P_{56} \\ P_{61} & P_{62} & P_{63} & P_{64} & P_{65} & P_{66} \end{bmatrix}\right\} \begin{pmatrix} U_0 \\ V_0 \\ W_0 \\ \bar{\gamma}_{XZ} \\ \bar{\gamma}_{YZ} \\ \bar{\epsilon}_{z_0} \end{pmatrix} = 0$$

(eq. B.15)

The upper three rows refer to the equilibrium equations in the upper facesheet, and the lower three rows to the equations for the lower facesheet. [C] is a stiffness matrix, [P] a load matrix and λ an eigenvalue solution.

The stiffness matrix coefficients are given by the following. Where terms have two signs the upper refers to the first coefficient given (for the upper facesheet) and the lower sign to the second coefficient (for the lower facesheet).

$$C_{11}, C_{41} = -A_1$$

$$C_{12}, C_{42} = A_3 + \frac{B_2}{R}$$

$$C_{13}, C_{43} = -\frac{A_{12}}{R}\alpha \pm A_5\frac{h}{2} + B_5 \pm \frac{B_2}{R}\beta\frac{h}{2}$$

$$C_{14}, C_{44} = \pm Q_1\alpha A_5\frac{h^3}{48} - Q_1\frac{A_{12}}{R}\alpha^2\frac{h^2}{8} \mp A_1\frac{h}{2} \pm Q_1\alpha\beta\frac{B_2}{R}\frac{h^3}{48} + Q_1\alpha B_5\frac{h^2}{8} \mp G_{xz}$$

$$C_{15}, C_{45} = \mp Q_2\beta A_5\frac{h^3}{48} + Q_2\frac{A_{12}}{R}\alpha\beta\frac{h^2}{8} \pm A_3\frac{h}{2} \mp Q_2\beta^2\frac{B_2}{R}\frac{h^3}{48} - Q_2\beta B_5\frac{h^2}{8} \pm \frac{B_2}{R}\frac{h}{2}$$

$$C_{16}, C_{46} = A_5\frac{h^2}{8} + \frac{B_2}{R}\beta\frac{h^2}{8} \mp \frac{A_{12}}{R}\alpha\frac{h}{2} \pm B_5\frac{h}{2}$$

$$C_{21}, C_{51} = A_3 + \frac{B_2}{R}$$

$$C_{22}, C_{52} = -A_2 - \frac{D_1}{R^2} + \frac{B_3}{R}$$

$$C_{23}, C_{53} = \frac{A_{22}}{R}\beta + \frac{B_1}{R^2} - B_6 + \frac{D_2}{R} \mp A_6\frac{h}{2} \pm \frac{B_8}{R}\frac{h}{2} \mp \frac{D_1}{R^2}\beta\frac{h}{2}$$

$$C_{24}, C_{54} = \mp Q_1\alpha A_6\frac{h^3}{48} + Q_1\frac{A_{22}}{R}\alpha\beta\frac{h^2}{8} \pm A_3\frac{h}{2} \pm Q_1\frac{B_8}{R}\alpha\frac{h^3}{48} + Q_1\alpha\frac{B_1}{R^2}\frac{h^2}{8} - Q_1\alpha B_6\frac{h^2}{8} \pm \frac{B_2}{R}\frac{h}{2} \mp \frac{Q_1}{R^2}\alpha\beta D_1\frac{h^3}{48} + \frac{Q_1}{R}\alpha D_2\frac{h^2}{8}$$

$$C_{25}, C_{55} = \pm Q_2 \beta A_6 \frac{h^3}{48} - Q_2 \frac{A_{22}}{R} \beta^2 \frac{h^2}{8} \mp A_2 \frac{h}{2} \mp Q_2 \beta \frac{B_8}{R} \frac{h^3}{48}$$
$$- Q_2 \beta \frac{B_1}{R^2} \frac{h^2}{8} + Q_2 \beta B_6 \frac{h^2}{8} \pm \frac{Q_2}{R^2} \beta^2 D_1 \frac{h^3}{48} - \frac{Q_2}{R} \beta D_2 \frac{h^2}{8}$$
$$\mp \frac{D_1}{R^2} \frac{h}{2} \mp G_{YZ}$$

$$C_{26}, C_{56} = - A_6 \frac{h^2}{8} \pm \frac{A_{22}}{R} \beta \frac{h}{2} + \frac{B_8}{R} \frac{h^2}{8} \pm \frac{B_1}{R^2} \frac{h}{2} \mp B_6 \frac{h}{2}$$
$$- \frac{D_1}{R^2} \beta \frac{h^2}{8} \pm \frac{D_2}{R} \frac{h}{2}$$

$$C_{31}, C_{61} = B_5 - \frac{A_{12}}{R} \alpha$$

$$C_{32}, C_{62} = \frac{A_{22}}{R} \beta - B_6 + \frac{B_1}{R^2} + \frac{D_2}{R}$$

$$C_{33}, C_{63} = -\frac{A_{22}}{R^2} \pm \frac{A_4}{R} \frac{h}{2} \mp B_7 \frac{h}{2} \pm \frac{B_1}{R^2} \beta \frac{h}{2} + \frac{B_4}{R} \pm \frac{D_2}{R} \beta \frac{h}{2} - D_3$$

$$C_{34}, C_{64} = \pm Q_1 \frac{A_4}{R} \alpha \frac{h^3}{48} \mp Q_1 B_7 \alpha \frac{h^3}{48} \pm Q_1 \frac{B_1}{R^2} \alpha \beta \frac{h^3}{48} \mp \frac{A_{12}}{R} \alpha \frac{h}{2}$$
$$\pm B_5 \frac{h}{2} - \frac{A_{22}}{R^2} Q_1 \alpha \frac{h^2}{8} + Q_1 \frac{B_4}{R} \alpha \frac{h^2}{8} \pm \frac{Q_1}{R} D_2 \alpha \beta \frac{h^3}{48}$$
$$- Q_1 D_3 \alpha \frac{h^2}{8} - G_{XZ} \alpha \frac{h}{2}$$

$$C_{35}, C_{65} = \mp Q_2 \frac{A_4}{R} \beta \frac{h^3}{48} \pm Q_2 B_7 \beta \frac{h^3}{48} \mp Q_2 \frac{B_1}{R^2} \beta^2 \frac{h^3}{48} \pm \frac{A_{22}}{R} \beta \frac{h}{2}$$
$$\mp B_6 \frac{h}{2} + \frac{A_{22}}{R^2} Q_2 \beta \frac{h^2}{8} - Q_2 \frac{B_4}{R} \beta \frac{h^2}{8} \mp \frac{Q_2}{R} D_2 \beta^2 \frac{h^3}{48}$$
$$\pm \frac{D_2}{R} \frac{h}{2} + Q_2 D_3 \beta \frac{h^2}{8} + G_{YZ} \beta \frac{h}{2}$$

$$C_{36}, C_{66} = - B_7 \frac{h^2}{8} + \frac{B_1}{R^2} \beta \frac{h^2}{8} + \frac{A_4}{R} \frac{h^2}{8} \mp \frac{A_{22}}{R^2} \frac{h}{2} \pm \frac{B_4}{R} \frac{h}{2} + \frac{D_2}{R} \beta \frac{h^2}{8}$$
$$\mp D_3 \frac{h}{2} \mp E_c$$

(eqs. B.16)

where the facesheet lay-up stiffness constants are given by :

$$A_1 = A_{11} \alpha^2 + A_{33} \beta^2$$

$$A_2 = A_{22} \beta^2 + A_{33} \alpha^2$$

$$A_3 = (A_{12} + A_{33})\alpha\beta$$

$$A_4 = A_{22}\beta^2 + A_{12}\alpha^2$$

$$A_5 = A_{11}\alpha^3 + (A_{12} + 2A_{33})\alpha\beta^2$$

$$A_6 = A_{22}\beta^3 + (A_{12} + 2A_{33})\alpha^2\beta$$

$$B_1 = B_{23}\alpha - B_{22}\beta$$

$$B_2 = B_{13}\alpha^2 - (B_{12} + B_{33})\alpha\beta + B_{23}\beta^2$$

$$B_3 = 2(B_{22}\beta^2 - 2B_{23}\alpha\beta + B_{33}\alpha^2)$$

$$B_4 = 2(B_{22}\beta^2 - 2B_{23}\alpha\beta + B_{12}\alpha^2)$$

$$B_5 = B_{11}\alpha^3 - 3B_{13}\alpha^2\beta + (B_{12} + 2B_{33})\alpha\beta^2 - B_{23}\beta^3$$

$$B_6 = B_{22}\beta^3 - 3B_{23}\alpha\beta^2 + (B_{12} + 2B_{33})\alpha^2\beta - B_{13}\alpha^3$$

$$B_7 = B_{11}\alpha^4 - 4B_{13}\alpha^3\beta + 2(B_{12} + 2B_{33})\alpha^2\beta^2 - 4B_{23}\alpha\beta^3 + B_{22}\beta^4$$

$$B_8 = 2B_{22}\beta^3 - 5B_{23}\alpha\beta^2 + (B_{12} + 2B_{33})\alpha^2\beta - B_{13}\alpha^3$$

$$D_1 = D_{33}\alpha^2 - 2D_{23}\alpha\beta + D_{22}\beta^2$$

$$D_2 = D_{22}\beta^3 - 3D_{23}\alpha\beta^2 + (D_{12} + 2D_{33})\alpha^2\beta - D_{13}\alpha^3$$

$$D_3 = D_{11}\alpha^4 - 4D_{13}\alpha^3\beta + 2(D_{12} + 2D_{33})\alpha^2\beta^2 - 4D_{23}\alpha\beta^3 + D_{22}\beta^4$$

(eqs. B.17)

If the critical axial and shear stress resultants in each facesheet are expressed in terms of the eigenvalue, λ, as:

$$\bar{N}_{x_1} = K_{x_1}\lambda \quad \text{... axial load, upper facesheet}$$

$$\bar{N}_{x_2} = K_{x_2}\lambda \quad \text{... axial load, lower facesheet}$$

(eqs. B.18)

$$\bar{N}_{xy_1} = K_{xy_1}\lambda \quad \text{... shear load, upper facesheet}$$

$$\bar{N}_{xy_2} = K_{xy_2}\lambda \quad \text{... shear load, lower facesheet}$$

The load matrix coefficients are then given by :

$$P_{11} = -K_{xY_1}\alpha\beta$$

$$P_{12} = -K_{xY_1}\alpha^2$$

$$P_{13} = 0$$

$$P_{14} = -K_{xY_1}\alpha\beta\frac{h}{2}$$

$$P_{15} = -K_{xY_1}\alpha^2\frac{h}{2}$$

$$P_{16} = 0$$

$$P_{21} = 0$$

$$P_{22} = -2K_{xY_1}\alpha\beta + K_{x_1}\alpha^2$$

$$P_{23} = -2K_{xY_1}\alpha\beta^2\frac{h}{2} + K_{x_1}\alpha^2\beta\frac{h}{2} + 2\frac{K_{xY_1}}{R}\alpha$$

$$P_{24} = -2Q_1K_{xY_1}\alpha^2\beta^2\frac{h^3}{48} + K_{x_1}Q_1\alpha^3\beta\frac{h^3}{48} + 2Q_1\frac{K_{xY_1}}{R}\alpha^2\frac{h^2}{8}$$

$$P_{25} = 2Q_2K_{xY_1}\alpha\beta^3\frac{h^3}{48} - K_{x_1}Q_2\alpha^2\beta^2\frac{h^3}{48} - 2Q_2\frac{K_{xY_1}}{R}\alpha\beta\frac{h^2}{8} + K_{x_1}\alpha^2\frac{h}{2} - 2K_{xY_1}\alpha\beta\frac{h}{2}$$

$$P_{26} = -2K_{xY_1}\alpha\beta^2\frac{h^2}{8} + 2\frac{K_{xY_1}}{R}\alpha\frac{h}{2} + K_{x_1}\alpha^2\beta\frac{h^2}{8}$$

$$P_{31} = 0$$

$$P_{32} = 2\frac{K_{xY_1}}{R}\alpha$$

$$P_{33} = 2\frac{K_{xY_1}}{R}\alpha\beta\frac{h}{2} - 2K_{xY_1}\alpha\beta + K_{x_1}\alpha^2$$

$$P_{34} = 2\frac{K_{xY_1}}{R}Q_1\alpha^2\beta\frac{h^3}{48} - 2K_{xY_1}Q_1\alpha^2\beta\frac{h^2}{8} + K_{x_1}Q_1\alpha^3\frac{h^2}{8}$$

$$P_{35} = -2\frac{K_{xY_1}}{R}Q_2\alpha\beta^2\frac{h^3}{48} + 2K_{xY_1}Q_2\alpha\beta^2\frac{h^2}{8} - K_{x_1}Q_2\alpha^2\beta\frac{h^2}{8} + 2\frac{K_{xY_1}}{R}\alpha\frac{h}{2}$$

$$P_{36} = 2\frac{K_{xY_1}}{R}\alpha\beta\frac{h^2}{8} - 2K_{xY_1}\alpha\beta\frac{h}{2} + K_{x_1}\alpha^2\frac{h}{2}$$

$$P_{41} = -K_{xY_2}\,\alpha\,\beta$$

$$P_{42} = -K_{xY_2}\,\alpha^2$$

$$P_{43} = 0$$

$$P_{44} = K_{xY_2}\,\alpha\,\beta\,\frac{h}{2}$$

$$P_{45} = K_{xY_2}\,\alpha^2\,\frac{h}{2}$$

$$P_{46} = 0$$

$$P_{51} = 0$$

$$P_{52} = -2\,K_{xY_2}\,\alpha\,\beta + K_{X_2}\,\alpha^2$$

$$P_{53} = 2\,K_{xY_2}\,\alpha\,\beta^2\,\frac{h}{2} - K_{X_2}\,\alpha^2\,\beta\,\frac{h}{2} + 2\,\frac{K_{X_2}}{R}\,\alpha$$

$$P_{54} = 2Q_1\,K_{xY_2}\,\alpha^2\beta^2\,\frac{h^3}{48} - Q_1\,\alpha^3\,\beta\,K_{X_2}\,\frac{h^3}{48} + 2Q_1\,\frac{K_{xY_2}}{R}\,\alpha^2\,\frac{h^2}{8}$$

$$P_{55} = -2Q_2\,K_{xY_2}\,\alpha\,\beta^3\,\frac{h^3}{48} + Q_2\,\alpha^2\beta^2\,\frac{h^3}{48} - 2Q_2\,\frac{K_{xY_2}}{R}\,\alpha\,\beta\,\frac{h^2}{8} - K_{X_2}\,\alpha^2\,\frac{h}{2} + 2\,K_{xY_2}\,\alpha\,\beta\,\frac{h}{2}$$

$$P_{56} = -2\,K_{xY_2}\,\alpha\,\beta^2\,\frac{h^2}{8} - 2\,\frac{K_{xY_2}}{R}\,\alpha\,\frac{h}{2} + K_{X_2}\,\alpha^2\,\beta\,\frac{h^2}{8}$$

$$P_{61} = 0$$

$$P_{62} = 2\,\frac{K_{xY_2}}{R}\,\alpha$$

$$P_{63} = -2\,\frac{K_{xY_2}}{R}\,\alpha\,\beta\,\frac{h}{2} - 2\,K_{xY_2}\,\alpha\,\beta - K_{X_2}\,\alpha^2$$

$$P_{64} = -2\,\frac{K_{xY_2}}{R}\,Q_2\,\alpha\,\beta^2\,\frac{h^3}{48} + 2\,K_{xY_2}\,Q_2\,\alpha\,\beta^2\,\frac{h^2}{8} - K_{X_2}\,Q_2\,\alpha^2\,\beta\,\frac{h^2}{8} - 2\,\frac{K_{xY_2}}{R}\,\alpha\,\frac{h}{2}$$

$$P_{65} = 2\,\frac{K_{xY_2}}{R}\,Q_2\,\alpha\,\beta^2\,\frac{h^3}{48} + 2\,K_{xY_2}\,Q_2\,\alpha\,\beta^2\,\frac{h^2}{8} - K_{X_2}\,Q_2\,\alpha^2\,\beta\,\frac{h^2}{8} - 2\,\frac{K_{xY_2}}{R}\,\alpha\,\frac{h}{2}$$

$$P_{66} = 2\,\frac{K_{xY_2}}{R}\,\alpha\,\beta\,\frac{h^2}{8} + 2\,K_{xY_2}\,\alpha\,\beta\,\frac{h}{2} - K_{X_2}\,\alpha^2\,\frac{h}{2}$$

(eqs. B.19)

For a given loading condition (defined by the relative values of K_{x1}, K_{x2}, K_{xy1} and K_{xy2}) the eigenvalues can be found which satisfy the matrix equilibrium equation (B.15). There are 6 eigenvalue solutions, of which only some are finite. These correspond to different buckling modes (eg. symmetric or antisymmetric) characterised by the eigenvectors. The critical eigenvalue for a particular mode can be found by varying the values of the wave parameters m & n until a minimum is found. The critical stress resultants are then simply found from equations (B.18).

The above theory is coded in a FORTRAN program described in Appendix C. This program calculates the matrix coefficients, extracts the eigenvalues and performs the eigenvalue minimisation with respect to the wave parameters if required.

Fig. B.1 WRINKLING THEORY SIGN CONVENTION

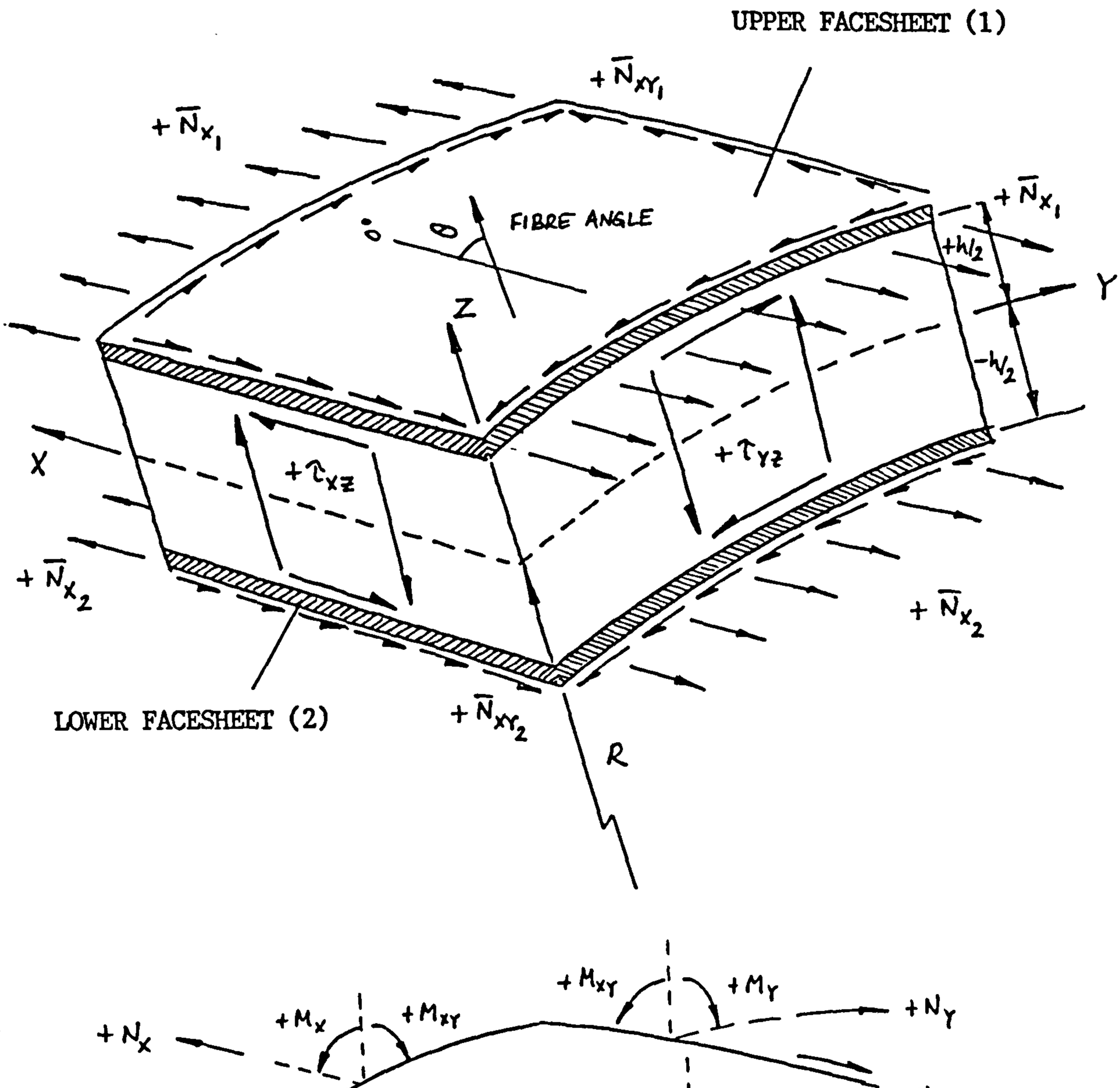

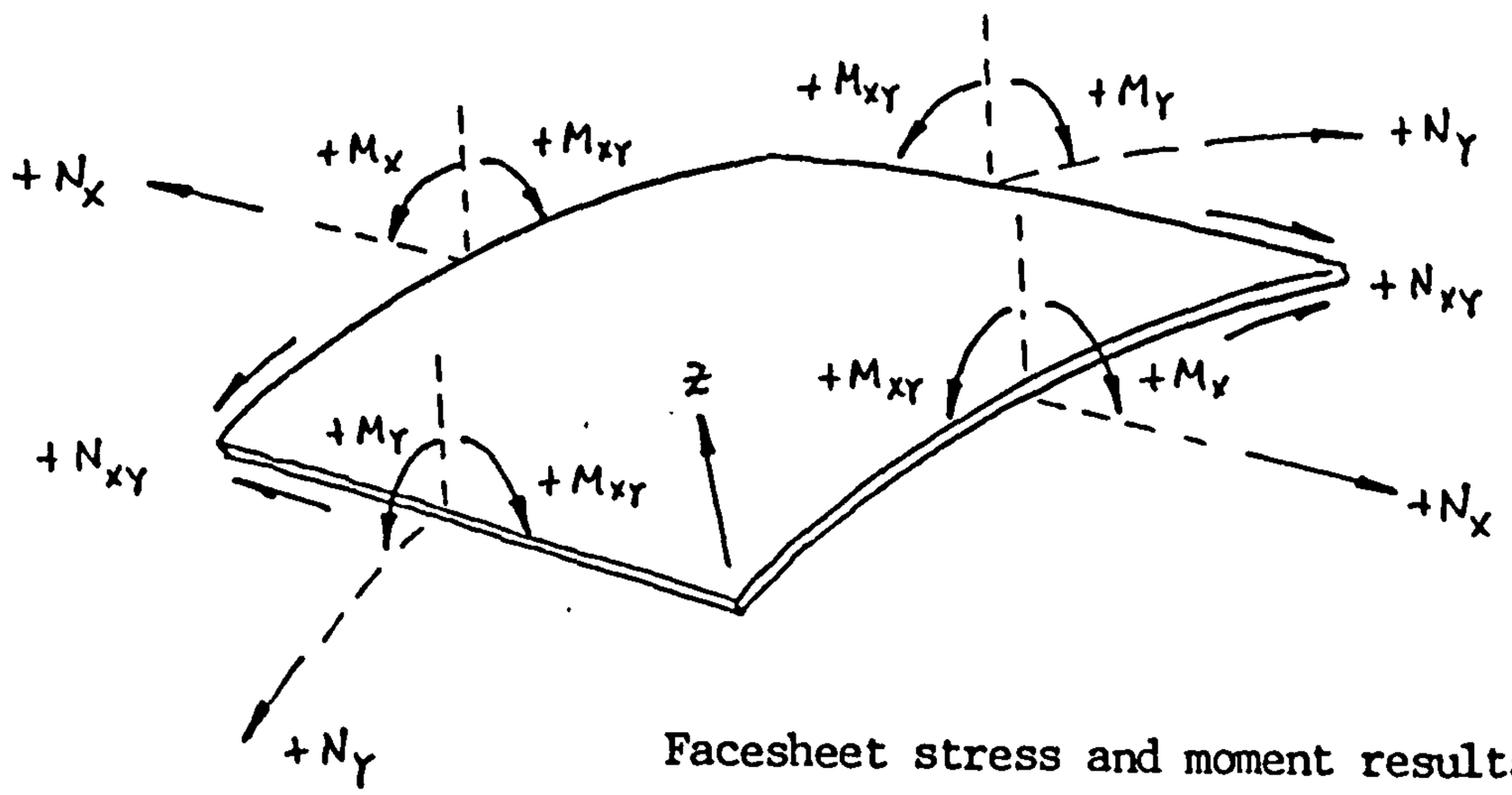

Facesheet stress and moment resultant sign convention.

APPENDIX C : WRINKLING ANALYSIS PROGRAM (WRINK)

Description

This program computes critical wrinkling loads for composite faced sandwich panels loaded by combinations of compression, shear and bending moment resultants in which the facesheets may be unbalanced about their own mid-plane. The theory behind the program is described in Chapter 6.2 and Appendix B. The user has the option of specifying the computation of the minimum critical wrinkling load which invokes a minimisation routine, or the calculation of the wrinkling load at various values of the wave parameters m & n to produce 'festoon' curves.

The program can also be used to compute general instability loads for single curvature panels or cylinders, subject to the restrictions given in Appendix B.

Input

The required input is :

FLAT/CURVED PANEL PROBLEM	1 = Flat Panel, or Wrinkling Problem 0 = Curved Panel/Cylinder Overall Buckling Problem.
PANEL DIMENSIONS	Radius of curvature R (only if curved panel or cylinder overall buckling problem). Width b, Length, a. Unless overall instability is being investigated, any reasonable dimensions can be specified.
FACESHEET PROPERTIES	Number of facesheet materials (including adhesive). E_1, E_2, ν_{12}, G_{12}, for each material.
FACESHEET LAY-UP	Total no. of plies in one facesheet. Material No, Angle (rel. to x-direction), thickness

	for each layer of upper facesheet from top downwards. Lower facesheet assumed to be symmetric.
CORE PROPERTIES	E_c, G_{xz}, G_{yz}, total thickness h.
LOAD RATIOS	Ratios of the axial and shear stress resultants in the upper (K_{x1} & K_{xy1}) and lower (K_{x2} & K_{xy2}) facesheets. See Table below for examples.
SOLUTION REQUIRED	0 = Festoon Curves 1 = Minimisation
FESTOON CURVE PARAMETERS	If specified. Start, finish and step size for m & n. m_{min}, m_{max}, Δ m n_{min}, n_{max}, Δ n
MINIMISATION PARAMETERS	If specified. Initial estimates for m & n, m_0 & n_0. Increments for gradient estimates Δm & Δn. Tolerance on critical values m^* & n^*.

(see example input data file)

Notes

(1) Load ratios for typical loading actions are given in the following table :

LOAD CONDITION	FACESHEET 1		FACESHEET 2	
	K_{x1}	K_{xy1}	K_{x2}	K_{xy2}
Pure Compression	$-\frac{1}{2}$	0	$-\frac{1}{2}$	0
Pure Flexure	$-\frac{1}{2}$	0	$+\frac{1}{2}$	0
Pure Shear	0	$+\frac{1}{2}$	0	$+\frac{1}{2}$

(2) Initial estimates for m & n can be found by using the specially orthotropic formula, with consistent panel dimensions. (Chapter 6, eq.(6.8)).

(3) Minimisation is usually well conditioned if Δm & Δn and the tolerance on m^* & n^* are taken to be about 1/100 th of the expected critical value for m^*.

Solution

The program first calculates the facesheet constitutive matrices which are then combined with the core properties to generate the 6 x 6 [C] stiffness matrix given in Appendix A. The [P] load matrix, also given in Appendix A, is calculated from the specified load ratios. The eigen problem is solved using standard NAG routines (X02AAF and F02BJF) for the particular values of m & n. If festoon curve output is requested, the program simply loops through the specified ranges of m & n. If the minimum eigenvalue is requested, a two dimensional minimisation is performed using a Newton-Raphson technique. The minimisation process alternates between m & n, treating them as continuous variables, until the specified tolerance on the minimum is achieved. The gradients and second derivatives w.r.t m & n are estimated by setting up and solving the eigen problem at 3 points separated by m & n whilst the other variable is held constant.

Output

If festoon curves are specified, the eigenvalues are output for the given ranges of m & n. If the minimum eigenvalue is specified, this is output along with the critical wrinkle wavelength and nodal line slope. The festoon curve option enables a check to be perfomed on the calculated minimum.

EXAMPLE INPUT FILE : (WRINK.DAT)

1	FLAT PLATE PROBLEM
0.300	PANEL WIDTH "b"
0.300	PANEL LENGTH "a"
2	NO. OF FACESHEET MATERIALS
42E9 15E9 0.23 4E9	E_1 E_2 ν_{12} G_{12} for MATERIAL 1
2.4E9 2.4E9 0.37 1.0E9	E_1 E_2 ν_{12} G_{12} for MATERIAL 2 (adhesive)
5	NO. OF PLIES PER FACESHEET (including adhesive layer)
1 45 0.10E-3	MATERIAL ANGLE THICKNESS FOR PLY 1
1 0 0.10E-3	" " " FOR PLY 2
1 90 0.10E-3	" " " FOR PLY 3
1 -45 0.10E-3	" " " FOR PLY 4
2 0 0.12E-3	" " " FOR PLY 5
	CORE PROPERTIES
310E6	E_c
186E6	G_{xz}
90E6	G_{yz}
10E-3	h
	LOAD RATIOS
-0.5	K_{x1}
-0.5	K_{x2}
0.0	K_{xy1}
0.0	K_{xy2}
1	MINIMISATION PROBLEM
50 0	INITIAL ESTIMATE $m^* = 50$, $n^* = 0$
1 1	$\Delta m = 1$, $\Delta n = 1$
1	TOLERANCE ON CRITICAL m and n

APPENDIX D ; SANDWICH PANEL OPTIMISATION PROGRAM (PANEL)

Description

This program performs a one dimensional optimisation of sandwich panel core depth for single curvature rectangular panels loaded in bending with natural frequency, material strength, wrinkling and dimpling design constraints. The panel may have composite facesheets with an unsymmetric lay-up about the facesheet mid-plane, but both facesheets are assumed to be symmetric about the panel mid-plane.

From a user supplied initial design (which must be unfeasible, ie. have a core thickness below the minimum) the program calculates values of the four design constraint functions and increments the core depth until all are satisfied. The analysis methods are described in Chapters 5, 6 and 7. For the calculation of critical wrinkling loads the program described in Appendix C is incorporated as a subroutine. As an initial estimate of the wrinkling waveform parameters which yield the minimum eigenvalue, the following are used :

$$m_0 = \frac{a}{\pi}\left(\frac{2E_c}{D_{11}h}\right)^{\frac{1}{4}}$$

$$n_0 = 0$$

m_0 is the critical number of axial half-wavelengths for specially orthotropic facesheets loaded in compression, and generally will be slightly lower than the actual critical value, m^*. n_0, the number of lateral half-wavelengths, is initially taken as zero since most lay-ups will have no nodal line slope under pure bending.

The program terminates by outputting the minimum core depth and panel mass for the given facesheet lay-up and core type which meets all the design constraints. Values of the constraints are given to indicate which of these are critical.

Input

The required input is :

PANEL DIMENSIONS	Length, a, Width, b and radius of curvature R of the panel. Set R to large number if panel is flat
VIBRATION STIFFNESS PARAMETERS	Panel mass per unit area, not including structure mass, assumed uniformly distributed, ρ . Design frequency requirement, f_D.
DESIGN BENDING MOMENT RESULTANT	M_x (N-mm/mm)
FACESHEET PROPERTIES	E_1, E_2, ν_{12}, G_{12}, X_T, X_C, Y_T, Y_C, S (allowables), ply thickness, t_{ply}, density, ρ_f.
FACESHEET LAY-UP	Total no. of plies per facesheet. Angles of plies relative to x-axis, for upper facesheet only from top downwards. Lower facesheet is assumed to be symmetrical.
CORE PROPERTIES	Cell size, d_c. E_c, G_{xz}, G_{yz}.
CORE DEPTH	Initial core depth estimate, max. allowable core depth, core depth increment (1 mm is practical).
CORE DENSITY	Effective core density (to account for any local densification), ρ_c, adhesive mass per unit area, ρ_a, for a single layer only.
KNOCK-DOWN FACTORS	k_1 for natural frequency prediction k_2 for facesheet material strength prediction k_3 for wrinkling prediction k_4 for dimpling prediction

WRINKLING MINIMISATION PARAMETERS	Δm & Δn for gradient estimates. Tolerance on m^* & n^*. Setting m = 1, n = 1 and tolerance = 1 found to give reasonable compromise between convergence and accuracy for most panels.

(see example input data file)

Solution

The sequence of calculations is shown in fig. 7.2 of Chapter 7.

Output

The program echoes the problem input data followed by the results of the optimisation. These consist of the optimum core depth and the corresponding panel mass breakdown per unit area, and values of the design constraints at the optimum. The predicted panel frequency is given along with the value of the constraint function (M.o.S). For the material failure constraint, the Tsai-Wu index and corresponding facesheet ply are also given. For the wrinkling constraint the critical wrinkling half-wavelength and nodal line slope are given.

(see example output results file)

EXAMPLE INPUT FILE : (PANEL.DAT)

0.550	PANEL LENGTH "a"
1.600	PANEL WIDTH "b"
1E12	RADIUS OF CURVATURE
0.3	NON-STRUCTURAL MASS PER UNIT AREA ρ
100.0	MIN. FREQUENCY REQUIREMENT
150.0	M_x DESIGN B.M. RESULATNT
175E9 6.8E9 0.30 3.75E9	E_1 E_2 v_{12} G_1
574E6 344E6 23E6 70E6 15E6	X_T X_C Y_T Y_C S
0.10E-3 1600	t_{ply} ρ_f
3	NO. PLIES PER FACESHEET
	FACESHEET LAY-UP ANGLES
30.0	1^{st} PLY
90.0	2^{nd} PLY
-30.0	3^{rd} PLY
	CORE PROPERTIES
4.8E-3	d_c
310E6	E_c
186E6	G_{xz}
90E6	G_{yz}
5E-3 50E-3 1E-3	h_{min} h_{max} Δh
32	EFFECTIVE CORE DENSITY
0.150	FILM ADHESIVE MASS PER UNIT AREA
1.0 1.0 0.4 1.0	KNOCK-DOWN FACTORS k_1 k_2 k_3 k_4
1.0 1.0 1.0	Δm Δn TOLERANCE

```
==========================================================
   COMPOSITE SPACECRAFT SANDWICH PANEL OPTIMISATION
==========================================================

PANEL DIMENSIONS
----------------
LENGTH ( X-DIRECTION ) = (.55CJE+C )
WIDTH  ( Y-DIRECTION ) = C.1bCJE+C1

PANEL LOADINGS
--------------
MASS PER UNIT AREA     = (.3JC.JE+C )
X-WISE MOMENT , MX     = (.15C )E+C 3

DESIGN FREQUENCY REQUIREMENT = 0.1 JC0E+C 3

FACESHEET MATERIAL PROPERTIES
-----------------------------

E1    = 0.1750E+12
E2    = 0.6800E+10
MU12  =  0.300
G12   = 0.3750E+10
XT    = 0.5740E+09
XC    = 0.3440E+09
YT    = 0.2300E+08
YC    = 0.7000E+08
SS    = 0.1500E+08

PLY THICKNESS = 0.1000E-02     DENSITY = 0.1600E+04

FACESHEET LAY-UP
----------------

  PLY          ANGLE
-------------------------

   1          0.3000E+02
   2          0.9000E+02
   3          -.3000E+02

CORE PROPERTIES
---------------

CELL SIZE      = 0.4800E-02
COMP. MODULUS = 0.3100E+09
XZ SHEAR MOD. = 0.1600E+09
YZ SHEAR MOD. = 0.9000E+08


EFF. DENSITY   = 0.3200E+02
ADHESIVE WT.   = 0.1500E+00
```

==========
ANALYSIS RESULTS
==========

CORE DEPTH = 0.7000E-02
EQUIVALENT FACESHEET LOADING = 0.2143E+03

PANEL STRUCTURE WEIGHT

FACESHEETS = 0.9000E+00 PER UNIT AREA
FILM ADHESIVE = 0.3000E+00 PER UNIT AREA
HONEYCOMB CORE = 0.2240E+00 PER UNIT AREA

TOTAL = 0.1464E+01 PER UNIT AREA

MASS OF RECTANGULAR PANEL = 0.1000E+01

1. STIFFNESS

NATURAL FREQUENCY = 0.1020E+02
M.O.S = 0.2492E-01

2. STRENGTH

MAX. TSAI-WU INDEX = 0.2867E+00
M.O.S = 0.7133E+00
CRITICAL LAYER = 3

3. WRINKLING

THEORETICAL LOAD = 0.1361E+06
ALLOWABLE LOAD = 0.7444E+05
M.O.S = 0.7122E+00
CRIT. 1/2 WAVELENGTH = 0.2000E-02
NODAL LINE SLOPE = -.2164E+00

4. DIMPLING

THEORETICAL LOAD = 0.2247E+06
ALLOWABLE LOAD = 0.2247E+06
M.O.S = 0.9247E+00

APPENDIX E : SPACECRAFT LATERAL FREQUENCY PROGRAM (FREQ)

Description

This program calculates lateral mode vibration frequencies for spacecraft idealised by a lumped mass and beam finite element method. The thrust tube is idealised by beams which include shear in addition to bending deformation, and the spacecraft is idealised by lumped masses and inertias. The beam element formulation is based on that of reference [46] and the stiffness and mass matrices are given in section 8.3.1 of Chapter 8. The program will either output lateral mode frequencies for a given spacecraft configuration with a particular thrust tube lay-up, or will compute frequencies of a particular mode as a function of two lay-up angle variables. For the latter option, output is either an isoparametric plot or an interpolated contour plot of frequency against the two angle variables.

Input

For a typical thrust tube and spacecraft representation refer to fig. E.1 for node and element numbering. The required input is :

NO. OF BEAM ELEMENTS	The thrust tube should be split into elements at lumped masses and changes in thrust tube stiffness
MASS INERTIA (at each node)	Lumped mass M_i and inertia I_i at i^{th} node. If zero use small values to prevent ill-conditioning of mass matrix.
LOWER INTERFACE RADIUS	Radius of thrust tube clamped base. (node 0)
THRUST TUBE DIMENSIONS (for each element)	Length L_j and upper radius R_j of j^{th} element.
FACESHEET PROPERTIES	Number of facesheet materials. E_1, E_2, ν_{12}, G_{12}, t_{ply} for each material.

SOLUTION REQUIRED — 1 = All lateral mode frequencies for given lay-up
2 = Selected mode frequency vs. lay-up angle variables

If solution code = 1 .....

FACESHEET LAY-UP — Total no. of plies in one facesheet.
(for each element) — Material No. Angle (rel. to axial direction)

Else if solution code = 2 ....

FIXED LAY-UP ANGLES — No. of fixed lay-up angles.
1^{st} fixed angle, 2^{nd} fixed angle etc.

FACESHEET LAY-UP — Total no. of plies in one facesheet.
(for each element) — Material No. Angle code

Code	Angle
0	0°
1	variable 1
2	variable 2
3	1^{st} fixed angle
4	2^{nd} fixed angle
	etc.

(note : negative code = negative angle)

MODE REQUIRED — 1 = 1^{st} mode
2 = 2^{nd} mode

PLOT REQUIRED — 0 = Isoparametric
1 = Contour

PLOTTING PARAMETERS — If Isoparametric ...
Flatness (typically 0.5)
View (0 = origin nearest corner

1 = rotate thro' 90°
2 = rotate thro' 180°)
If Contour Plot ...
No. of contours
Interpolation (0 = straight lines
1 = curves)

(see example input file)

Solution

The program computes the shell membrane constitutive matrices for each element of the thrust tube and then calculates the [K] element stiffness matrices, as described in section 8.3.1. The element stiffness matrices are assembled to form the global stiffness matrix. The global mass matrix is formed with the spacecraft lumped mass and inertias as diagonal terms. The eigen problem is solved using the standard NAG routine F02AEF. Plots of the lateral frequency as a function of two fibre angle variables are plotted using GINO subroutines.

Output

If the thrust tube lay-up is specified (solution code = 1), the program outputs the first n lateral modes, where n = 2 x no. of free nodes, and the corresponding mode shapes in terms of the lateral displacements and rotations at the nodes. Only the first 2 or 3 modes are likely to be accurate descriptions of the true modes. For variable thrust tube lay-ups, the selected mode frequency is plotted as a function of the two angle variables, and these are tabulated in a separate file.

EXAMPLE INPUT FILE : (FREQ.DAT)

(T-SAT SPACECRAFT)

3	NO. OF ELEMENTS
958 135	M_1 I_1
0.1 0.1	M_2 I_2
438 350	M_3 I_3
0.597	LAUNCHER INTERFACE RADIUS
0.550 0.535	L_1 R_1
0.300 0.500	L_2 R_2
0.775 0.500	L_3 R_3
1	NO. FACESHEET MATERIALS
175E9 6.8E9 0.30 3.75E9 0.100E-3	E_1 E_2 ν_{12} G_{12} t_{ply}
2	FREQ'Y AS FUNCTION OF FIBRE ANGLE
	VARIABLES REQUIRED
0	NO. OF FIXED ANGLES
8	FACESHEET LAY-UP FOR ELEMENT 1
1 1	
1 -1	0 = 0°
1 0	1 = VARIABLE 1
1 0	
1 0	
1 0	
1 -1	
1 1	

```
8
1    1
1   -1
1    0                    FACESHEET LAY-UP FOR ELEMENT 2
1    0
1    0
1    0
1   -1
1    1

4
1    2
1    0                    FACESHEET LAY-UP FOR ELEMENT 3
1    0
1   -2                    2 = VARIABLE 2

1                         FIRST MODE REQUIRED

1                         CONTOUR PLOT
20                        20 CONTOURS
1                         SMOOTH INTERPOLATION
```

APPENDIX F : THRUST TUBE MATERIAL STRENGTH PROGRAM (TTSTR)

Description

This program calculates the maximum ply Tsai-Wu failure index for composite thrust tubes loaded by axial and shear membrane stress resultants. The theory is based on that described in section 5.3 of Chapter 5. The user has the option of calculating the maximum Tsai-Wu index for a given lay-up under specified load cases, or of calculating the maximum Tsai-Wu index as a function of two lay-up angle variables. For the latter option the results are presented as either an isoparametric or contour plot of Tsai-Wu index against the two angle variables.

The program is intended for use in the optimisation of composite faced sandwich thrust tubes with symmetric fcaesheets. [B] matrix coupling in the shell constitutive matrix is therefore assumed to be zero. The program could equally be used for the analysis of monocoque composite thrust tubes, provided the lay-up is balanced.

Input

The required input is :

MATERIAL PROPERTIES — Number of facesheet materials.
E_1, E_2, v_{12}, G_{12}, t_{ply},
X_T, X_C, Y_T, Y_C, S for each material.

SOLUTION REQUIRED — 1 = Max. Tsai-Wu indices for given lay-up under specified load cases.
2 = Max. Tsai-Wu index vs. lay-up angle variables for a specified load case.

If solution code 1 ....

FACESHEET LAY-UP — Total no. of plies in one facesheet.
Material No. Angle (rel. to axial direction)

Else if solution code 2 ....

FACESHEET LAY-UP — Total no. of plies in one facesheet.
Material No. Angle Code

Code	Angle
0	0°
1	variable 1
2	variable 2

(for negative angle use negative code)

CORE THICKNESS — h (This can be any reasonable number since the core thickness does not determine facesheet stresses under membrane loading only)

If solution code 1 ....

APPLIED LOADS — No. of load cases.
N_x N_{xy} for each load case.

Else if solution code 2 ....

APPLIED LOADS — N_x N_{xy} single load case.

PLOT REQUIRED — 0 = Isoparametric
1 = Contour

PLOTTING PARAMETERS — If isoparametric ...
Flatness (typically 0.5)
View (0 = origin nearest corner
1 = rotate thro' 90°
2 = rotate thro' 180°)

If contour plot ...
No. of contours
Interpolation (0 = straight lines, 1 = curves)

(see example input file)

Solution

The program calculates the shell constitutive matrix, inverts it and applies the Tsai-Wu failure criterion to obtain a failure index for each ply in the lay-up under the given set of loads. These are compared and the maximum ply index is output. For a specified lay-up the calculation is repeated for each load case. For lay-ups in which the fibre angles are variable the maximum index is calculated at 5° intervals from 0° to 45° on a 10 x 10 grid. The results are displayed using GINO plotting subroutines which also perform the necessary interpolation for the contour plots.

Output

If solution option 1 is selected the program outputs the maximum Tsai-Wu index in the lay-up under each specified load case. The particular ply with the maximum index is also identified. If solution option 2 is selected the output is an isoparametric or contour plot of the maximum ply Tsai-Wu index as a function of the two ply angle variables. To give a reasonable scaling to the plots, Tsai-Wu indices of greater than 1.50 are truncated to this value. The Tsai-Wu index = 1.00 contour defines the boundary of the feasible and unfeasible regions for design optimisation.

EXAMPLE INPUT FILE : (TTSTR.DAT)

1	NO. OF FACESHEET MATERIALS
175E9 6.8E9 0.30 3.75E9 0.100E-3	E_1 E_2 ν_{12} G_{12} t_{ply}
574E6 344E6 23E6 70E6 15E6	X_T X_C Y_T Y_C S
1	MAX. INDEX FOR GIVEN LAY-UP UNDER SPECIFIED LOAD CASES
4	NO. OF PLIES PER FACESHEET
1 0	FACEHEET LAY-UP
1 45	
1 -45	
1 0	
10E-3	h
2	NO. OF LOAD CASES
-96E3 14E3	N_x N_{xy} LOAD CASE 1
-32E3 20E3	N_x N_{xy} LOAD CASE 2

APPENDIX G : BUCKLING ANALYSIS FOR COMPOSITE FACED SANDWICH CYLINDERS UNDER AXIAL COMPRESSION

This appendix develops the linear small deflection theory for orthotropic faced sandwich cylinders under axial compression described in section 8.5.2, based on the theory of Teichmann, Wang & Gerard. In the first part, the full buckling equilibrium matrix equation is derived which requires an eigenvalue solution, and in the second part the simplified solution for the special case of axisymmetric buckling is derived.

(1) General Solution

Refering to an element of cylindrical shell depicted in fig. G.1, assuming that all applied forces other than $\overline{N}_x$ are small and an infinite through-thickness core stiffness, the equilibrium equations at the onset of buckling are :

$$(a) \quad \frac{\partial N_x}{\partial x} + \frac{1}{R}\frac{\partial N_{x\theta}}{\partial \theta} = 0$$

$$(b) \quad \frac{1}{R}\frac{\partial N_\theta}{\partial \theta} + \frac{\partial N_{x\theta}}{\partial x} + \overline{N}_x \frac{\partial^2 v}{\partial x^2} - \frac{Q_\theta}{R} = 0$$

$$(c) \quad \frac{\partial Q_x}{\partial x} + \frac{1}{R}\frac{\partial Q_\theta}{\partial \theta} + \overline{N}_x \frac{\partial^2 w}{\partial x^2} + \frac{1}{R} N_\theta = 0 \qquad \text{(eqs. G.1)}$$

$$(d) \quad \frac{\partial M_x}{\partial x} + \frac{1}{R}\frac{\partial M_{x\theta}}{\partial \theta} - Q_x = 0$$

$$(e) \quad \frac{1}{R}\frac{\partial M_\theta}{\partial \theta} + \frac{\partial M_{x\theta}}{\partial x} - Q_\theta = 0$$

The strain-displacement relations for a curved element with constant through-thickness shear deformation are given by :

$$\epsilon_x = \frac{\partial u}{\partial x} \qquad \epsilon_\theta = \frac{1}{R}\left(\frac{\partial v}{\partial \theta} - w\right) \qquad \gamma_{x\theta} = \frac{1}{R}\frac{\partial u}{\partial \theta} + \frac{\partial v}{\partial x}$$

(eqs. G.2)

$$k_x = \frac{\partial \beta_x}{\partial x} \qquad k_\theta = \frac{1}{R}\frac{\partial \beta_\theta}{\partial \theta} \qquad k_{x\theta} = \frac{1}{R}\frac{\partial \beta_x}{\partial \theta} + \frac{\partial \beta_\theta}{\partial x}$$

where β_x & β_θ are the components of slope of the normal to the shell mid-plane and are given by :

$$\beta_x = \gamma_{xz} - \frac{\partial w}{\partial x} \qquad \beta_\theta = \gamma_{\theta z} - \frac{1}{R}\left(v + \frac{\partial w}{\partial \theta}\right) \qquad \text{(eqs. G.3)}$$

The shell constitutive relationship is given by :

$$\begin{Bmatrix} N_x \\ N_\theta \\ N_{x\theta} \\ M_x \\ M_\theta \\ M_{x\theta} \end{Bmatrix} = \left[\begin{array}{ccc:ccc} A_{11} & A_{12} & 0 & B_{11} & B_{12} & 0 \\ & A_{22} & 0 & & B_{22} & 0 \\ \text{SYM} & & A_{33} & \text{SYM} & & B_{33} \\ \hdashline B_{11} & B_{12} & 0 & D_{11} & D_{12} & 0 \\ & B_{22} & 0 & & D_{22} & 0 \\ \text{SYM} & & B_{33} & \text{SYM} & & D_{33} \end{array}\right] \begin{Bmatrix} \epsilon_x \\ \epsilon_\theta \\ \gamma_{x\theta} \\ k_x \\ k_\theta \\ k_{x\theta} \end{Bmatrix} \qquad \text{(eq. G.4)}$$

and the shear stress resultant-shear strain relationship for the core is :

$$Q_x = S_{xz}\,\gamma_{xz} \qquad Q_\theta = S_{\theta z}\,\gamma_{\theta z} \qquad \text{(eqs. G.5)}$$

Substituting equations (F.2) to (F.5) into the equilibrium equations (F.1) results in the 5 equations in terms of displacements and mid-plane slopes :

(a) $$A_{11}\frac{\partial^2 u}{\partial x^2} + \frac{A_{12}}{R}\left(\frac{\partial^2 v}{\partial x \partial \theta} - \frac{\partial w}{\partial x}\right) + B_{11}\frac{\partial^2 \beta_x}{\partial x^2} + \frac{B_{12}}{R}\frac{\partial^2 \beta_\theta}{\partial x \partial \theta}$$

$$+ \frac{A_{33}}{R}\left(\frac{1}{R}\frac{\partial^2 u}{\partial \theta^2} + \frac{\partial^2 v}{\partial x \partial \theta}\right) + \frac{B_{33}}{R}\left(\frac{1}{R}\frac{\partial^2 \beta_x}{\partial \theta^2} + \frac{\partial^2 \beta_\theta}{\partial x \partial \theta}\right) = 0$$

(b) $$\frac{A_{12}}{R}\frac{\partial^2 u}{\partial x \partial \theta} + \frac{A_{22}}{R^2}\left(\frac{\partial^2 v}{\partial \theta^2} - \frac{\partial w}{\partial \theta}\right) + \frac{B_{12}}{R}\frac{\partial^2 \beta_x}{\partial x \partial \theta} + \frac{B_{22}}{R}\frac{\partial^2 \beta_\theta}{\partial \theta^2}$$

$$+ A_{33}\left(\frac{1}{R}\frac{\partial^2 u}{\partial x \partial \theta} + \frac{\partial^2 v}{\partial x^2}\right) + B_{33}\left(\frac{1}{R}\frac{\partial^2 \beta_x}{\partial x \partial \theta} + \frac{\partial^2 \beta_\theta}{\partial x^2}\right) + \bar{N}_x\frac{\partial^2 v}{\partial x^2}$$

$$- \frac{S_{\theta z}}{R}\left(\beta_\theta + \frac{v}{R} + \frac{1}{R}\frac{\partial w}{\partial \theta}\right) = 0$$

$$-(c)\quad S_{xz}\left(\frac{\partial \beta_x}{\partial x}+\frac{\partial^2 w}{\partial x^2}\right)+\frac{S_{\theta z}}{R}\left(\frac{\partial \beta_\theta}{\partial \theta}+\frac{1}{R}\frac{\partial v}{\partial \theta}+\frac{1}{R}\frac{\gamma w}{\partial \theta^2}\right)+\overline{N}_x\frac{\partial^2 w}{\partial x^2}$$

$$+\frac{A_{12}}{R}\frac{\partial u}{\partial x}+\frac{A_{22}}{R^2}\left(\frac{\partial v}{\partial \theta}-w\right)+\frac{B_{12}}{R}\frac{\partial \beta_x}{\partial x^2}+\frac{B_{22}}{R^2}\frac{\partial \beta_\theta}{\partial \theta}\quad=\quad 0$$

$$(d)\quad B_{11}\frac{\partial^2 u}{\partial x^2}+\frac{B_{12}}{R}\left(\frac{\partial^2 v}{\partial x\partial \theta}-\frac{\partial w}{\partial x}\right)+D_{11}\frac{\partial^2 \beta_x}{\partial x^2}+\frac{D_{12}}{R}\frac{\partial^2 \beta_\theta}{\partial x\partial \theta}$$

$$+\frac{B_{33}}{R}\left(\frac{1}{R}\frac{\partial^2 u}{\partial \theta^2}+\frac{\partial^2 v}{\partial x\partial \theta}\right)+\frac{D_{33}}{R}\left(\frac{1}{R}\frac{\partial^2 \beta_x}{\partial \theta^2}+\frac{\partial^2 \beta_\theta}{\partial x\partial \theta}\right)$$

$$-S_{xz}\left(\beta_x+\frac{\partial w}{\partial x}\right)\quad=\quad 0$$

$$(e)\quad \frac{B_{12}}{R}\frac{\partial^2 u}{\partial x\partial \theta}+\frac{B_{22}}{R^2}\left(\frac{\partial^2 v}{\partial \theta^2}-\frac{\partial w}{\partial \theta}\right)+\frac{D_{12}}{R}\frac{\partial^2 \beta_x}{\partial x\partial \theta}+\frac{D_{22}}{R^2}\frac{\partial^2 \beta_\theta}{\partial \theta^2}$$

$$+B_{33}\left(\frac{1}{R}\frac{\partial^2 u}{\partial x\partial \theta}+\frac{\partial^2 v}{\partial x^2}\right)+D_{33}\left(\frac{1}{R}\frac{\partial^2 \beta_x}{\partial x\partial \theta}+\frac{\partial^2 \beta_\theta}{\partial x^2}\right)$$

$$-S_{\theta z}\left(\beta_\theta+\frac{v}{R}+\frac{1}{R}\frac{\partial w}{\partial \theta}\right)\quad=\quad 0 \qquad \text{(eqs. G.6)}$$

A solution to these equations can be found by assuming double trigonometric shape functions of the following form for the displacements and mid-plane slopes :

$$u = U \sin n\theta \cos\frac{m\pi x}{L}$$

$$v = V \cos n\theta \sin\frac{m\pi x}{L}$$

$$w = W \sin n\theta \sin\frac{m\pi x}{L} \qquad \text{(eqs. G.7)}$$

$$\beta_x = \overline{\beta}_x \sin n\theta \cos\frac{m\pi x}{L}$$

$$\beta_\theta = \overline{\beta}_\theta \cos n\theta \sin\frac{m\pi x}{L}$$

where,

m = no. of axial half waves

n = no. of cicumferential full waves

By performing the differentiation of these functions and substituting into the equilibrium equations (F.6), the following are obtained :

$$(a)\ \Big\{ \Big[-A_{11}\Big(\frac{\lambda}{R}\Big)^2 - A_{33}\Big(\frac{n}{R}\Big)^2\Big]U + \Big[-A_{12}\Big(\frac{\lambda}{R}\Big)\Big(\frac{n}{R}\Big) - A_{33}\Big(\frac{\lambda}{R}\Big)\Big(\frac{n}{R}\Big)\Big]V$$

$$+ \Big[-\frac{A_{12}}{R}\Big(\frac{\lambda}{R}\Big)\Big]W + \Big[-B_{11}\Big(\frac{\lambda}{R}\Big)^2 - B_{33}\Big(\frac{n}{R}\Big)^2\Big]\bar{\beta}_x$$

$$+ \Big[-B_{12}\Big(\frac{\lambda}{R}\Big)\Big(\frac{n}{R}\Big) - B_{33}\Big(\frac{\lambda}{R}\Big)\Big(\frac{n}{R}\Big)\Big]\bar{\beta}_\theta \Big\} \sin n\theta \cos\frac{\lambda x}{R} = 0$$

$$(b)\ \Big\{ \Big[-A_{12}\Big(\frac{\lambda}{R}\Big)\Big(\frac{n}{R}\Big) - A_{33}\Big(\frac{\lambda}{R}\Big)\Big(\frac{n}{R}\Big)\Big]U + \Big[-A_{22}\Big(\frac{n}{R}\Big)^2 - A_{33}\Big(\frac{\lambda}{R}\Big)^2 - \frac{S_{\theta z}}{R^2}$$

$$- \bar{N}_x\Big(\frac{\lambda}{R}\Big)^2\Big]V + \Big[-\frac{A_{22}}{R}\Big(\frac{n}{R}\Big) - \frac{S_{\theta z}}{R}\Big(\frac{n}{R}\Big)\Big]W + \Big[-B_{12}\Big(\frac{\lambda}{R}\Big)\Big(\frac{n}{R}\Big)$$

$$- B_{33}\Big(\frac{\lambda}{R}\Big)\Big(\frac{n}{R}\Big)\Big]\bar{\beta}_x + \Big[-B_{22}\Big(\frac{n}{R}\Big)^2 - B_{33}\Big(\frac{\lambda}{R}\Big)^2 - \frac{S_{\theta z}}{R}\Big]\bar{\beta}_\theta \Big\}$$

$$\cdot \cos n\theta \sin\frac{\lambda x}{R} = 0$$

$$(c)\ \Big\{ \Big[-\frac{A_{12}}{R}\Big(\frac{\lambda}{R}\Big)\Big]U + \Big[-\frac{S_{\theta z}}{R}\Big(\frac{n}{R}\Big) - \frac{A_{22}}{R}\Big(\frac{n}{R}\Big)\Big]V + \Big[-\frac{A_{22}}{R^2} - S_{xz}\Big(\frac{\lambda}{R}\Big)^2$$

$$- S_{\theta z}\Big(\frac{n}{R}\Big)^2 - \bar{N}_x\Big(\frac{\lambda}{R}\Big)^2\Big]W + \Big[-S_{xz}\Big(\frac{\lambda}{R}\Big) - \frac{B_{12}}{R}\Big(\frac{\lambda}{R}\Big)\Big]\bar{\beta}_x$$

$$+ \Big[-S_{\theta z}\Big(\frac{n}{R}\Big) - \frac{B_{22}}{R}\Big(\frac{n}{R}\Big)\Big]\bar{\beta}_\theta \Big\} \sin n\theta \sin\frac{\lambda x}{R} = 0$$

$$(d)\ \Big\{ \Big[-B_{11}\Big(\frac{\lambda}{R}\Big)^2 - B_{33}\Big(\frac{n}{R}\Big)^2\Big]U + \Big[-B_{12}\Big(\frac{\lambda}{R}\Big)\Big(\frac{n}{R}\Big) - B_{33}\Big(\frac{\lambda}{R}\Big)\Big(\frac{n}{R}\Big)\Big]V$$

$$+ \Big[-\frac{B_{12}}{R}\Big(\frac{\lambda}{R}\Big) - S_{xz}\Big(\frac{\lambda}{R}\Big)\Big]W + \Big[-D_{11}\Big(\frac{\lambda}{R}\Big)^2 - D_{33}\Big(\frac{n}{R}\Big)^2 - S_{xz}\Big]\bar{\beta}_x$$

$$+\left[-D_{12}\left(\frac{\lambda}{R}\right)\left(\frac{n}{R}\right)-D_{33}\left(\frac{\lambda}{R}\right)\left(\frac{n}{R}\right)\right]\bar{\beta}_\theta\Bigg\}\sin n\theta\cos\frac{\lambda x}{R}=0$$

$$(e)\Bigg\{\left[-B_{12}\left(\frac{\lambda}{R}\right)\left(\frac{n}{R}\right)-B_{33}\left(\frac{\lambda}{R}\right)\left(\frac{n}{R}\right)\right]U+\left[-B_{22}\left(\frac{n}{R}\right)^2-B_{33}\left(\frac{\lambda}{R}\right)^2-\frac{S_{Dz}}{R}\right]V$$

$$+\left[-\frac{B_{22}}{R}\left(\frac{n}{R}\right)-S_{\theta z}\left(\frac{n}{R}\right)\right]W+\left[-D_{12}\left(\frac{\lambda}{R}\right)\left(\frac{n}{R}\right)-D_{33}\left(\frac{\lambda}{R}\right)\left(\frac{n}{R}\right)\right]\bar{\beta}_x$$

$$+\left[-D_{22}\left(\frac{n}{R}\right)^2-D_{33}\left(\frac{\lambda}{R}\right)^2-S_{\theta z}\right]\bar{\beta}_\theta\Bigg\}\cos n\theta\sin\frac{\lambda x}{R}=0 \qquad \text{(eqs. G.8)}$$

where,

$$\lambda=\frac{m\pi R}{L}$$

Multiplying through by R and re-expressing the equations in matrix form results in a standard eigen problem, where the critical axial stress resultant is given by the lowest real eigenvalue solution :

$$\left\{\begin{bmatrix} C_{11} & C_{12} & C_{13} & C_{14} & C_{15}\\ C_{21} & C_{22} & C_{23} & C_{24} & C_{25}\\ C_{31} & C_{32} & C_{33} & C_{34} & C_{35}\\ C_{41} & C_{42} & C_{43} & C_{44} & C_{45}\\ C_{51} & C_{52} & C_{53} & C_{45} & C_{55}\end{bmatrix}-\psi\begin{bmatrix} 0 & 0 & 0 & 0 & 0\\ 0 & +\lambda^2 & 0 & 0 & 0\\ 0 & 0 & +\lambda^2 & 0 & 0\\ 0 & 0 & 0 & 0 & 0\\ 0 & 0 & 0 & 0 & 0\end{bmatrix}\right\}\begin{Bmatrix} U\\ V\\ W\\ \bar{\beta}_x\\ \bar{\beta}_\theta\end{Bmatrix}=0 \qquad \text{(eq. G.9)}$$

where the matrix coefficients are given by :

$$C_{11}=A_{11}\lambda^2+A_{33}n^2$$

$$C_{12}=A_{12}n\lambda+A_{33}n\lambda$$

$$C_{13}=A_{12}\lambda$$

$$C_{14}=B_{11}\lambda^2+B_{33}n^2$$

$$C_{15}=B_{12}n\lambda+B_{33}n\lambda$$

$$C_{21}=C_{12}$$

$$C_{22}=A_{22}n^2+A_{33}\lambda^2+S_{\theta z}$$

$$C_{23} = A_{22} n + S_{\theta z} n$$

$$C_{24} = B_{12} \lambda n + B_{33} n \lambda$$

$$C_{25} = B_{22} n^2 + B_{33} \lambda^2 + R S_{\theta z}$$

$$C_{31} = C_{13}$$

$$C_{32} = C_{23}$$

$$C_{33} = A_{22} + S_{xz} \lambda^2 + S_{\theta z} n^2$$

$$C_{34} = B_{12} \lambda + R S_{xz} \lambda$$

$$C_{35} = B_{22} n + R S_{\theta z} n$$

$$C_{41} = C_{14}$$

$$C_{42} = C_{24}$$

$$C_{43} = C_{34}$$

$$C_{44} = D_{11} \lambda^2 + D_{33} n^2 + R^2 S_{xz}$$

$$C_{45} = D_{12} n \lambda + D_{33} n \lambda$$

$$C_{51} = C_{15}$$

$$C_{52} = C_{25}$$

$$C_{53} = C_{35}$$

$$C_{54} = C_{45}$$

$$C_{55} = D_{22} n^2 + D_{33} \lambda^2 + R^2 S_{\theta z}$$

To solve the eigenvalue problem a standard NAG subroutine embodied in a FORTRAN program, described in Appendix G, is used. In order to find the minimum critical load to cause buckling, the eigenvalue must be minimised with respect to the wave parameters m & n. This minimisation is carried out in a subroutine included in the buckling program.

(2) Axisymmetric Solution

If the buckled mode shape is axisymmetric (fig. F.2), the number of circumferential buckles, n , is zero. Also, the following become zero :

$$v = 0 \qquad \beta_\theta = 0 \qquad \frac{\partial}{\partial\theta}, \frac{\partial^2}{\partial\theta^2} \ldots \text{etc.} = 0$$

The full set of equilibrium equations (F.6) are then reduced to a set of 3 in terms of the 3 remaining non-zero unknowns u, β_x & w :

$$(a) \qquad A_{11}\frac{\partial^2 u}{\partial x^2} - \frac{A_{12}}{R}\frac{\partial w}{\partial x} + B_{11}\frac{\partial^2 \beta_x}{\partial x^2} = 0$$

$$(b) \qquad \frac{A_{12}}{R}\frac{\partial u}{\partial x} - \frac{A_{22}}{R^2}w + (S_{xz} + \bar{N}_x)\frac{\partial^2 w}{\partial x^2} + \left(S_{xz} + \frac{B_{12}}{R}\right)\frac{\partial \beta_x}{\partial x} = 0$$

$$(c) \qquad B_{11}\frac{\partial^2 u}{\partial x^2} - \left(S_{xz} + \frac{B_{12}}{R}\right)\frac{\partial w}{\partial x} - S_{xz}\beta_x + D_{11}\frac{\partial^2 \beta_x}{\partial x^2} = 0 \qquad \text{(eqs. G.10)}$$

By differentiating and substituting these equations it is possible to reduce them to a single 5th order differential equation in terms of the w displacement only :

$$(k_4 \bar{N}_x + k_1)\frac{\partial^5 w}{\partial x^5} + (k_5 \bar{N}_x + k_2)\frac{\partial^3 w}{\partial x^3} + k_3\frac{\partial w}{\partial x} = 0 \qquad \text{(eq. G.11)}$$

where the coefficients are given in terms of the shell stiffnesses by :

$$k_1 = B_{11}\frac{k_6}{k_7} - D_{11}$$

$$k_2 = -\frac{k_8 k_6}{k_7}\frac{1}{S_{xz}} + \frac{D_{11}}{S_{xz}}\frac{A_{22}}{R^2} - \left(S_{xz} + \frac{B_{12}}{R}\right)^2\frac{1}{S_{xz}} + k_5$$

$$k_3 = -\frac{A_{22}}{R^2} - \frac{A_{12}}{R}\frac{k_8}{k_7}$$

$$K_4 = \frac{K_1}{S_{xz}}$$

$$K_5 = \frac{A_{12}}{R} B_{11} \frac{1}{K_7} + 1$$

$$K_6 = B_{11} \left(S_{xz} + \frac{B_{12}}{R} \right) - \frac{A_{12}}{R} D_{11}$$

$$K_7 = A_{11} \left(S_{xz} + \frac{B_{12}}{R} \right) - \frac{A_{12}}{R} B_{11}$$

$$K_8 = -\frac{1}{R} \left\{ A_{12} \left(S_{xz} + \frac{B_{12}}{R} \right) - \frac{A_{12}}{R} B_{11} \right\}$$

The differential equation (F.11) can be solved by assuming a buckled shape function for w of :

$$w = W \sin \frac{\lambda x}{R} \qquad \text{(eq. G.12)}$$

assuming simply supported ends.

Differentiating and substituting this function into the differential equation :

$$\left\{ \left(K_4 \bar{N}_x + K_1 \right) \left(\frac{\lambda}{R} \right)^5 - \left(K_5 \bar{N}_x + K_2 \right) \left(\frac{\lambda}{R} \right)^3 + K_3 \left(\frac{\lambda}{R} \right) \right\} \cos \frac{\lambda x}{R} = 0 \qquad \text{(eq. G.13)}$$

Re-arranging in terms of the critical stress resultant results in the following expression which must be minimised with respect to the wave parameter m.

$$\bar{N}_x = \frac{-K_1 \left(\frac{\lambda}{R} \right)^4 + K_2 \left(\frac{\lambda}{R} \right)^2 - K_3}{\left(\frac{\lambda}{R} \right)^2 \left(K_4 \left(\frac{\lambda}{R} \right)^2 - K_5 \right)} \qquad \text{(eq. G.14)}$$

For the particular case of a symmetric sandwich, ie. $B_{ij} = 0$, the coefficients are simplified and the above expression can be rewritten as :

$$\bar{N}_x = \frac{D_{11}\left(\frac{\lambda}{R}\right)^2 + \frac{A_{22}}{R^2}\left(1-\frac{A_{12}^2}{A_{11}A_{22}}\right)\left(\left(\frac{R}{\lambda}\right)^2 + \frac{D_{11}}{S_{xz}}\right)}{1 + \frac{D_{11}}{S_{xz}}\left(\frac{\lambda}{R}\right)^2} \qquad \text{(eq. G.15)}$$

Note that by setting S_{xz} to zero, equation (F.15) is simplified further to:

$$\bar{N}_x = D_{11}\left(\frac{m\pi}{L}\right)^2 + \frac{A_{22}}{R^2}\left(1-\frac{A_{12}^2}{A_{11}A_{22}}\right)\left(\frac{L}{m\pi}\right)^2 \qquad \text{(eq. G.16)}$$

Assuming m is continuous, the above expression can be minimised analytically by differentiating with respect to m^2 and setting to zero. This yields the familiar axial compression buckling equation for an orthotropic cylinder :

$$\bar{N}_{x\,MIN.} = \frac{2}{R}\left\{ A_{22}\left(1-\frac{A_{12}^2}{A_{11}A_{22}}\right) D_{11} \right\}^{\frac{1}{2}} \qquad \text{(eq. G.17)}$$

APPENDIX H : THRUST TUBE BUCKLING PROGRAM (BUCKL)

Description

This program performs general instability analysis of cylindrical shells of composite faced sandwich construction under axial and shear loading. The user can select from 9 possible solution options which enable the following to be computed : critical buckling loads under pure uniform axial compression, under pure torsion or both, festoon curves of critical buckling loads as functions of waveform parameters, the buckling interaction index for cylinders loaded by axial and shear stress resultants, and critical buckling loads or buckling interaction index as a function of ply angle variables for thrust tube design optimisation.

The program is based on the small deflection theory and subject to the limitations described in section 8.5 of Chapter 8. Thrust tubes with conical geometry can be analysed by assuming an equivalent cylindrical geometry.

Input

THRUST TUBE GEOMETRY	Small Radius, R_1, Large Radius, R_2, Length, L.
FACESHEET PROPERTIES	No. of facesheet materials. E_1, E_2, ν_{12}, G_{12}, t_{ply} for each material.
CORE PROPERTIES	E_c, G_{xz}, G_{yz}, h (G_{xz} refers to shear modulus in axial direction)
SOLUTION REQUIRED	1 = Critical Axial Buckling Load. 2 = Critical Torsional Buckling Load. 3 = Critical Axial and Torsional Loads. 4 = Festoon curves for Axial Buckling. 5 = Festoon curves for Torsional Buckling. 6 = Buckling Interaction Index.

For Given Lay-up

7 = Critical Axial Buckling Load.
8 = Critical Torsional Buckling Load.
9 = Buckling Interaction Index.

As fn. of 2 ply angle variables

If solution code = 1 to 6 ....

FACESHEET LAY-UP — No. of plies per facesheet.
Material No. Angle for each ply.

Else if solution code = 7 to 9 ....

FACESHEET LAY-UP — No. of plies per facesheet.
Material No. Angle Code for each ply.

Code	Angle
0	0°
1	variable 1
2	variable 2

(for negative angle use negative code)

If solution code = 4 or 5 (festoon curves) ....

FESTOON CURVE LIMITS — Start, finish and step size for m & n.
m_{min}, m_{max}, m_{step}
n_{min}, n_{max}, n_{step}

If solution code = 6 or 9 (interaction index) ....

KNOCK-DOWN FACTORS — To apply to theoretical axial & torsional loads k_a (axial), k_t (torsional).
See section 8.5.4 for discussion of knock-down factors.

If solution code = 6 ....

APPLIED LOADS — No. of load cases.
N_x N_{xy} for each load case.

If solution code = 9 ....

APPLIED LOADS — N_x N_{xy} single load case.

PLOT REQUIRED — 0 = Isoparametric
1 = Contour

PLOTTING PARAMETERS — If isoparametric ...
Flatness (typically 0.5)
View (0 = origin nearest corner
1 = rotate thro' 90°
2 = rotate thro' 180°)

If contour plot ...
No. of contours
Interpolation (0 = straight lines, 1 = curves)

(see example input file)

Solution

The sequence of computations is depicted in fig. H.1. After reading in the data, depending on the specified solution code, the program calculates the shell constitutive matrices and the critical buckling loads under pure compression and pure torsion. For the analysis of shells under combined loading the Interaction Buckling Index is calculated. The calculation of axial and torsional buckling loads for given values of the waveform parameters m & n is performed in separate subroutines based on the small deflection theories of Teichmann, Wang & Gerard[55] and March & Kuenzi[56]. These are described in detail in section 8.5 of Chapter 8 and Appendix G.

If the critical buckling loads are required these are found by a minimisation subroutine which minimises the buckling load with respect to m & n. The minimisation is performed with respect to integer values of m & n by locating the minimum buckling load of groups of m & n combinations +/- 1 about an initial estimate. The process continues for another group surrounding the updated critical m & n until the buckling load does not decrease any further. For axial buckling, an initial estimate of m = 1, n = 0 was assumed, for torsional buckling the initial estimate of the critical waveform parmaters was m = 1, n = 1. This method of minimsation was found to be satisfactory in nearly all cases. In certain instances where the rate of change of the buckling load with respect to m & n was small over a relatively large range the subroutine terminates prematurely, but because of the small rate of change this is sufficiently close to the true minimum.

For thrust tube design optimisation the critical buckling loads or interactive index is computed at 5° intervals between 0° and 45° for two fibre angle variables over a 10 x 10 grid. The results are displayed as an isoparametric or contour plot using GINO subroutines.

Output

Depending on the selected option, the program outputs critical axial and/or torsional buckling loads and/or the buckling interaction index and the corresponding values of the critical waveform parameters m^* & n^*. For thrust tube optimisation the output is in the form of an isoparametric or contour plot against the two ply angle variables. The buckling interaction index = 1.00 contour defines the boundary between the feasible and unfeasible design space.

EXAMPLE INPUT FILE : (BUCKL.DAT)

0.500 0.500 1.090	R_1 R_2 L
1	NO. OF FACESHEET MATERIALS
175E9 6.8E9 0.30 3.75E9 0.100E-3	E_1 E_2 ν_{12} G_{12} t_{ply}
310E6 186E6 90E6 10E-3	E_c G_{xz} G_{yz} h
9	BUCKLING INTERACTION INDEX FOR 2 ANGLE VARIABLE LAY-UPS.
4	PLIES PER FACESHEET
1 1	
1 2	FACESHEET LAY-UP 1 = VARIABLE 1
1 -2	2 = VARIABLE 2
1 -1	
0.5	k_a
0.6	k_t
-96E3 14E3	N_x N_{xy}
0	ISOPARAMETRIC PLOT
0.5	FLATNESS
0	VIEW

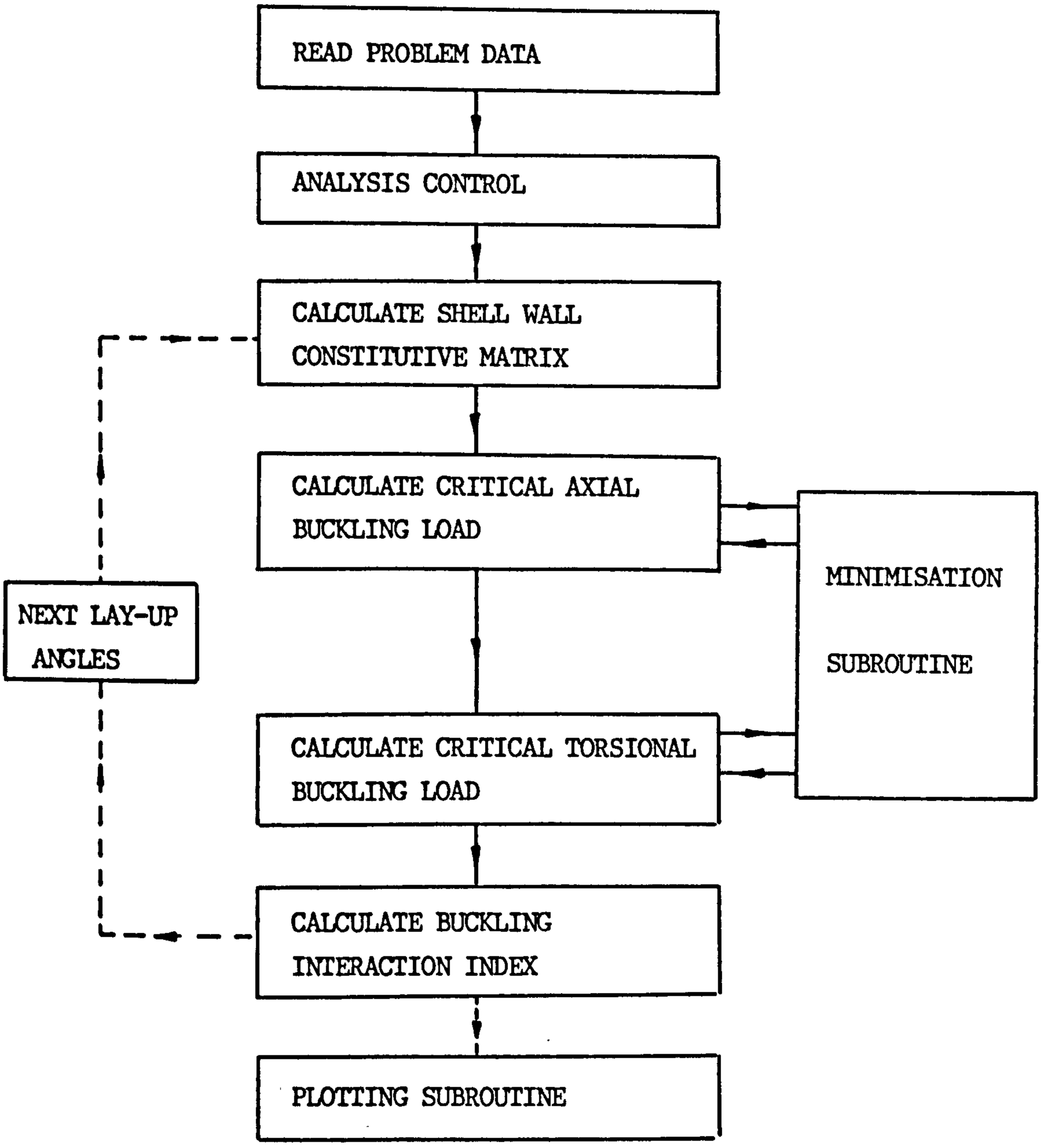

Fig. H.1 Thrust Tube Buckling Program (BUCKL): Sequence of Calculations.

APPENDIX I : PRIMUS SPACECRAFT

The PRIMUS (Primordial Sample Return Mission) spacecraft was a conceptual design study conducted by M.Sc. students at the College of Aeronautics, Cranfield, in 1988-1989. The spacecraft provided an example for the optimum design of a composite faced sandwich thrust tube, which is described in Chapter 8, section 8.9.

Mission

The spacecraft mission outline was to rendezvous with a comet, retrieve a core sample from the comet nucleus and return this to earth. Part of the spacecraft was to remain on the comet surface to transmit scientific data back to earth up to perihelion.

Configuration

The spacecraft configured to fly this mission is shown in figs. I.1 and I.2 (from reference (8.27)). It consisted of three separate modules: a Main Propulsion Stage (MPS), a Lander (LDR) and a Re-entry Capsule. The Main Propulsion Stage housed fuel & oxidiser tanks, the liquid motors and equipment for the cruise segments of the mission. It had an estimated mass of 5500 kg, of which the majority was fuel. The Lander contained science instruments and the core sample drill mechanism, it was fitted with 3 legs to support the complete spacecraft for landing on the comet surface. The Lander remains on the comet when the rest of the spacecraft returns to earth. It had an estimated mass of 600 kg. The Re-entry Capsule stores the core sample cryogenically for return to earth. It was conical shaped with thermal protection surfaces for atmospheric re-entry and had an estimated mass of 350 kg.

The spacecraft was configured for launch on Ariane 5 with the Lander inverted and attached to the top of the Main Propulsion Stage by a clamp band (fig. I.1). The Lander legs are retracted inwards to remain within the

allowable launcher volume. The Re-entry capsule is mounted to the top of the MPS and is contained internally between the MPS and LDR modules during launch and the outward cruise. The complete spacecraft stack interfaces with the launcher at the equipment bay mounting plane.

A thrust tube passed up through the full spacecraft stack, split into two parts: one in the MPS and one in the LDR. Both parts had a conical lower section and a cylindrical upper section. The thrust tube in the MPS acted as the adaptor to the launcher and provided the mounting for 3 hydrazine and 3 N_2O_4 tanks around its circumference. At its upper end, in the launch configuration, it provided the interface for the Lander and attachment for the Re-entry Capsule. The thrust tube within the Lander supported shear webs which transfered load from equipment inertia on launch and by shock loads from the legs on landing. The main body of the MPS was octagonal and the main body of the LDR was hexagonal, both built up of flat sandwich side panels and platforms.

ISSUE	MODIFICATION

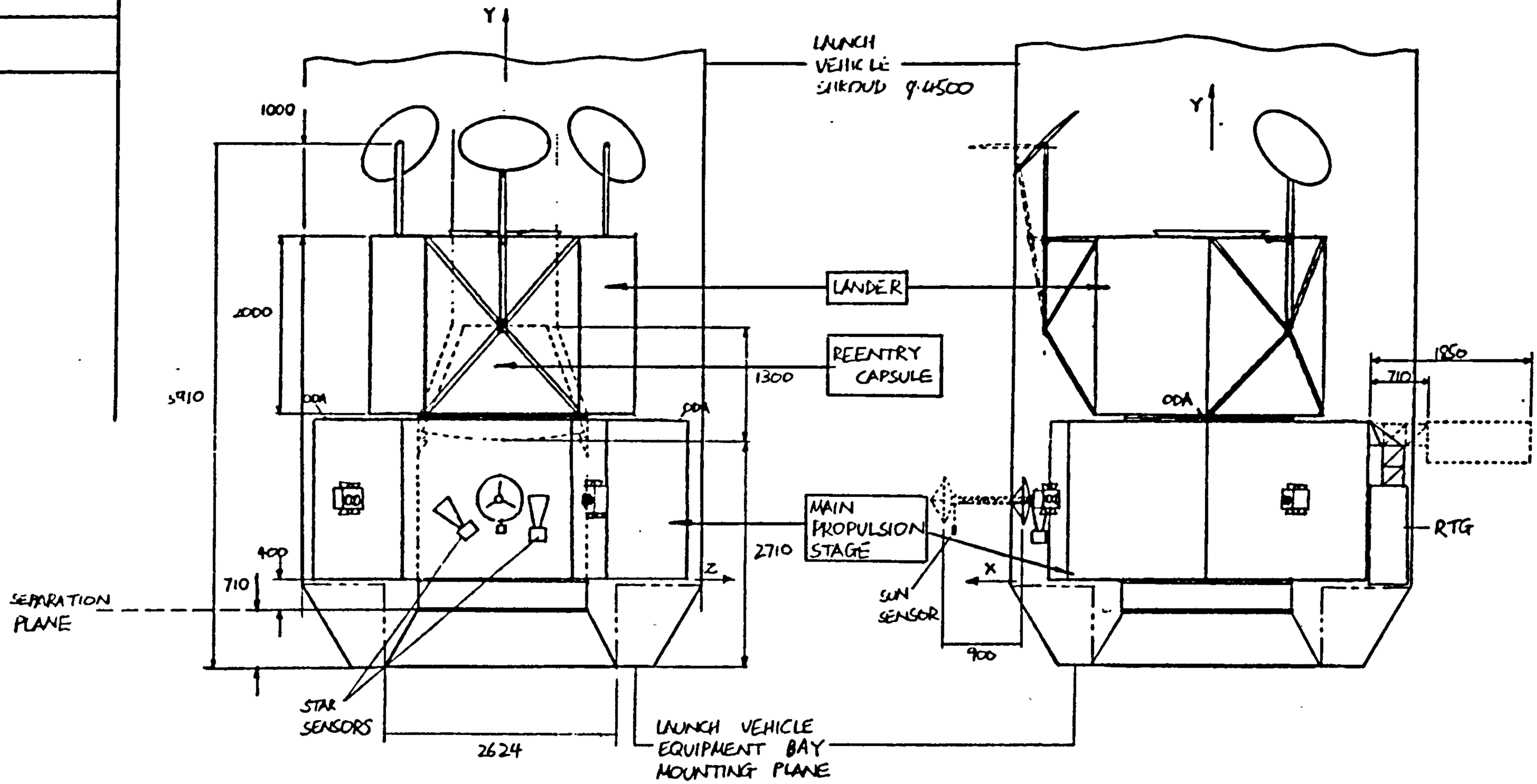

Fig. I.1 PRIMUS SPACECRAFT LAUNCH CONFIGURATION

422

THIRD ANGLE PROJECTION			SHEET SIZE A 3	ITEM	PART No.	DESCRIPTION	No. OFF	MAT'L	SPEC.	REMARKS
GENERAL TOLERANCE ON DIMENSIONS MACHINED UNMACHINED OTHER DIMENSIONS AS STATED	JOB No.	No. OF SETS REQ'D	SCALE 1:50	DRAWN	CHK'D	APPV'D	STRESS APPVD	TITLE:- MSC-51B		
WELD WHERE SHOWN THUS ⌒			FINISH	ISSUED BY				DRAWING No.		
MACHINE WHERE SHOWN THUS ✓	USED ON DRG.			CRANFIELD INSTITUTE OF TECHNOLOGY CRANFIELD.				SHT. OF SHEETS		

1 2 3 4 5 6 7 8